

**CHARACTERIZING MICROGLIAL RESPONSE TO AMYLOID:  
FROM NEW TOOLS TO NEW MOLECULES**

by  
**Priya Prakash**

**A Dissertation**

*Submitted to the Faculty of Purdue University  
In Partial Fulfillment of the Requirements for the degree of*

**Doctor of Philosophy**



Department of Chemistry  
West Lafayette, Indiana  
May 2021

**THE PURDUE UNIVERSITY GRADUATE SCHOOL**  
**STATEMENT OF COMMITTEE APPROVAL**

**Dr. Gaurav Chopra, Chair**

Department of Chemistry

**Dr. Jean-Christophe (Chris) Rochet**

Department of Medicinal Chemistry and Molecular Pharmacology

**Dr. Kavita Shah**

Department of Chemistry

**Dr. Bruce T. Lamb**

Stark Neurosciences Research Institute,  
Indiana University School of Medicine

**Approved by:**

Dr. Christine A. Hrycyna



*This thesis is dedicated to the women who raised me*

*My grandmother for her selfless love*

*My mother for all her sacrifices*

*My sister for being my rock*

## ACKNOWLEDGMENTS

First and foremost, I would like to express my most profound appreciation and gratitude to my Ph.D. advisor Dr. Gaurav Chopra for his continued support, mentorship, and encouragement. His unparalleled faith in me and his unwavering optimism in my work has been an immense source of motivation that has kept me going through this exciting scientific adventure. By encouraging me to think critically, ask tough questions, formulate bold ideas, challenge the academic norms, and persevere in the face of adversity, he has shaped me into becoming the scientist that I am today. I owe him a debt of thanks, and I look forward to our continued discussion and collaboration into the future. Next, I would like to express my sincere thanks to my thesis advisory committee members—Drs. Jean-Christophe (Chris) Rochet, Kavita Shah, and Bruce T. Lamb for providing constructive feedback and comments and supporting my professional development throughout my graduate career.

I am grateful to all the Chopra lab members for not only being supportive work colleagues and excellent collaborators but also for their friendships over the years. The following members were instrumental in contributing some of the methodologies described in this thesis. Dr. Jonathan Fine developed the bioinformatics methods used for all the omics data analysis (Appendix B). Dr. Krupal P. Jethava developed the chemistries used in the A $\beta$ <sup>pH</sup> probe (Chapter 4) and the multi-organelle-targeting pH-sensitive fluorophore probes (Chapter 5). Prageeth R. Wijewardhane performed some of the statistical analysis and generated select figures for the omics data (Chapter 7 and 8). Palak Manchanda has been an outstanding collaborator and has been immensely helpful in carrying out experiments related to microglial lipid droplet characterization in addition to other relevant microglial assays (Chapter 7). Dr. Caitlin E. Randolph helped with elucidating the lipid structures (Chapter 7). I would also like to thank other Chopra lab members, including Dr. Erin Kischuk, Armen Beck, Ahad Hossein, Joydeb Majumder, Asarasin (Sara) Adulnirath, Sheik Dawood, Harshit Arora, and Anisa Dunham, for valuable and uplifting discussions.

I am honored to have worked with some of the brightest and most talented undergraduate students who made significant contributions to this thesis. Their work ethic and commitment to research inspired me to be a better scientist and a mentor. Travis C. Lantz contributed to the development

of the recombinant A $\beta$  (Chapter 3). Gabrielle C. Williams developed the immunological assays for microglia and performed the drug-treatment experiments (Chapter 9). Dawn N. Tilley also contributed to the microglial drug-treatment experiments. Elizabeth A. Thayer optimized microglia's culture conditions and contributed to the initial lipidomics experiments (Chapter 7).

I want to thank some of the faculty and staff at Purdue for helping me with specific experiments. Dr. Christina R. Ferreira helped with the Multiple Reaction Monitoring-profiling experiments used to identify glial lipids and metabolites. Dr. Uma K. Aryal helped with the methods used in the proteomics experiments. Dr. Andy Schaber helped with some of the initial confocal and live-cell imaging work. Kathy Ragheb and Dr. Paul J. Robinson trained me on the concepts of flow cytometry. Victor Bernal-Crespo at the histology core helped with the staining of 5xFAD mouse brain tissues. I am also thankful to some of the drug discovery institute members, including Stephanie Winder, Stuart Michael, and Kaethe Beck, for helping me navigate Purdue administration. I would also like to thank my friends and colleagues from the PULSe program and at Purdue in general for their help, advice, and moral support via uplifting conversations over the years. Specifically, I want to thank Sayan Dutta, William B. Salloom, Kenneth Ikenna Onyedibe, and Drs. Paola Montenegro, Clement Opoku-Temeng, Johnny Wise, Ethan Hillman, and Stephen Miloro.

My sincere thanks to all my collaborators and co-authors from outside Purdue for their contribution to different aspects of the manuscripts highlighted in this thesis. Specifically—Dr. Shane A. Liddelow for not only being an enthusiastic collaborator but also for his scientific insight and mentorship. Dr. Kevin A. Guttenplan was the lead on the astrocyte project and provided the samples used for the proteomic, lipidomic, and metabolomic characterization of reactive astrocytes (Chapter 8). I am also thankful for other collaborators who performed some of the experiments detailed in the A $\beta^{\text{pH}}$  manuscript (Chapter 4), including Dr. David Attwell, Nils Korte, Pablo Izquierdo, Drs. Gord Fishell and Emilia Favuzzi, and Indigo VL Rose.

I am grateful to the following organizations for funding my work: Indiana CTSI for the Eli Lilly-Stark Neurosciences Predoctoral Research Fellowship in Neurodegeneration, the Purdue Research

Foundation Grant Award, Merck & Co., and the Peer-Reviewed Alzheimer's Research Partnership Award from the Department of Defense. The illustrations in this thesis were made using BioRender.

Finally, I am deeply thankful to my family for supporting me in my personal and professional endeavors. My grandmother, H.V. Jayalakshmi, for showering me with utmost love and affection. My sister and brother-in-law, Ramya Prakash and Venkatesh C. Ravichandran, for providing their unconditional support and being my home-away-from-home in a new country. My parents H.V. Vani and K.N. Surya Prakash, for prioritizing my education above anything else, giving me the freedom to be curious and independent, and believing in me as I carve my own path in life. I will forever be grateful for all your love and support.

## TABLE OF CONTENTS

LIST OF TABLES.....	16
LIST OF FIGURES .....	18
ABSTRACT.....	27
CHAPTER 1. THE MYSTERY AND MAGIC OF GLIA.....	31
1.1 Major cells of the central nervous system .....	31
1.2 Microglia—The resident immune cells of the CNS .....	32
1.3 The myriad functions of microglia .....	34
1.4 Astrocytes are key players of CNS immunity .....	39
1.5 References .....	41
CHAPTER 2. AN APPETITE FOR AMYLOID .....	47
2.1 Alzheimer’s Disease—An introduction .....	47
2.2 Amyloid beta .....	49
2.3 Microglial phagocytosis of A $\beta$ .....	51
2.4 A role for astrocytes in A $\beta$ phagocytosis .....	54
2.5 References .....	56
CHAPTER 3. PRODUCTION OF RECOMBINANT HUMAN AMYLOID BETA.....	59
3.1 Abstract.....	59
3.2 Introduction .....	59
3.3 Experimental design .....	61
3.4 Materials .....	62
3.5 Equipment.....	64
3.6 Procedure.....	65
3.6.1 Preparation of solutions.....	65
3.6.2 Expression of A $\beta$ (M1-42) peptide.....	65
3.6.3 A $\beta$ (M1-42) peptide purification using reverse-phase HPLC .....	69
3.6.4 Characterization of A $\beta$ (M1-42).....	74
3.7 Expected results and discussion .....	81
3.8 References .....	83
CHAPTER 4. GLIAL PHAGOCYTIC UPTAKE OF AMYLOID BETA .....	86

4.1	Abstract.....	86
4.2	Introduction .....	86
4.3	Results .....	89
4.3.1	Properties of a novel pH-dependent fluorescent conjugate of human A $\beta$ 1-42 .....	89
4.3.2	A $\beta^{\text{pH}}$ uptake into human and mouse microglial cell lines .....	93
4.3.3	Flow cytometry of A $\beta^{\text{pH}}$ phagocytic cells and staining of A $\beta^{\text{pH}}$ after phagocytosis in fixed primary cultured microglia and astrocytes .....	94
4.3.4	A $\beta^{\text{pH}}$ uptake by microglia and astrocytes in hippocampus, cortex, and retina.....	96
4.4	Discussion.....	103
4.5	Materials and methods.....	106
4.5.1	Animal ethics.....	106
4.5.2	Synthesis of pH-sensitive fluorescent human A $\beta$ conjugate with Protonex Green.....	107
4.5.3	Synthesis of pH-sensitive fluorescent human A $\beta$ 1-42 conjugate with pHrodo ....	108
4.5.4	Preparation of HFIP-treated A $\beta$ and A $\beta^{\text{pH}}$ stocks .....	108
4.5.5	Atomic Force Microscopy for analysis of A $\beta$ and A $\beta^{\text{pH}}$ aggregates .....	109
4.5.6	pH-dependent emission spectra of A $\beta$ conjugated with Protonex Green and A $\beta$ conjugated with pHrodo at various concentrations .....	109
4.5.7	pKa of Protonex Green 500 SE, A $\beta^{\text{pH}}$ , and RODO-A $\beta^{\text{pH}}$ .....	110
4.5.8	Concentration-dependent response of Protonex Green 500 SE and A $\beta^{\text{pH}}$ at acidic pH over time .....	110
4.5.9	Cell lines—culture and maintenance.....	111
4.5.10	Background fluorescence of PTXG and RODO in cells.....	111
4.5.11	Lactate Dehydrogenase activity cytotoxicity assay .....	111
4.5.12	Phagocytosis assay with live microglia.....	112
4.5.13	Effect of chloroquine and bafilomycin-A1 on fluorescence of A $\beta^{\text{pH}}$ in the cells .	113
4.5.14	Isolation and culture of primary mouse microglia .....	113
4.5.15	Flow cytometry analysis of BV2 and primary microglia phagocytosis .....	114
4.5.16	Confocal imaging of actin filaments and nuclei in the paraformaldehyde-fixed phagocytic microglial cells.....	115
4.5.17	Confocal Imaging of intracellular acidic organelles and nuclei in paraformaldehyde-fixed phagocytic microglial cells.....	115

4.5.18	Intracranial injection of A $\beta^{\text{pH}}$ , perfusion, and immunohistochemistry .....	116
4.5.19	Immunopanning and culture of primary astrocytes.....	117
4.5.20	Engulfment assay of A $\beta^{\text{pH}}$ by primary astrocytes .....	117
4.5.21	<i>In vivo</i> retinal engulfment of A $\beta^{\text{pH}}$ .....	118
4.5.22	Brain slice experiments .....	118
4.5.23	<i>In vivo</i> two-photon microscopy .....	119
4.6	Supporting information .....	120
4.6.1	Instrumentation used for chemical characterization of A $\beta^{\text{pH}}$ .....	120
4.6.2	Supporting movies.....	120
4.6.3	Supplemental text, figures and figure legends .....	121
4.7	Additional Information .....	142
4.7.1	Conflict Of Interest.....	142
4.7.2	Acknowledgment .....	142
4.7.3	Funding Sources .....	143
4.8	References .....	143
CHAPTER 5. PH-ACTIVABLE FLUORESCENT PROBES FOR TARGETING MICROGLIAL CELL ORGANELLES .....		149
5.1	Abstract.....	149
5.2	Main.....	149
5.3	Associated Content I: Chemical characterization.....	162
5.4	Associated content II: Biological experimentation .....	164
5.4.1	Animals .....	164
5.4.2	Culture and maintenance of BV2 microglia.....	164
5.4.3	Primary mouse microglia isolation and culture.....	164
5.4.4	Reconstitution of fluorescent probes in DMSO and cell treatment .....	165
5.4.5	Determination of metabolic activity of BV2 microglia with MTT assay .....	165
5.4.6	Determination of cytotoxicity of the probes on BV2 microglia with LDH assay. ....	166
5.4.7	Determination of cellular uptake of the fluorescent probes .....	167
5.4.8	Flow cytometry analysis.....	168
5.4.9	Confocal imaging .....	169
5.5	Associated content III: Chemical experimentation .....	172

5.6	References .....	191
CHAPTER 6. LIPIDS MODULATE MICROGLIAL CELL STATE AND FUNCTION .....		194
6.1	An introduction to lipids.....	194
6.2	The cellular lipid landscape is large and complex.....	195
6.3	Several Alzheimer's-risk genes are related to lipid metabolism .....	196
6.3.1	Lipoproteins—A “language” for cell-cell signaling .....	197
6.4	Lipids are key immunomodulators of microglial cell state and function .....	198
6.4.1	Phospholipids .....	199
6.4.2	Free fatty acids .....	201
6.4.3	Cholesterol .....	202
6.5	Lipid droplet accumulation in aged and/or diseased microglia.....	203
6.6	Concluding thoughts.....	204
6.7	References .....	205
CHAPTER 7. LIPIDOMIC AND METABOLOMIC CHARACTERIZATION OF MICROGLIA WITH AMYLOID.....		209
7.1	Introduction .....	209
7.2	Methods .....	210
7.2.1	BV2 cell culture and maintenance .....	210
7.2.2	Primary mouse microglia isolation and culture from adult mouse brains.....	210
7.2.3	Amyloid beta preparation and treatment .....	211
7.2.4	Microglia isolation from 5xFAD and WT mouse brains .....	212
7.2.5	Lipid and metabolite extraction by Bligh & Dyer method.....	212
7.2.6	Multiple Reaction Monitoring-profiling for lipidomics and metabolomics.....	213
7.2.7	Statistical and bioinformatic analysis pipeline.....	214
7.2.8	Metabolomic Pathway Analysis.....	215
7.2.9	Lipid droplet quantification via BODIPY staining and flow cytometry analysis .	215
7.2.10	IBA1 and DGAT2 staining of cortical regions of 5xFAD and WT mouse brains	216
7.3	Results .....	216
7.3.1	Overview of lipid changes in A $\beta$ -treated BV2 microglia .....	216
7.3.2	Select phospholipids were abundant in A $\beta$ -treated BV2 microglia at 24 hours ...	217



7.3.3	A $\beta$ -treatment caused depletion of select phospholipids and neutral lipids in BV2 microglia.....	217
7.3.4	Overview of cellular lipid profiles of A $\beta$ -treated primary mouse microglia .....	223
7.3.5	Increased cellular FFAs defines initial microglial state with A $\beta$ exposure.....	231
7.3.6	Prolonged exposure to A $\beta$ leads to TAG accumulation in primary microglia.....	231
7.3.7	TAG biosynthesis in mammalian cells.....	234
7.3.8	Microglia from 5xFAD female mice accumulate more lipid droplets compared to WT mice .....	235
7.3.9	Microglia from 5xFAD male mice show a subset of cells that accumulate more lipid droplets compared to WT mice.....	237
7.3.10	Age is a factor for lipid droplet accumulation in microglia .....	237
7.3.11	5xFAD microglia upregulate DGAT2—a lipid droplet-associated protein compared to WT microglia.....	240
7.3.12	Overview of the metabolite changes in A $\beta$ -treated primary microglia .....	241
7.3.13	Select lipids but several metabolites were identified in microglia conditioned media from A $\beta$ -treated primary microglia .....	247
7.3.14	Overview of the metabolite changes in 5xFAD microglia versus WT microglia .	248
7.4	Discussion.....	251
7.4.1	MRM-profiling of microglial lipidome and metabolome .....	251
7.4.2	New bioinformatics pipeline for lipidomics data analysis .....	251
7.4.3	Cultured microglia exhibit dramatic changes in their lipidome and metabolome with A $\beta$ treatment .....	252
7.4.4	Lipidomics and metabolomics of 5xFAD and WT microglia.....	253
7.4.5	Concluding thoughts .....	254
7.5	References .....	255
CHAPTER 8. PROTEOMIC, LIPIDOMIC, AND METABOLOMIC CHARACTERIZATION OF REACTIVE ASTROCYTES.....		259
8.1	Introduction .....	259
8.2	Profiling of reactive astrocytes and their conditioned medium.....	261
8.2.1	Sample preparation for the proteomic analysis of reactive astrocytes .....	261

8.2.2	Sample preparation for the proteomic analysis of reactive astrocyte conditioned medium .....	262
8.2.3	Liquid Chromatography-Mass Spectrometry/Mass Spectrometry.....	263
8.2.4	Data analysis .....	264
8.2.5	Reactive astrocytes and ACM upregulate several previously known as well as unknown unique proteins.....	266
8.3	Lipid and metabolite profiling of reactive astrocytes and their conditioned media .....	272
8.3.1	Sample preparation for lipidomics .....	272
8.3.2	MRM-profiling for lipids and metabolites .....	272
8.3.3	Data analysis .....	273
8.3.4	Saturated phosphatidylcholines are upregulated in reactive astrocytes .....	275
8.3.5	Long-chain saturated free fatty acids are upregulated in reactive ACM.....	278
8.3.6	Metabolome characterization of reactive astrocytes and their conditioned medium .. .....	282
8.4	Knocking out the <i>Elovl1</i> gene in reactive astrocytes changes their lipid profiles.....	286
8.5	Concluding thoughts.....	292
8.6	References .....	294
CHAPTER 9. MODULATING MICROGLIAL FUNCTION WITH STEROID COMPOUNDS .....		296
9.1	Abstract.....	296
9.2	Introduction .....	297
9.3	Materials and methods.....	300
9.3.1	Materials.....	300
9.3.2	BV2 microglial culture.....	300
9.3.3	Primary mouse microglia isolation and culture.....	300
9.3.4	Activation of BV2 microglia with LPS and drug treatment.....	301
9.3.5	Activation of primary mouse microglia with lipopolysaccharide and drug treatment .....	301
9.3.6	Enzyme Linked Immunosorbent Assay for TNF- $\alpha$ and IL-1 $\alpha$ production .....	301
9.3.7	Griess assay to evaluate Nitric Oxide production .....	302
9.3.8	Cell Titer Blue assay .....	302

9.3.9	Exploratory lipidomics .....	303
9.3.10	Data analysis .....	303
9.4	Results .....	304
9.4.1	BV2 microglial cells secrete TNF- $\alpha$ and IL-1 $\alpha$ with LPS activation.....	304
9.4.2	BV2 microglial cells secrete NO with LPS activation .....	304
9.4.3	Primary mouse microglial cells secrete TNF- $\alpha$ and IL-1 $\alpha$ but do not secrete NO with LPS activation at the tested concentrations .....	305
9.4.4	Dexamethasone reduced NO, TNF- $\alpha$ , and IL-1 $\alpha$ secretion from LPS-activated BV2 microglia .....	308
9.4.5	Steroid Treatment on CD11b <sup>+</sup> Cells .....	310
9.4.6	A few phosphatidylcholines are upregulated in LPS activated CD11b <sup>+</sup> cells with dexamethasone treatment.....	312
9.4.7	A few phosphatidylserines are downregulated in LPS activated CD11b <sup>+</sup> cells with dexamethasone treatment.....	313
9.5	Discussion.....	314
9.6	References .....	316
CHAPTER 10.	CHEMICAL NEUROIMMUNOLOGY—CURRENT AND FUTURE PERSPECTIVE .....	319
10.1	Preface .....	319
10.2	Beyond genes and proteins—Lipids and metabolites .....	319
10.3	Redefining glial cell states.....	320
10.4	New chemical tools to modulate glial function.....	321
10.5	New chemical techniques to characterize glial cell states.....	324
10.6	Departing thoughts .....	325
10.7	References .....	326
APPENDIX A.	ISOLATION AND CULTURE OF MICROGLIA FROM ADULT MOUSE BRAINS .....	328
A.1	Background.....	328
A.2	Reagents, buffers, and media preparation .....	328
A.3	Tissue dissociation and collection .....	330
A.4	Myelin removal .....	330

A.5	CD11b <sup>+</sup> cell selection .....	331
A.6	Seeding CD11b <sup>+</sup> cells .....	332
A.7	References .....	333
APPENDIX B. EXPLORATORY LIPIDOME AND METABOLOME ANALYSIS BY MULTIPLE REACTION MONITORING (MRM)-PROFILING .....		334
B.1	Background.....	334
B.2	Methods .....	334
B.2.1	Bligh & Dyer protocol for lipid and metabolite extraction .....	334
B.2.2	Multiple Reaction Monitoring (MRM)-profiling.....	335
B.3	Data analysis.....	336
B.4	References .....	337
APPENDIX C. PROTEOMIC ANALYSIS OF BV2 MICROGLIA WITH AMYLOID .....		339
C.1	Introduction .....	339
C.2	Methods .....	339
C.2.1	BV2 microglia cell culture .....	339
C.2.2	A $\beta$ 42 preparation and treatment.....	340
C.2.3	BV2 microglial phagocytosis of A $\beta$ 42.....	340
C.2.4	Protein extraction and digestion (Sample preparation for LC-MS/MS) .....	341
C.2.5	Data analysis .....	341
C.3	Results .....	341
C.3.1	BV2 microglia phagocytose A $\beta$ within 1 hour of treatment .....	341
C.3.2	Global proteomic changes in BV2 microglia with 1 hour A $\beta$ treatment .....	342
C.3.3	Upregulated proteins in BV2 microglia with 1 hour A $\beta$ treatment.....	345
C.3.4	Downregulated proteins in BV2 microglia with 1 hour A $\beta$ treatment.....	345
C.4	Concluding thoughts.....	348
C.5	References .....	349
APPENDIX D. PROTEOMIC ANALYSIS OF MYELOID-DERIVED SUPPRESSOR CELLS .....		350
D.1	Background.....	350
D.2	Method.....	351
D.3	Results .....	352

APPENDIX E. ONLINE RESOURCE FOR GLIAL OMICS DATASETS.....	355
VITA.....	361

## LIST OF TABLES

<b>Table 1-1</b> Receptors on microglia corresponding to target substrates for phagocytosis.....	38
<b>Table 3-1</b> Solvent gradient for the cleaning protocol done before and after peptide purification. .....	72
<b>Table 3-2</b> Solvent gradient for peptide purification. ....	73
<b>Table 7-1</b> The lipid classes screened, their corresponding abbreviation, and the total number of MRM transitions per class. ....	214
<b>Table 7-2</b> Differentially regulated lipids in A $\beta$ -activated BV2 microglia at 1 hour. ....	220
<b>Table 7-3</b> Differentially regulated lipids in A $\beta$ -activated BV2 microglia at 12 hours. ....	220
<b>Table 7-4</b> Upregulated lipids in A $\beta$ -activated BV2 microglia at 24 hours. ....	221
<b>Table 7-5</b> Downregulated lipids in A $\beta$ -activated BV2 microglia at 24 hours. ....	222
<b>Table 7-6</b> Upregulated lipids in A $\beta$ -activated primary microglia at 1 hour (A $\beta$ vs. Vehicle-treated microglia; FDR<0.1).....	226
<b>Table 7-7</b> Downregulated lipids in A $\beta$ -activated primary microglia at 1 hour (A $\beta$ vs. Vehicle-treated microglia; FDR<0.1).....	227
<b>Table 7-8</b> Upregulated lipids in A $\beta$ -activated primary microglia at 12 hours (A $\beta$ vs. Vehicle-treated microglia; FDR<0.1).....	228
<b>Table 7-9</b> Downregulated lipids in A $\beta$ -activated primary microglia at 12 hours (A $\beta$ vs. Vehicle-treated microglia; FDR<0.1).....	229
<b>Table 7-10</b> Differentially regulated lipids in A $\beta$ -activated primary microglia at 24 hours (A $\beta$ vs. Vehicle-treated microglia; FDR<0.1). ....	230
<b>Table 7-11</b> Top upregulated metabolites in A $\beta$ -activated primary microglia at 1 hour (A $\beta$ vs. Vehicle-treated microglia; FDR<0.1). ....	243
<b>Table 7-12</b> Top downregulated metabolites in A $\beta$ -activated primary microglia at 1 hour (A $\beta$ vs. Vehicle-treated microglia; FDR<0.1). ....	244
<b>Table 7-13</b> Differentially regulated metabolites in A $\beta$ -activated primary microglia at 12 hour (A $\beta$ vs. Vehicle-treated microglia; FDR<0.1). ....	244
<b>Table 7-14</b> Differentially regulated metabolites in A $\beta$ -activated primary microglia at 24 hour (A $\beta$ vs. Vehicle-treated microglia; FDR<0.1). ....	245
<b>Table 7-15</b> Top few upregulated metabolites in 5xFAD microglia vs. WT microglia (FDR<0.1) ..... .....	249
<b>Table 7-16</b> Downregulated metabolites in 5xFAD microglia vs. WT microglia (FDR<0.1) ....	250
<b>Table 8-1</b> Top 20 upregulated proteins in astrocytes. ....	268

<b>Table 8-2</b> Top 20 downregulated proteins in astrocytes. ....	269
<b>Table 8-3</b> Top 17 upregulated proteins in ACM. ....	271
<b>Table 8-4</b> Top 20 upregulated lipids in A1 reactive astrocytes.....	276
<b>Table 8-5</b> Top 20 downregulated lipids in A1 reactive astrocytes.....	277
<b>Table 8-6</b> Top 25 upregulated lipids in ACM. ....	280
<b>Table 8-7</b> Top 25 downregulated lipids in ACM. ....	281
<b>Table 8-8</b> Upregulated metabolites in reactive astrocytes. ....	283
<b>Table 8-9</b> Downregulated metabolites in reactive astrocytes.....	284
<b>Table 8-10</b> Upregulated metabolites in reactive ACM. ....	285
<b>Table 8-11</b> Downregulated metabolites in reactive ACM. ....	286
<b>Table 8-12</b> Top 20 downregulated lipids in <i>Elov11</i> -cKO reactive astrocytes compared to WT reactive astrocytes.....	288
<b>Table 8-13</b> Top 20 upregulated lipids in <i>Elov11</i> -cKO reactive astrocytes compared to WT reactive astrocytes.....	289
<b>Table 8-14</b> Top 19 downregulated lipids in <i>Elov11</i> -cKO reactive ACM compared to WT ACM. ....	290
<b>Table 8-15</b> Top 19 upregulated lipids in <i>Elov11</i> -cKO reactive ACM compared to WT ACM..	291
<b>Table 9-1</b> List of the compound, abbreviation used, class of compound, and indication that the compound has been approved for in the United States. N/A indicates not approved or discontinued. ....	299
<b>Table 9-2</b> Upregulated lipids in LPS activated CD11b <sup>+</sup> microglia due to dexamethasone treatment (FDR<0.1).....	313
<b>Table 9-3</b> Downregulated lipids in LPS activated CD11b <sup>+</sup> microglia due to dexamethasone treatment (FDR<0.1).....	313

## LIST OF FIGURES

- Figure 1.1** Major cells of the CNS. Neuron (myelinated) and Glial cells—Astrocyte (end feet visible), Oligodendrocyte, and Microglia. .... 31
- Figure 1.2** Immunohistochemical staining of microglia in the cortex of a wild type adult rat. Microglia are labeled with the IBA1 marker in red. (Left) The cells exhibit a rested, ramified morphology with several processes extending from the cell body. (Right) A magnified image of a single microglia cell. .... 33
- Figure 1.3** Immunofluorescence staining of microglia with the IBA1 marker in the cortical regions of 7 month old female mice. (Left) In a healthy mouse brain (wild type), microglia display long processes extending from the cell bodies. (Right) In a mouse model of Alzheimer’s disease (5xFAD), microglia appear to be dystrophic and hyper-reactive. .... 36
- Figure 1.4** The myriad functions of microglia. Pruning of neuronal synapses; Secretion of cytokines; Phagocytosis of A $\beta$  and  $\alpha$ Syn; Interaction with tumor cells via SIRP $\alpha$  and CD47. ... 37
- Figure 2.1** Characteristic features of healthy versus Alzheimer’s brain. .... 48
- Figure 2.2** Simplified mechanism of A $\beta$  secretion and plaque formation. A $\beta$  monomer is released from APP upon  $\beta$ - and  $\gamma$ -secretase activity into the extracellular microenvironment. A $\beta$  monomers form oligomers and later plaques consisting of various forms of A $\beta$  aggregates. .... 50
- Figure 2.3** Mechanism of microglial A $\beta$  phagocytosis. Phagocytosis is initiated with target (A $\beta$ ) recognition via the find me and eat me signals. The receptors are then involved in the engulfment of A $\beta$  into the phagosomes. The internalized A $\beta$  is enzymatically degraded by the hydrolytic enzymes in the acidic phagolysosomal compartments. .... 53
- Figure 3.1** Schematic diagram illustrating the experimental protocol for the expression and isolation of recombinant human A $\beta$ (M1-42) peptide from competent E. coli. Part 1. Isolation of the pET-Sac-A $\beta$ (M1-42) plasmid from the glycerol stock; Part 2. Transformation of BL21(DE3)pLysS and Rosetta(DE3)pLysS competent cells with the isolated Transformation of BL21(DE3)pLysS and Rosetta(DE3)pLysS competent cells with the isolated pET- pET-Sac-A $\beta$ (M1-42) plasmid; Part 3. Expression of the A $\beta$ (M1-42) peptide in 1 L liquid LB culture; Part 4. Harvesting and lysis of the cells using a probe sonicator followed by resuspension of the cell lysate in 8 M urea; and Part 5. Purification of the A $\beta$ (M1-42) peptide with preparative HPLC.. 62
- Figure 3.2** Transformed cells as colonies on the Luria Broth (LB) plate and the growing culture in liquid LB. (A) Colonies of transformed E. coli on solid LB. Red circles represent single colonies. (B) Single colony is picked from the plate and inoculated into 5 mL liquid LB and shaken at 37 °C overnight that makes a cloudy solution after incubation. (C) The next morning, this culture is inoculated into 1 L LB to grow the cells for the next 3 to 3.5 h until the optical density (OD) reaches 0.45. .... 67
- Figure 3.3** High-performance liquid chromatography (HPLC) set-up. (A) The water bath containing filtered reverse osmosis water is heated to ~ 80 °C. (B) Both columns are completely submerged in the water bath. One end of the guard column attached to the injection valve with



metal tubing and the other end of the guard column attached to the inlet of the primary C18 100 Å 5 µm 10 mm × 250 mm preparative column. The primary column is fed into the Combiflash. (C) 5 mL injection loop. (D) Collection of Aβ(M1-42) fractions eluted at 26 min. .... 72

**Figure 3.4** HPLC Chromatogram of urea-solubilized recombinant protein during purification. The Aβ(M1-42) peak elutes at 26 min at 95% acetonitrile with 0.1 % TFA, 5 % H<sub>2</sub>O with 0.1 % TFA. The urea salt from solution B elutes as a cluster of peaks between 5–7 min in 10% acetonitrile with 0.1 % TFA, 90 % H<sub>2</sub>O with 0.1 % TFA. The absorbance was taken at 214 nm. Inserted image of the white powder is the lyophilized peptide corresponding to the Aβ(M1-42) fractions collected at 26 min. .... 74

**Figure 3.5** MALDI-TOF mass spectra of Aβ(M1-42). A. The MALDI-TOF mass spectra of lyophilized Aβ(M1-42) in the range of m/z 2000 to 8000. The Aβ(M1-42) corresponds to the m/z 4642.21 peak. B. MALDI-TOF mass spectra of lyophilized carbamylated Aβ(M1-42) in the range of m/z 500 to 8000. Carbamylation peak (m/z 4685.34) appears ~ m/z 43 higher than the Aβ(M1-42) at m/z 4642.50 due to the extended exposure of the peptide to urea. A Voyager De-Pro MALDI-TOF mass spectrometer in positive linear mode was used with CHCA solution as the matrix for each spectrum. .... 75

**Figure 3.6** High-resolution Liquid Chromatography-Mass Spectrum (LC-MS) of Aβ(M1-42). The high-resolution mass spectrum was obtained using an Agilent 6550 iFunnel Q-TOF LC-MS in positive ion mode using electrospray ionization (ESI) with a fragmentor voltage of 175V. A. The chromatogram from the LC-MS showed a significant peak between 5–7 min while using 0.1% formic acid and methanol as the solvent system. B. Mass spectrum at time point 4.964 min resulting in the corresponding peaks: [M+3H]<sup>3+</sup> (m/z 1549.0935), [M+4H]<sup>4+</sup> (m/z 1162.0724), [M+5H]<sup>5+</sup> (m/z 929.8594), [M+6H]<sup>6+</sup> (m/z 775.0505), and [M+7H]<sup>7+</sup> (m/z 664.4722). C. The deconvolution of the mass spectrum in panel B was performed showing the peak corresponding to [M+H]<sup>+</sup> at m/z 4644.26 (calculated [M+H]<sup>+</sup> of m/z was done using the PEPTIDEMASS program). .... 76

**Figure 3.7** Western blot characterization of the recombinant human Aβ(M1-42) peptide. A. 10, 20, and 40 µg of the recombinant Aβ(M1-42) peptide was run on an SDS-PAGE gel and bands visualized using the 6E10 antibody with Western Blot. Lower concentrations of 10 and 20 µg show monomeric bands at 4 kDa while the 40 µg lane shows oligomeric bands at 14–17 kDa along with the monomeric band. All 3 concentrations show a slight amount of high molecular weight bands at 38–49 kDa suggesting a few aggregated forms of the peptide in the mixture. B. Synthetic human Aβ1-42 for reference shows similar monomeric bands at 10, 20, and 50 µg concentrations. More oligomers are present in the synthetic peptide. .... 78

**Figure 3.8** AFM characterization of the recombinant human Aβ(M1-42) peptide. The (A) synthetic Aβ(1-42) oligomers and (B) recombinant Aβ(M1-42) oligomers and/or (C) fibrils were prepared from HFIP- treated peptide films in 1× PBS buffer (pH 7.4) and analyzed by atomic force microscopy (AFM). Images (A) and (B) are 2 × 2 µm x–y scale and image (C) is 5 × 5 µm x–y scale. Left. 2-D image. Right. 3-D image. .... 80

**Figure 4.1** Synthesis and characterization of Aβ<sup>pH</sup>. (A) The Aβ<sup>pH</sup> is synthesized by conjugating the amine-reactive pH-sensitive Protonex Green dye to the side chain amine groups of the lysine residues and the N-terminal of human Aβ1-42 peptide. (B) The pH-sensitivity of the Aβ<sup>pH</sup> probe characterized at different concentrations from 0.1 µM to 5.0 µM. Increased fluorescence is

observed at acidic pH values of ~5.0 to ~2.0, covering the pH range of the intracellular acidic organelles. (C) Atomic Force Microscopy topographic images of A $\beta^{pH}$  oligomers compared to synthetic A $\beta$  oligomers. Left-2D topographic image of A $\beta^{pH}$  and synthetic A $\beta$  oligomers. Right-3D image (2 $\times$ 2  $\mu$ m x-y). (D) Live cell imaging of the phagocytic uptake of 1  $\mu$ M A $\beta^{pH}$  by BV2 and N9 mouse microglia and by HMC3 human microglia over 24 hours. (E) Quantification of A $\beta^{pH}$  phagocytic score by BV2, N9, and HMC3 microglial cells from the live cell images. (F) The phagocytic uptake of A $\beta^{pH}$  by BV2 cells is measured and quantified via flow cytometry analysis. Dot plot shows live (PI-) and A $\beta^{pH+}$  cells. No green fluorescence is measured in unstained cells (UC) and in dead cells stained with the PI only whereas it is measured in cells treated with 0.5 and 5.0  $\mu$ M A $\beta^{pH}$  for 1 hour (higher fluorescence is seen in cells exposed to the higher concentration of A $\beta^{pH}$ ). Data shown in terms of % max, by scaling each curve to mode = 100% (y-axis)..... 91

**Figure 4.2** Fluorescence of internalized A $\beta^{pH}$  is retained in fixed cells. (A) Confocal images of fixed HMC3, N9, and BV2 cells showing the uptake of A $\beta^{pH}$  (green). Cells are stained for acidic intracellular organelles (LysoTracker Red, confirming co-localization of the A $\beta^{pH}$  within the acidic intracellular organelles) and nuclei (DAPI, blue). No antibody is required to detect A $\beta^{pH}$ . (B) Primary mouse microglia grown in defined, reduced-serum media phagocytose A $\beta^{pH}$  *ex vivo*. Cells are fixed and stained for nuclei and show A $\beta^{pH}$  colocalized in the acidic organelles with LysoTracker Red. (C) The phagocytic uptake of A $\beta^{pH}$  by primary microglia is measured and quantified via flow cytometry analysis. Dot plot shows live (ZV-) and A $\beta^{pH+}$  cells. No green fluorescence is measured in unstained cells (UC) or dead cells stained with the ZV live/dead stain only whereas green fluorescence is measured in cells treated with 0.5, 1.0, and 2.0  $\mu$ M A $\beta^{pH}$  for 1 hour. Data shown in terms of % max, by scaling each curve to mode = 100% (y-axis). (D) Primary immunopanned rat astrocytes also phagocytose A $\beta^{pH}$  in serum-free conditions. Cells are fixed and stained for astrocyte specific GFAP antibody (red) and nuclei. (E) Uptake of A $\beta^{pH}$  over time by primary immunopanned astrocytes as observed in live cells in real time. (F) Quantification of uptake of 0.5, 1.0, and 2.0  $\mu$ M A $\beta^{pH}$  by primary astrocytes. .... 97

**Figure 4.3** A $\beta^{pH}$  is phagocytosed by both microglia and astrocytes in situ in rat hippocampal tissue sections. (A) Schematic of phagocytosis assay in rat hippocampal tissue slices. (B) Representative 2D maximum projection of a confocal z-stack showing microglia phagocytosing A $\beta^{pH}$ . Closeup of the indicated cell (yellow square) is shown on the right. Orthogonal projections at the level of the crosshairs show internalization of A $\beta^{pH}$  within the microglia. (C) Representative 2D maximum projection of a confocal z-stack showing astrocytes phagocytosing A $\beta^{pH}$ . Closeup of the indicated cell (yellow square) is shown on the right. Orthogonal projections at the level of the crosshairs show internalization of A $\beta^{pH}$  within the astrocyte. (D) Quantification of A $\beta^{pH}$  colocalized with microglia and astrocytes, as defined by IBA1<sup>+</sup> and GFAP<sup>+</sup> staining, respectively. Data shown as mean $\pm$ s.e.m. collected from 20 and 8 slices for microglia and astrocytes respectively (from 3 animals)..... 100

**Figure 4.4** A $\beta^{pH}$  is phagocytosed by cortical microglia and astrocytes in vivo and by rat retinal microglia in vivo. (A) Schematic of stereotaxic microinjection of A $\beta^{pH}$  in the somatosensory cortex of P7 mouse followed by staining of fixed tissue section after 24 and 72 hours. (B) Phagocytic uptake of A $\beta^{pH}$  by IBA1<sup>+</sup> microglia and GFAP<sup>+</sup> astrocytes in the periventricular white matter at the 24 hour timepoint. The box represents the region of the fluorescence image where high magnification confocal imaging was done. (C) IBA1<sup>+</sup> microglia show bright green fluorescence at 72 hour in the same region indicating presence of A $\beta^{pH}$  within the cells at this timepoint. GFAP<sup>+</sup> astrocytes do not show any green fluorescence in this region at this timepoint suggesting either

degradation of the peptide or insufficient  $A\beta^{pH}$  concentration for detectable phagocytic uptake by these cells. (D) Quantification of  $A\beta^{pH}$  fluorescence within IBA1<sup>+</sup> microglia and GFAP<sup>+</sup> astrocytes located in the pia and white matter regions show more  $A\beta^{pH}$  uptake by microglia compared to astrocytes. (E) Schematic of subretinal injection of  $A\beta^{pH}$  to evaluate its *in vivo* uptake by rat retinal microglia and astrocytes. (F) IBA1<sup>+</sup> rat retinal microglia phagocytose  $A\beta^{pH}$  *in vivo*. (G) Quantification of  $A\beta^{pH}$  uptake into retinal IBA1<sup>+</sup> microglia and GFAP<sup>+</sup> astrocytes. No fluorescence was detected in astrocytes at these 3 time points (n.d.). Data shown as mean $\pm$ s.e.m. from 2 animals. .... 101

**Figure 4.5**  $A\beta^{pH}$  is phagocytosed by microglia and astrocytes *in vivo* in the cerebral cortex. (A) Schematic of how  $A\beta^{pH}$  phagocytic uptake is imaged through a cranial window *in vivo* in real time using two-photon excitation microscopy. (B) *In vivo* two-photon imaging of the mouse barrel cortex before and after topical application of  $A\beta^{pH}$ . The fluorescence increases in cell somata (indicated by red circles) reflecting  $A\beta^{pH}$  uptake. (C) Quantification of mean  $A\beta^{pH}$  fluorescence in cell somata over time. The data were normalized to the maximum mean  $A\beta^{pH}$  fluorescence for each cell and then averaged. Data shown as mean $\pm$ s.e.m. N=59 somata from 2 animals. (D) 1.5 to 3 hours after *in vivo* two-photon imaging of  $A\beta^{pH}$ , animals were perfusion-fixed and cortical slices were stained for microglia, microglia lysosomes/endosomes and astrocytes using IBA1, CD68, and GFAP antibodies, respectively. (E) Quantification of  $A\beta^{pH}$  colocalization with IBA1, CD68, and GFAP suggests that most  $A\beta^{pH}$  is taken up by microglia and astrocytes *in vivo*. Data shown as mean $\pm$ s.e.m. N=12 stacks from 3 animals. .... 105

**Figure 5.1** Our strategy to prepare cell organelle targeting probes in one synthetic scheme with a common scaffold..... 151

**Figure 5.2** Absorption, Fluorescence spectrum of compound LysoShine 1, LysoShine 2, MitoShine at different pH solutions and their pKa values. Spectrum recorded at room temperature in PBS buffer at varying pH with 1% (v/v) of DMSO, in all cases probe concentration = 10  $\mu$ M. .... 158

**Figure 5.3** (a) Schematic for flow cytometry analysis in live cells. (b-d) Demonstrates the fluorescence of LysoShine 1, LysoShine 2, and MitoShine upon uptake by primary mouse microglia (live cells). Modal corresponds to a percentage of the maximum count. (e) Median fluorescence intensity (MFI) values for each probe. US Ctrl is unstained control. Gating strategy and flow plots with commercial dyes in supporting information. .... 159

**Figure 5.4** (a) Experimental design for fluorescence imaging of primary mouse microglial cells with the (b) LysoShine 1 and (c) LysoShine 2 (green). The localization of the compounds in the lysosomal acidic compartments is shown with the LysoTracker dye (red). Nuclear DNA is stained with DAPI (blue). Scale bars represent 200  $\mu$ m. .... 160

**Figure 5.5** Fluorescence imaging of primary mouse microglial cells with MitoShine. The localization of the compound was observed in mitochondria (magenta, MitoLite dye) as well as in the acidic lysosomal organelles (red, LysoTracker dye). (a) Magnified image with nuclear DNA is stained with DAPI (blue). Scale bars represent 50  $\mu$ m. .... 161

**Figure 6.1** Representative structures of select lipid classes. The main structure of a phospholipid is illustrated with the R2 position highlighted in yellow. The type of the phospholipid depends on the functional group at the R2 position. This is indicated in the following phospholipids shown in

yellow boxes. Other lipids drawn are ceramides, cholesteryl ester with a cholesterol backbone, and a triacylglycerol containing three acyl chains with a glycerol head group.....	196
<b>Figure 6.2</b> Rare and common variants contribute to Alzheimer's disease risk. Adapted from Karch & Goate, 2015[10]. Yellow thunderbolt symbol = genes associated with lipid metabolism. ....	197
<b>Figure 6.3</b> Lipids regulate microglial function. Examples: (L) Lipids act as ligands for TREM2 and affect downstream signaling. (R) Phosphatidylserine on cell membrane act as eat-me signal to initiate phagocytosis of apoptotic cells. ....	199
<b>Figure 6.4</b> Alois Alzheimer, 1911. glz: glia; gaz: neurons; P1/P2: senile plaques.....	204
<b>Figure 7.1</b> Schematic of experimental protocol for MRM-profiling of A $\beta$ -treatment and BV2 microglia. ....	217
<b>Figure 7.2</b> (a) Total number of cellular lipids for each class that were differentially regulated at 1, 12, and 24 hours of A $\beta$ treatment in BV2 microglia. Right: upregulated lipids, Left: downregulated lipids. (b) Lipids that were common between 1 and 24 hour of A $\beta$ treatment in BV2 microglia. ....	218
<b>Figure 7.3</b> PCA plots showing separation between lipids in A $\beta$ treated (red) and vehicle-treated BV2 microglia.....	219
<b>Figure 7.4</b> Schematic of experimental protocol for MRM-profiling of primary microglia. (a) Isolation, culture, and treatment of microglia. Microglia were isolated from adult C57B/6 mice and cultured in low-serum containing defined medium. Aggregated A $\beta$ 1-42 was added to the cells for 1, 12, or 24 hours. (b) Samples processing. The cell pellets and the conditioned medium were collected at each time point and subjected to Bligh & Dyer protocol for lipid extractions. Lipid were isolated from organic phase and metabolites were isolated from polar phase. (c) MRM-profiling and analysis. MRM-profiling of lipids and metabolites was performed to identify statistically significant lipids and metabolites in A $\beta$ treated versus vehicle-treated microglia. .	223
<b>Figure 7.5</b> Percent distribution of differentially regulated lipid classes in primary microglia at 1, 12, and 24 hours of A $\beta$ treatment (significant lipids). ....	225
<b>Figure 7.6</b> Principle Component Analysis (PCA) plots showing separation between lipids in A $\beta$ treated (red) and vehicle-treated primary microglia. ....	225
<b>Figure 7.7</b> Structures of C19:0, C20:0, and C22:0 were validated using gas-phase ion/ion chemistries. The plots on the left panel are from the standard lipids used to determine the mass of the lipid fragments upon neutral loss (NL). The plots on the right are from the microglia cell samples wherein the lipids with the same NL masses ( $m/z$ ) were identified thereby confirming the presence of the three saturated FFAs in the sample.....	232
<b>Figure 7.8</b> Total number of cellular lipid species for each lipid class that were (top) upregulated and (bottom) downregulated at 1, 12, and 24 hours of A $\beta$ treatment. The specific upregulated lipid species for the FFA (#) and TAG (\$) classes are listed in the boxes on top right. ....	233
<b>Figure 7.9</b> Working hypothesis to explain the microglial cell states due to FFA and TAG interplay due to initial and prolonged A $\beta$ treatment .....	234

<b>Figure 7.10</b> An overview of TAG biosynthesis in cells. Two pathways that lead to the production of TAGs in cells: the glycerol phosphate pathway and the monoacylglycerol pathway. ....	235
<b>Figure 7.11</b> BODIPY staining on acutely isolated CD11b <sup>+</sup> cells from WT and 5xFAD female mice. Gating strategy for flow cytometry analysis of (a) WT sample and (b) 5xFAD sample stained with BODIPY and DAPI. (c) No green fluorescence was measured in unstained cells (shown in black) whereas a strong green fluorescence signal was measured in DAPI <sup>-</sup> cells stained with BODIPY both in case of WT (shown in blue) and 5xFAD (shown in red). Data shown in terms of % max, by scaling each curve to mode = 100% (y-axis). (d) Comparison of BODIPY Median Fluorescence Intensity (MFI) normalized to WT (unpaired t-test, $P = .0016$ ). (n=2, where each group contained 1-2 female C57BL/6 mice and 1-2 female 5xFAD mice).....	236
<b>Figure 7.12</b> BODIPY staining on acutely isolated CD11b <sup>+</sup> cells from WT and 5xFAD male mice: Gating strategy for flow cytometry analysis of (a) WT sample (b) 5xFAD for BODIPY <sup>+</sup> cells. (c) No green fluorescence was measured in unstained cells (shown in black) where as a strong green fluorescence signal was measured in DAPI <sup>-</sup> cells treated 2 $\mu$ M BODIPY for 1 hour at 37°C both in case of WT (shown in blue) and 5xFAD (shown in red). Data shown in terms of % max, by scaling each curve to mode = 100% (y-axis). (d) Comparison of BODIPY Median Fluorescence Intensity (MFI) normalized to WT (unpaired t-test, $P = .0918$ ). (e) Dot plot for DAPI <sup>-</sup> cells in WT and 5xFAD sample showing BODIPY <sup>hi</sup> (Q2) and BODIPY <sup>lo</sup> (Q1) population (f) Comparison of Frequency of BODIPY <sup>hi</sup> cells in WT v/s 5xFAD (unpaired t-test, $P = .0254$ ). (n=1, containing 2 male C57BL/6 mice and 2 male 5xFAD mice) .....	238
<b>Figure 7.13</b> BODIPY staining on acutely isolated CD11b <sup>+</sup> cells from 3-4 month old WT and 5xFAD female mice: Gating strategy for flow cytometry analysis of (a) WT sample (b) 5xFAD sample for BODIPY <sup>+</sup> cells. (c) No green fluorescence was measured in unstained cells (shown in black) and a strong green fluorescence signal was measured in DAPI <sup>-</sup> cells treated 2 $\mu$ M BODIPY for 1 hour at 37°C both in case of WT (shown in blue) and 5xFAD (shown in red). Data shown in terms of % max, by scaling each curve to mode = 100% (y-axis). (d) Dot plot for DAPI <sup>-</sup> cells in WT and 5xFAD sample. (e) Comparison of BODIPY MFI relative to WT (unpaired t-test, $P = 0.7528$ ). (n=2, each group containing 1 female C57BL/6 mice and 1 female 5xFAD mice) 239	239
<b>Figure 7.14</b> DGAT2 expression in WT and 5xFAD microglia; 7-month-old female mice; Cortex; Scale bar is 50 $\mu$ m. ....	240
<b>Figure 7.15</b> Quantification of DGAT2 expression in WT and 5xFAD microglia. ....	241
<b>Figure 7.16</b> Principle Component Analysis (PCA) plots of metabolites in A $\beta$ treated (red) and vehicle-treated primary microglia. ....	242
<b>Figure 7.17</b> Pathway enrichment with differentially regulated metabolites in primary microglia with (a) 1 hour and (b) 24 hours of A $\beta$ treatment. ....	246
<b>Figure 7.18</b> PCA plots showing separation between metabolites in conditioned medium of A $\beta$ treated and vehicle-treated primary microglia. ....	248
<b>Figure 7.19</b> PCA plots showing separation between metabolites in 5xFAD and WT microglia. ....	248
<b>Figure 7.20</b> Pathway enrichment with differentially regulated metabolites in 5xFAD microglia. ....	250

<b>Figure 8.1</b> Activated microglia induce neurotoxic reactive astrocytes. Microglia become classically activated with several factors such as the bacterial endotoxin (LPS) and even signals arising from damaged neurons. These activated microglia release astrocyte-activating signals (TNF- $\alpha$ , IL-1 $\alpha$ , and C1q) that induce astrocytes to become reactive. These A1 or neuroinflammatory reactive astrocytes directly cause neuronal death via the secretion of an unknown neurotoxic factor. Only previously damaged neurons are susceptible to the reactive-astrocyte-induced death, however, the mechanism is still unknown. The identity of this astrocytic toxic factor was a mystery to date.....	260
<b>Figure 8.2</b> Sample preparation for proteomics of A1 reactive astrocytes and ACM. A total of 2694 and 75 proteins were identified in cells and ACM respectively. ....	263
<b>Figure 8.3</b> Number of significant proteins and PCA variation based on number of replicates of protein mass spectrometry that were required to have a non-zero spectral count to be considered for analysis. 4 of 10 (4x) was chosen for final analysis.....	265
<b>Figure 8.4</b> Number of differentially regulated proteins in reactive astrocytes and ACM. The cells had 75 upregulated and 101 downregulated proteins. The ACM had 17 upregulated and 0 downregulated proteins. Data based on the 4x analysis described above.....	265
<b>Figure 8.5</b> Principal component analysis (PCA) plots shows separation in the proteomes of reactive and control astrocytes. Variation in more than 90% of the sample and control data is seen in each category showcasing the separation of the reactive and control astrocytes and ACM proteome. ....	266
<b>Figure 8.6</b> Scatter plot shows the significant proteins in astrocytes due to their reactivity. Red and blue points indicate the proteins in highest and lowest abundance based on the Log <sub>2</sub> FC values respectively. Select relevant upregulated proteins like C3, CLU, SOD2, etc. are labeled. ....	267
<b>Figure 8.7</b> Scatter plot shows the significant proteins in ACM due to the reactivity of the astrocytes. Red and blue points indicate the proteins in highest and lowest abundance based on the logFC values respectively. ....	270
<b>Figure 8.8</b> Lipidomics pipeline for A1 astrocytes and ACM.....	273
<b>Figure 8.9</b> Number of differentially regulated lipids and metabolites in reactive astrocytes and ACM. Lipids are shown in black/grey and metabolites are shown in blue (dark/pale).....	274
<b>Figure 8.10</b> Principal component analysis (PCA) plots shows separation in the lipidome of reactive and control astrocytes. Variation in more than 70% of the sample and control data is seen in each category showcasing the separation of the reactive and control astrocytes and ACM lipidome. ....	274
<b>Figure 8.11</b> Heatmap of cell lipids demonstrating the lipid class-specific changes in control (C) and reactive (R) astrocytes. The clear transition from blue (downregulated) to red (upregulated) shows the changes in cellular states via lipid-mediated mechanisms.....	275
<b>Figure 8.12</b> Scatter plot of cell lipids shows the variation of the significant lipids from the unchanged lipids shown as grey points. Lipids in orange/red are upregulated and lipids in blue/purple are downregulated.....	278

<b>Figure 8.13</b> Heatmap of media lipids demonstrating the lipid class-specific changes in control (C) and reactive (R) astrocytes. The clear transition from blue (downregulated) to red (upregulated) shows the changes in cellular states via lipid-mediated mechanisms.....	279
<b>Figure 8.14</b> Scatter plot of media lipids shows the variation of the significant lipids from the unchanged lipids shown as grey points. Lipids in orange/red are upregulated and lipids in blue/purple are downregulated. C18:0, C16:0, C20:0, C19:0 are the highly upregulated lipids in the reactive ACM.....	282
<b>Figure 8.15</b> Principal component analysis (PCA) plots do not show slight but not complete separation in the metabolome of reactive and control astrocytes. ....	283
<b>Figure 8.16</b> Long chain and very long-chain fatty acid biosynthesis. <i>Elovl1</i> (red) is key in several steps of the synthesis to make saturated fatty acids. FAS is fatty acid synthase. ....	287
<b>Figure 8.17</b> Principal component analysis (PCA) plots shows separation in the lipidome of reactive and control astrocytes. Variation in more than 60% of the sample and control data is seen in each category showcasing the separation of the <i>Elovl1</i> -cKO reactive and control astrocytes and ACM lipidome. ....	287
<b>Figure 9.1</b> BV2 microglia produce TNF- $\alpha$ , IL-1 $\alpha$ , and NO with LPS activation. (A) Cell viability with LPS treatment is calculated by considering vehicle-treated cells as 100% viable. (B) NO production from BV2 cells is significantly increased with LPS. (C) Standard curve of TNF- $\alpha$ and (D) IL-1 $\alpha$ for ELISA using recombinant proteins. (E) BV2 secretion of TNF- $\alpha$ and (F) IL-1 $\alpha$ is significantly increased in the presence of LPS. ....	306
<b>Figure 9.2</b> CD11b <sup>+</sup> cells produce TNF- $\alpha$ and IL-1 $\alpha$ under the influence of LPS (50 ng/mL) activation. (A) Standard curve of TNF- $\alpha$ and (B) IL-1 $\alpha$ for ELISA using recombinant proteins. CD11b <sup>+</sup> cells secretion of (C) TNF- $\alpha$ (D) and IL-1 $\alpha$ is significantly increased in the presence of LPS. (E) Cell viability is normalized to control well which is considered 100% viable. LPS treatment does not alter the viability of CD11b <sup>+</sup> cells at the tested conditions. ....	307
<b>Figure 9.3</b> Select steroidal drugs reduce the secretion of NO, TNF- $\alpha$ , and IL-1 $\alpha$ by LPS-activated microglia. (A) DEX suppresses NO secretion by LPS-activated BV2 microglia at both 100 nM and (B) 1 $\mu$ M. (C) DEX significantly suppresses TNF- $\alpha$ secretion at 100 nM along with D4T, ETH, and ABL. (D) None of the drugs significantly reduce TNF- $\alpha$ at 1 $\mu$ M, however, DEX treatment has the most observable cytokine reduction at this dose. (E) DEX significantly suppresses IL-1 $\alpha$ secretion at both 100 nM and (F) 1 $\mu$ M. The secretion of NO, TNF- $\alpha$ , and IL-1 $\alpha$ with LPS treatment alone was selected as a control and set to 1.0. ....	309
<b>Figure 9.4</b> Schematic for evaluating NO, TNF- $\alpha$ , and IL-1 $\alpha$ in LPS-activated microglia upon drug treatment. ....	310
<b>Figure 9.5</b> CD11b <sup>+</sup> microglial secretion of IL-1 $\alpha$ with LPS activation and under the treatment of various steroid compounds, abi, d4t, dex, and eth. ....	311
<b>Figure 9.6</b> CD11b <sup>+</sup> microglial secretion of TN- $\alpha$ with LPS activation and under the treatment of various steroid compounds, abi, d4t, dex, and eth. ....	311
<b>Figure 9.7</b> Schematic for shotgun exploratory lipidomics performed on dexamethasone-treated activated microglial cells. ....	312

**Figure 10.1** Various neuronal and non-neuronal substrates that are implicated in neurodegenerative and neurological disorders. Microglia and astrocytes phagocytose these substrates in normal conditions but exhibit altered phagocytic capacities in diseased conditions. Conjugating these substrates with different types of fluorophores and probes will allow us to track their internalization by glial cells and separate these cells via FACS for their molecular characterization. .... 323

**Figure 10.2** Overview of my thesis. New Tools: Development of recombinant A $\beta$ , A $\beta^{\text{pH}}$ , and other pH-sensitive fluorophores to study A $\beta$ -specific phagocytosis and response in microglia (and astrocytes); Lipid Changes: Changes in microglial lipidome and metabolome landscape due to A $\beta$ , underlying mechanisms of lipid-induced cytotoxic and protective mechanisms; Reactive astrocytes: Characterizing reactive astrocytic proteome, lipidome, and metabolome. Lipidomics identified upregulation of saturated PCs and FFAs in reactive astrocytes and ACM, respectively. How these molecules influence microglial cell state and whether microglia develop a lipid droplet-rich phenotype in this environment warrants further investigation. .... 326



## ABSTRACT

Microglia are a population of specialized, tissue-resident immune cells that make up around 10% of total cells in our brain. They actively prune neuronal synapses, engulf cellular debris, and misfolded protein aggregates such as the Alzheimer's Disease (AD)-associated amyloid beta ( $A\beta$ ) by the process of phagocytosis. Intra and extracellular lipids and metabolites also influence microglial behavior. There are currently 10,000 different documented lipids, and the dysregulation in lipid metabolism is linked to AD. Yet, the changes in the global lipid and metabolite profiles in microglia are uncharacterized to date. In addition to phagocytosis, microglia also communicate with other cells like astrocytes and neurons in their environment and influence their behavior and function via protein and lipid molecules. Therefore, it is imperative to investigate the molecules that influence microglial cell state and function with respect to  $A\beta$  and neuroinflammation in general.

The overarching question of this work is, *How do microglia become dysfunctional in chronic inflammation?* Previous studies have demonstrated that microglia become dysfunctional and exhibit impaired phagocytosis in neurodegenerative brains. Defining the molecules that result in functional cell subsets based on  $A\beta$  removal and identifying the dysfunctional cell states will be crucial to understanding why the “altered” microglia fail to remove  $A\beta$  in AD. We developed new chemical tools to better understand and investigate the microglial response to  $A\beta$  *in vitro* and *in vivo*. Specifically, we introduce three new tools. (1) Recombinant human  $A\beta$  was developed via a rapid, refined, and robust method for expressing, purifying, and characterizing the protein. We showed that the recombinant  $A\beta$  behaves similarly to the synthetic  $A\beta$  and can be used in various assays to investigate microglial function. (2) A pH-sensitive fluorophore conjugate of  $A\beta$  (called  $A\beta^{pH}$ ) was developed to identify and separate  $A\beta$ -specific phagocytic and non-phagocytic glial cells *ex vivo* and *in vivo*. We demonstrated that microglia phagocytose  $A\beta^{pH}$  much more than astrocytes and that  $A\beta^{pH}$  can be used to monitor, for the first time,  $A\beta$ -specific phagocytosis in live animals in real-time. Thus,  $A\beta^{pH}$  can be used to identify the functional molecular markers of  $A\beta$  phagocytosis by sorting the  $A\beta$ -specific phagocytic and non-phagocytic glia for downstream proteomic, lipidomic, and metabolomic analysis. Identifying the *functional molecules* specific to these cell subsets will highlight the pathways unique to dysfunctional microglia in degeneration.

(3) New lysosomal, mitochondrial, and nuclei targeting pH-activable fluorescent probes (called LysoShine, MitoShine, and NucShine, respectively) were designed using a modular one-step synthetic strategy with a common reaction intermediate. We showed that the functional group transformation of a common core scaffold influences cellular localization and specificity of pH-activable fluorescent probes in live primary microglial cells. Together, these chemical tools can be utilized to study microglial phagocytic response to A $\beta$  and the downstream changes occurring to the subcellular organelles.

We next asked, *What changes occur to the lipid and metabolite profiles of microglia with A $\beta$ ?* While changes to microglial cell states have been previously delineated using single-cell sequencing technologies, characterizing the changes to microglial lipidome and metabolome have been challenging, mainly due to the lack of appropriate analytical methodologies. Here, we used a highly sensitive and robust technique called Multiple Reaction Monitoring-profiling to screen around 1500 unique lipid species categorized into ten main classes and around 700 metabolites in microglia that were exposed to A $\beta$  in culture. We found that microglia accumulate free fatty acids (FFAs) with initial A $\beta$  exposure but upregulate Triacylglycerides (TAGs) with prolonged A $\beta$  treatment. It is known from previous studies that excess FFA accumulation may be toxic to the cells. Thus, we hypothesized that microglia might overcome the FFA-induced cytotoxicity by producing an abundance of TAGs as a protective cellular mechanism. Interestingly, TAGs are also the significant components of lipid droplets (LDs)—which are the main energy storage compartments in the cells. We have demonstrated that microglia upregulate LDs in adult 5xFAD mice compared to the WT mice indicating a unique and previously undefined cellular response to A $\beta$ -induced chronic inflammation *in vivo*. Further, we have shown that Diacylglycerol O-acyltransferase 2 (DGAT2)—an LD-associated protein involved in TAG biosynthesis is upregulated in microglia in 5xFAD brains compared to microglia in WT brains. Taken together, these results indicate that the LD-rich microglia display a unique cellular mechanism that is “turned on” in order to overcome the stress related to acute and chronic inflammation.

The microglia-astrocyte cross-talk in health and disease is critical to the maintenance of tissue homeostasis. For example, astrocytic cholesterol is required for the survival and growth of microglia in a healthy brain. A recent study demonstrated that classically activated microglia

induce astrocytes to become “reactive” via the secretion of TNF- $\alpha$ , IL-1 $\alpha$ , and C1q. Further, reactive astrocytes were found to kill neurons and mature oligodendrocytes via the secretion of a toxic factor whose identity was a mystery to date. The molecular changes occurring in astrocytes due to their microglia-induced reactive state were not well defined. We have extensively characterized the proteome, lipidome, and metabolome of reactive astrocytes and their conditioned medium (comprising around 3660 proteins, 1500 lipids, 700 metabolites) in order to better delineate these changes. We show that astrocytes upregulate several proteins when they become reactive, including new and undefined proteins as well as the previously defined reactive astrocyte markers such as C3, LCN2, SERPING1, etc. Further, we show that the lipidome of astrocytes changes dramatically when they become reactive. Reactive astrocytes, along with their conditioned media, upregulate specific lipid classes, including phosphatidylcholines and long-chain saturated free fatty acids, respectively. These saturated lipids were found to be the astrocytic neurotoxic factor that killed neurons *in vitro* and *in vivo* upon reactivity. Overall, we provide the most comprehensive proteomic, lipidomic, and metabolomic characterization of reactive astrocytes to date that was instrumental in identifying the mysterious astrocytic neurotoxin, and these datasets will be helpful for probing microglia-astrocyte-neuron cross-talk in future studies.

Finally, we asked, *What compounds modulate the microglial inflammatory response?* We screened several FDA-approved steroidal compounds that are known to be potent anti-inflammatory molecules. We demonstrate that dexamethasone (DEX), a glucocorticoid agonist, reduces the production of inflammatory factors like nitric oxide, TNF- $\alpha$ , and IL-1 $\alpha$  by the lipopolysaccharide-activated microglia. We also show that DEX treatment induces lipidomic changes in microglia. Thus, these anti-inflammatory compounds may be used to modulate the microglial cell state and function in inflammation.

In conclusion, the work detailed in this thesis introduces new chemical tools for the characterization of microglial responses to A $\beta$ . We also highlight the lipid-related cellular and molecular changes occurring in microglia due to A $\beta$  in acute and chronic inflammation. Identifying the critical functional molecules involved in A $\beta$  response, metabolism, and signaling is essential for elucidating microglia’s role in health and disease. We also highlight the major molecular players involved in microglia-astrocyte cross-talk, thereby opening new avenues of investigation.

We put forward a final model wherein inflammatory proteins secreted by microglia directly influence astrocyte reactivity. The inflammatory lipid mediators secreted by reactive astrocytes may also influence microglial lipid metabolism and cell state. Finally, we propose chemical neuroimmunology to be the new frontier of neuroscience encompassing the development and use of chemical tools and techniques to investigate and modulate glial cell behavior and function in neuroinflammation and neurodegeneration.

## CHAPTER 1. THE MYSTERY AND MAGIC OF GLIA

### 1.1 Major cells of the central nervous system

Our central nervous system (CNS), comprising of the brain and the spinal cord, is made up of over a hundred billion cells that function together like a well-oiled machine to keep our entire body alive and active. While neurons are commonly referred to as the “basic building blocks” of the CNS, another equally—if not more!—important units are the non-neuronal cells called glia (Greek for “glue”). Glial cells are absolutely essential for the normal functioning of the CNS and regulate all aspects of its development, health, and disease[1], [2].

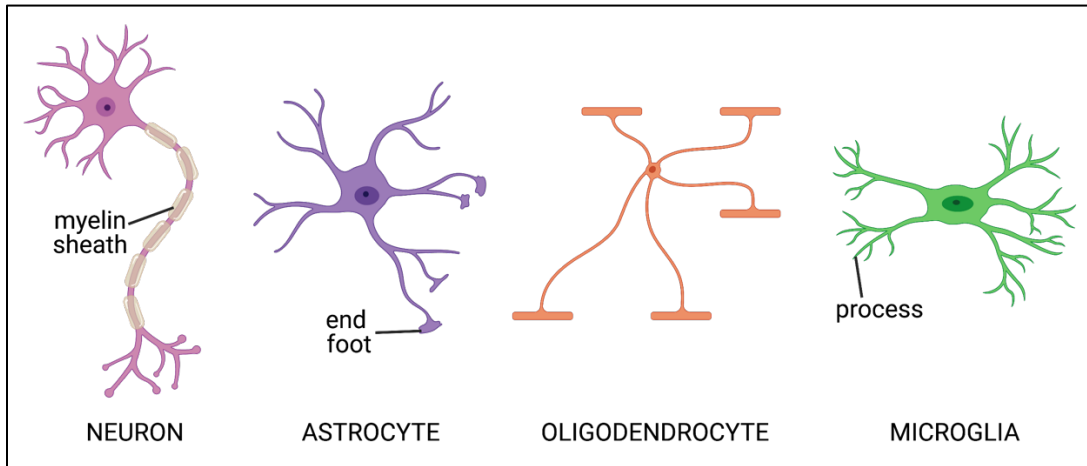


**Figure 1.1** Major cells of the CNS. Neuron (myelinated) and Glial cells—Astrocyte (end feet visible), Oligodendrocyte, and Microglia.

There are three main types of glial cells in the CNS: astrocytes, oligodendrocytes, and microglia. Astrocytes (“star-shaped cells”) are the largest glial cell population in the CNS (Figure 1.1). They are best known for some of their traditional functions like the promotion of neuronal development, production of trophic factors to support neuronal health, formation, function, and the phagocytic elimination of synapses, maintenance of the blood-brain barrier, control of neurotransmitter release and uptake, etc[1]. Oligodendrocytes are the myelinating cells of the CNS—they produce myelin, a lipid-rich fatty substance that provides the insulating sheath to the neuronal axons[1]. Microglia (“tiny glue”) are a small population of specialized immune cells that are vital for the regulation of

homeostasis[1]. They are the tissue-resident macrophages of the CNS and perform a myriad of immunological functions described in the sections below.

## 1.2 Microglia—The resident immune cells of the CNS

Microglia were first discovered by the Spanish neuroscientist Pío del Río Hortega in 1919[3]. In his paper, El “Tercer Elemento” de los Centros Nerviosos. I. La Microglía en Estado Normal (The “Third Element” of the Nervous Centers. I. The Microglia in Normal State), Río-Hortega wrote:

*‘As a result of our first observation, we are convinced that this new cell type is a glial cell and we call it microglia due to the tiny size of their soma, which is considerably smaller than that of fibrous and protoplasmic astrocytes.’*

Microglia make up around 10-15% total cells in the CNS[4]. Although microglia share many characteristics with the peripheral macrophages, they have distinct developmental origins and function. They originate from the yolk sac during early embryonic development around day 7-8 (in mice) and migrate to the brain where they permanently reside throughout one’s life[4]. The development of microglia is driven by the transcription factors interferon regulatory factor 8 (IRF8) and PU.1 along with the cytokine transforming growth factor- $\beta$  (TGF- $\beta$ )[5]. In contrast, peripheral macrophages originate from the hematopoietic stem cells in the bone marrow. Microglia are defined as CD11b<sup>+</sup>CD45<sup>low</sup> cells while peripheral macrophages are defined as CD11b<sup>+</sup>CD45<sup>high</sup> cells. Microglia also exhibit unique markers that are distinct from other immune cells. For example, they express the transmembrane protein 119 (TMEM119)[6], Spalt Like Transcription Factor 1 (SALL1)[7], Purinergic Receptor P2Y12 (P2RY12)[8], etc. Other markers used to identify microglia in the brain are Cx3CR1 known as the fractalkine receptor, Ionized calcium binding adaptor molecule 1 (IBA1), CD68, Triggering Receptor Expressed On Myeloid Cells 2 (TREM2), CD11b, F4/80, etc [9]. However, these markers are expressed on both the peripheral macrophages as well as microglia.

In a healthy brain, “resting” microglia exhibit a ramified morphology with elongated process to constantly survey their environment for external “eat me” signals originating from pathogens, cellular debris, misfolded protein aggregates, etc (Figure 1.2). However, when triggered by an inflammatory insult, microglia become “activated”, exhibit an amoeboid and dystrophic morphology, and undergo dramatic phenotypic and genotypic changes.

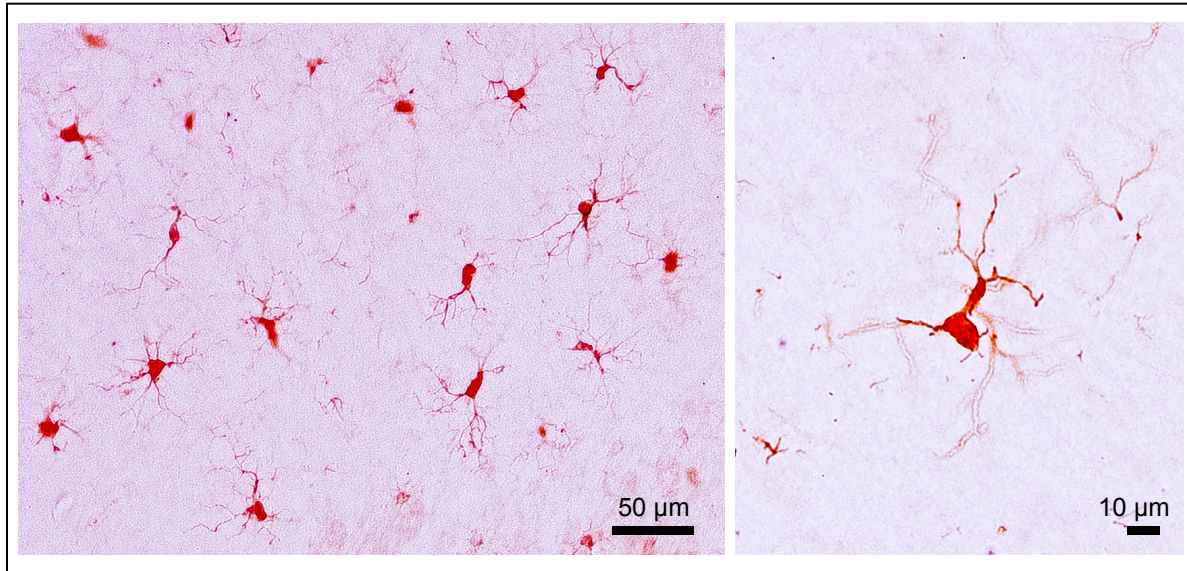


**Figure 1.2** Immunohistochemical staining of microglia in the cortex of a wild type adult rat. Microglia are labeled with the IBA1 marker in red. (Left) The cells exhibit a rested, ramified morphology with several processes extending from the cell body. (Right) A magnified image of a single microglia cell.

Traditionally, “activated” microglia were classified into two main phenotypes: M1 and M2 [10]. M1 microglial cells were considered to be the classically activated cells (activated by lipopolysaccharide or LPS or IFN- $\gamma$ ) expressing pro-inflammatory molecules like IL-1 $\beta$ , TNF- $\alpha$ , IL-6, nitric oxide (NO), etc[11]. M2 microglial cells were considered to be alternately activated (activated by IL-4 or IL-13) and expressed anti-inflammatory factors such as IL-10 and TGF- $\beta$ [11]. Over the years, this dual-phenotype classification of microglia has been largely refuted [10]. Today, we know that microglia are highly heterogeneous cells, even in a resting state in a healthy brain, where they can exhibit multiple distinct phenotypes and molecular markers[12]. The phenotypic, genotypic, and morphological diversity of microglia can be made apparent by their location in the brain parenchyma, the organism, the age and sex of the animal, local microenvironment, etc. The change to microglial phenotypes are dramatically exaggerated in a diseased or inflamed brain where disease-specific subpopulations of microglia have recently been identified. For example, single-cell RNA sequencing (scRNA-seq) has identified a unique microglia subtype in Alzheimer’s disease (AD) and amyotrophic lateral sclerosis (ALS) brains called Disease-Associated Microglia (or DAMs) that show distinct gene expression patterns linked to phagocytosis and lipid metabolism[13]. Another microglial subtype were identified to be localized to the developing corpus callosum and the myelin-rich cerebellar white matter and were termed

proliferative-region-associated microglia (PAMs)[14]. PAMs exhibit amoeboid morphology, are metabolically active and phagocytose newly formed oligodendrocytes. Glioma-associated microglia (GAMs) were identified in human gliomas which upregulated genes involving mitotic cell cycle, cell migration, cell adhesion, and extracellular matrix organization[15], [16]. Interestingly, human GAMs did not upregulate genes related to immune cell activation possibly suggesting a suppressed immune phenotype of microglia in glioblastoma. White matter associated microglia (WAMs) were also recently identified during aging. WAMs appear in the white matter regions and are dependent on TREM2 but independent of apolipoprotein E (APOE)[17]. It is hypothesized that WAMs may be protective for the clearance of degenerated myelin during aging and disease. These studies clearly demonstrate that microglial cell state and function is highly dependent on their local surrounding and that the signals arising from their environment can reprogram them into new and distinct functional states.

### **1.3 The myriad functions of microglia**

At birth, an infant's brain consists of roughly 15% more neurons than it would as an adult[18]. As we age, some of the neurons and the neuronal circuits become stronger while the remaining fade away[18]. Microglia actively prune away the unwanted neuronal synapses during development[19]. This process is therefore absolutely essential to the facilitation of neuronal plasticity and for shaping neuronal wiring in a healthy brain. When this pruning is somehow disrupted in children it could lead to the bases for developing certain neurological disorders such as schizophrenia and autism. But how do microglia identify the specific synapses to prune i.e. what molecules are involved in microglial-mediated synaptic pruning? One mechanism by which microglia recognize these low-activity synapses for pruning is via the identification of specific immune molecules called complement proteins[20]. Specifically, complement 3 or C3 proteins are "tagged" on synapses and act as eat-me signals thereby recruiting microglia to their location for their engulfment[21]. Microglia express the corresponding partner protein called C3 receptors (CR3) which identify the C3 molecules tagged on the synapses. Deleting the CR3/C3 signaling axis decreased the capacity for microglia to eliminate the synapses[21]. Thus, microglia play integral roles in shaping the brain structure and composition in a developing, healthy individual. As the professional phagocytes of the brain, microglia also engulf the pathogenic misfolded protein aggregates from their surroundings[22]. The disruption of their phagocytic function thus leads to



altered cell states and increased toxicity resulting in disease phenotypes. Phagocytosis is a fundamental process in cellular immunity and is described as the recognition, engulfment, and degradation of extracellular target substrates (that are larger than 0.5  $\mu\text{m}$  in size) by “professional phagocytes” namely, neutrophils, natural killer cells, and macrophages. Other cells like epithelial cells, fibroblasts, etc can also eliminate apoptotic cells from their environment[23]. When a phagocyte interacts with its target substrate, actin filaments in its plasma membrane depolymerize and extend to engulf the substrate within a specialized vesicle known as a phagosome. The phagosome matures by fusing with the lysosome to form a phagolysosome preparing the foreign substrate for digestion. As the phagosome matures into the phagolysosome, the pH of the vesicle gradually decreases to around 4.0 initiating enzymatic degradation of the substrate[24]. Microglial phagocytosis is a critical process for the maintenance of brain homeostasis throughout an individual’s lifespan.

In Alzheimer’s Disease (AD), 40-42 length peptides called amyloid beta ( $\text{A}\beta$ ) aggregate to form large extracellular toxic plaques that disrupt signaling between neurons and lead to neuronal death[25]. In a healthy brain environment, microglia would be able to phagocytose these  $\text{A}\beta$  aggregates consisting of oligomers and higher-order fibrils thereby preventing them from accumulating in the brain. However, in chronic inflammation, microglia fail to successfully phagocytose the  $\text{A}\beta$  plaques thereby allowing them to grow bigger and disrupt neural circuits and contribute to an increase in neuroinflammation[26]. Microglia in AD become highly dystrophic (Figure 1.3) and functionally impaired. The mechanisms underlying the altered states and function of microglia in AD are not well understood. Another characteristic feature of AD are accumulation of intracellular hyperphosphorylated tau proteins within the neurons[26]. When neurons start to disintegrate and die, they release these aggregated tau proteins into their extracellular milieu where they can cause similar damages to neurons leading to neuroinflammation. As the disease progresses, microglia fail to phagocytose  $\text{A}\beta$  as well as the tau proteins and the underlying cellular and molecular mechanisms related to these changes and cellular dysfunction are not well understood[27]. Further details of  $\text{A}\beta$  structure, their aggregation, and involvement in AD are discussed in Chapter 2.

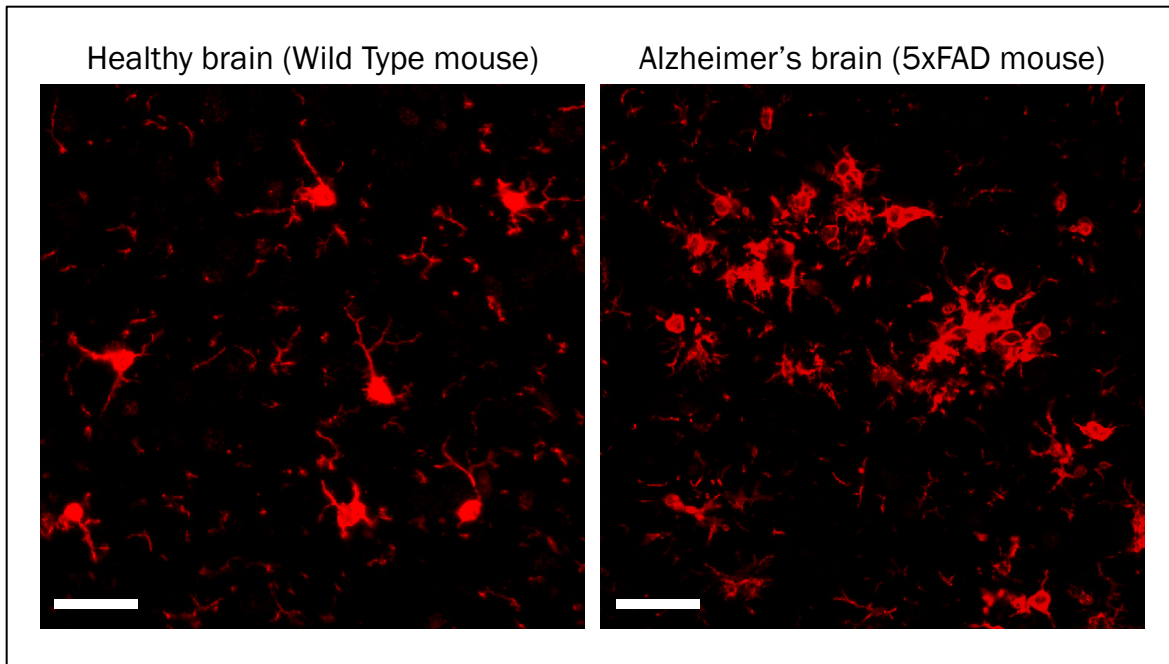


**Figure 1.3** Immunofluorescence staining of microglia with the IBA1 marker in the cortical regions of 7 month old female mice. (Left) In a healthy mouse brain (wild type), microglia display long processes extending from the cell bodies. (Right) In a mouse model of Alzheimer's disease (5xFAD), microglia appear to be dystrophic and hyper-reactive.

Parkinson's Disease (PD) is a neurodegenerative disorder characterized by the accumulation of  $\alpha$ -synuclein ( $\alpha$ Syn) proteins (major components of Lewy bodies) within dopaminergic neurons found in the midbrain[28]. Similar to tau proteins in AD, accumulated  $\alpha$ Syn proteins can "leak" from the damaged neurons into their extracellular space[28]. Active microglia would ideally phagocytose these  $\alpha$ Syn components preventing them from "seeding" to form further tissue damage. Microglia digest the engulfed  $\alpha$ Syn proteins by the process of autophagy to maintain tissue homeostasis[29]. It has been found that microglia with deficient autophagy-mechanisms can cause  $\alpha$ Syn accumulation and promote neurodegeneration[29]. Thus, both the extracellular mechanisms such as identifying target proteins via eat me signals and phagocytosis as well as intracellular mechanisms like lysosomal protein degradation and autophagy are essential to prevent events contributing to neurodegeneration. Microglia also phagocytose (or fail to do so) materials in other neurological conditions such as degrading myelin in Multiple Sclerosis (MS), degenerating motor neurons in Amyotrophic Lateral Sclerosis (ALS), prion proteins in prion diseases[30].

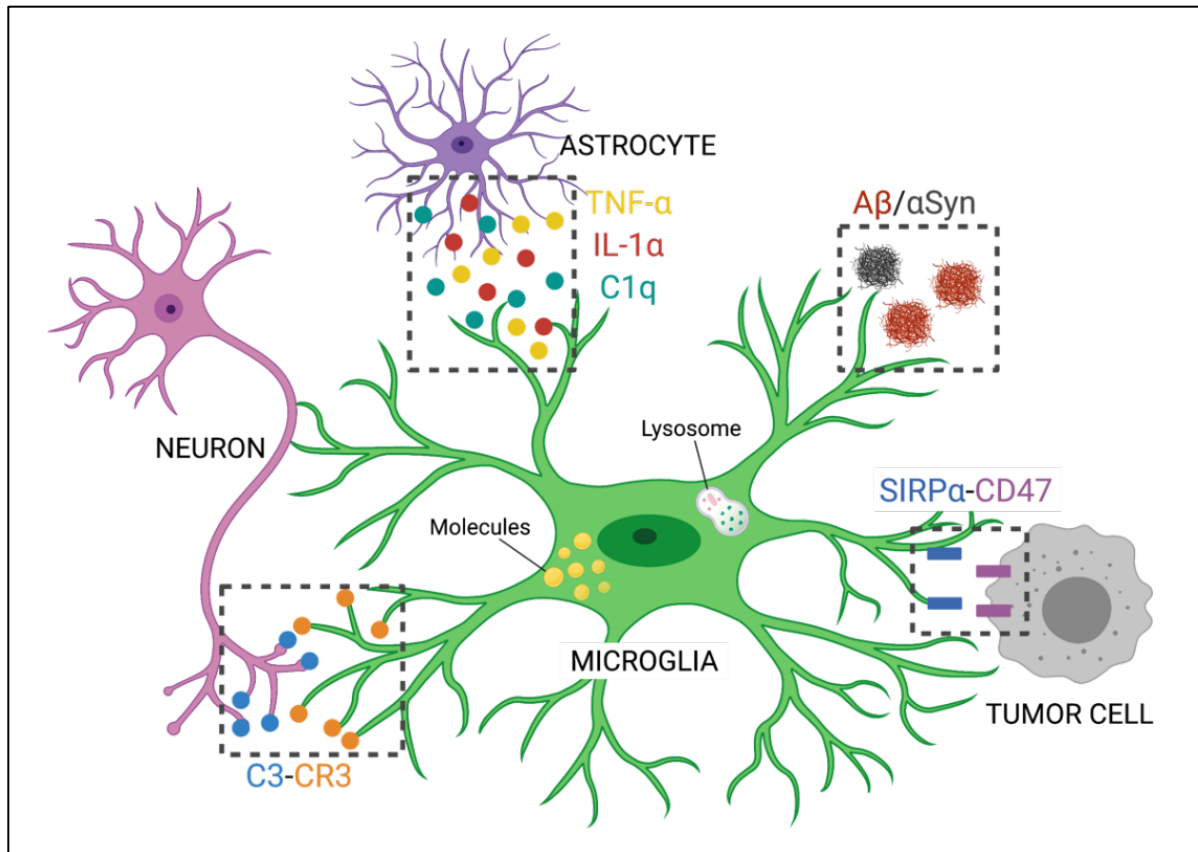


**Figure 1.4** The myriad functions of microglia. Pruning of neuronal synapses; Secretion of cytokines; Phagocytosis of A $\beta$  and  $\alpha$ Syn; Interaction with tumor cells via SIRP $\alpha$  and CD47.

Different substrate materials may be recognized and internalized by different protein receptors on the cell surface. For example, P2Y6 receptors recognize bacteria, A $\beta$  is recognized by the TREM2 and CD36 receptors, MERTK proteins recognize apoptotic cells, etc. (Table 1-1). There are several phagocytic receptors yet to be identified on microglia that may be essential for developing molecules to target the phagocytic function during disease pathogenesis. No doubt, microglial phagocytosis is integral to CNS homeostasis.

**Table 1-1** Receptors on microglia corresponding to target substrates for phagocytosis.

Target substrate	Corresponding receptors	References
Bacteria bioparticles	P2Y6R, TREM2	[31]
Zymosan bioparticles	TLR2/TLR6, CR3, Dectin-1	[32], [33], [34]
Apoptotic neurons	P2Y6R, Vitronectin receptors ( $\alpha v\beta 3$ or $\alpha v\beta 5$ integrins), MERTK, CR3, TREM2	[35]
Viable/live neurons	LRP, CRT	[36]
Apoptotic cells	MERTK, TIM4, uncharacterized phosphatidylserine receptors	[37], [38]
Amyloid $\beta$	TLRs, TREM2, CD36, CD47, $\alpha 6\beta 1$	[39], [40], [41]
$\alpha$ synuclein	TLR2/4, MRC1, Axl TAM, Fc $\gamma$ R, Clathrin	[42], [43], [44], [45], [46]
Myelin debris	CL-P1, LRP1, CR3, SRAI/II	[47], [48], [49]
Glioma tumor cells	Siglec-H	[50]

While microglia are known to become more “pro-inflammatory” in neurodegenerative disorders, glioma-associated microglia (GAMs) show the opposite phenotype in cancer microenvironments. Glioblastoma multiforme (GBM) is one of the most aggressive form of tumors in humans with very low survival rate—about 15 months of median survival[15]. GAMs in GBM exhibit “anti-inflammatory” or “pro-tumor” cell states with immunosuppressive function and reduced phagocytic capacity and are therefore unable to eliminate the tumor cells from the brain tissue. Thus, microglia in GBM promote tumor growth and hinder tumor cell death[15]. A noteworthy cellular cross-talk in the GBM microenvironment is the interaction between the SIRP $\alpha$  protein expressed on GAMs and CD47, a don’t-eat me signal present on glioma cells[51], [52]. This interaction renders the GAMs unable to engulf the tumor cells and hence disrupting this interaction may be beneficial for facilitating the clearance of CD47-expressing tumor cells.

In addition to phagocytosis, microglia actively secrete cytokines to influence their surroundings and affect the functions of their neighboring cells[22]. For example, when microglia become “classically activated” by an inflammatory trigger (for example, with lipopolysaccharide (LPS), a molecule shed by gram negative bacteria), they secrete cytokines such as tumor necrosis factor-

alpha (TNF- $\alpha$ ), interleukin one alpha (IL-1 $\alpha$ ), along with nitric oxide (NO) and other signaling molecules[53]. With the help of these cytokines, microglia actively communicate with other neuronal and non-neuronal glial cells like astrocytes and oligodendrocytes to regulate all aspects of brain function. A noteworthy cytokine-mediated mechanism was recently identified wherein cytokines released by activated microglia (TNF- $\alpha$  and IL-1 $\alpha$  along with the complement protein C1q) induce astrocytes to become “reactive” (or ‘A1’ phenotype) and kill neurons via the secretion of an unknown toxic factor[54]. Thus, activated microglia may cause neuronal death via reactive astrocytes and mediate neurodegeneration.

#### **1.4 Astrocytes are key players of CNS immunity**

Even though astrocytes are not traditional immune cells, they perform several immune cell-like functions and are key players of the CNS immunity. Just like microglia, astrocytes are also highly heterogeneous cells exhibiting various phenotypes depending on their location in the brain, sex and age of the organism, etc. Inflammatory stimuli or injury causes “resting” astrocytes to become reactive. A1 or neurotoxic reactive astrocytes are induced by a pathogen or a disease stimuli such as LPS[54]. These A1 astrocytes upregulate many complement cascade proteins such as C1R, C1S, C2, C3, C4, etc., and cause neuronal death by the direct secretion of toxic factors[54]. On the other hand, A2 or neurotrophic astrocytes are seen in injury (like ischemic stroke) wherein they secrete several healing neurotrophic factors that promote neuronal survival such as Brain-derived neurotrophic factor (BDNF), leukemia inhibitory factor (LIF), etc. These A2 or protective astrocytes are helpful in limiting the size of stroke or ischemic lesions as well as restoring the blood brain barrier[55]–[57].

Astrocytes are active phagocytes. They phagocytose synapses in the developing brain as well as in the adult brain[53]. They also secrete soluble substances that initiate synapse formation and function. They exhibit phagocytic capabilities towards neuronal cell debris[58], amyloid-beta (A $\beta$ ) aggregates[59], and other substrates and also secrete cytokines in response to inflammatory stimuli. Astrocytes and microglia act in a highly coordinated fashion wherein astrocytes even perform compensatory phagocytosis when microglia become dysfunctional in chronic inflammation[60]. The microglia-astrocyte cross-talk during inflammation is a critical event driving the changes in cell states and function in disease. For example, the A1 reactive astrocytes, upon induction by

activated microglia, directly affect neuronal survival by killing injured neurons and oligodendrocytes via an unknown toxic factor[54]. These A1 reactive astrocytes have drastically reduced phagocytic capacity and are unable to phagocytose synaptosomes and myelin debris[54]. Thus, “normal” as well as reactive astrocytes influence CNS development, health, and disease via their phagocytic function.

Like microglia, astrocytes play a role in the innate immune responses by secreting cytokines and chemokines in response to an inflammatory stimuli. In fact, one way by which microglia and astrocytes communicate with each other is by the expression and release of these factors, for example, in a model of traumatic brain injury, reactive astrocytes secrete chemokine ligand 2 or CCL2 that interacts with the corresponding chemokine receptor 2 or CCR2 expressed on microglia[61]. Another important effect of astrocytic cytokine and chemokine secretion is the recruitment and activation of peripheral immune cells into the brain microenvironment and modulation of the blood brain barrier (BBB). The reactivity of astrocytes and the type of inflammatory factor produced may also influence the reactivity of the surrounding immune cell. For example, the release of IFN- $\gamma$ , IL-12, etc. by astrocytes after injury or infection shifts microglia to a pro-inflammatory phenotype[62]. Astrocytes can also produce classical anti-inflammatory cytokines like IL-10 and TGF- $\beta$  that in turn also induced anti-inflammatory phenotypes in microglia or macrophages. Thus, the type of secretory factors by astrocytes are context dependent.

There is still much work to be done in understanding the adaptive immune responses in the CNS. Adaptive immunity is established by the T and B lymphocytes that generate specific responses to antigens with specialized receptors on their cell surface[63]. Unlike innate immunity that acts as a first line of defense and mounts a response almost immediately after an infection or injury, adaptive immunity is established as a slower, secondary response that is sustained for longer periods of time. Microglia and macrophages are classical cells of innate immunity in the CNS. They express scavenger receptors like CD36 and Receptor for advanced glycation endproducts (RAGE) that interacts directly with the infectious or toxic agent and secretes inflammatory factors in order to clear out the tissue damage[59]. There is some evidence that highlights astrocytes to be active components of the adaptive immune responses in CNS inflammation. Astrocytes are the main sources of chemoattractants like CCL5, CXCL10, CXCL12, etc. that recruit T and B cells.

CXCL10, for example, is a key ligand for CX3CR1 expressed on CD8<sup>+</sup> T cells during infection [64] and CXCL12 is a chemoattractant of T cells and B cells in models of multiple sclerosis[65]. Perhaps one of the most important features of astrocytes is the ability to upregulate major histocompatibility complex (MHC) class I and II molecules on their surface that directly interacts with CD8<sup>+</sup> and CD4<sup>+</sup> T cells[66]. In the periphery, these molecules are primarily expressed by antigen presenting cells (APCs) to recruit and activate T cells to mount an aggressive immune response during inflammation. Astrocytes, thus act as APCs in the CNS and may present phagocytosed components of cell debris, synapses, or neurons to the adaptive immune cells and “train” these cells to mount a sustained immune response to maintain CNS homeostasis. It is noteworthy that astrocytic endfeet are in constant interaction with peripheral leukocytes via the cerebral vasculature and blood vessels and these interactions may be exaggerated or suppressed during injury or disease. Thus, these regions of astrocyte endfeet-blood vessel interactions are worthy of further investigation in various disease paradigms to understand the cellular and molecular underpinnings of adaptive immunity in the CNS.

## 1.5 References

- [1] B. A. Barres, “The Mystery and Magic of Glia: A Perspective on Their Roles in Health and Disease,” *Neuron*, vol. 60, no. 3, pp. 430–440, Nov. 2008.
- [2] B. A. Barres, “What is a glial cell?,” *Glia*, vol. 43, no. 1, pp. 4–5, Jul. 2003.
- [3] J. del Río-Hortega Bereciartu, “Pío del Río-Hortega: The Revolution of Glia,” *Anat. Rec.*, vol. 303, no. 5, pp. 1232–1241, May 2020.
- [4] F. C. Bennett *et al.*, “A Combination of Ontogeny and CNS Environment Establishes Microglial Identity,” *Neuron*, vol. 98, no. 6, pp. 1170–1183.e8, Jun. 2018.
- [5] K. Kierdorf *et al.*, “Microglia emerge from erythromyeloid precursors via Pu.1-and Irf8-dependent pathways,” *Nat. Neurosci.*, vol. 16, no. 3, pp. 273–280, Mar. 2013.
- [6] M. L. Bennett *et al.*, “New tools for studying microglia in the mouse and human CNS,” *Proc. Natl. Acad. Sci. U. S. A.*, vol. 113, no. 12, pp. E1738–E1746, Mar. 2016.
- [7] A. Buttgereit *et al.*, “Sall1 is a transcriptional regulator defining microglia identity and function,” *Nat. Immunol.*, vol. 17, no. 12, pp. 1397–1406, Dec. 2016.
- [8] G. L. McKinsey *et al.*, “A new genetic strategy for targeting microglia in development and disease,” *Elife*, vol. 9, pp. 1–34, Jun. 2020.

- [9] A. M. Jurga, M. Paleczna, and K. Z. Kuter, “Overview of General and Discriminating Markers of Differential Microglia Phenotypes,” *Front. Cell. Neurosci.*, vol. 14, p. 198, Aug. 2020.
- [10] R. M. Ransohoff, “A polarizing question: Do M1 and M2 microglia exist,” *Nature Neuroscience*, vol. 19, no. 8. Nature Publishing Group, pp. 987–991, 01-Aug-2016.
- [11] Y. Tang and W. Le, “Differential Roles of M1 and M2 Microglia in Neurodegenerative Diseases,” *Molecular Neurobiology*, vol. 53, no. 2. Humana Press Inc., pp. 1181–1194, 01-Mar-2016.
- [12] V. Stratoulis, J. L. Venero, M. Tremblay, and B. Joseph, “Microglial subtypes: diversity within the microglial community,” *EMBO J.*, vol. 38, no. 17, Sep. 2019.
- [13] H. Keren-Shaul *et al.*, “A Unique Microglia Type Associated with Restricting Development of Alzheimer’s Disease,” *Cell*, vol. 169, no. 7, pp. 1276–1290.e17, Jun. 2017.
- [14] Q. Li *et al.*, “Developmental Heterogeneity of Microglia and Brain Myeloid Cells Revealed by Deep Single-Cell RNA Sequencing,” *Neuron*, vol. 101, no. 2, pp. 207–223.e10, Jan. 2019.
- [15] D. H. Gutmann and H. Kettenmann, “Microglia/Brain Macrophages as Central Drivers of Brain Tumor Pathobiology,” *Neuron*, vol. 104, no. 3. Cell Press, pp. 442–449, 06-Nov-2019.
- [16] E. C. Wright-Jin and D. H. Gutmann, “Microglia as Dynamic Cellular Mediators of Brain Function,” *Trends Mol. Med.*, vol. 25, no. 11, pp. 967–979, 2019.
- [17] S. Safaiyan, S. Besson-Girard, T. Gberk Kaya, M. Brendel, O. Gokce, and M. Simons Correspondence, “White matter aging drives microglial diversity,” *Neuron*, Feb. 2021.
- [18] J. Sakai, “How synaptic pruning shapes neural wiring during development and, possibly, in disease,” *Proc. Natl. Acad. Sci. U. S. A.*, vol. 117, no. 28, pp. 16096–16099, Jul. 2020.
- [19] R. C. Paolicelli *et al.*, “Synaptic pruning by microglia is necessary for normal brain development,” *Science (80-. )*, vol. 333, no. 6048, pp. 1456–1458, Sep. 2011.
- [20] B. Stevens *et al.*, “The Classical Complement Cascade Mediates CNS Synapse Elimination,” *Cell*, vol. 131, no. 6, pp. 1164–1178, Dec. 2007.
- [21] D. P. Schafer *et al.*, “Microglia Sculpt Postnatal Neural Circuits in an Activity and Complement-Dependent Manner,” *Neuron*, vol. 74, no. 4, pp. 691–705, May 2012.
- [22] A. Aguzzi, B. A. Barres, and M. L. Bennett, “Microglia: Scapegoat, saboteur, or something else?,” *Science*, vol. 339, no. 6116. pp. 156–161, 2013.



- [23] S. Gordon, “Phagocytosis: An Immunobiologic Process,” *Immunity*, vol. 44, no. 3. pp. 463–475, 2016.
- [24] A. Aderem and D. M. Underhill, “Mechanisms of phagocytosis in macrophages,” *Annu. Rev. Immunol.*, vol. 17, pp. 593–623, 1999.
- [25] D. J. Selkoe, “Alzheimer’s disease,” *Cold Spring Harbor Perspectives in Biology*, vol. 3, no. 7. pp. 1–16, 2011.
- [26] D. J. Selkoe, “The molecular pathology of Alzheimer’s disease,” *Neuron*, vol. 6, no. 4. pp. 487–498, 1991.
- [27] D. V. Hansen, J. E. Hanson, and M. Sheng, “Microglia in Alzheimer’s disease,” *J. Cell Biol.*, vol. 217, no. 2, pp. 459–472, Feb. 2018.
- [28] A. Samii, J. G. Nutt, and B. R. Ransom, “Parkinson’s disease,” in *Lancet*, 2004, vol. 363, no. 9423, pp. 1783–1793.
- [29] M. S. Ho, “Microglia in parkinson’s disease,” in *Advances in Experimental Medicine and Biology*, vol. 1175, Springer New York LLC, 2019, pp. 335–353.
- [30] D. A. Galloway, A. E. M. Phillips, D. R. J. Owen, and C. S. Moore, “Phagocytosis in the brain: Homeostasis and disease,” *Front. Immunol.*, vol. 10, no. MAR, Apr. 2019.
- [31] E. N. N’Diaye *et al.*, “TREM-2 (triggering receptor expressed on myeloid cells 2) is a phagocytic receptor for bacteria,” *J. Cell Biol.*, vol. 184, no. 2, pp. 215–223, 2009.
- [32] D. M. Underhill, “Macrophage recognition of zymosan particles,” *J. Endotoxin Res.*, vol. 9, no. 3, pp. 176–180, 2003.
- [33] V. Le Cabec, S. Carréno, A. Moisand, C. Bordier, and I. Maridonneau-Parini, “Complement Receptor 3 (CD11b/CD18) Mediates Type I and Type II Phagocytosis During Nonopsonic and Opsonic Phagocytosis, Respectively,” *J. Immunol.*, vol. 169, no. 4, pp. 2003–2009, 2002.
- [34] J. Herre *et al.*, “Dectin-1 uses novel mechanisms for yeast phagocytosis in macrophages,” *Blood*, vol. 104, no. 13, pp. 4038–4045, 2004.
- [35] K. Takahashi, C. D. P. Rochford, and H. Neumann, “Clearance of apoptotic neurons without inflammation by microglial triggering receptor expressed on myeloid cells-2,” *J. Exp. Med.*, vol. 201, no. 4, pp. 647–657, 2005.
- [36] M. Fricker, M. J. Oliva-Martín, and G. C. Brown, “Primary phagocytosis of viable neurons by microglia activated with LPS or A $\beta$  is dependent on calreticulin/LRP phagocytic signalling,” *J. Neuroinflammation*, vol. 9, 2012.

- [37] R. S. Scott *et al.*, “Phagocytosis and clearance of apoptotic cells is mediated by MER,” *Nature*, vol. 411, no. 6834, pp. 207–211, 2001.
- [38] C. Nishi, S. Toda, K. Segawa, and S. Nagata, “Tim4- and MerTK-Mediated Engulfment of Apoptotic Cells by Mouse Resident Peritoneal Macrophages,” *Mol. Cell. Biol.*, vol. 34, no. 8, pp. 1512–1520, 2014.
- [39] Y. Zhao *et al.*, “TREM2 Is a Receptor for  $\beta$ -Amyloid that Mediates Microglial Function,” *Neuron*, vol. 97, no. 5, pp. 1023–1031.e7, Mar. 2018.
- [40] F. L. Yeh, Y. Wang, I. Tom, L. C. Gonzalez, and M. Sheng, “TREM2 Binds to Apolipoproteins, Including APOE and CLU/APOJ, and Thereby Facilitates Uptake of Amyloid-Beta by Microglia,” *Neuron*, vol. 91, no. 2, pp. 328–340, Jul. 2016.
- [41] J. Koenigsnecht and G. Landreth, “Microglial phagocytosis of fibrillar  $\beta$ -amyloid through a  $\beta$ 1 integrin-dependent mechanism,” *J. Neurosci.*, vol. 24, no. 44, pp. 9838–9846, Nov. 2004.
- [42] E. Janda, L. Boi, and A. R. Carta, “Microglial phagocytosis and its regulation: A therapeutic target in parkinson’s disease?,” *Front. Mol. Neurosci.*, vol. 11, 2018.
- [43] D. Lecca *et al.*, “Boosting phagocytosis and anti-inflammatory phenotype in microglia mediates neuroprotection by PPAR $\gamma$  agonist MDG548 in Parkinson’s disease models,” *Br. J. Pharmacol.*, vol. 175, no. 16, pp. 3298–3314, 2018.
- [44] L. Fourgeaud *et al.*, “TAM receptors regulate multiple features of microglial physiology,” *Nature*, vol. 532, no. 7598, pp. 240–244, 2016.
- [45] S. Cao, D. G. Standaert, and A. S. Harms, “The gamma chain subunit of Fc receptors is required for alpha-synuclein-induced pro-inflammatory signaling in microglia,” *J. Neuroinflammation*, vol. 9, 2012.
- [46] J. Liu, Y. Zhou, Y. Wang, H. Fong, T. M. Murray, and J. Zhang, “Identification of proteins involved in microglial endocytosis of  $\alpha$ -synuclein,” *J. Proteome Res.*, vol. 6, no. 9, pp. 3614–3627, 2007.
- [47] J. F. J. Bogie *et al.*, “Scavenger receptor collectin placenta 1 is a novel receptor involved in the uptake of myelin by phagocytes,” *Sci. Rep.*, vol. 7, 2017.
- [48] A. Gaultier *et al.*, “Low-density lipoprotein receptor-related protein 1 is an essential receptor for myelin phagocytosis,” *J. Cell Sci.*, vol. 122, no. 8, pp. 1155–1162, Apr. 2009.
- [49] F. Reichert and S. Rotshenker, “Complement-receptor-3 and scavenger-receptor-AI/II mediated myelin phagocytosis in microglia and macrophages,” *Neurobiol. Dis.*, vol. 12, no. 1, pp. 65–72, 2003.

- [50] J. Kopatz *et al.*, “Siglec-h on activated microglia for recognition and engulfment of glioma cells,” *Glia*, vol. 61, no. 7, pp. 1122–1133, Jul. 2013.
- [51] G. Hutter *et al.*, “Microglia are effector cells of CD47-SIRP $\alpha$  antiphagocytic axis disruption against glioblastoma,” *Proc. Natl. Acad. Sci. U. S. A.*, vol. 116, no. 3, pp. 997–1006, Jan. 2019.
- [52] F. Li *et al.*, “Blocking the CD47-SIRP $\alpha$  axis by delivery of anti-CD47 antibody induces antitumor effects in glioma and glioma stem cells,” *Oncoimmunology*, vol. 7, no. 2, Feb. 2018.
- [53] J. B. Zuchero and B. A. Barres, “Glia in mammalian development and disease,” *Dev.*, vol. 142, no. 22, pp. 3805–3809, Nov. 2015.
- [54] S. A. Liddelow *et al.*, “Neurotoxic reactive astrocytes are induced by activated microglia,” *Nature*, vol. 541, no. 7638, pp. 481–487, Jan. 2017.
- [55] J. R. Faulkner, J. E. Herrmann, M. J. Woo, K. E. Tansey, N. B. Doan, and M. V. Sofroniew, “Reactive Astrocytes Protect Tissue and Preserve Function after Spinal Cord Injury,” *J. Neurosci.*, vol. 24, no. 9, pp. 2143–2155, Mar. 2004.
- [56] D. J. Myer, “Essential protective roles of reactive astrocytes in traumatic brain injury,” *Brain*, vol. 129, no. 10, pp. 2761–2772, Jul. 2006.
- [57] L. Li *et al.*, “Protective role of reactive astrocytes in brain ischemia,” *J. Cereb. Blood Flow Metab.*, vol. 28, no. 3, pp. 468–481, Mar. 2008.
- [58] N. M. Wakida *et al.*, “Phagocytic response of astrocytes to damaged neighboring cells,” *PLoS One*, vol. 13, no. 4, 2018.
- [59] R. S. Jones, A. M. Minogue, T. J. Connor, and M. A. Lynch, “Amyloid- $\beta$ -induced astrocytic phagocytosis is mediated by CD36, CD47 and RAGE,” *J. Neuroimmune Pharmacol.*, vol. 8, no. 1, pp. 301–311, Mar. 2013.
- [60] H. Konishi *et al.*, “Astrocytic phagocytosis is a compensatory mechanism for microglial dysfunction,” *EMBO J.*, vol. 39, no. 22, p. e104464, Nov. 2020.
- [61] M. He *et al.*, “Astrocyte-derived CCL2 is associated with m1 activation and recruitment of cultured microglial cells,” *Cell. Physiol. Biochem.*, vol. 38, no. 3, pp. 859–870, Mar. 2016.
- [62] F. O. Martinez, L. Helming, and S. Gordon, “Alternative activation of macrophages: An immunologic functional perspective,” *Annual Review of Immunology*. 2009.

- [63] A. Waisman, R. S. Liblau, and B. Becher, “Innate and adaptive immune responses in the CNS,” *The Lancet Neurology*, vol. 14, no. 9. Lancet Publishing Group, pp. 945–955, 01-Sep-2015.
- [64] B. Zhang, Y. K. Chan, B. Lu, M. S. Diamond, and R. S. Klein, “CXCR3 Mediates Region-Specific Antiviral T Cell Trafficking within the Central Nervous System during West Nile Virus Encephalitis,” *J. Immunol.*, 2008.
- [65] M. Krumbholz *et al.*, “Chemokines in multiple sclerosis: CXCL12 and CXCL13 up-regulation is differentially linked to CNS immune cell recruitment,” *Brain*, 2006.
- [66] Y. Dong and E. N. Benveniste, “Immune function of astrocytes,” *Glia*, vol. 36, no. 2, pp. 180–190, Nov. 2001.

## CHAPTER 2. AN APPETITE FOR AMYLOID

The amyloid beta peptide is one of the key pathological features of Alzheimer's disease. The aggregation of amyloid beta into oligomers and fibrils causes damage to neurons as well as activation of glial cells. Microglia phagocytose the peptide aggregates in the early stages of the disease but the dysfunctional state of microglia in later disease stages is hypothesized to contribute to disease progression and increased neuroinflammation. This chapter focusses on Alzheimer's disease, characteristics of the amyloid beta ( $A\beta$ ) peptide and the role of microglial as well as astrocytic phagocytosis of  $A\beta$ .

### 2.1 Alzheimer's Disease—An introduction

Alzheimer's Disease (AD) is the most common type of dementia affecting more than 40 million individuals worldwide. Ranking sixth in the top ten causes of deaths in the United States (WHO, 2019)[1], it is the only disease that has no cure, no prevention, and no proven way to slow its progression. As of 2020, AD is the most expensive disease costing the nation around \$226 billion and the costs are expected to increase five-fold (over \$1 trillion) by the year 2050[1]. These staggering statistics calls for an immediate need for effective and innovative therapeutic strategies to combat this devastating disease.

AD is characterized by progressive neurodegeneration resulting in cognitive decline and memory loss. Pathologically, it is characterized by progressive extracellular protein deposits and neuron death as well as gliosis (Figure 2.1). Besides aging, one of the most common risk factors for AD is the inheritance of the Apolipoprotein E- $\epsilon$ 4 (APOE $\epsilon$ 4) polymorphic gene[2]. Produced by the astrocytes in the CNS, the APOE protein is essential for cholesterol transport in the bloodstream and to the neurons. It is estimated that 40-60% of the individuals diagnosed with AD carry one or two copies of the APOE $\epsilon$ 4 gene[1]. Other recently discovered genetic factors that increase the risk of developing AD are mutations in PSEN1/PSEN2, APP, CLU, INPP5D, SORL1, ABCA7, SLC24A4, TREM2, etc.[3] Although many hypotheses exist to explain the causes and consequences of the underlying cellular and molecular mechanisms involved in AD, the eventual decline in the physiological conditions remains universal. Individuals affected by AD show

progressive deterioration in cognition and memory accompanied by additional symptoms such as erratic mood swings, speaking and writing problems, poor judgement, paranoia and hallucinations, withdrawal from daily activities, changes in personality and decline in the overall quality of life[1].

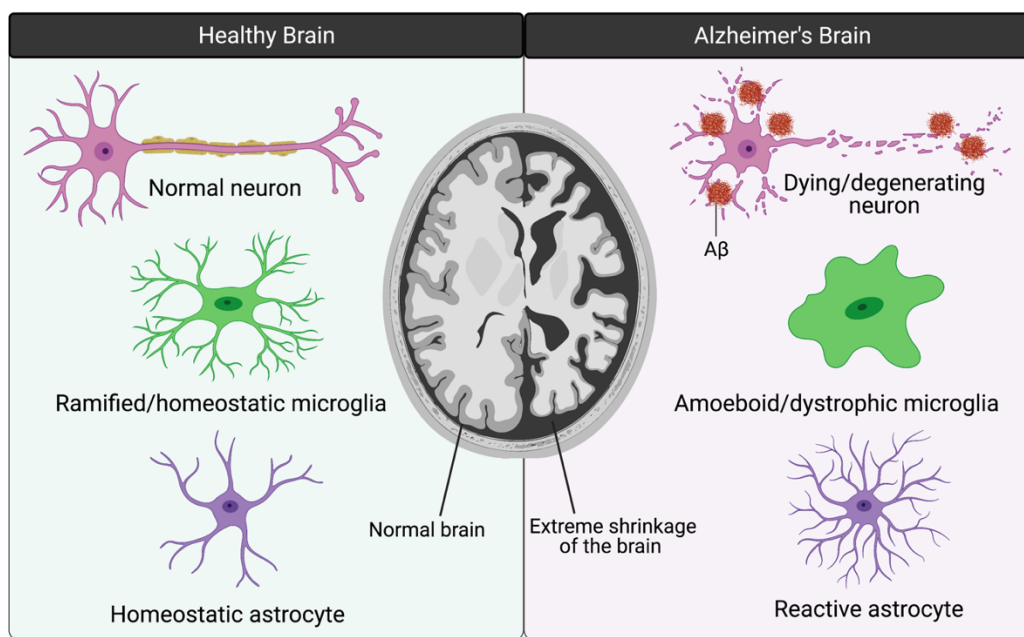


**Figure 2.1** Characteristic features of healthy versus Alzheimer's brain.

Although no drug exists to treat AD itself, five drugs have been approved by the FDA since 1993 to treat the disease symptoms. Between 2002 to 2020 alone, there have been around 300 failed clinical trials conducted by Eli Lilly, Roche, Johnson & Johnson, Pfizer, and other giant pharmaceutical companies. Out of the five FDA approved drugs, donepezil (1996), rivastigmine (2000) and galantamine (2001) are cholinesterase inhibitors used to treat mild to moderate AD[1]. These compounds inhibit the breakdown of acetylcholine (ACh) – a neurotransmitter essential for memory, attention, decision making, and thinking. It has been shown that individuals with AD produce less ACh in their brains as the disease progresses and therefore, these drugs can only be used for a short term. Moderate to severe AD is treated with an N-Methyl-D-aspartate (NMDA) receptor antagonist called memantine (2003). In normal levels, glutamate – a neurotransmitter, is involved in learning and memory. Defected neural cells of AD have been shown to release excess amounts of glutamate that leads to increased neural damage and death. Memantine binds to NMDA receptors on neurons and therefore inhibits the activity of glutamate. The fifth approved drug is a

combination of donepezil and memantine to increase effectivity of the treatment. A few other drugs currently being tested are  $\beta$ - and  $\gamma$ -secretase inhibitors—enzymes that modulate pathogenic proteins in AD ( $A\beta$  and tau), active monoclonal antibodies, etc.

Today, the world is in a dire need of a novel therapy for AD by either inhibiting nerve cell death or delaying the damage. Treatments that directly target  $A\beta$  production and/or degradation have all been unsuccessful so far. An alternate immunotherapeutic strategy may be to harness microglia and astrocytes to mitigate inflammation and slow down disease progression. Treatments that encompass multiple cellular targets through diverse pathway interventions may be promising.

## **2.2 Amyloid beta**

A hallmark characteristic of AD is the abnormal accumulation of amyloid beta ( $A\beta$ ), a ~4 kDa peptide that is cleaved from the much larger Amyloid Precursor Protein (APP), an integral transmembrane glycoprotein, is sequentially broken down by  $\beta$ - and  $\gamma$ -secretases on neuronal cell membranes. The  $A\beta$  fragments produced can be of any length consisting of 37-49 amino acid residues[4], however,  $A\beta$ 40 and  $A\beta$ 42 are the most common isoforms and the  $A\beta$ 42 fragment is the major toxic peptide found in the brains of AD patients. Misfolded  $A\beta$  monomers accumulate to form soluble oligomers that can be toxic to the neighboring neurons[5]. The progressive buildup of the oligomers leads to the formation of insoluble protein aggregates, mainly to be in the fibrillar form, and are known as senile plaques which are thought to be the major culprit in AD (Figure 2.2). Recently, studies have shown that  $A\beta$  oligomers are more toxic than the plaques and may be the key player of disease toxicity[6].  $A\beta$  oligomers can also get deposited on the blood capillaries and restrict cerebral blood flow and thus oxygen supply to the brain[7].

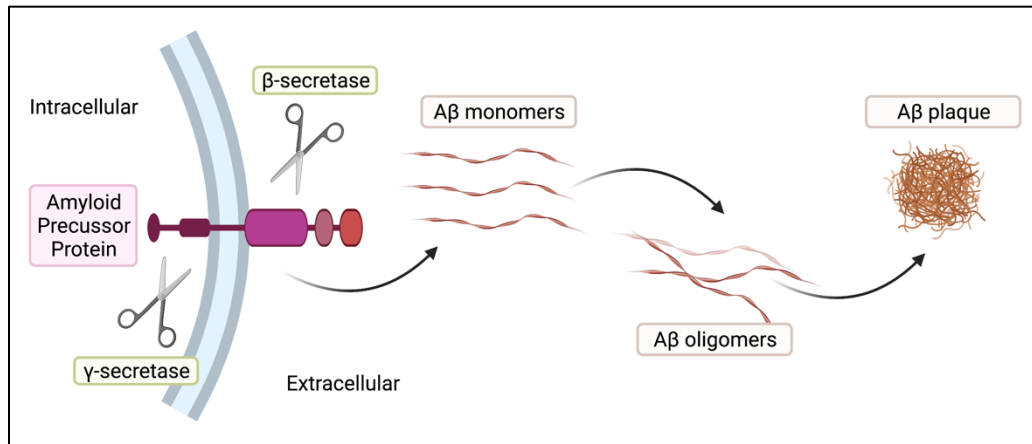


**Figure 2.2** Simplified mechanism of A $\beta$  secretion and plaque formation. A $\beta$  monomer is released from APP upon  $\beta$ - and  $\gamma$ -secretase activity into the extracellular microenvironment. A $\beta$  monomers form oligomers and later plaques consisting of various forms of A $\beta$  aggregates.

An alternate hypothesis that has emerged in the recent years is the role for A $\beta$  as an antimicrobial peptide (AMP). Studies have demonstrated that A $\beta$  oligomers exhibit antimicrobial properties and protects against fungal and bacterial infections in mouse, worm, and cell culture models of AD[8], [9]. These studies argue that A $\beta$  fibrillation is a necessary mechanism to entrap microbial peptides within the plaques in order to prevent their propagation into the neighboring cells causing their destruction and death. Thus, A $\beta$  may exhibit a protective or damaging role and these studies need further careful evaluation in the clinical AD models.

In addition to extracellular A $\beta$  deposits, intracellular accumulation of hyperphosphorylated tau proteins are another hallmark of AD pathology. Alterations in the signaling pathways and the aberrant neural networks can also be characterized by the build-up of hyperphosphorylated tau proteins within the nerve cell bodies. The tau protein aggregates that form the neurofibrillary tangles disrupt the cytoskeletal backbone of the neurons that eventually leads to the disintegration of the transport system within the cell and overall collapse of the cellular structure.

The misfolded proteins are known to induce immune responses upon binding to receptors on astrocytes and microglial cells causing inflammation in the affected regions of the brain and further promote disease progression. Some of the inflammatory factors such as IL-1 $\beta$ , IL-6, IL-12, IFN- $\gamma$ , TNF- $\alpha$ , NO, and ROS are shown to be upregulated in the cerebrospinal fluid (CSF) of AD patients as well as in the brains of AD mice and therefore have been the focus of new therapeutic



approaches to treat neuroinflammation in AD. However, the levels of these molecules may be highly dependent on the disease stage which needs further investigation.

### **2.3 Microglial phagocytosis of A $\beta$**

The precise role of microglia in AD is still unclear. Microglia are required for phagocytosis of A $\beta$  and tau aggregates, dying neurons, and cell debris to maintain CNS homeostasis. In addition to phagocytosis, microglia also secrete inflammatory molecules towards their target substrates. How these two processes are affected through the course of AD and how a functional balance is maintained between microglial phagocytosis and its neurotoxic inflammatory phenotype still remains elusive.

Newly formed A $\beta$  monomers are released to the extracellular space where they are cleared by multiple mechanisms including (i) drainage by the interstitial fluid and CSF [10], (ii) transport across the blood vessels where they enter the circulation and are cleared up by the liver, and/or (iii) by microglial and astrocytic phagocytosis. When A $\beta$  is released into the extracellular space, they can be “carried by” chaperone proteins like APOE that influence their metabolism, aggregation, transport, and clearance. APOE is a lipid transport protein (a lipoprotein) expressed as three different isoforms: APOE2, APOE3, and APOE4. E3 is the most common isoform, and E4 is responsible for a genetic predisposition to AD, increasing the disease risk by approximately 3-fold more than the E3 allele, whereas E2 decreases AD risk[11]. Astrocytes and microglia secrete APOE into the interstitial fluid (ISF) of the brain. The interaction and binding of A $\beta$  and APOE in the ISF influences their endocytic clearance. The binding of APOE to A $\beta$  taken up by the cells through receptor-mediated endocytosis mediated by LRP5 (Low Density Lipoprotein Receptor (LDLR)-related proteins). LDLRs regulate aggregation and also the cellular uptake of A $\beta$ . LRP5 and RAGE proteins also regulate the transport of A $\beta$  across the BBB[12], [13]. The protein-protein association of A $\beta$  with APOE thus directly influences A $\beta$  levels in the brain and the dysregulation in APOE function may result in aggregation of A $\beta$  in AD.

Microglia can phagocytose and degrade A $\beta$  and its various aggregated states. Exposure to A $\beta$  “activates” microglia i.e. causes a change in cell state from a homeostatic to reactive phenotype along with a cascade of downstream changes. In the early stages of AD, microglia may readily

clear up the A $\beta$  monomers as well as the soluble oligomers and thereby delay disease progression by limiting senile plaque formation. One of the first studies to note a relationship between microglial reactivity and association with A $\beta$  plaques was published in 1998. This study demonstrated an increased number of intensely labeled microglia with enlarged cell bodies clustered in and around the plaques in a transgenic mouse model of AD[14]. Today, we know that microglia closely associate with A $\beta$  and exhibit dramatic changes in their transcriptomes and proteomes with functional deficits[15]. While these plaque-associated microglia show genomic changes and are unable to efficiently phagocytose the plaques, it may be hypothesized that these microglial subsets exhibit a “suppressed” or “exhausted” cell states. It is therefore important to evaluate the functional consequences of these changes that can eventually be targeted to boost microglial uptake of A $\beta$  using immunomodulatory therapies.

Phagocytosis is an evolutionarily conserved process in cellular immunity. It is described as the recognition, engulfment, and degradation of solid extracellular substrates ( $>0.5\ \mu\text{m}$ ) by “professional phagocytes” namely, neutrophils, natural killer cells, and macrophages[16]. Phagocytosis was first observed in transparent starfish larvae in 1884 by Elie Metchnikoff [17]. Other cells like epithelial cells, fibroblasts, pericytes, lymphocytes, etc can also eliminate apoptotic cells and other debris from their environment under special circumstances. Phagocytosis is a receptor-mediated process and is dependent on actin-filament polymerization i.e., when a phagocyte interacts with its target substrate, actin filaments in its plasma membrane depolymerize and extend to engulf the substrate within a specialized vesicle known as a phagosomes. Maturation of the phagosome involves its fusion with the lysosome to form a phagolysosome that prepares the foreign substrate for digestion. During the maturation of the phagosome, the pH of the intracellular vesicle gradually decreases to around 4.0 thereby initiating the enzymatic degradation of the target substrate (Figure 2.3).

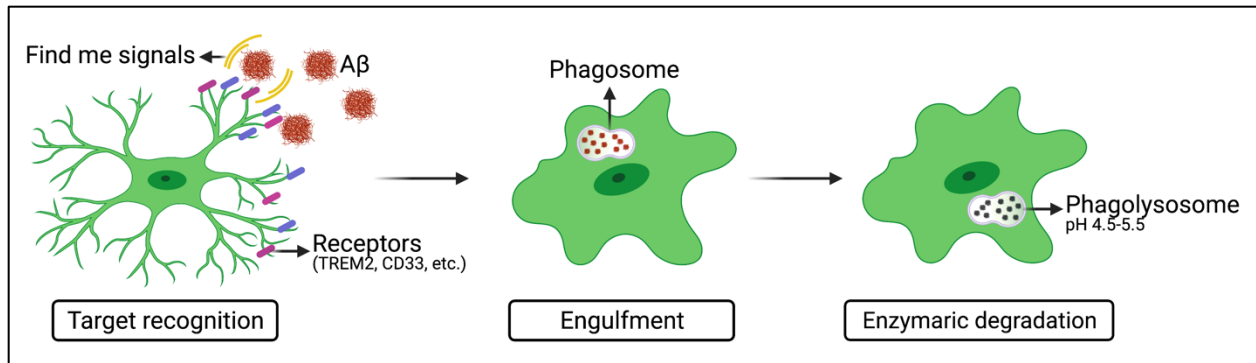


**Figure 2.3** Mechanism of microglial Aβ phagocytosis. Phagocytosis is initiated with target (Aβ) recognition via the find me and eat me signals. The receptors are then involved in the engulfment of Aβ into the phagosomes. The internalized Aβ is enzymatically degraded by the hydrolytic enzymes in the acidic phagolysosomal compartments.

Microglial membrane receptors bind to Aβ leading to cellular “activation”, Aβ phagocytosis and clearance. Several receptors on microglial surface have already been identified to specifically bind and respond to Aβ. For example, scavenger receptors including scavenger receptor A-1 (SCARA-1), MARCO, scavenger receptor B-1 (SCARB-1), CD36 and the receptor for advanced glycation end product (RAGE)[18], selected G-protein coupled receptors (GPCRs) including peptide receptor 2 (FPR2) and chemokine-like receptor 1 (CMKLR1)[19], toll-like receptors (TLRs) including TLR2, TLR4, and the co-receptor CD14[20], TREM2[21], etc (Table 1-1). While some receptors trigger an inflammatory immune response towards extracellular Aβ, some others participate in Aβ clearance by specifically binding to and internalizing Aβ fibrils into the cellular phagosomes. Identifying Aβ-specific receptors of phagocytosis is important. Microglia must be differentially targeted to enhance the phagocytosis of Aβ plaques but not viable neurons or glial cells in chronic inflammatory environments of diseased brains. Targeting these receptors at various stages of AD progression to specifically phagocytose microglia may be a promising immunotherapeutic approach to clear the Aβ plaques from the brain microenvironment. There is a need to identify additional receptors that are Aβ specific in order to enhance Aβ uptake and modulate microglial function. Innovative analytical techniques such as proteomics and lipidomics may identify new and previously unknown microglial targets of Aβ.

Microglial uptake of Aβ is followed by their proteolytic degradation within the cells. It has previously been shown that an imbalance in the degradation of Aβ may lead to their biochemical

and pathological deposition in the brain parenchyma as well as in the CSF[22]. A $\beta$ -degrading proteases include neprilysin, endothelin-converting enzymes, insulin-degrading enzyme, plasmin, matrix metalloproteinases, Cathepsin D, etc., that degrade A $\beta$  in the extracellular environment. Once A $\beta$  aggregates are internalized into the cells via phagocytosis, they are encompassed within the acidic phagosomes that later fuses with the lysosomes to form phagolysosomes and begins the initiation of their intracellular degradation. The phagolysosomes are progressively acidified to around pH 4.5 where they activate the hydrolytic degradative enzymes. Mutations in the genes that encode these enzymes may thus contribute to dysregulated degradation of A $\beta$  resulting in cellular dysfunction.

## **2.4 A role for astrocytes in A $\beta$ phagocytosis**

While astrocytes are best known for some of their traditional functions like the promotion of neuronal development[23], formation as well as the phagocytic elimination of synapses[23], and maintenance of the blood-brain barrier[24], they also exhibit phagocytic capabilities towards pathogenic neuronal substrates like A $\beta$  aggregates[25]. How astrocytes contribute to A $\beta$  phagocytosis and the underlying molecular mechanisms delineating the astrocytic uptake and degradation of A $\beta$  is not well characterized.

Astrocytes closely associate with A $\beta$  plaques in AD brains[26]–[29]. Human astrocytes can internalize A $\beta$  in vitro but this uptake is limited with an increase in A $\beta$  size[30]. Astrocytic uptake of A $\beta$  is thus dependent on the conformation and aggregated state of A $\beta$  (i.e. smaller A $\beta$  oligomers are more rapidly internalized than larger A $\beta$  fibrils). Furthermore, cytochalasin D, a well-known potent inhibitor of actin polymerization and phagocytosis, inhibited microglial uptake of A $\beta$  in culture but could not inhibit astrocytic A $\beta$  uptake[30]. Therefore, it can be hypothesized that the mechanism of A $\beta$  phagocytosis by astrocytes may be different than microglial uptake of A $\beta$ .

A few phagocytosis-specific receptors are identified in astrocytes. For example, astrocytes use the MEGF10 and MERTK pathways to phagocytose or prune neuronal synapses and contribute to the refinement of neural circuits[31]. What astrocytic receptors are specific to A $\beta$  phagocytosis? LDLR-Related Protein 4 (LRP4), a type I single transmembrane protein of the LDL receptor

family was recently identified to be involved in the process of astrocytic A $\beta$  clearance[32]. LRP family members serve as important receptors for several ligands, including APOE, agrin, etc., and influence lipid metabolism and cholesterol homeostasis in the CNS[33]. Another member of the LDLR-Related protein family, namely, LRP1 also participates in the phagocytosis and degradation of A $\beta$  by astrocytes and therefore impacts A $\beta$  deposition and pathology in AD[34]. There is no doubt that the LDLR family of proteins plays a critical role in lowering A $\beta$  levels in the brain. Thus, modulating astrocytic levels of LDLR appears to be a potential approach for enhancing the clearance of A $\beta$  via astrocytes.

Given that astrocytes are the major producers of APOE in the brain, the contribution of astrocytic APOE (and APOJ) in A $\beta$  clearance and degradation should not be discounted. By binding to A $\beta$ , APOE/J suppress A $\beta$  levels and deposition in the brain and regulate the extracellular A $\beta$  metabolism. An interesting evidence from the study mentioned previously [32] was that astrocytic LRP4 mediated A $\beta$  uptake without the participation from APOE i.e. APOE binding of A $\beta$  was not required for LRP4-mediated A $\beta$  clearance by astrocytes. This poses the question: *What receptors mediate the uptake of APOE-bound A $\beta$  by astrocytes?* Identifying such receptors may be key in targeting astrocytes to influence extracellular A $\beta$  levels during AD progression. (TREM2 on microglia, for example, participates in the phagocytosis of APOE-bound A $\beta$ . Similar mechanisms need to be investigated with respect to astrocytes.)

Similar to microglia, astrocytes may also exhibit dysfunctional states in AD brains. Astrogliosis is observed in inflamed brains in various disease paradigms and these changes in astrocytic cell states may also influence cellular behavior and functions towards external stimuli. It is also well worth noting that the neurotoxic or A1 reactive astrocytes exhibited reduced phagocytosis of synaptosomes[35] and may show similar effects with respect to A $\beta$ . This is yet to be tested. Recently, up to 57 differentially regulated genes were identified in plaque-associated microglia and astrocytes in AD tissue using spatial transcriptomics techniques[36]. Most of these genes were involved in the complement cascade, the endosomal-lysosomal system, and other aspects of the glial immune response. While several such studies have identified the A $\beta$ -mediated genetic changes in glial cells, it is important to note the functional consequences of such genetic changes.

That is, *What are the functions gained or lost in the dystrophic or reactive glial cells that associate with A $\beta$  plaques in vivo?* Identifying the proteins, lipids, and metabolites in A $\beta$ -associated astrocytes (as well as microglia) in AD may answer this question. There are several new and unknown astrocytic protein and lipid markers yet to be discovered for A $\beta$  clearance. Although the phagocytosis of A $\beta$  is primarily studied in the context of microglia—the brain's professional phagocytes, there is no doubt that given their prominence in the CNS, A $\beta$  clearance by astrocytes is a vital mechanism in the brain.

## 2.5 References

- [1] “2020 Alzheimer’s disease facts and figures,” Alzheimer’s Dement., 2020.
- [2] L. Ungar, A. Altmann, and M. D. Greicius, “Apolipoprotein E, gender, and Alzheimer’s disease: An overlooked, but potent and promising interaction,” Brain Imaging Behav., 2014.
- [3] C. M. Karch and A. M. Goate, “Alzheimer’s disease risk genes and mechanisms of disease pathogenesis,” Biological Psychiatry, vol. 77, no. 1. pp. 43–51, 2015.
- [4] J. Nunan and D. H. Small, “Regulation of APP cleavage by alpha-, beta- and gamma-secretases,” FEBS Lett., 2000.
- [5] E. N. Cline, M. A. Bicca, K. L. Viola, and W. L. Klein, “The Amyloid- $\beta$  Oligomer Hypothesis: Beginning of the Third Decade,” Journal of Alzheimer’s Disease. 2018.
- [6] L. N. Zhao, H. Long, Y. Mu, and L. Y. Chew, “The toxicity of amyloid  $\beta$  oligomers,” International Journal of Molecular Sciences. 2012.
- [7] R. Nortley et al., “Amyloid  $\beta$  oligomers constrict human capillaries in Alzheimer’s disease via signaling to pericytes,” Science (80-. ), vol. 365, no. 6450, 2019.
- [8] S. J. Soscia et al., “The Alzheimer’s disease-associated amyloid  $\beta$ -protein is an antimicrobial peptide,” PLoS One, 2010.
- [9] D. K. V. Kumar et al., “Amyloid- $\beta$  peptide protects against microbial infection in mouse and worm models of Alzheimer’s disease,” Sci. Transl. Med., 2016.
- [10] J. J. Iliff et al., “A paravascular pathway facilitates CSF flow through the brain parenchyma and the clearance of interstitial solutes, including amyloid  $\beta$ ,” Sci. Transl. Med., 2012.

- [11] L. C. Löwe, C. Gaser, and K. Franke, “The effect of the APOE genotype on individual BrainAGE in normal aging, Mild cognitive impairment, and Alzheimer’s Disease,” *PLoS One*, 2016.
- [12] R. Deane et al., “RAGE mediates amyloid- $\beta$  peptide transport across the blood-brain barrier and accumulation in brain,” *Nat. Med.*, 2003.
- [13] M. Shibata et al., “Clearance of Alzheimer’s amyloid- $\beta$ 1-40 peptide from brain by LDL receptor-related protein-1 at the blood-brain barrier,” *J. Clin. Invest.*, 2000.
- [14] S. A. Frautschy et al., “Microglial response to amyloid plaques in APPsw transgenic mice,” *Am. J. Pathol.*, vol. 152, no. 1, pp. 307–17, Jan. 1998.
- [15] H. Keren-Shaul et al., “A Unique Microglia Type Associated with Restricting Development of Alzheimer’s Disease,” *Cell*, vol. 169, no. 7, pp. 1276-1290.e17, Jun. 2017.
- [16] S. Gordon, “Phagocytosis: An Immunobiologic Process,” *Immunity*, vol. 44, no. 3. pp. 463–475, 2016.
- [17] S. Gordon, “Phagocytosis: The Legacy of Metchnikoff,” *Cell*. 2016.
- [18] B. R. Choi et al., “Increased expression of the receptor for advanced glycation end products in neurons and astrocytes in a triple transgenic mouse model of Alzheimer’s disease,” *Exp. Mol. Med.*, 2014.
- [19] L. Peng et al., “The chemerin receptor CMKLR1 is a functional receptor for amyloid- $\beta$  peptide,” *J. Alzheimer’s Dis.*, 2014.
- [20] K. Tahara, H. D. Kim, J. J. Jin, J. A. Maxwell, L. Li, and K. I. Fukuchi, “Role of toll-like receptor signalling in A $\beta$  uptake and clearance,” *Brain*, 2006.
- [21] Y. Zhao et al., “TREM2 Is a Receptor for  $\beta$ -Amyloid that Mediates Microglial Function,” *Neuron*, vol. 97, no. 5, pp. 1023-1031.e7, Mar. 2018.
- [22] N. Iwata et al., “Identification of the major A $\beta$ 1-42-degrading catabolic pathway in brain parenchyma: Suppression leads to biochemical and pathological deposition,” *Nat. Med.*, 2000.
- [23] N. J. Allen, “Astrocyte regulation of synaptic behavior,” *Annu. Rev. Cell Dev. Biol.*, vol. 30, no. 1, pp. 439–463, Oct. 2014.
- [24] B. A. Barres, “What is a glial cell?,” *Glia*, vol. 43, no. 1, pp. 4–5, Jul. 2003.
- [25] R. S. Jones, A. M. Minogue, T. J. Connor, and M. A. Lynch, “Amyloid- $\beta$ -induced astrocytic phagocytosis is mediated by CD36, CD47 and RAGE,” *J. Neuroimmune Pharmacol.*, vol. 8, no. 1, pp. 301–311, Mar. 2013.

- [26] H. M. Wisniewski and J. Wegiel, "Spatial relationships between astrocytes and classical plaque components," *Neurobiol. Aging*, 1991.
- [27] S. Kato, T. Gondo, Y. Hoshii, M. Takahashi, M. Yamada, and T. Ishihara, "Confocal observation of senile plaques in Alzheimer's disease: Senile plaque morphology and relationship between senile plaques and astrocytes," *Pathol. Int.*, vol. 48, no. 5, pp. 332–340, May 1998.
- [28] D. R. Thal, C. Schultz, F. Dehghani, H. Yamaguchi, H. Braak, and E. Braak, "Amyloid  $\beta$ -protein ( $A\beta$ )-containing astrocytes are located preferentially near N-terminal-truncated  $A\beta$  deposits in the human entorhinal cortex," *Acta Neuropathol.*, vol. 100, no. 6, pp. 608–617, Dec. 2000.
- [29] R. G. Nagele, M. R. D'Andrea, H. Lee, V. Venkataraman, and H. Y. Wang, "Astrocytes accumulate  $A\beta$ 42 and give rise to astrocytic amyloid plaques in Alzheimer disease brains," *Brain Res.*, vol. 971, no. 2, pp. 197–209, May 2003.
- [30] H. M. Nielsen, R. Veerhuis, B. Holmqvist, and S. Janciauskiene, "Binding and uptake of  $A\beta$ 1-42 by primary human astrocytes in vitro," *Glia*, 2009.
- [31] W. S. Chung et al., "Astrocytes mediate synapse elimination through MEGF10 and MERTK pathways," *Nature*, vol. 504, no. 7480, pp. 394–400, Dec. 2013.
- [32] H. Zhang et al., "A Role of Low-Density Lipoprotein Receptor-Related Protein 4 (LRP4) in Astrocytic Ab Clearance," *J. Neurosci.*, vol. 40, no. 28, pp. 5347–5361, 2020.
- [33] J. Herz and D. K. Strickland, "LRP: A multifunctional scavenger and signaling receptor," *J. Clin. Invest.*, vol. 108, no. 6, pp. 779–784, Sep. 2001.
- [34] C. C. Liu et al., "Astrocytic LRP1 mediates brain  $A\beta$  clearance and impacts amyloid deposition," *J. Neurosci.*, vol. 37, no. 15, pp. 4023–4031, Apr. 2017.
- [35] S. A. Liddelow et al., "Neurotoxic reactive astrocytes are induced by activated microglia," *Nature*, vol. 541, no. 7638, pp. 481–487, Jan. 2017.
- [36] W. T. Chen et al., "Spatial Transcriptomics and In Situ Sequencing to Study Alzheimer's Disease," *Cell*, 2020.



## CHAPTER 3. PRODUCTION OF RECOMBINANT HUMAN AMYLOID BETA

This chapter has been reproduced under a Creative Commons Attribution 4.0 International License (<http://creativecommons.org/licenses/by/4.0/>) and minor changes to original text have been made to format the original article as a thesis chapter.

Prakash P\*, Lantz TC\*, Jethava KP, Chopra G. Rapid, Refined, and Robust Method for Expression, Purification, and Characterization of Recombinant Human Amyloid beta 1-42. *Methods and Protocols*. 2019; 2(2):48.  
<https://doi.org/10.3390/mps2020048>

### 3.1 Abstract

Amyloid plaques found in the brains of Alzheimer's disease patients primarily consists of amyloid beta 1-42 (A $\beta$ 42). Commercially, A $\beta$ 42 is synthesized using high-throughput peptide synthesizers resulting in the presence of impurities and the racemization of amino acids that affects its aggregation properties. Furthermore, the repeated purchase of even a small quantity (~1 mg) of commercial A $\beta$ 42 can be expensive for academic researchers. Here, we describe a detailed methodology for robust expression of recombinant human A $\beta$ (M1-42) in Rosetta(DE3)pLysS and BL21(DE3)pLysS competent *E. coli* using standard molecular biology techniques with refined and rapid one-step analytical purification techniques. The peptide is isolated and purified from transformed cells using an optimized reverse-phase high-performance liquid chromatography (HPLC) protocol with commonly available C18 columns, yielding high amounts of peptide (~15–20 mg per 1 L culture) within a short period of time. The recombinant human A $\beta$ (M1-42) forms characteristic aggregates similar to synthetic A $\beta$ 42 aggregates as verified by western blotting and atomic force microscopy to warrant future biological use. Our rapid, refined, and robust technique produces pure recombinant human A $\beta$ (M1-42) that may be used to synthesize chemical probes and in several downstream in vitro and in vivo assays to facilitate Alzheimer's disease research.

### 3.2 Introduction

Amyloid beta 1-42 (A $\beta$ 42) is a small ~4 kDa peptide produced when the amyloid precursor protein expressed on neuronal membranes is sequentially cleaved by  $\beta$ -secretase and  $\gamma$ -secretase [1]. A $\beta$  exists as several variants ranging from 36 to 43 amino acid residues [2]. However, the main

component of the toxic amyloid plaques found in the brains of Alzheimer's Disease (AD) patients is composed of the A $\beta$ 42 isoform [3]. The extracellular accumulation of A $\beta$ 42 in the brain over time contributes to neuronal dysfunction and death leading to progressive memory loss and cognitive decline [4].

Several therapeutics currently in preclinical and clinical trials for AD are focused on targeting the cellular and molecular mechanisms related to A $\beta$ 42 [5,6]. Thus, there is an immediate need for further understanding of A $\beta$ 42's biological function and its effect on both neurons and non-neuronal glial cells [7–9]. Researchers commonly use commercially-available synthetic A $\beta$ 42 for their experiments. However, the repeated purchase of synthetic A $\beta$ 42 can be expensive (~ \$300 for 1 mg of peptide). Synthesizing A $\beta$ 42 in a traditional biochemistry laboratory has additional hurdles, such as 1) being expensive due to high instrument costs and 2) challenging due to the high hydrophobicity of the peptide that can affect the yield and efficiency of the procedure. The C-terminal sequence of A $\beta$ 42 in particular is known to be resistant to solid-phase peptide synthesis and is therefore called a “difficult sequence” peptide [10]. Furthermore, the presence of impurities and the racemization of amino acids during the synthesis of A $\beta$  affects its aggregation properties. It has been shown that synthetic A $\beta$  has lower aggregation kinetics and decreased neurotoxicity compared to recombinant human A $\beta$  [11]. Thus, recombinant human A $\beta$  is not only cheaper and easier to produce than the synthetic peptide but it is also free of enantiomers and is therefore better for investigating the biochemical and biological activity of A $\beta$ .

Here, we present an alternate and refined approach for the rapid, easy, and low-cost production and purification of recombinant human A $\beta$ 42 containing an exogenous N-terminus methionine, denoted as A $\beta$ (M1-42). The pET-Sac-A $\beta$ (M1-42) plasmid was developed previously by Walsh et al. and expresses A $\beta$ (M1-42) in *E. coli* cells [12]. In this original protocol, a combination of anion-exchange chromatography and centrifugal filtration was used to purify the peptide. Further, it was demonstrated that the exogenous methionine does not affect the kinetics and the fibrillation process of A $\beta$ (M1-42) compared to A $\beta$ 42 [12]. Thus, the recombinant human A $\beta$ (M1-42) and synthetic A $\beta$ 42 both exhibit aggregate-forming properties. The concentration-dependent aggregation kinetics of the A $\beta$ (M1-42) and its variants with different N-terminal sequence extensions have also been previously evaluated [13]. In this protocol, we will focus on the

expression of the recombinant A $\beta$ (M1-42) peptide, its one-step purification using HPLC, and the morphology characterization of the purified peptide.

Recently, Yoo et al. published a protocol where the A $\beta$ (M1-42) peptide was purified using reverse-phase high-performance liquid chromatography (HPLC) [14]. We have further expanded and optimized this protocol with the following changes to provide improved versatility to the method: 1) We have expressed the pET- Sac-A $\beta$ (M1-42) plasmid in Rosetta(DE3)pLysS cells (a BL21 derivative designed to enhance the expression of eukaryotic proteins) in addition to the BL21(DE3)pLysS cells; 2) We have performed the purification of the peptide with HPLC using the commonly available C18 columns with optimized solvent system conditions; 3) We have provided characteristic details of the peptide with Matrix-Assisted Laser Desorption/Ionization Time-Of-Flight Mass Spectrometry (MALDI-TOF MS) and verified its characteristic aggregate formations in different conditions by western blotting and Atomic Force Microscopy (AFM) to warrant future biological use.

### **3.3 Experimental design**

The protocol detailed in this paper can be divided into five parts (Figure 3.1). The pET-Sac-A $\beta$ (M1-42) plasmid is isolated (Part 1), transformed in the competent *E. coli* (Part 2), and the expression of A $\beta$ (M1-42) peptide is induced in a large quantity of bacterial culture (Part 3). Expressing human A $\beta$ (M1-42) in *E. coli* is a highly efficient and feasible method to produce large quantities of the peptide. Our protocol can be completed within a week's time (~ five days if starting from the beginning or three days if using the transformed bacteria for generating more cultures for peptide purification) and a yield of around 15–20 mg of the peptide per 1 L of the culture can be obtained. The equipment utilized for the expression and purification of the peptide are readily available in not only biological labs, but also in synthetic chemistry and chemical biology labs, therefore promoting widespread use of the method.

The expressed peptides are present as inclusion bodies within the bacterial cells that are then isolated by repeated sonification and lysed with Tris/EDTA buffers followed by dissolution of the peptide into 8M urea buffer (Part 4). The peptide is ultimately purified by reverse-phase HPLC using the C18 columns with an optimized solvent system for peptide purification (Part 5). C18

columns are popular and conventionally used for the separation of small molecules and low molecular weight peptides. Typically a relatively large (43 residues) and hydrophobic peptide like A $\beta$ (M1-42) [3] is not separated with a C18 column. However, heating the column between 60–80 °C results in a single peak during separation of pure A $\beta$ (M1-42) peptide with yields similar to alternative protocols [12–14]. The lyophilized peptide is characterized by mass spectrometry to verify the identity of the peptide and to detect any impurities present. The aggregation characteristics of the recombinant A $\beta$ (M1-42) are similar to the synthetic A $\beta$ 42 peptide as per AFM and western blotting with monoclonal antibody.

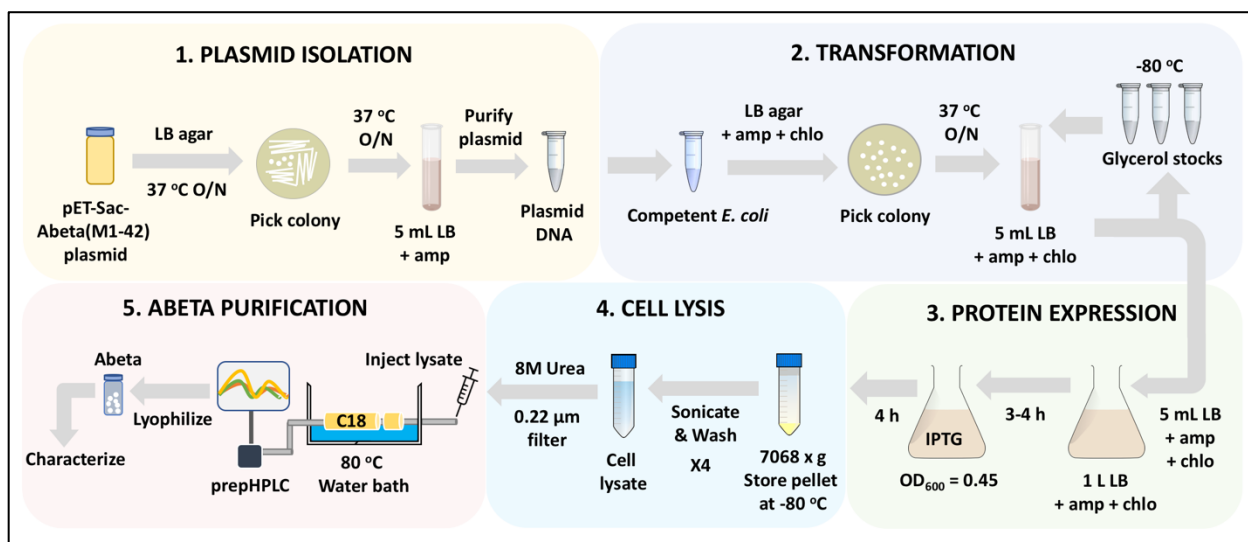


**Figure 3.1** Schematic diagram illustrating the experimental protocol for the expression and isolation of recombinant human A $\beta$ (M1-42) peptide from competent *E. coli*. Part 1. Isolation of the pET-Sac-A $\beta$ (M1-42) plasmid from the glycerol stock; Part 2. Transformation of BL21(DE3)pLysS and Rosetta(DE3)pLysS competent cells with the isolated Transformation of BL21(DE3)pLysS and Rosetta(DE3)pLysS competent cells with the isolated pET- pET-Sac-A $\beta$ (M1-42) plasmid; Part 3. Expression of the A $\beta$ (M1-42) peptide in 1 L liquid LB culture; Part 4. Harvesting and lysis of the cells using a probe sonicator followed by resuspension of the cell lysate in 8 M urea; and Part 5. Purification of the A $\beta$ (M1-42) peptide with preparative HPLC.

### 3.4 Materials

- pET-Sac-A $\beta$ (M1-42) plasmid (Addgene, Watertown, MA, USA; Cat. no.: 71875)
- Tryptone (Fisher Scientific, Waltham, MA, USA; Cat. no.: BP1421-500)
- Yeast Extract (Fisher Scientific, Waltham, MA, USA; Cat. no.: BP9727-500)

- LB Agar (Miller, Granulated) (Fisher Scientific, Waltham, MA, USA; Cat. no.: BP9724-500)
- Ampicillin (VWR International, Radnor, PA, USA, Cat. no.: 80055-786)
- Chloramphenicol (Fisher Scientific, Waltham, MA, USA; Cat. no.: AAJ67273AB)
- Plasmid Miniprep System (Promega, Madison, WI, USA; Cat. no.: A12222)
- Rosetta™(DE3)pLysS Competent Cells (MilliporeSigma, Burlington, MA, USA; Cat. no.: 70956-3)
- Isopropyl  $\beta$ -D-1- thiogalactopyranoside (IPTG) (Fisher Scientific, Waltham, MA, USA; Cat. no.: 15-529-019)
- Tris hydrochloride (Tris-HCl) (Fisher Scientific, Waltham, MA, USA; Cat. no.: BP153-500)
- Urea (Invitrogen, Carlsbad, CA, USA; Cat. no.: 15505-035)
- 0.22  $\mu$ m non-sterile hydrophilic PVDF syringe filter (Fisher Scientific, Waltham, MA, USA; Cat. no.: 09-719-000)
- HPLC grade Acetonitrile (Fisher Scientific, Waltham, MA, USA; Cat. no.: A998-4)
- Purified anti- $\beta$ -Amyloid, 1-16 Antibody (BioLegend, San Diego, CA, USA; Cat. no.: 803001)
- HRP Goat anti-mouse IgG (minimal x-reactivity) Antibody (BioLegend, San Diego, CA, USA; Cat. no.: 405306)
- SuperSignal West Pico Chemiluminescent Substrate (Fisher Scientific, Waltham, MA, USA; Cat. no.: 34080)
- 1,1,1,3,3,3-Hexafluoroisopropyl alcohol (Chem-Impex International, Wood Dale, IL, USA; Cat. no.: 00080)
- Hamilton syringe with a Teflon plunger and a sharp needle [Hamilton Company, Reno, NV, USA; Part. no.: 81343]
- Mica sheet (Ted Pella, Redding, CA, USA; Cat. no.: 50)
- Aluminum coated silicon probes with resonant frequency  $\sim$ 300 kHz and 40 N/m force constant (Ted Pella, Redding, CA, USA; Cat. no.: TAP300AL-G-10)
- Phosphate-buffered saline (PBS), 10x at pH 7.4 (Alfa Aesar, Haverhill, MA, USA; Cat. no.: J62036-K7)

### 3.5 Equipment

- Benchtop incubator shaker (New Brunswick™ Excella® E24) (Eppendorf, Hamburg, Germany; Cat. no.: M1352-0000)
- Sonicator Ultrasonic Homogenizer (125W) with 1/4" Probe (Qsonica, Newton, CT, USA; Cat. no.: Q700-110 and 4435)
- CO2 Incubator (New Brunswick™ Galaxy® 48S) (Eppendorf, Hamburg, Germany; Cat. no.: CO48S-120-0000)
- Centrifuge (Sorvall LYNX 6000) with a Swinging-Bucket Rotor (BIOFlex™ HC) (Thermo Fisher Scientific, Waltham, MA USA; Cat. no.: 75006591 and 75003000)
- UV-Visible Spectrophotometer (JASCO, Easton, MD, USA; Cat. no.: V-730)
- Microplate reader for nucleic acid quantification (Take3™ Micro-Volume plate) with Gen5 Software (BioTek, Winooski, VT, USA; Cat. no.: TAKE3)
- Combiflash EZ prep UV/ELSD (Teledyne ISCO, Lincoln, NE, USA; Cat. no.: 218J00936)
- RediSep Prep 10 × 250 mm C18 100A, 5 µm column (Teledyne ISCO, Lincoln, NE, USA; Cat. no.: 692203809)
- RediSep Prep Guard 20 × 30 mm, C18Aq, 100A, 5 µm (Teledyne ISCO, Lincoln, NE, USA; Cat. no.: 692203805)
- GenPure UV/UF × CAD plus Ultrapure Water Purification System (Thermo Fisher Scientific, Waltham, MA USA; Cat. no.: 41956240)
- Rotary evaporator and water bath (EYELA, Keyland Court Bohemia, NY, USA; Cat. no.: N-1110 and SB-1200)
- Dry Bath with heating block (Thermo Fisher Scientific, Waltham, MA USA; Cat. no.: 88870002)
- Labconco Freezone 12 Liter Console Freeze Dry System (Lyophilizer) (Labconco, Kansas City, MO, USA; Cat. no.: 710612000)
- Voyager-DE PRO (MALDI-TOF mass spectrometer) (Applied Biosystems, Foster City, CA, USA;)
- For AFM: Veeco Multimode instrument with NanoScope V controller

### 3.6 Procedure

#### 3.6.1 Preparation of solutions

Use ultrapure water to prepare all the solutions in the protocol. Make liquid Luria Broth (LB) by dissolving 10 g tryptone, 10 g NaCl, and 5 g yeast extract in 1 L water. Autoclave the liquid LB and bring to room temperature before adding the antibiotics. Prepare solid LB as 3.2 g of LB agar mix in 100 mL water. Autoclave the broth and allowed to cool before adding the antibiotics as follows: (i) 100 mg/L ampicillin for antibiotic selection during amplification of the pET-Sac-A $\beta$ (M1-42) plasmid in LB media and (ii) 100 mg/L ampicillin and 34 mg/L chloramphenicol for maintenance and expression of the A $\beta$ (M1-42) peptide in Rosetta(DE3)pLysS and BL21(DE3)pLysS strains (i.e., for transformed bacteria). For solid LB preparation, pour the media with the antibiotics on to the Petri dishes and keep in the biosafety cabinet with lids open to allow the media to solidify. Prepare these plates in bulk and refrigerate at 4 °C for future use to save time during the protocol. For cell lysis steps, make two buffers: (i) Buffer A containing 10 mM Tris/HCl and 1 mM EDTA in water (pH 8.0), (ii) Buffer B containing 8 M urea, 10 mM Tris/HCl, and 1 mM EDTA in water (pH 8.0). Prepare fresh buffers each time. For peptide purification with preparative HPLC, make: (i) Solvent A as 0.1% trifluoroacetic acid (TFA) in water and (ii) Solvent B as 0.1% TFA in acetonitrile (Table 3-1). TFA is a common ion-pairing agent used in reverse phase-HPLC to enhance the separation of large hydrophobic peptides and is volatile and easily removed from the purified peptide. Acetonitrile is a common organic solvent used to elute peptides as it has low viscosity and is easy to evaporate off.

#### 3.6.2 Expression of A $\beta$ (M1-42) peptide

Time for Completion: 55:30 h

##### 3.6.2.1 Isolation of the pET-Sac-A $\beta$ (M1-42) plasmid

Time for Completion: 31:00 h

**Note:** The bacterial growth on solid agar as well as in liquid culture are performed at 37 °C temperature which is the optimal growth temperature for E. coli cells.

1. Streak the bacteria onto a solid LB agar plate containing 100 mg/L ampicillin using a sterile loop. Note: The pET-Sac-A $\beta$ (M1-42) plasmid arrives as a bacterial agar stab culture.
2. Keep the plate overnight for ~ 16 h in the incubator at 37 °C for the colonies to grow.
3. The next day, pick a single colony from the plate (Figure 3.2-A) using a sterile loop or a sterile 10  $\mu$ L pipet tip and inoculate into 5 mL of liquid LB containing 100 mg/L ampicillin.
4. Keep the culture in a shaking incubator at 220 rpm and 37 °C overnight for ~ 16 h.
5. The next day, isolate the plasmid (Figure 3.1, Part 1) from the culture using the plasmid isolation miniprep kit following instructions per the user manual.
6. Measure the concentration of the plasmid at 260 nm absorbance using a spectrophotometer for nucleic acid quantification. Note: Typical plasmid yield is around 45-55 ng/ $\mu$ L from 5 mL liquid LB culture.

### ***3.6.2.2 Transformation of pET-Sac-A $\beta$ (M1-42) plasmid into competent *E. coli* by heat shock method***

Time for Completion: 01:30 h

1. To transform the A $\beta$ (M1-42) plasmid into *E. coli* (Figure 3.1, Part 2), thaw the frozen vials of Rosetta(DE3)pLysS cells or BL21(DE3)pLysS competent cells (20–50  $\mu$ L) on ice.
2. Once thawed, add around 1–2  $\mu$ L of the isolated plasmid (to have 50–100 ng total DNA) to the cells and gently flick the tube a few times to mix the plasmid with the cells.
3. Incubate the cells and the plasmid mixture on ice for 20 min and then place the tube in a 42 °C water bath for 45 s to facilitate the transformation of plasmid into the cells via heat shock method.
4. After heat shock, immediately place the tubes on ice for 2 mins.
5. Inoculate the transformed bacteria into 500  $\mu$ L of liquid LB media without any antibiotics and keep the tube in the 37 °C shaker for 1 h at 220 rpm.

**CRITICAL STEP:** The transformed bacteria is first inoculated in liquid LB media without any antibiotics for 1 h to allow the bacteria to express the antibiotic resistance proteins necessary for future steps.



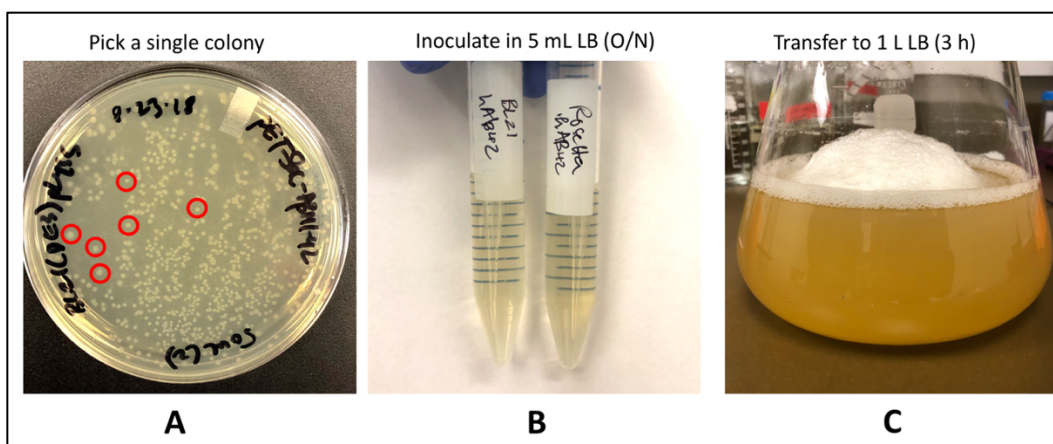


**Figure 3.2** Transformed cells as colonies on the Luria Broth (LB) plate and the growing culture in liquid LB. (A) Colonies of transformed *E. coli* on solid LB. Red circles represent single colonies. (B) Single colony is picked from the plate and inoculated into 5 mL liquid LB and shaken at 37 °C overnight that makes a cloudy solution after incubation. (C) The next morning, this culture is inoculated into 1 L LB to grow the cells for the next 3 to 3.5 h until the optical density (OD) reaches 0.45.

### 3.6.2.2 Expression of $A\beta(M1-42)$ peptide by the transformed *E. coli*

Time for Completion: 23:00 h

1. After 1 h, spread around 25–30  $\mu$ L (out of 500  $\mu$ L) of the transformed cells onto solid LB agar plates containing 100 mg/L ampicillin and 34 mg/L chloramphenicol using a sterile glass spreader.
2. Let the plates sit in the biosafety cabinet for 5 min to allow the cells to absorb on the solid LB.
3. Next, keep the plates overnight in the incubator at 37 °C for the transformed colonies to grow.

**CRITICAL STEP:** It is best to use a lower volume of the transformed cells (25–30  $\mu$ L) as this results in more single colonies that are easier to pick and prevents overcrowding on the plate.

4. The next day, pick a single colony from the plate using a sterile loop or a sterile 10  $\mu$ L pipet tip and inoculate into 5 mL of liquid LB containing 100 mg/L ampicillin and 34 mg/L chloramphenicol (first culture).
5. **OPTIONAL STEP:** At the same time, pick another single colony of the transformed bacteria and inoculate into a second 5 mL liquid LB media containing 100 mg/L ampicillin

and 34 mg/L chloramphenicol for overnight growth (second culture). This culture will be used to make frozen glycerol stocks for future use.

6. Place both the cultures in the shaking incubator at 220 rpm at 37 °C overnight (16 h) (Figure 3.2-B).
7. The following day, inoculate the first 5 mL culture into a large 2 L Erlenmeyer flask containing 1 L liquid LB media with 100 mg/L ampicillin and 34 mg/L chloramphenicol (Figure 3.2-C).
8. Keep this 1 L culture at 220 rpm and 37 °C until the cell density reaches an optical density (OD) value between 0.40 to 0.45 at 600 nm (OD<sub>600</sub>).

**CRITICAL STEP:** The BL21(DE3)pLysS cells reach an OD<sub>600</sub> between 0.40 to 0.45 in 3 h time, whereas the Rosetta(DE3)pLysS cells requires around 3.5–4.0 h to reach an OD<sub>600</sub> between 0.40 to 0.45. It is best to measure the OD of the culture at regular 20 min intervals starting from the 3-h time point before proceeding to the next step.

9. **OPTIONAL STEP:** The second 5 mL culture of transformed bacteria is used to make 25% glycerol stocks by adding 500 µL of 50% glycerol to 500 µL bacterial culture and is frozen at –80 °C for future use. A –80 °C frozen glycerol stock of the transformed bacteria is thawed for use in the future for inoculating 5 mL liquid LB containing 100 mg/L ampicillin and 34 mg/L chloramphenicol to grow additional cultures of the transformed bacteria containing the Aβ(M1-42) plasmid. Note: Frozen aliquots of 250–500 µL glycerol stocks may be stored for future use. It is recommended that the stored aliquots of glycerol stock be thawed 1–2 times only. Additionally, some of the frozen stock may be scrapped and thawed for inoculation.

**CRITICAL STEP:** This step serves as a starting point for all future experiments performed for the isolation of the Aβ(M1-42) peptide (Figure 3.1, Part 3). It is important to note that this step is critical for reducing the time taken for the entire protocol along with saving the reagents used for peptide expression.

10. Once the OD<sub>600</sub> of the 1 L culture reaches 0.40 to 0.45, induce protein expression by adding isopropyl β-D-1- thiogalactopyranoside (IPTG) to obtain a final concentration of 0.1 mM in 1 L of the liquid LB media. Note: Add 1 mL of 0.1 M IPTG stock solution prepared in water to obtain a final concentration of 0.1 mM in 1 L LB media.

Note: IPTG induction must occur early in the exponential growth phase to form insoluble inclusion bodies, which are essential for the isolation procedure.

11. Keep the culture again on the shaking incubator at 220 rpm and 37 °C for additional an 4 h in the presence of IPTG to allow the cells to express the A $\beta$ (M1-42) peptide.

12. After 4 h, centrifuge the 1 L culture at 7068 $\times$  g at 4 °C for 25 min.

Note: The cultures are centrifuged at 4 °C temperature to arrest cell growth and metabolism.

Note: Our centrifuge allowed for a maximum speed of 7068 $\times$  g with the corresponding swinging bucket rotor (see section 3.5. Equipment). Hence, this speed was used to collect the transformed cells from the 1 L cultures. The cells may also be pelleted by centrifuging the cultures at 2800 $\times$  g if using a JA-10 rotor [14].

13. Discard the supernatant liquid LB and resuspend the pelleted cells in 25 mL of 1 $\times$  PBS and transfer the thick cell suspension to a 50 mL falcon tube using a 10 mL pipet.

14. Centrifuge the cells at 7068 $\times$  g at 4 °C for 25 min and discard the 1 $\times$  PBS supernatant.

15. **PAUSE STEP:** Store the pelleted cells at –80 °C until the next day or when ready for cell lysis.

### 3.6.3 A $\beta$ (M1-42) peptide purification using reverse-phase HPLC

Time for Completion: 05:40 h

#### 3.6.3.1 *Cell lysis and resuspension*

Time for Completion: 02:24 h

Note: Cell lysis steps involving sonication and centrifugation is performed at 4 °C to prevent denaturation of the protein. It is critical for the pH of the buffers to be set at 8.0 to improve solubility of the peptide and prevent its aggregation. The peptide is thus maintained in alkaline conditions since it is known to aggregate at lower pH of 5.5. with lower solubility [15].

1. To lyse the cells (Figure 3.1, Part 4), resuspend the cell pellet in 25 mL Buffer A. Cut the tip off a 1 mL pipette tip to efficiently dissociate the thick pellet in the buffer.

2. Disrupt the cell pellet mechanically by mixing the cells with Buffer A. Place the tube in an ice bucket containing ice and water and introduce the sonicator probe into the cell mixture. Note: Ensure that the cell mixture remains cold throughout the sonication.

3. Sonicate the cells at 30 s pulse with an amplitude of 60% for 2 min until the lysate appears homogenous. Note: Four 30 s on/off cycles for a total of 4 min.

**CRITICAL STEP:** To increase the lysis efficiency, sonicate the cell pellet in the original 50 mL frozen falcon tube since transferring the cell mixture to containers with a large surface area reduces the lysis efficiency.

4. Centrifuge the sonicated mixture at 7068× g for 25 min at 4 °C and discard the supernatant. Note: The sonicated mixture was centrifuged at 7068× g based on the maximum speed allowed on our centrifuge and swinging bucket rotor (see section 3.5 Equipment). This speed was sufficient to collect the pellet from the cell lysis at the bottom of the tube. The sonicated mixture may also be centrifuged at higher speeds of up to 38,000× g if using the JA-18 rotor to collect the pellet [14].

5. Repeat the sonication and centrifugation steps (steps 1 to 4) three more times.

6. Resuspend the pellet in 20 mL of freshly prepared Buffer B and sonicate as above until the solution appears clear.

**CRITICAL STEP:** Purification (Section 3.6.3.2) should be performed immediately after the peptide is dissolved in 8 M urea solution (Buffer B). Extended exposure of the peptide to urea is known to cause carbamylation of lysine residues.

**CRITICAL STEP:** Due to the inconsistencies of mechanical lysis using the sonicator, the solution may appear to be cloudy. Note: Prepare fresh Buffer B every time. The pH of the buffers is critical for the complete dissolution of the peptide fraction.

7. Centrifuge the solution at 7068× g for 25 min at 4 °C to remove any foam that may have appeared during the sonication step and to pellet unwanted insoluble cell debris, if any.

Finally, filter the supernatant through a 0.22 µm non-sterile hydrophilic PVDF syringe filter using a 30 mL syringe to obtain a clear solution.

8. **OPTIONAL STEP:** Prior to purification, MALDI-TOF MS may be performed on the urea-solubilized recombinant peptide to confirm the presence of Aβ(M1-42) in the solution (data not shown). Since the solution contains additional salts, the solution must be passed through a C18 Zip Tip resin to remove the salts in order to obtain a clear spectrum.

### 3.6.3.2 *Peptide purification using reverse-phase HPLC*

Time for Completion: 03:16 h

**Equipment set-up for peptide purification:** Heat a water bath containing reverse osmosis water using a commercially-available sous vide between 60 to 80 °C (Figure 3.3-A). Completely submerge both the guard and the primary columns in the water bath (Figure 3.3-B). It is recommended to set up the water bath with the submerged columns at least 4 hours prior to purification to allow the water bath to reach 60 to 80 °C and the temperature of the columns to equilibrate. Note: As it is common for many silica-based C18 columns to degrade at higher temperatures, different columns have different recommended heating limits. Refer to your column manual or manufacturing guide to identify the column's recommended heating limit. Heating of the guard and primary columns is necessary to prevent the recombinant peptide from sticking to the column and to improve yield of the peptide.

Place the solvent lines from the CombiFlash HPLC instrument into the Solvent A and Solvent B bottles. Next, prime the system with Solvent B followed by Solvent A to clear the solvent lines of any previous residual solvents. Then clean the column by injecting 4 mL of Buffer B into the 5 mL injection loop (Figure 3.3-C) and run the solvent gradient for the cleaning protocol provided in Table 1.

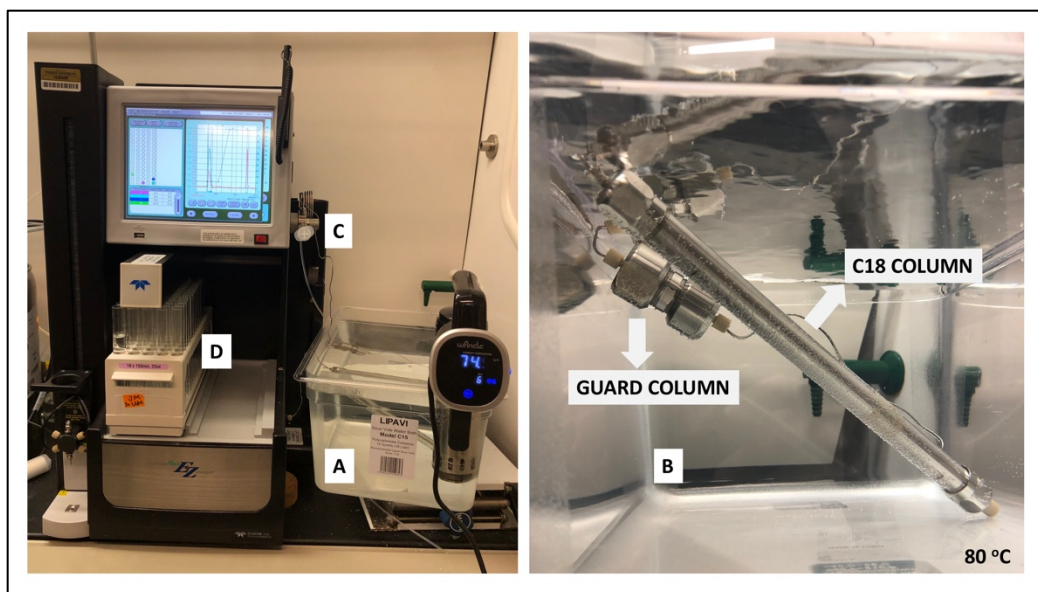


**Figure 3.3** High-performance liquid chromatography (HPLC) set-up. (A) The water bath containing filtered reverse osmosis water is heated to ~ 80 °C. (B) Both columns are completely submerged in the water bath. One end of the guard column attached to the injection valve with metal tubing and the other end of the guard column attached to the inlet of the primary C18 100 Å 5 µm 10 mm × 250 mm preparative column. The primary column is fed into the Combiflash. (C) 5 mL injection loop. (D) Collection of Aβ(M1-42) fractions eluted at 26 min.

**Table 3-1** Solvent gradient for the cleaning protocol done before and after peptide purification.

% Solvent A <sup>1</sup>	% Solvent B <sup>2</sup>	Elapsed Time (min)
90	10	0
90	10	5
10	90	10
10	90	20

<sup>1</sup> Solvent A = H<sub>2</sub>O with 0.1% TFA; <sup>2</sup> Solvent B = Acetonitrile with 0.1% TFA

1. Place a rack of clean and dry 18 × 150 mm glass test tubes (Figure 3.3-D) in the instrument.
2. Run the solvent gradient as per the cleaning protocol in Table 1 at a flow rate of 5 mL/min.
3. Equilibrate the column with the starting solvent system in Table 2 at a flow rate of 5 mL/min. And inject 4 mL of the filtered solution obtained from section 3.2.1 step 8 into the HPLC injection loop for separation (Figure 3.3-C).

4. Run the solvent gradient described in Table 3-2 and collect peaks detected at 214 nm. Note: A $\beta$ (M1-42) typically elutes at 26 min.
5. Upon completion of the purification protocol, clean the column with the solvent gradient described in Table 3-1.
6. Repeat the cleaning and purification steps three more times or until all the solution is used.
7. Combine the collected A $\beta$ (M1-42) fractions eluted at 26 min (Figure 3.4).
8. Evaporate off the acetonitrile under reduced pressure at 65 °C using a rotary evaporator until a cloudy aqueous solution remains.
9. Freeze the solution at –80 °C and then submerge in liquid nitrogen for 5 min.
10. Perform overnight lyophilization at –90 °C at 0.003 mbar pressure to obtain the white A $\beta$ (M1-42) powder (Figure 3.4).
11. **PAUSE STEP** Store the lyophilized peptide at –80 °C until further characterization.

**Table 3-2** Solvent gradient for peptide purification.

% Solvent A <sup>1</sup>	% Solvent B <sup>2</sup>	Elapsed Time (min)
90	10	0
90	10	9
5	95	19
5	95	27

<sup>1</sup> Solvent A = H<sub>2</sub>O with 0.1% TFA; <sup>2</sup> Solvent B = Acetonitrile with 0.1% TFA

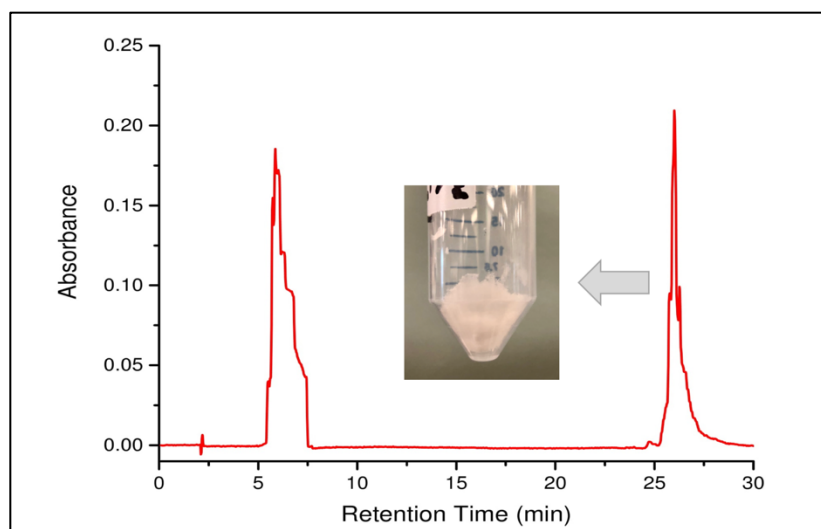


**Figure 3.4** HPLC Chromatogram of urea-solubilized recombinant protein during purification. The A $\beta$ (M1-42) peak elutes at 26 min at 95% acetonitrile with 0.1 % TFA, 5 % H<sub>2</sub>O with 0.1 % TFA. The urea salt from solution B elutes as a cluster of peaks between 5–7 min in 10% acetonitrile with 0.1 % TFA, 90 % H<sub>2</sub>O with 0.1 % TFA. The absorbance was taken at 214 nm. Inserted image of the white powder is the lyophilized peptide corresponding to the A $\beta$ (M1-42) fractions collected at 26 min.

### 3.6.4 Characterization of A $\beta$ (M1-42)

#### 3.6.4.1 Characterization of A $\beta$ (M1-42) using MALDI-TOF MS and high-resolution LC-MS

Time for Completion: 00:45 h

1. Dissolve a small quantity of A $\beta$ (M1-42) in water and dilute in water until the sample is approximately 100  $\mu$ g/mL.
2. Thoroughly mix 1  $\mu$ L of the A $\beta$ (M1-42) solution (analyte) with 1  $\mu$ L of  $\alpha$ -cyano-4-hydroxycinnamic acid (CHCA) matrix solution (10 mg/mL CHCA in 0.1% TFA).
3. Spot the analyte/matrix mixture on a MALDI target plate and allow to dry.
4. Obtain the MALDI-TOF mass spectra on a Voyager-DE PRO from 1000–22000 Da in the positive ion mode with an accelerating voltage of 25,000 V (Figure 3.5).
5. Further dilute the analyte solution prepared for the MALDI-TOF MS and inject into the Agilent 6550 iFunnel Q-TOF LC-MS in positive mode and fragment using electrospray ionization (ESI) with a fragmentor voltage of 175V (Figure 3.6).



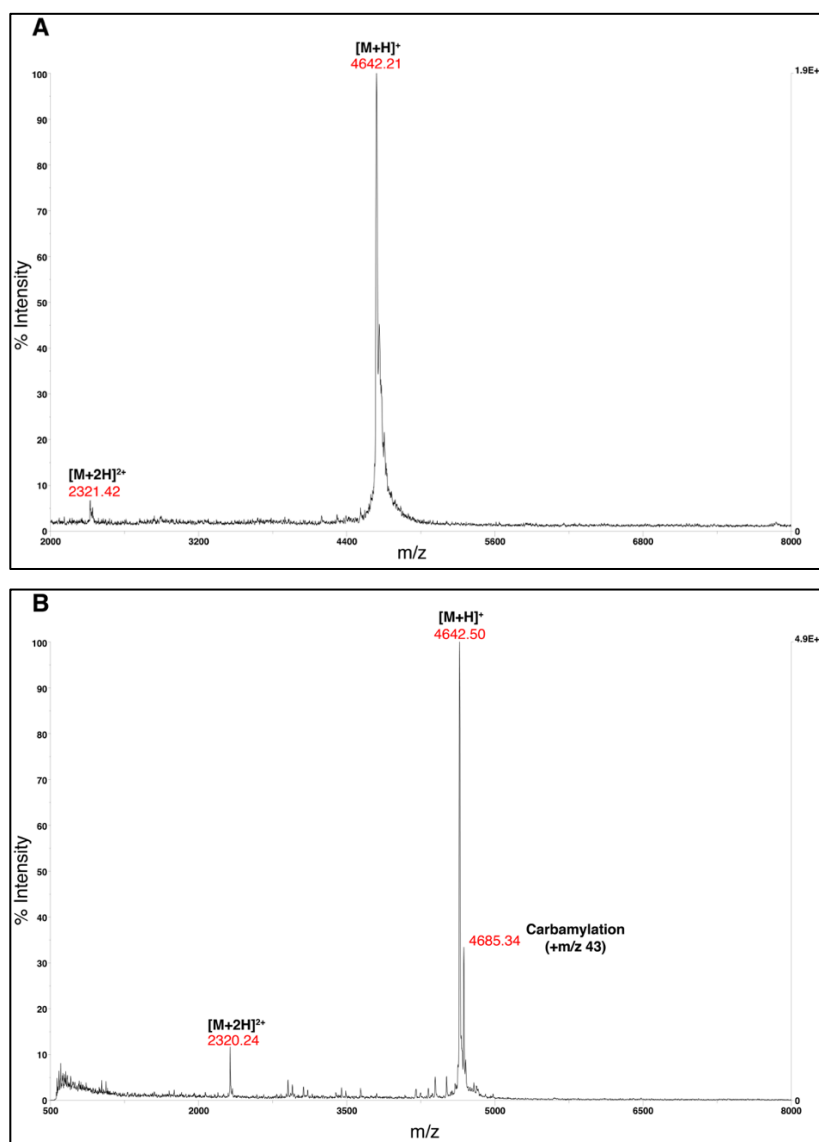


**Figure 3.5** MALDI-TOF mass spectra of Aβ(M1-42). A. The MALDI-TOF mass spectra of lyophilized Aβ(M1-42) in the range of m/z 2000 to 8000. The Aβ(M1-42) corresponds to the m/z 4642.21 peak. B. MALDI-TOF mass spectra of lyophilized carbamylated Aβ(M1-42) in the range of m/z 500 to 8000. Carbamylation peak (m/z 4685.34) appears ~ m/z 43 higher than the Aβ(M1-42) at m/z 4642.50 due to the extended exposure of the peptide to urea. A Voyager De-Pro MALDI-TOF mass spectrometer in positive linear mode was used with CHCA solution as the matrix for each spectrum.

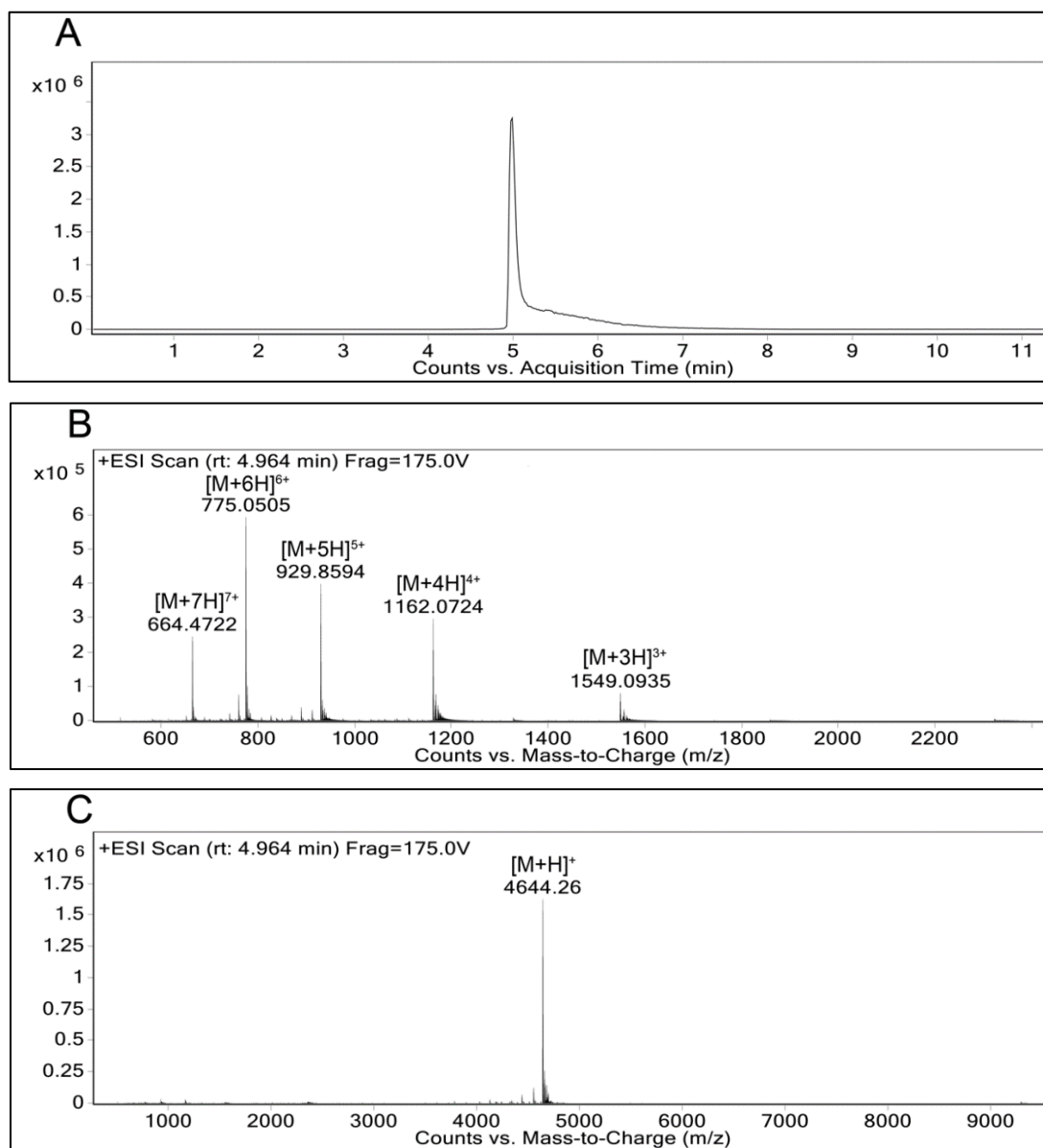


**Figure 3.6** High-resolution Liquid Chromatography-Mass Spectrum (LC-MS) of A $\beta$ (M1-42). The high-resolution mass spectrum was obtained using an Agilent 6550 iFunnel Q-TOF LC-MS in positive ion mode using electrospray ionization (ESI) with a fragmentor voltage of 175V. A. The chromatogram from the LC-MS showed a significant peak between 5–7 min while using 0.1% formic acid and methanol as the solvent system. B. Mass spectrum at time point 4.964 min resulting in the corresponding peaks: [M+3H]<sup>3+</sup> (m/z 1549.0935), [M+4H]<sup>4+</sup> (m/z 1162.0724), [M+5H]<sup>5+</sup> (m/z 929.8594), [M+6H]<sup>6+</sup> (m/z 775.0505), and [M+7H]<sup>7+</sup> (m/z 664.4722). C. The deconvolution of the mass spectrum in panel B was performed showing the peak corresponding to [M+H]<sup>+</sup> at m/z 4644.26 (calculated [M+H]<sup>+</sup> of m/z was done using the PEPTIDEMASS program).

### 3.6.4.2 *Western blot characterization of the purified A $\beta$ (M1-42) peptide*

Time for Completion: Two Days

1. To perform western blotting, the lyophilized peptide from HPLC was dissolved in 1,1,1,3,3,3-hexafluoro-2-propanol (HFIP) to prepare monomers of A $\beta$ (M1-42) as per the previously established protocols [16,17].
2. When the peptide is dried overnight in the chemical hood, dissolve 1 mg of the peptide in 221  $\mu$ L DMSO to obtain a final concentration of 1.0 mM.
3. Load the peptide on 12% Sodium Dodecyl Sulfate Polyacrylamide Gel Electrophoresis (SDS-PAGE) at different concentrations (10, 20, and 40  $\mu$ g per 40  $\mu$ L total well volume) and run the gel at 115 V for 1 h and 20 min or until the loading buffer line reaches the bottom of the gel.
4. Transfer the gel to a nitrocellulose membrane at 10 V for 35 min.
5. After transfer, boil the membrane in PBS for 5 min, then incubate on a rocker with blocking buffer (5% milk in Tris-buffered saline, 0.1% Tween 20 (TBST)) for 1 h.
6. After blocking, incubate the membrane in the blocking buffer containing the 6E10 monoclonal antibody (with target specificity to the human A $\beta$  peptide) overnight on a rocker at 4 °C.
7. The next morning, wash the membrane 3 times for 10 min each with TBST and incubate with the secondary antibody (HRP-conjugated goat anti-mouse antibody) on the rocker for 1 h.
8. Washed again three times for 10 min each with TBST and develop in the dark room using chemiluminescence reagents as per the manufacturer's protocol.
9. Run the synthetic A $\beta$ (1-42) in the same gel with the same protocol for comparison (Figure 3.7).

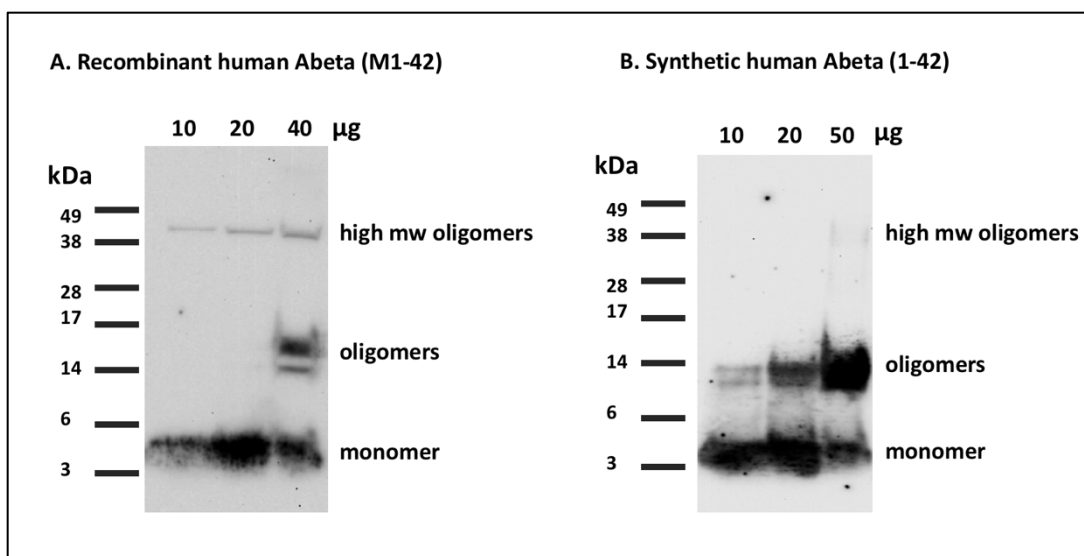


**Figure 3.7** Western blot characterization of the recombinant human Aβ(M1-42) peptide. A. 10, 20, and 40 μg of the recombinant Aβ(M1-42) peptide was run on an SDS-PAGE gel and bands visualized using the 6E10 antibody with Western Blot. Lower concentrations of 10 and 20 μg show monomeric bands at 4 kDa while the 40 μg lane shows oligomeric bands at 14–17 kDa along with the monomeric band. All 3 concentrations show a slight amount of high molecular weight bands at 38–49 kDa suggesting a few aggregated forms of the peptide in the mixture. B. Synthetic human Aβ(1-42) for reference shows similar monomeric bands at 10, 20, and 50 μg concentrations. More oligomers are present in the synthetic peptide.

#### 3.6.4.3 Characterization of Aβ(M1-42) oligomers by atomic force microscopy

Time for Completion: Two days

**Preparing Aβ(M1-42) monomers:** The synthetic Aβ(1-42) and the lyophilized Aβ(M1-42) powder are used to prepare 1 mM solution with 215 μL of 1,1,1,3,3,3-Hexafluoro-2-propanol (HFIP). Handle the HFIP carefully using a 1 mL glass Hamilton syringe with a Teflon plunger and a sharp needle. Start by incubating the clear Aβ(M1-42) and synthetic Aβ(1-42) solution at room temperature for 30 min. Next, transfer 100 μL aliquots (~0.45 mg) to microcentrifuge tubes and leave the tubes open in the fume hood overnight for the HFIP to evaporate. The next morning, dry the sample under high vacuum for 1 h without heating to remove any remaining traces of HFIP and moisture. This results in thin clear films of monomeric peptides at the bottom of the tubes which are stored at –80 °C until further use.

1. To evaluate the aggregation property of the recombinant A $\beta$ (M1-42) with respect to the synthetic A $\beta$ (1-42), the protocol established by Stine et al. is used to prepare A $\beta$  oligomers and fibrils [16,17].
2. In brief, allow the tubes containing monomeric peptide films to equilibrate at room temperature for a few minutes and prepare 5 mM of synthetic A $\beta$ (1-42) and recombinant A $\beta$ (M1-42) DMSO stocks by adding 20  $\mu$ L of cell-grade DMSO to each tube containing ~0.45 mg of the peptide.
3. Pipet the solution thoroughly by scraping down the sides of the tube and vortexed for ~30 s followed by bath sonication for 10 min to ensure complete resuspension of the peptide film.

**CRITICAL STEP:** This stock solution is used immediately as the starting material for oligomeric A $\beta$  preparation.

4. To prepare A $\beta$  oligomers, mix 2  $\mu$ L of the freshly resuspended 5 mM of synthetic A $\beta$ (1-42) and recombinant A $\beta$ (M1-42) in DMSO with 98  $\mu$ L of 1 $\times$  PBS (filtered) to make 100  $\mu$ M solution. To prepare A $\beta$  fibrils, mix 98  $\mu$ L of 10 mM HCl (filtered) to 2  $\mu$ L of freshly resuspended 5 mM of recombinant A $\beta$ (M1-42) in DMSO.
5. Vortex the solution thoroughly for 15 s and incubate at 4  $^{\circ}$ C (for oligomers) and at 37  $^{\circ}$ C (for fibrils) for 24 h.
6. After 24 h, prepare the samples for AFM with proper sterile technique in the hood as follows: Dilute the 100  $\mu$ M samples to a concentration of 30  $\mu$ M in filtered water.
7. Mount the mica sheet on 15 mm stainless steel pucks.
8. Immediately before sample plating, remove a few layers of the mica sheet using adhesive tape to reveal a featureless surface for the absorption of the peptide.
9. Next, pretreat the mica surface with ~5–8  $\mu$ L of filtered 1M HCl for 30 s and rinse with 2–3 drops of ultrapure water (filtered) using the 1 mL syringe.
10. **CRITICAL STEP:** Hold the mica plate at a 45 $^{\circ}$  angle to wash with drops of water. Immediately after cleaning, spot the peptide sample onto mica and incubate for 3 min.
11. Gently rinse the mica with 2–3 drops of water using the 1 mL syringe and dry with several gentle pulses of clean compressed air or nitrogen gas.
12. Incubate the samples at room temperature for a few hours until imaging.

13. Perform the AFM imaging using a multimode AFM equipped with aluminum-coated silicon probes with  $\sim 300$  kHz resonant frequency and 40 N/m force constant under the tapping mode.
14. Finally, perform image analysis using the NanoScope Analysis software.

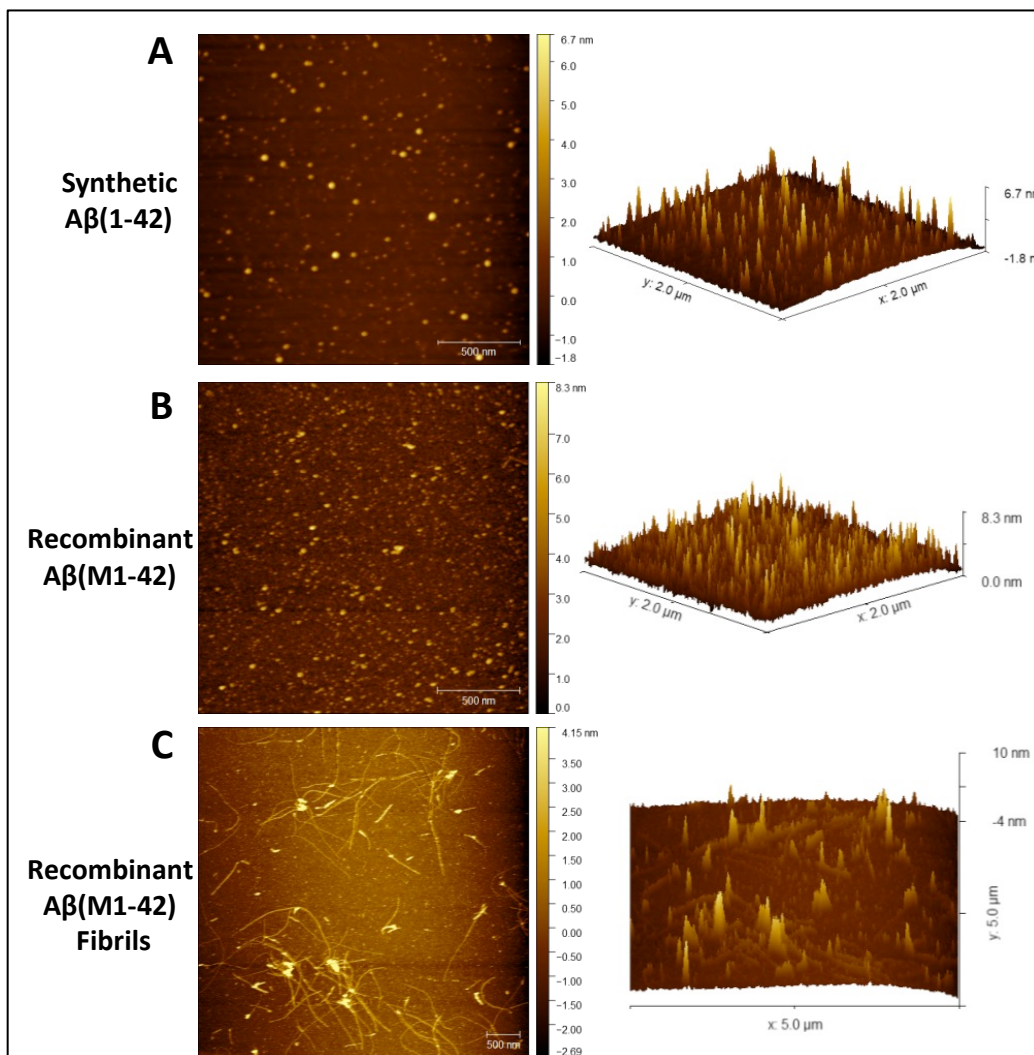


**Figure 3.8** AFM characterization of the recombinant human  $A\beta(M1-42)$  peptide. The (A) synthetic  $A\beta(1-42)$  oligomers and (B) recombinant  $A\beta(M1-42)$  oligomers and/or (C) fibrils were prepared from HFIP- treated peptide films in  $1\times$  PBS buffer (pH 7.4) and analyzed by atomic force microscopy (AFM). Images (A) and (B) are  $2 \times 2 \mu\text{m}$  x-y scale and image (C) is  $5 \times 5 \mu\text{m}$  x-y scale. Left. 2-D image. Right. 3-D image.

### 3.7 Expected results and discussion

A handful of methodologies have been published in recent years that show expression of A $\beta$ 42 in *E. coli* using standard molecular biology techniques, such as transformation and bacterial cell culture. The major differences among these methodologies have been the isolation and purification methods used to obtain purified peptide samples. The purification of the peptides expressed from cells is challenging due to the many different techniques proposed combined with limited resources available in a traditional biochemistry or chemical biology laboratory. For example, previously, nickel affinity chromatography was used to purify A $\beta$ 42 fusion proteins with N-terminal His-affinity tag [18] or as an extended polypeptide of His-tagged ubiquitin [19]. Both these methods require additional steps from which A $\beta$ 42 has to be eventually cleaved requiring extra time, reagents, as well as comprising on the final peptide yield. Another method used NaOH treatment followed by ultracentrifugation to isolate and purify the insoluble inclusion bodies expressed in the *E. coli* [20]. This purification method reduces the peptide purity and yield (~ 4 mg of peptide obtained). Walsh et al. [12] used ion exchange chromatography and Yoo et al. [14] used preparative HPLC equipped with a C8 column for A $\beta$ (M1-42) purification.

In this paper, we present a highly detailed alternate and refined approach for the rapid, easy, and low-cost production and purification of recombinant human A $\beta$ 42. By using alternate tools for peptide purification, we provide additional versatility to the protocol. Expected results and some critical points of consideration during the protocol are as follows. During the cell lysis and resuspension step, it is important to avoid leaving the peptide in 8M urea after cell lysis for a long period of time. Exposing the lysate to a high concentration of urea solution is known to cause carbamylation of the lysine residues [21]. Carbamylation can be seen in the MALDI-TOF MS by the presence of a secondary peak  $m/z$  43 higher than the peak  $m/z$  4642.50 corresponding to [M+H]<sup>+</sup> (Figure 3.5-B). Our HPLC system has a 5 mL injection loop, which limits the amount of sample that can be loaded onto the column. In Yoo et al. method, the cell lysate in 8 M urea was further diluted before injecting in the column [14]. We decided not to dilute the urea-solubilized fraction of the cell lysate in our protocol due to the smaller volume of the injection loop allowing for fewer batch runs thereby reducing the time taken for purification without reducing the purity of the peptide. The mass characterization of the final peptide shows that the final peptide obtained with very few impurities (Figure 3.6).

Using western blotting of recombinant A $\beta$ (M1-42) and synthetic A $\beta$ 42, we demonstrated that the purified peptide mixture contains large quantities of monomers as seen in the 4 kDa region (Figure 3.7). A higher concentration of the peptide shows oligomeric forms of the peptide that appear between 14–17 kDa (trimers and tetramers). Overall, we show that the recombinant A $\beta$ (M1-42) peptide epitope can be recognized by the monoclonal 6E10 antibody that is specific for human A $\beta$ 42, suggesting future biological use of our recombinant A $\beta$ (M1-42). Interestingly, the recombinant A $\beta$ (M1-42) peptide showed higher molecular weight (HMW) oligomeric bands in the 38–49 kDa region that were not visible with synthetic A $\beta$ 42. Increased levels of such HMW oligomers are seen in the cerebrospinal fluid samples from Alzheimer's patients [22]. Thus, HMW oligomers are of huge importance for understanding the etiology of Alzheimer's disease [23]. We further characterized the aggregation property of recombinant A $\beta$ (M1-42) using atomic force microscopy (AFM). The recombinant peptide formed large oligomers of different sizes (some greater than 20 nm, not shown) compared to the synthetic peptide that formed mostly uniform oligomers during the same time (Figure 3.8). The recombinant A $\beta$ (M1-42) also formed characteristic fibrils similar to those formed by synthetic A $\beta$ 42 [17]. It has been previously shown that the recombinant A $\beta$ 42 aggregates faster and is more neurotoxic than synthetic A $\beta$ 42 [11]. Overall, the recombinant A $\beta$ (M1-42) formed characteristic oligomers under similar aggregation conditions as the synthetic A $\beta$ 42. Further characterization may be necessary to evaluate the concentration-dependent aggregation kinetics of the recombinant A $\beta$ (M1-42) [13].

Thus, the A $\beta$ (M1-42) peptide could be used for several downstream in vitro and in vivo applications such as cell-based drug screening, neuroinflammation cell culture, animal models, etc., and for the synthesis and development of novel A $\beta$ -related biorthogonal chemical and fluorescent probes to facilitate the advancement of neurological disease research.

**Author Contributions:** Conceptualization, P.P., T.C.L., and G.C.; methodology, P.P., T.C.L., and K.P.J.; validation, P.P., T.C.L., and K.P.J.; investigation, P.P., T.C.L., and K.P.J.; resources, G.C.; writing—original draft preparation, P.P.; writing—review and editing, T.C.L., K.P.J., and G.C.; supervision, G.C.; project administration, G.C.; funding acquisition, G.C.;



**Funding:** This research was supported by Startup Funds to G.C. from Department of Chemistry, Purdue University and Purdue Research Foundation (PRF) Research Grant award to G.C.

**Acknowledgments:** We thank the following individuals at Purdue University: Dr. Herman Sintim at Department of Chemistry for providing the Rosetta(DE3)pLysS cells and the resources for bacterial work including the laminar flow cabinet, sonicator, 37 °C incubator, and shaker; Dr. Gregory H. Hockerman at Department of Medicinal Chemistry and Molecular Pharmacology for providing the BL21(DE3)pLysS cells; Connie Bonham at Analytical Mass Spectrometry Facility for assistance with MALDI-TOF/MS.

**Conflicts of Interest:** The authors declare no conflict of interest.

### 3.8 References

- [1] Hamley, I.W. The Amyloid Beta Peptide: A Chemist's Perspective. Role in Alzheimer's and Fibrillization. *Chem. Rev.* 2012, 112, 5147–5192.
- [2] Jarrett, J.T.; Berger, E.P.; Lansbury, P.T. The carboxy terminus of the beta. amyloid protein is critical for the seeding of amyloid formation: Implications for the pathogenesis of Alzheimer's disease. *Biochem.* 1993, 32, 4693–4697.
- [3] Murphy, M.P.; Levine, H. Alzheimer's Disease and the  $\beta$ -Amyloid Peptide. *J. Alzheimer's Dis.* 2010, 19, 311–323.
- [4] Ballard, C.; Gauthier, S.; Corbett, A.; Brayne, C.; Aarsland, D.; Jones, E. Alzheimer's Disease. *Lancet* 2011, 377, 1019–1031, doi:10.1016/S0140-6736(10)61349-9.
- [5] Doig, A.J.; Del Castillo-Frias, M.P.; Berthoumieu, O.; Tarus, B.; Nasica-Labouze, J.; Sterpone, F.; Nguyen, P.H.; Hooper, N.M.; Faller, P.; Derreumaux, P. Why Is Research on Amyloid- $\beta$  Failing to Give New Drugs for Alzheimer's Disease? *ACS Chem. Neurosci.* 2017, 8, 1435–1437.
- [6] Cummings, J.; Lee, G.; Ritter, A.; Zhong, K. Alzheimer's Disease Drug Development Pipeline: 2018. *Alzheimer's Dement. Transl. Res. Clin. Interv.* 2018, doi:10.1016/j.trci.2018.03.009.
- [7] Zuroff, L.; Daley, D.; Black, K.L.; Koronyo-Hamaoui, M. Clearance of cerebral A $\beta$  in Alzheimer's disease: Reassessing the role of microglia and monocytes. *Cell. Mol. Life Sci.* 2017, 74, 2167–2201.

- [8] Frost, G.R.; Li, Y.-M. The role of astrocytes in amyloid production and Alzheimer's disease. *Open Boil.* 2017, 7, 170228.
- [9] Gomez-Arboledas, A.; Davila, J.C.; Sanchez-Mejias, E.; Navarro, V.; Nuñez-Diaz, C.; Sanchez-Varo, R.; Sanchez-Mico, M.V.; Trujillo-Estrada, L.; Fernandez-Valenzuela, J.J.; Vizuete, M.; et al. Phagocytic Clearance of Presynaptic Dystrophies by Reactive Astrocytes in Alzheimer's Disease. *Glia* 2018, doi:10.1002/glia.23270.
- [10] Tickler, A.K.; Clippingdale, A.B.; Wade, J.D. Amyloid- $\beta$  as a "Difficult Sequence" in Solid Phase Peptide Synthesis. *Protein Pept. Lett.* 2004, doi:10.2174/0929866043406986.
- [11] Finder, V.H.; Vodopivec, I.; Nitsch, R.M.; Glockshuber, R. The Recombinant Amyloid- $\beta$  Peptide A $\beta$ 1–42 Aggregates Faster and Is More Neurotoxic than Synthetic A $\beta$ 1–42. *J. Mol. Boil.* 2010, 396, 9–18.
- [12] Walsh, D.M.; Thulin, E.; Minogue, A.M.; Gustavsson, N.; Pang, E.; Teplow, D.B.; Linse, S. A facile method for expression and purification of the Alzheimer's disease-associated amyloid  $\beta$ -peptide. *FEBS J.* 2009, 276, 1266–1281.
- [13] Szczepankiewicz, O.; Linse, B.; Meisl, G.; Thulin, E.; Frohm, B.; Frigerio, C.S.; Colvin, M.T.; Jacavone, A.C.; Griffin, R.G.; Knowles, T.; et al. N-Terminal Extensions Retard A $\beta$ 42 Fibril Formation but Allow Cross-Seeding and Coaggregation with A $\beta$ 42. *J. Am. Chem. Soc.* 2015, 137, 14673–14685.
- [14] Yoo, S.; Zhang, S.; Kreutzer, A.G.; Nowick, J.S. An Efficient Method for the Expression and Purification of A $\beta$ (M1-42). *Biochemistry* 2018, doi:10.1021/acs.biochem.8b00393.
- [15] Teplow, D.B. Preparation of Amyloid  $\beta$ -Protein for Structural and Functional Studies. *Methods in Enzymology* 2006, 413, 20–33.
- [16] Stine, W.B.; Dahlgren, K.N.; Krafft, G.A.; LaDu, M.J. In Vitro Characterization of Conditions for Amyloid- $\beta$  Peptide Oligomerization and Fibrillogenesis. *J. Biol. Chem.* 2003, doi:10.1074/jbc.M210207200.
- [17] Stine, W.B.; Jungbauer, L.; Yu, C.; Ladu, M.J. Preparing Synthetic A $\beta$  in Different Aggregation States. *Methods Mol. Biol.* 2011, doi:10.1007/978-1-60761-744-0\_2.
- [18] Chhetri, G.; Pandey, T.; Chinta, R.; Kumar, A.; Tripathi, T. An improved method for high-level soluble expression and purification of recombinant amyloid-beta peptide for in vitro studies. *Protein Expr. Purif.* 2015, 114, 71–76.
- [19] Lee, E.K.; Hwang, J.H.; Shin, D.Y.; Kim, D.I.; Yoo, Y.J. Production of recombinant amyloid- $\beta$  peptide 42 as an ubiquitin extension. *Protein Expr. Purif.* 2005, 40, 183–189.

- [20] Hoarau, M.; Malbert, Y.; Irague, R.; Hureau, C.; Faller, P.; Gras, E.; André, I.; Remaud-Siméon, M. A Robust and Efficient Production and Purification Procedure of Recombinant Alzheimers Disease Methionine-Modified Amyloid- $\beta$  Peptides. PLoS ONE 2016, doi:10.1371/journal.pone.0161209.
- [21] Sun, S.; Zhou, J.Y.; Yang, W.; Zhang, H. Inhibition of Protein Carbamylation in Urea Solution Using Ammonium-Containing Buffers. Anal. Biochem. 2014, doi:10.1016/j.ab.2013.10.024.
- [22] Fukumoto, H.; Tokuda, T.; Kasai, T.; Ishigami, N.; Hidaka, H.; Kondo, M.; Allsop, D.; Nakagawa, M. High-molecular-weight  $\beta$ -amyloid oligomers are elevated in cerebrospinal fluid of Alzheimer patients. FASEB J. 2010, 24, 2716–2726.
- [23] Bernstein, S.L.; Dupuis, N.F.; Lazo, N.D.; Wytttenbach, T.; Condron, M.M.; Bitan, G.; Teplow, D.B.; Shea, J.-E.; Ruotolo, B.T.; Robinson, C.V.; et al. Amyloid- $\beta$  protein oligomerization and the importance of tetramers and dodecamers in the aetiology of Alzheimer's disease. Nat. Chem. 2009, 1, 326–331.

## CHAPTER 4. GLIAL PHAGOCYTOTIC UPTAKE OF AMYLOID BETA

This chapter has been reproduced under a Creative Commons Attribution 4.0 International License (<http://creativecommons.org/licenses/by/4.0/>) and minor changes to original text have been made to format the original article as a thesis chapter.

Prakash P\*, Jethava KP\*, Korte N\*, Izquierdo P\*, Favuzzi E, Rose I, Guttenplan K, Dutta S, Rochet J-C, Fishell G, Liddel S, Attwell D, Chopra G. Monitoring phagocytic uptake of amyloid  $\beta$  into glial cell lysosomes in real time. (In revision at *Chemical Science*). Preprint available on bioRxiv.

doi: <https://doi.org/10.1101/2020.03.29.002857>

### 4.1 Abstract

Phagocytosis by glial cells is essential to regulate brain function during health and disease. Therapies for Alzheimer's disease (AD) have primarily focused on targeting antibodies to amyloid  $\beta$  ( $A\beta$ ) or enzymes that make it, and while removal of  $A\beta$  by phagocytosis is protective early in AD it remains poorly understood. Impaired phagocytic function of glial cells during later stages of AD likely contributes to worsened disease outcome, but the underlying mechanisms of how this occurs remain unknown. We have developed a human  $A\beta$ 1-42 analogue ( $A\beta^{pH}$ ) that exhibits green fluorescence upon internalization into the acidic organelles of cells but is non-fluorescent at physiological pH. This allowed us to image, for the first time, glial uptake of  $A\beta^{pH}$  in real time in live animals. Microglia phagocytose more  $A\beta^{pH}$  than astrocytes in culture, in brain slices and in vivo.  $A\beta^{pH}$  can be used to investigate the phagocytic mechanisms responsible for removing  $A\beta$  from the extracellular space, and thus could become a useful tool to study  $A\beta$  clearance at different stages of AD.

### 4.2 Introduction

Glial cells make up more than half of the cells of the central nervous system (CNS) and are vital to the regulation of brain function [1]. Microglia are specialized CNS-resident macrophages that respond to pathogens and injury by clearing cell debris, misfolded protein aggregates and damaged neurons by the process of phagocytosis [2]. Mature microglia in the adult brain exhibit a ramified morphology and constantly survey their surroundings for "eat me" signals [3] present on or released from apoptotic cells, microbes, protein deposits, dysfunctional synapses and other target

substrates. After CNS injury or during neurodegenerative diseases like Alzheimer's disease (AD) microglia become "reactive", and change morphology, becoming rod-like or amoeboid [4], and actively engage with their environment by secreting inflammatory cytokines like TNF- $\alpha$  and IL-1 $\alpha$ . These cytokines cause functional changes in astrocytes, microglia themselves and other cells [5,6].

During phagocytosis, proteins on the microglial cell surface, such as the Toll-Like Receptors (TLRs), Fc receptors, and scavenger receptors including CD36 and the receptor for advanced glycation end products (RAGE) among others, recognize the "eat-me" signals and engulf the target substrates into intracellular compartments called phagosomes [7–10]. The phagosomes mature by fusing with lysosomes to form highly acidic phagolysosomes and mobilize the phagocytosed material for enzymatic degradation. The pH of phagosomal organelles during this maturation process is progressively reduced [11] from 6.0 to around 5.0-4.5. Although microglia are the "professional phagocytes" of the CNS, astrocytes are also competent phagocytic cells with important roles both during health, and in response to injury or in disease [12–15]. Recent evidence has demonstrated the phagocytic abilities of reactive astrocytes towards cellular debris in CNS injury [16]. Together, reactive microglia and astrocytes play a crucial role in clearing extracellular debris and cellular components and aid in remodeling the tissue environment during disease.

AD is characterized by the generation of soluble oligomers of amyloid  $\beta$  (A $\beta$ ) that have numerous downstream actions, including reducing cerebral blood flow [17], inhibiting glutamate uptake which may cause hyperexcitability of neurons [18], and inducing hyperphosphorylation of the cytoskeletal protein tau [19,20] which leads to synaptic dysfunction and cognitive decline. Ultimately A $\beta$  oligomers are deposited as extracellular plaques in the brain, a hallmark of AD, which contribute to neuroinflammation and neuronal death [21]. The main A $\beta$  species generated excessively in AD is A $\beta$ 1-42, which is a small ~4.5 kDa peptide produced by the cleavage of amyloid precursor protein on neuronal membranes by  $\beta$ - and  $\gamma$ -secretases [22,23]. Removal of A $\beta$  from the extracellular space by phagocytosis into microglia and astrocytes, as well as by clearance across endothelial cells into the blood or lymph vessels, is thought to limit the build-up of the extracellular A $\beta$  concentration. However, AD pathology occurs when A $\beta$  generation outweighs its removal [20]. Thus, to understand the onset of plaque deposition during AD (and perhaps how to

prevent it) it is essential to understand molecular mechanisms underlying glial phagocytosis and degradation of A $\beta$ . A method that can monitor this process, especially in real time *in vivo*, will facilitate identification of the receptors that bind to A $\beta$  and initiate its phagocytic clearance. This will allow investigation of why glia that surround A $\beta$  plaques in AD show impaired phagocytic function [5,24,25], and why in inflammatory conditions microglia may increase their phagocytic capacity depending on their state of activation [26,27].

Current methods to study glial phagocytosis involve the use of fluorescent latex beads [28] or particles of zymosan [29] or *E. coli* [30] conjugated to non-pH dependent fluorophores like fluorescein and rhodamine31. A non-pH dependent particle makes it difficult to clearly determine whether the particle is inside the phagosomes or outside the cell during live-cell monitoring (Figure 4.S1-A). Some bioparticles can be labeled with pH-sensitive dyes such as pHrodo, however, these currently available pH-sensitive dyes are not suitable for labeling disease-specific pathogenic molecules like A $\beta$  for *in vivo* use. While non-pH sensitive fluorophore conjugates of A $\beta$  have been used to evaluate A $\beta$  phagocytosis [28,32], they have several disadvantages for live-cell imaging and cannot be used for selective identification and isolation of phagocytic cells *in vivo*. First, pH-insensitive fluorophore conjugated A $\beta$  peptides exhibit sustained fluorescence in the extracellular space (at physiological pH) thus contributing a noisy background that hinders the clear visualization of live phagocytic cells (Figure 4.S1-B). Second, in live-cell imaging and in fluorescence-activated cell sorting (FACS) of live cells, it is difficult to differentiate between A $\beta$  molecules that are internalized by the cells versus A $\beta$  molecules that are stuck to the cell surface.

To address these issues, we have developed a pH-dependent fluorescent conjugate of human A $\beta$ 1-42, which we call A $\beta^{\text{pH}}$ , and characterized it using mass spectrometry, atomic force microscopy and imaging of its uptake into cells *in vitro* and *in vivo*. We show the functionality of the A $\beta^{\text{pH}}$  probe for identifying phagocytic microglia and astrocytes in several different biological model systems such as cell lines, primary cell cultures, brain tissue slices, and *in vivo* in brain and retina. A $\beta^{\text{pH}}$  retains an aggregation phenotype similar to that of synthetic A $\beta$  *in vitro* and exhibits increased green fluorescence within the acidic pH range of 5.0 to 4.5 but not at the extracellular and cytoplasmic physiological pH values of 7.4 and 7.1, respectively. A $\beta^{\text{pH}}$  can be used to visualize phagocytosis in live cells in real time without the use of any A $\beta$ -specific antibody. It is internalized

by glial cells (both astrocytes and microglia) in live rat hippocampal tissue sections in situ. Stereotaxic injection of A $\beta^{\text{pH}}$  into the mouse somatosensory cortex in vivo leads to its uptake by astrocytes and microglia, following which microglia retain the A $\beta^{\text{pH}}$  within the cells up to 3 days in vivo unlike astrocytes. Similarly, microglia in retinal tissues retain the A $\beta^{\text{pH}}$  within the cells for up to 3 days but no signal was detected in astrocytes. Finally, we show, for the first time, real-time phagocytosis of A $\beta$  into microglia and astrocytes in mouse cortex in vivo by two-photon excitation microscopy.

### 4.3 Results

#### 4.3.1 Properties of a novel pH-dependent fluorescent conjugate of human A $\beta$ 1-42

We synthesized a new pH-sensitive fluorescent dye-labelled phagocytic A $\beta$  probe for imaging both in vitro and *in vivo*, and for cell sorting which allows for downstream analysis of functional subtypes of cells. We used a facile bioconjugation strategy to make our new probe safe for use with live cells in vitro and with live animals in vivo. The A $\beta^{\text{pH}}$  conjugate was synthesized at the microgram scale by linking the synthetic human A $\beta$ 1-42 peptide to the amine-reactive Protonex Green 500, SE (PTXG) fluorophore (Figure 4.1-A). We selected PTXG based on its ability to gain fluorescence in acidic environments and thus emit fluorescence specifically at the low pH of 5.0-4.5 found within lysosomes—a property of only a few commercial dyes. Conjugation of the fluorophore was performed at the side chain amine groups of the lysine residues within, and at the N-terminal of, human A $\beta$ 1-42 peptide. The conjugation was confirmed with matrix-assisted laser desorption/ionization-mass spectrometry (MALDI-MS) (Figures 4.S2-A, 4.S2-B) that indicated the conjugation of PTXG with the A $\beta$ 1-42 peptide (molecular weight >4.5K) by removal of succinimidyl ester (SE) as a leaving group. Additionally, proton nuclear magnetic resonance (1H-NMR) analysis of A $\beta^{\text{pH}}$  also demonstrated the presence of PTXG as well as A $\beta$ 1-42 peptide (Figures 4.S3-A to C). The spectrum of A $\beta$ 1-42 peptide obtained from attenuated total reflection Fourier transform infrared spectroscopy (ATR-FTIR) also shows a strong absorption peak at 1625 cm<sup>-1</sup> confirming carbonyl functional group of amide bonds (Figure 4.S4-A) and the spectrum of PTXG shows the presence of amide and ester group with absorption peaks at 1668 and 1727 cm<sup>-1</sup>, respectively (Figure 4.S4-B). The conjugated product A $\beta^{\text{pH}}$  shows a distinct peak at 1674 cm<sup>-1</sup> confirming amide bond formation between the A $\beta$ 1-42 peptide and PTXG dye, as expected (Figure

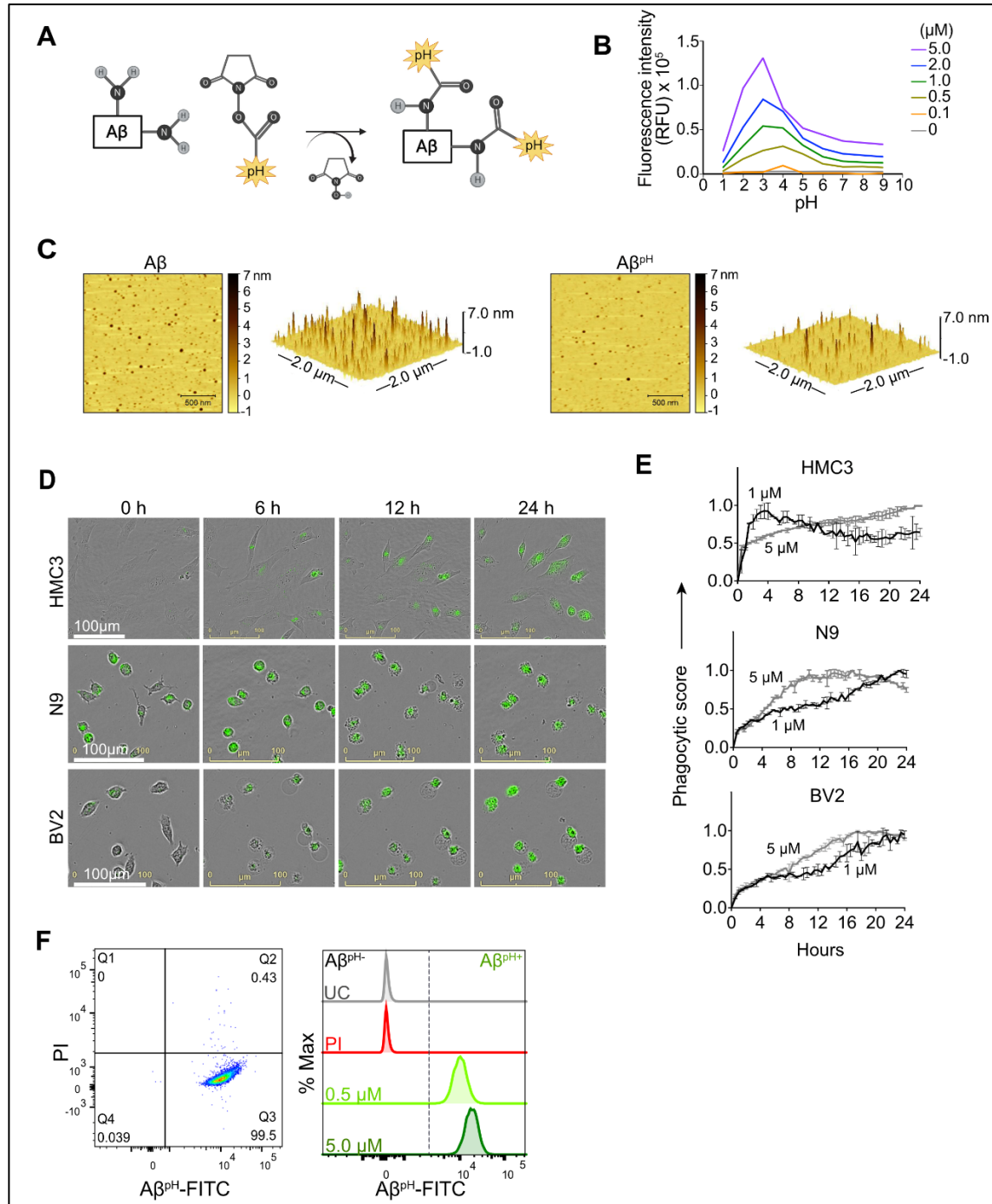
4.S4-C). Collectively, these experiments confirm the formation of the peptide-dye conjugate. We also synthesized another conjugate of A $\beta$ 1-42 with the pHrodo-Red, NHS fluorophore (RODO) and confirmed conjugate formation from the MALDI-MS spectrum (Figure 4.S5).

The pH-sensitivity of the PTXG and RODO-conjugated A $\beta$  were assessed by measuring their fluorescence intensities at various pH values. Notably, the pKa of a dye may shift when conjugated with a protein or peptide and this would change the pH-sensitivity of the conjugated product. [33] The PTXG-conjugated A $\beta$  showed increased fluorescence at pH less than  $\sim$ 5.5 at concentrations of 0.5, 1.0, 2.0 and 5.0  $\mu$ M whereas PTXG alone showed increased fluorescence at pH  $\sim$ 4.5 at concentrations of 0.5, 1.0, 2.0 and 5.0  $\mu$ M with excitation/emission wavelengths of 443/505 nm. The pKa of PTXG-conjugated A $\beta$  and PTXG alone were 5.2–5.9 and 4.4–4.7 at concentrations of 0.5, 1.0, 2.0 and 5.0  $\mu$ M, respectively (Figure 4.S6-A). The PTXG dye clearly shows increased fluorescence around pH  $\sim$ 4.5 whereas PTXG-conjugated A $\beta$  shows a pH-sensitivity of  $\sim$ 5.5 that lies within the pH range of lysosomes thus making it suitable for our study. On the other hand, the RODO-conjugated A $\beta$  had a pKa value of 6.2–6.4 (at 5, 2, 1, 0.5  $\mu$ M) (Figure 4.S6-B). It is known that the amine-reactive forms of the RODO dye has a pKa of  $\sim$ 7.3 in solution and shifts to about  $\sim$ 6.5 upon conjugation [34] that is similar to the pKa value we observed for RODO-conjugated A $\beta$ . Further, the PTXG-A $\beta$  conjugate showed a maximum fluorescence intensity between 500-510 nm in the acidic pH range (Figure 4.S7-A). The PTXG-A $\beta$  conjugate exhibited low fluorescence intensity at pH values  $>$  6.0 including at the physiological extracellular pH of 7.4. In contrast, the RODO-conjugated A $\beta$  displayed varying fluorescence intensities at different pH values for the same concentrations (Figure 4.S7-B). Overall, these experiments show that the pKa shifts towards phagosomal pH range when PTXG is conjugated to A $\beta$  (average pKa  $\sim$ 5.5) compared to the PTXG alone (average pKa  $\sim$ 4.5) whereas RODO-conjugated A $\beta$  has a pKa of  $\sim$ 6.3 that is more alkaline and close to the endosomal pH range of around 6.4–6.5. We also tested to see if the unconjugated PTXG and RODO dyes were endogenously taken up by the cells. BV2 microglia treated with PTXG alone showed very low fluorescence indicating minimal uptake of the dye compared to cells treated with the PTXG-A $\beta$  conjugate. The cells treated with RODO alone showed high fluorescence indicating higher dye uptake (at 1  $\mu$ M, the cells showed almost 50% fluorescence with RODO compared to the RODO-A $\beta$  conjugate) (Figure 4.S8) limiting its in vivo use. Neither of the two dyes were toxic to the cells in culture (Figure 4.S9).



**Figure 4.1** Synthesis and characterization of  $A\beta^{pH}$ . (A) The  $A\beta^{pH}$  is synthesized by conjugating the amine-reactive pH-sensitive Protonex Green dye to the side chain amine groups of the lysine residues and the N-terminal of human  $A\beta$ 1-42 peptide. (B) The pH-sensitivity of the  $A\beta^{pH}$  probe characterized at different concentrations from 0.1  $\mu$ M to 5.0  $\mu$ M. Increased fluorescence is observed at acidic pH values of  $\sim$ 5.0 to  $\sim$ 2.0, covering the pH range of the intracellular acidic organelles. (C) Atomic Force Microscopy topographic images of  $A\beta^{pH}$  oligomers compared to synthetic  $A\beta$  oligomers. Left-2D topographic image of  $A\beta^{pH}$  and synthetic  $A\beta$  oligomers. Right-3D image ( $2 \times 2 \mu$ m x-y). (D) Live cell imaging of the phagocytic uptake of 1  $\mu$ M  $A\beta^{pH}$  by BV2 and N9 mouse microglia and by HMC3 human microglia over 24 hours. (E) Quantification of  $A\beta^{pH}$  phagocytic score by BV2, N9, and HMC3 microglial cells from the live cell images. (F) The phagocytic uptake of  $A\beta^{pH}$  by BV2 cells is measured and quantified via flow cytometry analysis. Dot plot shows live (PI-) and  $A\beta^{pH+}$  cells. No green fluorescence is measured in unstained cells (UC) and in dead cells stained with the PI only whereas it is measured in cells treated with 0.5 and 5.0  $\mu$ M  $A\beta^{pH}$  for 1 hour (higher fluorescence is seen in cells exposed to the higher concentration of  $A\beta^{pH}$ ). Data shown in terms of % max, by scaling each curve to mode = 100% (y-axis).

Figure 4.1 continued



In order to validate that PTXG-A $\beta$  fluorescence increase in the acidic environment of the phagosome, we measured the fluorescence of the PTXG-A $\beta$  conjugate in cells treated with two different lysosomotropic compounds chloroquine (CQ) and bafilomycin A (BF). [36] Increased cellular PTXG-A $\beta$  fluorescence was measured with CQ (100  $\mu$ M) but we did not see any change in fluorescence with BF (100 nM) treatment (Figure 4.S10), possibly due to their different mode of action. Thus, summarizing the above-experiments, we believe that the PTXG-A $\beta$  conjugate outperforms the RODO-A $\beta$  conjugate due to the following reasons: (i) a narrower range of fluorescence, (ii) minimal background uptake, (iii) the long-term sustained fluorescence intensity of PTXG-A $\beta$  (Figure 4.S11), and (iv) a more suitable pK<sub>a</sub> value. Thus, the PTXG-A $\beta$  conjugate performed better and was chosen for all further experiments (termed A $\beta^{pH}$  henceforth in the paper). Lastly, we wanted to determine whether A $\beta^{pH}$  exhibits aggregation properties similar to the aggregation of synthetic, non-conjugated A $\beta$ . The A $\beta$ 1-42 and A $\beta^{pH}$  oligomers were prepared from hexafluoroisopropanol (HFIP) treated peptide films in PBS pH 7.4 buffer at 4 °C. Atomic force microscopy (AFM) revealed that the ability of A $\beta^{pH}$  to aggregate is similar, in size and height, to that of the non-conjugated A $\beta$  (Figure 4.1C) suggesting that A $\beta^{pH}$  is suitable for biological use [38,39].

### 4.3.2 A $\beta^{pH}$ uptake into human and mouse microglial cell lines

To visualize phagocytosis of A $\beta^{pH}$  in real time in live microglial cells, immortalized human microglial clone 3 (HMC3) cells and mouse BV2 and N9 microglial cells were treated with 1, 2 and 5.0  $\mu$ M concentrations of A $\beta^{pH}$  and live-cell images were acquired every 30 minutes for 24 hours (Figure 4.1D). We observed internalization and increased fluorescence of A $\beta^{pH}$  (implying phagocytosis) by HMC3 cells. The fluorescence was quantified as a *Phagocytic Score*, i.e. relative fluorescence compared to initial time (t=0) normalized over the 24-hour period (see Methods). For HMC3 cells there was an initial rapid phase of fluorescence (score) increase followed either by a slower increase in fluorescence at 5  $\mu$ M A $\beta^{pH}$  concentration or a slow decrease of fluorescence from its peak value at 1  $\mu$ M and 2  $\mu$ M A $\beta^{pH}$  concentration (Figures 4.1E, 4.S12). This suggests rapid initial uptake of A $\beta^{pH}$ , followed by intracellular degradation of A $\beta^{pH}$  which occurs either more rapidly than the influx (giving a slow decline) or less rapidly than the influx (giving a slowed increase) (Figure 4.S12). Cells that did not phagocytose A $\beta^{pH}$  did not display any green fluorescence thereby differentiating A $\beta^{pH}$ -specific phagocytic and non-phagocytic microglial cells

in real time. Rodent microglial cell lines (BV2 and N9) showed a peak of Phagocytic Score at 12-16 hours for N9 and 16-20 hours for BV2 at 5  $\mu\text{M}$   $\text{A}\beta^{\text{pH}}$  treatment, compared to the HMC3 human microglial cell line that showed a gradual increase in phagocytosis over the 24-hour treatment period for the same concentration. Interestingly, for the lower  $\text{A}\beta^{\text{pH}}$  doses of 1  $\mu\text{M}$  and 2  $\mu\text{M}$ , the peak value of Phagocytic Score for HMC3 cells was within the initial 4 hours compared to the gradual increase for the rodent cell lines over the 24 hour period (Figure 4.S12). Using live-cell imaging, we also observed interesting morphological differences over time between phagocytic and non-phagocytic microglial cells. During the initial 2 hours, many cells displayed an elongated, branched morphology followed by acquisition of an amoeboid morphology during subsequent time points when phagocytosis was occurring, as indicated by increased fluorescence (Movies 4.S1-3). Thus, the  $\text{A}\beta^{\text{pH}}$  reporter can be used to visualize  $\text{A}\beta$ -specific phagocytosis in real-time and can be used in experiments to evaluate enhancement or inhibition of microglial phagocytosis for *in vitro* screening of drug candidates for AD.

#### **4.3.3 Flow cytometry of $\text{A}\beta^{\text{pH}}$ phagocytic cells and staining of $\text{A}\beta^{\text{pH}}$ after phagocytosis in fixed primary cultured microglia and astrocytes**

We next determined whether  $\text{A}\beta^{\text{pH}}$  can be used to analyze phagocytosing cells using flow cytometry. By adding  $\text{A}\beta^{\text{pH}}$  to BV2 cells *in vitro*, we show that live microglial cells that phagocytose  $\text{A}\beta^{\text{pH}}$  can be easily analyzed with flow cytometry without the need for traditional dyes or antibodies to detect  $\text{A}\beta$  (Figure 4.1F, 4.S13-A). Phagocytic uptake of  $\text{A}\beta^{\text{pH}}$  by BV2 microglia was evident with a green fluorescence peak within live cells when the cells were treated with 0.5  $\mu\text{M}$  and 5.0  $\mu\text{M}$   $\text{A}\beta^{\text{pH}}$  for 1 hour in culture, with unstained and live/dead stained cells as controls. There was a slight increase in  $\text{A}\beta^{\text{pH}}$  fluorescence at 1 hour when the  $\text{A}\beta^{\text{pH}}$  concentration was increased 10-fold. The green fluorescence signal indicates internalization of  $\text{A}\beta^{\text{pH}}$  into the cellular acidic organelles, thereby avoiding detection of peptide sticking to the cell surface.  $\text{A}\beta^{\text{pH}}$  fluorescence after phagocytosis is sufficiently bright to enable FACS experiments, allowing single cell analysis of  $\text{A}\beta^{\text{pH}+}$  phagocytic and  $\text{A}\beta^{\text{pH}-}$  non-phagocytic microglia and other glial cells.

Fixing cells that have internalized  $\text{A}\beta^{\text{pH}}$ , and using specific antibodies and dyes to study specific molecular processes, can help identify molecular mechanisms involved during  $\text{A}\beta$  phagocytosis. To determine whether  $\text{A}\beta^{\text{pH}}$  can maintain its fluorescence in fixed cells, we used primary mouse

CD11b<sup>+</sup> microglial cells isolated from 3-5 month old mice as well as BV2, N9, and HMC3 microglia. After A $\beta$ <sup>pH</sup> (5.0  $\mu$ M) treatment for 2 hours, the cells were fixed in 4% paraformaldehyde followed by addition of red phalloidin dye (a podosome core marker for F-actin) to visualize actin filaments and the cell body with confocal microscopy (Figure 4.S14-A,B). Confocal imaging of the fixed A $\beta$ <sup>pH</sup>-treated microglia showed green fluorescence within the red actin filaments thereby confirming the uptake of A $\beta$ <sup>pH</sup> peptides by the cells. Further, LysoTracker DND-99 was used to confirm localization of A $\beta$ <sup>pH</sup> within acidic organelles such as phagosomes or phagolysosomes. The co-localization of green fluorescent A $\beta$ <sup>pH</sup> along with the red signal from the LysoTracker dye confirmed the presence of A $\beta$ <sup>pH</sup> within acidic phagolysosomes after 2 hours in HMC3, N9, and BV2 microglia cell lines (Figures 4.2-A, 4.S14-C). Similarly, uptake of A $\beta$ <sup>pH</sup> into intracellular acidic organelles was also confirmed in CD11b<sup>+</sup> primary microglia that were cultured in reduced-serum TIC medium [40] (Figure 4.2-B). Finally, we also detected the green fluorescence signal within CD11b<sup>+</sup> primary microglia (A $\beta$ <sup>pH+</sup> cells) at 0.5, 1.0, and 2.0  $\mu$ M A $\beta$ <sup>pH</sup> concentrations via flow cytometry (Figures 4.2-C, 4.S13-B) after 1 hour of treatment, and found an increase in fluorescence with A $\beta$ <sup>pH</sup> concentration. The unstained and live/dead stained cells were used as controls. Microglia recognize and phagocytose A $\beta$  peptides through scavenger receptors such as Toll-Like Receptor 2 (TLR2), Cluster of Differentiation 14 (CD14), and Triggering Receptors Expressed on Myeloid Cells 2 (TREM2) [41–43]. Studies have shown that deletion of, or mutations in A $\beta$ -specific receptors, such as TREM2, leads to increased A $\beta$  seeding [44,45]. Thus, the A $\beta$ <sup>pH</sup> reporter that we have developed could serve as a valuable chemical tool to delineate the role of receptor proteins involved in A $\beta$  uptake by glial cells, using specific antibodies or CRISPR-Cas9 genetic screens.

In addition to microglia, astrocytes have been shown to exhibit phagocytic characteristics after ischemic injury [16] and can phagocytose extracellular A $\beta$  [28]. Therefore, we tested whether primary immunopanned cultured mouse astrocytes phagocytosed A $\beta$ <sup>pH</sup>. Indeed, this was the case, with retention of the phagocytic A $\beta$ <sup>pH</sup> signal after methanol-fixation and staining of cells with GFAP antibody (Figure 4.2-D). A $\beta$ <sup>pH</sup> phagocytosis could also be detected with live cell imaging (Figure 4.2-E). Quantification of A $\beta$ <sup>pH</sup> uptake at different concentrations showed internalization increasing for approximately 1 hour, followed by a sustained fluorescence within the cells which may reflect a balance between phagocytosis and degradation of the probe (Figure 4.2-F). Thus,

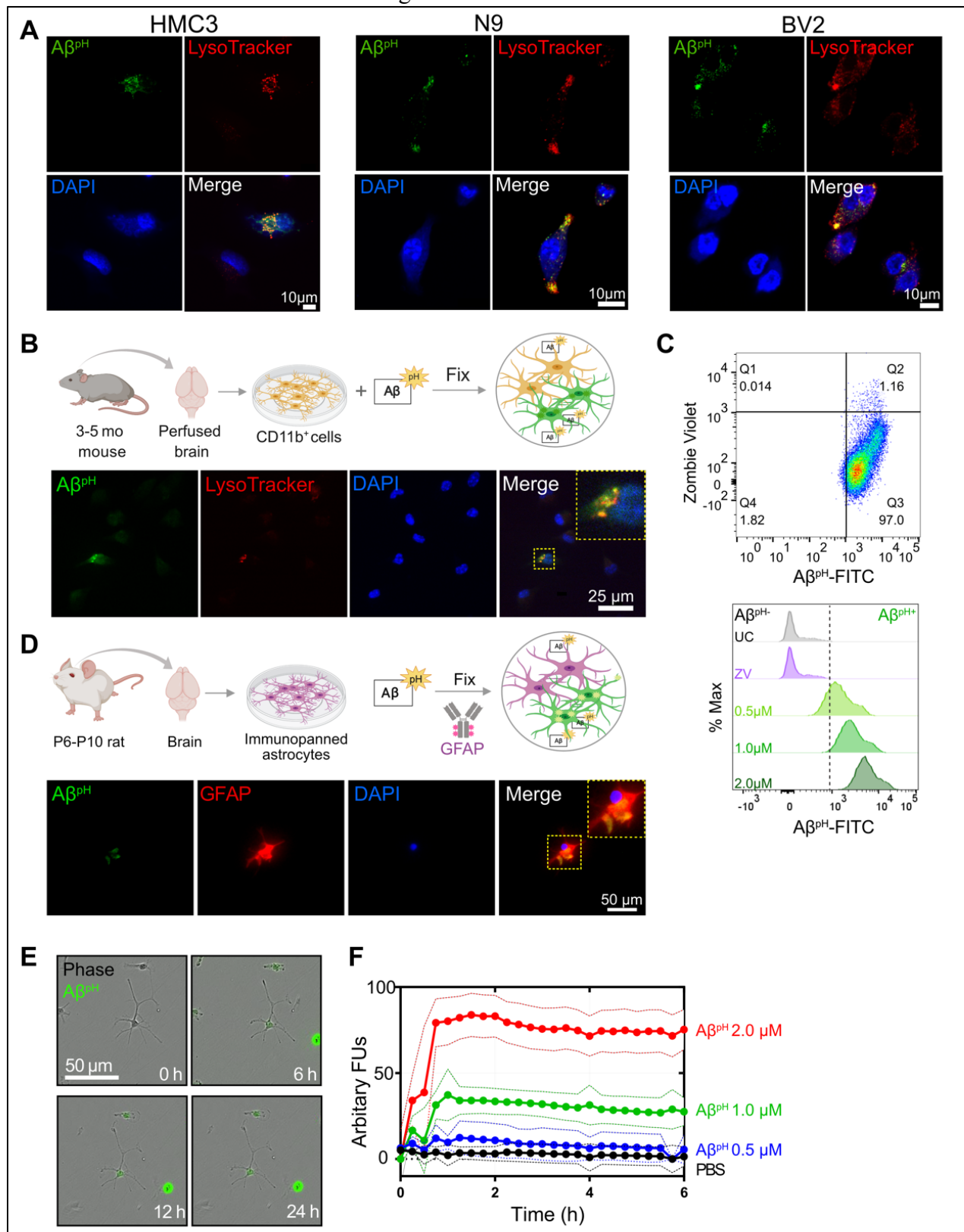
A $\beta^{pH}$  may be a viable candidate for concentration- and time-dependent studies of glial cell phagocytosis *in vitro*. The sustained fluorescence of A $\beta^{pH}$  seen for up to 6 hours inside cultured microglia and astrocytes suggests that it is chemically stable under physiological conditions – allowing for long-term use *in vivo*.

#### **4.3.4 A $\beta^{pH}$ uptake by microglia and astrocytes in hippocampus, cortex, and retina**

To assess phagocytic uptake of A $\beta^{pH}$  in the hippocampus, a brain area that is crucial for learning and memory, we applied 5  $\mu$ M A $\beta^{pH}$  (for 1.5 hours at 37 °C) to live hippocampal slices from postnatal day 12 (P12) rat. The tissue slices were then fixed and stained with glial cell specific antibodies (Figure 4.3-A). Microglia phagocytosed A $\beta^{pH}$  as seen by the localization of A $\beta^{pH}$  within the IBA1<sup>+</sup> myeloid cells in these tissues (Figure 4.3-B). Our experiments revealed green fluorescent signal both within IBA1<sup>+</sup> microglial cells as well as outside the IBA1<sup>+</sup> cells (Figure 4.S15), presumably reflecting phagocytic uptake of A $\beta^{pH}$  by cells other than microglia, such as astrocytes. Indeed, staining with GFAP antibody demonstrated internalization of A $\beta^{pH}$  within GFAP<sup>+</sup> astrocytes (Figure 4.3-C). Summing over cells, approximately 60% of the internalized A $\beta^{pH}$  was phagocytosed by microglia and 40% by astrocytes (Figure 4.3-D). Interestingly, in astrocytes the phagocytosed A $\beta^{pH}$  was distributed more homogeneously throughout the GFAP area than the phagocytosed A $\beta^{pH}$  in IBA1 stained microglia. This is expected since in microglia the acidic compartments (where A $\beta^{pH}$  is present) are mostly juxtanuclear whereas IBA1 is known to be enriched in podosomes and podonuts [46]. In contrast, in astrocytes the acidic compartments occur all over the cell body [47].

**Figure 4.2** Fluorescence of internalized  $A\beta^{pH}$  is retained in fixed cells. (A) Confocal images of fixed HMC3, N9, and BV2 cells showing the uptake of  $A\beta^{pH}$  (green). Cells are stained for acidic intracellular organelles (LysoTracker Red, confirming co-localization of the  $A\beta^{pH}$  within the acidic intracellular organelles) and nuclei (DAPI, blue). No antibody is required to detect  $A\beta^{pH}$ . (B) Primary mouse microglia grown in defined, reduced-serum media phagocytose  $A\beta^{pH}$  *ex vivo*. Cells are fixed and stained for nuclei and show  $A\beta^{pH}$  colocalized in the acidic organelles with LysoTracker Red. (C) The phagocytic uptake of  $A\beta^{pH}$  by primary microglia is measured and quantified via flow cytometry analysis. Dot plot shows live (ZV<sup>-</sup>) and  $A\beta^{pH+}$  cells. No green fluorescence is measured in unstained cells (UC) or dead cells stained with the ZV live/dead stain only whereas green fluorescence is measured in cells treated with 0.5, 1.0, and 2.0  $\mu$ M  $A\beta^{pH}$  for 1 hour. Data shown in terms of % max, by scaling each curve to mode = 100% (y-axis). (D) Primary immunopanned rat astrocytes also phagocytose  $A\beta^{pH}$  in serum-free conditions. Cells are fixed and stained for astrocyte specific GFAP antibody (red) and nuclei. (E) Uptake of  $A\beta^{pH}$  over time by primary immunopanned astrocytes as observed in live cells in real time. (F) Quantification of uptake of 0.5, 1.0, and 2.0  $\mu$ M  $A\beta^{pH}$  by primary astrocytes.

Figure 4.2 continued





We next tested the A $\beta^{pH}$  probe in different in vivo settings. After intracranial injection of A $\beta^{pH}$  into the somatosensory cortex of wild-type P7 C57BL/6J mice (Figure 4.4-A), phagocytosis of the A $\beta^{pH}$  by IBA1<sup>+</sup> microglia and GFAP<sup>+</sup> astrocytes was assessed by fixing the corresponding tissue sections at 24 and 72 hours after injection. At 24 hours, A $\beta^{pH}$  was observed in the injected area and appeared to be enclosed within cell bodies. There was less astrocyte uptake of A $\beta^{pH}$  compared to uptake by microglia, which may be a result of a reactive response by astrocytes that has been shown to downregulate phagocytic pathways in some states [5] (Figure 4.4-B, D). At 72 hours after the A $\beta^{pH}$  injection there was also A $\beta^{pH}$  visible at the pial surface and in the periventricular white matter. With increased magnification, we observed cell bodies containing A $\beta^{pH}$  that were positive for the IBA1 microglial marker (Figure 4.4-C) but the GFAP<sup>+</sup> astrocytes localized at the injection site showed very little A $\beta^{pH}$  signal (Figure 4.4-D). Thus, microglia engulf the majority of the A $\beta^{pH}$  under these conditions in vivo with astrocytes also contributing to removal at early times.

Next, we injected A $\beta^{pH}$  into the vitreous of the eye in postnatal rats to eliminate possible complications due to glial scarring resulting from cortical injection, and low penetration through the blood-brain barrier as a result of peripheral delivery (Figure 4.4-E). We injected 1  $\mu$ L of A $\beta^{pH}$  intravitreally and left the animals for 3, 24, or 72 hours. At the end of the experiment, retinæ were removed, fixed in 4% paraformaldehyde, and whole mount retinal preparations were made. Astrocytes and microglia in the retinal ganglion cell layer were labelled with GFAP and IBA1 antibodies respectively, and co-localization with the fluorescent signal from the injected A $\beta^{pH}$  probe was determined. We observed that IBA1<sup>+</sup> microglia contained A $\beta^{pH}$  at all time points, but we did not detect any A $\beta^{pH}$  signal in GFAP<sup>+</sup> astrocytes (Figure 4.4-F,G). The A $\beta^{pH}$  positive microglia were less visible in the retina compared to other brain regions, suggesting that clearance from the eye was more rapid than clearance from the brain parenchyma as observed in other experiments (above).

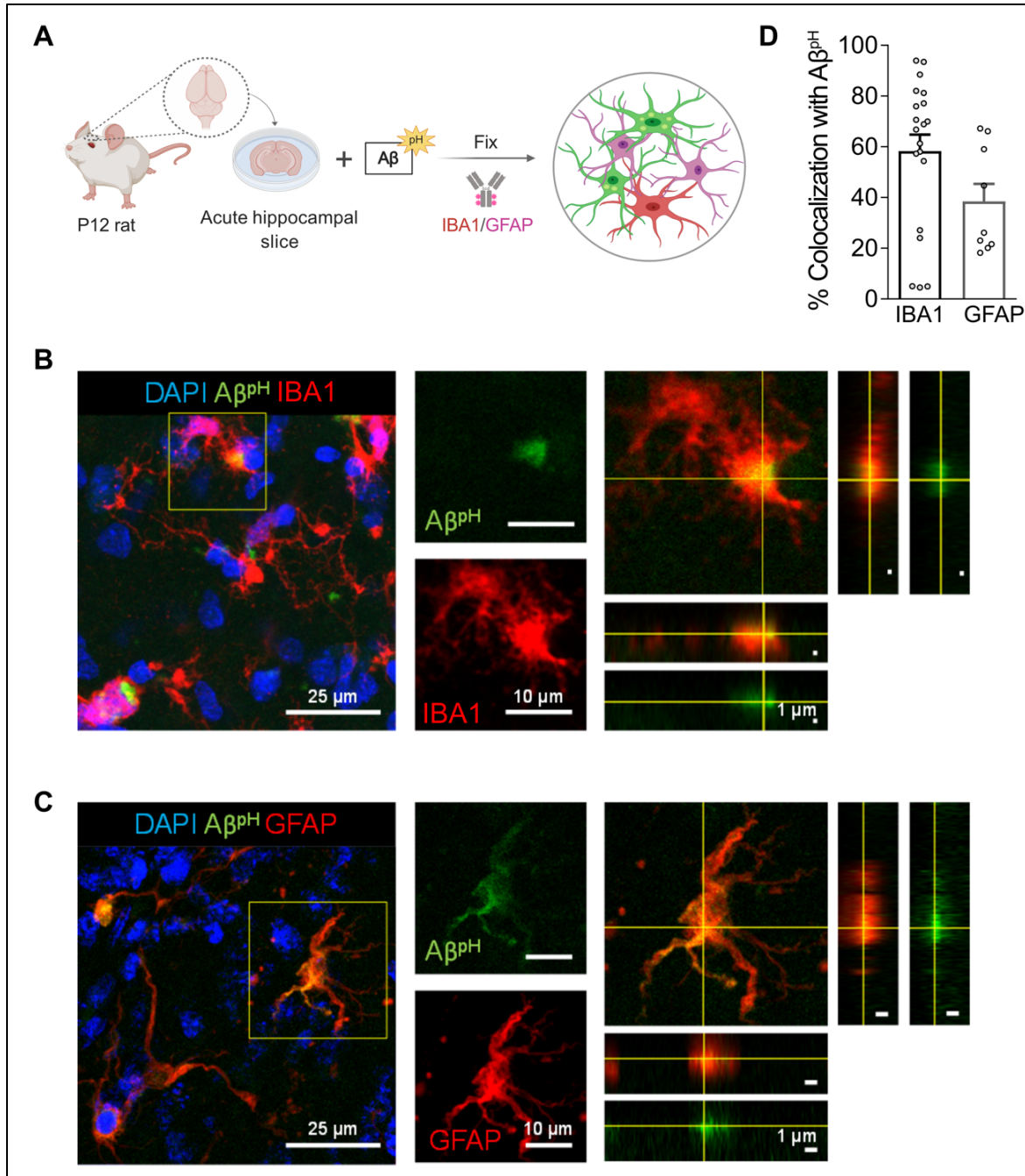
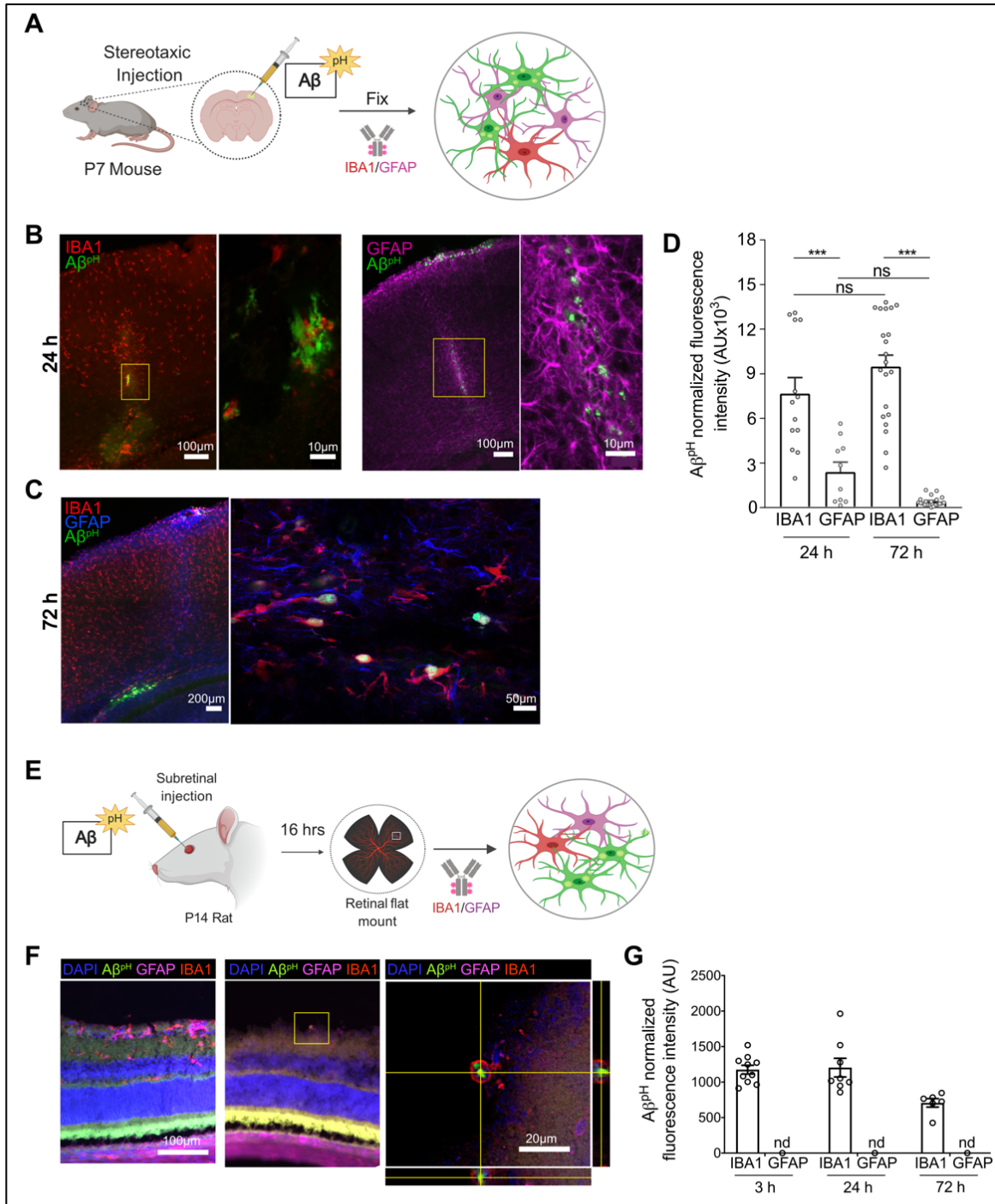


**Figure 4.3** Aβ<sup>pH</sup> is phagocytosed by both microglia and astrocytes in situ in rat hippocampal tissue sections. (A) Schematic of phagocytosis assay in rat hippocampal tissue slices. (B) Representative 2D maximum projection of a confocal z-stack showing microglia phagocytosing Aβ<sup>pH</sup>. Closeup of the indicated cell (yellow square) is shown on the right. Orthogonal projections at the level of the crosshairs show internalization of Aβ<sup>pH</sup> within the microglia. (C) Representative 2D maximum projection of a confocal z-stack showing astrocytes phagocytosing Aβ<sup>pH</sup>. Closeup of the indicated cell (yellow square) is shown on the right. Orthogonal projections at the level of the crosshairs show internalization of Aβ<sup>pH</sup> within the astrocyte. (D) Quantification of Aβ<sup>pH</sup> colocalized with microglia and astrocytes, as defined by IBA1<sup>+</sup> and GFAP<sup>+</sup> staining, respectively. Data shown as mean ± s.e.m. collected from 20 and 8 slices for microglia and astrocytes respectively (from 3 animals).

**Figure 4.4**  $A\beta^{pH}$  is phagocytosed by cortical microglia and astrocytes *in vivo* and by rat retinal microglia *in vivo*. (A) Schematic of stereotaxic microinjection of  $A\beta^{pH}$  in the somatosensory cortex of P7 mouse followed by staining of fixed tissue section after 24 and 72 hours. (B) Phagocytic uptake of  $A\beta^{pH}$  by IBA1<sup>+</sup> microglia and GFAP<sup>+</sup> astrocytes in the periventricular white matter at the 24 hour timepoint. The box represents the region of the fluorescence image where high magnification confocal imaging was done. (C) IBA1<sup>+</sup> microglia show bright green fluorescence at 72 hour in the same region indicating presence of  $A\beta^{pH}$  within the cells at this timepoint. GFAP<sup>+</sup> astrocytes do not show any green fluorescence in this region at this timepoint suggesting either degradation of the peptide or insufficient  $A\beta^{pH}$  concentration for detectable phagocytic uptake by these cells. (D) Quantification of  $A\beta^{pH}$  fluorescence within IBA1<sup>+</sup> microglia and GFAP<sup>+</sup> astrocytes located in the pia and white matter regions show more  $A\beta^{pH}$  uptake by microglia compared to astrocytes. (E) Schematic of subretinal injection of  $A\beta^{pH}$  to evaluate its *in vivo* uptake by rat retinal microglia and astrocytes. (F) IBA1<sup>+</sup> rat retinal microglia phagocytose  $A\beta^{pH}$  *in vivo*. (G) Quantification of  $A\beta^{pH}$  uptake into retinal IBA1<sup>+</sup> microglia and GFAP<sup>+</sup> astrocytes. No fluorescence was detected in astrocytes at these 3 time points (n.d.). Data shown as mean $\pm$ s.e.m. from 2 animals.

Figure 4.4 continued



The *in vivo* investigation of A $\beta$  phagocytosis described above consists of imaging fixed tissue sections with confocal microscopy. To date, phagocytosis of A $\beta$  has not been observed in live animals in real time. Using A $\beta^{\text{pH}}$ , we observed phagocytic uptake in live mice in real time using two-photon microscopy (Movies 4.S4, 4.S5). Here, 5.0  $\mu\text{M}$  A $\beta^{\text{pH}}$  was applied onto the cortical surface of live mice through a cranial window for 10 minutes during two-photon imaging of the barrel cortex (Figure 4.5-A). This showed an increase in green fluorescence in the cell somata after A $\beta^{\text{pH}}$  application, indicating phagocytic uptake of A $\beta^{\text{pH}}$  (Figure 4.5-B). Quantification of the fluorescence within the cell somata showed rapid A $\beta^{\text{pH}}$  uptake after the peptide was added to the cranial window followed by stabilization of the signal at around 20 minutes (Figure 4.5-C). The brains were later fixed by cardiac paraformaldehyde perfusion and stained with antibodies to identify the cell types mediating the A $\beta^{\text{pH}}$  uptake. Phagocytosed green A $\beta^{\text{pH}}$  was present in IBA1 labeled microglia and colocalized with the microglia/macrophage lysosomal protein CD68, and A $\beta^{\text{pH}}$  was also seen in GFAP<sup>+</sup> astrocytes (Figure 4.5-D). Integrating the fluorescence over the different classes of labeled cells showed that about 70% of the phagocytosed A $\beta^{\text{pH}}$  was taken up by microglia and about 25% by astrocytes (Figure 4.5-E). These percentages are similar to those seen in the brain slice experiments described above. Thus, microglial uptake of A $\beta^{\text{pH}}$  dominates over astrocyte uptake.

#### 4.4 Discussion

The phagocytic capacity of glial cells has been measured using traditional dyes and fluorophore-labeled particles such as fluorescein or rhodamine-coated *E. coli* and beads, however, these experiments entail some major drawbacks: 1) difficulty in differentiating between adherent versus internalized particles, 2) use of additional reagents (like trypan blue or ethidium bromide) and additional experimental steps required to quench the extracellular fluorescence prior to analysis by flow cytometry and imaging [48], 3) quenching of the fluorescence within the acidic environment of the phagosomes, and 4) lack of specificity of the neuronal target substrate (beads, *E. coli*, zymosan, etc.) [49]. Here, we have synthesized a pH-sensitive fluorogenic A $\beta$  reporter, A $\beta^{\text{pH}}$ , at a microgram scale and characterized the reporter in detail (Figures 4.1-A-C, 4.S2-11). We show that the A $\beta^{\text{pH}}$  is well suited for detection in the acidic environment of the lysosomal organelles with pH of 5.0-4.5. The PTXG dye has an acidic pKa of 4.4-4.7 in DMEM/F12 cell culture medium and exhibits a gain of fluorescence in the acidic environments. Upon conjugation with A $\beta$ , the pKa

of A $\beta^{\text{pH}}$  probe shifts to 5.2-5.9, which is in the range of acidic lysosomal organelles and is thus ideal for future mechanistic studies. Moreover, the unconjugated PTXG dye exhibits low to no background fluorescence signal, compared to other commercial dyes such as pHrodo-Red SE, justifying its *in vitro* and *in vivo* use. We demonstrated the functionality of A $\beta^{\text{pH}}$  in mouse and human microglial cell lines, in primary microglia and astrocyte cultures *in vitro*, in acute hippocampal slices from mouse brains, in mice *in vivo* using stereotaxic injections followed by fixation, and in live mice *in vivo* via two-photon imaging. The A $\beta^{\text{pH}}$  reporter is a powerful tool for answering questions related to mechanisms of A $\beta$  phagocytosis and cellular inflammatory responses, and for developing therapeutic strategies to promote A $\beta$  clearance.

We observed phagocytic uptake of A $\beta^{\text{pH}}$  in three different microglial cell lines and in primary glial cell cultures in real-time (Figures 4.1-D-E, 4.2-E-F) and by using confocal imaging (Figure 4.2-A-B, D). We showed the utility of A $\beta^{\text{pH}}$  to be used without the need for any antibodies to identify or detect A $\beta$  using flow cytometry (Figures 4.1-F, 4.2-C) which will greatly benefit experimental design and outcome by reducing the number of steps required in assays. While microglia cultured *in vitro* and *ex vivo* do not completely recapitulate the transcriptomes of microglia *in vivo* [50], microglial cell culture models provide a convenient system for screening chemical and biological molecules in a rapid and high-throughput manner. We also demonstrated the utility of A $\beta^{\text{pH}}$  in functional assays to evaluate cellular phagocytosis. Further, we demonstrated the phagocytic uptake of A $\beta^{\text{pH}}$  in live tissue hippocampal slices that preserve the three-dimensional nature of the cell microenvironment and can serve as an additional useful model to study A $\beta$ -related biology in a tissue environment. Microglia were more efficient in internalizing A $\beta^{\text{pH}}$  than astrocytes *in situ* (Figures 4.3-A-D). During the period of this assay it is unlikely that astrocytes would have become reactive so it appears that A $\beta$  clearance is not just a property of reactive astrocytes [51–53]. The astrocytes most closely associated with neurodegeneration appear to be of a reactive phenotype that downregulates phagocytic pathways [5], suggesting that the engulfment of A $\beta^{\text{pH}}$  by astrocytes is a normal physiological function of these cells (although this may change with disease progression).

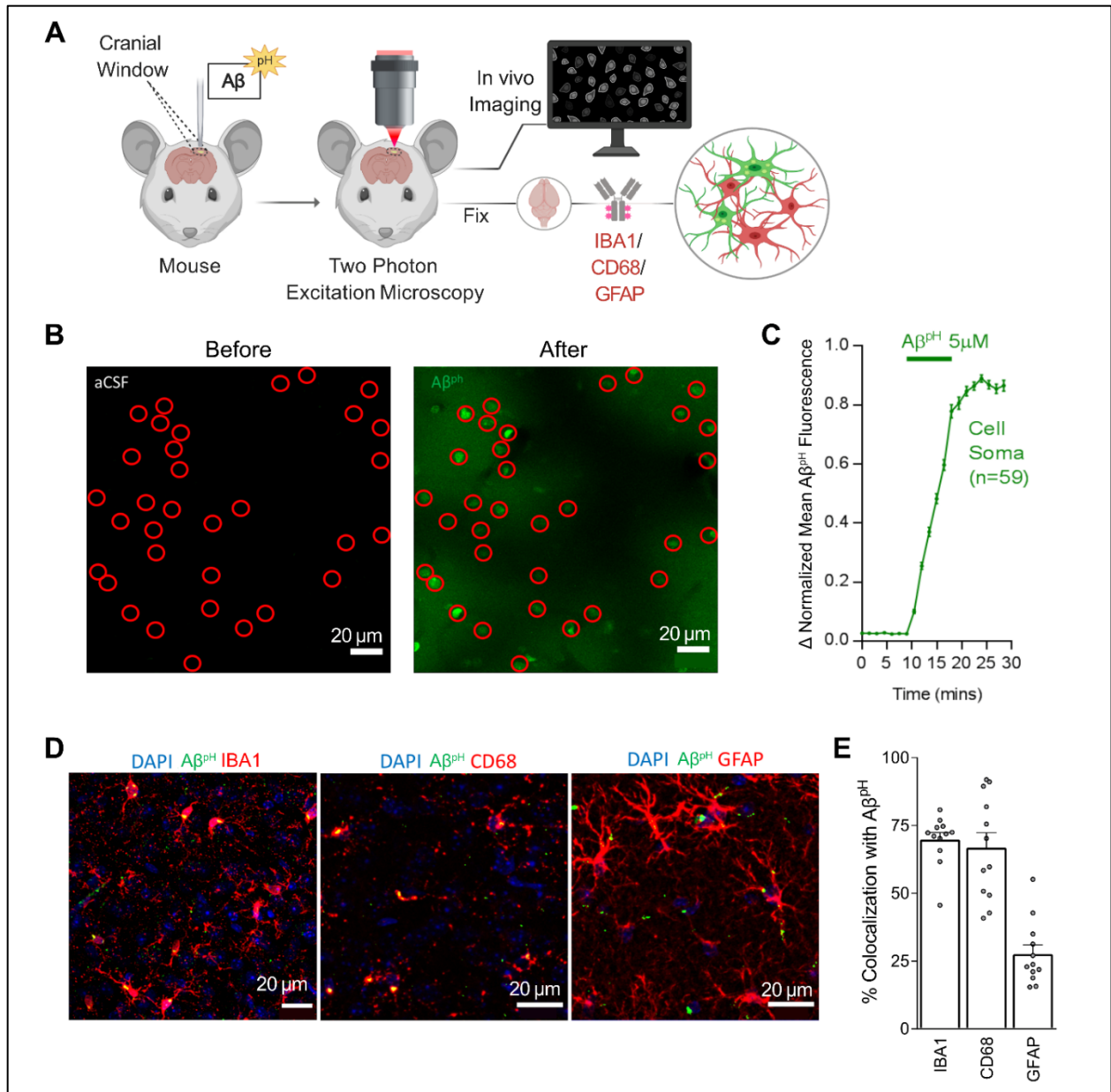


**Figure 4.5** Aβ<sup>pH</sup> is phagocytosed by microglia and astrocytes in vivo in the cerebral cortex. (A) Schematic of how Aβ<sup>pH</sup> phagocytic uptake is imaged through a cranial window in vivo in real time using two-photon excitation microscopy. (B) *In vivo* two-photon imaging of the mouse barrel cortex before and after topical application of Aβ<sup>pH</sup>. The fluorescence increases in cell somata (indicated by red circles) reflecting Aβ<sup>pH</sup> uptake. (C) Quantification of mean Aβ<sup>pH</sup> fluorescence in cell somata over time. The data were normalized to the maximum mean Aβ<sup>pH</sup> fluorescence for each cell and then averaged. Data shown as mean ± s.e.m. N=59 somata from 2 animals. (D) 1.5 to 3 hours after in vivo two-photon imaging of Aβ<sup>pH</sup>, animals were perfusion-fixed and cortical slices were stained for microglia, microglia lysosomes/endosomes and astrocytes using IBA1, CD68, and GFAP antibodies, respectively. (E) Quantification of Aβ<sup>pH</sup> colocalization with IBA1, CD68, and GFAP suggests that most Aβ<sup>pH</sup> is taken up by microglia and astrocytes in vivo. Data shown as mean ± s.e.m. N=12 stacks from 3 animals.

Most importantly, we demonstrated the utility of using of A $\beta^{pH}$  in various in vivo models. Stereotaxic injection of A $\beta^{pH}$  into the mouse somatosensory cortex was followed by uptake by microglia and astrocytes (Figures 4.4-A-D), injecting A $\beta^{pH}$  into the vitreous of the eye was followed by uptake by retinal microglia (Figures 4.4-E-G), and the real-time uptake of A $\beta^{pH}$  by microglia and astrocytes was demonstrated in vivo in live mice using two-photon microscopy (Figures 4.5-A-C). We confirmed the identity of the cells observed with two-photon excitation by using IBA1 to label microglia, CD68 (a phagocytosis-specific marker) to label microglia and macrophages, and GFAP to label astrocytes (Figures 4.5-D-E). The time course of uptake in vivo was rapid, with phagocytosed A $\beta^{pH}$  fluorescence reaching a peak level within 20 minutes (this may reflect a balance between continued phagocytosis and intracellular degradation). Approximately two thirds of the A $\beta^{pH}$  was phagocytosed by microglia and one third by astrocytes, again on a time scale too rapid for astrocytes to have become reactive.

The development of A $\beta^{pH}$ , in particular the ease with which it can be produced in the lab, will facilitate the characterization of different populations of cells that remove (or do not remove) A $\beta$  by phagocytosis in various conditions, including AD, trauma-induced amyloidopathy and Down's syndrome. Combining this tracer with transgenic labeling of microglia (e.g. *Tmem119*-tdTomato mice [54] which exhibit red fluorescence in microglia) or other cell types will allow the transcriptome and proteome of different subpopulations of heterogeneous phagocytic cells to be defined (including cells of different age [25,55,56], and sex [57]), facilitating the discovery of new mechanisms, targets and functional biomarkers. Understanding the clearance of A $\beta$  is fundamental to understanding the onset of AD [58,59], and having a quantitative technique to assess A $\beta$  phagocytosis should contribute significantly to this. We expect that A $\beta^{pH}$  will become a useful tool to facilitate the study of impaired phagocytic function mechanisms in vivo during chronic inflammation in neurodegenerative diseases.

## **4.5 Materials and methods**

### **4.5.1 Animal ethics**

Animal maintenance and isolation of primary microglia were performed according to Purdue Animal Care and Use Committee guidelines and approval (protocol number 1812001834).



Injection of A $\beta^{\text{pH}}$  into the retina of rats were completed in accordance with the National Institute of Health Stanford University's Administrative Panel on Laboratory Animal Care. Purification of rat primary astrocyte was completed in accordance with NYU Langone School of Medicine's Institutional Animal Care and Use Committee (IACUC) guidelines and approval. All rats were housed with ad libitum food and water in a 12 hour light/dark cycle. Standard Sprague Dawley rats (Charles River, #400) were used in all retinal experiments. Animal maintenance and experimental procedure for the intracranial stereotaxic injections of A $\beta^{\text{pH}}$  in mice were performed according to the guidelines established by the IACUC at Harvard Medical School (protocol number IS00001269). Experiments on brain slices and in vivo 2-photon imaged mice were carried out under a UK government license (PPL 70/8976, awarded after local ethical review and UK Home Office assessment) to David Attwell, in accordance with all relevant animal legislation in the UK.

#### **4.5.2 Synthesis of pH-sensitive fluorescent human A $\beta$ conjugate with Protonex Green**

Human amyloid-beta (A $\beta$ 1-42) was purchased from AnaSpec., Inc (Cat. #AS-20276), Protonex<sup>TM</sup> Green 500 SE was from AAT Bioquest, Inc. (Cat. #21215), and pHrodo-Red SE was from Thermo Fisher Scientific (Cat. #P36600). To 200  $\mu\text{L}$  aliquot of A $\beta$ 1-42 (1 mg/mL in 1M NaHCO<sub>3</sub>, pH ~8.3) was added 10 equivalents of Protonex-Green 500 (PTXG), SE dye (88  $\mu\text{L}$  from 5 mM stock in anhydrous DMSO) and incubated at room temperature for 3 hours in the dark (vial wrapped in aluminum foil: note: add 100  $\mu\text{L}$  ultrapure water if the solution becomes viscous). The additional 5 equivalents of PTXG, SE dye (44  $\mu\text{L}$  from 5 mM DMSO stock) was added and incubated under the same conditions for 3 hours. The crude reaction mixture was diluted with 1 mL ultrapure water and the conjugated product was dialyzed by Pierce Protein Concentrators at 4500 g for 30-45 minutes in a swinging bucket centrifuge to remove the small molecular weight fragments. [Pierce Protein Concentrators PES, 3K Molecular Weight Cut-Off (MWCO); Thermo Fisher Scientific, Cat #PI88514, note: prior use, wash and centrifuge protein concentrator with 1 mL ultrapure water to remove any preservatives] The resulting concentrated solution was diluted with 0.5 mL ultrapure water and dialyzed again for 15-30 minutes as done previously. Then the concentrated solution was diluted with 0.2 mL ultrapure water and lyophilized overnight to get the A $\beta^{\text{pH}}$  powder.

Finally, MALDI-MS spectrum was recorded to confirm the chemical conjugation of PTXG with A $\beta$ 1-42.

#### **4.5.3 Synthesis of pH-sensitive fluorescent human A $\beta$ 1-42 conjugate with pHrodo**

A solution containing A $\beta$ 1-42 (570  $\mu$ g, 12.63 nmol) was prepared in 1M NaHCO<sub>3</sub> (pH 8.3, 570  $\mu$ L) and the pHrodo Red-NHS (1 mg) stock solution was prepared in anhydrous DMSO (150  $\mu$ L) (~10.2 mM). Next, the A $\beta$  solution (570  $\mu$ L) and pHrodo stock solution (0.6314  $\mu$ mol, 61.5  $\mu$ L of stock solution) were mixed and incubated at room temperature for 6 hours while wrapped with aluminum foil. This crude reaction mixture was then diluted with ultrapure water (1 mL) and the conjugated product was dialyzed by Pierce Protein Concentrators (PES, 3K MWCO, note: prior use, wash and centrifuge protein concentrator with 1 mL ultrapure water to remove any preservatives) at 4500 g for 30-45 minutes in a swinging bucket centrifuge to remove the small molecular weight fragments. The resulting concentrated solution was diluted with ultrapure water (0.5 mL) and dialyzed again for 15-30 minutes as before. Then the concentrated solution was diluted with 0.2 mL ultrapure water and lyophilized overnight to get the RODO-A $\beta$ <sup>pH</sup> powder. Finally, the MALDI-MS spectrum was recorded to confirm the chemical conjugation of pHrodo-Red fluorophore to the A $\beta$  peptide.

#### **4.5.4 Preparation of HFIP-treated A $\beta$ and A $\beta$ <sup>pH</sup> stocks**

A $\beta$  or A $\beta$ <sup>pH</sup> was dissolved in HFIP and prepared as previously described [37]. Briefly, 1 mM A $\beta$  solution was prepared by adding HFIP directly to the vial (0.5 mg A $\beta$  or A $\beta$ <sup>pH</sup> in 93.35  $\mu$ L HFIP). The peptide should be completely dissolved. The solution was incubated at room temperature for at least 30 min. HFIP was allowed to evaporate in the open tubes overnight in the fume hood and then dried down under high vacuum for 1 hour without heating to remove any remaining traces of HFIP and moisture, leaving a thin clear film of peptide at the bottom of the tubes. The tubes containing dried peptides were stored at -20 °C until further use. To make oligomers, 5 mM A $\beta$  DMSO stock was prepared by adding 22  $\mu$ L fresh dry DMSO to 0.5 mg of dried peptide film. To ensure complete resuspension of peptide film, the mixture was pipetted thoroughly, scraping down the sides of the tube near the bottom. The suspension was vortexed well (~30 seconds) and pulsed in a microcentrifuge to collect the solution at the bottom of the tube and the 5 mM A $\beta$  DMSO

solution was sonicated for 10 minutes. This preparation was used as the starting material for preparing the aggregated A $\beta$  incubated at 4 °C for 24 hours for analysis by Atomic Force Microscopy.

#### **4.5.5 Atomic Force Microscopy for analysis of A $\beta$ and A $\beta^{pH}$ aggregates**

We followed the previously published detailed protocols for analyzing A $\beta$  and A $\beta^{pH}$  aggregates by Atomic Force Microscopy (AFM) [37,38]. Briefly, sample preparation was performed with sterile techniques using sterile media and MilliQ-water. A 10 mL syringe with ultrapure water equipped with a 0.22  $\mu$ m filter was filled and the initial 1–2 mL was discarded through syringe filter output. 1M HCl and 1x PBS buffer were also filtered through 0.22  $\mu$ m filter. The samples were prepared for spotting on mica by diluting to final concentrations of 10–30  $\mu$ M in water. Immediately before sample delivery, top few layers of mica were cleaved away using an adhesive tape to reveal a clean, flat, featureless surface. The fresh surface was pretreated with ~5-8  $\mu$ L of filtered 1M HCl for 30 seconds and rinsed with two drops of water (note: the mica was held at a 45° angle and washed with water to allow the water coming out of the syringe filter to roll over the mica). If necessary, the remaining water was absorbed with fiber-free tissue paper/wipes by keeping paper on the edge of the mica. Immediately, the sample was spotted onto mica and incubated for 3 minutes followed by rinsing with three drops of water and blow drying with several gentle pulses of compressed air. Samples were then kept in a dust-free box and incubated on benchtop for a few minutes to hours at room temperature until analysis. AFM imaging was performed with Veeco Multimode with NanoScope V controller with NanoScope Software using the Silicon AFM probes, TAP300 Aluminum reflex coating (Ted Pella, Inc. Cat# TAP300AL-G-10) at ~300 kHz resonant frequency and ~40 N/m force constant in the tapping mode.

#### **4.5.6 pH-dependent emission spectra of A $\beta$ conjugated with Protonex Green and A $\beta$ conjugated with pHrodo at various concentrations**

The cell culture medium was supplemented with dilute HCl and NaOH solutions to obtain different solutions of pH ranging from 1.0 to 9.0 for the assay. Lyophilized powder of A $\beta$  conjugated with pHrodo (RODO-A $\beta^{pH}$ ) and A $\beta$  conjugated with Protonex Green® (PTXG-A $\beta^{pH}$ ) was dissolved in cell culture medium to make stock solutions and kept at 37 °C for 24 hours to pre-aggregate the peptide conjugates. From the stock solutions, different dilutions for each pH condition were

prepared at concentrations of 0.5, 1.0, 2.0, and 5.0  $\mu\text{M}$  in a 96-well plate (100  $\mu\text{L}$ /well). Fluorescence intensity of each well containing  $\text{A}\beta^{\text{pH}}$  was obtained on a Cytation<sup>TM</sup> 5 imaging multi-mode reader (BioTek Instruments) at 443/505 nm excitation/emission wavelengths. The fluorescence intensity of each pH-solution and  $\text{A}\beta^{\text{pH}}$ -concentration in relative fluorescence units (RFU) was plotted using GraphPad Prism software.

#### **4.5.7 pKa of Protonex Green 500 SE, $\text{A}\beta^{\text{pH}}$ , and RODO- $\text{A}\beta^{\text{pH}}$**

The cell culture medium DMEM/F12 (Corning Cat.# MT15090CV) was supplemented with dilute HCl and NaOH solutions to obtain different pH solutions (pH range 3.85, 4.03, 4.26, 4.46, 4.88, 5.02, 5.30, 5.67, 6.22, 6.44, 6.94, 7.40, 8.31) for the assay. From the stock solutions (5 mM of PTXG and 100  $\mu\text{M}$  of  $\text{A}\beta^{\text{pH}}$ ) different dilutions for each pH condition were prepared at concentrations of 5.0, 2.0, 1.0, 0.5  $\mu\text{M}$  in a 384-well plate with 40  $\mu\text{L}$ /well total volume (Corning NBS plate, cat #3575). Fluorescence intensity of each well containing PTXG and  $\text{A}\beta^{\text{pH}}$  was obtained on a Varioskan LUX imaging multi-mode reader (Thermo Scientific) at excitation/emission wavelengths 443/505 nm for PTXG or  $\text{A}\beta^{\text{pH}}$  and excitation/emission wavelengths 466/590 nm for RODO- $\text{A}\beta^{\text{pH}}$ . The fluorescence intensity was normalized by dividing each value by the highest value obtained for 5  $\mu\text{M}$  concentration. The fluorescence intensity of each pH-solution vs Normalized fluorescence intensity for each concentration was plotted using three replicates and processed using GraphPad Prism software.

#### **4.5.8 Concentration-dependent response of Protonex Green 500 SE and $\text{A}\beta^{\text{pH}}$ at acidic pH over time**

Solutions of Protonex Green 500, SE<sup>®</sup> (PTXG) and  $\text{A}\beta$  conjugated with PTXG ( $\text{A}\beta^{\text{pH}}$ ) were prepared in the cell culture medium at concentrations of 0, 0.1, 0.5, 1.0, 2.0, 5.0  $\mu\text{M}$  and a 50  $\mu\text{L}$  aliquot of each solution was transferred in duplicates into the wells of a 96-well plate. To measure the fluorescence of PTXG and  $\text{A}\beta^{\text{pH}}$  solutions under acidic conditions at different concentrations, 7.5  $\mu\text{L}$  of pH 1.0 solution (hydrochloric acid in media) was added to each well to obtain a final pH of 3.0. Fluorescence intensities of the acidic solutions were measured at an excitation/emission wavelength of 443/505 nm on A Cytation 5 multimode plate reader (BioTek, Inc). Next, to initiate aggregation of  $\text{A}\beta^{\text{pH}}$ , the plate was incubated at 37°C with 5%  $\text{CO}_2$  and fluorescence was measured

at 2, 6, 12, and 24-hour time points. The change in fluorescence intensities of the PTXG and A $\beta^{pH}$  aggregates was analyzed over time using GraphPad Prism software.

#### **4.5.9 Cell lines—culture and maintenance**

BV2 and N9 mouse microglial cell lines were generously gifted by Dr. Linda J. Van Eldik (University of Kentucky, USA). The BV-2 cell line was developed in the lab of Dr. Elisabetta Blasi at the University of Perugia, Italy. Cells were maintained at 37°C and 5% CO<sub>2</sub> in DMEM (Dulbecco's Modified Eagle's Medium)/Hams F-12 50/50 Mix (Corning #10-090-CV) supplemented with 10% FBS (Atlanta Biologicals), 1% L-Glutamine (Corning #25-005-CI), and 1% Penicillin/Streptomycin (Invitrogen). HMC3 human microglial cell line was a gift from Dr. Jianming Li (Purdue University, USA) who originally obtained the cells from ATCC. These cells were maintained at 37°C and 5% CO<sub>2</sub> in DMEM supplemented with 10% FBS and 1% penicillin/streptomycin.

#### **4.5.10 Background fluorescence of PTXG and RODO in cells**

BV2 cells were seeded at a concentration of 10,000 cells in 200  $\mu$ L per well in a 96-well flat-bottom plate (Falcon) for 16 hours (overnight). The next day, the media was aspirated, and the cells were treated with 1.0  $\mu$ M or 0.5  $\mu$ M of PTXG, PTXG-A $\beta^{pH}$ , RODO, and RODO-A $\beta^{pH}$  and placed in a 37 °C incubator for 2 hours respectively. Next, the fluorescence of PTXG and PTXG-A $\beta^{pH}$  was measured at 443/505 nm and the fluorescence of RODO, and RODO-A $\beta^{pH}$  was measured at 560/585 nm using a fluorescence plate reader (Attune NxT, Thermo Fisher Scientific, USA) to evaluate the cellular fluorescence indicating uptake of the unconjugated and A $\beta$ -conjugated dyes.

#### **4.5.11 Lactate Dehydrogenase activity cytotoxicity assay**

The cytotoxicity of the PTXG and RODO dyes were evaluated with lactate dehydrogenase (LDH) assay per manufacturers protocol (CyQUANT LDH Cytotoxicity Assay; Thermo #C20300). Briefly, 5000 BV2 cells/100  $\mu$ L were seeded onto the wells of a 96-well flat bottom plate (Falcon) for 16 hours (overnight). The next day, the cells were treated with the PTXG and RODO dyes (25, 12.5, 6.25, 3.125, 1.56, 0.78, and 0.39  $\mu$ M) for 24 hours. Cells without any dye treatment were

used as a negative control (to measure the spontaneous LDH activity). Cells treated with the provided lysis buffer were used as the positive controls (to measure the maximum LDH activity that is later set to 100%). The % cytotoxicity of the PTXG and RODO dyes were calculated per the equation below and the data was plotted for n=3 biological replicates, mean+sd.

$$\% \text{ Cytotoxicity} = \frac{[\text{PTXG or RODO-treated LDH activity} - \text{Spontaneous LDH activity}]}{[\text{Maximum LDH activity} - \text{Spontaneous LDH activity}]}$$

#### 4.5.12 Phagocytosis assay with live microglia

Cells were seeded at 5000 cells per well (200  $\mu\text{L}$  per well) in a 96-well flat bottom plate (Falcon) for approximately 16 hours (overnight). For all cell assays, the lyophilized  $\text{A}\beta^{\text{pH}}$  conjugate was dissolved in the culture medium to prepare a stock solution and was pre-aggregated by placing the stock solution at 37  $^{\circ}\text{C}$  for 24 hours. Further dilution for cell treatment was performed in culture media and the diluted solution was filtered using a 0.22  $\mu\text{m}$  syringe filter prior to cell treatment. The adherent cells (BV2, N9, HMC3) were treated with a final concentration of  $\text{A}\beta^{\text{pH}}$  at a final concentration of 0, 0.1, 0.5, 1.0, 2.0, and 5.0  $\mu\text{M}$  by replacing one-half of the culture medium (100  $\mu\text{L}$ ) with a stock  $\text{A}\beta^{\text{pH}}$  solution at 2x concentration. Two technical replicates were used for each treatment concentration. The plates were immediately placed in an IncuCyte S3 Live-Cell Analysis System (Essen BioScience) and four images per well were captured at 30-minute time intervals for 24 hours. The fluorescence intensity, cell confluence, and the integrated fluorescence intensity data were obtained and analyzed using the GraphPad Prism software.

The  $\text{A}\beta^{\text{pH}}$  uptake was measured as the *Phagocytic Score* metric, defined as a normalized value relative to the initial fluorescence intensity at t=0 and calculated as:

$$\text{Phagocytic Score} = \frac{\text{Relative Total Intensity (t)}}{\text{Maximum Relative Total Integrated Intensity}}$$

where, Relative Total Integrated Intensity (t) is defined as Total Integrated Intensity (t)–Total Integrated Intensity (t=0) for each concentration and cell type.

The Total integrated intensity is defined as the total sum of A $\beta$ <sup>pH</sup> fluorescence intensity in the entire image and given by the expression  $((CU \times \mu m^2)/Image)$  as defined by IncuCyte. We captured 4 images per well with multiple replicates for each A $\beta$ <sup>pH</sup> concentration and for each cell type. These images were used to calculate the value of Total integrated intensity,  $((CU \times \mu m^2)/Image)$ . The individual units are defined as: CU = Average mean intensity (the average of the A $\beta$ <sup>pH</sup>'s mean fluorescence intensity in each cell in an image),  $\mu m^2$  = Average area (the average area of the A $\beta$ <sup>pH</sup>'s in each cell in an image).

The Maximum Relative Total Integrated Intensity is the maximum value of Relative Total Integrated Intensity over the 24-hour period. Such a normalization gives Phagocytic Score values between 0 and 1 to compare different concentrations across different cell types. The maximum peak indicates the time when the degradation is equal to the uptake for each concentration and cell type. All other values show an interplay between uptake or degradation compared to time,  $t=0$ , shown by either increase or decrease in fluorescence that is also observed visually. The corresponding videos (Movies 1-3) during live cell imaging were taken on IncuCyte S3 Live-Cell Analysis System (Essen BioScience) and stabilized using the Blender version 2.82a software ([www.blender.org](http://www.blender.org)).

#### **4.5.13 Effect of chloroquine and bafilomycin-A1 on fluorescence of A $\beta$ <sup>pH</sup> in the cells**

BV2 cells were seeded at a concentration of 10,000 cells in 200  $\mu$ L per well in a 96-well-flat bottom plate (Falcon) for 16 hours (overnight). The next day, the media was aspirated and the cells were treated with 100  $\mu$ M chloroquine (CQ) or 100 nM bafilomycin (BF) and placed in a 37 °C incubator. After 2 hours, the media was removed and replaced with 100 nM of A $\beta$ <sup>pH</sup>. After 2 hours, the media was removed, and the cells were detached from the plates using cold 1x PBS and gentle pipetting. The fluorescence of A $\beta$ <sup>pH</sup> in the cells were analyzed by flow cytometry (Attune NxT, Thermo Fisher Scientific, USA). The data was plotted for n=3 biological replicates, mean+sd.

#### **4.5.14 Isolation and culture of primary mouse microglia**

CD11b<sup>+</sup> primary microglia were isolated from adult mice aged around 7 months (male and female) and cultured as follows. Mice were euthanized with CO<sub>2</sub> following the Purdue University Animal

Care and Use Committee guidelines and brains were transcardially perfused with ice-cold PBS. The perfused brains were dissected and cut into small 1 mm<sup>3</sup> pieces before homogenizing them in DPBS<sup>++</sup> containing 0.4% DNase I on a tissue dissociator (Miltenyi Biotec) at 37 °C for 35 mins. The cell suspension was filtered through a 70 µm filter and myelin was removed two times, first using Percoll PLUS reagent followed by myelin removal beads using LS columns (Miltenyi Biotec). After complete myelin removal, CD11b<sup>+</sup> cells were selected from the single cell suspension using the CD11b beads (Miltenyi Biotec) as per the manufacturer's instructions. The CD11b<sup>+</sup> cells were finally resuspended in microglia growth media made in DMEM/F12 (Corning Cat. #MT15090CV), further diluted in TIC (TGF-β, IL-34, and cholesterol) media [40] with 2% FBS before seeding 0.1x10<sup>6</sup> cells per 500 µL in a well of a 24-well plate (Corning Cat. #353847). The cells were maintained in TIC media at 37 °C and 10% CO<sub>2</sub> with media change every other day until the day (around 10-14 div) of the phagocytosis assay (around 10-14 div).

#### **4.5.15 Flow cytometry analysis of BV2 and primary microglia phagocytosis**

BV2 microglial cells were seeded at a density of 250k cells/well in a 6-well plate for around 14 hours overnight. The next morning, the cells were treated with 0.5 µM and 5 µM Aβ<sup>PH</sup> and placed in a 37 °C incubator for 1 hour, after which the plate was brought to the hood, placed on ice to stop phagocytosis, and cell culture medium containing Aβ<sup>PH</sup> was aspirated. The cells were washed once with cold PBS. Next, the cells were treated with ice cold PBS containing 2 mM EDTA for 2 minutes on ice to detach the cells from the wells. The cells were then centrifuged at 1400 rpm for 3 minutes. The supernatant was aspirated, and the cell pellets were re-suspended in FACS buffer (PBS, 25 mM HEPES, 2 mM EDTA, and 2% FBS). Five minutes before analysis of each sample, propidium iodide (PI; Thermo Fisher Scientific, Cat. #P1304MP) was added to the sample (40 ng/mL cell suspension) for staining of dead cells. Phagocytosis of Aβ<sup>PH</sup> by primary microglial cells was analyzed on div 10-14 in a similar manner. Cells were treated with Aβ<sup>PH</sup> for 1 hour and detached from the plate using cold PBS and 2 mM EDTA. After centrifuging the cell suspension, the cell pellet was resuspended in 0.1 mL PBS for live/dead staining. Here, Zombie Violet, ZV, (BioLegend, #423113) was used to evaluate cell viability (1:100 per 10<sup>6</sup> cells in 0.1 mL) for 15 mins followed by PBS wash. Finally, the cells were resuspended in FACS buffer and taken for analysis. Cells exhibiting green fluorescence were captured on the FITC channel upon gating for



live cells on Attune NxT flow cytometer (Invitrogen). The files were then analyzed on FlowJo V10 software. Briefly, at least 90% of the total cells were first gated on SSC-A vs FSC-A plot and the single cells within this gate were selected on the FSC-H vs FSC-A plot. From the single cells, the live and dead cells were identified from the viability dye. PI<sup>-</sup> and ZV<sup>-</sup> cells were considered as live cells and PI<sup>+</sup> and ZV<sup>+</sup> cells were taken as dead cells on the histogram plots. Finally, A $\beta$ <sup>pH<sup>+</sup></sup> or A $\beta$ <sup>pH<sup>-</sup></sup> cells were identified within the live cell population in the A $\beta$ <sup>pH</sup> histogram plot on the FITC channel.

#### **4.5.16 Confocal imaging of actin filaments and nuclei in the paraformaldehyde-fixed phagocytic microglial cells**

For labeling the cells with phalloidin and DAPI, 20,000 cells/250  $\mu$ L were plated in 14 mm microwells of 35 mm glass bottom dishes (MatTek #P35G-1.5-14-C) and kept overnight. The cells were treated with 5.0  $\mu$ M A $\beta$ <sup>pH</sup> for 2 hours on the next day. Then the medium was aspirated, and cells were fixed with 4% paraformaldehyde for 20 minutes, and then gently washed once with PBS. Phalloidin-iFluor 594 reagent (Abcam, Cat. #ab176757; 1000x stock) was diluted to 1x in PBS and added to the fixed cells for 10 minutes for staining the actin filaments. To label the nuclei, DAPI was diluted to a concentration of 1  $\mu$ g/mL. The cells were washed again with PBS followed by a 10-minute incubation with the diluted DAPI solution. Finally, the DAPI solution (Invitrogen, Cat. #D3571) was aspirated and the fixed cells treated with 2-3 drops of ProLong Gold Antifade Mountant (Invitrogen #P36930) before imaging. Fluorescence images of phagocytic microglial cells were captured using 40x and 60x objectives on a Nikon AR-1 MP confocal laser microscope. Images were obtained using the NIS Elements microscope imaging software.

#### **4.5.17 Confocal Imaging of intracellular acidic organelles and nuclei in paraformaldehyde-fixed phagocytic microglial cells**

LysoTracker Red DND-99 (Thermo Fisher Scientific, Cat. #L7528) was used for labeling the intracellular organelles of the cells to observe the subcellular localization of A $\beta$ <sup>pH</sup> sensors inside the cells after phagocytosis. 20,000 cells/250  $\mu$ L were plated in 14 mm microwells of 35 mm glass bottom dishes (MatTek #P35G-1.5-14-C) and kept overnight. The cells were treated with 5.0  $\mu$ M A $\beta$ <sup>pH</sup> for 2 hours on the next day. Then the A $\beta$ <sup>pH</sup>-containing medium was aspirated and replaced

with 200  $\mu$ L of media containing 100 nM concentration of the LysoTracker dye and the cells were incubated in a 37 °C, 5% CO<sub>2</sub> incubator for 30 minutes. Finally, the cells were fixed and treated with DAPI to stain the nuclei followed by 2-3 drops of ProLong Gold Antifade Mountant using the above-mentioned protocol. Fluorescence images of phagocytic microglial cells were captured using 40x and 60x objectives on a Nikon AR-1 MP confocal laser microscope. Images were obtained using the NIS Elements microscope imaging software.

#### **4.5.18 Intracranial injection of A $\beta$ <sup>pH</sup>, perfusion, and immunohistochemistry**

Lyophilized A $\beta$ <sup>pH</sup> was dissolved in Hank's Balanced Salt Solution (HBSS no calcium, no magnesium, no phenol red, ThermoFisher #14175079) to obtain a 100  $\mu$ M stock solution that was then briefly vortexed and sonicated in a bath sonicator for 1 minute and used immediately for intracranial injections or stored at -80 °C. For intracranial injections, the stock solution was diluted in HBSS to obtain a 10  $\mu$ M working solution and kept on ice to prevent aggregation. Postnatal day 7 mice were anesthetized with isoflurane and were mounted on a stereotaxic frame. Two lots of 250 nL of A $\beta$ <sup>pH</sup> working solution were unilaterally injected in the somatosensory cortex of wild-type C57BL/6J mice using a Nanoliter Injector (anteroposterior -2.3 mm; mediolateral +2.3 mm; dorsoventral -0.5 mm for lower layers and -0.2 mm for upper layers, relative to Lambda) at an injection rate of 100 nL/minute followed by 2 additional minutes to allow diffusion. 24 or 72 hours after injections, animals were deeply anesthetized with sodium pentobarbital by intraperitoneal injection and then transcardially perfused with PBS 1x followed by 4% paraformaldehyde (PFA) in PBS. Brains were dissected out, post-fixed for two hours at 4 °C, and cryoprotected in a 30% sucrose-PBS solution overnight at 4°C. Then, tissue was sectioned at 40  $\mu$ m on a sliding microtome (Leica). Free-floating brain sections were permeabilized by incubating with 0.3% Triton X-100 in PBS for 1 hour and then blocked for 3 hours (0.3% Triton X-100 and 10% normal donkey serum), followed by incubation with primary antibodies in 0.3% Triton X-100 and 10% normal donkey serum overnight at 4°C. The next day, brains were rinsed in PBS 1x for 1 hour, incubated with the appropriate secondary antibodies for 2 hours at room temperature, rinsed again in PBS, incubated with DAPI and mounted using Fluoromount-G (SouthernBiotech, #0100-01). During perfusion and immunohistochemistry all solutions were maintained at neutral pH. The following primary antibodies were used: mouse anti-GFAP (1:200, Sigma #G3893-100UL) and

rabbit anti-IBA1 (1:500, Wako Chemicals, #019-1974). The secondary antibodies used were donkey anti-mouse-IgG1 647 (Invitrogen, #A21241) and donkey anti-rabbit 594 (ThermoFisher, #A-21207). Tissue samples were imaged on a ZEISS Axio Imager and a ZEISS LSM 800 confocal using a 20x objective. A $\beta^{\text{pH}}$  fluorescence signal was quantified using ImageJ. First, cell contour was manually drawn using IBA1 or GFAP signal and mean fluorescence intensity in the A $\beta^{\text{pH}}$  channel was measured. Next, the selection was moved to a nearby region with no obvious A $\beta^{\text{pH}}$  fluorescence signal and mean fluorescence intensity in the A $\beta^{\text{pH}}$  channel was measured (background). Normalized fluorescence intensity for each cell was calculated as A $\beta^{\text{pH}}$  fluorescence signal minus background. Data were analyzed by one-way ANOVA followed by the Sidak's post hoc analysis for comparisons of multiple samples using GraphPad Prism 7 (GraphPad Software).

#### **4.5.19 Immunopanning and culture of primary astrocytes**

Astrocytes were purified by immunopanning from the forebrains of P5 Sprague Dawley rats (Charles River) forebrains and cultured as previously described [60]. In brief, cortices were enzymatically disrupted (using papain) and then mechanically dissociated to produce a single-cell suspension that was incubated on several negative immunopanning plates to remove microglia, endothelial cells and oligodendrocyte lineage cells. Positive selection for astrocytes was with an ITGB5-coated panning plate. Isolated astrocytes were cultured in a defined, serum-free base medium containing 50% neurobasal, 50% DMEM, 100 U/ml penicillin, 100  $\mu\text{g}/\text{mL}$  streptomycin, 1 mM sodium pyruvate, 292  $\mu\text{g}/\text{mL}$  L-glutamine, 1 $\times$  SATO and 5  $\mu\text{g}/\text{mL}$  of N-acetyl cysteine. This medium was supplemented with the astrocyte-required survival factor HBEGF (Peprotech, 100-47) at 5 ng/mL [60]. Cells were plated at 5,000 cells/well in 12-well plates coated with poly-D-lysine and maintained at 10% CO<sub>2</sub>.

#### **4.5.20 Engulfment assay of A $\beta^{\text{pH}}$ by primary astrocytes**

Astrocytes were maintained for 1 week in culture and checked for their reactivity state using qPCR5 before addition of A $\beta^{\text{pH}}$ . The cells were treated with 0.5, 1.0, or 2.0  $\mu\text{M}$  A $\beta^{\text{pH}}$  and imaged continuously with still images taken every 5 minutes with an IncuCyte S3 System epifluorescence time lapse microscope to analyze engulfed A $\beta^{\text{pH}}$  particles. For image processing analysis, we took 9 images per well using a 20x objective lens from random areas of the 12-well plates and calculated

the phagocytic index by measuring the area of engulfed A $\beta$ <sup>pH</sup> particles (fluorescence signal) normalized to the area of astrocytes, using ImageJ.

#### **4.5.21 *In vivo* retinal engulfment of A $\beta$ <sup>pH</sup>**

P14 Sprague Dawley rats were anaesthetized with 2.5% inhaled isoflurane in 2.0 l O<sub>2</sub> per min. Once non-responsive, animals received a 1  $\mu$ L intravitreal injection of A $\beta$ <sup>pH</sup>, or PBS. Retinae were collected for immunofluorescence analyses at 3, 24, and 72 hours. At collection, eyeballs were removed, fixed in 4% PFA overnight, and washed in PBS, and retinae were dissected and whole-mounts placed on silanized glass slides. Retinae were blocked with 10% heat-inactivated normal goat serum for 2 hours at room temperature. Incubation with primary antibodies to GFAP (Dako, A0063, 1:5000) and IBA1 (WAKO, 019-19741, 1:500) diluted in 5% goat serum in PBS was followed by detection with AlexaFluor fluorescent secondary antibodies (Thermo, 1:1000).

#### **4.5.22 Brain slice experiments**

Rats at postnatal day 12 (P12) were sacrificed by cervical dislocation followed by decapitation, and 250  $\mu$ m sagittal hippocampal slices were prepared on a Leica VT 1200S vibratome at 4°C in oxygenated solution containing (mM): 124 NaCl, 26 NaHCO<sub>3</sub>, 2.5 KCl, 1 NaH<sub>2</sub>PO<sub>4</sub>, 10 glucose, 2 CaCl<sub>2</sub>, 1 MgCl<sub>2</sub>, 1 kynurenic acid. Acute slices were allowed to recover for 2.5 hours at room temperature before being transferred to 24-well plates and incubated with 5  $\mu$ M A $\beta$ <sup>pH</sup> in HEPES-based aCSF (140 mM NaCl, 10 mM HEPES, 2.5 mM KCl, 1 mM NaH<sub>2</sub>PO<sub>4</sub>, 10 mM glucose, 2 mM CaCl<sub>2</sub>, and 1 mM MgCl<sub>2</sub>) for 1.5 hours at 37 °C. Following incubation, slices were quickly rinsed in cold phosphate-buffered saline (PBS) and fixed in 4% paraformaldehyde (PFA) for 45 minutes at room temperature. For immunolabeling, slices were permeabilized and blocked in buffer containing 10% horse serum and 0.02% Triton X-100 in PBS for 2 hours at room temperature, followed by incubation with goat anti-IBA1 (Abcam, ab5076) or chicken anti-GFAP (Abcam, ab4674) primary antibodies diluted 1:500 in blocking buffer for 12 hours at 4°C. Following four 10 minute washes in PBS, donkey anti-goat IgG 647 (ThermoFisher, A21447) or donkey anti-chicken IgG 649 (Jackson, 703-495-155) secondary antibodies diluted 1:1000 in blocking buffer were applied for 4 hours at room temperature. Finally, slices were incubated in DAPI for 30 minutes, rinsed in PBS and mounted. Imaging was done using a Zeiss LSM700

confocal microscope and a 20x objective, where 10  $\mu\text{m}$  image stacks at 1  $\mu\text{m}$  step interval were acquired. For analysis, the percentage of  $\text{A}\beta^{\text{pH}}$  signal within microglial or astroglial cells was calculated by binarizing the microglia or astrocyte channel, creating a mask and multiplying it by the raw  $\text{A}\beta^{\text{pH}}$  signal. The fluorescence intensity of  $\text{A}\beta^{\text{pH}}$  colocalizing with either cell type mask was then expressed as a percentage of the total  $\text{A}\beta^{\text{pH}}$  signal across the field.

#### **4.5.23 *In vivo* two-photon microscopy**

Adult mice bred on a C57BL/6 background aged ~4-6 months (P123 to P203) were anesthetized using urethane (1.55 g/kg given intraperitoneally). Adequate anesthesia was ensured by confirming the absence of a withdrawal response to a paw pinch. Body temperature was maintained at  $36.8 \pm 0.3^\circ\text{C}$  and eyes were protected from drying by applying polyacrylic acid eye drops (Dr Winzer Pharma). The trachea was cannulated and mice were mechanically ventilated with medical air supplemented with oxygen using a MiniVent (Model 845). A headplate was attached to the skull using superglue and mice were head fixed to a custom-built stage. A craniotomy of approximately 2 mm diameter was performed over the right primary somatosensory cortex, immediately caudal to the coronal suture and approximately 2 to 4 mm laterally from the midline. The dura was removed and 2% agarose in HEPES-buffered aCSF was used to create a well filled with HEPES-buffered aCSF during imaging.

Two-photon excitation was performed using a Newport-Spectraphysics Ti:sapphire MaiTai laser pulsing at 80 MHz, and a Zeiss LSM710 microscope with a 20x water immersion objective (NA 1.0). Fluorescence was evoked using a wavelength of 920 nm. The mean laser power under the objective did not exceed 25 mW. Image stacks were taken in 2  $\mu\text{m}$  depth increments (50-200  $\mu\text{m}$  from the cortical surface) every 1.5 min for approximately 30 minutes. Five  $\mu\text{M}$   $\text{A}\beta^{\text{pH}}$  in HEPES-based aCSF was applied to the cortical surface for 10 minutes and then replaced with HEPES-based aCSF. Animals were transcardially perfused with ice-cold PBS followed by 4% PFA in PBS at 1.5 or 3 hours after pH  $\text{A}\beta^{\text{pH}}$  application. Brains were post-fixed in PFA for 12 hours at  $4^\circ\text{C}$  and 100  $\mu\text{m}$  sagittal sections were prepared using a vibratome. Slices were permeabilized and blocked for 12 hours and incubated with rabbit anti-IBA1 (1:500, Synaptic Systems, 234006), rat anti-mouse CD68 (1:500, Bio-Rad, MCA1957) or chicken anti-GFAP (1:500, Abcam, ab4674) primary antibodies for 24 hours at  $4^\circ\text{C}$ . Following washes in PBS, donkey anti-rabbit IgG 647 (1:500,

ThermoFisher, A31573), goat anti-rat IgG 647 (1:500, ThermoFisher, A21247) or donkey anti-chicken IgG 649 (1:300, Jackson, 703-495-155) was applied for 12 hours at 4°C. Image stacks (23 µm deep) were acquired at 1 µm interval in the cerebral cortex and analysis was done as for in situ experiments.

## 4.6 Supporting information

Instrumentation, detailed chemical characterization of Aβ<sup>pH</sup> (MALDI-MS, <sup>1</sup>H-NMR, FTIR), movies, flow cytometry, and confocal microscopy supporting data are given in this section.

### 4.6.1 Instrumentation used for chemical characterization of Aβ<sup>pH</sup>

- MALDI-MS spectra were obtained using Applied Biosystems Voyager DE PRO instrument (Main parameters: Number of laser shots: 100/spectrum, Laser intensity: variable 2500 to 3300, Laser repetition rate: 20.0 Hz, accelerating voltage 25000 V).
- <sup>1</sup>H-NMR spectra were obtained in DMSO-d<sub>6</sub> solvent using a Bruker AV-III-500-HD 500 MHz NMR instrument.
- ATR-FTIR spectra were recorded using Thermo Fisher Nicolet FTIR instrument.
- AFM images were recorded using Veeco Multimode instrument with NanoScope V controller

### 4.6.2 Supporting movies

- **Movie 4.S1** <https://youtu.be/2gmwNXQ1nsc> - Phagocytosis of Aβ<sup>pH</sup> by HMC3 cells. Phagocytic uptake of Aβ<sup>pH</sup> by HMC3 cells. The green fluorescent intensity within the cells increases over time with increased Aβ<sup>pH</sup> uptake. The cell at the center of the frame engulfs a neighboring cell (during the 5 hour time point) by forming a phagocytic cup (seen at the 4 hour time point).
- **Movie 4.S2** <https://youtu.be/jQW0Aj1B8sI> - Phagocytosis of Aβ<sup>pH</sup> by BV2 cells. Phagocytic uptake of Aβ<sup>pH</sup> by BV2 microglia is confirmed by the appearance of green fluorescence within the acidic phagosomes of the cells. A change from the ramified state to the amoeboid state is observed visually during this process.

- **Movie 4.S3** <https://youtu.be/kjOWvxxd3do> - Phagocytosis of A $\beta$ pH by N9 cells. Phagocytic uptake of A $\beta$ pH by N9 microglia demonstrated by the appearance of green fluorescence within the cells.
- **Movie 4.S4** <https://youtu.be/nlJmXnXcf0A> - In vivo imaging of A $\beta$ pH in mouse cortex. In vivo two-photon imaging of the barrel cortex before and after topical application of A $\beta$ pH for 16 frames (intensity enhanced).
- **Movie 4.S5** [https://youtu.be/AiY\\_09Mdc3Q](https://youtu.be/AiY_09Mdc3Q) - In vivo imaging of A $\beta$ pH in mouse cortex. In vivo two-photon imaging of the barrel cortex before and after topical application of A $\beta$ pH. The fluorescence increase in cell somata indicates A $\beta$ pH uptake.

#### 4.6.3 Supplemental text, figures and figure legends

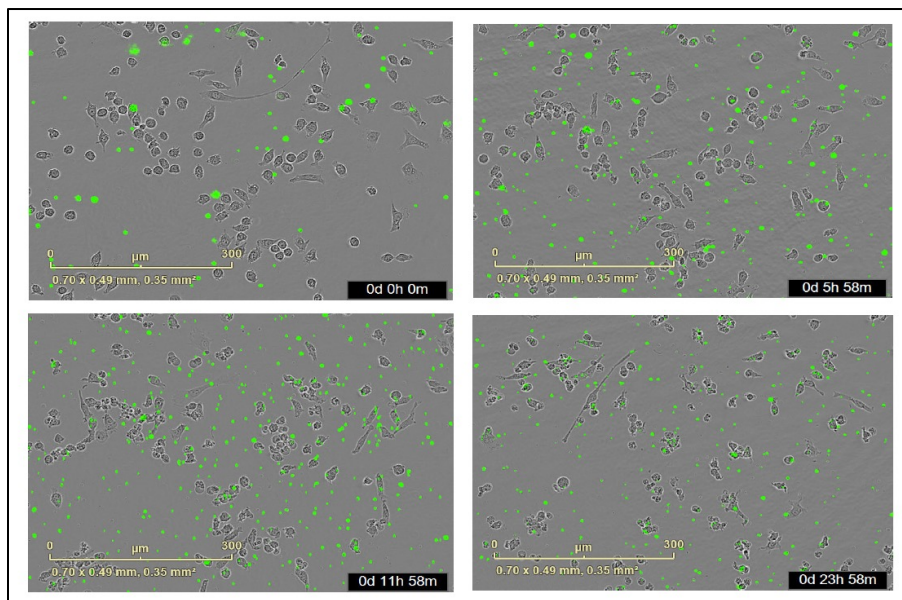


**Figure 4.S1-A.** Live cell imaging of 1  $\mu$ m fluorescent latex beads (Sigma-Aldrich, #L1030) applied to BV2 cells for 24 hours (~0, 6, 12, and 24 hours). It is difficult to determine if the beads are within or outside the cell bodies.

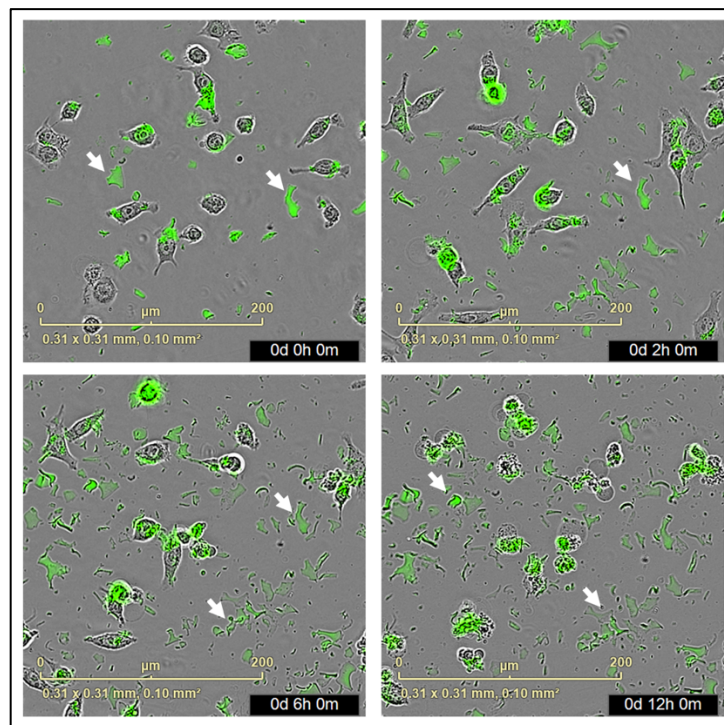


**Figure 4.S1-B.** Live cell imaging of BV2 mouse microglia treated with (pH-independent) fluorescein-labeled A $\beta$  peptides (AnaSpec, Inc. #23525-05) at 0, 2, 6, and 12 hour time points. High background noise is observed in addition to non-specific fluorescence in and around the microglial cells.

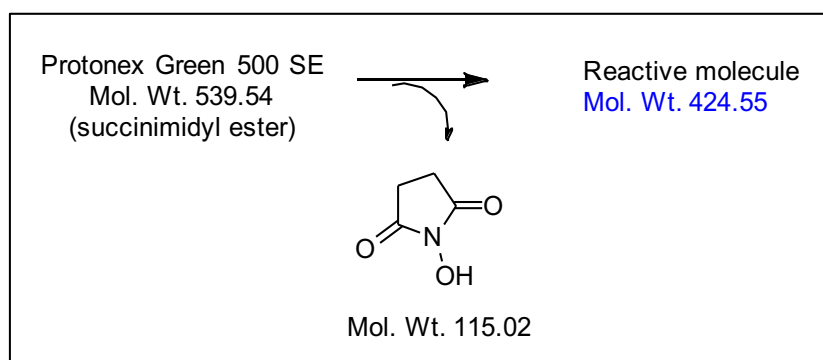


**Figure 4.S2-A.** The mass calculation for the reactive part of Protonex Green 500, SE after conjugation with an amine functional group of A $\beta$ <sub>1-42</sub>. The Protonex Green 500, SE is a succinimidyl ester of active dye molecule (molecular weight 539.54) and the leaving group *N*-hydroxy succinimide has a molecular weight of 115.02. Therefore, the reactive fragment has a molecular weight of 424.55.



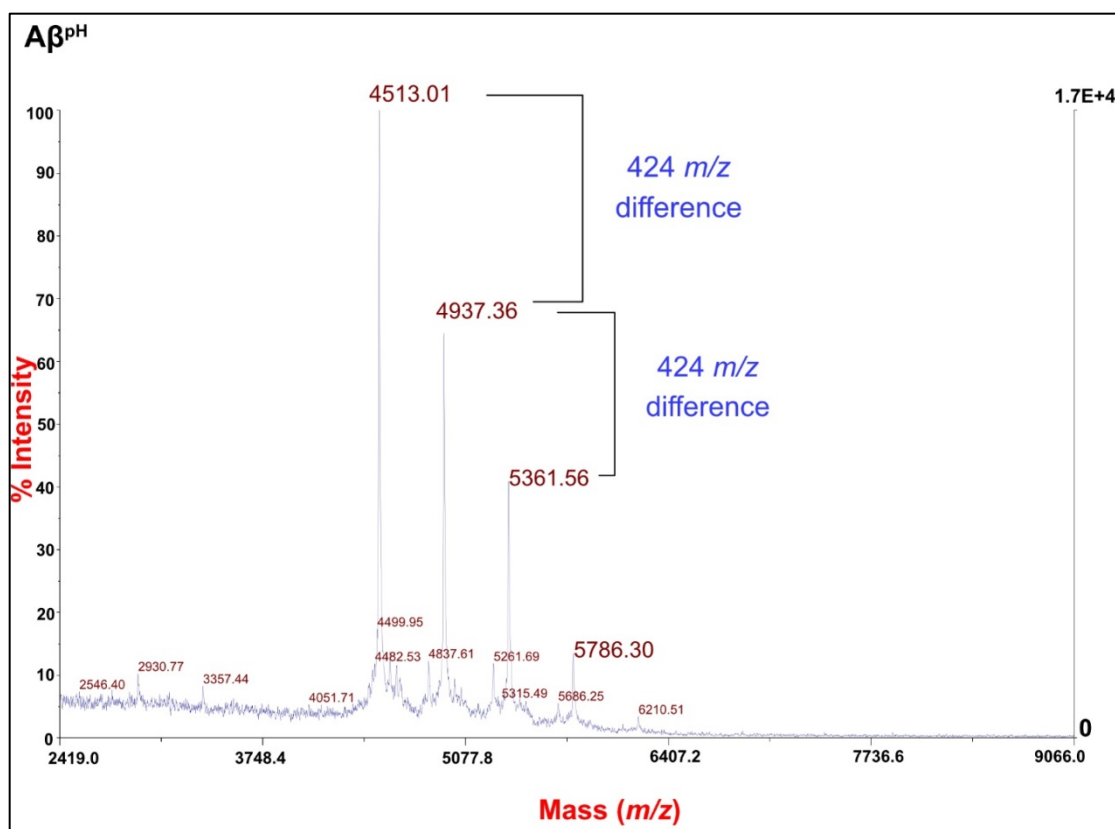


**Figure 4.S2-B.** MALDI-MS spectrum [%intensity vs. Mass ( $m/z$ )] for A $\beta$ -Protonex Green conjugate (A $\beta^{\text{pH}}$ ) corresponding to  $m/z$  of 5357.06 and 4932.87. The  $m/z$  difference of 424 indicates the addition of reactive fragment of Protonex Green 500, SE upon conjugation with an amine functional groups present in A $\beta_{1-42}$ .

Proton nuclear magnetic resonance ( $^1\text{H}$ -NMR) spectrum shows a chemical shift for protons. A chemical shift is a relative resonant frequency to a standard magnetic field. Chemical shift ( $\delta$ ) is usually expressed in parts per million (ppm). The position and number of chemical shifts are used to determine the structure and functional groups present in a molecule. For example, chemical shifts for aliphatic protons are in 0.5 to 5.0 ppm region and for aromatic protons are in 6.5 to 9 ppm region depending upon the electrochemical environment of protons. This basis was used to identify aliphatic and aromatic protons in the  $^1\text{H}$ -NMR spectrum of PTXG, A $\beta_{1-42}$ , PTXG-A $\beta^{\text{pH}}$  shown in Figures S3A-S3C, respectively.

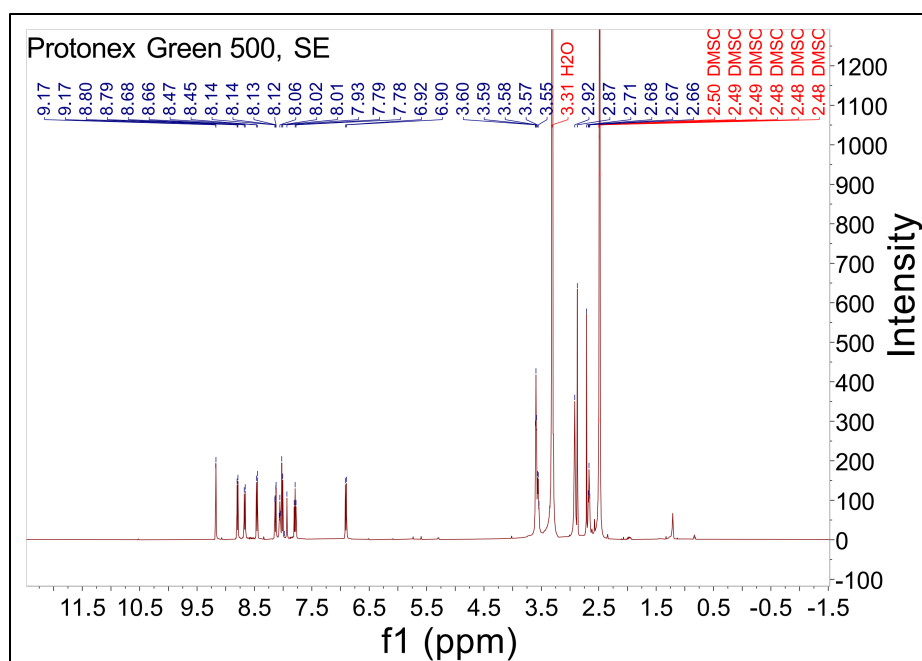


**Figure 4.S3-A.**  $^1\text{H}$ -NMR spectrum [Intensity vs. ppm] of the Protonex Green 500, SE in  $\text{DMSO-}d_6$ . shows the presence of aliphatic (2.0 to 4.0 ppm region) and aromatic protons (6.5 to 9.5 ppm region) to chemically characterize the material used for the reaction.

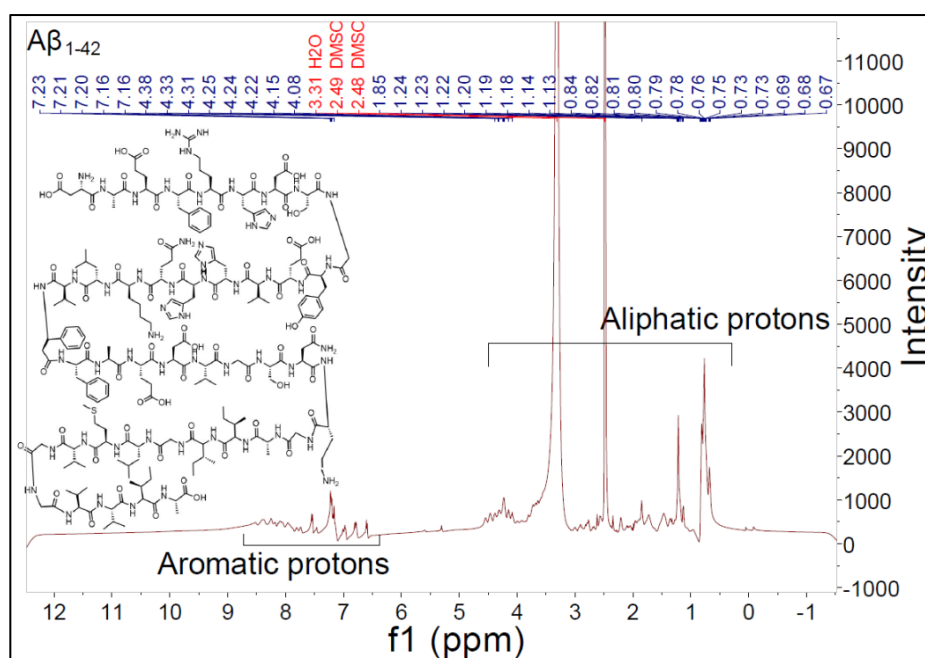


**Figure 4.S3-B.**  $^1\text{H}$ -NMR spectrum [Intensity vs. ppm] of  $\text{A}\beta_{1-42}$  in  $\text{DMSO-}d_6$ . The  $\text{A}\beta_{1-42}$  peptide has amino acids containing aromatic (phenyl, 4-hydroxyphenyl, imidazolyl rings) and aliphatic (side chains and peptide backbone) functional groups. The  $^1\text{H}$ -NMR spectrum of  $\text{A}\beta_{1-42}$  confirms the presence of protons arising from aliphatic and aromatic functional group-containing amino acids to characterize the material used for the reaction.

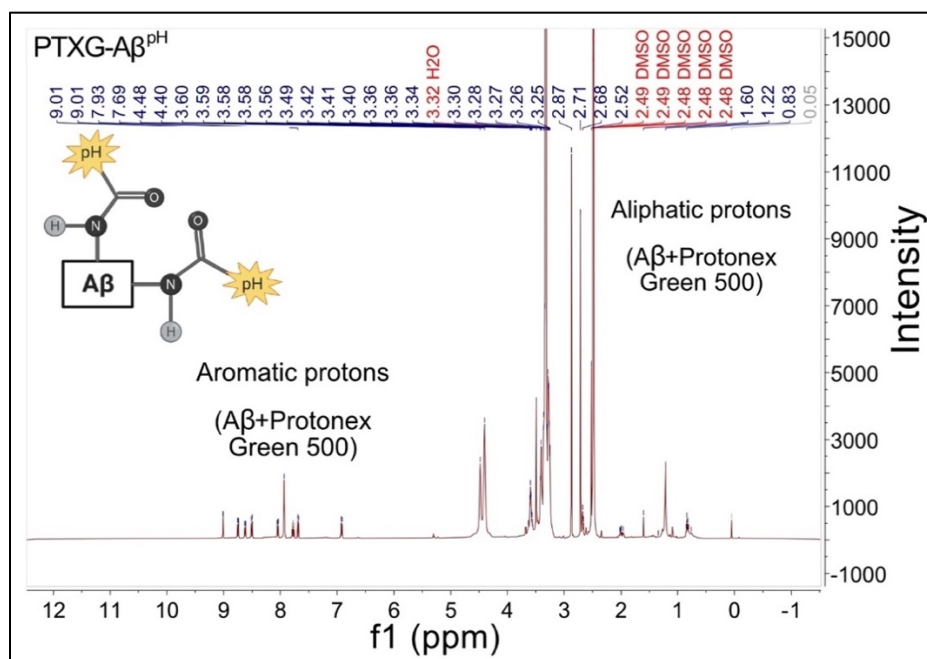


**Figure 4.S3-C.**  $^1\text{H}$ -NMR spectrum [Intensity vs. ppm] of the synthetic Protonex Green-conjugated A $\beta$  (PTXG-A $\beta^{\text{pH}}$ ) in DMSO- $d_6$ . The spectrum exhibits peaks at aliphatic and aromatic regions that are present due to functional groups present in both Protonex Green 500 and A $\beta_{1-42}$  (compared to Figures S3A, S3B) confirms the conjugation of Protonex Green 500 with A $\beta_{1-42}$ .

Fourier Transform InfraRed (FTIR) spectroscopy utilizes the frequencies associated with the bonds in a molecule that typically vibrate around  $4000\text{ cm}^{-1}$  to  $400\text{ cm}^{-1}$ , known as the Infrared region of the electromagnetic spectrum. This region is associated with specific frequencies that change the vibration patterns of chemical bonds, resulting in an FTIR spectrum. A typical FTIR spectrum is visualized in a graph of infrared light absorbance (or transmittance) on the y-axis vs. frequency or wavenumber ( $\text{cm}^{-1}$ ) on the x-axis. In general, the FTIR-spectrum is unique for an individual chemical entity and a change in structure or a functional group can be identified by comparing changes in these spectra. For example, carbonyl ( $\text{C}=\text{O}$ ) is a functional group that is easily identified by FTIR spectroscopy due to a prominent bond stretching vibration peak at unique wavenumber range of around  $1670\text{--}1820\text{ cm}^{-1}$ . Since carbonyl ( $\text{C}=\text{O}$ ) groups are present on carboxylic acids, aldehydes, amides, anhydrides, esters, and ketones, unique wavenumbers in FTIR spectrum confirm these specific types of carbonyl groups. Furthermore, chemical modification results in a change in wavenumber to identify changes between specific carbonyl group types. This basis was used to identify chemical changes in the Attenuated Total Reflection

Fourier Transform InfraRed (ATR-FTIR) spectrum of A $\beta_{1-42}$ , PTXG, PTXG-A $\beta^{\text{pH}}$  shown in Figures S4A-S4B, respectively.

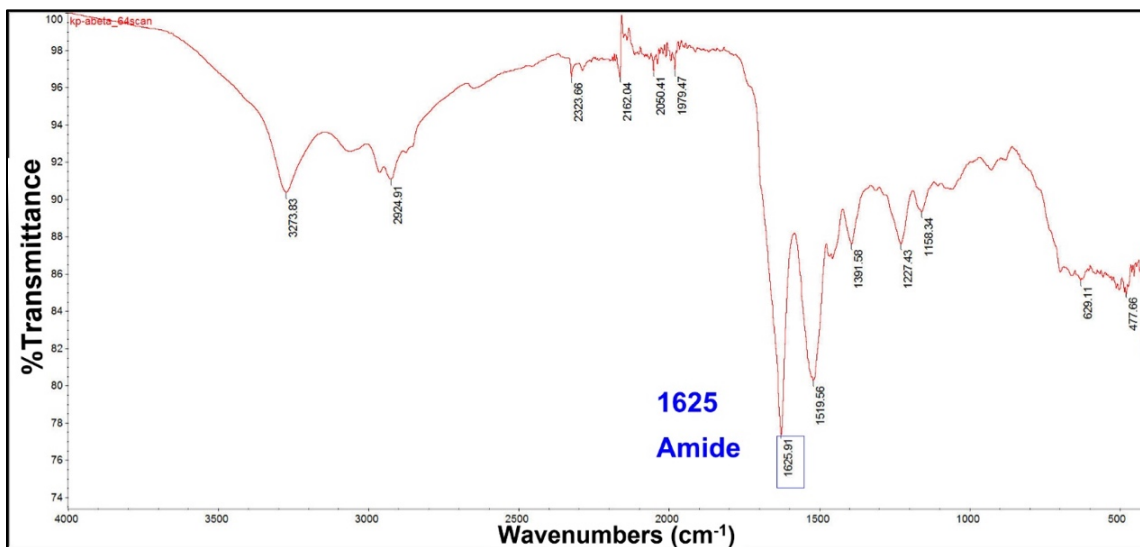


**Figure 4.S4-A.** ATR-FTIR spectrum [%Transmittance vs. Wavenumbers ( $\text{cm}^{-1}$ )] of the A $\beta_{1-42}$ . The ATR-FTIR shows the intense signal at  $1625 \text{ cm}^{-1}$  correspondence to carbonyl ( $\text{C}=\text{O}$ ) stretching frequencies in amide bonds of the peptide.

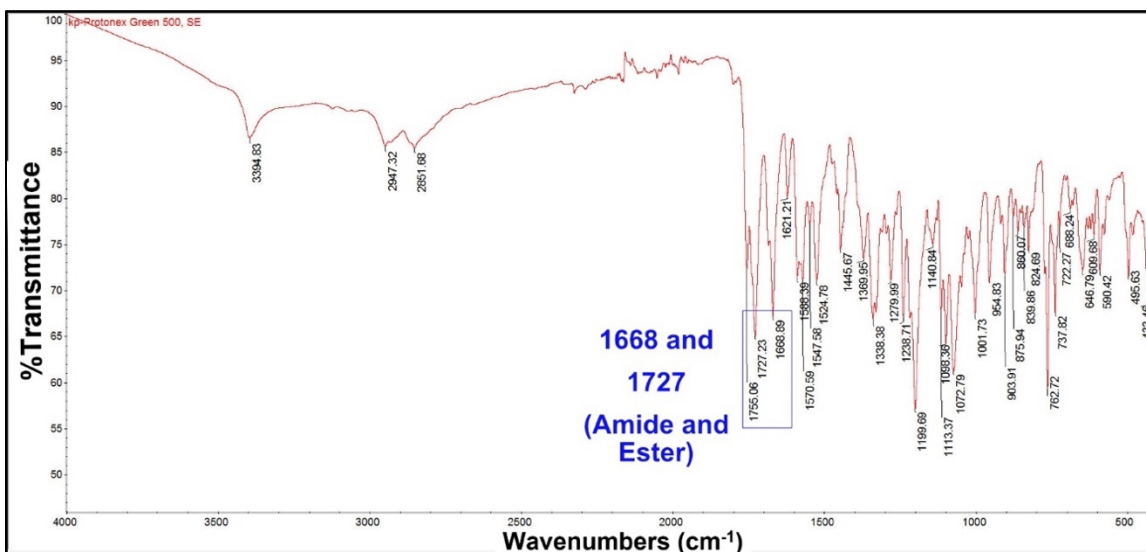


**Figure 4.S4-B.** ATR-FTIR spectrum [%Transmittance vs. Wavenumbers ( $\text{cm}^{-1}$ )] of the Protonex Green 500, SE (PTXG). The PTXG chemical structure has amide and ester functional groups and the spectrum shows expected two intense signals at  $1668$  and  $1727 \text{ cm}^{-1}$  corresponding to carbonyl ( $\text{C}=\text{O}$ ) stretching frequencies in amide and ester functional groups, respectively.

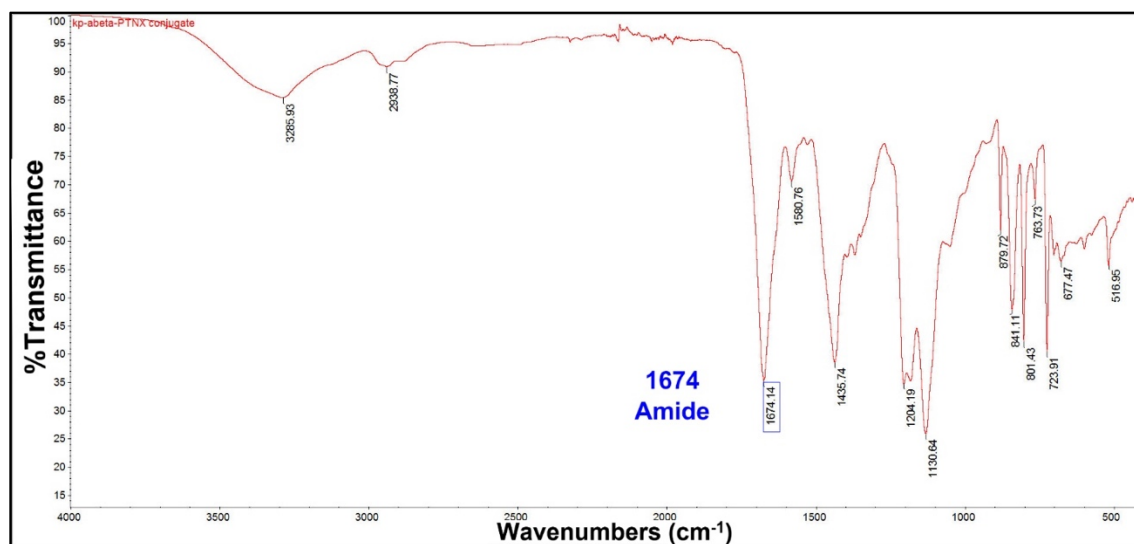


**Figure 4.S4-C.** ATR-FTIR spectrum [%Transmittance vs. Wavenumbers ( $\text{cm}^{-1}$ )] of the PTXG- $\text{A}\beta$  conjugate ( $\text{PTXG-A}\beta^{\text{pH}}$ ) shows the change in stretching frequencies of carbonyl ( $\text{C=O}$ ) of the amide functional group compared to Figures S4A-S4B. No peak at  $1727\text{ cm}^{-1}$  of the ester functional group as shown in Figure S4B, suggests a change in the chemical structure of PTXG because of amide bond formation with an amine functional group of  $\text{A}\beta_{1-42}$ .

Taken together Figures S4A-S4C show chemical characterization of unconjugated  $\text{A}\beta$ , PTXG and conjugated PTXG- $\text{A}\beta$  using  $^1\text{H-NMR}$  and ATR-FTIR spectroscopy.

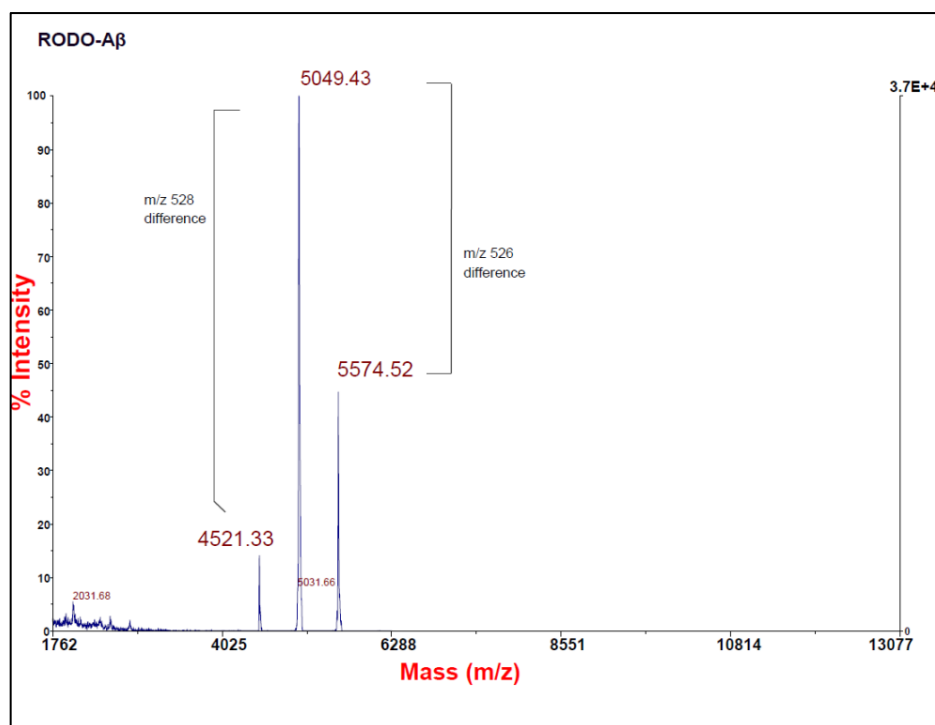
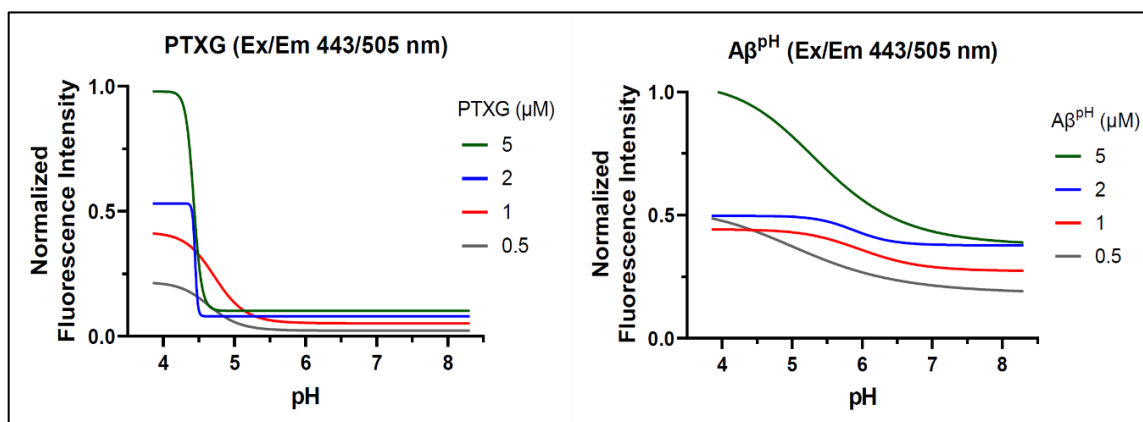


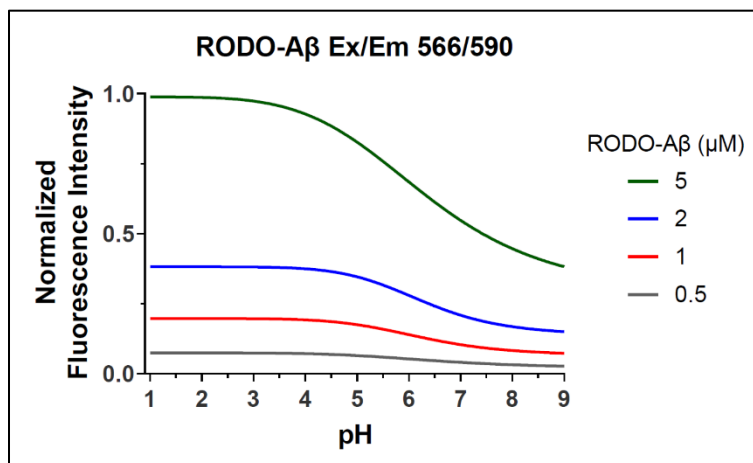
**Figure 4.S5.** MALDI-MS spectrum [%intensity vs. Mass ( $m/z$ )] for pHrodo Red conjugate of A $\beta$  (RODO-A $\beta^{\text{pH}}$ ) corresponding to  $m/z$  of 5049.43 and 5574.42. These  $m/z$  peaks are emerging from the conjugation of pHrodo Red (molecular weight of reactive fragment  $\sim 527$ ) with an amine functional group of A $\beta_{1-42}$ .



PTXG Conc.	5 $\mu$ M	2 $\mu$ M	1 $\mu$ M	0.5 $\mu$ M
pKa	4.4	4.4	4.7	4.6

PTXG-A $\beta$ (A $\beta^{pH}$ ) Conc.	5 $\mu$ M	2 $\mu$ M	1 $\mu$ M	0.5 $\mu$ M
pKa	5.4	5.8	5.9	5.2

**Figure 4.S6-A.** pKa of Protonex Green 500, SE<sup>®</sup> (PTXG) and A $\beta^{pH}$ . Emission spectrum of PTXG and A $\beta^{pH}$  at concentration 5.0, 2.0, 1.0, 0.5  $\mu$ M in a 384-well plate with 40  $\mu$ L/well total volume in different pH solutions (pH range 3.85, 4.03, 4.26, 4.46, 4.88, 5.02, 5.30, 5.67, 6.22, 6.44, 6.94, 7.40, 8.31) prepared in DMEM/F12 cell culture medium. Ex/Em is 443/505 nm. The fluorescence intensity was normalized by dividing each value by the highest value obtained for 5  $\mu$ M concentration. pKa was calculated using GraphPad Prism software. pKa value at each concentration is shown in the table. Legend shows colors for concentrations of PTXG and A $\beta^{pH}$  ( $\mu$ M).



RODO-A $\beta$ Conc.	5 $\mu$ M	2 $\mu$ M	1 $\mu$ M	0.5 $\mu$ M
pKa	6.3	6.3	6.2	6.4

**Figure 4.S6-B.** pKa of RODO-A $\beta$ . Emission spectrum of PTXG and A $\beta^{\text{pH}}$  at concentration 5.0, 2.0, 1.0, 0.5  $\mu$ M in a 384-well plate with 40  $\mu$ L/well total volume in different pH solutions (pH range 3.85, 4.03, 4.26, 4.46, 4.88, 5.02, 5.30, 5.67, 6.22, 6.44, 6.94, 7.40, 8.31) prepared in DMEM/F12 cell culture medium. Ex/Em is 566/590 nm. The fluorescence intensity was normalized by dividing each value by the highest value obtained for 5  $\mu$ M concentration. pKa was calculated using GraphPad Prism software. pKa value at each concentration is shown in the table. Legend shows colors for concentrations of RODO-A $\beta$  ( $\mu$ M).



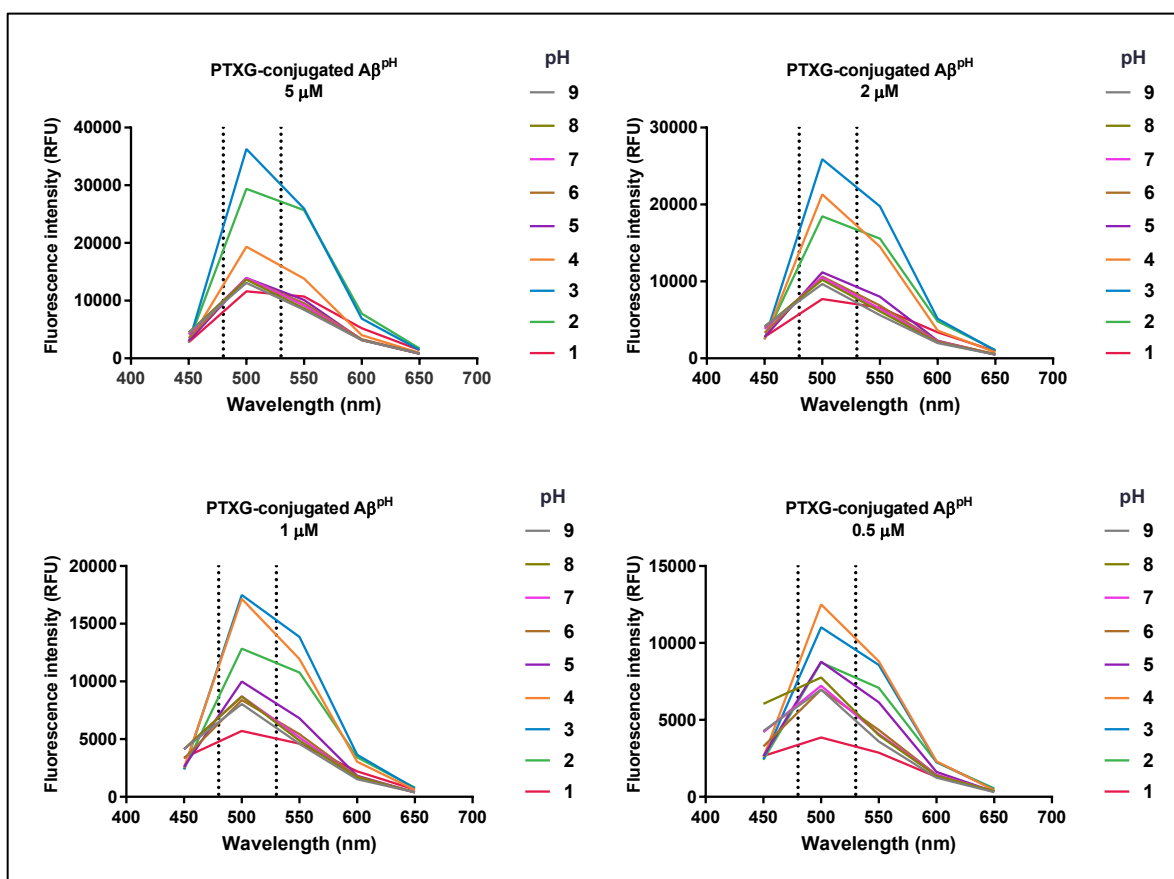


**Figure 4.S7-A.** pH-dependent emission spectra of Protonex Green (PTXG) conjugated Aβ at various concentrations. The emission spectra of the PTXG-Aβ<sup>pH</sup> reporter showing larger fluorescence intensity for acidic pH and limited fluorescence at the physiological pH of 7.4. Dotted lines highlight the region of maximum emission. Legend shows color code for pH 1 to 9.

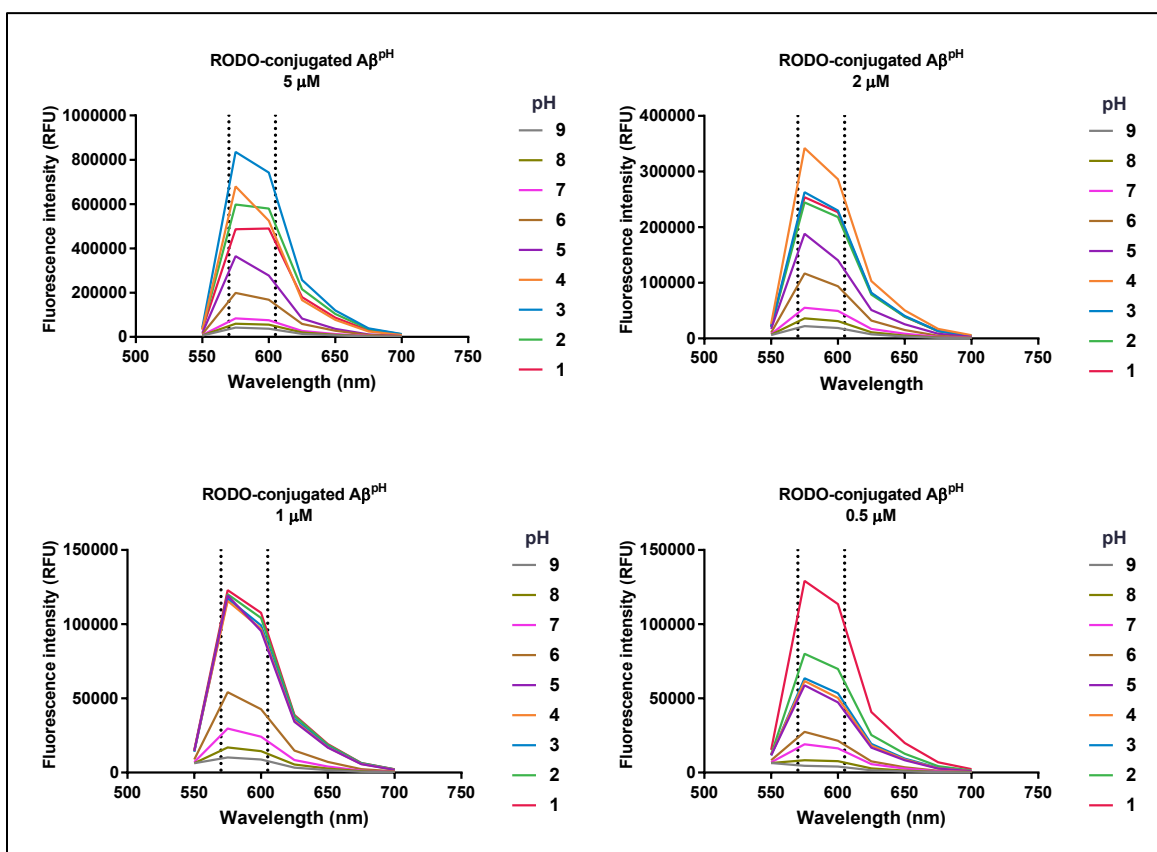


**Figure 4.S7-B.** pH-dependent emission spectra of pHrodo Red (RODO) conjugated Aβ at various concentrations. The emission spectra of the RODO-Aβ<sup>pH</sup> reporter showing maximum fluorescence over a large pH range of 1.0 to 5.0 along with differences between concentrations. Dotted lines highlight the region of maximum emission. Legend shows color code for pH 1 to 9.

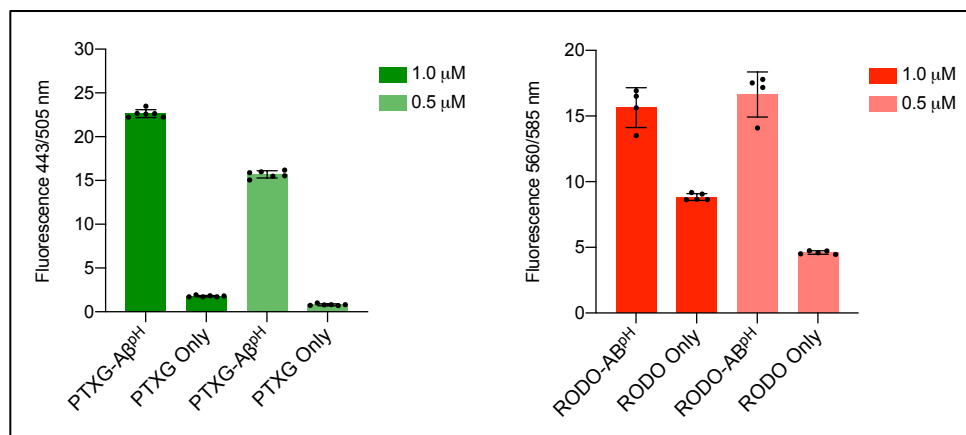


**Figure 4.S8.** Background fluorescence of PTXG and RODO in cells. BV2 microglia were treated with 1.0 μM or 0.5 μM of PTXG, PTXG-Aβ<sup>pH</sup>, RODO, and RODO-Aβ<sup>pH</sup> for 2 hours and fluorescence measured using a microplate reader. Microglial cells treated with PTXG alone showed very low fluorescence indicating less uptake of the dye alone compared to cells treated with PTXG-Aβ<sup>pH</sup>. Cells treated with RODO alone showed high background uptake (almost 50% fluorescence compared to the cell treated with RODO-Aβ<sup>pH</sup> at higher concentrations) indicating high background of this dye (media fluorescence subtracted from all).

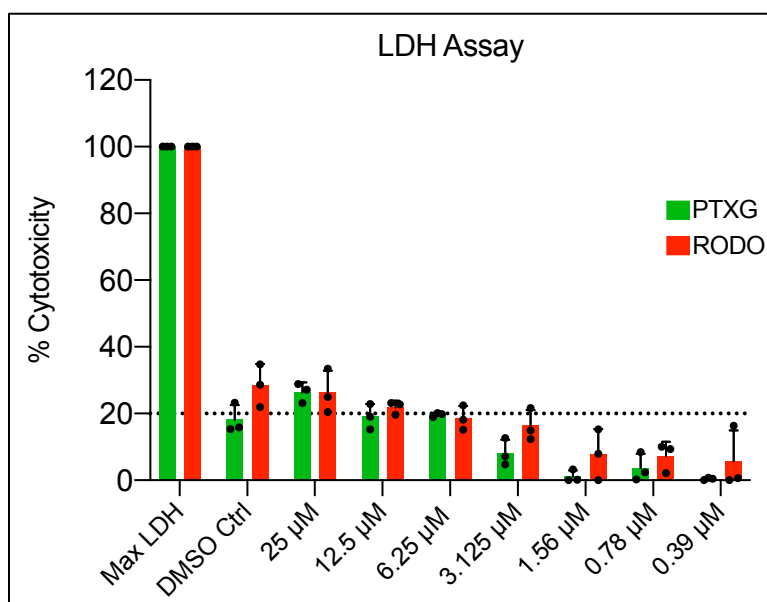


**Figure 4.S9.** Toxicity of PTXG and RODO dyes. BV2 microglia were treated with different concentrations of PTXG and RODO for 24 hours. Lactate dehydrogenase (LDH) assay was performed per manufacturer's instructions (CyQUANT LDH Cytotoxicity Assay; Thermo #C20300) to determine the toxicity of PTXG and RODO on microglia. Both PTXG and RODO dyes exhibited very low to almost no toxicity to BV2 microglial cells (24 hrs treatment). At the highest dose tested (25 μM), both dyes showed around 30% cytotoxicity. However, at 12.5 μM and below, the dyes showed 20% (dotted line) or less cytotoxicity.

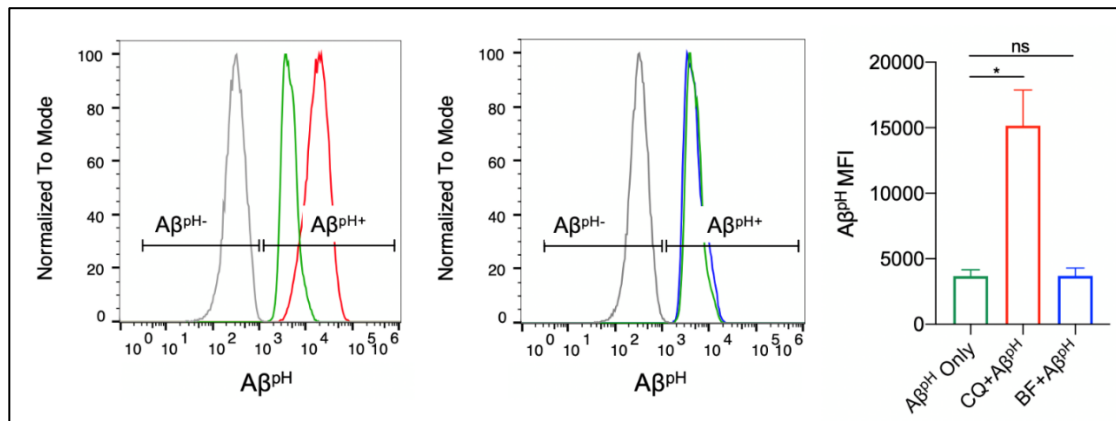


**Figure 4.S10.** Effect of chloroquine (CQ) and bafilomycin-A1 (BF) on fluorescence of A $\beta^{\text{pH}}$  in the cells. BV2 microglia were treated with 100  $\mu\text{M}$  CQ or 100 nM BF for 2 hours. The media was removed and replaced with 100 nM of A $\beta^{\text{pH}}$ -containing media for another 2 hours. The cells were then removed from the plates and A $\beta^{\text{pH}}$  uptake was analyzed by flow cytometry. BV2 microglial cells showed increase in A $\beta^{\text{pH}}$  fluorescence under CQ treatment (100  $\mu\text{M}$ , 2 hrs). The cells showed no difference in A $\beta^{\text{pH}}$  fluorescence under BF treatment (100 nM, 2 hrs).

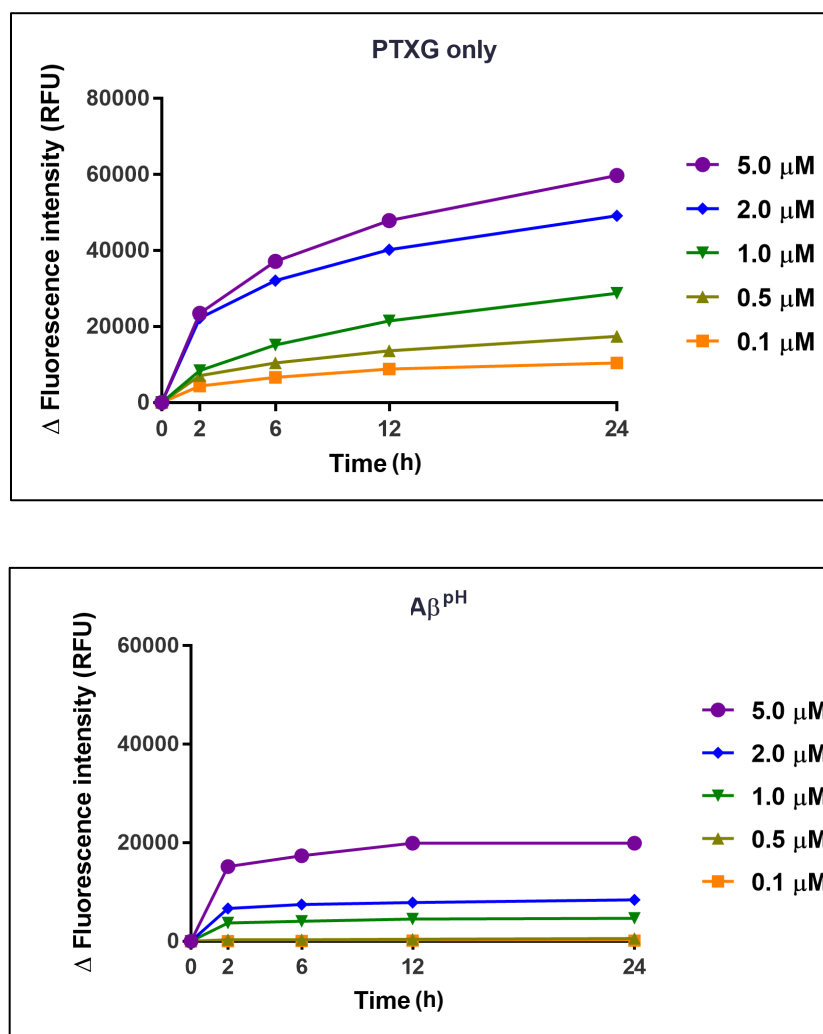


**Figure 4.S11.** Concentration-dependent response of PTXG and PTXG-conjugated A $\beta$  (A $\beta^{\text{pH}}$ ) at acidic pH over time. Fluorescence intensity of the PTXG-conjugated A $\beta$  (A $\beta^{\text{pH}}$ , bottom plot) in acidic condition of pH 3.0 over a 24 hour period. Top plot shows the fluorescence intensity of PTXG alone.

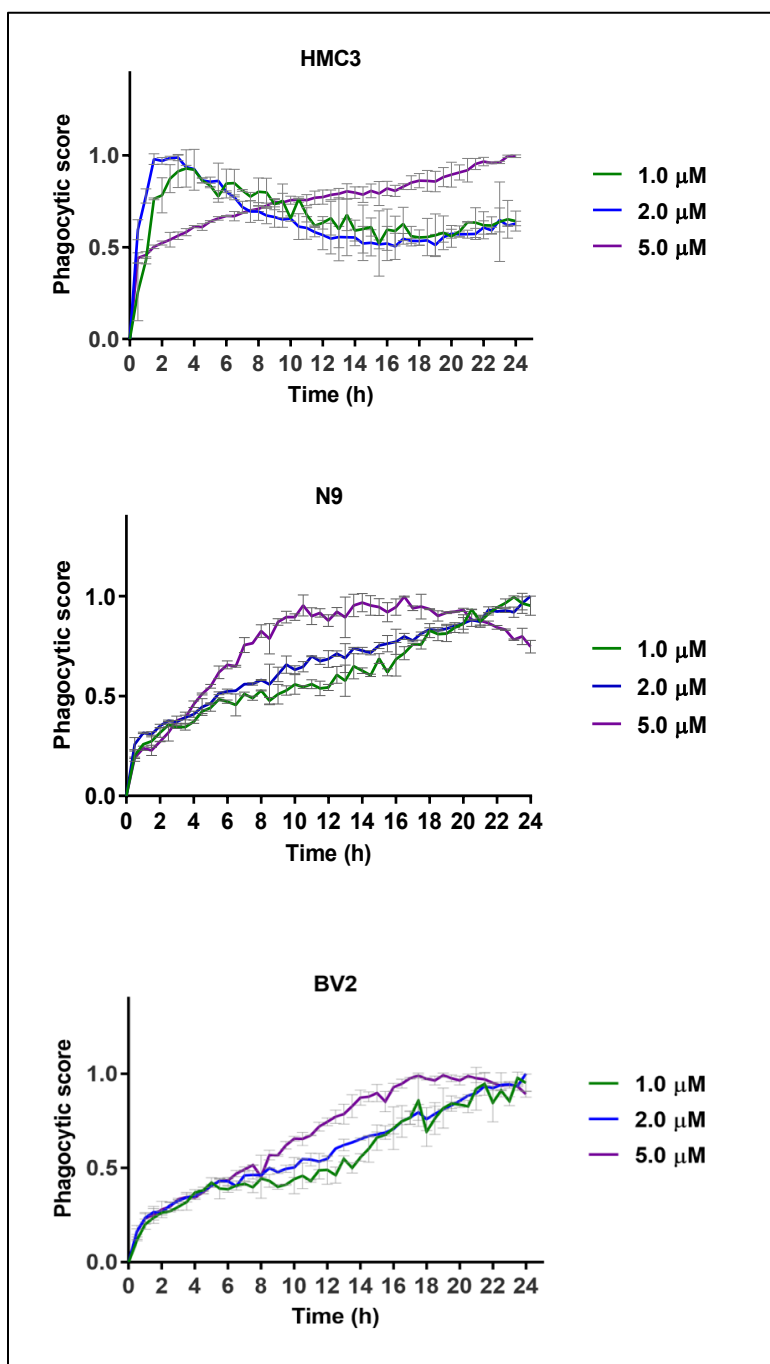


**Figure 4.S12.** Change in Phagocytic Score over time. For human microglia (HMC3, top), 5  $\mu\text{M}$  of  $\text{A}\beta^{\text{pH}}$  leads to a gradual increase in phagocytic score over time. At lower concentrations of 1 and 2  $\mu\text{M}$   $\text{A}\beta^{\text{pH}}$ , increased phagocytic score is observed peaking between 2 to 6 hours indicating maximum fluorescence intensity over 24 hours compared to starting ( $t=0$ ) time point. This is followed by progressive decrease in phagocytic score indicating decreased uptake or increased degradation compared to  $t=0$  time point and ultimately flattening out after 14 hours. In mouse N9 (center) and BV2 (bottom) microglia, higher  $\text{A}\beta^{\text{pH}}$  concentration (5  $\mu\text{M}$ ) results in higher phagocytic score over time peaking at 12-16 hours for N9 and 16-20 hours for BV2 compared to no peaks at 1 and 2  $\mu\text{M}$   $\text{A}\beta^{\text{pH}}$  treatment.

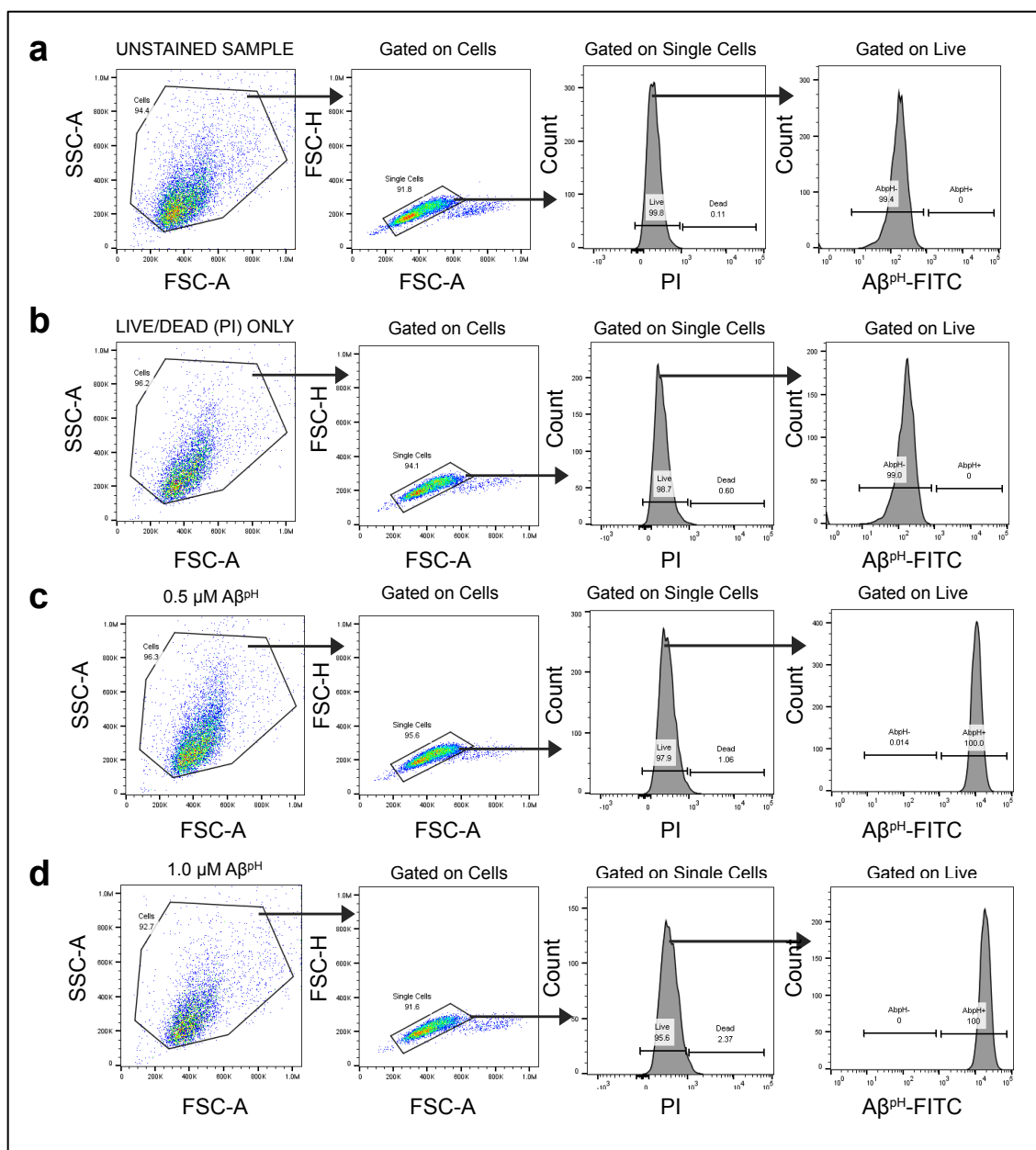


**Figure 4.S13-A.** Gating strategy for flow cytometry analysis of Aβ<sup>PH</sup> by BV2 microglia. a. Unstained sample i.e. cells only. b. Cells with live/dead stain only. Propidium iodide (PI) was used as a live/dead stain (indicating dead cells). c. Cells treated with 0.5 μM Aβ<sup>PH</sup> for 1 hour. d. Cells treated with 1.0 μM Aβ<sup>PH</sup> for 1 hour.

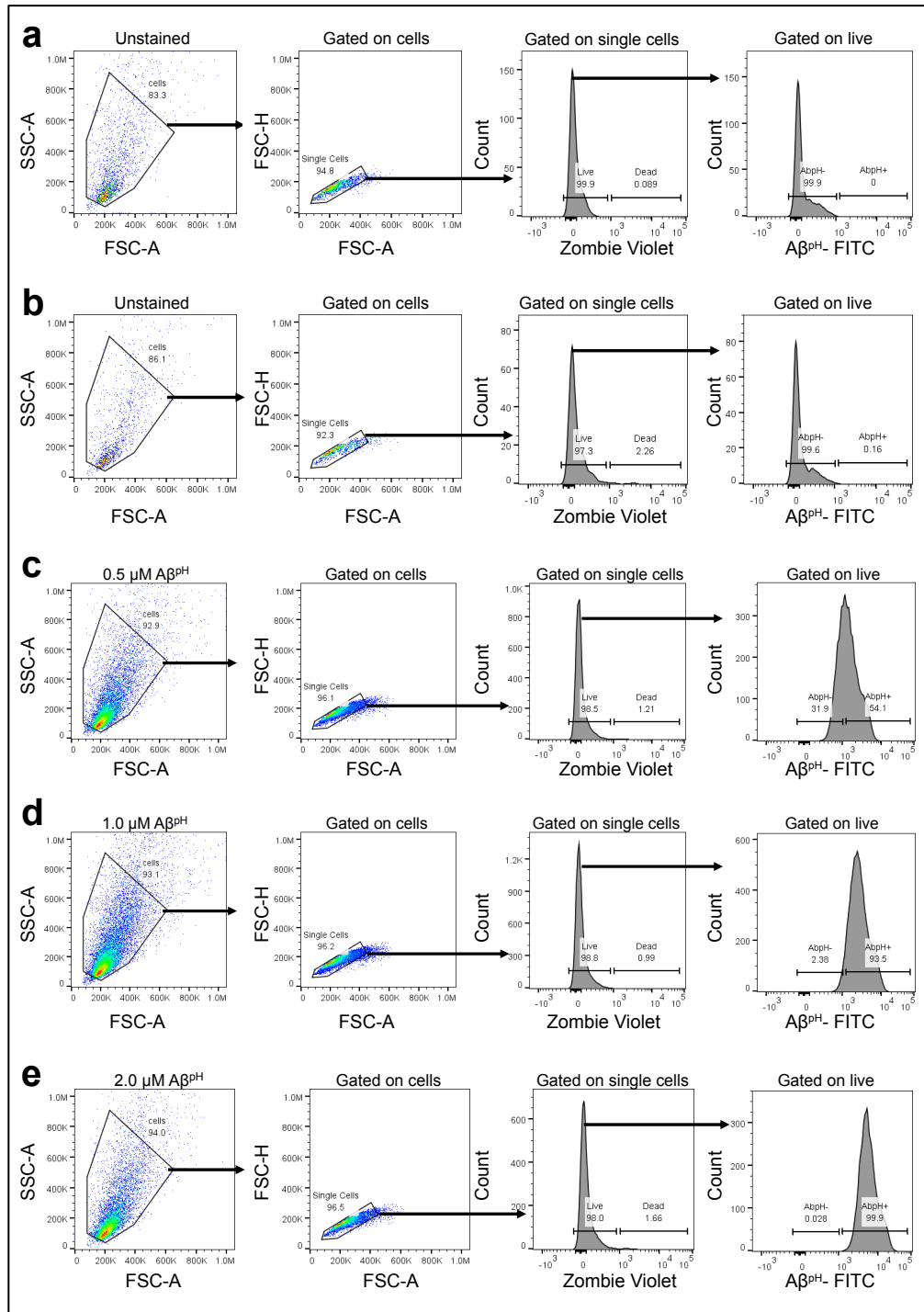


**Figure 4.S13-B.** Gating strategy for flow cytometry analysis of Aβ<sup>pH</sup> by primary microglia. a. Unstained sample i.e. cells only. b. Cells with live/dead stain only. Zombie violet was used as a live/dead stain (indicating dead cells). Cells were treated with c. 0.5 μM, d. 1.0 μM, and e. 2.0 μM Aβ<sup>pH</sup> for 1 hour.



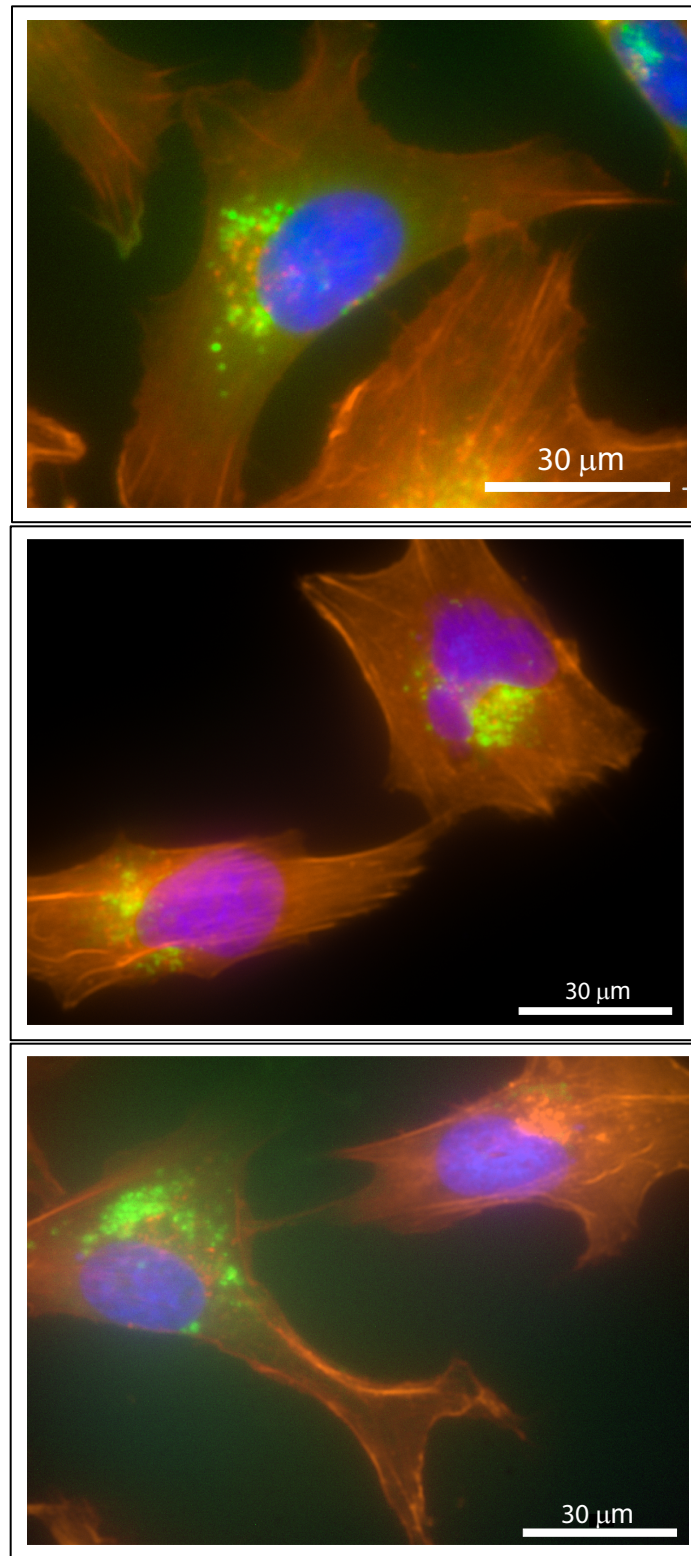


**Figure 4.S14-A.** Imaging phagocytosis of Aβ<sup>pH</sup> (green) in fixed HMC3 cells stained with phalloidin (red) and DAPI (blue).

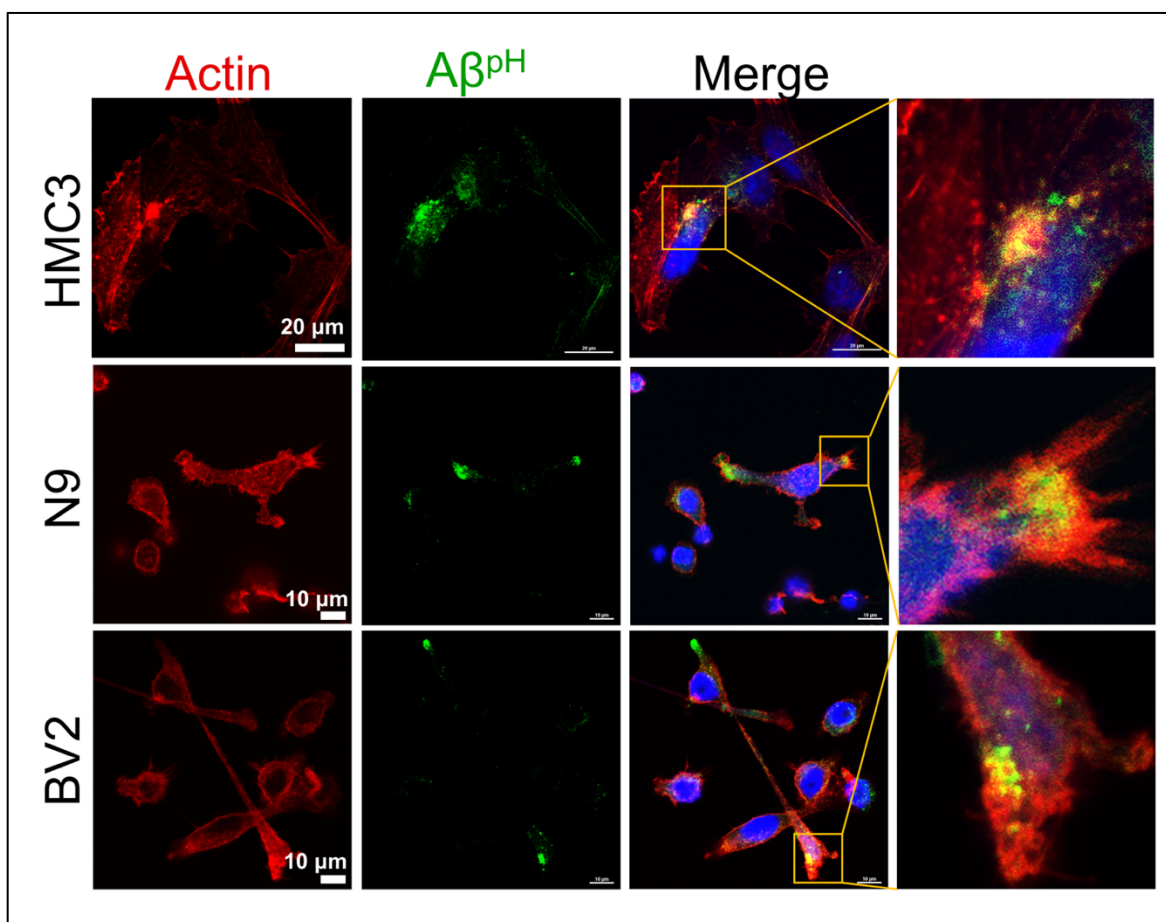


**Figure 4.S14-B.** Confocal images of fixed HMC3, N9, and BV2 cells showing the uptake of Aβ<sup>pH</sup> (green). Cells are stained for actin (red) and nuclei (blue) and retain the green Aβ<sup>pH</sup> signal after fixing.

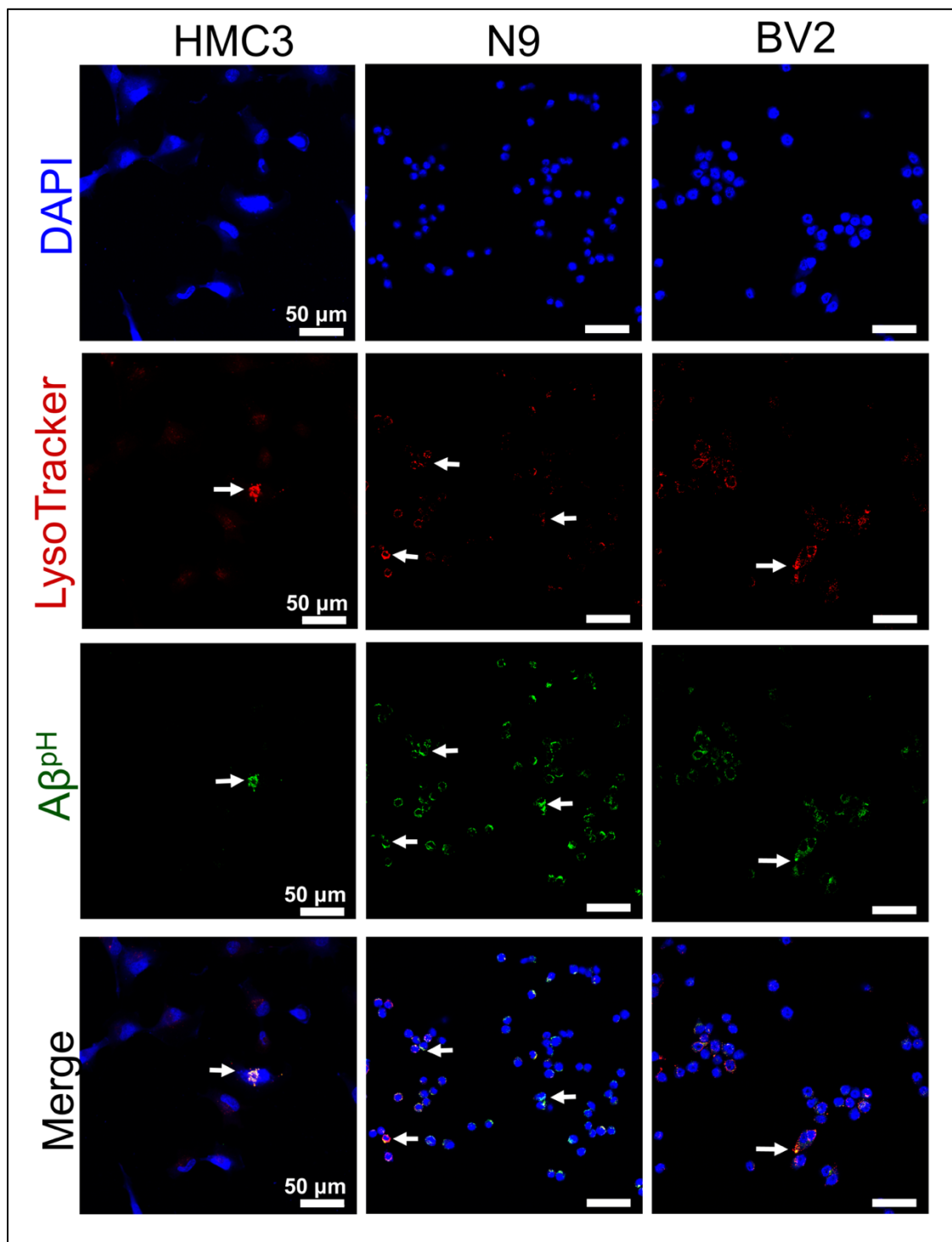


**Figure 4.S14-C.** Confocal images of fixed HMC3, N9, and BV2 cells showing the uptake of Aβ<sup>pH</sup> (green) as indicated by the white arrows. Cells are stained for acidic intracellular organelles (LysoTracker, red) and nuclei (DAPI, blue).

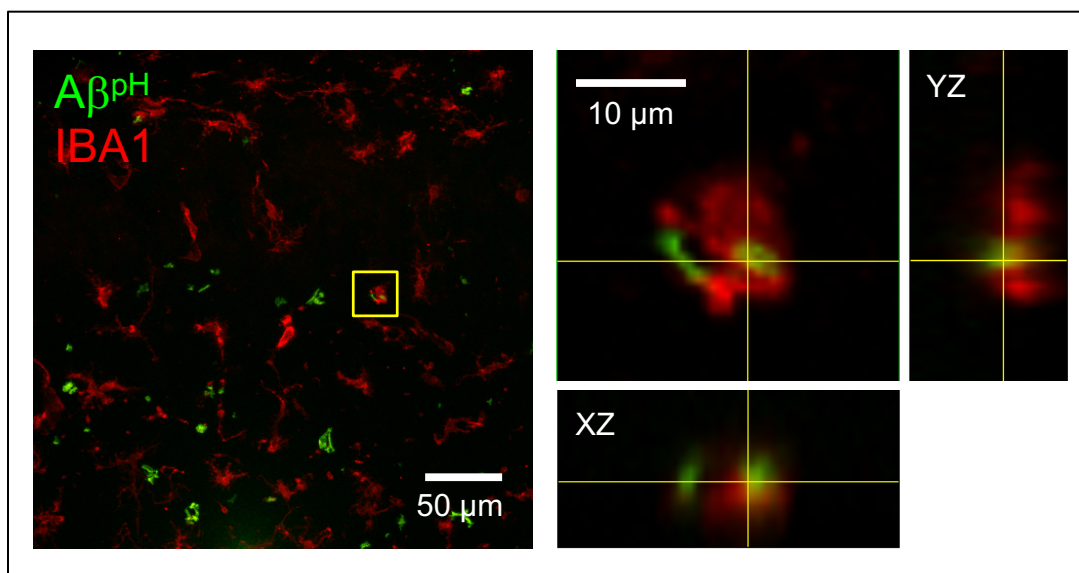


**Figure 4.S15.** Uptake of A $\beta^{\text{pH}}$  (green) by IBA1 $^{+}$  microglia (red) in acute hippocampal slices from a P12 rat. The A $\beta^{\text{pH}}$  is taken up by microglia shown by overlap of green and red fluorescence (images on right). Green fluorescence of A $\beta^{\text{pH}}$  outside microglial cells (red) indicates uptake into cells other than microglia.

## 4.7 Additional Information

### 4.7.1 Conflict Of Interest

Shane Liddelow is an academic founder of AstronauTx Ltd. Other authors declare no competing financial interests.

### 4.7.2 Acknowledgment

We thank Sheik Dawood for help with registering the videos. We also thank Dr. Andy Schaber, Imaging Facility Director, Bindley Bioscience Center at Purdue University and Dr. Joydeb Majumder for assistance with confocal imaging; Prof. J. Paul Robinson and Kathy Ragheb at the Purdue University Cytometry Laboratories for flow cytometry assistance. The cartoon schematics in the figures were created using BioRender.com.

### 4.7.3 Funding Sources

This work was supported, in part, by a Purdue University start-up package from the Department of Chemistry at Purdue University, an award from Purdue Research Foundation, Purdue Integrative Data Science Institute award, Ralph W. and Grace M. Showalter Research Trust award, the Jim and Diann Robbers Grant for New Investigators award, National Institutes of Health, National Center for Advancing Translational Sciences ASPIRE Design Challenge awards and the United States Department of Defense USAMRAA award # W81XWH2010665 to Gaurav Chopra. Additional support, in part by, the Stark Neurosciences Research Institute, the Indiana Alzheimer Disease Center, Eli Lilly and Company, the Indiana Clinical and Translational Sciences Institute grant # UL1TR002529 from the National Institutes of Health, National Center for Advancing Translational Sciences, and the Purdue University Center for Cancer Research funded by National Institutes of Health grant # P30 CA023168 are also acknowledged. The content is solely the responsibility of the authors and does not necessarily represent the official views of the National Institutes of Health. Work in the Attwell lab was supported by Wellcome Trust Investigator Awards 099222 and 219366 to David Attwell, by a Wellcome Trust 4-year PhD studentship to Pablo Izquierdo, and by a BBSRC LIDo PhD studentship to Nils Korte. Emilia Favuzzi was supported by EMBO (ALTF 444-2018). Kevin A. Guttenplan was supported by the Wu Tsai Neuroscience Institute Interdisciplinary Scholar Award from Stanford University. Work in the Liddelow lab was supported by NYU School of Medicine, generous anonymous donors, the Blas Frangione Foundation, and the Cure Alzheimer's Foundation. The Rochet lab was supported by grants from the Branfman Family Foundation and Purdue Research Foundation to Jean-Christophe Rochet. Priya Prakash and Sayan Dutta acknowledge support from Eli Lilly-Stark Neurosciences Research Institute-CTSI predoctoral fellowships. Gaurav Chopra is the Director of Merck-Purdue Center for Measurement Science funded by Merck Sharp & Dohme Corp., a subsidiary of Merck & Co., Inc., Kenilworth, NJ, U.S.A.

### 4.8 References

- [1] J. B. Zuchero and B. A. Barres, "Glia in mammalian development and disease," *Development*, vol. 142, no. 22, pp. 3805–3809, Nov. 2015.
- [2] Q. Li and B. A. Barres, "Microglia and macrophages in brain homeostasis and disease," *Nat. Rev. Immunol.*, vol. 18, no. 4, pp. 225–242, Apr. 2018.

- [3] A. Nimmerjahn, F. Kirchhoff, and F. Helmchen, “Resting microglial cells are highly dynamic surveillants of brain parenchyma in vivo.,” *Science*, vol. 308, no. 5726, pp. 1314–8, May 2005.
- [4] A. D. Bachstetter *et al.*, “Disease-related microglia heterogeneity in the hippocampus of Alzheimer’s disease, dementia with Lewy bodies, and hippocampal sclerosis of aging,” *Acta Neuropathol. Commun.*, vol. 3, no. 1, p. 32, Dec. 2015.
- [5] S. A. Liddelow *et al.*, “Neurotoxic reactive astrocytes are induced by activated microglia,” *Nature*, vol. 541, no. 7638, pp. 481–487, Jan. 2017.
- [6] A. F. Lloyd and V. E. Miron, “The pro-remyelination properties of microglia in the central nervous system,” *Nat. Rev. Neurol.*, vol. 15, no. 8, pp. 447–458, Aug. 2019.
- [7] M. L. Hanke and T. Kielian, “Toll-like receptors in health and disease in the brain: mechanisms and therapeutic potential.,” *Clin. Sci. (Lond.)*, vol. 121, no. 9, pp. 367–87, Nov. 2011.
- [8] E. Okun, M. P. Mattson, and T. V Arumugam, “Involvement of Fc receptors in disorders of the central nervous system.,” *Neuromolecular Med.*, vol. 12, no. 2, pp. 164–78, Jun. 2010.
- [9] J. Husemann, J. D. Loike, R. Anankov, M. Febbraio, and S. C. Silverstein, “Scavenger receptors in neurobiology and neuropathology: Their role on microglia and other cells of the nervous system,” *Glia*, vol. 40, no. 2, pp. 195–205, Nov. 2002.
- [10] S. Hong and B. Stevens, “Microglia: Phagocytosing to Clear, Sculpt, and Eliminate,” *Dev. Cell*, vol. 38, no. 2, pp. 126–128, Jul. 2016.
- [11] J. Canton, “Phagosome maturation in polarized macrophages,” *J. Leukoc. Biol.*, vol. 96, no. 5, pp. 729–738, Nov. 2014.
- [12] N. M. Wakida *et al.*, “Phagocytic response of astrocytes to damaged neighboring cells,” *PLoS One*, vol. 13, no. 4, 2018.
- [13] W.-S. Chung *et al.*, “Astrocytes mediate synapse elimination through MEGF10 and MERTK pathways,” *Nature*, vol. 504, no. 7480, pp. 394–400, Dec. 2013.
- [14] J. Doherty, M. A. Logan, O. E. Tasdemir, and M. R. Freeman, “Ensheathing Glia Function as Phagocytes in the Adult Drosophila Brain,” *J. Neurosci.*, vol. 29, no. 15, pp. 4768–4781, Apr. 2009.
- [15] Y. Fuentes-Medel, M. A. Logan, J. Ashley, B. Ataman, V. Budnik, and M. R. Freeman, “Glia and muscle sculpt neuromuscular arbors by engulfing destabilized synaptic boutons and shed presynaptic debris,” *PLoS Biol.*, vol. 7, no. 8, 2009.

- [16] Y. M. Morizawa *et al.*, “Reactive astrocytes function as phagocytes after brain ischemia via ABCA1-mediated pathway,” *Nat. Commun.*, vol. 8, no. 1, p. 28, Dec. 2017.
- [17] R. Nortley *et al.*, “Amyloid  $\beta$  oligomers constrict human capillaries in Alzheimer’s disease via signaling to pericytes,” *Science (80-. )*, vol. 365, no. 6450, p. eaav9518, Jul. 2019.
- [18] M. Lei *et al.*, “Soluble A $\beta$  oligomers impair hippocampal LTP by disrupting glutamatergic/GABAergic balance,” *Neurobiol. Dis.*, vol. 85, pp. 111–121, 2016.
- [19] C. Sato *et al.*, “Tau Kinetics in Neurons and the Human Central Nervous System.,” *Neuron*, vol. 97, no. 6, pp. 1284–1298.e7, Mar. 2018.
- [20] J. M. Long and D. M. Holtzman, “Alzheimer Disease: An Update on Pathobiology and Treatment Strategies.,” *Cell*, vol. 179, no. 2, pp. 312–339, Oct. 2019.
- [21] M. T. Heneka *et al.*, “Neuroinflammation in Alzheimer’s disease,” *Lancet Neurol.*, vol. 14, no. 4, pp. 388–405, Apr. 2015.
- [22] R. J. O’Brien and P. C. Wong, “Amyloid precursor protein processing and Alzheimer’s disease.,” *Annu. Rev. Neurosci.*, vol. 34, no. 1, pp. 185–204, Jul. 2011.
- [23] D. J. Selkoe, “Alzheimer’s Disease: Genes, Proteins, and Therapy.”
- [24] G. Krabbe *et al.*, “Functional impairment of microglia coincides with Beta-amyloid deposition in mice with Alzheimer-like pathology.,” *PLoS One*, vol. 8, no. 4, p. e60921, Apr. 2013.
- [25] A. M. Floden and C. K. Combs, “Microglia demonstrate age-dependent interaction with amyloid- $\beta$  fibrils.,” *J. Alzheimers. Dis.*, vol. 25, no. 2, pp. 279–93, Jul. 2011.
- [26] H. Sarlus and M. T. Heneka, “Microglia in Alzheimer’s disease,” *J. Clin. Invest.*, vol. 127, no. 9, pp. 3240–3249, Sep. 2017.
- [27] P. D. Wes, I. R. Holtzman, E. W. G. M. Boddeke, T. Möller, and B. J. L. Eggen, “Next generation transcriptomics and genomics elucidate biological complexity of microglia in health and disease,” *Glia*, vol. 64, no. 2, pp. 197–213, 2016.
- [28] R. S. Jones, A. M. Minogue, T. J. Connor, and M. A. Lynch, “Amyloid- $\beta$ -induced astrocytic phagocytosis is mediated by CD36, CD47 and RAGE,” *J. Neuroimmune Pharmacol.*, vol. 8, no. 1, pp. 301–311, Mar. 2013.
- [29] J. Koenigsknecht and G. Landreth, “Microglial phagocytosis of fibrillar beta-amyloid through a  $\beta$ 1 integrin-dependent mechanism.,” *J. Neurosci.*, vol. 24, no. 44, pp. 9838–46, Nov. 2004.

- [30] S. Ribes *et al.*, “Toll-Like Receptor Prestimulation Increases Phagocytosis of *Escherichia coli* DH5 and *Escherichia coli* K1 Strains by Murine Microglial Cells,” *Infect. Immun.*, vol. 77, no. 1, pp. 557–564, Jan. 2009.
- [31] S. Hassan, K. Eldeeb, P. J. Millns, A. J. Bennett, S. P. H. Alexander, and D. A. Kendall, “Cannabidiol enhances microglial phagocytosis via transient receptor potential (TRP) channel activation,” *Br. J. Pharmacol.*, vol. 171, no. 9, pp. 2426–2439, May 2014.
- [32] D. M. Paresce, R. N. Ghosh, and F. R. Maxfield, “Microglial Cells Internalize Aggregates of the Alzheimer’s Disease Amyloid  $\beta$ -Protein Via a Scavenger Receptor,” *Neuron*, vol. 17, no. 3, pp. 553–565, Sep. 1996.
- [33] L. D. Lavis, T. J. Rutkoski, and R. T. Raines, “Tuning the pKa of fluorescein to optimize binding assays,” *Anal. Chem.*, vol. 79, no. 17, pp. 6775–6782, Sep. 2007.
- [34] “pHrodo™ Red.” Thermo Fisher Scientific.
- [35] L. Ma, Q. Ouyang, G. C. Werthmann, H. M. Thompson, and E. M. Morrow, “Live-cell Microscopy and Fluorescence-based Measurement of Luminal pH in Intracellular Organelles,” *Front. Cell Dev. Biol.*, vol. 5, no. AUG, p. 71, Aug. 2017.
- [36] S. Lu, T. Sung, N. Lin, R. T. Abraham, and B. A. Jessen, “Lysosomal adaptation: How cells respond to lysosomotropic compounds,” *PLoS One*, vol. 12, no. 3, Mar. 2017.
- [37] P. Prakash, T. C. Lantz, K. P. Jethava, and G. Chopra, “Rapid, Refined, and Robust Method for Expression, Purification, and Characterization of Recombinant Human Amyloid beta 1-42,” *Methods Protoc.*, vol. 2, no. 2, p. 48, 2019.
- [38] W. B. Stine, L. Jungbauer, C. Yu, and M. J. Ladu, “Preparing synthetic A $\beta$  in different aggregation states,” in *Methods in Molecular Biology*, vol. 670, 2011, pp. 13–32.
- [39] W. B. Stine, K. N. Dahlgren, G. A. Krafft, and M. J. LaDu, “In Vitro Characterization of Conditions for Amyloid- $\beta$  Peptide Oligomerization and Fibrillogenesis,” *J. Biol. Chem.*, vol. 278, no. 13, pp. 11612–11622, Mar. 2003.
- [40] C. J. Bohlen, F. C. Bennett, A. F. Tucker, H. Y. Collins, S. B. Mulinyawe, and B. A. Barres, “Diverse Requirements for Microglial Survival, Specification, and Function Revealed by Defined-Medium Cultures,” *Neuron*, vol. 94, no. 4, pp. 759–773.e8, May 2017.
- [41] S. Liu *et al.*, “TLR2 Is a Primary Receptor for Alzheimer’s Amyloid Peptide To Trigger Neuroinflammatory Activation,” *J. Immunol.*, vol. 188, no. 3, pp. 1098–1107, Feb. 2012.
- [42] Y. Liu *et al.*, “LPS receptor (CD14): a receptor for phagocytosis of Alzheimer’s amyloid peptide,” *Brain*, vol. 128, no. 8, pp. 1778–1789, Aug. 2005.



- [43] Y. Zhao *et al.*, “TREM2 Is a Receptor for  $\beta$ -Amyloid that Mediates Microglial Function,” *Neuron*, vol. 97, no. 5, pp. 1023–1031.e7, Mar. 2018.
- [44] S. Parhizkar *et al.*, “Loss of TREM2 function increases amyloid seeding but reduces plaque-associated ApoE,” *Nat. Neurosci.*, vol. 22, no. 2, pp. 191–204, Feb. 2019.
- [45] G. Kleinberger *et al.*, “TREM2 mutations implicated in neurodegeneration impair cell surface transport and phagocytosis,” *Sci. Transl. Med.*, vol. 6, no. 243, pp. 243ra86–243ra86, Jul. 2014.
- [46] T. A. Siddiqui, S. Lively, C. Vincent, and L. C. Schlichter, “Regulation of podosome formation, microglial migration and invasion by  $\text{Ca}^{2+}$ -signaling molecules expressed in podosomes,” *J. Neuroinflammation*, vol. 9, no. 1, p. 770, Dec. 2012.
- [47] O. E. Tasdemir-Yilmaz and M. R. Freeman, “Astrocytes engage unique molecular programs to engulf pruned neuronal debris from distinct subsets of neurons,” *Genes Dev.*, vol. 28, no. 1, pp. 20–33, Jan. 2014.
- [48] J. Nuutila and E.-M. Lilius, “Flow cytometric quantitative determination of ingestion by phagocytes needs the distinguishing of overlapping populations of binding and ingesting cells,” *Cytom. Part A*, vol. 65A, no. 2, pp. 93–102, Jun. 2005.
- [49] C.-W. Chow, G. P. Downey, and S. Grinstein, “Measurements of Phagocytosis and Phagosomal Maturation,” *Curr. Protoc. Cell Biol.*, vol. 22, no. 1, pp. 15.7.1–15.7.33, Mar. 2004.
- [50] O. Butovsky *et al.*, “Identification of a unique TGF- $\beta$ -dependent molecular and functional signature in microglia,” *Nat. Neurosci.*, vol. 17, no. 1, pp. 131–143, Jan. 2014.
- [51] Q. Xiao *et al.*, “Enhancing astrocytic lysosome biogenesis facilitates A $\beta$  clearance and attenuates amyloid plaque pathogenesis,” *J. Neurosci.*, vol. 34, no. 29, pp. 9607–20, Jul. 2014.
- [52] J. A. Fernández-Albarral *et al.*, “Retinal glial changes in Alzheimer’s disease – A review,” *J. Optom.*, vol. 12, no. 3, pp. 198–207, Jul. 2019.
- [53] A. Gomez-Arboledas *et al.*, “Phagocytic clearance of presynaptic dystrophies by reactive astrocytes in Alzheimer’s disease,” *Glia*, vol. 66, no. 3, pp. 637–653, Mar. 2018.
- [54] C. Ruan *et al.*, “A novel Tmem119-tdTomato reporter mouse model for studying microglia in the central nervous system,” *Brain. Behav. Immun.*, vol. 83, pp. 180–191, Jan. 2020.
- [55] W. J. Streit, N. W. Sammons, A. J. Kuhns, and D. L. Sparks, “Dystrophic Microglia in the Aging Human Brain,” *Glia*, vol. 45, no. 2, pp. 208–212, 2004.

- [56] W. J. Streit, H. Braak, Q. S. Xue, and I. Bechmann, “Dystrophic (senescent) rather than activated microglial cells are associated with tau pathology and likely precede neurodegeneration in Alzheimer’s disease,” *Acta Neuropathol.*, vol. 118, no. 4, pp. 475–485, 2009.
- [57] D. Guneykaya *et al.*, “Transcriptional and Translational Differences of Microglia from Male and Female Brains,” *Cell Rep.*, vol. 24, no. 10, pp. 2773–2783.e6, Sep. 2018.
- [58] A. Mildner *et al.*, “Distinct and non-redundant roles of microglia and myeloid subsets in mouse models of Alzheimer’s disease,” *J. Neurosci.*, vol. 31, no. 31, pp. 11159–71, Aug. 2011.
- [59] S. A. Grathwohl *et al.*, “Formation and maintenance of Alzheimer’s disease  $\beta$ -amyloid plaques in the absence of microglia,” *Nat. Neurosci.*, vol. 12, no. 11, pp. 1361–1363, Nov. 2009.
- [60] L. C. Foo *et al.*, “Development of a Method for the Purification and Culture of Rodent Astrocytes,” *Neuron*, vol. 71, no. 5, pp. 799–811, Sep. 2011.

## CHAPTER 5. PH-ACTIVABLE FLUORESCENT PROBES FOR TARGETING MICROGLIAL CELL ORGANELLES

Manuscript in review.

Jethava KP\*, Prakash P\*, Manchanda P, Arora H, Chopra G. One Scaffold—Different Organelles Sensors: pH-Activable Fluorescent Probes for Targeting Live Primary Microglial Cell Organelles.

### 5.1 Abstract

Targeting live cell organelles is important for imaging and to understand and control specific biochemical processes. Typically, fluorescent probes with distinct structural scaffolds have been used for targeting specific cell organelle. Herein, we aimed to design modular one-step synthetic strategies using a common reaction intermediate to develop new lysosomal, mitochondrial and nucleus targeting pH-activable fluorescent probes that are all based on a single boron dipyrromethane analogs. The divergent cell organelle targeting was achieved by synthesizing pH-activable fluorescent probes with specific functional groups changes to the main scaffold resulting in differential fluorescence and pKa. Specifically, we show that the functional group transformation of the same scaffold influences cellular localization and specificity of pH-activable fluorescent probes in live primary microglial cells with pKa's ranging from ~4.5-6.0. We introduce a structure-organelle-relationship (SOR) framework targeting the nucleus (NucShine), lysosomes (LysoShine) and mitochondria (MitoShine) in primary mouse microglial cells. This work will result in future applications of SOR beyond imaging to target and control organelle-specific biochemical processes in disease-specific models.

### 5.2 Main

Fluorescent organic materials have proven to be extremely useful for biological and biomedical science. [1a] Specifically, high-sensitivity fluorescent imaging of cellular organelles with enhanced spatial resolution allows direct visualization of dynamic cellular processes. [1b] Small-molecule fluorescent probes are essential tools to monitor changes in biological processes in cellular organelles. These include imaging lysosomes, [2a-b] mitochondria, [2c] Golgi apparatus, [2d] nucleus [2f] among many others, and fluorescent probes are useful to track their abundance,

localization, and function in cells. Lysosomes mainly act as a cellular ‘recycling plant’ to maintain intracellular and extracellular homeostasis [2a] via the breakdown of carbohydrates, lipids, proteins, nucleic acids, cellular debris and other foreign pathogens. Mitochondria is the cellular ‘power plant’ that contains enzymes responsible for energy production needed for biochemical reactions and for energy metabolism to maintain cellular health. In addition, lysosomal and mitochondrial crosstalk is critical for cells and its dysfunction leads to diseases including neurodegeneration. [2e] Often, imaging of cell organelles, irrespective of pH-activable property, involves specific fluorescent probes having different scaffolds that are prepared separately by multistep synthesis. In that context, a conceptual divergent synthetic strategy delivering a distinct organelle targeting from the same basic scaffold has remained elusive.

Microglia, the immune cells in the brain and macrophages in the periphery phagocytose (or engulf) extracellular material such as bacteria, virus, misfolded proteins, cell debris, etc. from their microenvironment into lysosomes for degradation. [3a] Lysosomes are membrane-bound acidic organelles containing several enzymes (hydrolases, proteases, lipases, etc.) to actively breakdown the phagocytosed material. [3b] Microglial cells are an excellent model for examining phagocytosis as well as lysosomal and mitochondrial activity ex vivo and in vivo. [3c] Microglia are the professional phagocytes in the brain that play a critical role in brain health and development. [3d] It is known that microglial lysosomes are unable to effectively degrade a large quantity of phagocytosed amyloid-beta aggregates, which may be contributing to neurodegeneration during later stages of Alzheimer’s disease. [3e] Furthermore, during neurodegeneration microglia releases dysfunctional mitochondria into their environment thereby exacerbating neuroinflammation. [3f] It is, therefore, crucial to develop pH-activable chemical probes that target lysosomes and mitochondria to understand such cellular processes. [3c] Fortunately, we can exploit the lysosomal acidic environment of pH 4.5 – 5.5 [2a,4a] to develop pH-activable fluorescent probes to visualize, track, and investigate lysosomal processes in live and fixed cells and in vivo. [3c] For targeting mitochondria, we can exploit the negatively charged inner membrane of mitochondria to design a fluorescent probe with a positively charged functional group. [4b] Importantly, the maintenance of a particular alkaline matrix (pH ~8) by pumping out protons dictates the normal physiological function of mitochondria. [4c] However, during disease pathogenesis, impaired mitochondria undergo mitophagic elimination through lysosomal fusion. [2e]

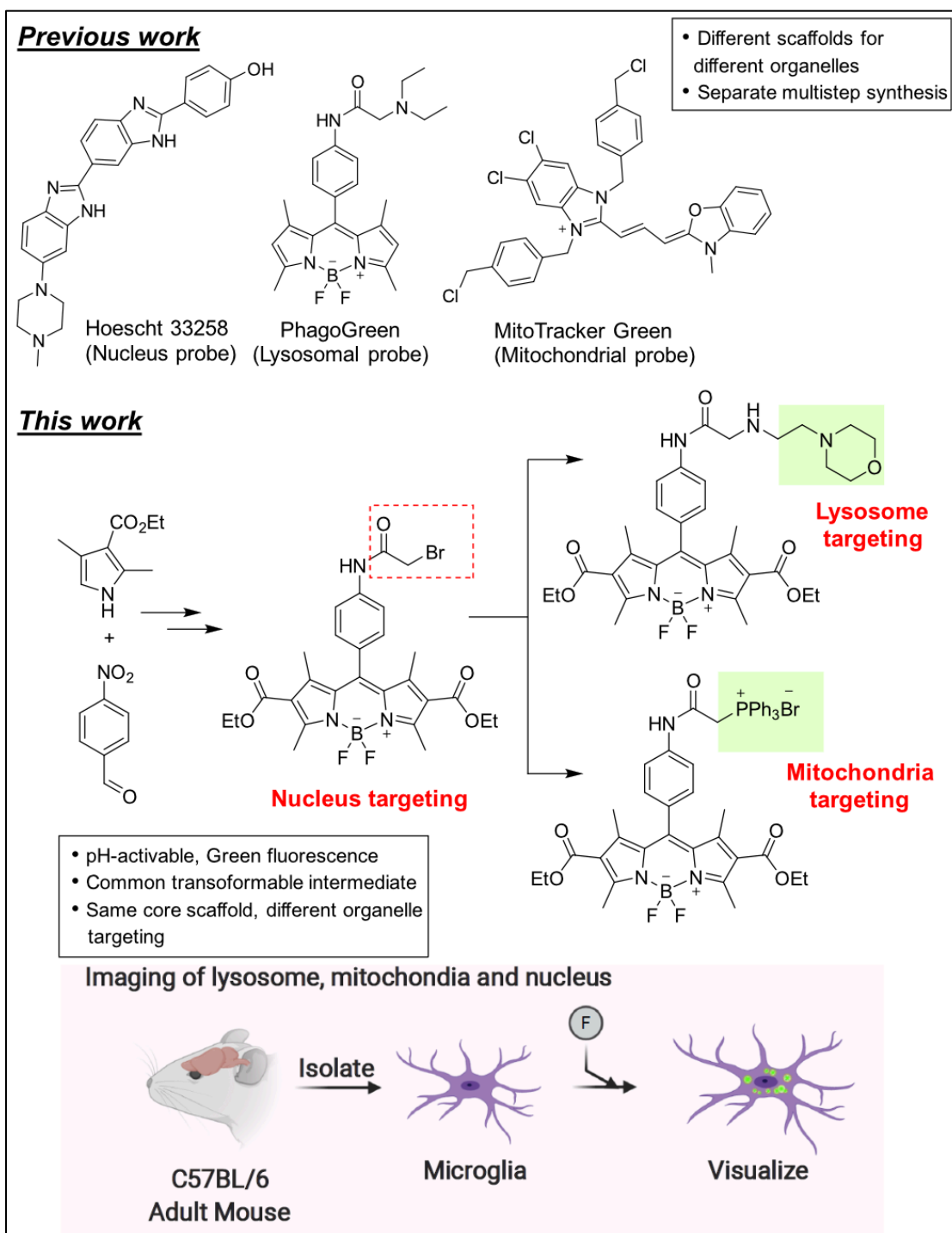


**Figure 5.1** Our strategy to prepare cell organelle targeting probes in one synthetic scheme with a common scaffold.

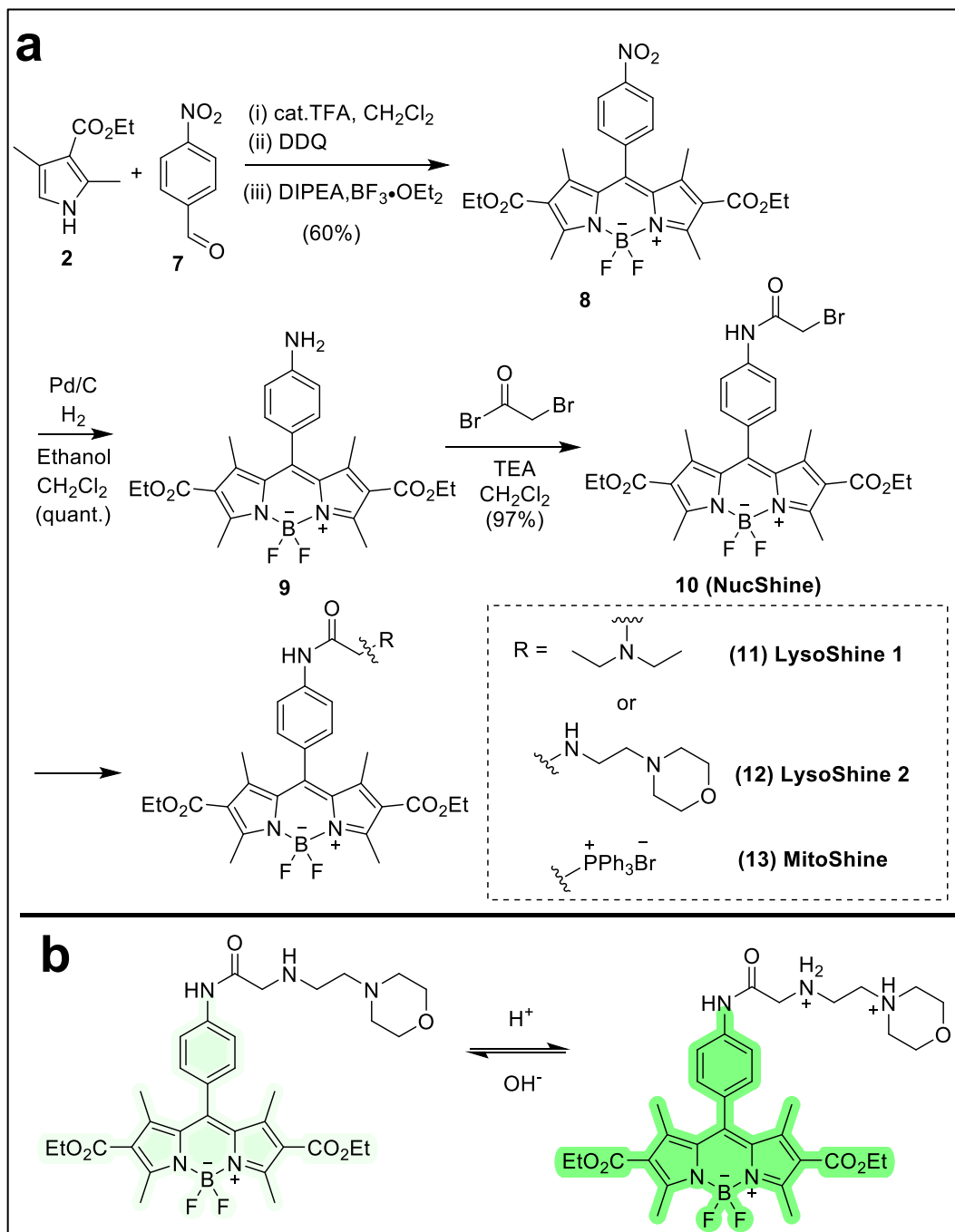
Moreover, understanding the crosstalk between mitochondria and lysosomes using targeted fluorescent probes is important for the investigation of cellular processes leading to disease pathogenesis. [4d] Nonetheless, if mitochondrial targeting fluorescent probe that has acidic pH-activable property, then such fluorescent probes could be useful to track mitochondrial fusion with acidic lysosomes.

The rational design of pH-activable fluorescent probes should satisfy several parameters: (i) ability to emit high fluorescence at lysosomal acidic pH and negligible fluorescence at cytosolic neutral pH, (ii) cellular permeability and uptake, (iii) non-specific binding to other cellular components, and (iv) good solubility. Several pH-activable fluorescent probes contain rhodamine, [5a] coumarin, [5b] naphthalimide, [4b] cyanine [4e-f] and 4,4-difluoro boron dipyrromethane (known as BODIPY) based scaffolds. [5c] The widely used are BODIPY-based scaffolds [5d] due to a variety of synthetic routes to introduce diverse functionalities [6a-b] for desired photophysical and spectroscopic properties. However, this process is not robust and minor changes in the substituents can significantly affect spectroscopic properties. Furthermore, if we can develop a synthetic strategy that could furnish divergent cell organelle targeting fluorescent probes, would not only reduce the chemical burden but also afford a convenient synthesis of fluorescent probes from a single synthetic intermediate.

Representative fluorescent probes with different chemical scaffolds that specifically target nucleus (Hoescht 33258), [2g] lysosome (PhagoGreen) [6b] or mitochondria (MitoTracker Green<sup>TM</sup>) [2f] are shown in Figure 1. Here, we report a new modular design strategy for developing ratiometric BODIPY-based fluorescent probes targeting lysosomes, mitochondria and the nucleus that are highly fluorescent at acidic pH levels compared to cytosolic pH levels (Figure 1). During the course of the present study, we identified an interesting synthetic intermediate that is an excellent nucleus targeting fluorescent probe. We identified organelle targeting pH-activable fluorescent probes that are cell-permeable, and non-toxic to the cells. One of the most common starting materials to prepare BODIPY probes is 2,4-dimethyl-1H-pyrrole (Scheme S1, compound 1) that exists as a liquid at room temperature. We used ethyl 2,4-dimethyl-1H-pyrrole-3-carboxylate (2) that is solid at room temperature, easy to handle, well-tolerated under reaction conditions, and underrepresented in the literature to prepare boron dipyrromethene scaffold (3). [6c] The additional

functional group on the pyrrole ring system can serve as a handle for late-stage functionalization. Substitutions of BODIPY have significant effects on the excitation/emission property of a fluorescent probe but have only been studied at the 1,3,5,7-positions in scaffold 3, using compound 1 but not compound 2 (Scheme S1).

Previous reports suggest that N,N-dimethylaniline functional group can be used to prepare pH-activable probes. Urano and Kobayashi et al. [7a] and Kikuchi et al. [7b] independently reported -NMe<sub>2</sub> containing probe with pK<sub>a</sub> 4.3 and 4.5, respectively. Therefore, we strategically designed compound 5 to be synthesized in two steps (see Scheme S2) using 2,4-dimethyl-1H-pyrrole-3-carboxylate (2) and 4-(N,N-dimethylamine) benzaldehyde (4). Interestingly, the absorbance and fluorescence property of 5 showed the high fluorescence at pH 2.0 or less that was significantly different from similar probes reported in the literature (Figure S1). [7a-b] This suggests that the ethylester functional group played a role in the pH-sensitive property of compound 5. Notably, the Knoevenagel condensation between a methyl group at position 3 or 5 of BODIPY scaffold and substituted benzaldehyde was used to introduce extended conjugation to fine-tune the pH-sensitive property towards bathochromic (red) fluorescence shift. Specifically, compound 5 was reacted with 4-hydroxybenzaldehyde or 4-hydroxy 3-nitro benzaldehyde using piperidine, acetic acid as additives, and anhydrous toluene as a solvent under reflux condition to obtain expected conjugated products 6a-b (Scheme S2). [7c,d] However, 6a-b were sparingly soluble in an aqueous medium and 6a did not generate a fluorescence spectrum as solubility was affected by pH buffers. Compound 6b was soluble in a mixture of DMSO: acetonitrile and showed pH-sensitivity with significant fluorescence at pH less than 6 (Figure S2) due to the presence of a nitro group at ortho-position to the hydroxyl group. [7e] However, poor solubility of these compounds does not warrant its use in primary cells and for future in vivo applications.



**Scheme 5.1** (a) Synthetic route for the synthesis of pH-activable NucShine (**10**), LysoShine probes (**11** and **12**) and MitoShine (**13**) probe; (b) A plausible response mechanism of the pH-activable probe (representative example)



To overcome these challenges, we designed another synthetic route to achieve a facile and modular synthesis of pH-activable fluorescent probes targeting lysosomes, mitochondria and the nucleus (Scheme 1a). Herein, we envisioned preparing an important synthetic intermediate that can be transformed into different organelle targeting probes in one step. Using the common synthetic intermediate, we installed functional groups that target a specific cell organelle individually. For example, we planned to synthesize pH-responsive lysosome targeting probes, using morpholine as a lysosome-targeting moiety. [1a,5c,8a-b] The BODIPY fluorophore can be fine-tuned by the photo-induced electron transfer (PET) mechanism of the lone pair electrons of a nitrogen atom in the morpholine as well as secondary amine functional group (Scheme 1b). A similar mechanism can be envisioned when the diethylamine group is present. We started the synthesis of designed pH-responsive probes by the reaction of compound 2 with 4-nitro benzaldehyde (compound 7) afforded compound 8 as a brownish-black solid. The nitro compound 8 was reduced successfully into amine-containing compound 9 using Pd/C in ethanol: CH<sub>2</sub>Cl<sub>2</sub> solvent mixture. Next, compound 9 readily reacted with bromo acetyl bromide to give 10 with excellent yields. The –CH<sub>2</sub>Br handle provides easy access to substitute with an amine functional group-containing reactant to get the final product. We used diethylamine and 2-aminoethyl morpholine substrate to synthesize compounds 11 (LysoShine 1) and 12 (LysoShine 2), respectively. We noticed that –CH<sub>2</sub>Br in intermediate 10 could serve as a useful synthon to introduce another targeting moiety such as cationic triphenylphosphine for mitochondria targeting. Therefore, we prepared a mitochondrial probe (compound 13) also using intermediate 10 when reacted with triphenylphosphine under the inert condition and named compound 13 as MitoShine.

Next, we investigated the absorption and fluorescent properties of LysoShine 1, LysoShine 2, and MitoShine (Figure 2). The LysoShine 1 in different pH solutions of phosphate buffer (1% DMSO in 1M PBS) has an absorption centered around 500 nm and emission maximum at 505 nm with 480 nm excitation. LysoShine 1 is highly fluorescent at pH 4 compared to reduced fluorescence that gradually decreased from pH 5 to 7 (pK<sub>a</sub> of 5.4, Figure 2). On the other hand, LysoShine 2 (max. absorption 500 nm, max. emission 512 nm, excitation 480 nm) showed better pH-sensitivity with a gradual increase for pH less than 6 (pK<sub>a</sub> of 6.0). We tested the mitochondrial targeting property of MitoShine (max. absorption 505 nm, max. emission 535 nm, excitation 480 nm). Interestingly, MitoShine showed significantly higher fluorescence at pH 4 compared to other pH

values (Figure 2) with a pKa of 4.4 suggesting possible use to image mitochondria-lysosome crosstalk. We also tested the photophysical property of the important synthetic intermediate compound 10 (absorption maximum 505 nm, max, emission 510 nm at excitation 480 nm, pKa 3.2, Figure S3). Unlike, compound 6a-b, LysoShine 1 and 2, MitoShine maintains its solubility upon addition of pH solutions (final DMSO concentration 1%), so we considered it as compatible for further biological experiments with cells.

Next, we performed a series of experiments with BV2 microglia cell line and with primary microglia isolated from mouse brains towards applications in biological systems. We performed MTT assay with 1, 5 and 10  $\mu$ M concentrations of the probes at 24 hours with BV2 microglia to measure the effect on metabolic activity (Figure S4). All the compounds maintained 80% or higher cellular metabolic activity except for MitoShine, which maintained a high cellular metabolic activity at 1  $\mu$ M but only 10% activity at 5  $\mu$ M or higher concentrations. We also assessed the cytotoxicity of the probes on BV2 using the lactate dehydrogenase (LDH) assay that measures the levels of LDH released by dying cells into the cell culture medium. In 2 hours assay, LysoShine 1 and 2 did not show any cytotoxicity at any tested doses. Contrarily MitoShine showed no cytotoxicity at 1 and 5  $\mu$ M, it showed less than 10% cytotoxicity at 10  $\mu$ M (Figure S5a). In 24 hours treatment, LysoShine 1 and 2 showed less than 10% cytotoxicity at all the tested doses compared to MitoShine that showed around 20% cytotoxicity at higher doses of 10  $\mu$ M and 5  $\mu$ M (Figure S5b). Therefore, the lower metabolic activity of the cells at higher concentrations of MitoShine for 24 hours may lead to cytotoxicity. For a fluorescent probe, it is essential to have high cell permeability. So, we also checked the uptake efficiency of synthesized probes. In 2 hour treatment, almost all probes showed uptake efficiency around 80% or higher at all doses except for MitoShine that showed 30% of uptake at 10  $\mu$ M (Figure S6). Next, having important information (fluorescent property, cytotoxicity and uptake efficiency) in hand, we focused on the cell imaging experiments and flow cytometry analysis to test these pH-activable probes in primary microglia. Notably, compound 10 is one of the important intermediate and found to be cell permeable (Figure S6) as well as not cytotoxic (Figure S4) to BV2 cells. Interestingly, MitoTracker Green has a -CH<sub>2</sub>Cl functional group while compound 10 has -CH<sub>2</sub>Br. Whereas previously reported microglia specific probes have -CH<sub>2</sub>Cl group. [7f] So, it would be interesting to test the behavior of compound 10 inside the cell. So, first, we checked the localization of compound 10,

which showed high fluorescence at pH less than 3 (Figure S3). Interestingly, in the confocal imaging, we observed bright green puncta that colocalized with nuclei staining dye DAPI (Figure S8). For nucleus targeting, DAPI and Hoechst dyes are the most widely used dyes in the field and only a few novel nucleus targeting probes have been reported due to the challenges of nucleus targeting such as poor target efficiency, membrane impermeability etc. [2f-g] The compound 10 (named NucShine) satisfy these requirements and potentially a new nucleus targeting probe. These observations motivated us to explore—how transforming one functional group to another impacts the cell organelle targeting ability of these pH-activable probes in primary mouse microglia.

We performed flow cytometry analysis to evaluate the intensity of the fluorescent signals of the probes in primary mouse microglia (Figure 3a) for future cell sorting applications. The cells treated with the fluorescent probes at 10  $\mu$ M for 2 hours showed increased green fluorescence compared to the cells treated with the vehicle only (unstained control) thereby clearly discriminating between the probe-treated and untreated cells (Figure 3b-d). Furthermore, LysoShine 1 showed higher fluorescent intensity than LysoShine 2 within the cells (Figure 3 along with the commercially available LysoTracker dye, or with (ii) MitoShine probe and the MitoLite dye, we were able to identify over 95% of the live cells that are LysoShine+LysoTracker+ and around 87% of live cell subset that was MitoShine+MitoLite+ (Figure S7). The ability to identify the probe-specific individual cells also demonstrates the possibility of sorting the cell subsets for downstream analysis in the future.

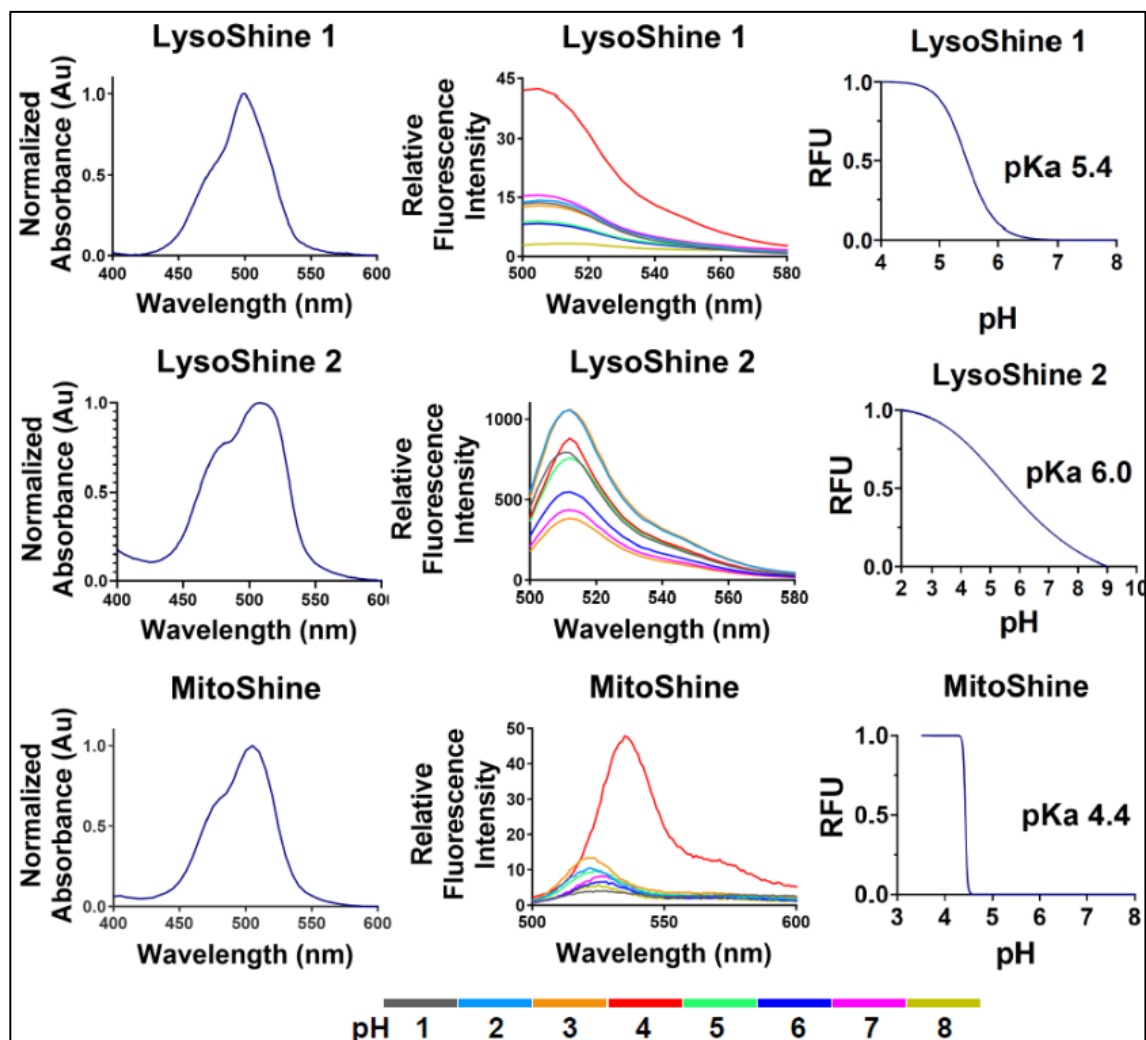


**Figure 5.2** Absorption, Fluorescence spectrum of compound LysoShine 1, LysoShine 2, MitoShine at different pH solutions and their pKa values. Spectrum recorded at room temperature in PBS buffer at varying pH with 1% (v/v) of DMSO, in all cases probe concentration = 10  $\mu$ M.

Next, to confirm the localization of the fluorescent probes within the lysosomal organelles, we performed confocal imaging of the probes with primary microglia (**Figure 4a**). The green fluorescent signal of LysoShine 1 and LysoShine 2 appeared as several bright puncta around the nuclei as well as in the cytosolic regions of the cells. The localization of the probes into the intracellular acidic organelles was confirmed by co-staining with the commercially available LysoTracker Red DND-99 dye (**Figure 4b-c**). We obtained similar fluorescence in BV2 microglia (**Figure S9**). The LysoShine probes clearly co-localized with the LysoTracker dye within the acidic lysosomes and not with DAPI-labelled nuclei, confirming targeting in cells.

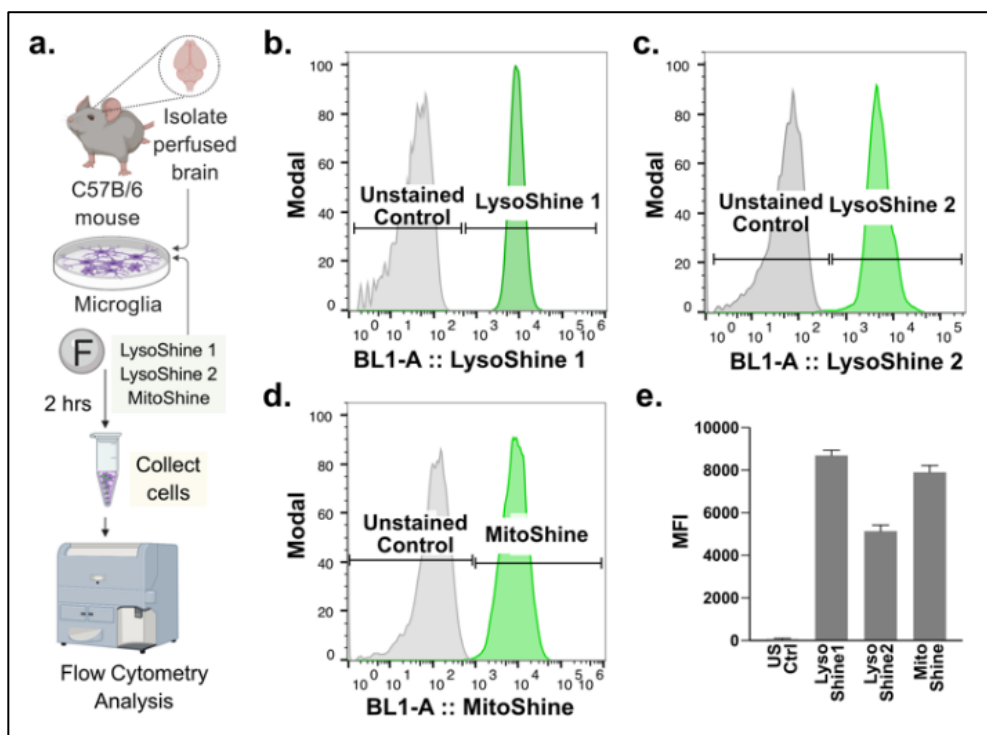


**Figure 5.3** (a) Schematic for flow cytometry analysis in live cells. (b-d) Demonstrates the fluorescence of LysoShine 1, LysoShine 2, and MitoShine upon uptake by primary mouse microglia (live cells). Modal corresponds to a percentage of the maximum count. (e) Median fluorescence intensity (MFI) values for each probe. US Ctrl is unstained control. Gating strategy and flow plots with commercial dyes in supporting information.

The localization of the mitochondrial probe, MitoShine, was similarly evaluated in primary microglia with confocal imaging. The cells showed a bright green fluorescent signal and the green puncta with MitoShine within the cells clearly co-localized with MitoLite, a commercial mitochondrial dye (**Figure S10a**). Interestingly, we observed several other regions (green puncta)

labeled with MitoShine that did not overlap with MitoLite (**Figure S10b**) suggesting that localization of the MitoShine probe may be localizing in other organelle along with the mitochondria. Interestingly, in a separate experiment, we observed an overlap of the MitoShine probe with LysoTracker, an acidic lysosomal dye (**Figure S10c**).

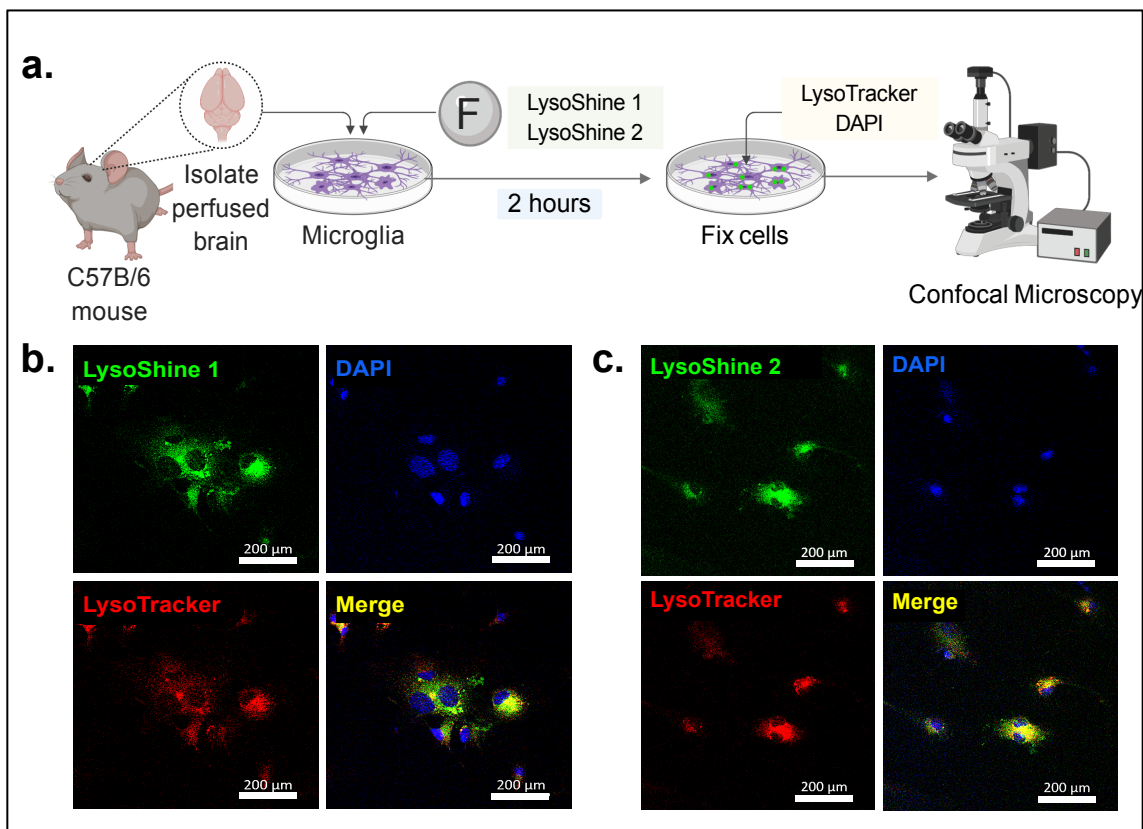


**Figure 5.4** (a) Experimental design for fluorescence imaging of primary mouse microglial cells with the (b) LysoShine 1 and (c) LysoShine 2 (green). The localization of the compounds in the lysosomal acidic compartments is shown with the LysoTracker dye (red). Nuclear DNA is stained with DAPI (blue). Scale bars represent 200 μm.

We asked if MitoShine could be used to study mitochondrial transport and recycling as a means to dynamically monitor organelle quality [4d] or identify mitophagic elimination through lysosomal fusion. [2e] We therefore treated the primary microglia with MitoShine for 2 hours and later with both LysoTracker and MitoLite at the same time. Confocal imaging demonstrated the colocalization of MitoShine in both mitochondrial as well as in lysosomal organelles (**Figure 5**). In addition, overlapping both channels of LysoTracker and MitoLite dyes indicates the merging of

mitochondria and lysosomes in these cells (**Figure S11**) suggesting the possible use of MitoShine for mitochondrial-lysosomal fusion processes for future biological applications.

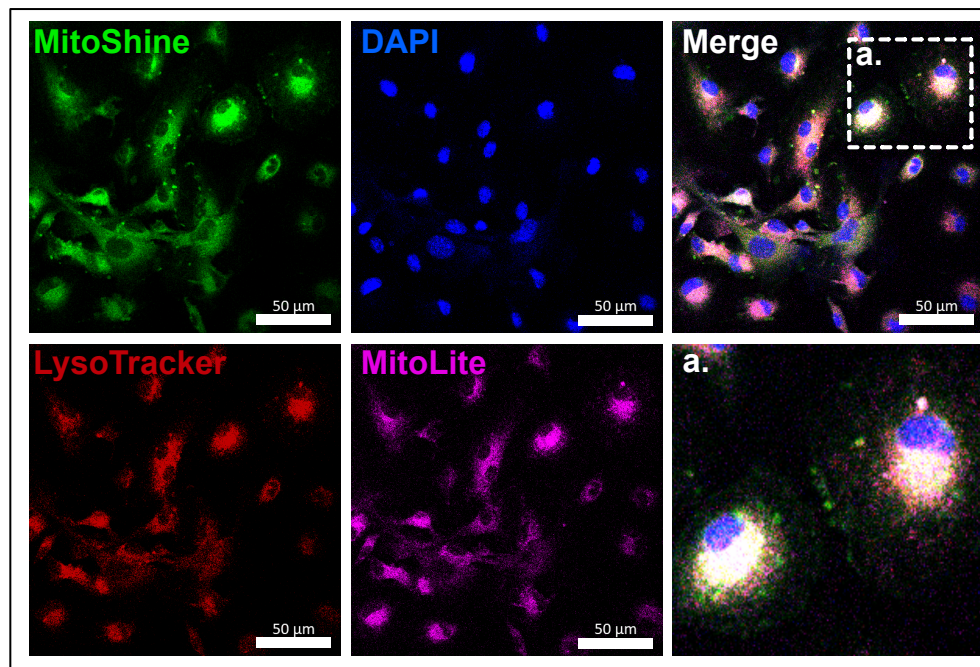
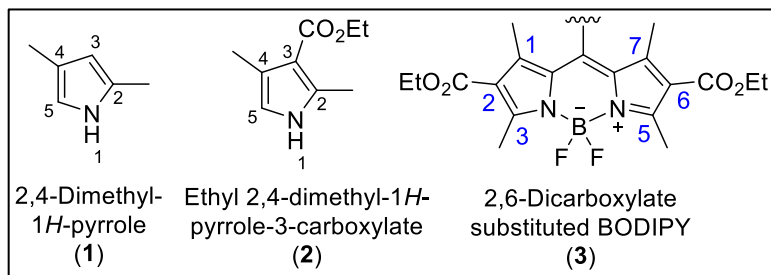


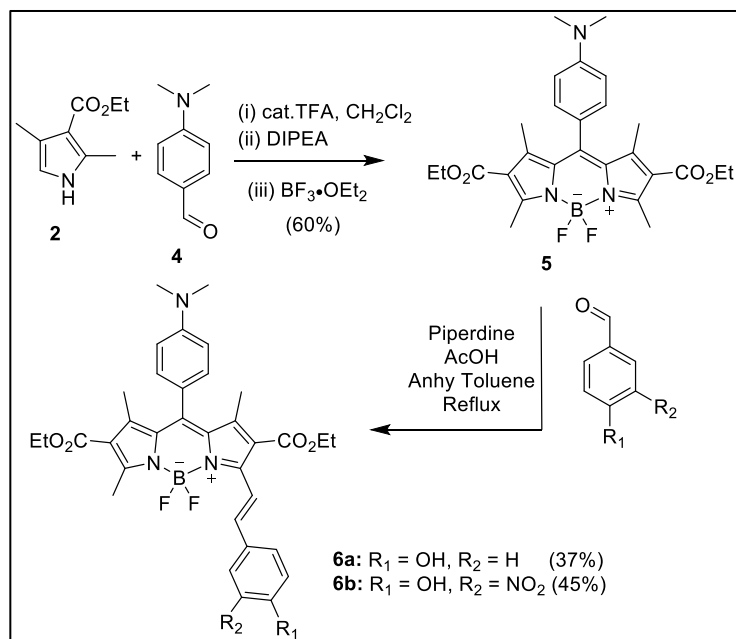
**Figure 5.5** Fluorescence imaging of primary mouse microglial cells with MitoShine. The localization of the compound was observed in mitochondria (magenta, MitoLite dye) as well as in the acidic lysosomal organelles (red, LysoTracker dye). (a) Magnified image with nuclear DNA is stained with DAPI (blue). Scale bars represent 50  $\mu\text{m}$ .

In summary, we have developed a modular synthetic strategy for pH-activable fluorescent BODIPY probes to achieve divergent targeting of cellular organelles that are tested in primary cells and available for future biological use in vivo. We showed how the transformation of a critical synthetic intermediate containing bromomethyl group into various derivatives results in a distinct targeting ability of the probe affording lysosomal, mitochondrial and nucleus targeting probes. The synthesized fluorescent probes have high fluorescence at acidic lysosomal pH compared to cytosolic neutral pH. The pH-activable property of fluorescent probes was utilized for targeting lysosomes and mitochondria in primary mouse microglial cells. Besides, the synthetic intermediate or the probes with free amine group can also be used for several bioconjugation reactions, including targeting a protein of interest such as the A $\beta$ (1-42) peptide [3c,8c] to investigate target-specific microglial uptake towards specific cellular organelles. Further derivatization of pH-activable probes and biological applications will be explored in the future.

### 5.3 Associated Content I: Chemical characterization



**Scheme S1.** Strategy to synthesize BODIPY scaffold 3 with ethylester functional group



**Scheme S2.** Synthetic route for the approach towards the synthesis of pH-activable probes with extended conjugation



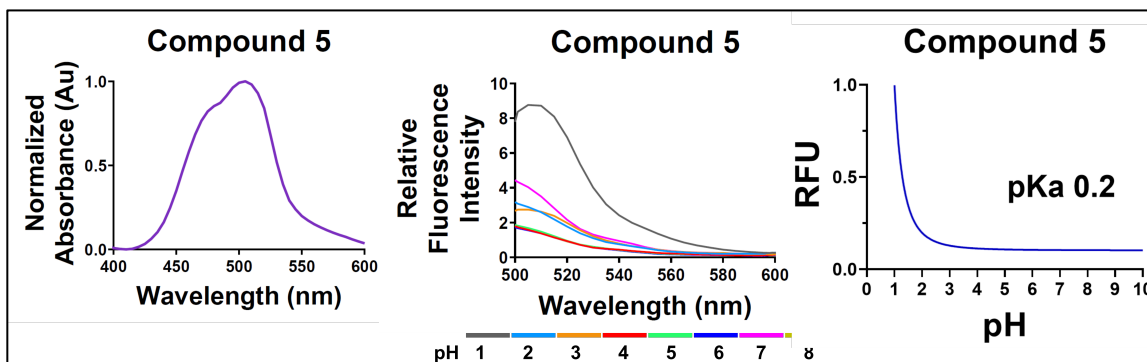


**Figure S1.** Absorption and fluorescence spectrum of compound 5 at 10  $\mu$ M concentration in PBS (1% DMSO). The absorption maximum 505 nm, excitation/emission 480/512 nm, pKa 0.2 were observed. The pH solutions were prepared in 1M PBS buffer using dilute sodium hydroxide or hydrochloric acid.

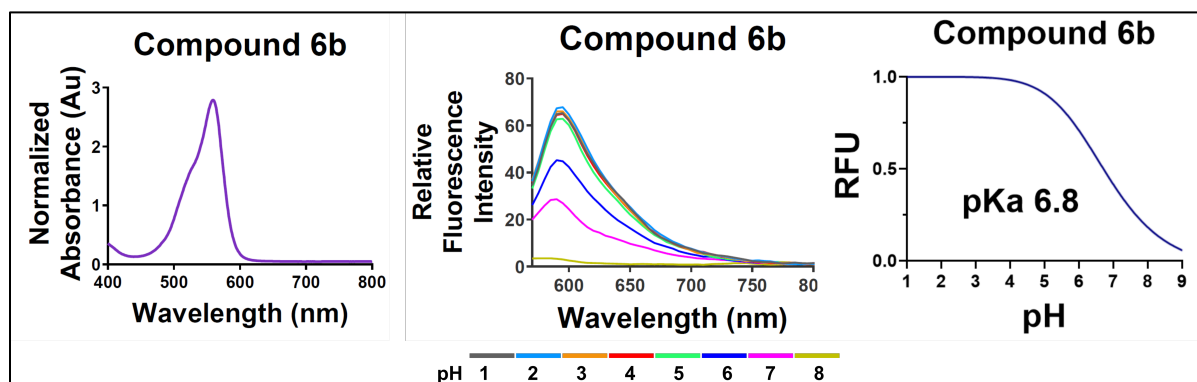


**Figure S2.** Absorption and fluorescence spectrum of compounds 6b at 10  $\mu$ M concentration in PBS [20% DMSO:MeCN (1:1 mixture)]. The absorption maximum 560 nm, excitation/emission 550/590 nm, pKa 6.8 were observed. The compound 6a-b were sparingly soluble in the aqueous medium, so the absorbance and fluorescence spectrum were recorded using a mixture of phosphate buffer containing 20% DMSO:MeCN (1:1). No florescent spectrum was recorded for compound 6a as it was not soluble and precipitated out after addition of pH solutions. pH solutions were prepared in 1M PBS buffer using dilute sodium hydroxide or hydrochloric acid.

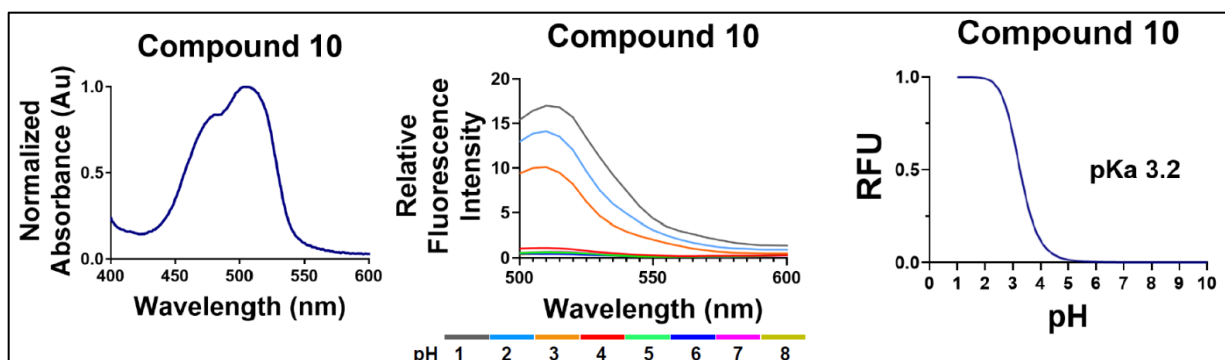


**Figure S3.** Absorption and fluorescence spectrum of compound 10 (NucShine) at 50  $\mu$ M concentration in PBS (2% DMSO). The absorption maximum 505 nm, excitation/emission 480/510 nm, and pKa 3.2 were observed. The pH solutions were prepared in 1M PBS buffer using dilute sodium hydroxide or hydrochloric acid.

## 5.4 Associated content II: Biological experimentation

### 5.4.1 Animals

All mice were handled according to the Purdue Animal Care and Use Committee (PACUC) guidelines. Adult C57BL/6 mice (5-7 months old) bred in house were used for isolating microglia.

### 5.4.2 Culture and maintenance of BV2 microglia

BV2 mouse microglia cells were generously gifted by Dr. Linda J. Van Eldik (University of Kentucky, USA). The BV-2 cell line was developed in the lab of Dr. Elisabetta Blasi at the University of Perugia, Italy. Cells were maintained at 37  $^{\circ}$ C and 5% CO<sub>2</sub> in DMEM/Hams F-12 50/50 Mix supplemented with 10% Fetal Bovine Serum (FBS), 1% L-Glutamine, and 1% Penicillin/Streptomycin. For imaging experiments, 70,000 cells/2 mL/well were seeded on glass coverslips (Corning #12-553-450) in 6-well plates (Corning #08-772-1B). For flow cytometry experiments, 20,000 cells/0.5 mL were seeded in 24-well plates (Corning #3526).

### 5.4.3 Primary mouse microglia isolation and culture

A detailed protocol for the isolation and culture of primary microglia from adult mouse brains is previously described (Prakash P, Jethava KP, et al. bioRxiv 2020). Briefly, CD11b<sup>+</sup> primary microglia were isolated from adult C57BL/6 mice aged 5-7 months of age (both male and female sexes) and cultured as follows. Mice were euthanized with CO<sub>2</sub> following the PACUC guidelines,

perfused brains were removed and cut into small pieces before homogenizing them in DPBS++ with 0.4% DNase-I on the tissue dissociator at 37 °C. After filtering the cells through a 70 µm filter, myelin was removed two times, first using gradient centrifugation with Percoll PLUS reagent followed by the use of myelin removal beads on the magnetic column separators. After myelin removal, CD11b<sup>+</sup> cells were selected from the single cell suspension using the CD11b<sup>+</sup> beads as per the manufacturer's instructions. The CD11b<sup>+</sup> cells were finally resuspended in microglia growth media, further diluted in TIC (TGF-β, IL-34, and cholesterol containing) media containing 2% FBS before seeding 0.1x10<sup>6</sup> cells/500 µL/well of a 24-well plate. The cells were maintained at 37 °C and 10% CO<sub>2</sub> with half-media change every other day until the day of compound treatment (around 12-14 div). For confocal imaging experiments, around 50,000 cells/2mL cells were sub-cultured at the center of 35mm glass-bottom imaging dishes (FluoroDish™ #FD35).

#### **5.4.4 Reconstitution of fluorescent probes in DMSO and cell treatment**

The dried fluorescent probes powders were resuspended in cell grade DMSO to prepare 5 mM stock solutions. This stock was used to make a 1, 5, or 10 mM dilution of the probe in cell culture media. The diluted probe solutions were filtered through 0.22 µm filters before adding to the cells.

#### **5.4.5 Determination of metabolic activity of BV2 microglia with MTT assay**

Murine microglial BV2 cells (10,000 cells/well) were seeded in a 96 well plate and cultured for 24 hours at 37 °C in a 5% CO<sub>2</sub> incubator. Next day, the media was aspirated, and the cells were rinsed twice with PBS (pH 7.4) followed by treatment with 1, 5, or 10 µM of the probe solution made in DMSO (final DMSO concentration = 0.05%) for 24 hours in the incubator. Next, the media was aspirated and 20 µL of 5 mg/mL 3-(4,5dimethylthiazol-2-yl)-2,5-diphenyltetrazolium bromide (MTT) solution was added to the cells and then incubated for three hours. The MTT solution was then removed and 100 µL DMSO was added to dissolve the violet formazan crystals. The plate was shaken for 5 minutes using an orbital shaker. The absorbance value at 450 nm was recorded and the percent cell metabolic activity was calculated as the ratio of sample absorbance to control absorbance.

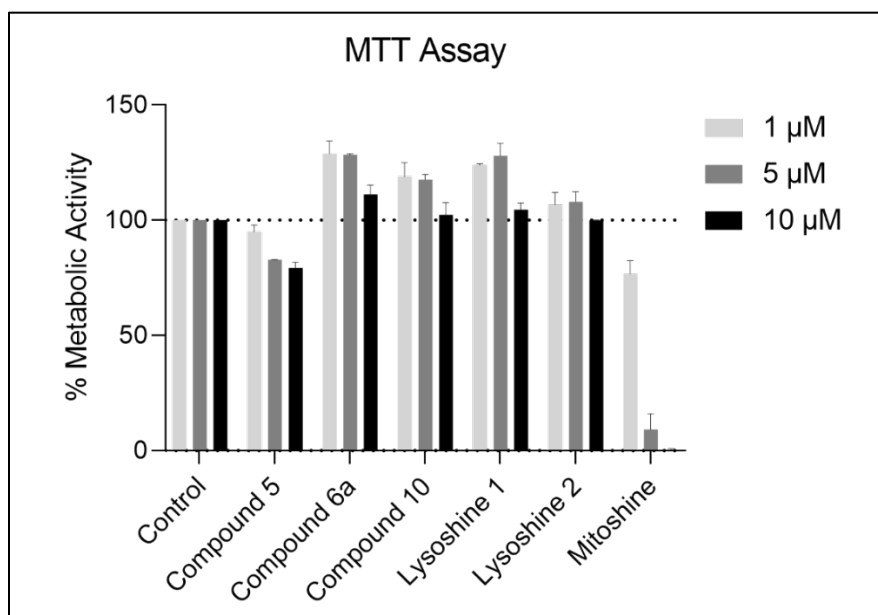


**Figure S4.** Effect of the fluorescent probes at 1, 5 or 10  $\mu\text{M}$  concentration on the metabolic activity of BV2 microglia. BV2 microglia were treated with different concentration (1, 5, 10  $\mu\text{M}$ ) of the fluorescent probes for 24 hours prior to performing the MTT assay. Bars depict  $n=3$  data with SD. Effect of the probes on the metabolic activity is calculated relative to the DMSO controls set to 100% metabolic activity.

#### 5.4.6 Determination of cytotoxicity of the probes on BV2 microglia with LDH assay

The cytotoxicity of the fluorescent probes was determined using the Invitrogen™ CyQUANT™ LDH Cytotoxicity Assay kit which measures the release of Lactate dehydrogenase (LDH) from the dead and dying cells. The assay was performed per the manufacturer's protocol. Briefly, BV2 cells (5000 cells/100  $\mu\text{L}$ /well) were seeded in a 96 well plate and cultured for 24 hours at 37 °C in a 5% CO<sub>2</sub> incubator. After 24 hours, the media was removed, and the cells were treated with 1, 5, or 10  $\mu\text{M}$  of the probes for 2 or 24 hours of incubation. Three additional wells were treated with the given lysis buffer for 45 minutes (positive control). After the corresponding incubation period, the total LDH release was measured using a fluorescent plate reader. The cells without any probe treatment correspond to spontaneous LDH release and were taken as negative control and the cells treated with the lysis buffer correspond to maximum LDH release. The percentage cytotoxicity of the probes was determined as follows:

$$\% \text{ cytotoxicity} = \frac{[\text{Probe-treated LDH activity} - \text{Spontaneous LDH activity}] \times 100}{[\text{Maximum LDH activity} - \text{Spontaneous LDH activity}]}$$

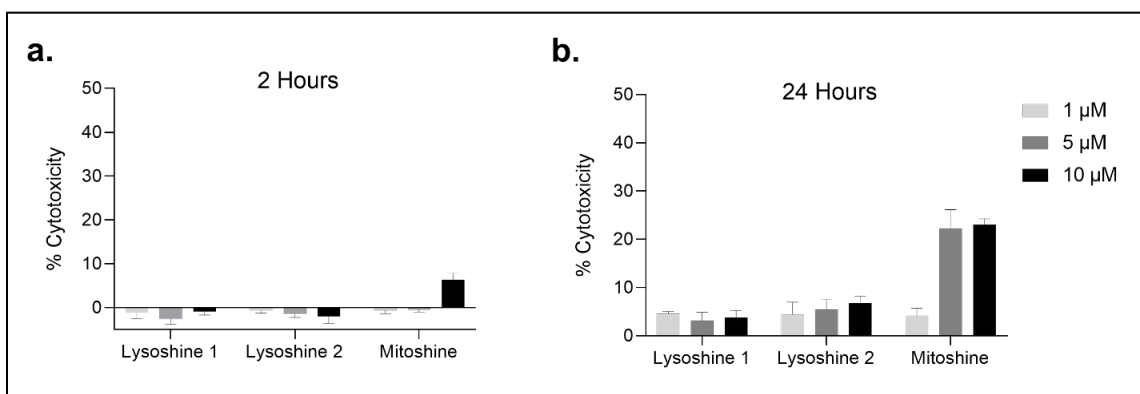


**Figure S5.** Percent cytotoxicity of the LysoShine 1, LysoShine 2, and MitoShine fluorescent probes. Percent (%) cytotoxicity after a) 2 hours treatment, b) 24 hours treatment with the probes was calculated relative to % cytotoxicity of maximum LDH positive control that was set to 100% (not shown) as described in the protocol above. Bars depict n=2 data with SD.

#### 5.4.7 Determination of cellular uptake of the fluorescent probes

Cellular uptake of the fluorescent probes was determined in-vitro as described previously (Zhang J, Yang M, et al. Journal of Materials Chemistry B. 2015). Briefly, BV2 cells (20,000 cells/well) were seeded in a 96 well plate and cultured overnight at 37 °C in a 5% CO<sub>2</sub> incubator. Next day, the media was removed, and the cells were treated with 1, 5, or 10 μM of the probes for 2 hours. After incubation, the supernatant was collected, and the absorbance was recorded at the respective absorbance maxima of the probe. This was compared with absorbance of the probe in media without cells. The percent cellular uptake was calculated as percentage of the ratio of absorbance of the supernatant to the absorbance of probe solution without cells:

$$\% \text{ Uptake Efficiency} = 1 - \frac{[A_{\text{supernatant}}] \times 100}{[A_{\text{probe}}]}$$

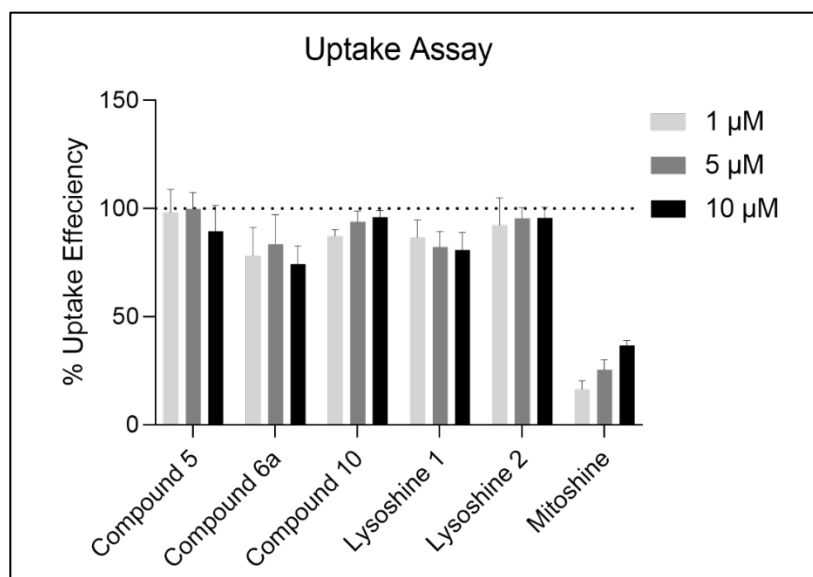


**Figure S6.** Percent uptake efficiency of the fluorescent probes in BV2 microglia. Cellular uptake of the probe at different concentrations after two hours of incubation. The % uptake efficiency was determined as the percentage of probe taken up by cells out of the total amount of probe in the initial incubation solution. Bars depict n=3 data with SD.

#### 5.4.8 Flow cytometry analysis

Primary mouse microglia were treated with 1, 5, or 10 mM fluorescent probes for 2 hours for the cells to uptake the probe. The media was then aspirated, and the cells were incubated with 100 nM LysoTracker (1 mM stock from Thermo #L7528) or with 0.5x MitoLite (1000-fold dilution from 500x stock of AAT Bioquest #22678) for 1.5 hours. The media was aspirated and 500  $\mu$ L/well of cold (4  $^{\circ}$ C) phosphate buffered saline was added to the cells. The cells were gently detached from the plates and transferred to corresponding vials. Finally, 0.1  $\mu$ g/mL of DAPI was added to the suspended cells (500  $\mu$ L volume) for 3 mins before analyzing the cells on the Attune NxT flow cytometer (Invitrogen). All the cells were first gated on the side and forward scatter plot (SSC vs. FSC) followed by gating the live cells using the DAPI nuclear stain. Around 10-20 thousand cells were gated from the live cells in order to analyze the cellular fluorescence signal corresponding to the LysoShine/LysoTracker or Mitoshine/MitoLite probes.

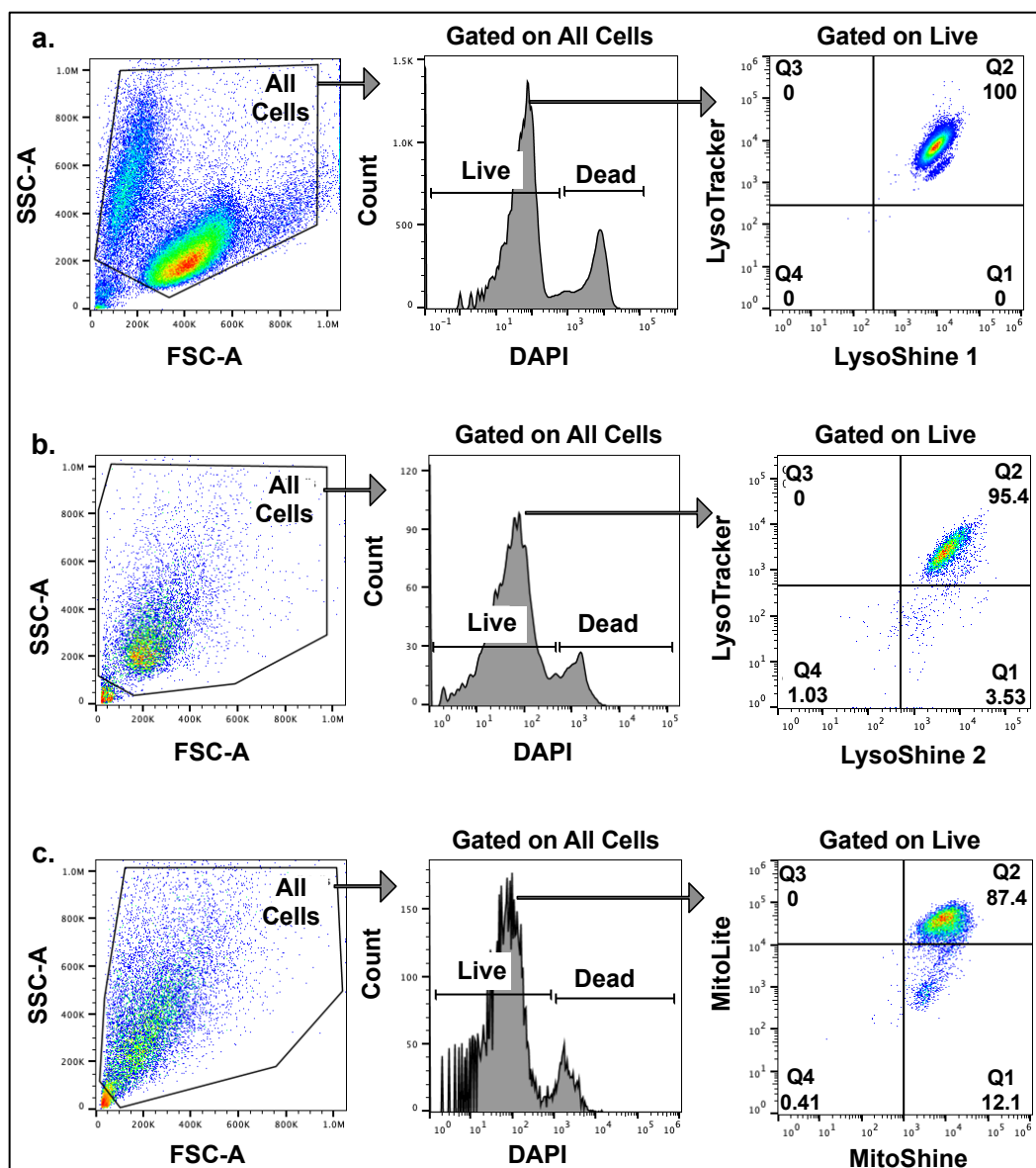


**Figure S7.** Gating strategy for flow cytometry analysis of primary mouse microglia treated with the fluorescent probes. All cells selected in the SSC-A vs FSC-A plots were used to visualize and quantify live and dead cells stained with DAPI dye. From this, live cells were selected to identify and quantify the (a, b) LysoTracker+LysoShine+ cells or (c) MitoLite+MitoShine+ cells.

#### 5.4.9 Confocal imaging

The localization of the fluorescent probes were visualized using confocal microscopy. The cells were incubated with 10 mM probe for 2 hours and then the media was aspirated. The cells were then incubated with 100 nM LysoTracker (1 mM stock from Thermo #L7528) or with 0.5x MitoLite (1000-fold dilution from 500x stock of AAT Bioquest #22678) for 1.5 hours. The media

was aspirated, and the cells were fixed with 4% paraformaldehyde for 10 mins followed by nuclear staining with 1 mM/mL DAPI for 5 mins. For BV2 microglia grown on glass coverslips, the coverslips were removed from the wells and transferred to glass slides with a drop of anti-fade reagent (Thermo Fisher Scientific #P36930). For primary mouse microglia grown in 35 mm glass-bottom dishes, the cells were treated with a few drops of the anti-fade reagent and taken for imaging. The images were captured on a Zeiss LSM 880 Upright Confocal microscope equipped with Plan-Apochromat 20x/0.8 objective.

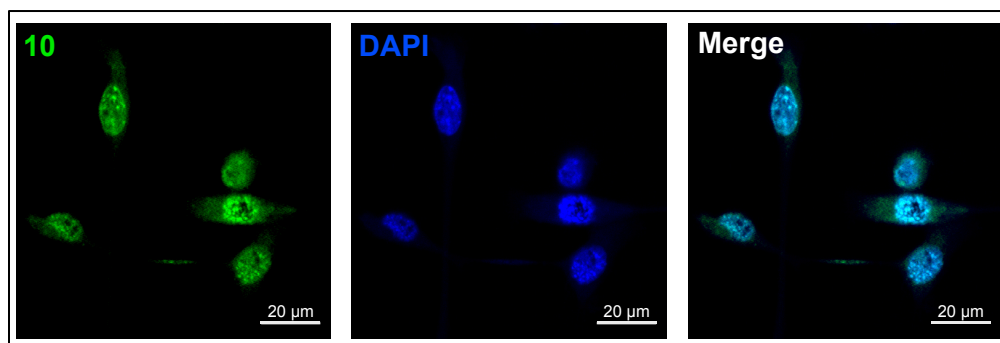


**Figure S8.** Compound 10 localizes to the nuclei. The compound 10 (green) (NucShine) localizes to the nuclei (blue) in BV2 microglia. Scale bars represent 20 µm.

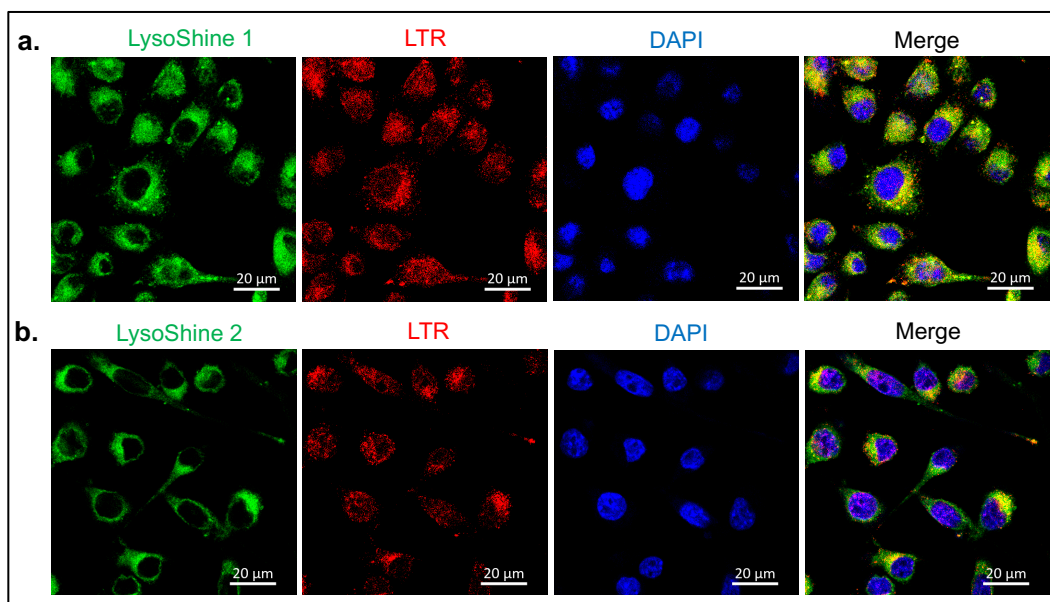


**Figure S9.** Confocal Imaging of Lysosomal probes LysoShine 1 and LysoShine 2 in BV2 microglia. Confocal images depicting the co-localization of (a) LysoShine 1 and (b) LysoShine 2 lysosomal probes (green) with LysoTracker Red DND-99 (LTR, red) in BV2 microglia. Nuclei are stained with DAPI (blue). Scale bars represent 20 µm.



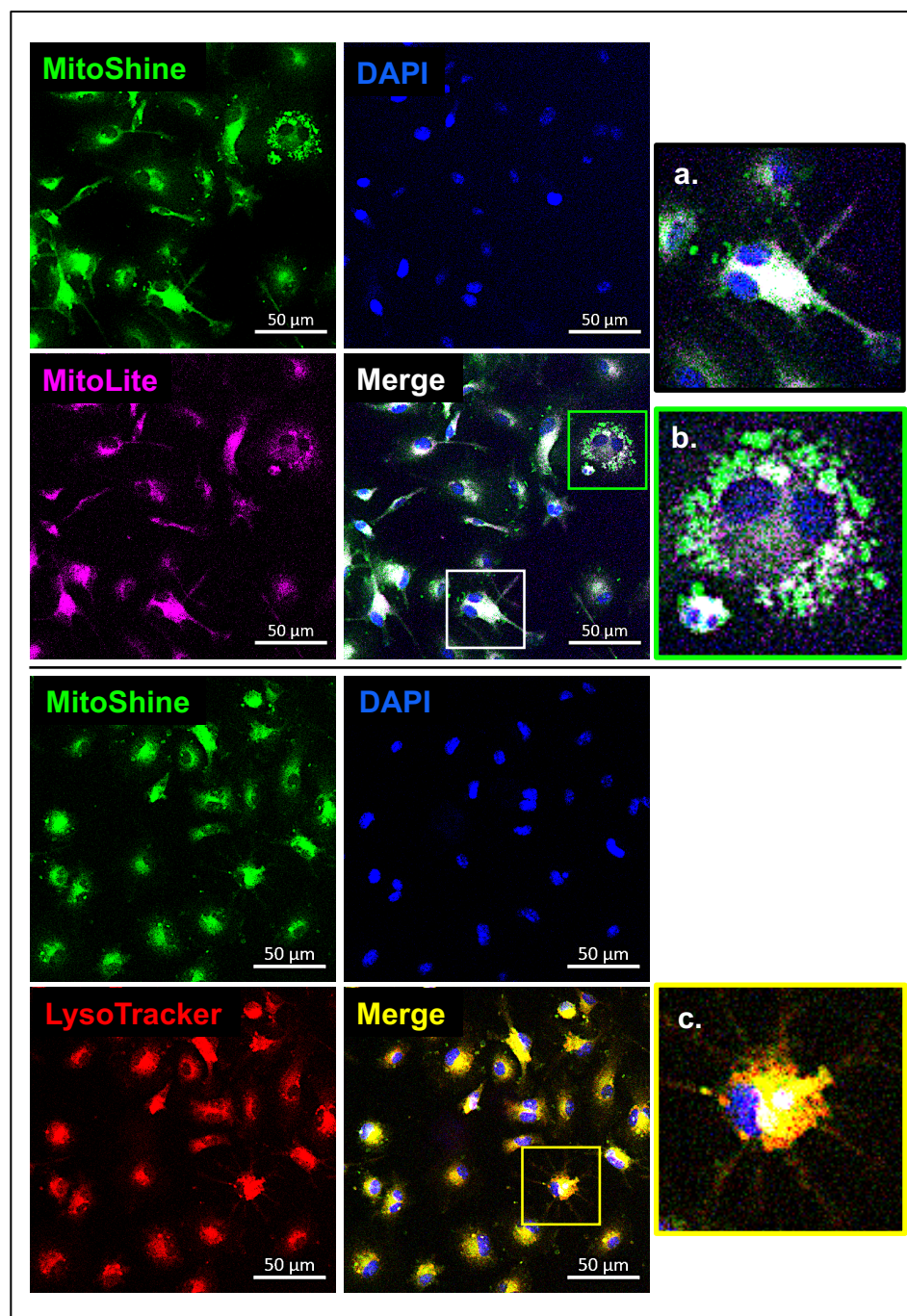


**Figure S10.** Confocal imaging of primary mouse microglial cells with MitoShine. The localization of the compound was observed in mitochondria (magenta) and acidic lysosomal organelles (red). Magnified images on the far-right show MitoShine localization in (a) non-mitochondria (likely lysosomes), (b) mitochondria, and (c) lysosomes. Nuclear DNA is stained with DAPI (blue). Scale bars represent 50  $\mu\text{m}$ .

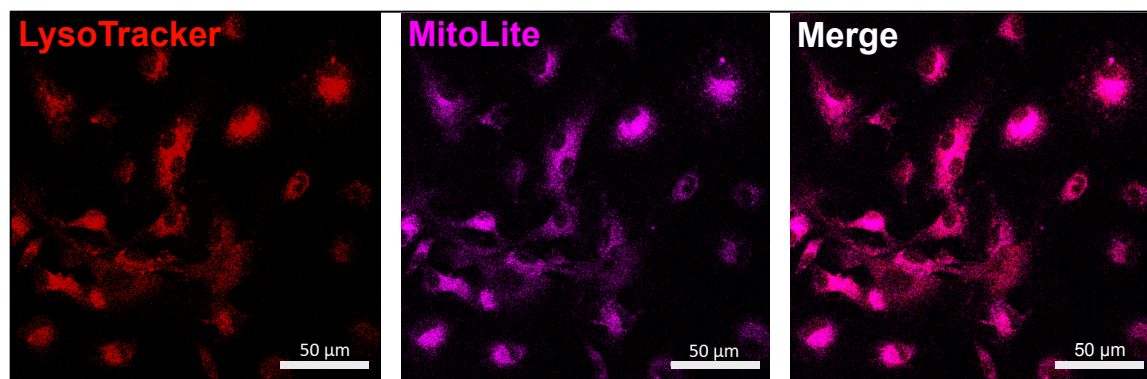
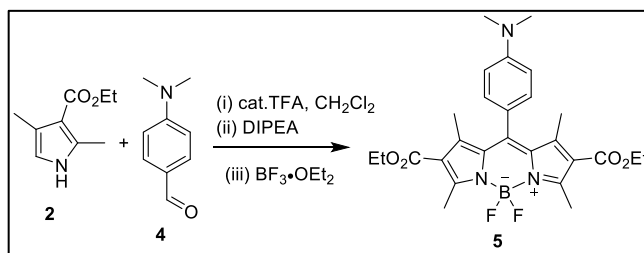


**Figure S11.** Overlap of lysosomes and mitochondria in primary microglia. The overlap of mitochondria (magenta) and acidic lysosomal organelles (red) observed via confocal microscope during co-treatment with MitoShine florescent probe. Scale bars represent 50  $\mu\text{m}$ .

## 5.5 Associated content III: Chemical experimentation

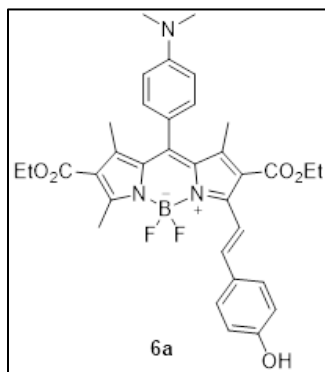
Unless noted otherwise, all reagents and solvents were purchased from commercial sources and used as received. All reactions were performed in either round bottom flask with septum or microwave vial with seal septum. The proton ( $^1\text{H}$ ) and carbon ( $^{13}\text{C}$ ) NMR spectra were obtained using a 500 MHz using  $\text{Me}_4\text{Si}$  as an internal standard and are reported in  $\delta$  units. Coupling constants (J values) are reported in Hz. Silica gel column chromatography was performed on Teledyne ISCO (EZprep model) instrument. High-resolution mass spectra (HRMS) were obtained using the electron spray ionization (ESI) technique and as TOF mass analyzer. Organic solvents and starting materials were used as received. The absorption and fluorescence spectra were process by GraphPad Prism software (version 9).

**Procedure for the synthesis of Diethyl 10-(4-(dimethylamino)phenyl)-5,5-difluoro-1,3,7,9-tetramethyl-5H-4λ4,5λ4-dipyrrolo[1,2-c:2',1'-f][1,3,2]diazaborinine-2,8-dicarboxylate (5, kpgc02s254)**



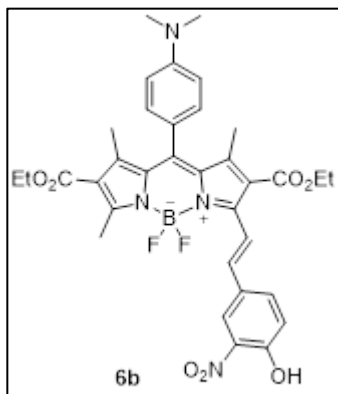
A clean oven dried 500 mL round bottom flask with a magnetic stir bar, charged with 2,4-Dimethyl-1H-pyrrole-3-carboxylic acid ethyl ester (2 equiv., 3 mmol, 502 mg) and 4-(Dimethylamino) benzaldehyde (1 equiv., 1.5 mmol, 224 mg) in anhydrous CH<sub>2</sub>Cl<sub>2</sub> (300 mL). The solution was purged with Argon twice. Then, 1 drop of trifluoro acetic acid was added under inert reaction condition and reaction was allowed to stir at room temperature for 24 hours. The reaction was monitored by TLC. Next, septum was removed and DDQ (1 equiv., 1.5 mmol) was added quickly. Again, the reaction mixture was purged with Argon and stirred at room temperature for 15 min. The immediate color change to dark purple was observed. The solvent was partially removed and compound was isolated over short pad of alumina (neutral) using 1-10% methanol in dichloromethane as an eluent as a dark red solid powder. The product was immediately used for the next step. In a clean oven dried round bottom flask (500 mL) with a stir bar, a mixture of the resulting compound, anhydrous DCM (200 mL) and diisopropyl ethylamine (5 mL) was added under inert atmosphere. The solution was stirred for 10 minutes. BF<sub>3</sub>•OEt<sub>2</sub> (5 mL) was added slowly and stirred for additional 5 hours under inert atmosphere. The crude product was extracted with dichloromethane: water, washed with brine, dried over sodium sulfate. Further, compound was purified using flash silica column chromatography with 0-1% methanol in dichloromethane as an eluent and a brownish-purple solid product (460 mg, yield 60%) was obtained. If needed, the purification can be repeated. <sup>1</sup>H NMR (500 MHz, CDCl<sub>3</sub>): δ 7.03 (d, J = 8.8 Hz, 2H), 6.80 (d, J = 8.7 Hz, 2H), 4.28 (q, J = 7.1, 7.1, 7.1 Hz, 4H), 3.05 (s, 6H), 2.82 (d, J = 1.4 Hz, 6H), 1.78 (s, 6H), 1.33 (t, J = 7.1, 7.1 Hz, 6H); <sup>13</sup>C NMR (126 MHz, CDCl<sub>3</sub>) δ 190.36, 164.52, 158.76, 151.15, 147.76, 147.60, 132.20, 128.80, 122.13, 121.14, 112.43, 111.01, 60.13, 40.23, 40.11, 14.96, 14.32, 14.16; HRMS (ESI) m/z: [M - H]<sup>+</sup> calcd for C<sub>27</sub>H<sub>31</sub>BF<sub>2</sub>N<sub>3</sub>O<sub>4</sub> 510.2376; Found 510.2380.

**Procedure for the synthesis of diethyl (E)-10-(4-(dimethylamino)phenyl)-5,5-difluoro-3-(4-hydroxystyryl)-1,7,9-trimethyl-5H-4l4,5l4-dipyrrolo[1,2-c:2',1'-f][1,3,2]diazaborinine-2,8-dicarboxylate (**6a**, kpgc02s264)**



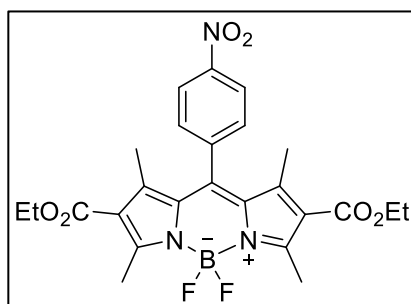
In a clean oven dried microwave vial with a stir bar, a mixture of compound **5** (30 mg, 0.058 mmol, 1 equiv), 4-hydroxybenzaldehyde (7 mg, 0.058 mmol, 1 equiv), piperidine (100  $\mu$ L), acetic acid (100  $\mu$ L), activated molecular sieve (500 mg) were added and the vial was sealed and purged with Argon. Then, anhydrous toluene (2 mL) was added, and reaction mixture was stirred at 120  $^{\circ}$ C (reflux) for 45 minutes. The reaction was monitored by TLC (Silica, 10% ethylacetate in dichloromethane). The reaction mixture was cooled to room temperature and washed three times with water. The organic phase was dried over sodium sulfate and the organic solvent was evaporated under reduced pressure. The residue was purified by silica gel flash column chromatography (CombiFlash) using 0-20% ethylacetate in dichloromethane to afford the desired compound **6a** as reddish-purple solid (13 mg, yield 37%).  $^1\text{H}$  NMR (500 MHz, Acetone)  $\delta$  8.58 (s, 1H), 7.25 – 7.19 (m, 2H), 6.90 (dd,  $J$  = 8.7, 4.9 Hz, 4H), 6.71 (d,  $J$  = 8.6 Hz, 2H), 6.55 (d,  $J$  = 16.3 Hz, 1H), 5.87 (d,  $J$  = 16.2 Hz, 1H), 4.25 (dq,  $J$  = 19.4, 7.1, 7.1, 7.1 Hz, 4H), 3.05 (s, 6H), 2.69 (s, 3H), 1.86 (s, 3H), 1.32 (t,  $J$  = 7.1, 7.1 Hz, 3H), 1.19 (t,  $J$  = 7.1, 7.1 Hz, 3H);  $^{13}\text{C}$  NMR (126 MHz,  $\text{CDCl}_3$ )  $\delta$  212.05, 169.69, 168.64, 163.48, 162.65, 161.54, 156.34, 152.20, 151.45, 148.78, 141.03, 136.87, 136.71, 134.73, 133.47, 132.67, 127.02, 125.27, 125.08, 121.64, 120.46, 117.71, 65.61, 65.25, 19.76, 19.25, 19.20, 19.13, 18.83; HRMS (ESI)  $m/z$ :  $[\text{M} + \text{H}]^+$  calcd for  $\text{C}_{34}\text{H}_{37}\text{BF}_2\text{N}_3\text{O}_5$  616.2794; Found 616.2799.

**Procedure for the synthesis of diethyl (E)-10-(4-(Dimethylamino)phenyl)-5,5-difluoro-3-(4-hydroxy-3-nitrostyryl)-1,7,9-trimethyl-5H-414,514-dipyrrolo[1,2-c:2',1'-f][1,3,2]diazaborinine-2,8-dicarboxylate (6b, kpgc02s270)**



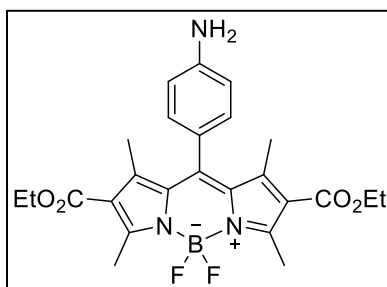
In a clean oven dried microwave vial with a stir bar, a mixture of compound 5 (51.1 mg, 0.1 mmol, 1 equiv), 4-hydroxy-3-nitro benzaldehyde (16.7 mg, 0.1 mmol, 1 equiv), piperidine (100 uL), acetic acid (100 uL), activated molecular sieve (500 mg) were added and purged with Argon. Then, anhydrous toluene (2 mL) was added, and reaction mixture was stirred at 120 °C (reflux) for 12 hours. The reaction was monitored by TLC (Silica, 10% ethylacetate in dichloromethane). The reaction mixture was cooled to room temperature and washed three times with water. The organic phase was dried over sodium sulfate and the organic solvent was evaporated under reduced pressure. The residue was purified by silica gel flash column chromatography (CombiFlash) using 0-30% ethylacetate in dichloromethane to afford the desired compound 6a as dark purple solid (29 mg, yield 45%); <sup>1</sup>H NMR (500 MHz, CDCl<sub>3</sub>) δ 10.73 (s, 1H), 8.48 – 8.42 (m, 2H), 8.22 (d, J = 2.2 Hz, 1H), 7.92 (dd, J = 8.8, 2.2 Hz, 1H), 7.66 – 7.54 (m, 3H), 7.40 (d, J = 16.5 Hz, 1H), 7.22 (d, J = 8.8 Hz, 1H), 4.32 (dq, J = 18.1, 7.1, 7.1, 7.1 Hz, 4H), 2.88 (s, 3H), 1.67 (s, 3H), 1.54 (s, 6H), 1.32 (dt, J = 14.6, 7.1, 7.1 Hz, 6H); <sup>13</sup>C NMR (126 MHz, CDCl<sub>3</sub>) δ 164.95, 163.85, 161.44, 155.68, 152.31, 148.79, 147.28, 144.16, 141.15, 137.16, 135.39, 133.66, 131.64, 129.65, 124.84, 124.47, 120.76, 118.20, 61.29, 60.58, 29.72, 15.31, 14.23, 14.11, 13.77; HRMS (ESI) m/z: [M + H]<sup>+</sup> calcd for C<sub>34</sub>H<sub>36</sub>BF<sub>2</sub>N<sub>4</sub>O<sub>7</sub> 661.2645; Found 661.2652.

**Procedure for the synthesis of Diethyl 5,5-difluoro-1,3,7,9-tetramethyl-10-(4-nitrophenyl)-5H-4λ4,5λ4-dipyrrolo[1,2-c:2',1'-f][1,3,2]diazaborinine-2,8-dicarboxylate (8, kpgc02s273)**



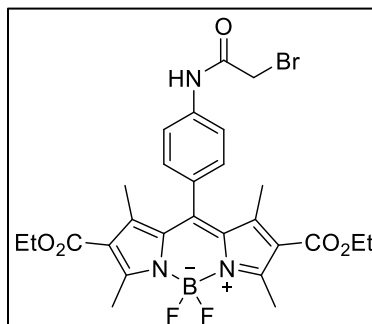
4-Nitrobenzaldehyde (2.0 mmol, 302 mg, 1 equiv) and 2,4-Dimethyl-1H-pyrrole-3-carboxylic acid ethyl ester (4.0 mmol, 669 mg, 2 equiv) were dissolved in 350 mL of anhydrous CH<sub>2</sub>Cl<sub>2</sub> under Argon atmosphere. One drop of TFA was added, and the solution was stirred at room temperature overnight. When TLC monitoring (silica; CH<sub>2</sub>Cl<sub>2</sub>) showed complete consumption of the aldehyde, a solution of 2,3-Dichloro-5,6-dicyano-1,4-benzoquinone (DDQ, 908 mg, 4.0 mmol) in CH<sub>2</sub>Cl<sub>2</sub> was added, and stirring was continued for 20 minutes under Argon atmosphere. The reaction mixture was washed with water, dried over sodium sulfate, filtered, and evaporated. The compound was purified by short (manual) column chromatography over neutral alumina (CH<sub>2</sub>Cl<sub>2</sub>). The brown powder thus obtained and 5 mL of N,N-Diisopropylethylamine (DIPEA) were dissolved in 200 mL of toluene under an Argon atmosphere. Then 5 mL of BF<sub>3</sub>•Et<sub>2</sub>O was added dropwise, and the solution was stirred at room temperature for 30 min. The reaction mixture was washed with water, dried over sodium sulfate, filtered, and evaporated. The compound was purified by silica gel column chromatography (CH<sub>2</sub>Cl<sub>2</sub>/n-hexane = 1/1) to give an orange-red solid (620 mg, yield 60%). <sup>1</sup>H NMR (500 MHz, CDCl<sub>3</sub>) δ 8.44 (d, J = 8.7 Hz, 2H), 7.57 – 7.52 (m, 2H), 4.29 (q, J = 7.2, 7.1, 7.1 Hz, 4H), 2.84 (s, 6H), 1.64 (s, 6H), 1.33 (t, J = 7.1, 7.1 Hz, 6H); <sup>13</sup>C NMR (126 MHz, CDCl<sub>3</sub>) δ 163.96, 160.60, 148.74, 146.97, 142.28, 141.22, 130.72, 129.52, 124.82, 123.14, 60.48, 15.13, 14.27, 14.02; HRMS (ESI) m/z: [M - H]<sup>+</sup> calcd for C<sub>25</sub>H<sub>25</sub>BF<sub>2</sub>N<sub>3</sub>O<sub>6</sub> 512.1805; Found 512.1801.

**Procedure for the synthesis of diethyl 10-(4-aminophenyl)-5,5-difluoro-1,3,7,9-tetramethyl-5H-4l4,5l4-dipyrrolo[1,2-c:2',1'-f][1,3,2]diazaborinine-2,8-dicarboxylate (9, kpgc02s274)**



To a solution of nitro-compound 8 (0.5 mmol) in 120 mL of degassed EtOH:CH<sub>2</sub>Cl<sub>2</sub> (1:1), was added a suspension of Pd/C (50 mg, 10% mol) in EtOH under inert atmosphere. The resulting mixture was stirred at room temperature under H<sub>2</sub> (1 atm, balloon) for 12 hours. When the reaction was completed, inorganic solids were removed by filtration through Celite® pad and washed with several portions of CH<sub>2</sub>Cl<sub>2</sub>. The TLC showed a small amount of impurities. The product was purified by flash chromatography using 0-20% CH<sub>2</sub>Cl<sub>2</sub>: MeOH. The silica in cartridge and column was neutralized by passing acetone (containing 0.5% triethylamine). The orange colored solid was obtained quantitatively. <sup>1</sup>H NMR (500 MHz, CDCl<sub>3</sub>) δ 6.99 (d, J = 8.4 Hz, 2H), 6.81 (d, J = 8.4 Hz, 2H), 4.28 (q, J = 7.1, 7.1, 7.1 Hz, 4H), 2.82 (s, 6H), 1.78 (s, 6H), 1.33 (t, J = 7.1, 7.1 Hz, 6H); <sup>13</sup>C NMR (126 MHz, CDCl<sub>3</sub>) δ 164.44, 159.01, 147.82, 146.95, 132.05, 128.91, 123.81, 122.29, 115.69, 60.17, 14.96, 14.31, 14.05; HRMS (ESI) m/z: [M + H]<sup>+</sup> calcd for C<sub>25</sub>H<sub>29</sub>BF<sub>2</sub>N<sub>3</sub>O<sub>4</sub> 484.2219; Found 484.2225.

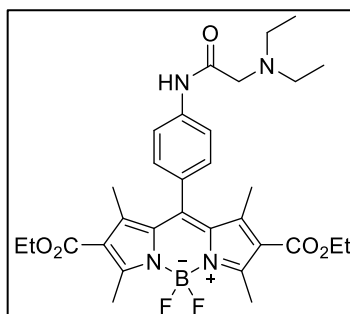
**Procedure for the synthesis of diethyl 10-(4-(2-bromoacetamido)phenyl)-5,5-difluoro-1,3,7,9-tetramethyl-5H-4l4,5l4-dipyrrolo[1,2-c:2',1'-f][1,3,2]diazaborinine-2,8-dicarboxylate (10, kpgc02s276)**



A solution of NH<sub>2</sub>-compound 9 (60 mg, 0.12 mmol) in CH<sub>2</sub>Cl<sub>2</sub> (3 mL) was kept in ice-bath. Triethylamine (0.14 mmol, 19  $\mu$ L) was added to a solution and then bromoacetyl bromide (0.14 mmol, 12  $\mu$ L) was added slowly. It was stirred at room temperature. Once precipitation was observed within 5 minutes, reaction mixture was directly quenched with 10 mL CH<sub>2</sub>Cl<sub>2</sub> and saturated sodium bicarbonate solution. The organic layer was collected and removed under reduced pressure. The product was obtained in quantitative yield as bright orange solid (72 mg, 97% yield). <sup>1</sup>H NMR (500 MHz, CDCl<sub>3</sub>):  $\delta$  8.48 (bs, 1H), 7.82 – 7.76 (m, 2H), 7.29 – 7.21 (m, 2H), 4.27 (q, J = 7.1, 7.1, 7.1 Hz, 4H), 4.06 (s, 2H), 2.82 (s, 6H), 1.70 (s, 6H), 1.32 (t, J = 7.1, 7.1 Hz, 6H); <sup>13</sup>C NMR (126 MHz, CDCl<sub>3</sub>):  $\delta$  164.28, 163.73, 159.61, 147.57, 145.06, 138.64, 131.56, 130.68, 128.73, 122.59, 120.49, 60.31, 46.23, 29.39, 15.03, 14.28, 13.95; HRMS (ESI) m/z: [M + H]<sup>+</sup> calcd for C<sub>27</sub>H<sub>30</sub>BBBrF<sub>2</sub>N<sub>3</sub>O<sub>5</sub> 604.14030; Found 604.1438.

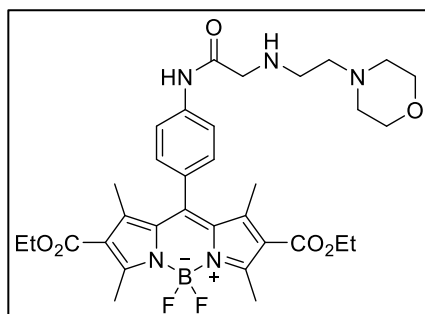


**Procedure for the synthesis of Diethyl 10-(4-(2-(diethylamino)acetamido)phenyl)-5,5-difluoro-1,3,7,9-tetramethyl-5H-4λ4,5λ4-dipyrrolo[1,2-c:2',1'-f][1,3,2]diazaborinine-2,8-dicarboxylate (LysoShine 1, kpgc02s277)**



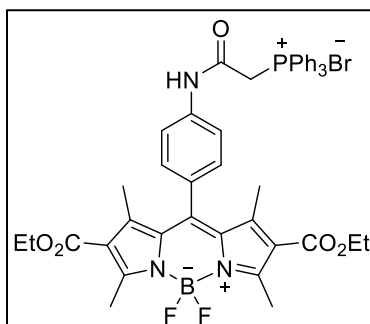
In a screw cap vial, to a solution of 10 (20 mg, 0.033 mmol) in acetone (1 mL) was added diethylamine (0.066 mmol, 2 equiv, 7  $\mu$ L) and stirred at 60  $^{\circ}$ C for 1 hour. The reaction was monitored by TLC (silica, CH<sub>2</sub>Cl<sub>2</sub>: EtOAc 9:1). Immediately, the reaction mixture was directly loaded on a cartridge and product was eluted in CH<sub>2</sub>Cl<sub>2</sub>: MeOH (95:5) using flash chromatography. The product was obtained as orange solid (11 mg, 56% yield). <sup>1</sup>H NMR (500 MHz, CDCl<sub>3</sub>):  $\delta$  9.63 (bs, 1H), 7.79 (d, J = 8.5 Hz, 2H), 7.22 (d, J = 8.5 Hz, 2H), 4.27 (q, J = 7.1, 7.1, 7.1 Hz, 4H), 3.19 (s, 2H), 2.82 (s, 6H), 2.69 (q, J = 7.1, 7.1, 7.1 Hz, 4H), 2.16 (s, 1H), 1.72 (s, 6H), 1.32 (t, J = 7.2, 7.2 Hz, 6H), 1.13 (t, J = 7.1, 7.1 Hz, 6H); <sup>13</sup>C NMR (126 MHz, CDCl<sub>3</sub>)  $\delta$  170.50, 164.30, 159.46, 147.65, 145.60, 139.19, 131.67, 129.58, 128.64, 122.51, 119.89, 60.24, 58.13, 48.75, 14.99, 14.29, 14.03, 12.41; HRMS (ESI) m/z: [M + H]<sup>+</sup> calcd for C<sub>31</sub>H<sub>40</sub>BF<sub>2</sub>N<sub>4</sub>O<sub>5</sub> 597.3060; Found 597.3065.

**Procedure for the synthesis of diethyl 5,5-difluoro-1,3,7,9-tetramethyl-10-(4-(2-((2-morpholinoethyl)amino)acetamido)phenyl)-5H-4λ4,5λ4-dipyrrolo[1,2-c:2',1'-f][1,3,2]diazaborinine-2,8-dicarboxylate (LysoShine 2, kpgc02s280)**



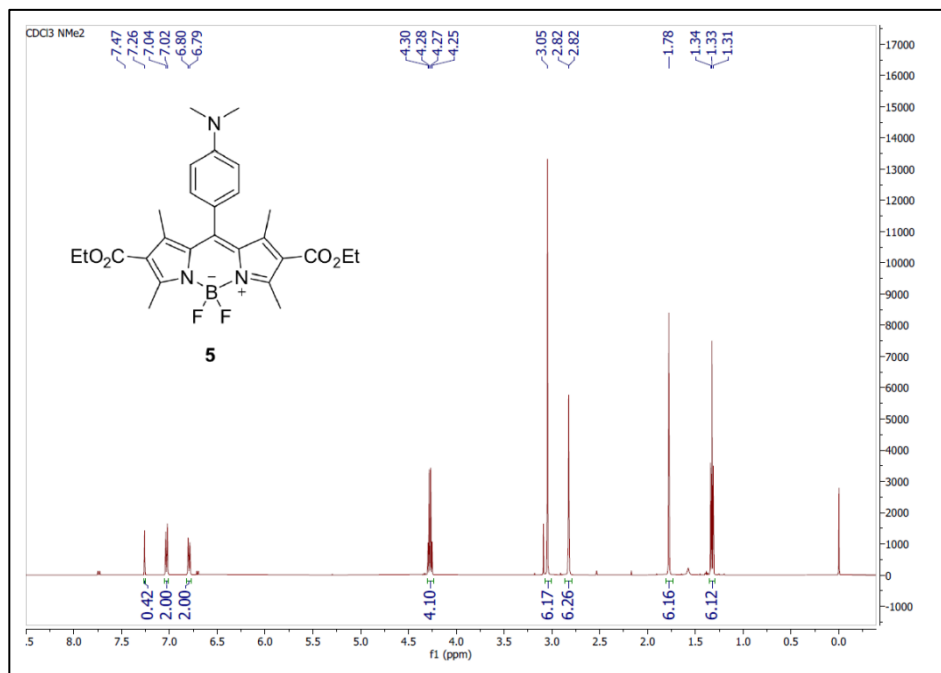
To a solution of 10 compound (20 mg, 0.033 mmol) in acetone (1 mL) was added 4-(2-aminoethyl)morpholine (0.066 mmol, 2 equiv, ~9  $\mu$ L) and stirred at 60 °C for 1 hour. The reaction was monitored by TLC (silica, CH<sub>2</sub>Cl<sub>2</sub>: EtOAc 9:1) and a new polar product was observed. Immediately, the reaction mixture was directly loaded on a cartridge and product was eluted with gradient of 0-10% methanol in dichloromethane. The product was obtained as Dark orange solid (10 mg, 46% yield). <sup>1</sup>H NMR (500 MHz, CDCl<sub>3</sub>)  $\delta$  9.68 (bs, 1H), 7.82 (d, J = 8.5 Hz, 2H), 7.22 (d, J = 8.5 Hz, 2H), 4.27 (q, J = 7.1, 7.1, 7.1 Hz, 4H), 3.71 (t, J = 4.7, 4.7 Hz, 4H), 3.43 (s, 2H), 2.82 (s, 8H), 2.56 – 2.50 (m, 2H), 2.50 – 2.44 (m, 4H), 1.71 (s, 6H), 1.32 (t, J = 7.1, 7.1 Hz, 6H); <sup>13</sup>C NMR (126 MHz, CDCl<sub>3</sub>)  $\delta$  170.44, 164.30, 159.46, 147.63, 145.55, 139.21, 131.65, 129.63, 128.60, 122.51, 120.06, 66.94, 60.26, 58.11, 53.71, 53.18, 46.39, 15.01, 14.29, 13.95; HRMS (ESI) m/z: [M + H]<sup>+</sup> calcd for C<sub>33</sub>H<sub>43</sub>BF<sub>2</sub>N<sub>5</sub>O<sub>6</sub> 654.3274; Found 654.3280.

**Procedure for the synthesis of (2-((4-(2,8-bis(ethoxycarbonyl)-5,5-difluoro-1,3,7,9-tetramethyl-5H-4l4,5l4-dipyrrolo[1,2-c:2',1'-f][1,3,2]diazaborinin-10-yl)phenyl)amino)-2-oxoethyl)triphenylphosphonium bromide (MitoShine, kpgc02s286)**

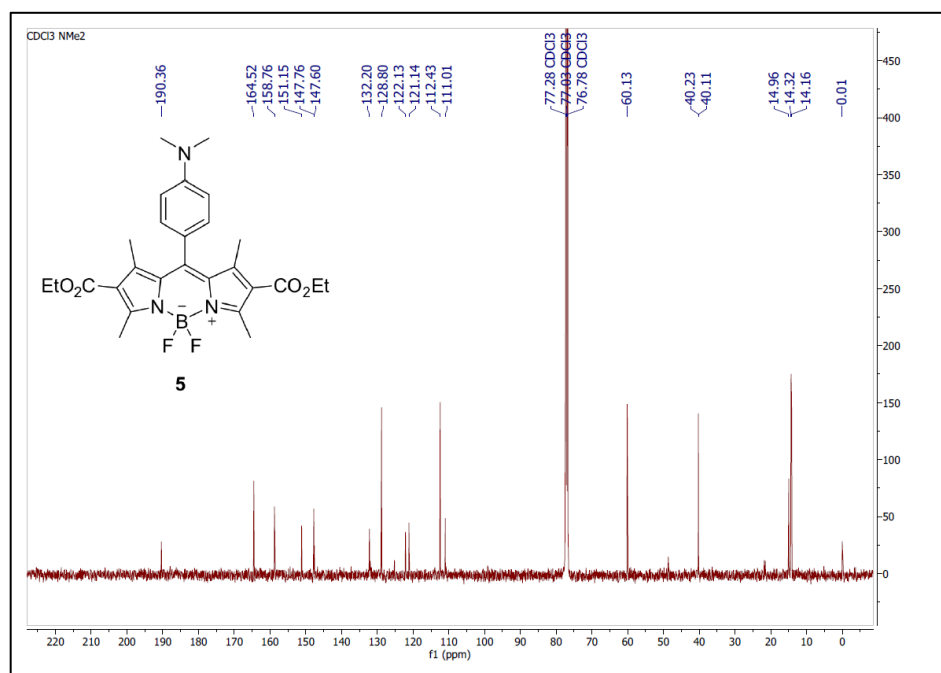


To a solution of 10 (37 mg, 0.06 mmol) in anhydrous acetonitrile (2 mL), triphenylphosphine (0.18 mmol, 3 equiv, 48 mg) was added and stirred at reflux condition overnight. The reaction was monitored by TLC (silica, CH<sub>2</sub>Cl<sub>2</sub>: EtOAc 9:1) and a new polar product was observed. Immediately, the reaction mixture was directly loaded on a cartridge and product was eluted in CH<sub>2</sub>Cl<sub>2</sub>: MeOH (90:10). The product was obtained as greenish orange solid (30 mg, 63% yield). <sup>1</sup>H NMR (500 MHz, CDCl<sub>3</sub>) δ 11.68 (bs, 1H), 7.90 – 7.76 (m, 10H), 7.70 – 7.63 (m, 6H), 7.14 – 7.09 (m, 2H), 5.16 (d, J = 14.4 Hz, 2H), 4.28 (q, J = 7.1, 7.1, 7.1 Hz, 4H), 2.81 (s, 6H), 2.63 (s, 1H), 2.17 (s, 2H), 1.65 (s, 6H), 1.36 – 1.30 (m, 6H); <sup>13</sup>C NMR (126 MHz, CDCl<sub>3</sub>) δ 164.34, 147.73, 135.27, 134.11, 134.03, 130.34, 130.23, 128.17, 120.83, 117.64, 60.23, 29.28, 14.98, 14.29, 13.85; HRMS (ESI) m/z: [M - Br]<sup>+</sup> calcd for C<sub>45</sub>H<sub>44</sub>BF<sub>2</sub>N<sub>3</sub>O<sub>5</sub>P<sup>+</sup> 786.3074; Found 786.3079.

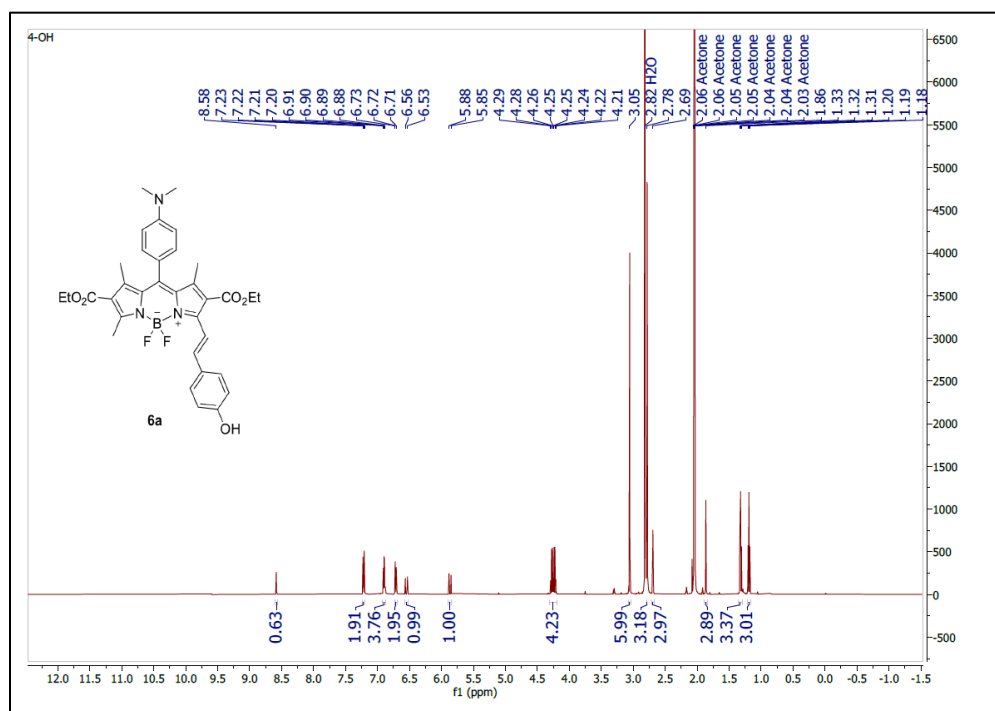
## <sup>1</sup>H and <sup>13</sup>C NMR spectra



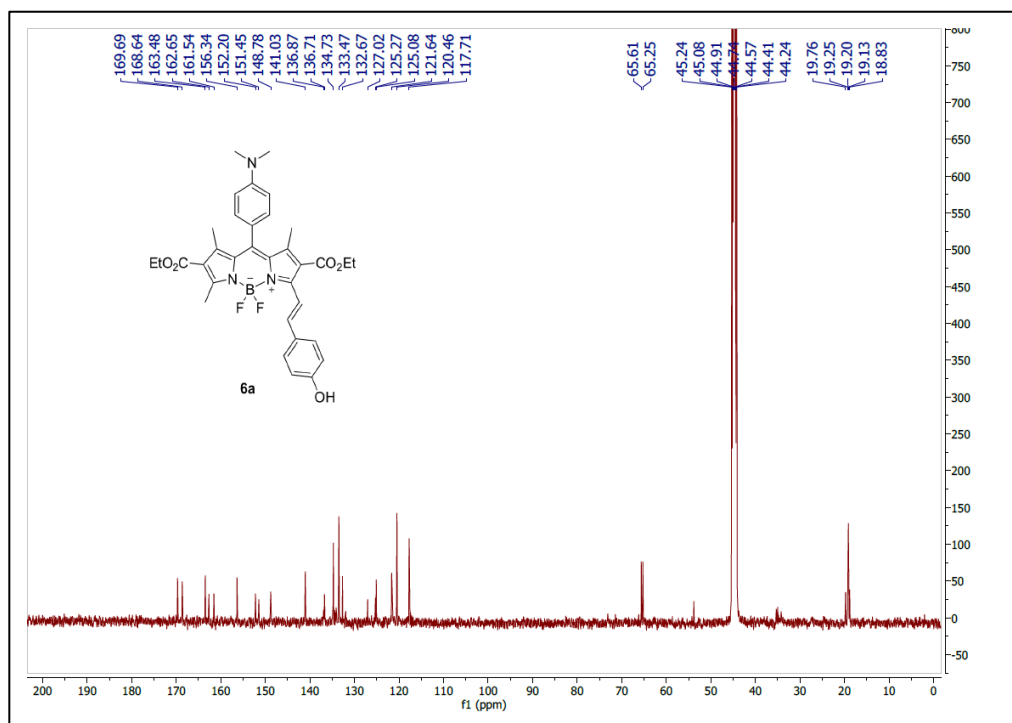
<sup>1</sup>H-spectrum of Diethyl 10-(4-(dimethylamino)phenyl)-5,5-difluoro-1,3,7,9-tetramethyl-5H-4λ4,5λ4-dipyrrolo[1,2-c:2',1'-f][1,3,2]diazaborinine-2,8-dicarboxylate (5)



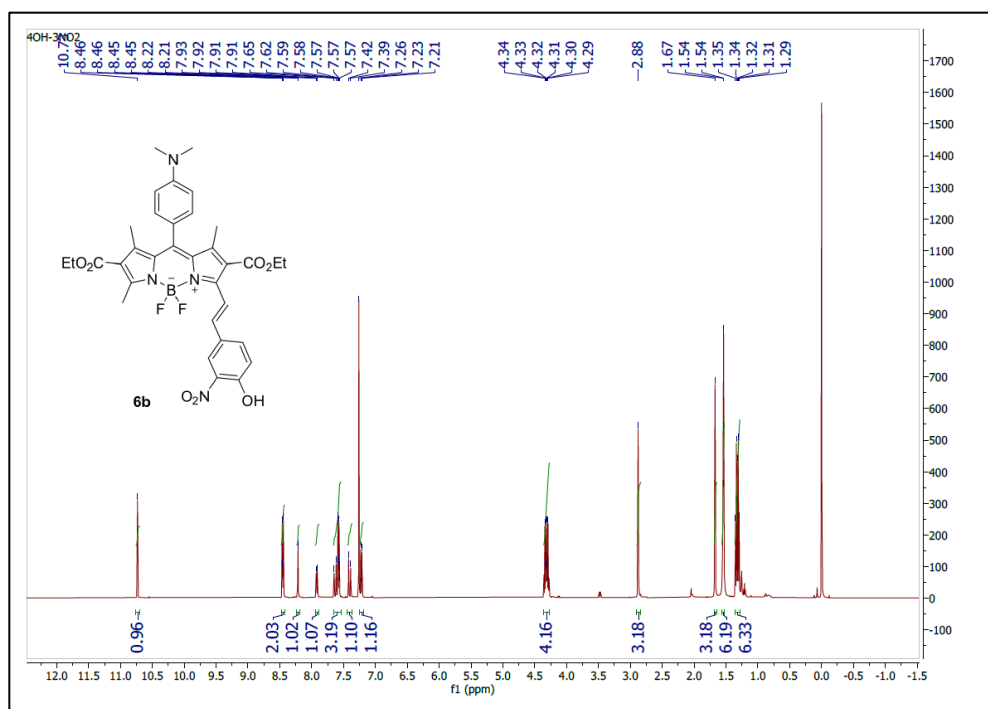
<sup>13</sup>C-spectrum of Diethyl 10-(4-(dimethylamino)phenyl)-5,5-difluoro-1,3,7,9-tetramethyl-5H-4λ4,5λ4-dipyrrolo[1,2-c:2',1'-f][1,3,2]diazaborinine-2,8-dicarboxylate (5)



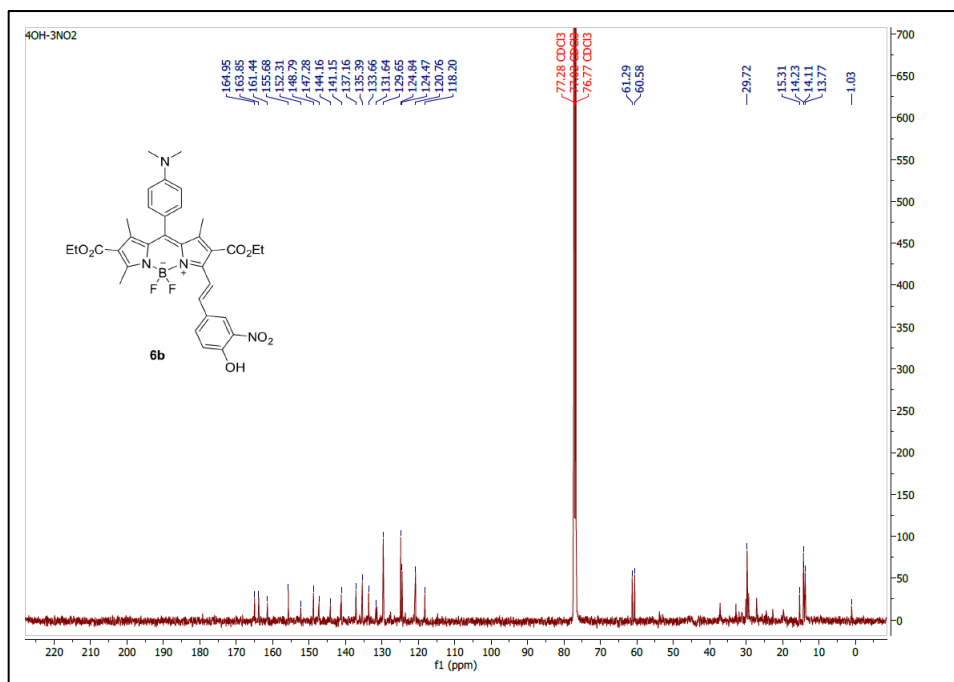
<sup>1</sup>H-spectrum of (E)-10-(4-(Dimethylamino)phenyl)-5,5-difluoro-3-(4-hydroxystyryl)-1,7,9-trimethyl-5H-414,514-dipyrrolo[1,2-c:2',1'-f][1,3,2]diazaborinine-2,8-dicarboxylate (6a)



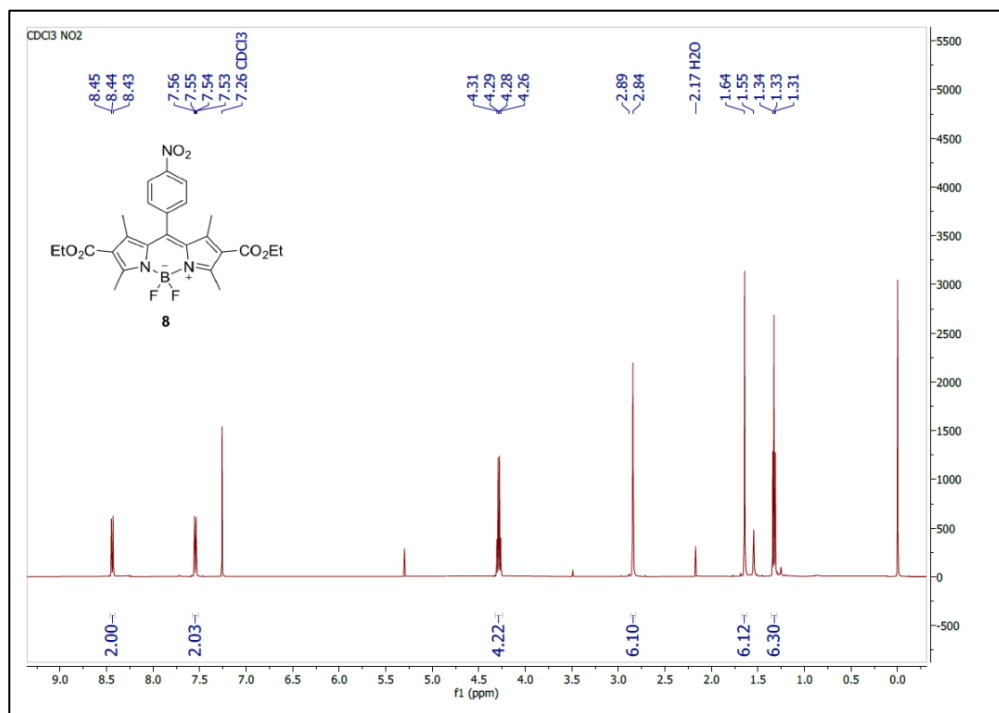
<sup>13</sup>C-spectrum of (E)-10-(4-(Dimethylamino)phenyl)-5,5-difluoro-3-(4-hydroxystyryl)-1,7,9-trimethyl-5H-414,514-dipyrrolo[1,2-c:2',1'-f][1,3,2]diazaborinine-2,8-dicarboxylate (6a)



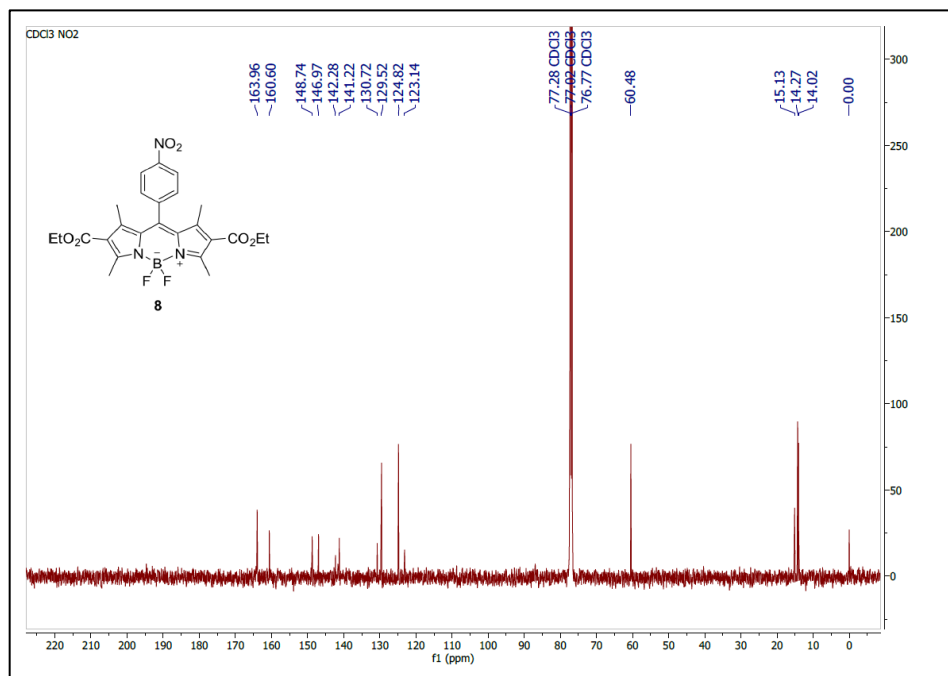
<sup>1</sup>H-spectrum Diethyl (E)-10-(4-(dimethylamino)phenyl)-5,5-difluoro-3-(4-hydroxy-3-nitrostyryl)-1,7,9-trimethyl-5H-414,514-dipyrrolo[1,2-c:2',1'-f][1,3,2]diazaborinine-2,8-dicarboxylate (6b)



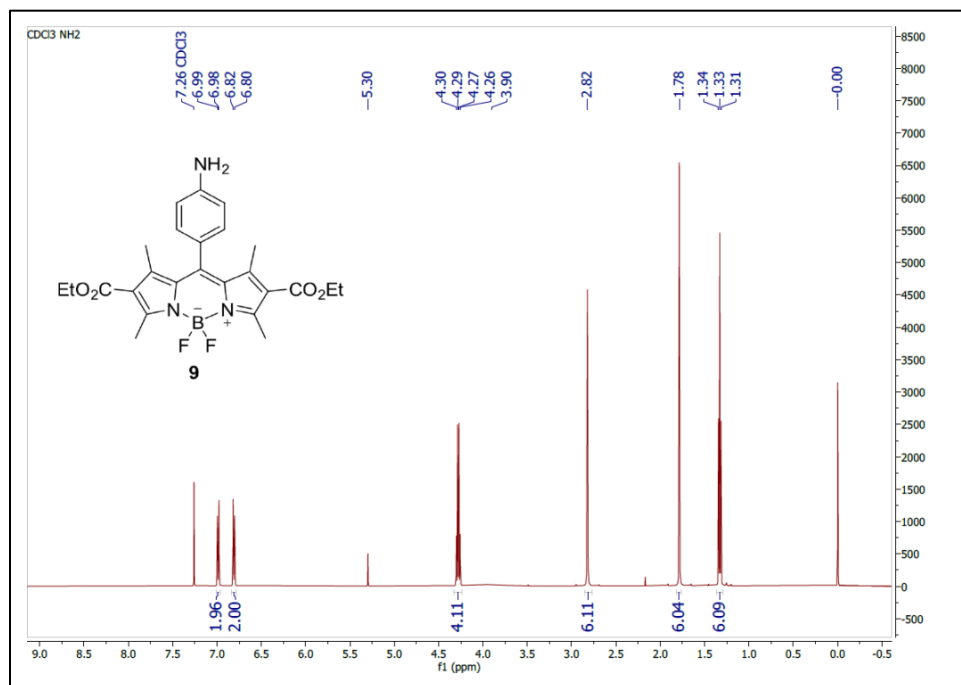
<sup>13</sup>C-spectrum of Diethyl (E)-10-(4-(dimethylamino)phenyl)-5,5-difluoro-3-(4-hydroxy-3-nitrostyryl)-1,7,9-trimethyl-5H-414,514-dipyrrolo[1,2-c:2',1'-f][1,3,2]diazaborinine-2,8-dicarboxylate (6b)



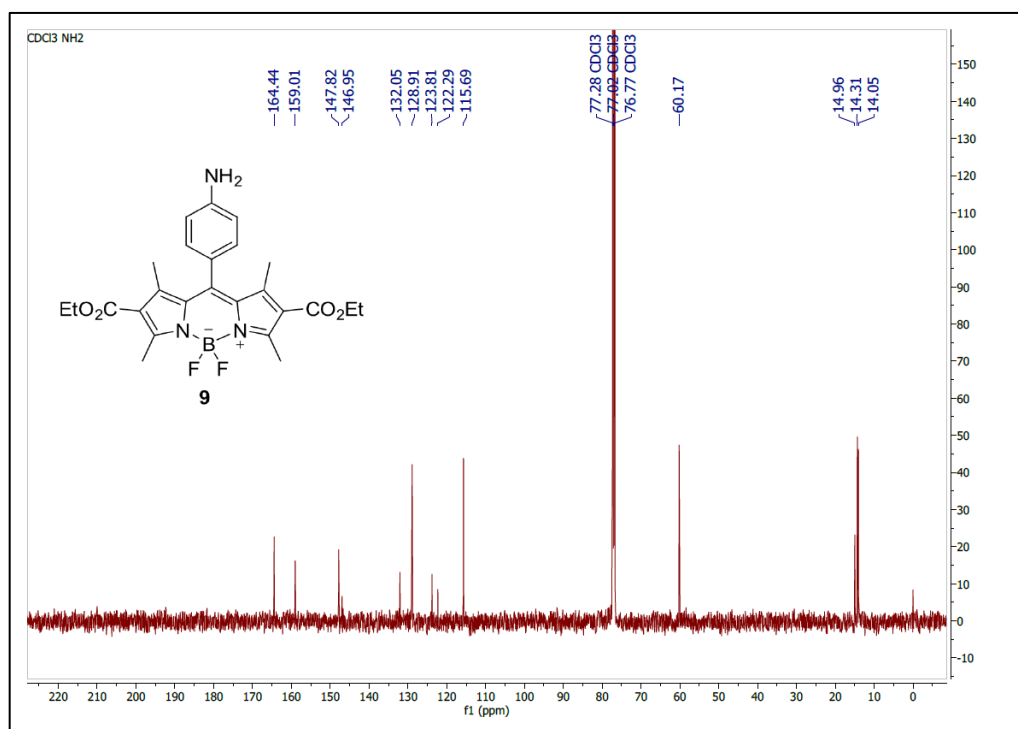
<sup>1</sup>H-spectrum of Diethyl 5,5-difluoro-1,3,7,9-tetramethyl-10-(4-nitrophenyl)-5H-4λ4,5λ4-dipyrrolo[1,2-c:2',1'-f][1,3,2]diazaborinine-2,8-dicarboxylate (8)



<sup>13</sup>C-spectrum of Diethyl 5,5-difluoro-1,3,7,9-tetramethyl-10-(4-nitrophenyl)-5H-4λ4,5λ4-dipyrrolo[1,2-c:2',1'-f][1,3,2]diazaborinine-2,8-dicarboxylate (8)

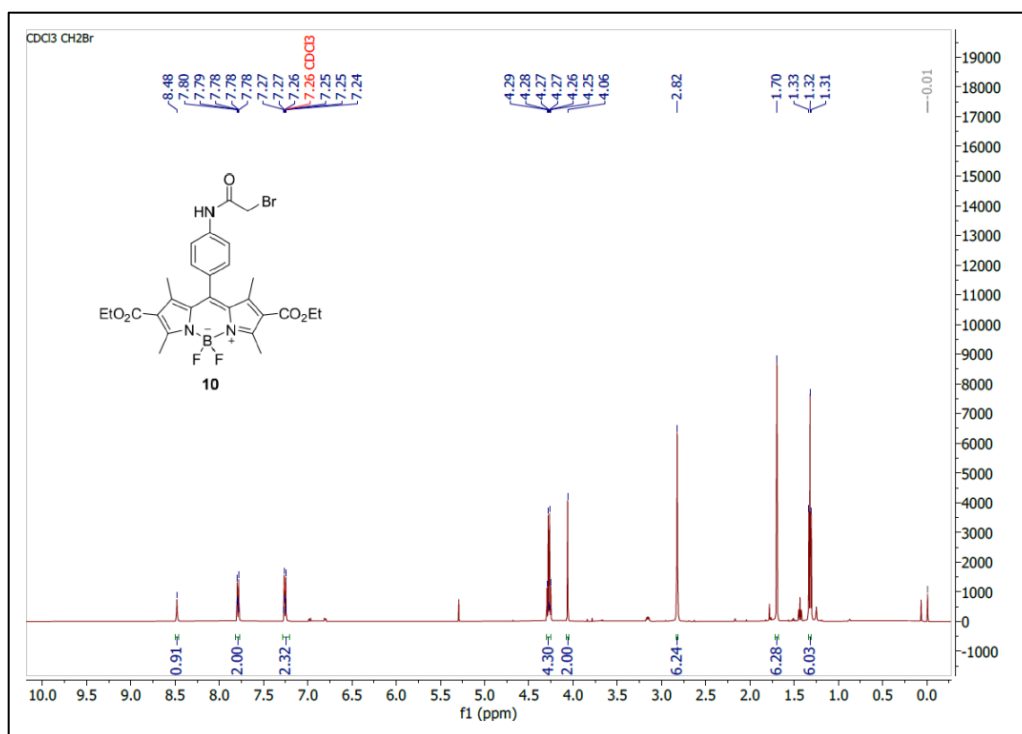


<sup>1</sup>H-spectrum of Diethyl 10-(4-aminophenyl)-5,5-difluoro-1,3,7,9-tetramethyl-5H-414,514-dipyrrolo[1,2-c:2',1'-f][1,3,2]diazaborinine-2,8-dicarboxylate (9)

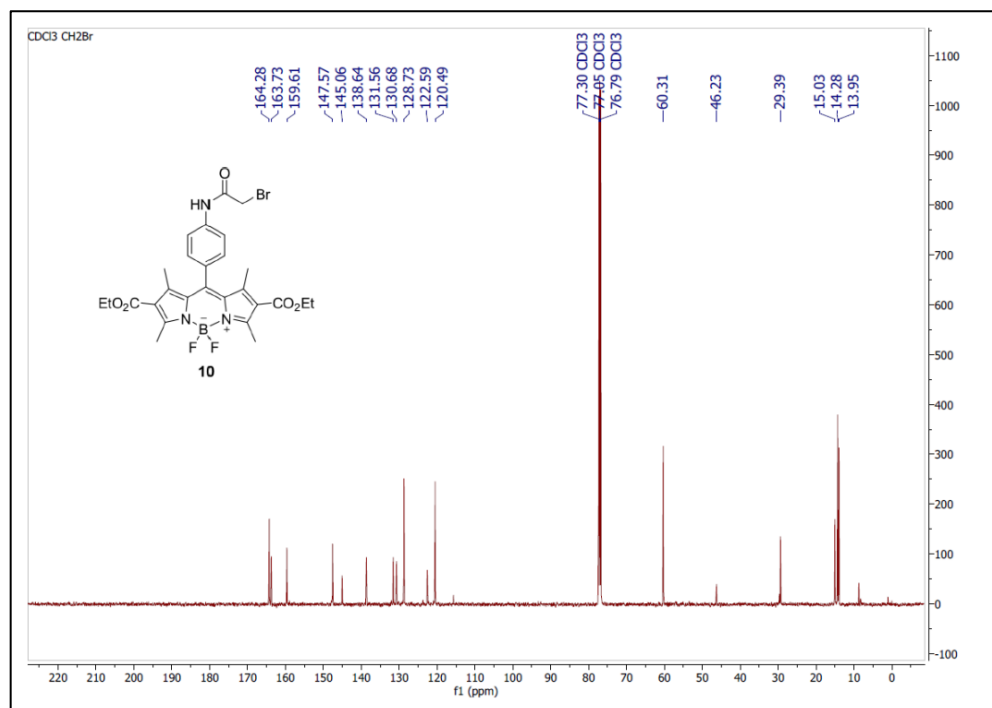


<sup>13</sup>C-spectrum of Diethyl 10-(4-aminophenyl)-5,5-difluoro-1,3,7,9-tetramethyl-5H-414,514-dipyrrolo[1,2-c:2',1'-f][1,3,2]diazaborinine-2,8-dicarboxylate (9)

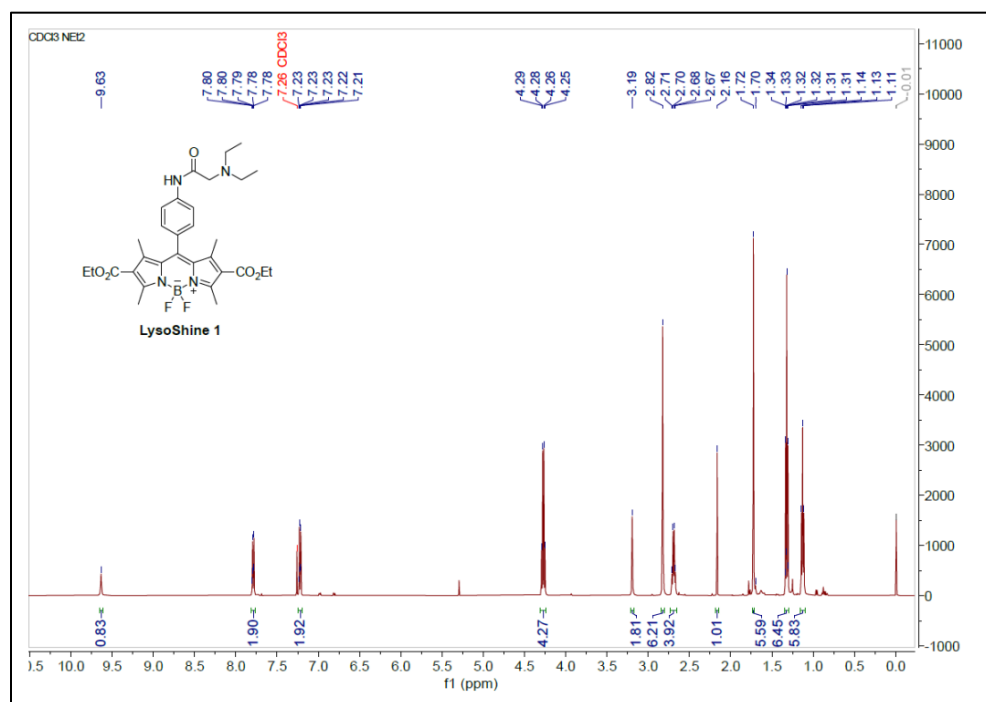




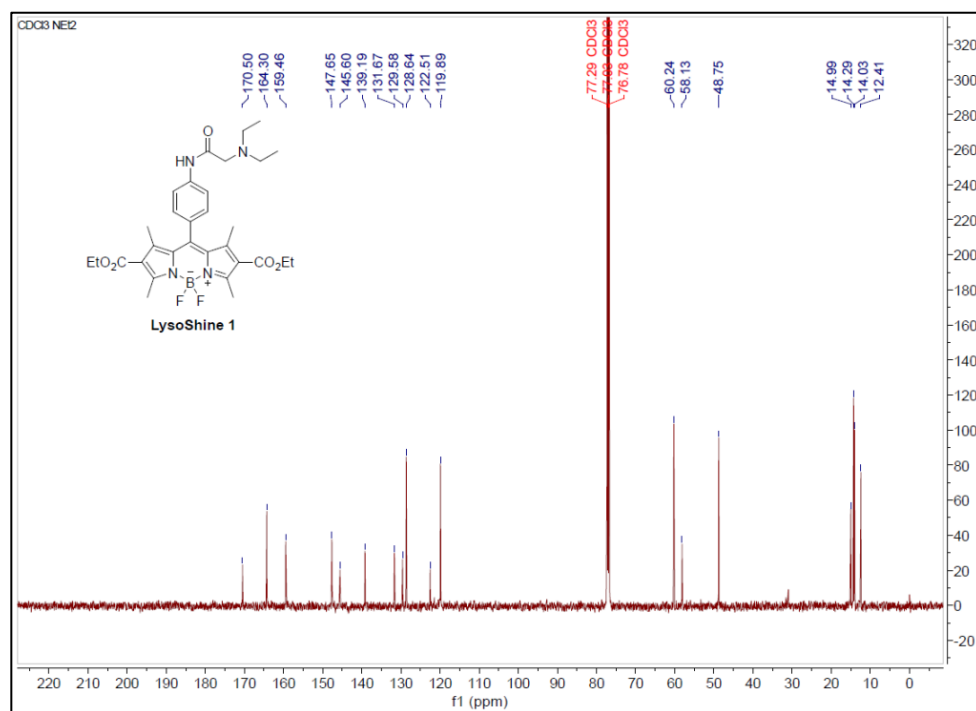
<sup>1</sup>H-spectrum of Diethyl 10-(4-(2-bromoacetamido)phenyl)-5,5-difluoro-1,3,7,9-tetramethyl-5H-4,14,5,14-dipyrrolo[1,2-c:2',1'-f][1,3,2]diazaborinine-2,8-dicarboxylate (10)



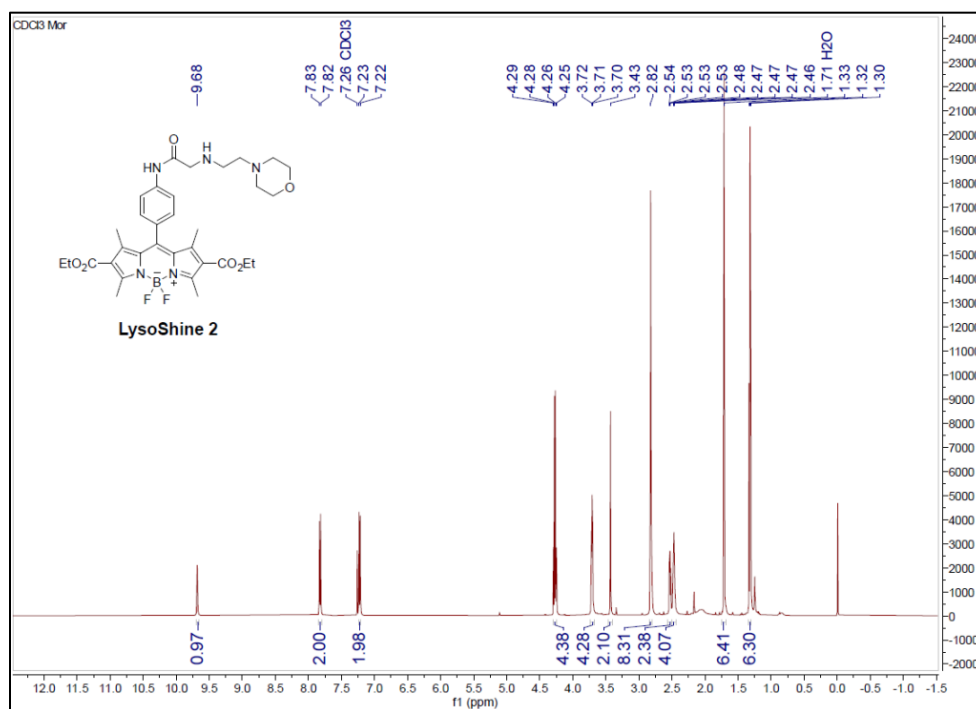
<sup>13</sup>C-spectrum of Diethyl 10-(4-(2-bromoacetamido)phenyl)-5,5-difluoro-1,3,7,9-tetramethyl-5H-4,14,5,14-dipyrrolo[1,2-c:2',1'-f][1,3,2]diazaborinine-2,8-dicarboxylate (10)



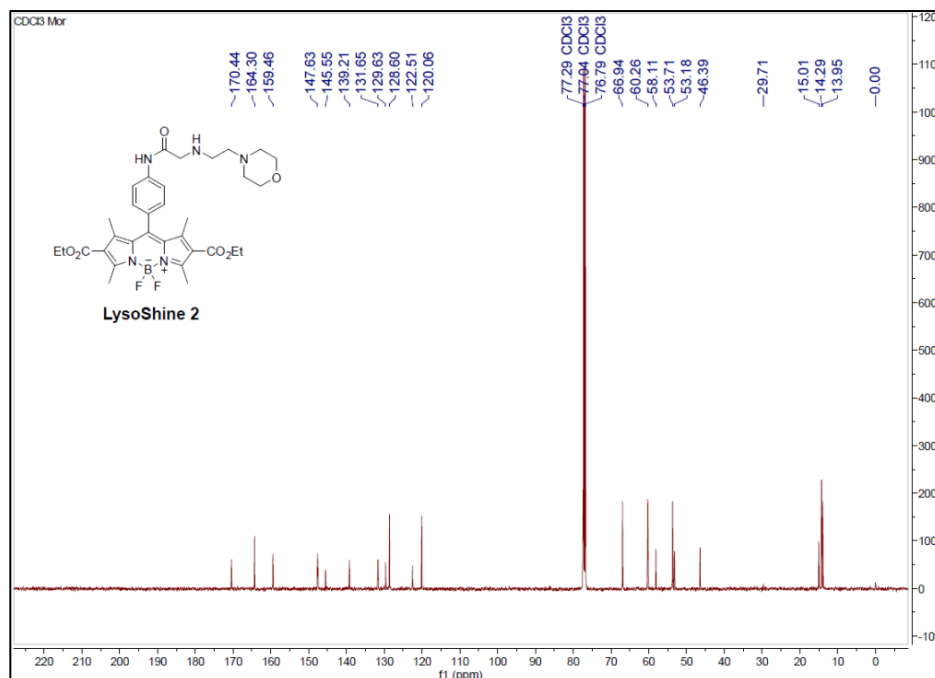
<sup>1</sup>H-spectrum of Diethyl 10-(4-(2-(diethylamino)acetamido)phenyl)-5,5-difluoro-1,3,7,9-tetramethyl-5H-4λ4,5λ4-dipyrrolo[1,2-c:2',1'-f][1,3,2]diazaborinine-2,8-dicarboxylate (LysoShine 1)



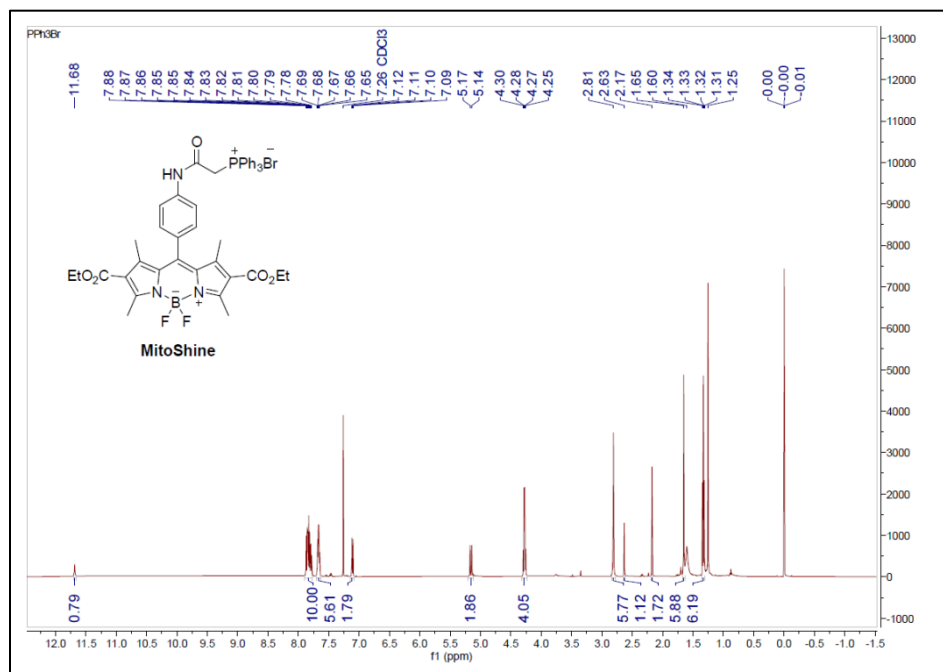
<sup>13</sup>C-spectrum of Diethyl 10-(4-(2-(diethylamino)acetamido)phenyl)-5,5-difluoro-1,3,7,9-tetramethyl-5H-4λ4,5λ4-dipyrrolo[1,2-c:2',1'-f][1,3,2]diazaborinine-2,8-dicarboxylate (LysoShine 1)



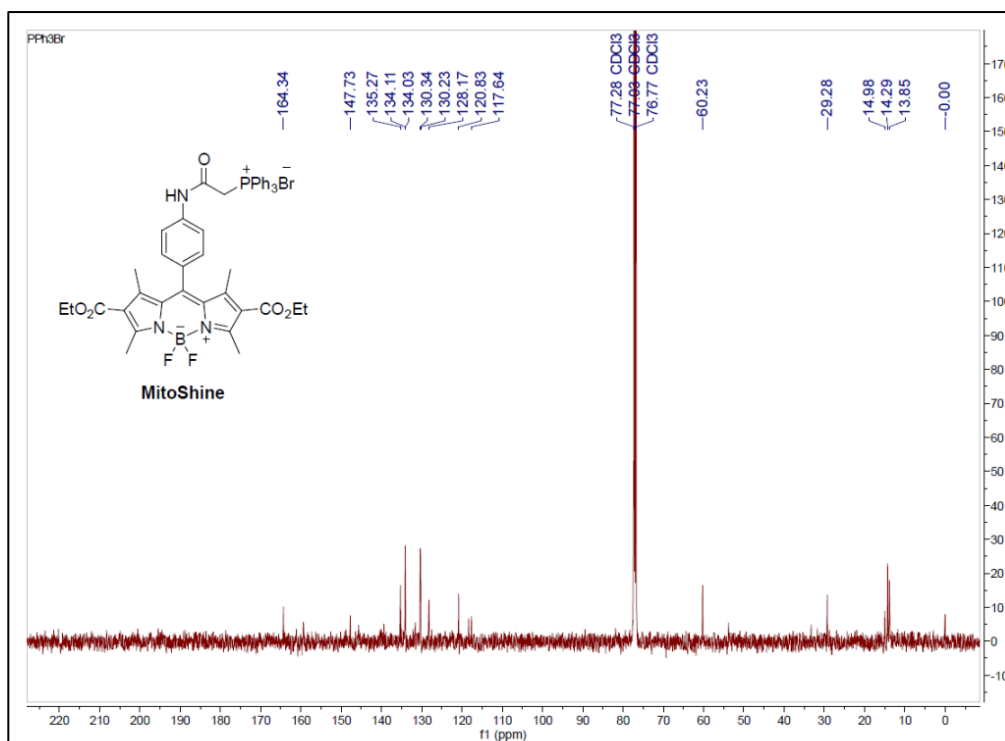
<sup>1</sup>H-spectrum of Diethyl 5,5-difluoro-1,3,7,9-tetramethyl-10-(4-(2-((2-morpholinoethyl)amino)acetamido)phenyl)-5H-4λ4,5λ4-dipyrrolo[1,2-c:2',1'-f][1,3,2]diazaborinine-2,8-dicarboxylate (LysoShine 2)



<sup>13</sup>C-spectrum of Diethyl 5,5-difluoro-1,3,7,9-tetramethyl-10-(4-(2-((2-morpholinoethyl)amino)acetamido)phenyl)-5H-4λ4,5λ4-dipyrrolo[1,2-c:2',1'-f][1,3,2]diazaborinine-2,8-dicarboxylate (LysoShine 2)



<sup>1</sup>H-spectrum of (2-((4-(2,8-Bis(ethoxycarbonyl)-5,5-difluoro-1,3,7,9-tetramethyl-5H-414,514-dipyrrolo[1,2-c:2',1'-f][1,3,2]diazaborinin-10-yl)phenyl)amino)-2-oxoethyl)triphenylphosphonium bromide (MitoShine)



<sup>13</sup>C-spectrum of (2-((4-(2,8-Bis(ethoxycarbonyl)-5,5-difluoro-1,3,7,9-tetramethyl-5H-414,514-dipyrrolo[1,2-c:2',1'-f][1,3,2]diazaborinin-10-yl)phenyl)amino)-2-oxoethyl)triphenylphosphonium bromide (MitoShine)

## 5.6 References

- [1a] J. Zhang, R. E. Campbell, A. Y. Ting and R. Y. Tsien, *Nat. Rev. Mol. Cell Biol.*, 2002, 3, 906–918.
- [1b] T. Kowada, H. Maeda and K. Kikuchi, *Chem. Soc. Rev.*, 2015, 44, 4953–4972.
- [2a] J. Han and K. Burgess, *Chem. Rev.*, 2010, 110, 2709–2728.
- [2b] J. T. Hou, W. X. Ren, K. Li, J. Seo, A. Sharma, X. Q. Yu, J. S. Kim, *Chem. Soc. Rev.*, 2017, 46, 2076–90.
- [2c] A. R. Sarkar, C. H. Heo, L. Xu, H. W. Lee, H. Y. Si, J. W. Byun, H. M. Kim, *Chem. Sci.*, 2016, 7, 766–73.
- [2d] L. Fan, X. Wang, J. Ge, F. Li, C. Zhang, B. Lin, S. Shuang and C. Dong, *Chem. Commun.*, 2019, 55, 6685–88.
- [2e] C. M. Deus, K. F. Yambire, P. J. Oliveira, N. Raimundo, *Trends Mol. Med.*, 2020, 26, 71–88.
- [2f] Gao P., Pan W., Li N. and Tang B. *Chem. Sci.*, 2019, 10, 6035-6071.
- [2g] Bucevičius, J., Lukinavičius, G. and Gerasimaitė, R., *Chemosensors* 2018, 6, 18.
- [3a] S. Gordon, *Immunity*, 2016, 44, 463–475.
- [3b] H. Xu and D. Ren, *Annu. Rev. Physiol.*, 2015, 77, 57–80.
- [3c] P. Prakash, K. P. Jethava, N. Korte, P. Izquierdo, E. Favuzzi, I. Rose, K. A. Guttenplan, S. Dutta, C. Rochet, G. Fishell, S. Liddelow, D. Attwell and G. Chopra, *bioRxiv*, DOI:10.1101/2020.03.29.002857.
- [3d] J. B. Zuchero and B. A. Barres, *Development*, 2015, 142, 3805–3809.
- [3e] D. M. Paresce, H. Chung and F. R. Maxfield, *J. Biol. Chem.*, 1997, 272, 29390–7.
- [3f] A. U. Joshi, P. S. Minhas, S. A. Liddelow, B. Haileselassie, K. I. Andreasson, G. W. Dorn and D. Mochly-Rosen, *Nat. Neurosci.*, 2019, 22, 1635-1648.
- [4a] R. E. Lawrence and R. Zoncu, *Nat. Cell Biol.*, 2019, 21, 133–142.
- [4b] X. Liu, L. Wang, T. Bing, N. Zhang and D. Shangguan, *ACS Appl. Bio Mater.*, 2019, 2, 1368–1375.
- [4c] M. H. Lee, N. Park, C. Yi, J. H. Han, J. H. Hong, K. P. Kim, D. H. Kang, J. L. Sessler, C. Kang and J. S. Kim, *J. Am. Chem. Soc.*, 2014, 136, 14136–14142.

- [4d] M. I. Sánchez, Y. Vida, E. Pérez-Inestrosa, J. L. Mascareñas, M. E. Vázquez, A. Sugiura and J. Martínez-Costas, *Sci. Rep.*, 2020, 10, 3528.
- [4e] Mu H., Miki K., Harada H., Tanaka K., Nogita K., and Ohe K., *ACS Sens.* 2021, 6, 1, 123–129.
- [4f] Cooper, M.E., Gregory, S., Adie, E., and Kalinka S., *J. Fluoresc.*, 2002, 12, 425–429.
- [5a] Y. Zhang, S. Xia, M. Fang, W. Mazi, Y. Zeng, T. Johnston, A. Pap, R. L. Luck and H. Liu, *Chem. Commun.*, 2018, 54, 7625–7628.
- [5b] D. Cao, Z. Liu, P. Verwilt, S. Koo, P. Jangjili, J. S. Kim and W. Lin, *Chem. Rev.*, 2019, 119, 10403–10519.
- [5c] J. L. Zhu, Z. Xu, Y. Yang and L. Xu, *Chem. Commun.*, 2019, 6629–6671.
- [5d] H. Lu, J. MacK, Y. Yang and Z. Shen, *Chem. Soc. Rev.*, 2014, 43, 4778–4823.
- [6a] N. Boens, V. Leen and W. Dehaen, *Chem. Soc. Rev.*, 2012, 41, 1130–1172.
- [6b] A. Vázquez-Romero, N. Kielland, M. J. Arévalo, S. Preciado, R. J. Mellanby, Y. Feng, R. Lavilla and M. Vendrell, *J. Am. Chem. Soc.*, 2013, 135, 16018–16021.
- [6c] N. O. Didukh, V. P. Yakubovskiy, Y. V. Zatsikha, G. T. Rohde, V. N. Nemykin and Y. P. Kovtun, *J. Org. Chem.*, 2019, 84, 2133–2147.
- [7a] Y. Urano, D. Asanuma, Y. Hama, Y. Koyama, T. Barrett, M. Kamiya, T. Nagano, T. Watanabe, A. Hasegawa, P. L. Choyke and H. Kobayashi, *Nat. Med.*, 2009, 15, 104–109.
- [7b] T. Kowada, J. Kikuta, A. Kubo, M. Ishii, H. Maeda, S. Mizukami and K. Kikuchi, *J. Am. Chem. Soc.*, 2011, 133, 17772–17776.
- [7c] H. Xiong, P. Kos, Y. Yan, K. Zhou, J. B. Miller, S. Elkassih and D. J. Siegwart, *Bioconjugate Chem.*, 2016, 27, 1737–1744.
- [7d] M. H. Chua, T. Kim, Z. L. Lim, T. Y. Gopalakrishna, Y. Ni, J. Xu, D. Kim and J. Wu, *Chem. - A Eur. J.*, 2018, 24, 2232–2241.
- [7e] M. Grossi, M. Morgunova, S. Cheung, D. Scholz, E. Conroy, M. Terrile, A. Panarella, J. C. Simpson, W. M. Gallagher and D. F. O'Shea, *Nat. Commun.*, 2016, 7, 1–13.
- [7f] Leong C., Lee S. C., Ock J., Li X., See P., Park S. J., Ginhoux F., Yun S. W., Chang Y. T., *Chem. Commun.* 2014, 50(9), 1089–1091.
- [8a] S. L. Shen, X. P. Chen, X. F. Zhang, J. Y. Miao and B. X. Zhao, *J. Mater. Chem. B*, 2015, 3, 919–925.

- [8b] T. H. Chen, S. Zhang, M. Jaishi, R. Adhikari, J. Bi, M. Fang, S. Xia, Y. Zhang, R. L. Luck, R. Pati, H. M. Lee, F. T. Luo, A. Tiwari and H. Liu, *ACS Appl. Bio Mater.*, 2018, 1, 549–560.
- [8c] P. Prakash, T. C. Lantz, K. P. Jethava, G. Chopra, *Methods Protoc.* 2019, 2 (2), 48.

## CHAPTER 6. LIPIDS MODULATE MICROGLIAL CELL STATE AND FUNCTION

### 6.1 An introduction to lipids

Lipids are a diverse range of hydrophobic or amphipathic small molecules including fatty acids and their derivatives that are soluble in organic solvents such as hydrocarbons, chloroform, benzene, ethers, and alcohols[1]. A comprehensive definition of lipids was proposed more recently by Dr. William Walker Christie, creator of The Lipid Library (<https://lipidlibrary.aocs.org/>)—one of the largest lipid repositories in the world. He proposed a new definition for lipids based on structural criteria as follows:

*“Lipids comprise a heterogeneous class of predominantly hydrophilic organic molecules of relatively low molecular weight (commonly <1000) that are defined by the presence either of linear alkyl chains, usually with even-numbers of carbon atoms and saturated or unsaturated with double bonds in characteristic positions, or of isoprene units in linear or cyclic structures. These can contain variable numbers of oxygenated substituents such as carboxylic acid or hydroxyl groups, and/or other heteroatoms, but especially nitrogen in amines, for example. Often, these are linked covalently to glycerol, carbohydrates, phosphate and other small polar entities, which can render the molecules more amphiphilic.”*

Lipids are the basic building blocks of cellular membrane and provide structural stability, motility, and flexibility to cells. They allow the embedding of membrane-spanning proteins within the lipid bilayer and directly signal to them during normal cellular functions. Subtle differences in lipid metabolism can provide key insights into cell states and even disease pathologies. One can appreciate that lipids (the lipid bilayer) lie at the frontier between a cell and its environment. Thus, both the structural and signaling aspects of lipids are integral to the maintenance of cell state and function. Lipids make up an integral part of the CNS physiology. The brain contains the second-largest lipid content in the human body—second only to the adipose tissue. From insulating axons for neuronal conduction to regulating signaling events on the cell membrane, lipids play a vital role in all aspects of cell survival and function.



## 6.2 The cellular lipid landscape is large and complex

The International Lipid Classification and Nomenclature Committee under the sponsorship of the LIPID MAPS Consortium (<https://www.lipidmaps.org/>) has classified lipids into eight main categories with each category containing its own subclassification hierarchy[1], [2]. These eight main classes of lipids are: fatty acyls, glycerolipids, glycerophospholipids, sphingolipids, sterol lipids, prenol lipids, saccharolipids, and polyketides. Each lipid classes contains hundreds, if not thousands, of “lipid species” based on the length of the acyl chain, presence or absence of C=C bonds in the acyl chains, the number of C=C bonds, the location of C=C bonds, the functional groups associated with the structures, etc. Thus, each lipid class contains unique sub-classes of molecules and exhibit extensive structural diversity (Figure 6.1). The location of the lipids within the cells also contribute to their functional characteristics. In an active cell, lipids orchestrate all aspects of cellular processes including signaling events, phagocytosis, migration, energy production, transcriptional events, etc. One can thus appreciate the complexity of the cellular “lipidome” by considering all the possible permutations and combinations of the lipid structures.

According to LipidPedia, it is estimated that millions of lipids can be identified or computationally generated[3], however, no single database can provide information on all the lipids. There are also a large number of lipids that are yet to be identified constituting “the dark lipidome” which may uncover new and previously details about cell biology and metabolism. Thus, analytical tools and techniques are instrumental to uncovering the cellular lipidome in the context of health and disease.

Even though several lipids have been identified to date, the roles of specific lipids in glial cells has not been well understood. Lipids directly influence microglial function by modulating membrane proteins on the cell surface, yet, only a handful of studies have shown changes in specific metabolites in microglia in inflammatory environments. The dysregulation in lipid metabolism in glial cells also contributes to AD pathogenesis and other neurological disorders. Thus, the identification of specific lipids that affect glial cellular response and function in disease will serve as functional biomarkers and targets for next generation of therapeutics.

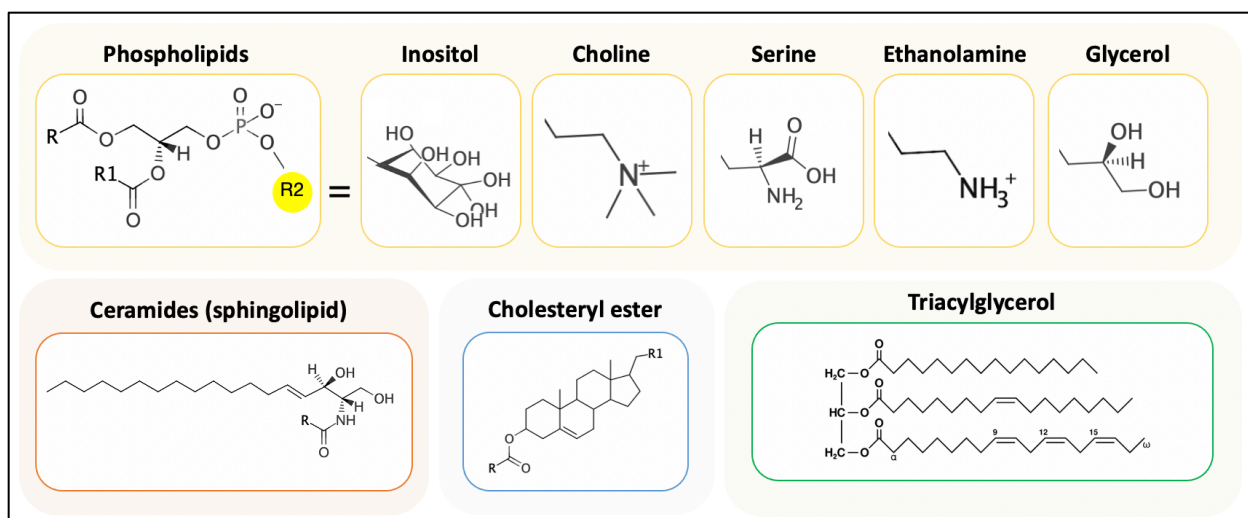


**Figure 6.1** Representative structures of select lipid classes. The main structure of a phospholipid is illustrated with the R2 position highlighted in yellow. The type of the phospholipid depends on the functional group at the R2 position. This is indicated in the following phospholipids shown in yellow boxes. Other lipids drawn are ceramides, cholesteryl ester with a cholesterol backbone, and a triacylglycerol containing three acyl chains with a glycerol head group.

### 6.3 Several Alzheimer's-risk genes are related to lipid metabolism

Alzheimer's disease is a huge burden to society. Currently, it has no cure or approved treatments and there have been several failed clinical trials by big pharma[4], [5]. Lipids play a key role in regulating cellular functions, are critical for immune cell modulation and signaling[6], and are just as important as proteins and genes[7]. Lipid deposits were first observed in AD brains by Alois Alzheimer in 1907[8] and are since considered to be critical in AD pathology. Several disease-risk genes that are implicated in AD are directly related to lipid metabolism and function such as TREM2, INPP5D, APOE, etc (Figure 6.2). For example, cholesterol, an essential lipid is carried by the Apolipoprotein E (APOE) in the brain and mutations in APOE is one of the primary disease-risk gene for AD[9] that is also known to affect A $\beta$  uptake by microglia[6]. Yet, there are several new and unknown astrocytic protein and lipid markers yet to be discovered for A $\beta$ -specific clearance that will directly affect AD pathogenesis and may also serve as functional biomarkers for disease diagnosis. Therefore, tools developed to identify microglia phagocytosis specificity will form the basis for the identification of protein and lipid targets that are essential to develop new immunomodulatory drugs. Further, the new lipid modulators of glial cell state and function will identify new cellular and molecular mechanisms underlying brain physiology in health and disease.

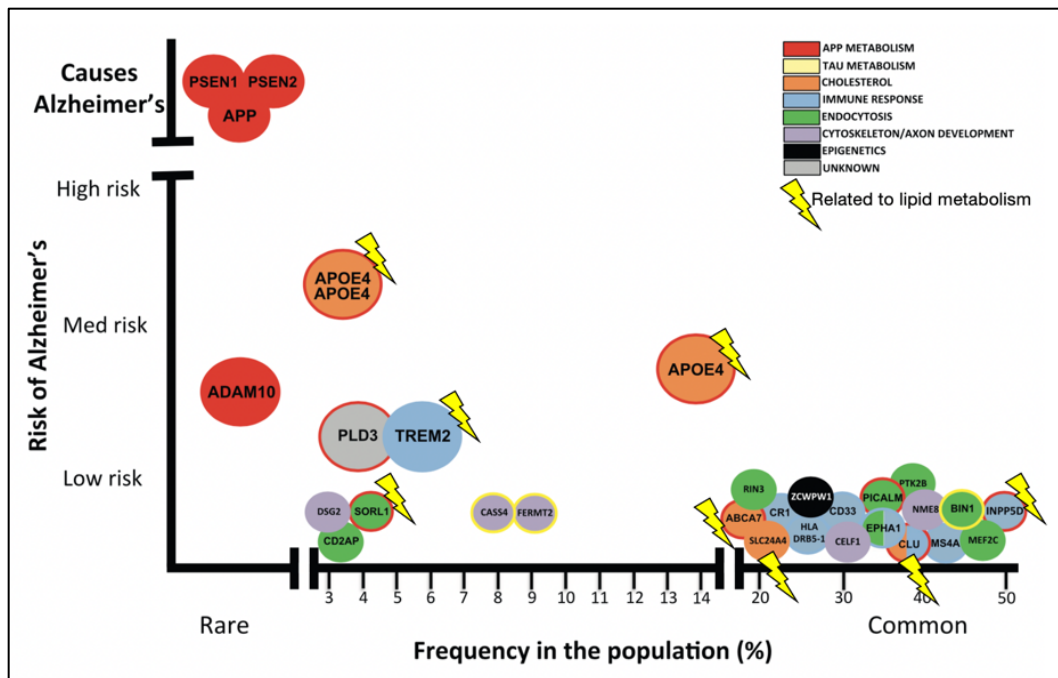


**Figure 6.2** Rare and common variants contribute to Alzheimer's disease risk. Adapted from Karch & Goate, 2015[10]. Yellow thunderbolt symbol = genes associated with lipid metabolism.

### 6.3.1 Lipoproteins—A “language” for cell-cell signaling

Lipoproteins are chaperone proteins in the CNS that carry or transport lipids between cells in order to maintain lipid homeostasis in the tissue environment. They are implicated in the onset and progression of several neurodegenerative disorders including AD. The most abundant lipoproteins in the brain are apolipoprotein E (APOE) and APOJ (also called as clusterin) which are endogenously expressed by astrocytes[11] and microglia[12]. Mutations in both the *APOE* and *APOJ* genes are linked to AD risk; specifically, the *APOE4* isoform has been extensively linked to AD and the lipidation of *APOE4* (i.e. carrying cholesterol and phospholipids) alters its metabolism and receptor binding ability. Lipoproteins also interact with neurons by binding to proteins on the neuronal membrane such as the amyloid precursor protein (APP), among others. They can be internalized into the cells via the low-density lipoprotein receptors (LDLR), low-density lipoprotein receptor-related protein 1 (LRP1), heparan sulfate proteoglycans (HSPGs), etc. [13]. One of the ways these lipoproteins induce pathological states in the brain is by affecting the A $\beta$  aggregation and clearance[14] and by inducing the activation of microglia as well as astrocytes.

The failure of lipoprotein-binding of A $\beta$  may result in increased extracellular A $\beta$  accumulation thereby leading to progressive plaque formation. The type of lipids contained in the lipoproteins may also have varying effects on the states of cells that they interact with. Thus, it is critical to better understand lipoprotein functions, especially in the context of A $\beta$  metabolism, interactions with specific cells in the CNS, and the mechanism of their lipidation in the context of health and disease.

#### **6.4 Lipids are key immunomodulators of microglial cell state and function**

In addition to genes and proteins, lipids are increasingly recognized as vital biomolecules for microglial behavior and function. What specific membrane and intracellular lipids regulate microglial phagocytosis? There are currently 10,000 different documented lipids, and the dysregulation in lipid metabolism is linked to AD and other neurological diseases.[15], [16] However, the changes in the global cellular lipid landscape and specific lipid molecules that modulate glial function in AD remains largely uncharacterized till date. Lipids directly influence microglial function by modulating membrane proteins on the cell surface. For example, lipids promote phagocytosis by acting as ligands to transmembrane proteins like Triggering receptor expressed on myeloid cells 2 (TREM2) and Low-Density Lipoprotein Receptors (LDLRs)[17]–[19]. Apoptotic cells expose phosphatidylserines on their membranes that act as “eat me” signals and recruit microglia to facilitate their phagocytic uptake (Figure 6.3). Cell membrane lipids like phospholipids and cholesterol closely interact with A $\beta$  and affect the aggregative properties of A $\beta$  via membrane induced fibrilization phenomenon[20]. It has also been shown that lipids reprogram microglia into disease reactive phenotypes when the cells are exposed to A $\beta$  in culture[21], [22]. Only a handful of studies have shown changes in specific metabolites in microglia in inflammatory environments[23]. A recent study showed that A $\beta$  treatment causes a significant metabolic alternation in microglia by switching them from respiratory to glycolytic states[21], [22]. No doubt, glial cell states and functions are governed by the changes in their lipid and metabolite signatures.

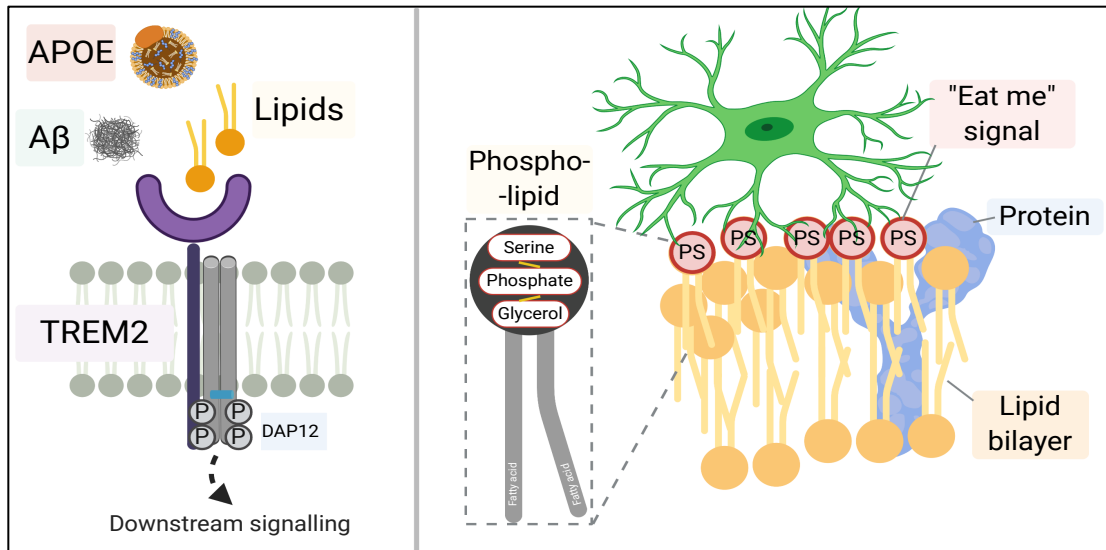


**Figure 6.3** Lipids regulate microglial function. Examples: (L) Lipids act as ligands for TREM2 and affect downstream signaling. (R) Phosphatidylserine on cell membrane act as eat-me signal to initiate phagocytosis of apoptotic cells.

#### 6.4.1 Phospholipids

Phospholipids (also known as Glycerophospholipids) are the major components of the cell membrane. They comprise of a glycerol backbone, two non-polar fatty acid tails, a phosphate group substituted with one of the following polar head groups—inositol (PI), choline (PC), serine (PS), ethanolamine (PE), or glycerol (PG).

PIs are especially abundant in the brain tissue, where they can amount to 10% of the phospholipids, but they are also present in all tissues, cell types and membranes. PIs are signaling lipids and can act as cell membrane identifiers based on their location within the cell. For example, PI(4,5)P<sub>2</sub> marks the plasma membrane, PI(3)P defines the identity of early endosomes, and PI(3,5)P<sub>2</sub> defined the late endosomes[24]. Just like PSs, PIs are present entirely in the inner leaflet of the plasma membrane under normal conditions. Under cellular stress or apoptosis, they may be exposed to the extracellular space due to the cell membrane “flips” over thereby causing them to become eat-me signals for phagocytosis. PIs also act as second messengers, precursors to other signaling molecules and regulators[25]. Several proteins that directly interact with PIs have been shown to regulate the innate immune responses in microglia. For example, Phosphatidylinositol 4,5-bisphosphate (PIP<sub>2</sub>), an important lipid regulator of membrane signaling and remodeling

processes, has been shown to influence Toll-like receptor (TLR) signaling in microglia[26]. TLRs are key transducers of immune responses such as inflammation, phagocytosis, and autophagy. Interestingly, certain PI species are also shown to be “over expressed” (or become increasingly abundant) upon microglial activation as observed via mass spectrometry (MS)-based lipid profiling. For example, an unusual inositol phospholipid molecule, PI(20:4/20:4), was shown to be increased by 300% after activation of macrophages[27]. Since PI(20:4/20:4) was formed and degraded rapidly in the cells, this molecule was suggested to have a role in regulating cell signaling events. Such studies further support the notion that bioactive lipids may be used as cellular biomarkers to detect changes in cell states in different pathological conditions.

PCs are the most abundant phospholipids and are the major constituents of plasma membranes and play a large role in the membrane-mediated cell signaling events[28]. Changes in PC levels have been shown to affect microglial reactivity during injury. One study demonstrated an increase in arachidonic acid-containing PC (specifically [PC(16:0/20:4)+K]<sup>+</sup>) to be associated with reactive microglia and astrocytes in the spinal cord after peripheral nerve injury[29]. Thus, this PC lipid species could serve as a marker to identify reactive glia in the spinal cord in this injury condition. Oxidized lipids may contribute to enhanced inflammation in the CNS during disease. Specifically, exogenous oxidized PCs (OxPCs) are considered to be potent neurotoxins and are found in Multiple Sclerosis (MS) lesions in the brain that drive neurodegeneration. It was recently found that microglia directly interact with these toxic OxPCs in a TREM2-dependent manner (TREM2<sup>high</sup> microglia were required for OxPC elimination) and may help prevent further neuronal damage in MS[30]. Microglia protected neurons against OxPC toxicity *in vitro* and the loss of microglia exacerbated OxPC-mediated neurodegeneration *in vivo*[30]. These findings demonstrate how specific lipid species regulate microglial function (and/or how microglia regulate the levels of lipids in the CNS) in a disease environment and play a major role in maintaining brain homeostasis via lipid regulation.

PSs (also called as PtdSer) are exclusively located in the inner leaflets of healthy cell membranes but are exposed to the extracellular space in dying cells. The exposed PS molecules act as “eat me” signals to recruit microglia (and astrocytes) for the phagocytic clearance of dying cells and debris[31]. This process is widely observed during brain development wherein excess synapses

need to be eliminated to support enhanced neuron-neuron connections and neuronal plasticity. The neuronal synapses that are ready to be “eaten off” (or pruned) express high levels of PSs on their outer membranes for microglial phagocytosis[31]. Aberrant expression of PSs may thus affect neuronal connectivity during brain development leading to neurodevelopmental disorders. What specific PS species regulate this process has not been well defined and warrants further research. When microglia become inherently dysfunction during disease and are phagocytically incapable of clearing the dying neurons and other cells, targeting the PS molecules on the cell membranes via chemical modulation may be a feasible approach to enhance debris clearance. It is worth noting that microglial-uptake of apoptotic cells is receptor mediated[31]. Specific receptors on microglia directly bind to PS thereby initiating phagocytosis. For example, Triggering receptor expressed on myeloid cells 2 (TREM2) and G protein-coupled Receptor 56 (GPR56) facilitate microglial engulfment of neurons by direct binding to PS[32], [33].

#### **6.4.2 Free fatty acids**

Fatty acids comprise of carboxylic acid with long aliphatic chains which can either be saturated (no C=C double bonds) or unsaturated (one or more C=C double bonds). Fatty acids are usually found in their esterified form, namely, triglycerides, phospholipids, and cholesteryl esters. The presence of fatty acids in their standalone form (as free fatty acids; FFAs) may be an indication of dysregulated lipid homeostasis and inflammation in the tissue microenvironment. For example, palmitic acid, a saturated free fatty acid containing an aliphatic chain with 16 carbon atoms (C16:0) is one of the main FFA that promotes metabolic inflammation and is known to be toxic to cells *in vitro*[34] and *in vivo*. Saturated FFAs induce microglial reactivity by activating microglial TLR4 receptor signaling[35] which further triggers a cascade of inflammatory events. It is also suggested that palmitic acid impairs the protective responses of microglia by affecting their phagocytic ability and migratory activity. Specifically, palmitic acid was shown to suppress microglial phagocytic capacity and migratory ability under IFN- $\gamma$ -induced inflammatory condition[34]. Interestingly, other studies have shown that palmitic acid may induce an alternate-phenotype in microglia by enhancing their phagocytic capacity and turning on genes like *Arg1* (arginase 1) in culture[36] which is widely characterized as an anti-inflammatory marker. Of course, one must exercise caution in drawing conclusions from studies done in cultured microglial cells, especially in serum containing media conditions as these *in vitro* cell culture models do not accurately recapitulate

microglia in physiological *in vivo* conditions. Other relevant saturated FFAs that are implicated in microglia-mediated inflammation are stearic acid (C18:0), arachidic acid (C20:0), etc. It is interesting to note that while saturated FFAs are associated with pro-inflammatory or neurotoxic cellular phenotypes, unsaturated FFAs like oleic acid (C18:1), arachidonic acid (20:4), docosahexaenoic acid (22:6) are associated with anti-inflammatory or neuroprotective cellular phenotypes. More studies need to be performed *in vivo* in order to better understand how saturated and unsaturated free fatty acids influence microglial phenotype and behavior and how these changes may contribute to disease pathogenesis.

### 6.4.3 Cholesterol

The CNS contains around 23% of total cholesterol in the body all of which is made locally within the CNS since the blood brain barrier prevents the entry of cholesterol-containing lipoproteins into the brain. Most of the brain's cholesterol is found as insulating sheaths on axons along with sphingolipids. As stated previously, cholesterol is mainly present in its esterified form as cholesteryl esters (CEs) and similarly, CEs break down to produce free cholesterol and fatty acids. Astrocytes and mature oligodendrocytes are the major cholesterol-producing cells in the brain. The secreted cholesterol is carried into the extracellular space in association with the APOE/J chaperone proteins and is critical for the regulation of neuronal function. High concentrations of astrocyte-derived cholesterol is also required for microglial survival (along with TGF- $\beta$ 2 and CSF-1) *in vitro* and *in vivo*[37]. Since microglia express lower levels of cholesterol biosynthesis genes compared to astrocytes and matured oligodendrocytes, it was inferred that microglia are deficient at producing cholesterol autonomously and therefore are dependent on the other CNS cells *in vivo* or direct cholesterol supplementation *in vitro* for their survival. Cholesterol also plays a huge role in A $\beta$  metabolism via the APOE-A $\beta$  signaling axis. Free cholesterol associated with the lipid rafts on the plasma membrane are linked to an increased aggregation of A $\beta$  via similar pathways. However, how microglia metabolize cholesterol is still unclear. Further, it is important to understand how cholesterol modulates microglial function and the underlying mechanisms of cholesterol signaling in microglia.

The phagocytic clearance of cholesterol is a major function of microglia in the CNS. A recent study demonstrated that cholesterol bound to APOE is phagocytosed via the TREM2 receptor on



microglial membrane[38]. It was shown that microglia deficient in *Trem2* were associated with cholesterol efflux defects thereby proposing a new mechanism for microglial-mediated lipid sensing and brain cholesterol metabolism. Furthermore, dysfunctional microglia observed in aged and disease brains exhibit altered phenotypes and are unable to efficiently clear the myelin debris via phagocytosis. It was found that aged microglia with defective lipid metabolism were unable to metabolize cholesteryl esters which in turn triggered cholesterol crystal formation[39]. The formation of these cholesterol crystals were damaging to the microglial lysosomes and triggered severe inflammatory events via the activation of the inflammasome pathway[39].

## **6.5 Lipid droplet accumulation in aged and/or diseased microglia**

In 1911, Dr. Alois Alzheimer observed “glial cells with large adipose saccules” surrounding A $\beta$  plaques while investigating the brain tissue section of his dementia patient (Figure 6.4). This was perhaps the first cell subtype classification of glia classified by Alzheimer himself. These observations are found in his beautiful illustrations and renditions of brain slices. Over a hundred years passed by with little progress in our understanding of what these lipid-rich glial cells are and what they do. Today, with the advent of high-resolution confocal microscopy, we are able to visualize lipid-rich compartments (now called lipid droplets) in glial cells in human and rodent tissue. Interestingly, we are also able to observe lipid-droplet containing glial cells encompassing A $\beta$  plaques in AD tissues. Sc-RNAseq analysis has identified dysregulation in lipid metabolism-related genes in microglia around A $\beta$  plaques[40].

Why (rather how) are these microglia able to migrate towards the A $\beta$  plaques but unable to engulf them is still a big mystery. What intra and extracellular events contribute to lipid droplet accumulation in A $\beta$ -associated microglia and what are the consequential functional deficits in microglia due to this unique lipid-rich phenotype is still not clear. Does the inherent functional deficits lead to lipid accumulation is also not known. But why is this important? i.e. why is it important to delineate whether the lipid accumulation in microglia results in dysregulated function or whether the functional deficits leads to lipid accumulation in microglia? Answering these questions will give us insights into how we may modulate microglial functions via new and novel drugs, tools, or molecules. If we are able to trigger microglia to phagocytose A $\beta$  before they

become dysfunctional, perhaps we can slow down the process of progressive plaque formation and eventual AD progression.

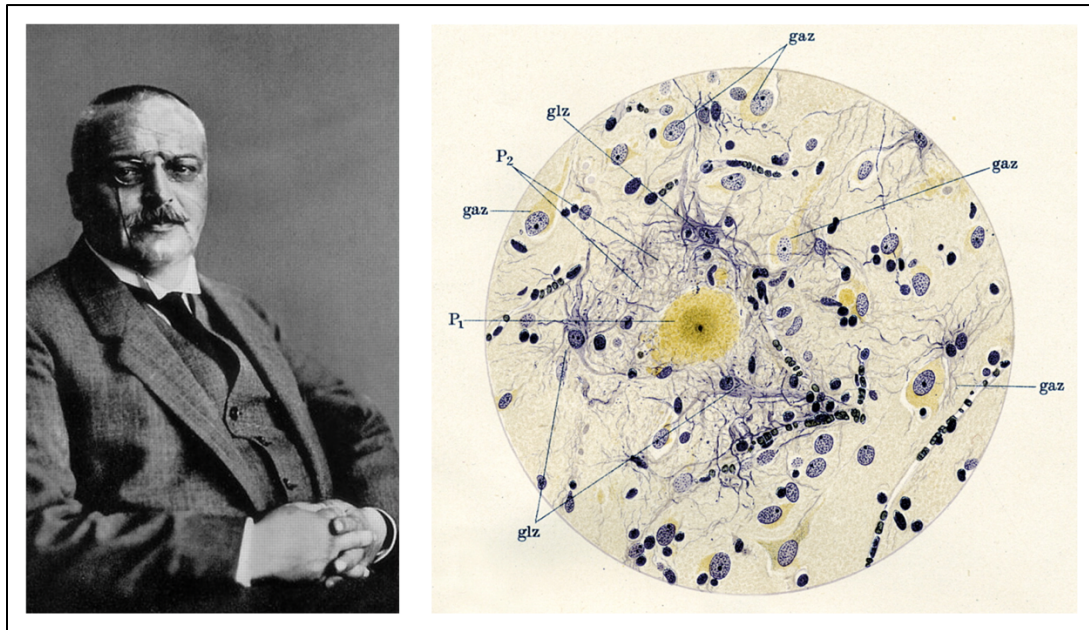


**Figure 6.4** Alois Alzheimer, 1911. glz: glia; gaz: neurons; P1/P2: senile plaques.

Lipid droplet-accumulating microglia (termed LDAM) were recently identified in aged human and rodent brains[41]. It was shown that LDAMs are functionally defective in phagocytosis, produce high levels of reactive oxygen species, and secrete proinflammatory cytokines. Additionally, healthy or “normal” microglia treated with LPS *in vitro* (direct treatment) or *in vivo* (via intraperitoneal injection) also developed into LDAM suggesting that this phenotype is not unique to aging only but can also be observed with inflammation. This study raises several interesting questions: Do microglia or a subset of microglia in AD and other neurodegenerative disorders also exhibit this LDAM phenotype? What proteins are involved in the formation of LDs in microglia? Does the elimination of LDs in microglia (and hence the LDAM phenotype) enhance their phagocytic capacity?

## 6.6 Concluding thoughts

No doubt, lipids play a huge role in regulating all aspects of microglial cell state and function. Several lipid classes were not discussed in this chapter including sphingolipids, ceramides, etc. but

are still critically involved in all aspects of microglial behavior. One can also appreciate the vastness of the cellular lipid landscape and the added complexity with increased structural diversity of lipids. Hundreds, if not thousands of lipids are yet to be identified and these lipids make up the “dark lipidome”. Several of the unidentified lipids may be involved in critical disease-related pathways and may even serve as cellular biomarkers to diagnose disease pathology. The selected few studies mentioned in this chapter also highlights the importance of evaluating the changes to the global lipidome profiles of glial cells rather than investigating changes to individual lipids. Like proteins, lipids also interact with each other and work together to regulate functional changes as a result of an inflammatory trigger such as LPS or A $\beta$ . Thus, analyzing how several lipid classes change together may lead to the identification of new glial cell states and even form the basis of analyzing diseases from a lipid-centric view in parallel to a gene-centric and a protein-centric view. New analytical tools involving robust lipidomic methods will identify more lipids and map them to the cell types in the CNS. The following chapter will focus on how A $\beta$  regulates microglial global lipid profiles *in vitro* and in the 5xFAD mouse model of AD.

## 6.7 References

- [1] E. Fahy *et al.*, “A comprehensive classification system for lipids,” *J. Lipid Res.*, vol. 46, no. 5, pp. 839–861, 2005.
- [2] E. Fahy *et al.*, “Update of the LIPID MAPS comprehensive classification system for lipids,” *Journal of Lipid Research*, vol. 50, no. SUPPL. J Lipid Res, Apr-2009.
- [3] T. C. Kuo and Y. J. Tseng, “LipidPedia: A comprehensive lipid knowledgebase,” *Bioinformatics*, vol. 34, no. 17, pp. 2982–2987, Sep. 2018.
- [4] R. Vandenberghe *et al.*, “Bapineuzumab for mild to moderate Alzheimer’s disease in two global, randomized, phase 3 trials,” *Alzheimer’s Res. Ther.*, vol. 8, no. 1, p. 18, Dec. 2016.
- [5] R. S. Doody *et al.*, “Phase 3 Trials of Solanezumab for Mild-to-Moderate Alzheimer’s Disease,” *N. Engl. J. Med.*, vol. 370, no. 4, pp. 311–321, Jan. 2014.
- [6] F. L. Yeh, Y. Wang, I. Tom, L. C. Gonzalez, and M. Sheng, “TREM2 Binds to Apolipoproteins, Including APOE and CLU/APOJ, and Thereby Facilitates Uptake of Amyloid-Beta by Microglia,” *Neuron*, vol. 91, no. 2, pp. 328–340, Jul. 2016.
- [7] J. A. Hamilton, C. J. Hillard, A. A. Spector, and P. A. Watkins, “Brain uptake and utilization of fatty acids, lipids and lipoproteins: Application to neurological disorders,” in *Journal of Molecular Neuroscience*, 2007, vol. 33, no. 1, pp. 2–11.

- [8] R. A. Stelzmann, H. Norman Schnitzlein, and F. Reed Murtagh, "An english translation of alzheimer's 1907 paper, 'über eine eigenartige erkankung der hirnrinde,'" *Clin. Anat.*, vol. 8, no. 6, pp. 429–431, 1995.
- [9] L. Puglielli, R. E. Tanzi, and D. M. Kovacs, "Alzheimer's disease: The cholesterol connection," *Nat. Neurosci.*, vol. 6, no. 4, pp. 345–351, Apr. 2003.
- [10] C. M. Karch and A. M. Goate, "Alzheimer's disease risk genes and mechanisms of disease pathogenesis," *Biological Psychiatry*, vol. 77, no. 1. pp. 43–51, 2015.
- [11] R. W. Mahley, "Apolipoprotein E: Cholesterol transport protein with expanding role in cell biology," *Science*, vol. 240, no. 4852. Science, pp. 622–630, 1988.
- [12] T. Uchihara *et al.*, "ApoE immunoreactivity and microglial cells in Alzheimer's disease brain," *Neurosci. Lett.*, vol. 195, no. 1, pp. 5–8, Jul. 1995.
- [13] G. Bu, "Apolipoprotein e and its receptors in Alzheimer's disease: Pathways, pathogenesis and therapy," *Nature Reviews Neuroscience*, vol. 10, no. 5. NIH Public Access, pp. 333–344, May-2009.
- [14] L. M. Ittner and J. Götz, "Amyloid- $\beta$  and tau - A toxic pas de deux in Alzheimer's disease," *Nat. Rev. Neurosci.*, vol. 12, no. 2, pp. 67–72, Feb. 2011.
- [15] G. Di Paolo and T.-W. Kim, "Linking lipids to Alzheimer's disease: cholesterol and beyond," *Nat. Rev. Neurosci.*, vol. 12, no. 5, pp. 284–296, May 2011.
- [16] M. W. Wong, N. Braidy, A. Poljak, R. Pickford, M. Thambisetty, and P. S. Sachdev, "Dysregulation of lipids in Alzheimer's disease and their role as potential biomarkers," *Alzheimer's Dement.*, vol. 13, no. 7, pp. 810–827, Jul. 2017.
- [17] A. A. Nugent *et al.*, "TREM2 Regulates Microglial Cholesterol Metabolism upon Chronic Phagocytic Challenge," *Neuron*, vol. 105, no. 5, pp. 837-854.e9, Mar. 2020.
- [18] J. M. Basak, P. B. Verghese, H. Yoon, J. Kim, and D. M. Holtzman, "Low-density lipoprotein receptor represents an apolipoprotein E-independent pathway of A $\beta$  uptake and degradation by astrocytes," *J. Biol. Chem.*, vol. 287, no. 17, pp. 13959–13971, Apr. 2012.
- [19] H. Zhang *et al.*, "A Role of Low-Density Lipoprotein Receptor-Related Protein 4 (LRP4) in Astrocytic Ab Clearance," *J. Neurosci.*, vol. 40, no. 28, pp. 5347–5361, 2020.
- [20] Z. Niu, Z. Zhang, W. Zhao, and J. Yang, "Interactions between amyloid  $\beta$  peptide and lipid membranes," *Biochimica et Biophysica Acta - Biomembranes*, vol. 1860, no. 9. pp. 1663–1669, 2018.

- [21] S. H. Baik *et al.*, “A Breakdown in Metabolic Reprogramming Causes Microglia Dysfunction in Alzheimer’s Disease,” *Cell Metab.*, vol. 30, no. 3, pp. 493-507.e6, 2019.
- [22] F. C. Bennett and S. A. Liddelow, “Microglia Metabolic Breakdown Drives Alzheimer’s Pathology,” *Cell Metab.*, vol. 30, no. 3, pp. 405–406, Sep. 2019.
- [23] I. El Ghazi *et al.*, “Changes in the NMR metabolic profile of human microglial cells exposed to lipopolysaccharide or morphine,” *J. Neuroimmune Pharmacol.*, vol. 5, no. 4, pp. 574–581, 2010.
- [24] A. Wallroth and V. Haucke, “Phosphoinositide conversion in endocytosis and the endolysosomal system,” *Journal of Biological Chemistry*, vol. 293, no. 5. American Society for Biochemistry and Molecular Biology Inc., pp. 1526–1535, 02-Feb-2018.
- [25] D. V. Olivença, I. Uliyakina, L. L. Fonseca, M. D. Amaral, E. O. Voit, and F. R. Pinto, “A mathematical model of the phosphoinositide pathway,” *Sci. Rep.*, vol. 8, no. 1, pp. 1–12, Dec. 2018.
- [26] T. T. N. Nguyen *et al.*, “Phosphatidylinositol 4-phosphate 5-kinase  $\alpha$  contributes to Toll-like receptor 2-mediated immune responses in microglial cells stimulated with lipoteichoic acid,” *Cell. Signal.*, vol. 38, pp. 159–170, Oct. 2017.
- [27] L. Gil-de-Gómez *et al.*, “A Phosphatidylinositol Species Acutely Generated by Activated Macrophages Regulates Innate Immune Responses,” *J. Immunol.*, vol. 190, no. 10, pp. 5169–5177, May 2013.
- [28] G. Van Meer, D. R. Voelker, and G. W. Feigenson, “Membrane lipids: Where they are and how they behave,” *Nature Reviews Molecular Cell Biology*, vol. 9, no. 2. NIH Public Access, pp. 112–124, Feb-2008.
- [29] D. Xu *et al.*, “Increased arachidonic acid-containing phosphatidylcholine is associated with reactive microglia and astrocytes in the spinal cord after peripheral nerve injury,” *Sci. Rep.*, vol. 6, no. 1, pp. 1–11, May 2016.
- [30] Y. Dong *et al.*, “Oxidized phosphatidylcholines found in multiple sclerosis lesions mediate neurodegeneration and are neutralized by microglia,” *Nat. Neurosci.*, vol. 24, no. 4, pp. 489–503, Feb. 2021.
- [31] M. Maruoka and J. Suzuki, “Regulation of phospholipid dynamics in brain,” *Neuroscience Research*. Elsevier Ireland Ltd, 18-Jan-2021.
- [32] T. Li *et al.*, “A splicing isoform of GPR56 mediates microglial synaptic refinement via phosphatidylserine binding,” *EMBO J.*, vol. 39, no. 16, Aug. 2020.

- [33] N. Scott-Hewitt *et al.*, “Local externalization of phosphatidylserine mediates developmental synaptic pruning by microglia,” *EMBO J.*, vol. 39, no. 16, Aug. 2020.
- [34] N. Yanguas-Casás *et al.*, “Sex differences in the phagocytic and migratory activity of microglia and their impairment by palmitic acid,” *Glia*, vol. 66, no. 3, pp. 522–537, Mar. 2018.
- [35] Z. Wang *et al.*, “Saturated fatty acids activate microglia via Toll-like receptor 4/NF- $\kappa$ B signalling,” *Br. J. Nutr.*, vol. 107, no. 2, pp. 229–241, Jan. 2012.
- [36] L. M. Tracy, F. Bergqvist, E. V. Ivanova, K. T. Jacobsen, and K. Iverfeldt, “Exposure to the saturated free fatty acid palmitate alters BV-2 microglia inflammatory response,” *J. Mol. Neurosci.*, vol. 51, no. 3, pp. 805–812, Nov. 2013.
- [37] C. J. Bohlen, F. C. Bennett, A. F. Tucker, H. Y. Collins, S. B. Mulinyawe, and B. A. Barres, “Diverse Requirements for Microglial Survival, Specification, and Function Revealed by Defined-Medium Cultures,” *Neuron*, vol. 94, no. 4, pp. 759–773.e8, May 2017.
- [38] E. C. Damisah, A. Rai, and J. Grutzendler, “TREM2: Modulator of Lipid Metabolism in Microglia,” *Neuron*, vol. 105, no. 5, pp. 759–761, 2020.
- [39] L. Cantuti-Castelvetri *et al.*, “Defective cholesterol clearance limits remyelination in the aged central nervous system,” *Science (80-. )*, vol. 359, no. 6376, pp. 684–688, Feb. 2018.
- [40] H. Keren-Shaul *et al.*, “A Unique Microglia Type Associated with Restricting Development of Alzheimer’s Disease,” *Cell*, vol. 169, no. 7, pp. 1276–1290.e17, Jun. 2017.
- [41] J. Marschallinger *et al.*, “Lipid-droplet-accumulating microglia represent a dysfunctional and proinflammatory state in the aging brain,” *Nat. Neurosci.*, vol. 23, no. 2, pp. 194–208, Feb. 2020.

## CHAPTER 7. LIPIDOMIC AND METABOLOMIC CHARACTERIZATION OF MICROGLIA WITH AMYLOID

Manuscript in preparation.

Prakash P, Wijewardhane PR, Manchanda P, Randolph CE, Thayer EA, Chopra G. Lipidomic and metabolomic characterization of microglia reveals distinct cell states with amyloid.

### 7.1 Introduction

Given the critical role of lipids in regulating signaling events and mediating microglial phenotype, we asked *What changes occur in the global lipid and metabolite landscape of microglia with A $\beta$ ?* Using an exploratory mass spectrometry technique known as Multiple Reaction Monitoring (MRM)-Profiling (Appendix B), the changes to cellular as well as the secretory lipid and metabolites were profiled with 1, 12, and 24 hours of A $\beta$  treatment. Around 1500 different lipid species divided into 10 main lipid classes and around 700 metabolites were screened in A $\beta$ -treated microglia and microglia conditioned medium (MCM). An initial microglial cell state was identified that was caused by an increase in cellular free fatty acids (FFAs) due to initial A $\beta$  exposure. With prolonged A $\beta$  treatment, microglia produced an abundance of Triacylglycerides (TAGs), which are the major components of lipid droplets previously observed in microglia[1]. It may be hypothesized that an abundance of TAGs formation (or perhaps lipid droplet formation) is a protective mechanism in microglia in order to overcome free fatty acids-induced cytotoxicity[2] during an acute inflammatory trigger in the form of A $\beta$ . The secretory lipids and metabolites identified in the MCM revealed a unique A $\beta$ -specific lipid-secretome of microglia. Select FFAs identified in A $\beta$ -treated microglia *ex vivo* were also identified in microglia in 5xFAD brains. We also provide a useful web resource for probing the differentially expressed lipid species in A $\beta$ -treated microglia and MCM (Appendix C). We also highlight the pathways implicated with these lipid and metabolite changes in microglia. Additionally, 5xFAD microglia showed an increase in lipid droplet accumulation in a sex-specific manner wherein female microglia exhibited a homogenous lipid droplet accumulation in the cells compared to a subset of male microglia which showed an abundance of lipid droplet within the cells. Finally, we identified DGAT2, a protein involved in TAG production within lipid droplets to be significantly highly expressed in 5xFAD microglia compared to WT microglia. Thus, this study highlights the key lipid and metabolite-

mediated microglial cell states associated with A $\beta$  *ex vivo* and *in vivo* in 5xFAD brains and the datasets produced further advance the toolsets required to explore microglial biology.

## **7.2 Methods**

### **7.2.1 BV2 cell culture and maintenance**

BV2 mouse microglial cell line, a generous gift from Dr. Linda J. Van Eldik (University of Kentucky, USA), was originally developed in the lab of Dr. Elisabetta Blasi at the University of Perugia, Italy. BV2 cells were cultured in DMEM/F12 medium containing 10% FBS (Atlanta Biologicals), 1% Penicillin/Streptomycin (Invitrogen), and 1% L-Glutamine (Corning #25-005-CI). The cells were maintained in 37 °C incubator with 5% CO<sub>2</sub>. Cells were sub-cultured when they reached 80% confluency and used for the experiments.

### **7.2.2 Primary mouse microglia isolation and culture from adult mouse brains**

CD11b<sup>+</sup> primary microglia were isolated from adult mice aged around 7 months (male and female) and cultured as follows. Mice were euthanized with CO<sub>2</sub> following the Purdue University Animal Care and Use Committee guidelines. After confirming their unresponsiveness to toe pinch, the mice were transcardially perfused with ice-cold PBS and perfused brains were immediately dissected and placed in ice-cold dounce buffer (DPBS<sup>++</sup> with 0.4% DNase I). The brains were chopped into small 1 mm<sup>3</sup>-sized pieces and each brain was transferred to a C-tube containing 5 mL dounce buffer. The tissue was thoroughly dissociated at 37 °C on an Octo-Heat Dissociator on the 37C\_ABDK setting for 30 mins. Next, the cell suspension was taken to the hood and filtered through a 70  $\mu$ m filter. The volume of the cell suspension was brought to 32.5 mL to which 10 mL of 1x Percoll PLUS (9 mL Percoll PLUS + 1 mL DPBS<sup>++</sup> containing Mg<sup>2+</sup> and Ca<sup>2+</sup>) reagent was added and the suspension centrifuged on slow break at 500 x g for 15 mins at 4 °C. The supernatant containing the myelin was aspirated and cell pellet was resuspended in 1.8 mL MACS buffer (0.5% BSA + 2 mM EDTA in 1x PBS) to which 200  $\mu$ L myelin removal beads was added. The suspension was gently mixed and incubated at 4 °C for 15 mins. Next, the cell suspension was diluted with 18 mL of MACS buffer and centrifugated on slow break at 300 x g for 10 mins at 4 °C (the same centrifugation setting was used from this step onwards). The supernatant was aspirated and the cells with the beads were passed through the LS column. The pass-through solution containing the



unlabeled cells (i.e. cells of interest) was collected on ice and the cell suspension again centrifuged as above. The cell pellet was now resuspended in 90 uL MACS buffer + 10 uL CD11b beads and incubated for 15 mins at 4 °C. The cell suspension was diluted with 1 mL MACS buffer and centrifuged as above. The pellet was now resuspended in 500 uL MACS buffer and passed through a LS column for positive selection of CD11b<sup>+</sup> cells. The CD11b<sup>+</sup> cells collected in the LS column were plunged out into a chilled 15 mL falcon tube and the cell suspension was centrifuged as above. After centrifugation, the MACS buffer supernatant was aspirated and the cell pellet was finally resuspended in 500 uL microglia growth medium (MGM) to make a stock cell suspension. The total cell number was counted using a hemocytometer and the stock cell suspension was diluted further in MGM containing TGF- $\beta$ , IL-34, and cholesterol (TIC media) with 2% FBS to obtain around 0.2x10<sup>6</sup> cells/mL concentration. Finally, around 0.1x10<sup>6</sup> cells were seeded per well in 500 uL total MGM in a 24-well plate. The cells were maintained at 37 °C in a 10% CO<sub>2</sub> incubator. Half the media was changed the following day and every other day after until the day of the experiment which was around 12-14 div.

### **7.2.3 Amyloid beta preparation and treatment**

The solid A $\beta$ 1-42 (A $\beta$ ) (Anaspec #20276) peptide obtained from the manufacturer was first dissolved in HFIP as previously described to create monomers. From the HFIP-treated A $\beta$ , a 100 uM stock solution was prepared in TIC media for primary microglia and in 20 mM NaOH, pH 10.5 for BV2 microglia. Peptide aggregation was initiated by incubating the solution at 37 °C for 24 hours as before. Following 24 hours, the peptide was either used directly on the cells or stored at -80 °C until treatment. The peptide was diluted in the culture medium and filtered through a 0.22  $\mu$ m syringe filter before treatment on cells.

BV2 microglia were seeded overnight in a 6-well plate at a concentration of 0.1x10<sup>6</sup> cells/mL/well. The next morning, the cells were treated with 500 nM A $\beta$ 1-42 or vehicle control for 1, 12, or 24 hours. After the respective time points, the treatment-media was aspirated and the cells were washed 3x times with ice-cold PBS, detached with 0.25% trypsin, and centrifuged at 500 x g for 6 mins at 4 °C. The supernatant was discarded, and pelleted cells were frozen in -80 °C. Cells from 4 independent experiments were used for direct injection-MS/MS and MRM-profiling experiment.

Primary microglia were treated similarly with 500 nM A $\beta$ 1-42 or vehicle control for 1, 12, or 24 hours. After the respective time points, the conditioned media from each well were collected and stored at -80 °C. The cells were detached from the wells with 0.25% trypsin and collected in 1x PBS before pelleting them at 500 x g for 6 mins at 4 °C. The supernatant was aspirated and cell pellets were also stored at -80 °C along with the conditioned media for lipid and metabolite extraction.

#### **7.2.4 Microglia isolation from 5xFAD and WT mouse brains**

Microglia (CD11b<sup>+</sup>) cells were isolated from 5xFAD and WT mouse brains (3-5 months or 5-7 months of age, depending on the experiment) as detailed in the protocol in section 7.2.2 above. For the lipidomics and metabolomics experiments, the isolated cells were pelleted at 4 °C and stored at -80 °C until the day of lipid and metabolite extraction as detailed in section 7.2.5. For lipid droplet quantification experiments, the isolated cells were further processed for BODIPY staining and flow cytometry analysis as detailed in section 7.2.9 below.

#### **7.2.5 Lipid and metabolite extraction by Bligh & Dyer method**

Lipid and metabolite extracts from cells and conditioned media were prepared using a slightly modified Bligh & Dyer extraction procedure. The frozen cell pellets from BV2 and primary microglia were thawed for 10 mins at room temperature. To the pellets, 200  $\mu$ L ultrapure water was added and gently pipetted to promote cell lysis. Next, 450  $\mu$ L methanol, and 250  $\mu$ L HPLC grade chloroform was added. The samples were mixed, vortexed for 10 seconds resulting in a one-phase solution that were then incubated at 4 °C for 15 mins. After that, 250  $\mu$ L ultrapure water and 250  $\mu$ L chloroform was added resulting in a biphasic solution. The cell and conditioned media samples were centrifuged at 16,000 x g for 10 mins resulting in three phases in the tubes. The bottom is the organic phase that contains the lipids and was transferred to new tubes, the middle phase consisting of proteins were discarded and the upper polar phase containing the metabolites were also transferred to new tubes. The solvents from the organic phase and the polar phase were evaporated in a speed-vac leaving behind the dried lipid and metabolite extracts in the tubes. The dried lipid extracts were dissolved in acetonitrile/methanol/ 300 mM ammonium acetate (3:6.65:0.35 v/v/v) to make stock solution and the dried metabolite extracts were dissolved in

water/methanol (1:1) to make stock solution. The lipid and metabolite stock solutions were diluted further as described below before running them on the mass spectrometer.

#### **7.2.6 Multiple Reaction Monitoring-profiling for lipidomics and metabolomics**

MRM-profiling of the extracted lipids and metabolites was performed as described previously. Sample preparation was carried out by diluting the lipid and metabolite stock solutions in the injection solvent (acetonitrile:methanol:ammonium acetate 300 mM 3:6.65:0.35 (v/v)). The injection solvent alone without any lipids or metabolites was used as the “blank” sample. The injection solvent containing the quantitative mass spec internal standard consisting of a mixture of 13 deuterated lipid internal standards at a concentration of 100 µg/mL each (Avanti Polar Lipids, #330731) was used as the “quality control” sample to monitor their peaks over time to confirm proper working of the instrument. Finally, 8 µL of the diluted lipid or metabolite sample was delivered to the ESI source of an Agilent 6410 triple quadrupole mass spectrometer to acquire the MS data by flow injection (no chromatographic separation). This method enabled the interrogation of the relative amounts of numerous lipid species within ten major classes of lipids based on the LipidMaps database. Triacylglycerides (TAGs) were divided into 2 separate methods (TAG1 and TAG2) based on the fatty acid residues’ neutral losses selected as the product ions for the ion transitions. Specifically, TAG1 method screens for 16:0, 16:1, 18:0 and 18:1 fatty acids and TAG 2 method screens for 18:2, 20:0, and 20:4 fatty acids. The raw MS data obtained for lipids and metabolites was analyzed using an in-house script and the lists containing MRM transitions along with the respective ion intensity values were exported for statistical and bioinformatic analysis.

**Table 7-1** The lipid classes screened, their corresponding abbreviation, and the total number of MRM transitions per class.

Serial number	Lipid class	Abbreviation	Total number MRM transitions
1	Acyl carnitines	AC	64
2	Cholesteryl esters	CE	57
3	Ceramides	Cer	81
4	Free fatty acids	FFA	36
5	Phosphatidylcholine and sphingomyelin	PC and SM	149
6	Phosphatidylethanolamine	PE	152
7	Phosphatidylglycerol	PG	152
8	Phosphatidylinositol	PI	148
9	Phosphatidylserine	PS	148
10	Triacylglycerols 1	TAG1	196
11	Triacylglycerols 2	TAG2	189

### 7.2.7 Statistical and bioinformatic analysis pipeline

All statistics for the comparisons of MRM transitions of the lipids and metabolites between A $\beta$ -treated microglia compared to vehicle-treated microglia were calculated using the edgeR package. Here, the ion count for a given molecule (lipid or metabolite) was referred to using the subscript  $s$  for the sample (cell replicate for a class of analyte) and  $b$  for the specific molecule (lipid or metabolite). An additional ‘intercept’ sample was added to model the experimental blank performed using just the injection media to ensure that all comparisons are significant with respect to this blank control. The edgeR package fits a generalized linear model to the following log-linear relationship for the mean-variance:  $\log \mu_{bs} = X_b^T \beta_g + \log N_s$ , for each molecule  $b$  in sample  $s$  where the sum of all ion intensity for sample  $s$  sums to  $N_s$ . This allowed for the calculation of the coefficient of variation (CV) for the ion count for a molecule in a sample ( $y_{bs}$ ) using the following relationship:  $CV^2(y_{bs}) = 1/\mu_{bs} + \Phi_b$ , where  $\Phi_b$  is the dispersion of the molecule. This dispersion term was estimated using the common dispersion method. These values were used to calculate the

associated log-fold change between the A $\beta$ -treated and vehicle-treated control microglia and the p-values were obtained using the likelihood ratio test. These p-values were then adjusted for multiple testing using the Benjamini-Hochberg (BH) method to obtain false discovery rates (FDRs). The lipid or metabolite was considered relevant or significant when fold change>0.5 and FDR<0.1.

### **7.2.8 Metabolomic Pathway Analysis**

Metabolomic Pathway Analysis (MetPA) was generated by MetaboAnalyst version 4.0 software package. For input, a list of all the tentative structural identities for the MRMs which were statistically significant from either cells or conditioned media taken from 1, 12, and 24 hour time points were entered as a list of compound names. Next, the parameters for the pathway analysis—i.e. the pathway library, the algorithm for pathway enrichment analysis, as well as the algorithm for topological analysis were specified. Specifically, the *Mus musculus* Kyoto Encyclopedia of Genes and Genomes (KEGG) or Small Molecule Pathway Database (SMPDB) was chosen as the library and the default specific pathway analysis algorithms, namely, hypergeometric test for over representation analysis and relative-betweenness centrality for pathway topology analysis were chosen. Pathways with p-value <0.05 were taken into consideration to be significant and discussed in this paper.

### **7.2.9 Lipid droplet quantification via BODIPY staining and flow cytometry analysis**

The microglial (CD11b<sup>+</sup>) cells from perfused brains of 5-7 months old female 5xFAD mice and age and sex-matched WT control mice were isolated. The cells were resuspended in 1x PBS and the total cell number was evaluated using a hemocytometer. The cells were then divided into different microcentrifuge tubes and pelleted in a centrifuge. The supernatant was removed and the cells were resuspended in 2  $\mu$ M BODIPY dye diluted in 1x PBS. The cells were then stained with the BODIPY dye for 1 hour at 37 °C (the tubes were left in the 37 °C incubator for 1 hour). After staining, the cells were pelleted in a centrifuge, the supernatant containing the BODIPY dye in PBS was removed and the cells were resuspended in around 500  $\mu$ L FACS buffer. The cells were analyzed on the Attune NxT flow cytometer (Invitrogen). Three minutes before analysis of each sample, DAPI was added to the sample (0.1  $\mu$ g/ mL cell suspension) for staining of dead cells. The

cells were gated on the forward and side scatter to remove any debris and doublets or triplets. Next, the cells appearing in the live gate were selected and the DAPI-stained dead cells were gated out. The live cells were then gated for their BODIPY expression. Appropriate controls for each dye including unstained cells were incorporated in the experiments for the accurate analysis of the flow plots.

#### **7.2.10 IBA1 and DGAT2 staining of cortical regions of 5xFAD and WT mouse brains**

For the staining of brain cortical tissue sections, the isolated mouse brains were post-fixed in paraformaldehyde followed by embedding in OCT and snap frozen over dry ice. The tissue was sectioned coronally on a vibratome to obtain the cortical slices of 10  $\mu$ m thickness that were then mounted on charged glass slides for staining procedure. The slides were dried for 30-60 mins in a 60 °C oven. After drying, all slides were deparaffinized through 3 changes of xylene and rehydrated through a gradient of ethanol to water. After deparaffinization, antigen retrieval was performed using a Tris-EDTA pH 9.0 solution at a temperature of 95 °C for 20 mins. Slides were cooled for 20 mins at room temperature (RT) and transferred to Tris buffer with Tween 20 detergent (TBST). The rest of the staining was carried out at RT using a BioCare Intellipath Stainer. The slides were incubated in 2.5% normal horse serum for 20 mins. Excess reagent was blown off and both primary antibodies, IBA1 (Abcam, ab48004) and DGAT (Abcam, ab237613) were applied at a dilution of 1:100 for 30 minutes. Slides were rinsed twice in TBST and secondary antibodies applied for 30 minutes. Donkey anti-goat AlexaFluor555 antibody was applied at 1:500 for 30 min (Invitrogen, A21432) and the goat anti-rabbit Dylight 488 secondary antibody (Invitrogen, DI-1488) was applied for 30 mins. Slides were rinsed twice in TBST and DAPI counterstain (Invitrogen, EN62248) applied at 1  $\mu$ g/mL for 10 minutes. Slides were rinsed in water and cover-slipped using Prolong Gold (Invitrogen, P36934). The images were taken using a Leica Versa8 whole-slide scanner and analyzed on Aperio ImageScope (Leica).

### **7.3 Results**

#### **7.3.1 Overview of lipid changes in A $\beta$ -treated BV2 microglia**

Cultured BV2 microglia were treated with 500 nM of A $\beta$  for 1 hour, 12 hours, or 24 hours to quantify the effect of changes in lipids over time. The total lipid content extracted from cell pellets

were subjected to MRM-profiling. A $\beta$ -treatment for 1 hour caused depletion of 5 lipids in BV2 microglia including 3 PS lipids (PSo(18:1), PS(14:1), and PSp (16:0)), 1 FFA, and 1 CE. PS on neuronal cell surface has been previously characterized as an “eat me” signal on neurons and other cells for microglial recognition and phagocytosis, however, the implications of PS on microglial surface itself is not well understood. It is quite possible that the initial acute exposure of A $\beta$  on cultured microglia causes them to become apoptotic.

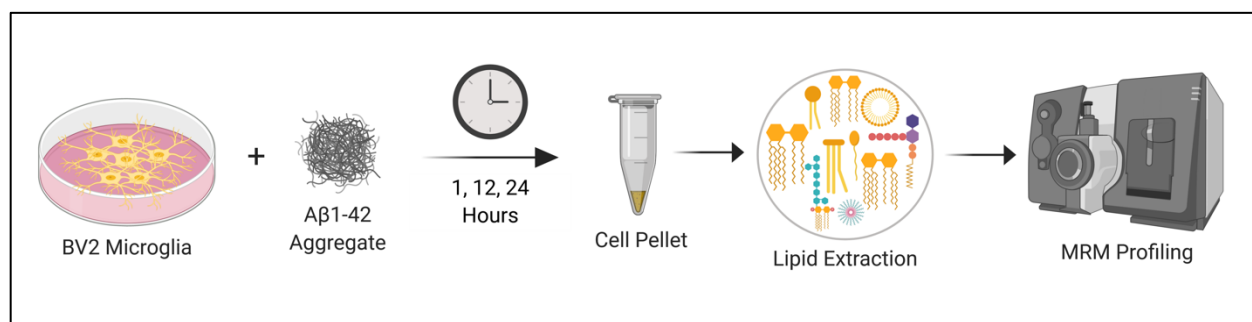


**Figure 7.1** Schematic of experimental protocol for MRM-profiling of A $\beta$ -treatment and BV2 microglia.

### 7.3.2 Select phospholipids were abundant in A $\beta$ -treated BV2 microglia at 24 hours

Out of the 152 MRMs related to PEs that were scanned, MRM-profiling revealed 19 PEs that were distinct between A $\beta$ -treated and vehicle-treated BV2 microglia at 24 hours. Furthermore, all of the 19 MRMs related to PEs were found to be 0.3x to 1.4x times more abundant at this timepoint whereas none of these PEs changed at 1 and 12 hour time points. Similarly, 4 MRMs related to PCs (out of 149 total PC and SM ion transitions) and 3 MRMs related to PI (out of 148 total ion transitions) exhibited differential profiles between the two groups with both the classes being around 0.3x times more abundant in the A $\beta$ -treated microglia compared to control BV2 microglia.

### 7.3.3 A $\beta$ -treatment caused depletion of select phospholipids and neutral lipids in BV2 microglia

While certain phospholipids were upregulated with A $\beta$  treatment at 24 hours, other classes of lipids including ceramides, cholesteryl esters, and triacylglycerols were downregulated in the same cells. The 24 hour A $\beta$  treatment significantly affected the abundance of PGs in these cells. Out of 152 PG total transitions, the presence of 6 lipids was significantly reduced with A $\beta$ -treatment. The acyl

chain lengths of all the 6 lipids were between 20 to 30 and all of them were saturated lipids. Similarly, 6 ceramides out of 81 transitions, 4 out of 148 PS transitions, 4 out of 385 total TAG transitions, and 2 out of 57 CE transitions were found to be depleted in A $\beta$ -treated BV2 microglia.

The downregulation of PSo(18:0) and PS(14:1) that were common in BV2 microglia with A $\beta$  treatment from 1 to 24 hours is noteworthy. The expression of PS on cell membranes indicates the activation of apoptotic mechanisms followed by their recognition, engagement, and removal via phagocytosis[3]. Here, the downregulation of PS in BV2 microglia with A $\beta$  exposure over time may suggest an “activated” state of BV2 cells. In neuronal co-cultures with microglia, it has been shown that PS expression on neurons can activate rat microglia towards an anti-inflammatory phenotype[3], [4]. It remains to be seen if PS expression on microglia indeed influence the neighboring microglia to exhibit anti- or pro-inflammatory states of activation.

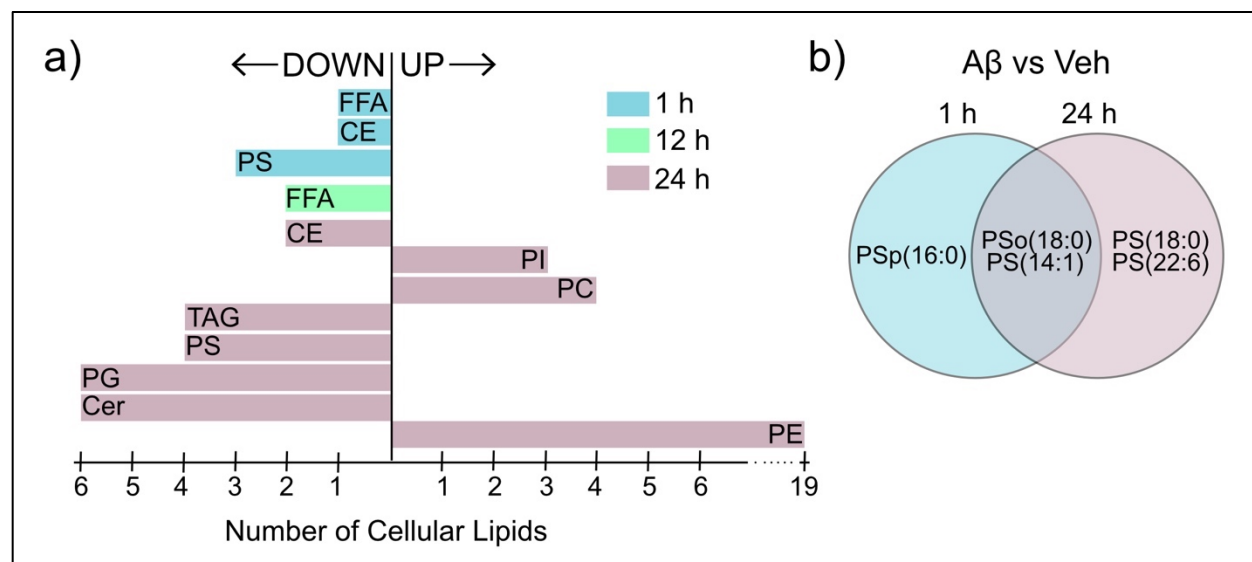


**Figure 7.2** (a) Total number of cellular lipids for each class that were differentially regulated at 1, 12, and 24 hours of A $\beta$  treatment in BV2 microglia. Right: upregulated lipids, Left: downregulated lipids. (b) Lipids that were common between 1 and 24 hour of A $\beta$  treatment in BV2 microglia.

PCA plots generated based on the significantly different lipids showed distinct separation of the A $\beta$  and vehicle-treated microglial groups and principle components (PCs) 1 and 2 explained 97.2% of the dataset variance for 1 hour indicating dramatic changes occurring in BV2 microglial lipidome at this initial time point. Next, PCA plots accounted for 100% variation in dataset for 12



hour, and 87.9% for 24 hour treatment. Taken together, these results demonstrate that *in vitro* A $\beta$  exposure for 24 hours correlates with increased presence of certain select phospholipids like PE, PC, and PI lipids in BV2 microglia, possibly indicating changes to cell membrane due to their A $\beta$ -mediated activated status.

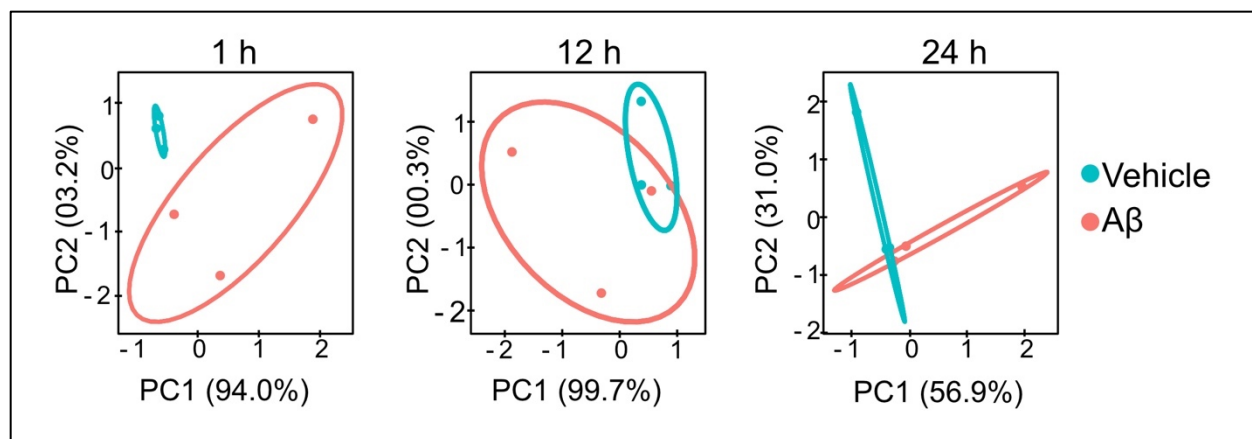


**Figure 7.3** PCA plots showing separation between lipids in A $\beta$  treated (red) and vehicle-treated BV2 microglia.

**Table 7-2** Differentially regulated lipids in A $\beta$ -activated BV2 microglia at 1 hour.

Lipids	MRM Transition	Log <sub>2</sub> FC	P value	FDR
<b>Upregulated Lipids</b>				
N/A				
<b>Downregulated Lipids</b>				
PSo (18:0)	512.3348 -> 327.3348	-1.871	9.87E-30	1.32E-26
PS (14:1)	468.2358 -> 283.2358	-1.683	1.27E-24	8.44E-22
15:1 Cholesteryl ester	626.5532 -> 369.1	-0.676	2.76E-05	0.01228
PSp (16:0)	482.2879 -> 297.2879	-0.599	2.16E-04	0.07172
C15:1	239.3 -> 239.3	-0.584	2.69E-04	0.07172

**Table 7-3** Differentially regulated lipids in A $\beta$ -activated BV2 microglia at 12 hours.

Lipid	Transition	Log <sub>2</sub> FC	P value	FDR
<b>Upregulated Lipids</b>				
N/A				
<b>Downregulated Lipids</b>				
C18:0	283.3 -> 283.3	-0.879	1.74E-06	0.00232
C16:0	255.3 -> 255.3	-0.682	1.98E-04	0.13193

**Table 7-4** Upregulated lipids in A $\beta$ -activated BV2 microglia at 24 hours.

<b>Lipid</b>	<b>Transition</b>	<b>Log<sub>2</sub>FC</b>	<b>P value</b>	<b>FDR</b>
PEo (38:6)	750.5433 -> 609.5433	1.416	1.11E-21	1.47E-18
PE (18:1)	480.3086 -> 339.3086	1.36	4.24E-20	2.83E-17
PE (22:6)	526.2929 -> 385.2929	1.044	1.64E-12	7.28E-10
PE (38:0)	776.6165 -> 635.6165	0.716	9.38E-07	1.56E-04
PE (20:3)	504.3086 -> 363.3086	0.685	3.49E-06	4.65E-04
PE (21:0)	524.3348 -> 383.3348	0.564	1.39E-04	0.013194
PE (20:4)	502.2929 -> 361.2929	0.528	3.21E-04	0.027958
PE (18:2)	478.2929 -> 337.2929	0.512	5.07E-04	0.037548
PE (18:0)	482.3242 -> 341.3242	0.497	7.15E-04	0.043373
PI (38:3)	906.5802 -> 629.5802	0.451	0.002040423	0.097139

**Table 7-5** Downregulated lipids in A $\beta$ -activated BV2 microglia at 24 hours.

<b>Lipid</b>	<b>Transition</b>	<b>Log<sub>2</sub>FC</b>	<b>P value</b>	<b>FDR</b>
PSo (18:0)	512.3348 -> 327.3348	-0.959	4.88E-11	1.63E-08
PS (14:1)	468.2358 -> 283.2358	-0.851	5.25E-09	1.40E-06
PG (24:0)	628.392 -> 439.392	-0.841	1.22E-08	2.72E-06
16:0 Cholesteryl ester	642.5845 -> 369.1	-0.751	2.77E-07	5.27E-05
15:0 Campesteryl ester_simulated	642.6002 -> 369.1	-0.707	1.30E-06	1.92E-04
Cer(t18:0/20:0(2OH))	628.6 -> 282.4	-0.647	9.90E-06	0.001199
PG (20:0)	572.3294 -> 383.3294	-0.639	1.45E-05	0.001609
PG (30:0)	712.4859 -> 523.4859	-0.609	3.81E-05	0.003905
Cer(d18:0/20:0(2OH))	612.6 -> 266.4	-0.523	3.36E-04	0.027958
PS (22:6)	570.2828 -> 385.2828	-0.513	4.96E-04	0.037548
PG (28:0)	684.4546 -> 495.4546	-0.508	5.97E-04	0.041865
PS (18:0)	526.3141 -> 341.3141	-0.501	6.78E-04	0.043373
PG (26:0)	656.4233 -> 467.4233	-0.495	7.89E-04	0.045712
Cer(d14:2(4E,6E)/16:0)	480.4 -> 206.3	-0.494	7.16E-04	0.043373
TAG(54:1)_FA 20:0	906.8 -> 577.8	-0.468	0.00157851	0.085553
TAG(54:2)_FA 18:1	904.8 -> 605.8	-0.461	0.001918592	0.094722
Cer(t18:0/24:0(2OH))	684.7 -> 282.4	-0.461	0.001604525	0.085553
Cer(t18:0/22:0(2OH))	656.6 -> 282.4	-0.451	0.001911221	0.094722

### 7.3.4 Overview of cellular lipid profiles of A $\beta$ -treated primary mouse microglia

Even though microglia isolated from rodent brains and cultured *ex vivo* (termed primary microglia) do not completely recapitulate the transcriptomic profile of microglia *in vivo*[5], primary microglia grown in serum-free or reduced-serum conditions with highly defined medium can still closely preserve the *in vivo* cellular phenotypes[6]. Here, we isolated microglia from adult (7 month old) mice and cultured them in low-serum containing defined media in order to evaluate the changes in their lipid and metabolite profiles upon A $\beta$  treatment. Interestingly, out of all the lipids analyzed, FFAs were the most differentially regulated lipids with the initial time points of 1 and 12 hour A $\beta$  treatment (32% and 36% of the total differential lipids in the cells respectively) and TAGs were the most differentially regulated at 24 hours. The amount of TAGs increased in primary microglia from 1 to 24 hours indicating the effect of A $\beta$  stress on cellular neutral lipids with further implications to their phenotypes discussed below.

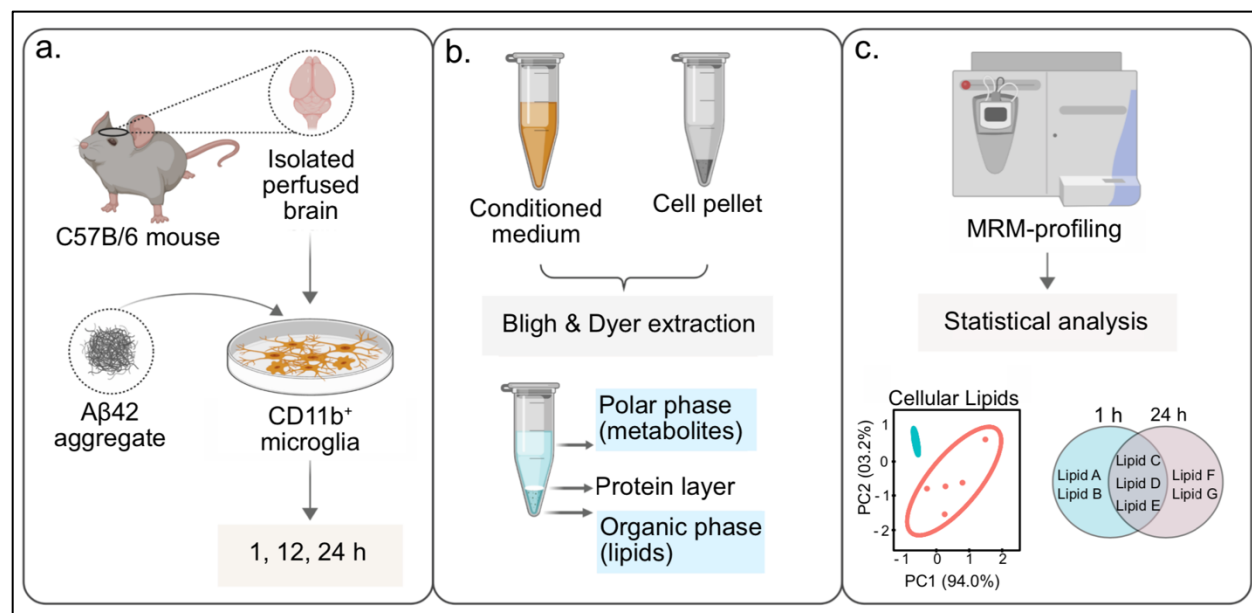


**Figure 7.4** Schematic of experimental protocol for MRM-profiling of primary microglia. (a) Isolation, culture, and treatment of microglia. Microglia were isolated from adult C57B/6 mice and cultured in low-serum containing defined medium. Aggregated A $\beta$ 1-42 was added to the cells for 1, 12, or 24 hours. (b) Samples processing. The cell pellets and the conditioned medium were collected at each time point and subjected to Bligh & Dyer protocol for lipid extractions. Lipid were isolated from organic phase and metabolites were isolated from polar phase. (c) MRM-profiling and analysis. MRM-profiling of lipids and metabolites was performed to identify statistically significant lipids and metabolites in A $\beta$  treated versus vehicle-treated microglia.

In primary microglia activated by A $\beta$  for 1 hour, 32 MRM transitions were found to be significant (FDR<0.1) out of which 22 were abundant and 10 were found to be depleted compared to the vehicle-treated control cells. Three saturated FFAs, namely, C20:0, C22:0, and C19:0 were the most abundant lipids in the A $\beta$ -treated cells. Among the phospholipids, 4 PEs and 2 PGs were uniquely identified in the A $\beta$  activated microglia. We note that PCs with 32 acyl chain length with 1 to 3 C=C double bonds were upregulated with A $\beta$  activation whereas longer chain length PCs which 38-42 carbon atoms and 2 to 10 C=C double bonds were depleted in these cells. Additionally, 3 TAGs and 2 ACs, which are both localized in the intracellular space and participate in fatty acid metabolism, were uniquely identified in these cells.

With 12 hour activation of A $\beta$ , a total of 22 lipids were found to be significantly regulated between A $\beta$  and control-treated microglia out of which 14 lipids were upregulated and 8 lipids were depleted in A $\beta$ -activated cells. The upregulated lipids included 5 FFAs, 3 CEs, 1 AC, 1 TAG, and 3 PS that are well uniquely identified in the A $\beta$ -activated primary microglia. 3 classes of phospholipids, namely, PGs, PI, and PE were uniquely identified in control microglia alone. Over time, with 24 hour A $\beta$  activation, the number of significantly regulated lipids between the two cell groups reduced to 16 out of which TAGs and PGs were found to be abundant in the A $\beta$ -activated primary microglia.

There were 8 common lipids (all tentative attributions) identified in the 1 and 24 hour datasets possibly indicating common mechanisms correlated to the continued activation state of microglia due to A $\beta$  exposure. Specifically, 20:3 campesteryl ester, C20:0 (arachidic acid), PG20:0, and PG 20:3 were found to be upregulated in A $\beta$ -activated primary microglia over time i.e. from 1 to 24 hours. Cerotic acid (C(26:0)), C(26:1), and C(30:0) were consistently downregulated with A $\beta$ -activation over time at 1 and 24 hour treatments. Interestingly, TAG(54:0) containing C18:0 as one of the fatty acyl residues was upregulated at 1 hour but downregulated with 24 hours of A $\beta$  exposure.

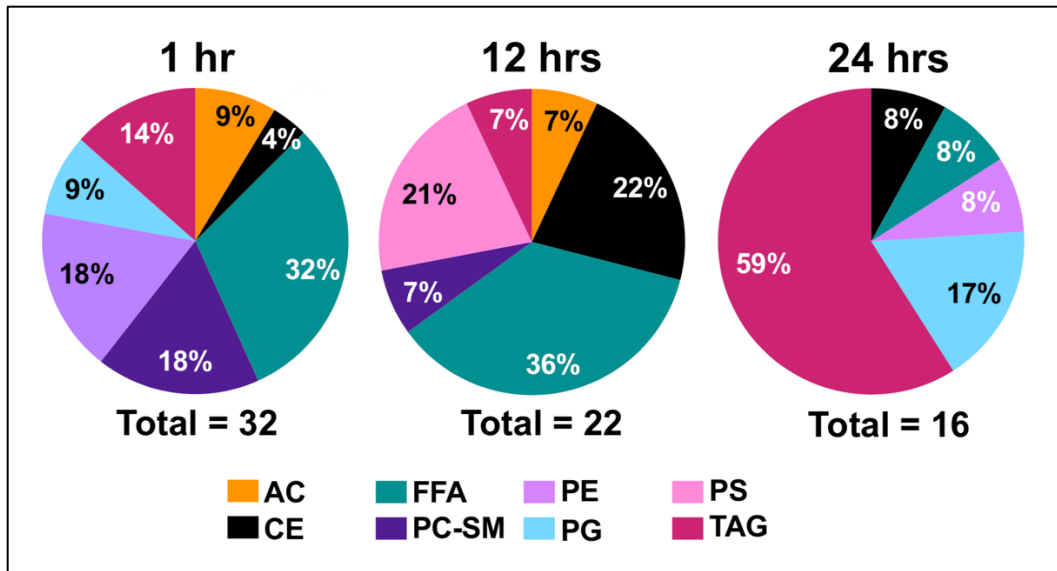


**Figure 7.5** Percent distribution of differentially regulated lipid classes in primary microglia at 1, 12, and 24 hours of A $\beta$  treatment (significant lipids).

PCA plots generated based on the significantly different lipids in primary microglia showed distinct separation of the A $\beta$  and vehicle-treated microglial groups and principle components (PCs) 1 and 2 explained 70.5% of the dataset variance for 1 hour, 64.7% for 12 hour, and 65.1% for 24 hour treatment. We hypothesize that the heterogeneity of primary microglial cultures compared to the primarily homogenous BV2 cell line contributes to the increased differences in the lipid profiles within the different groups of A $\beta$ -activated primary microglia in our data.

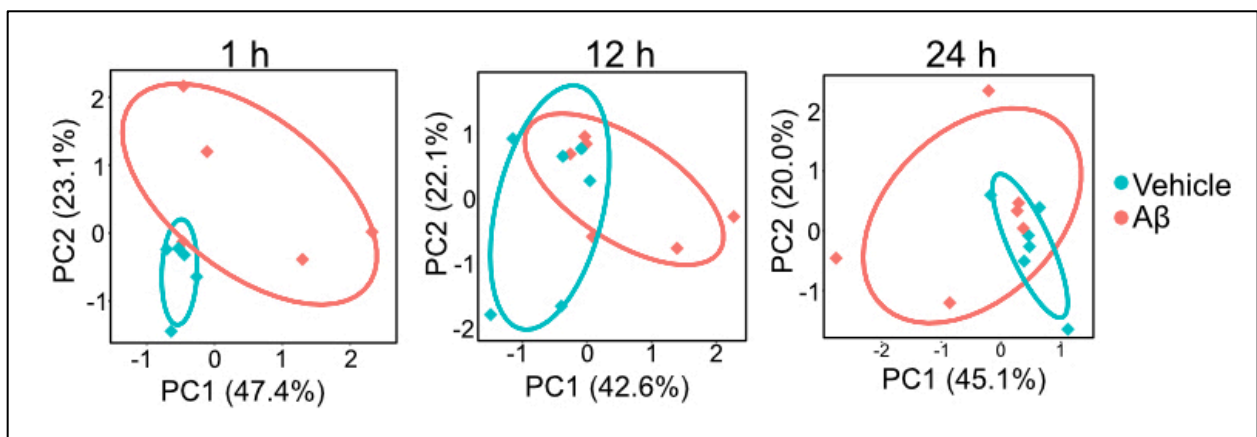


**Figure 7.6** Principle Component Analysis (PCA) plots showing separation between lipids in A $\beta$  treated (red) and vehicle-treated primary microglia.

**Table 7-6** Upregulated lipids in A $\beta$ -activated primary microglia at 1 hour (A $\beta$  vs. Vehicle-treated microglia; FDR<0.1).

Lipid	MRM Transition	Log <sub>2</sub> FC	P Value	FDR
C20:0	311.3 -> 311.3	1.6879832	1.68E-46	2.27E-43
C22:0	339.3 -> 339.3	1.5109162	5.75E-38	3.88E-35
PE (18:1)	480.3086 -> 339.3086	0.7482792	1.42E-10	6.41E-08
C19:0	297.3 -> 297.3	0.7069199	8.84E-10	2.98E-07
C22:6	327.3 -> 327.3	0.6208289	7.16E-08	1.93E-05
PE (34:2)	716.5226 -> 575.5226	0.5757071	7.24E-07	1.09E-04
20:3 Campesterol ester	706.6158 -> 369.1	0.5742709	6.41E-07	1.08E-04
PCo(32:3)	714.5 -> 184.1	0.5544737	1.97E-06	2.66E-04
TAG(54:0)_FA 18:0	908.9 -> 607.896	0.5135383	9.71E-06	0.00106718
PG (20:0)	572.3294 -> 383.3294	0.5087903	1.19E-05	0.00106718
PC (32:2)	730.5 -> 184.1	0.5063731	1.13E-05	0.00106718
C17:1	267.3 -> 267.3	0.4841384	2.61E-05	0.00207368
PG (24:0)	628.392 -> 439.392	0.4583927	7.75E-05	0.00580467
C20:1	309.3 -> 309.3	0.3990322	5.20E-04	0.03342873
(13Z,16Z)-docosadienoylcarnitine	480.4 -> 85.1	0.3911683	7.13E-04	0.04371419
TAG(50:1)_FA 18:1	852.8 -> 553.8	0.3904579	8.94E-04	0.04824671
PE (20:1)	508.3399 -> 367.3399	0.3892501	8.56E-04	0.04810491
C18:2	279.3 -> 279.3	0.3838601	8.46E-04	0.04810491
PE (34:1)	718.5383 -> 577.5383	0.3767449	0.00108065	0.05606932
Stearidonyl carnitine	420.3 -> 85.1	0.3678706	0.00141397	0.0657741
TAG(52:0)_FA 18:0	880.8 -> 579.8	0.3585599	0.00198752	0.08937235
PC (32:1)	732.6 -> 184.1	0.353215	0.00211613	0.09208578



**Table 7-7** Downregulated lipids in A $\beta$ -activated primary microglia at 1 hour (A $\beta$  vs. Vehicle-treated microglia; FDR<0.1).

<b>Lipid</b>	<b>MRM Transition</b>	<b>Log<sub>2</sub>FC</b>	<b>P Value</b>	<b>FDR</b>
C26:1	393.3 -> 393.3	-0.59348436	2.56E-07	5.76E-05
C30:0	451.4 -> 451.4	-0.57888311	5.03E-07	9.69E-05
PSo (18:0)	512.3348 -> 327.3348	-0.50494455	1.14E-05	0.00106718
C26:0	395.3 -> 395.3	-0.50441227	1.17E-05	0.00106718
PS (14:1)	468.2358 -> 283.2358	-0.48775788	2.25E-05	0.00189665
C18:3	277.3 -> 277.3	-0.41904571	2.71E-04	0.01922269
PC (42:10)	854.6 -> 184.1	-0.4099137	3.94E-04	0.02659761
PS (36:8)	776.4498 -> 591.4498	-0.37300527	0.00120207	0.05791414
PCo(38:5)	794.6 -> 184.1	-0.37282045	0.00119193	0.05791414
PCo(42:2)	856.7 -> 184.1	-0.35429765	0.00219109	0.09236833

**Table 7-8** Upregulated lipids in A $\beta$ -activated primary microglia at 12 hours (A $\beta$  vs. Vehicle-treated microglia; FDR<0.1).

Lipid	Transition	Log <sub>2</sub> FC	P Value	FDR
20:2 Cholesteryl ester, 18:1 Stigmasteryl ester, 18:2 Sitosteryl ester	694.6158 -> 369.1	0.9068327	1.27E-24	1.72E-21
24:1 Cholesteryl ester, 22:0 Stigmasteryl ester, 22:1 Sitosteryl ester	752.6941 -> 369.1	0.8783231	3.32E-23	2.24E-20
16:3 Cholesteryl ester	636.5376 -> 369.1	0.8427626	1.61E-21	7.24E-19
(5Z,8Z)- tetradecadienoylcarnitine	368.3 -> 85.1	0.5782358	4.75E-11	1.07E-08
C26:1	393.3 -> 393.3	0.4346097	6.21E-07	1.05E-04
C15:1	239.3 -> 239.3	0.3780742	1.45E-05	0.0019591
PS (14:1)	468.2358 -> 283.2358	0.360846	3.48E-05	0.00427023
PSo (18:0)	512.3348 -> 327.3348	0.3510625	5.61E-05	0.00586269
C26:0	395.3 -> 395.3	0.3471851	6.77E-05	0.00652399
PC (42:4)	866.7 -> 184.1	0.3430496	1.06E-04	0.00894984
C16:1	253.3 -> 253.3	0.3304944	1.52E-04	0.01203494
TAG(60:8)_FA 20:0	976.9 -> 647.9	0.3117654	4.54E-04	0.03403174
PS (28:0)	680.4498 -> 495.4498	0.2932297	7.87E-04	0.05307606
C20:1	309.3 -> 309.3	0.2752723	0.00158406	0.09713142

**Table 7-9** Downregulated lipids in A $\beta$ -activated primary microglia at 12 hours (A $\beta$  vs. Vehicle-treated microglia; FDR<0.1).

<b>Lipid</b>	<b>Transition</b>	<b>Log<sub>2</sub>FC</b>	<b>P Value</b>	<b>FDR</b>
PG (24:0)	628.392 -> 439.392	-0.72904752	1.85E-16	6.24E-14
PG (26:0)	656.4233 -> 467.4233	-0.58644359	4.07E-11	1.07E-08
PG (20:0)	572.3294 -> 383.3294	-0.50682421	1.04E-08	2.00E-06
TAG(48:1)_FA 16:0	822.8 -> 549.8	-0.4169503	3.31E-06	4.97E-04
TAG(54:3)_FA 18:1	902.8 -> 603.8	-0.35653754	5.65E-05	0.00586269
PEo (36:2)	730.5746 -> 589.5746	-0.35182886	7.73E-05	0.00695318
PI (36:1)	882.5802 -> 605.5802	-0.30868941	4.86E-04	0.03451893
PG (28:0)	684.4546 -> 495.4546	-0.28376368	0.00145624	0.09354617

**Table 7-10** Differentially regulated lipids in A $\beta$ -activated primary microglia at 24 hours (A $\beta$  vs. Vehicle-treated microglia; FDR<0.1).

Lipid	Transition	Log <sub>2</sub> FC	P Value	FDR
<b>Upregulated Lipids</b>				
TAG(52:3)_FA 18:1	874.8 -> 575.8	0.7224398	5.38E-11	7.25E-08
TAG(54:3)_FA 18:1	902.8 -> 603.8	0.5379654	8.75E-07	3.26E-04
PG (20:0)	572.3294 -> 383.3294	0.5357878	9.66E-07	3.26E-04
PG (24:0)	628.392 -> 439.392	0.5272322	1.36E-06	3.67E-04
TAG(52:2)_FA 18:1	876.8 -> 577.8	0.4893567	7.72E-06	0.00173599
TAG(52:3)_FA 18:2	874.8 -> 577.8	0.4554288	3.57E-05	0.00602319
C20:0	311.3 -> 311.3	0.4518256	2.96E-05	0.0057059
20:3 Campesteryl ester	706.6158 -> 369.1	0.4369285	5.54E-05	0.00747216
TAG(50:2)_FA 16:0	850.8 -> 577.8	0.4326664	7.44E-05	0.00912263
TAG(52:3)_FA 16:0	874.8 -> 601.8	0.3954692	3.27E-04	0.03388214
TAG(50:3)_FA 16:0	848.8 -> 575.8	0.3770093	6.02E-04	0.05411171
PE (20:4)	502.2929 -> 361.2929	0.354025	0.00109327	0.09217607
<b>Downregulated Lipids</b>				
C26:1	393.3 -> 393.3	-0.57900188	9.03E-08	6.09E-05
C26:0	395.3 -> 395.3	-0.43818416	5.11E-05	0.00747216
TAG(54:0)_FA 18:0	908.9 -> 607.896	-0.42057757	1.20E-04	0.01344779
C30:0	451.4 -> 451.4	-0.38130443	4.23E-04	0.04074293

### **7.3.5 Increased cellular FFAs defines initial microglial state with A $\beta$ exposure**

FFAs were the most differentially regulated lipids that were abundant in microglia with initial A $\beta$  exposure. Three saturated FFAs, namely, C20:0, C22:0, and C19:0 were the most abundant lipids in these cells. Several studies conducted in peripheral macrophages have indicated that the accumulation of FFAs in cells results in lipotoxicity and fatty acid-induced apoptosis[7]–[9]. Our data showed an upregulation of FFAs in microglia with initial treatment to A $\beta$ , thereby suggesting an initial cell state due to the direct response to an environmental inflammatory insult. It has also been shown in peripheral immunity that saturated and unsaturated FFAs differ in their contributions to lipotoxicity (accumulation of excess lipids leading to cell dysfunction or cell death). Specifically, the presence of saturated FFA alone may cause cellular toxicity and cell death. However, in the presence of both saturated and unsaturated FFAs, it has been shown that the unsaturated FFAs are required to sequester the saturated FFAs in order to metabolize them into TAGs within the lipid droplets[2] via the initiation of the glycerol phosphate pathway[10]. Lipotoxicity from accumulated long chain FFAs may thus be specific to saturated FFAs[11]–[13] (as seen with our astrocyte studies), however, this mechanism may vary with respect to cell type and environment.

### **7.3.6 Prolonged exposure to A $\beta$ leads to TAG accumulation in primary microglia**

With prolonged A $\beta$  exposure, we see an upregulation of TAGs and a depletion of FFAs in microglia which indicates a shift in microglial metabolic state. A similar switch in lipid processing is seen in the periphery, specifically in the adipocytes that have a unique capacity to store excess FFAs in the form of triglyceride in lipid droplets. It was also recently shown that microglia accumulate lipid droplets that are rich with TAGs with age[1], however, whether these lipid droplets are protective or detrimental to microglial cell state and function has not been well defined. We hypothesize that TAG accumulation in response to increased cellular levels of FFAs may be a general metabolic phenomenon in microglia in response to acute inflammatory triggers like A $\beta$ . It must be noted that TAGs serve as the predominant form of energy storage in mammalian cells[10]. We thus speculate that primary microglial cells may be entering a “hibernation” state by producing an abundance of TAGs due to the prolonged effect A $\beta$  induced inflammation in culture.

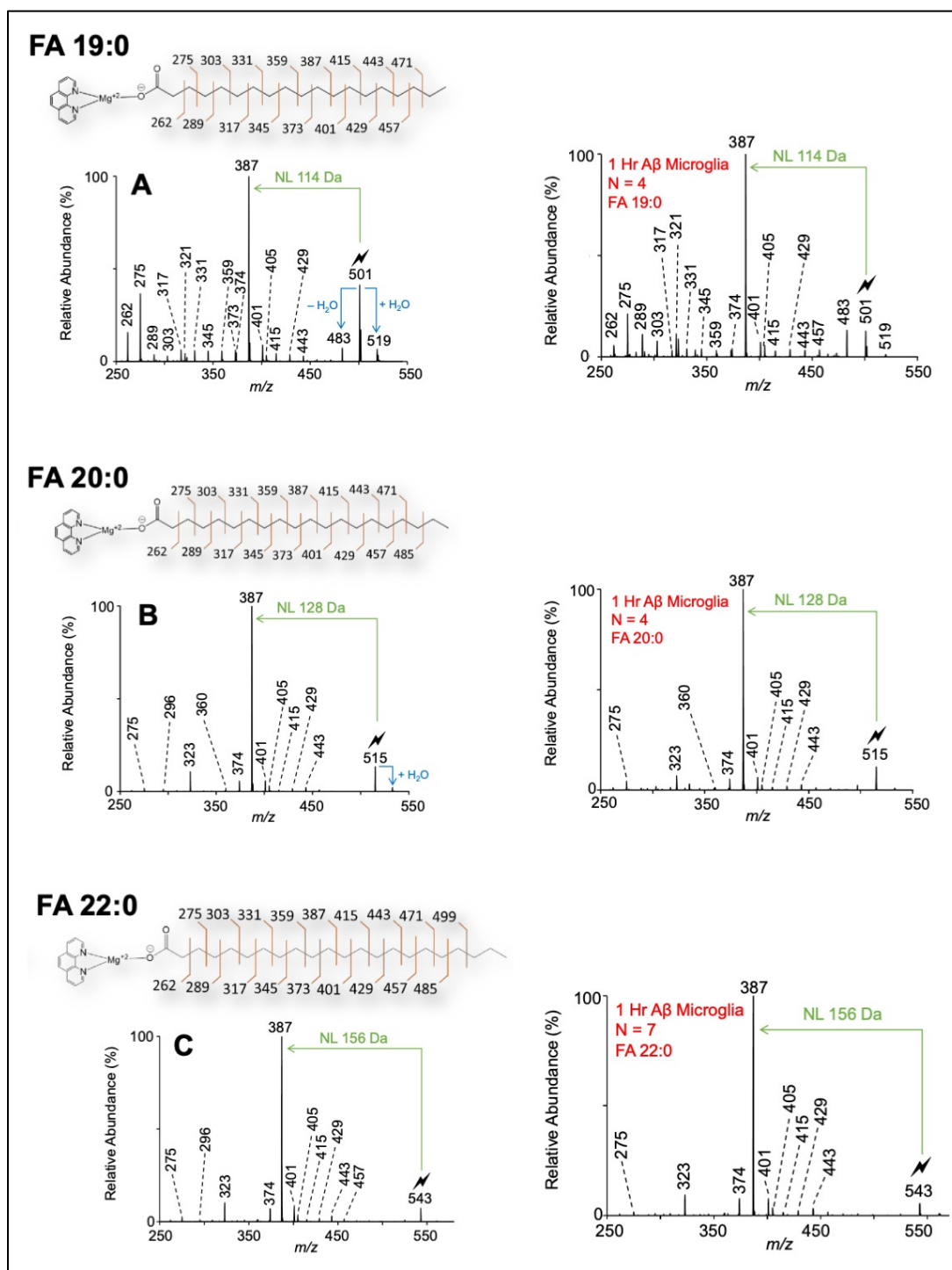


**Figure 7.7** Structures of C19:0, C20:0, and C22:0 were validated using gas-phase ion/ion chemistries. The plots on the left panel are from the standard lipids used to determine the mass of the lipid fragments upon neutral loss (NL). The plots on the right are from the microglia cell samples wherein the lipids with the same NL masses ( $m/z$ ) were identified thereby confirming the presence of the three saturated FFAs in the sample.

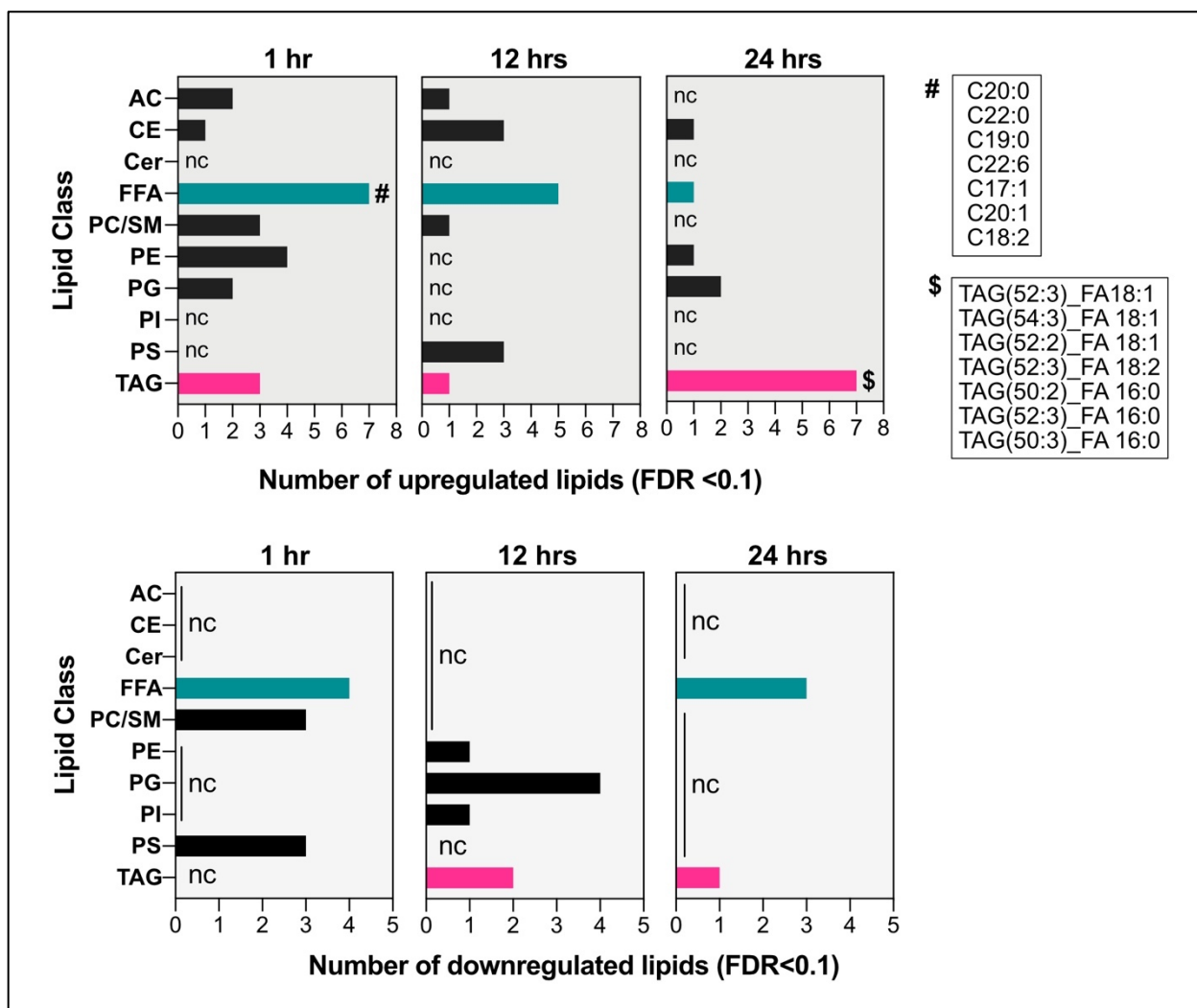


**Figure 7.8** Total number of cellular lipid species for each lipid class that were (top) upregulated and (bottom) downregulated at 1, 12, and 24 hours of A $\beta$  treatment. The specific upregulated lipid species for the FFA (#) and TAG (\$) classes are listed in the boxes on top right.

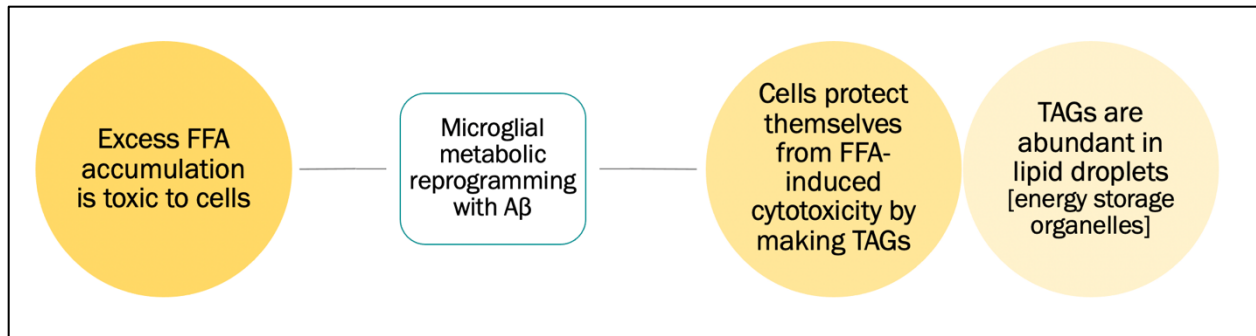


**Figure 7.9** Working hypothesis to explain the microglial cell states due to FFA and TAG interplay due to initial and prolonged A $\beta$  treatment

### 7.3.7 TAG biosynthesis in mammalian cells

Given the abundance of TAGs with prolonged A $\beta$  treatment *ex vivo*, we next asked *What genes (and proteins) are involved in the biosynthesis of TAGs in mammalian cells?* Identifying the specific genes and proteins involved in TAG biosynthesis will be useful in modulating microglial states by reprogramming their cellular metabolism in inflammation. There are two pathways that lead to the production of TAGs in cells: 1) the glycerol phosphate pathway and 2) the monoacylglycerol pathway. The former pathway is “turned on” in all cells at all times during normal cell function and survival. The later pathway is unique to lipid droplets and involves two major enzyme classes: MGAT (Monoacylglycerol acyltransferases) and DGAT (Diacylglycerol acyltransferases). Interestingly, single cell RNA sequencing study has previously demonstrated that the *Dgat2* gene is upregulated in WT microglia upon lipopolysaccharide treatment compared to the WT control microglia[14]. This suggests a possible role for DGAT2 protein in microglia in response to an inflammatory trigger. Thus, evaluating the gene and protein expression of DGAT2 in microglia with A $\beta$  treatment (acute inflammation) as well as in microglia isolated from 5xFAD mice (chronic inflammation) may identify this lipid-associated protein to be unique to microglia under inflammation.



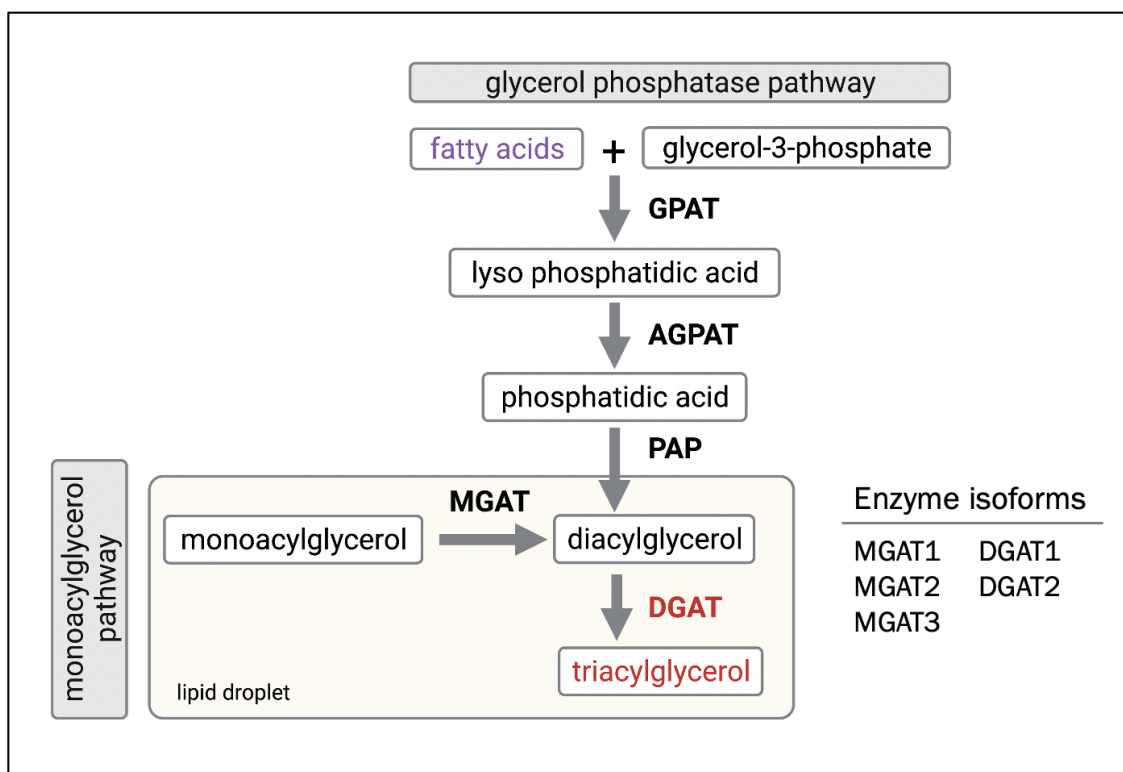


**Figure 7.10** An overview of TAG biosynthesis in cells. Two pathways that lead to the production of TAGs in cells: the glycerol phosphate pathway and the monoacylglycerol pathway.

### 7.3.8 Microglia from 5xFAD female mice accumulate more lipid droplets compared to WT mice

Since TAGs are predominantly found in lipid droplets (LDs) within the cells, we asked if microglia in a diseased brain environment would show an abundance of LDs due to inflammation. 5xFAD mice are an aggressive model for AD which express human APP and PSEN1 transgenes with a total of five AD-linked mutations[15], [16]. 5xFAD mice exhibit the A $\beta$  pathology starting 2-3 months of age with increased microgliosis and inflammation. We thus used adult male and female mice in order to evaluate if 5xFAD mice exhibited an abundance of LDs due to their A $\beta$  pathology and chronic inflammation compared to age-matched WT mice. LDs are tiny cellular organelles surrounded by a lipid monolayer and have a core comprising mostly of neutral lipids including cholesteryl esters and TAGs. Neutral lipids can be stained with the BODIPY dye 493/503 nm. Indeed, female microglia (CD11b<sup>+</sup> cells) from 5xFAD mice exhibited increased LDs (BODIPY<sup>+</sup> cells) compared to microglia isolated from WT mice. We observed that all the microglial cells (homogenous population) from 5xFAD mice showed an increase in BODIPY fluorescence

compared to the WT female microglia (1.5 fold increase) suggesting greater LD accumulation in these cells.

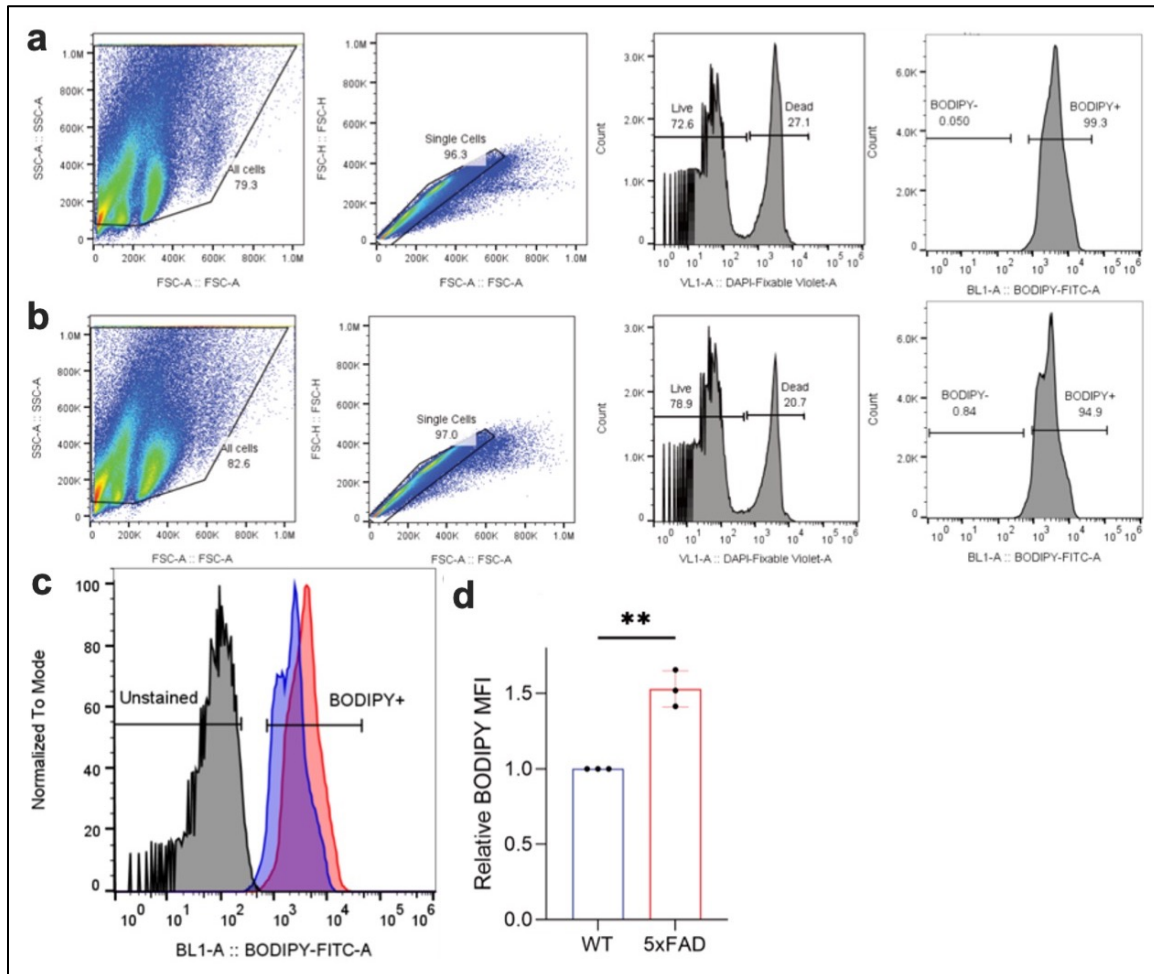


**Figure 7.11** BODIPY staining on acutely isolated CD11b+ cells from WT and 5xFAD female mice. Gating strategy for flow cytometry analysis of (a) WT sample and (b) 5xFAD sample stained with BODIPY and DAPI. (c) No green fluorescence was measured in unstained cells (shown in black) whereas a strong green fluorescence signal was measured in DAPI- cells stained with BODIPY both in case of WT (shown in blue) and 5xFAD (shown in red). Data shown in terms of % max, by scaling each curve to mode = 100% (y-axis). (d) Comparison of BODIPY Median Fluorescence Intensity (MFI) normalized to WT (unpaired t-test,  $P = .0016$ ). (n=2, where each group contained 1-2 female C57BL/6 mice and 1-2 female 5xFAD mice)

### **7.3.9 Microglia from 5xFAD male mice show a subset of cells that accumulate more lipid droplets compared to WT mice**

It is well-known that incidence of Alzheimer's disease is higher in females than males. We next asked if 5-7 months old 5xFAD male mice have lipid associated microglia. We found no significant change in MFI of BODIPY<sup>+</sup> microglial cells between WT and 5xFAD males overall. However, there was a subset of cells which have higher BODIPY expression suggesting increase in lipid droplets. This is in contrast to lipid accumulation in female 5xFAD mice suggesting differences in inflammation between sexes. In conclusion, only a subset of male microglia isolated from 5xFAD mice showed an increase LD-accumulated microglia compared to WT male microglia thereby indicating a sex specificity in microglial LD accumulation.

### **7.3.10 Age is a factor for lipid droplet accumulation in microglia**

A recent study showed that microglia in aged brains accumulated more LDs compared to microglia from young brains[1]. Further, it was shown that these lipid droplet-accumulating microglia exhibited a dysfunctional phenotype with reduced phagocytic capacity. Thus, age is an important factor for evaluating lipid droplet formation in microglia that may lead to cellular dysfunction and alerted phenotypes during inflammation. Thus, we asked if age is a factor that affects lipid accumulating microglia in 5xFAD female mice, as it is known that severe amyloid-beta pathology in the brain in these mice occurs from ages 3-4 month onwards. Interestingly, we found no significant difference in the BODIPY<sup>+</sup> microglial cells in 5xFAD female mice compared to age-matched WT female mice thereby suggesting the lipid accumulated dysfunction may occur over a longer period of time. This is in contrast with our previous finding that demonstrated a stark difference in LDs in microglia from older female mice (5-7 months of age) further proving that age is a factor for lipid droplet accumulation in microglia.

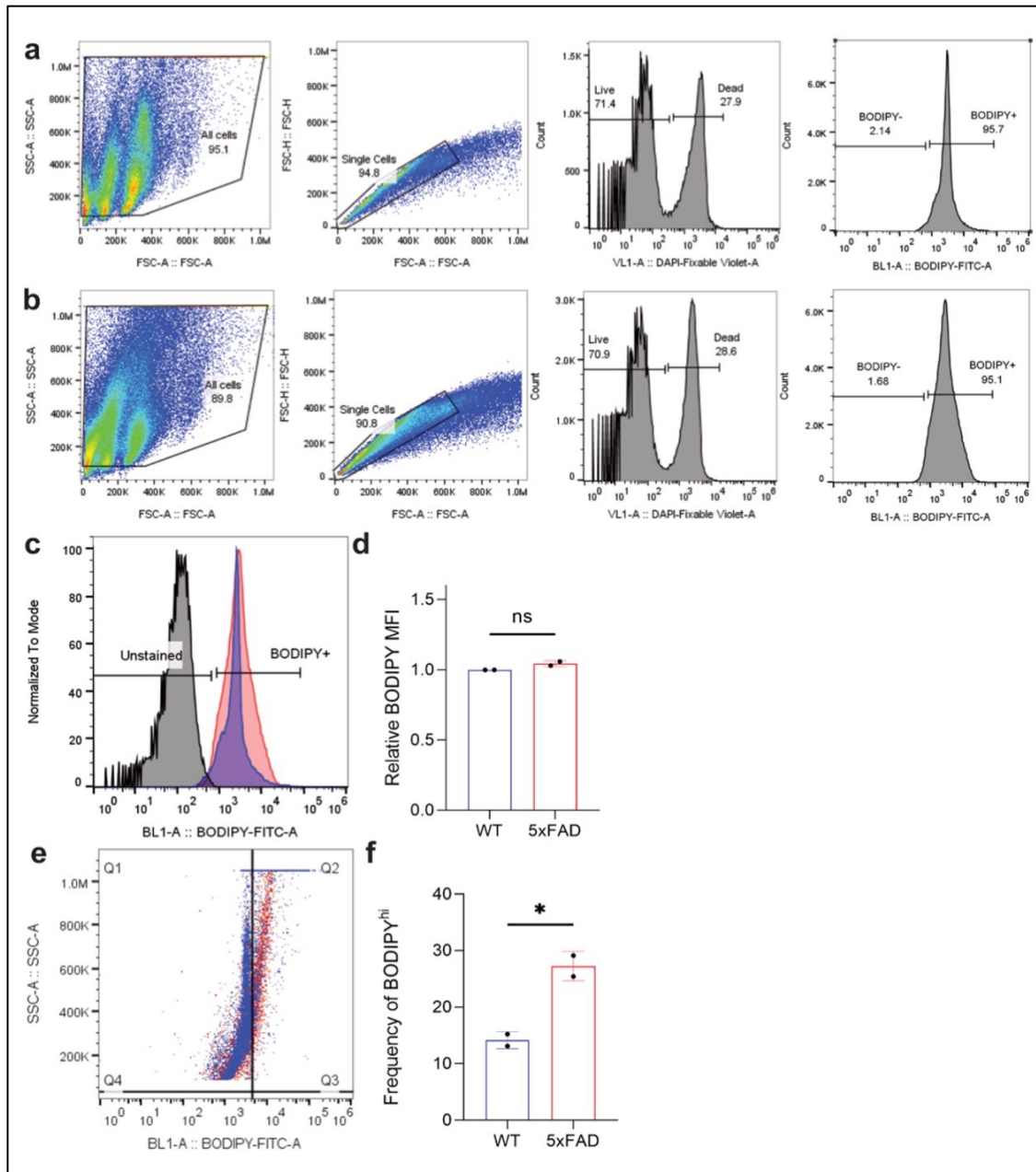


**Figure 7.12** BODIPY staining on acutely isolated CD11b<sup>+</sup> cells from WT and 5xFAD male mice: Gating strategy for flow cytometry analysis of (a) WT sample (b) 5xFAD for BODIPY<sup>+</sup> cells. (c) No green fluorescence was measured in unstained cells (shown in black) whereas a strong green fluorescence signal was measured in DAPI- cells treated 2 $\mu$ M BODIPY for 1 hour at 37°C both in case of WT (shown in blue) and 5xFAD (shown in red). Data shown in terms of % max, by scaling each curve to mode = 100% (y-axis). (d) Comparison of BODIPY Median Fluorescence Intensity (MFI) normalized to WT (unpaired t-test,  $P = .0918$ ). (e) Dot plot for DAPI- cells in WT and 5xFAD sample showing BODIPY<sup>hi</sup> (Q2) and BODIPY<sup>lo</sup> (Q1) population (f) Comparison of Frequency of BODIPY<sup>hi</sup> cells in WT v/s 5xFAD (unpaired t-test,  $P = .0254$ ). (n=1, containing 2 male C57BL/6 mice and 2 male 5xFAD mice)

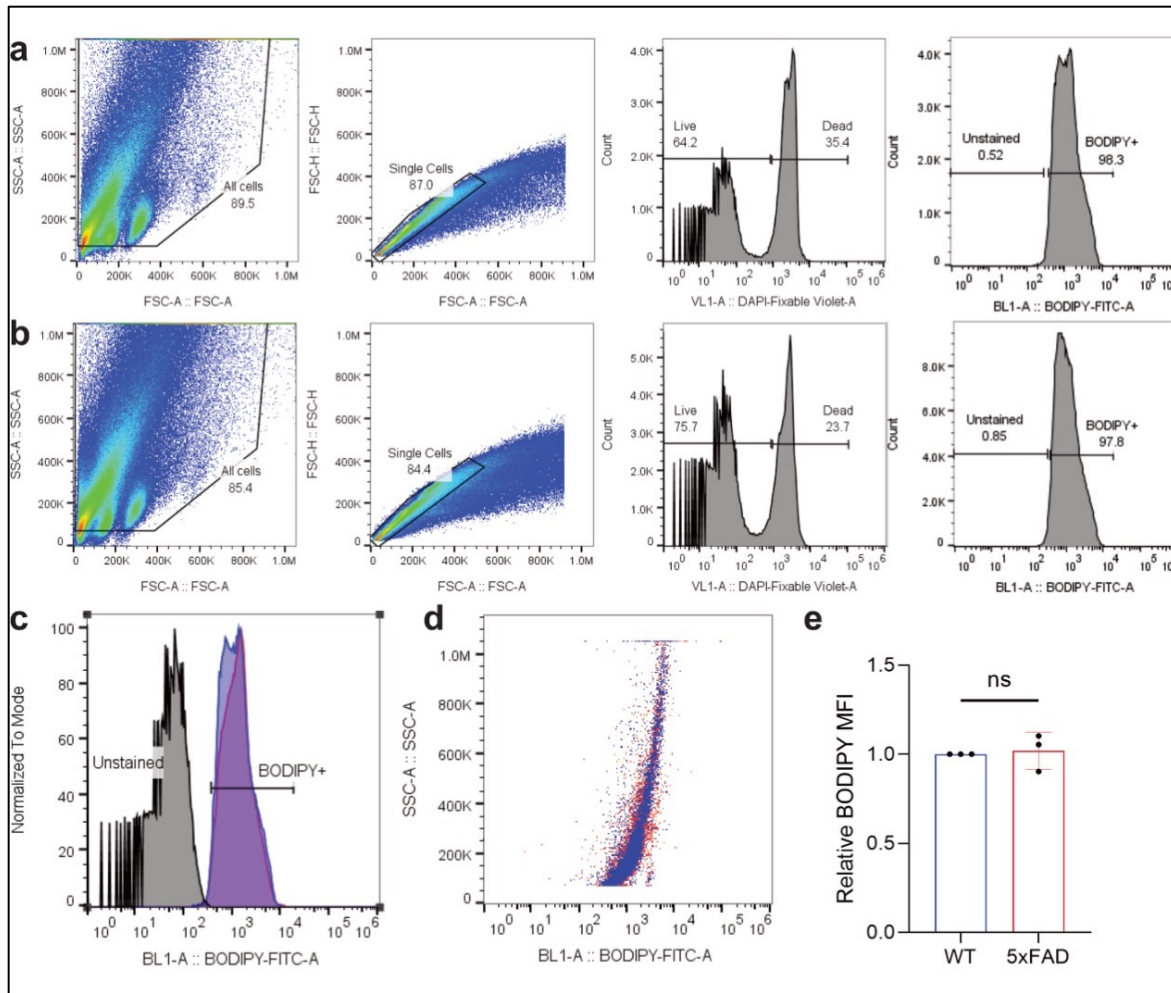


**Figure 7.13** BODIPY staining on acutely isolated CD11b<sup>+</sup> cells from 3-4 month old WT and 5xFAD female mice: Gating strategy for flow cytometry analysis of (a) WT sample (b) 5xFAD sample for BODIPY<sup>+</sup> cells. (c) No green fluorescence was measured in unstained cells (shown in black) and a strong green fluorescence signal was measured in DAPI<sup>-</sup> cells treated 2 $\mu$ M BODIPY for 1 hour at 37°C both in case of WT (shown in blue) and 5xFAD (shown in red). Data shown in terms of % max, by scaling each curve to mode = 100% (y-axis). (d) Dot plot for DAPI<sup>-</sup> cells in WT and 5xFAD sample. (e) Comparison of BODIPY MFI relative to WT (unpaired t-test,  $P=0.7528$ ). (n=2, each group containing 1 female C57BL/6 mice and 1 female 5xFAD mice)



### 7.3.11 5xFAD microglia upregulate DGAT2—a lipid droplet-associated protein compared to WT microglia

We stained the cortical regions of the 5xFAD and WT mouse brains to determine the expression of the microglial DGAT2 protein. Indeed, the 5xFAD regions showed an increased expression of DGAT2 within microglia compared to the WT brains. We also observed the expression of DGAT2 in regions outside of IBA1, which may be occurring in other glial cells or even neurons in the environment.

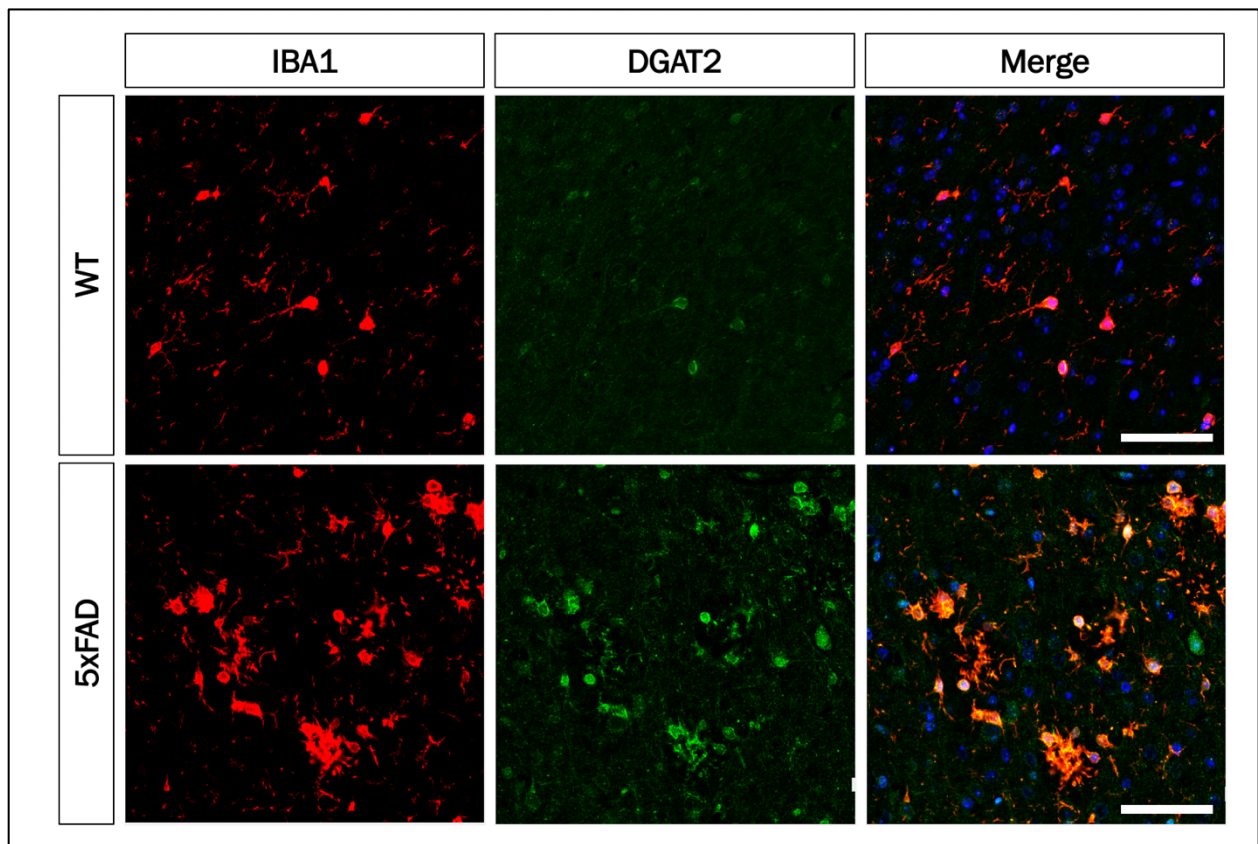


**Figure 7.14** DGAT2 expression in WT and 5xFAD microglia; 7-month-old female mice; Cortex; Scale bar is 50  $\mu$ m.

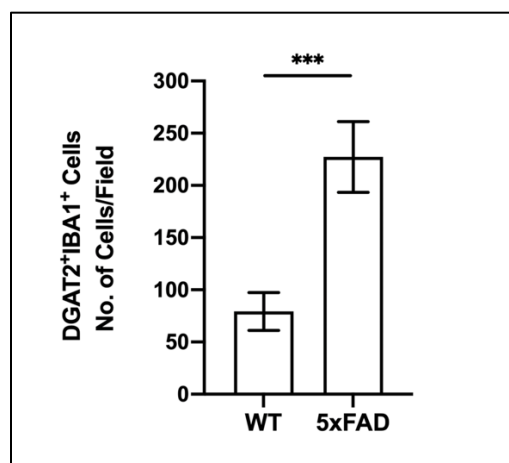


**Figure 7.15** Quantification of DGAT2 expression in WT and 5xFAD microglia.

### 7.3.12 Overview of the metabolite changes in A $\beta$ -treated primary microglia

Little is known about the metabolic changes that occur with microglia are exposed to A $\beta$ . We used MRM-profiling to screen several MRMs related to metabolites in the cells at 1, 12, and 24 hour time points to identify the metabolic changes associated with microglial response to A $\beta$ . At 1 hour, 42 MRMs were found to be significant out of which 7 MRMS were upregulated in A $\beta$ -activated primary microglia, namely, MRMs reported for D-mannitol, 2-isopropylmalate, meso-erythritol, dulcitol (i.e. galactitol), oxoglutaric acid, and L-Aspartic Acid. Out of the 33 MRMs that were downregulated in A $\beta$ -activated primary microglia, the ones related to L-2-aminobutyric acid, D(-)-hydroxy butyric acid, and inosine were the top 3 most downregulated metabolites. Additional MRMs downregulated in these microglia included the ones related to valine, L-serine, L-leucine, L-phenylalanine, arginine, etc. At 12 hours, 5 significant MRMs were found to be identified in A $\beta$  treated microglia. Out of these, the ones related to uracil and cryptoxanthin were upregulated and malic acid, mannitol, and hexanoyl carnitine were downregulated upon A $\beta$ -activation. For 24 hour A $\beta$  treatment, 17 MRMs were found to be significant out of which 9 were upregulated and 8 were downregulated. Out of the upregulated metabolites, D-mannitol, dulcitol, creatine, and 2-isopropylmalate were the top upregulated metabolites and alanine, asparagine, tyrosine, tryptophan were the top downregulated metabolites in the 24 hour A $\beta$  treated primary microglia.

Out of the several upregulated and downregulated MRMs with A $\beta$  treatment, namely MRMs related to D-mannitol, dulcitol, and 2-isopropylmalate were upregulated whereas L-tryptophan, L-tyrosine, and asparagine were downregulated with both 1 and 24 hours of A $\beta$  exposure. PCA plots generated based on the significantly different metabolites in showed distinct separation of the A $\beta$  and vehicle-treated microglial groups and principle components (PCs) 1 and 2 explained 94.1% of the dataset variance for 1 hour, 63.8% for 12 hour, and 50.6% for 24 hour treatment.

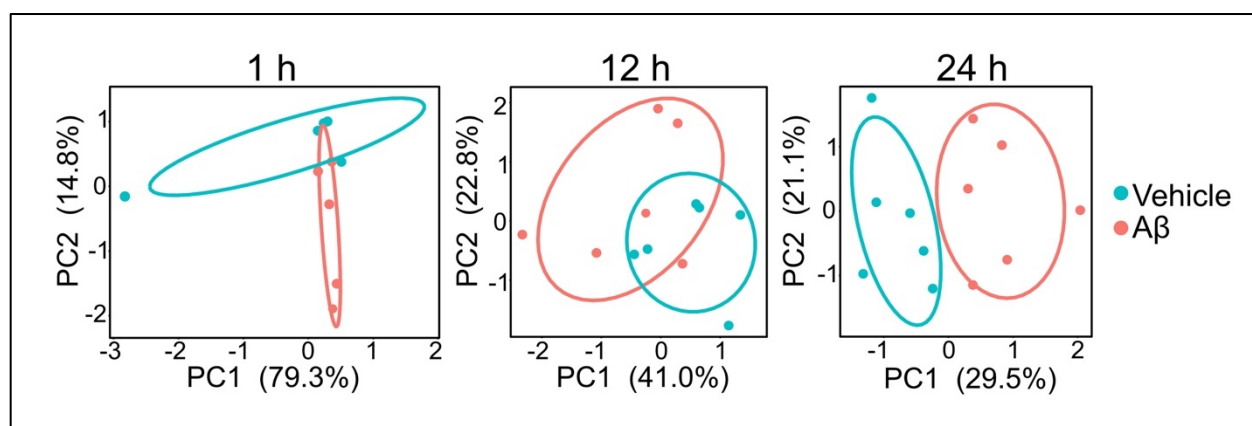


**Figure 7.16** Principle Component Analysis (PCA) plots of metabolites in A $\beta$  treated (red) and vehicle-treated primary microglia.



**Table 7-11** Top upregulated metabolites in A $\beta$ -activated primary microglia at 1 hour (A $\beta$  vs. Vehicle-treated microglia; FDR<0.1).

Metabolite	Transition	Log <sub>2</sub> FC	P Value	FDR
<b>Upregulated Metabolites</b>				
5_D-Mannitol	183.1 -> 98	1.119432	1.51E-14	3.61E-12
5_2-isopropylmalate; 6_2-Isopropylmalic acid	177.1 -> 95	0.8638686	2.62E-09	1.34E-07
5_2-isopropylmalate; 6_2-Isopropylmalic acid	177.1 -> 95	0.8638686	2.62E-09	1.34E-07
5_DL-3,4- Dihydroxymandelic acid	167 -> 85	0.7728525	1.12E-07	4.23E-06
4_meso-Erythritol	145 -> 104	0.7169791	6.91E-07	2.36E-05
6_Dulcitol (i.e. Galactitol)	183.1 -> 57	0.6254315	1.62E-05	4.70E-04
7_Oxoglutaric acid; 9_Oxoglutaric acid	147 -> 65	0.4902308	6.69E-04	0.01370532
7_Oxoglutaric acid; 9_Oxoglutaric acid	147 -> 65	0.4902308	6.69E-04	0.01370532
6_L-Aspartic Acid	134 -> 43	0.4786743	9.59E-04	0.01809804

**Table 7-12** Top downregulated metabolites in A $\beta$ -activated primary microglia at 1 hour (A $\beta$  vs. Vehicle-treated microglia; FDR<0.1).

Metabolite	Transition	Log <sub>2</sub> FC	P Value	FDR
1_L-2-Aminobutyric acid	104.1 -> 58.1	-1.99951996	5.35E-41	3.84E-38
4_D(-)-hydroxy butyric acid	105.1 -> 45	-1.33603878	9.00E-20	3.23E-17
4_Inosine	269.1 -> 137	-1.09278393	8.55E-14	1.53E-11
3_L-Isoleucine	132.1 -> 44	-0.93994631	8.90E-11	1.06E-08
2_Valine	118.1 -> 55.1	-0.92998546	1.40E-10	1.44E-08
1_L-Proline	116.1 -> 70.1	-0.92406621	1.92E-10	1.72E-08
2_L-Leucine	132.1 -> 44.1	-0.91813413	2.34E-10	1.87E-08
4_L-Serine	106.1 -> 60	-0.9054735	5.24E-10	3.75E-08
5_L-Phenylalanine	166.1 -> 120.1	-0.87196206	1.73E-09	1.04E-07
3_L-Leucine	132.1 -> 43.1	-0.8723496	1.71E-09	1.04E-07

**Table 7-13** Differentially regulated metabolites in A $\beta$ -activated primary microglia at 12 hour (A $\beta$  vs. Vehicle-treated microglia; FDR<0.1).

Metabolite	Transition	Log FC	P Value	FDR
<b>Upregulated Metabolites</b>				
5_Uracil	113 -> 70	0.7235503	3.69E-19	2.65E-16
1_Cryptoxanthin	552.4 -> 551.4	0.6748845	7.86E-17	2.82E-14
<b>Downregulated Metabolites</b>				
4_Malic acid	135 -> 45	-0.40094818	4.28E-07	1.02E-04
5_D-Mannitol	183.1 -> 98	-0.37255321	2.45E-06	4.38E-04
2_Hexanoylcarnitine	260.2 -> 85	-0.34536343	2.12E-05	0.00290658

**Table 7-14** Differentially regulated metabolites in A $\beta$ -activated primary microglia at 24 hour (A $\beta$  vs. Vehicle-treated microglia; FDR<0.1).

Metabolite	Transition	Log FC	P Value	FDR
<b>Upregulated Metabolites</b>				
5_D-Mannitol	183.1 -> 98	1.2448087	2.10E-78	1.50E-75
6_Dulcitol (i.e. Galactitol)	183.1 -> 57	0.4299163	1.62E-10	3.86E-08
4_Creatine	132.1 -> 87.1	0.3497849	2.25E-07	4.03E-05
5_2-isopropylmalate; 6_2-Isopropylmalic acid	177.1 -> 95	0.2950935	7.94E-06	9.49E-04
5_2-isopropylmalate; 6_2-Isopropylmalic acid	177.1 -> 95	0.2950935	7.94E-06	9.49E-04
4_Inosine	269.1 -> 137	0.2751627	4.26E-05	0.00436289
3_Creatine	132.1 -> 90.1	0.2511287	1.44E-04	0.01031651
5_Palmitic acid	255.2 -> 71.1	0.2234703	9.79E-04	0.05852064
4_Arginine	175.1 -> 116.1	0.2138322	0.00123665	0.06333396
<b>Downregulated Metabolites</b>				
2_Alanine	90 -> 72	-0.468447	1.69E-12	6.07E-10
5_Asparagine	133.1 -> 74	-0.31526667	3.67E-06	5.26E-04
4_L-Tyrosine	182.1 -> 165.1	-0.25577092	1.32E-04	0.01031651
3_Alanine	90 -> 45	-0.25337629	1.31E-04	0.01031651
5_L-Tryptophan	205.1 -> 146.1	-0.22874298	4.98E-04	0.03245536
1_Cryptoxanthin	552.4 -> 551.4	-0.21892497	0.00116295	0.06333396
5_Glyceraldehyde 3-phosphate	171 -> 73	-0.21783819	0.00145894	0.06973713
4_L-Tryptophan	205.1 -> 188.1	-0.20892149	0.001796	0.08048345

Next, we performed pathway analysis based on tentative attribution of the MRMs in order to obtain an overview of the most impacted pathways due to A $\beta$  exposure. All the differentially regulated metabolites that were significant (FDR<0.1) at the 3 timepoints were combined (62 significant metabolites) and analyzed to determine the possible metabolic pathways affected with A $\beta$  exposure. Significant KEGG pathways associated with A $\beta$  activation were aminoacyl-tRNA biosynthesis, alanine, aspartate and glutamate metabolism, valine, leucine and isoleucine biosynthesis, phenylalanine, tyrosine and tryptophan biosynthesis, and arginine and proline metabolism. Some of the significant Small Molecule Pathway Database (SMPDB) pathways associated with A $\beta$  activation were malate-aspartate shuttle, arginine and proline metabolism, oxidation of branched chain fatty acids, beta-alanine metabolism, etc.

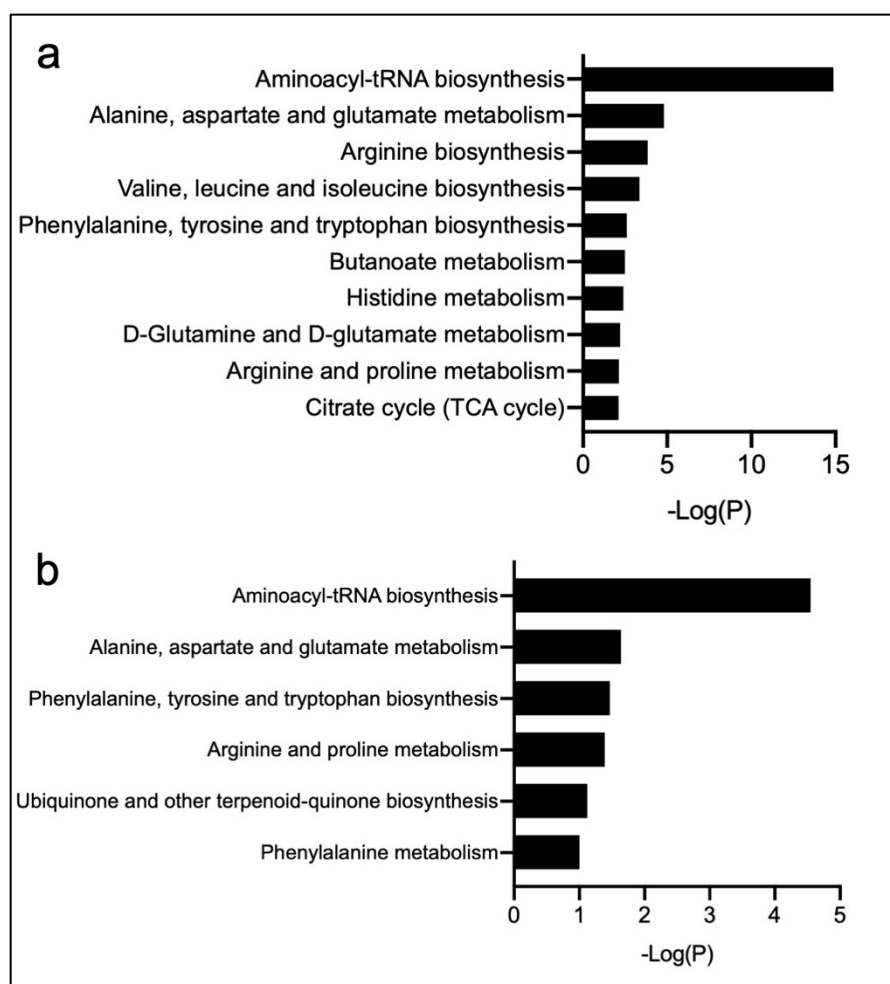


**Figure 7.17** Pathway enrichment with differentially regulated metabolites in primary microglia with (a) 1 hour and (b) 24 hours of A $\beta$  treatment.

### **7.3.13 Select lipids but several metabolites were identified in microglia conditioned media from A $\beta$ -treated primary microglia**

In addition to investigating the changes in the cellular -omics profiles, we also evaluated the changes in the secretory lipids and metabolites by analyzing the microglia conditioned media with A $\beta$  exposure. We cultured the primary microglia exclusively in low-serum defined media to reduce the non-specific activation caused by serum. There were no statistically significant lipids identified in the primary microglial conditioned media with 1 hour of A $\beta$  treatment. At 12 hours, 5 MRMs were significant out of which PI (36:0) and PIp (38:6) were upregulated and 2-Hydroxymyristoylcarnitine, and 17:0 cholesteryl ester were downregulated with A $\beta$  treatment. Only one lipid, namely, 2-hydroxymyristoylcarnitine was found to be downregulated in the conditioned media at 24 hours after treatment.

In contrast to lipids, several metabolites were identified and found to be significant in the conditioned media with A $\beta$  treatment. These metabolites characterize the dynamic lipid-secretome of A $\beta$ -activated microglia that is known to play a critical role in remodeling the tissue microenvironment[17] and alter cellular response such as phagocytosis[18]. With 1 hour A $\beta$  treatment, all the significant metabolites were found to be downregulated in the conditioned media out of which D-mannitol, dulcitol, diphenylamine, and sucrose were the top most downregulated metabolites. At the 12 hour time point, 11 metabolites were found to be upregulated in the conditioned media, out of which diphenylamine, cryptoxanthin, atenolol, cytidine, malic acid, L-serine, and stearic acid were some of the top most upregulated metabolites. Sphingosine, theanine, and L-phenylalanine were the 3 downregulated metabolites at this time point. At 24 hour A $\beta$  treatment, 18 metabolites were found to be upregulated whereas 9 metabolites were downregulated. Diphenylamine, alanine, cytidine, L-tryptophan, and L-threonine were some of the top most upregulated metabolites and spermidine, pantothenic acid, caprylic acid, and D-glucose were amongst the downregulated metabolites. PCA plots revealed the clear separation between the differentially regulated metabolites in the conditioned media obtained from A $\beta$  and vehicle-treated microglial groups and principle components (PCs) 1 and 2 explained 84.3% of the dataset variance for 1 hour, 66.8% for 12 hour, and 54.9% for 24 hour treatment.

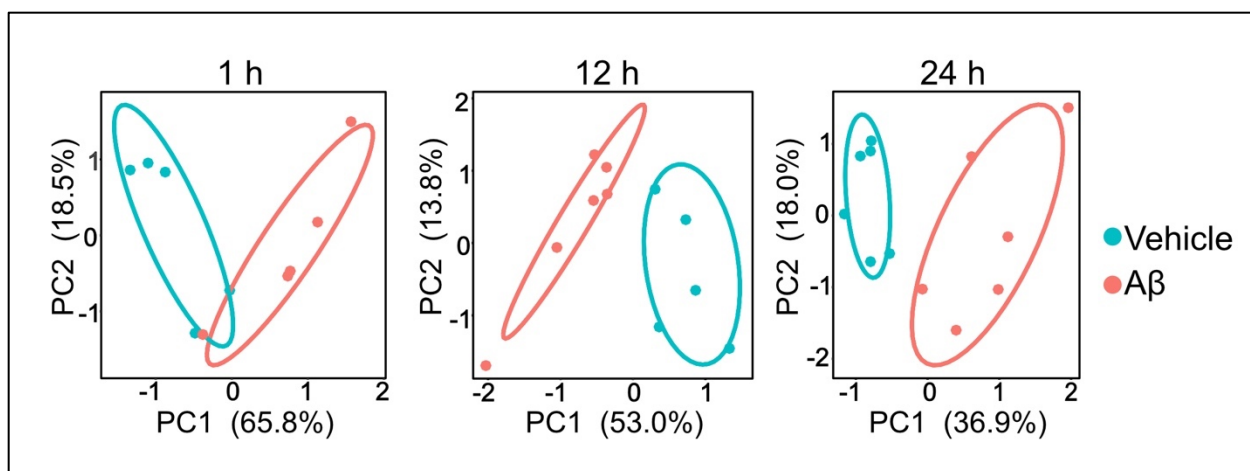


**Figure 7.18** PCA plots showing separation between metabolites in conditioned medium of Aβ treated and vehicle-treated primary microglia.

All the differentially regulated MRMs related to metabolites that were significant ( $FDR < 0.1$ ) at the 3 timepoints were combined (63 significant metabolites) and analyzed to determine the metabolic pathways affected with Aβ exposure. Pathway analysis of the media metabolites revealed phenylalanine, tyrosine and tryptophan biosynthesis, starch and sucrose metabolism, sphingolipid metabolism, valine, leucine and isoleucine biosynthesis, galactose metabolism, and alanine, aspartate and glutamate metabolism pathways to be significant with Aβ exposure.

#### 7.3.14 Overview of the metabolite changes in 5xFAD microglia versus WT microglia

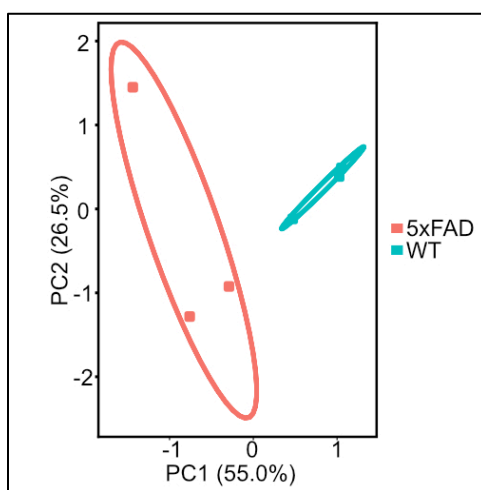


**Figure 7.19** PCA plots showing separation between metabolites in 5xFAD and WT microglia.

**Table 7-15** Top few upregulated metabolites in 5xFAD microglia vs. WT microglia (FDR<0.1)

Metabolite	Log <sub>2</sub> FC	P value	FDR
meso-Erythritol	2.48020968	4.56E-57	3.67E-54
Oxoglutaric acid	2.12437726	2.90E-43	1.17E-40
Creatine	1.6324726	4.17E-27	8.38E-25
L-Leucine	1.60818126	1.61E-26	2.59E-24
Oxoglutaric acid	1.57535138	2.79E-25	3.74E-23
L-Isoleucine	1.55181223	7.42E-25	8.53E-23
(+)-?-Tocopherol	1.3361818	8.49E-19	8.53E-17
L-Leucine	1.10217628	1.79E-13	1.44E-11
Acetylcarnitine	1.03402268	4.17E-12	3.05E-10
L-Carnitine	0.99056987	4.05E-11	2.51E-09
Acetyl-carnitine	0.97107745	7.44E-11	4.27E-09
Creatine	0.77818322	2.04E-07	9.12E-06
L-Carnitine	0.77299099	2.60E-07	1.05E-05
2-Hydroxylauroylcarnitine, 3-hydroxydodecanoylcarnitine	0.76538933	2.32E-07	9.83E-06
Oxoglutaric acid	0.72020495	1.63E-06	6.23E-05
Free Carnitine	0.71119619	1.81E-06	6.62E-05
L-Glutamate; Glutamic acid	0.67441331	5.95E-06	2.08E-04
Free Carnitine	0.67154835	6.45E-06	2.16E-04
L-Lysine	0.62374237	2.98E-05	9.22E-04
Hypoxanthine	0.60901038	4.93E-05	0.00141528

**Table 7-16** Downregulated metabolites in 5xFAD microglia vs. WT microglia (FDR<0.1)

Metabolite	Log <sub>2</sub> FC	P value	FDR
Caprylic acid	-1.7913354	1.26E-31	3.37E-29
Allantoin	-1.1882384	2.18E-15	1.95E-13
L-Phenylalanine	-1.0064427	2.44E-11	1.63E-09
D-Ribulose 5-phosphate	-0.9119494	7.87E-10	4.22E-08
Progesterone	-0.9064298	1.22E-09	6.14E-08
Zeaxanthin	-0.8095686	5.58E-08	2.64E-06
D-Erythrose 4-phosphate	-0.6356192	1.91E-05	6.13E-04
D-Fructose 6-phosphate	-0.6141149	3.37E-05	0.00100254
D-Lactose	-0.5994224	5.32E-05	0.00147629
Alanine	-0.4998841	7.61E-04	0.01529114
Alanine	-0.4739926	0.00144104	0.02574656
Sucrose	-0.4181048	0.00486556	0.07380957
NADH	-0.4033975	0.00704898	0.09981982

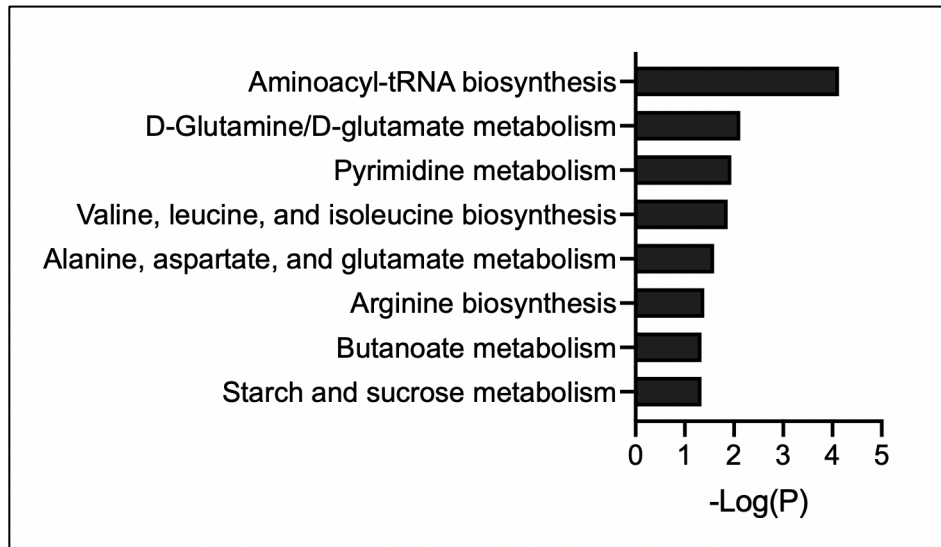


**Figure 7.20** Pathway enrichment with differentially regulated metabolites in 5xFAD microglia.



## 7.4 Discussion

### 7.4.1 MRM-profiling of microglial lipidome and metabolome

This is the first study to demonstrate the global changes in the lipid and metabolite landscape of microglia with A $\beta$  exposure *ex vivo* and in the 5xFAD mouse model *in vivo*. We have shown the effectiveness of MRM-profiling as an exploratory approach to characterize the lipidome and metabolome of microglial cells and their lipid-secretome present in their conditioned media. Specifically, we profiled the changes in 10 different classes of lipids comprising 1,372 total MRM transitions and 717 MRM transitions for metabolites. MRM-profiling is especially suitable for the analysis of microglia, where we are limited by large sample size (i.e., cell number—only around 10-15% of cells in the brain are microglia), since it avoids the chromatographic dilution and separation of the sample for untargeted lipidomics, which are necessary to screen a large number of samples. While most Mass Spectrometry (MS) exploratory approaches for small molecule profiling are based on LC separation and full mass scans followed by product ion scans, MRM-profiling relies on direct sample injection and functional group monitoring using neutral loss and precursor MS/MS scans. In conventional product ion MS/MS, we detect signals associated with individual molecules, but MRM initially focusses at the functional group level. The most discriminant precursor/product transitions observed from screens of representative pooled samples are used to analyze individual samples in minimum times using very small amounts of sample. Even though MRM-profiling also faces most of the challenges related to the difficulty of identifying the molecular structure of small molecules, the advantageous features of sensitivity and speed of MRM-profiling have been recently demonstrated by its application on biomarker discovery for several disease conditions[19]–[21].

### 7.4.2 New bioinformatics pipeline for lipidomics data analysis

Further, we have developed a new methodology for statistical analysis to identify the significant and differentially regulated lipids and metabolites in our samples. Traditional methods use an unweighted Welch T-Test to determine statistical significance for a given lipid between the control and treatment groups[22]. This approach has two issues: (1) it assumes that the mean of each lipid measure in a group (A $\beta$  treated or vehicle-treated) follows a normal distribution, and (2) it does not adjust the p-value for multiple testing from the same biological samples. To address these

issues, we use a statistical method developed for measurements which follow a negative binomial distribution as the lipid intensities appear to follow this distribution. These values are then adjusted to account for multiple testing.

#### **7.4.3 Cultured microglia exhibit dramatic changes in their lipidome and metabolome with A $\beta$ treatment**

BV2 and primary microglia constitute two *in vitro* cellular models of microglia, yet they exhibit stark differences in their transcriptomes[5]. As expected, we observed differences in the lipid profiles of BV2 and primary mouse microglia at 1, 12, and 24 hour time points of A $\beta$  treatment. While PS(14:1) and PSo(18:0) were upregulated in primary microglia with 1-hour A $\beta$  treatment, they were downregulated in BV2 microglia under similar conditions. Interestingly, PG(20:0) and PG(24:0) were commonly upregulated in both BV2 and primary microglia with 24-hour A $\beta$  activation. For all further evaluation, we focused on primary microglia since they were cultured in a highly optimized and defined culture medium[6] that

TAGs are primarily found in the cytoplasm and are stored as lipid droplets in mammalian cells. High levels of TAGs were recently found in LPS-activated BV2 and primary microglia.[1] They were found to be the major component of lipid droplets in lipid-droplet-associated microglia (LDAM) in neurodegenerative brains[1]. In our experiments, long chain length TAG species consisting of 50, 52, and 54 residues and different saturation/unsaturation states (0 to 3 double bonds) were upregulated in primary microglia at 1 and 24 hours of A $\beta$  activation. Among free fatty acids, we found arachidic acid (C(20:0)) to be upregulated and cerotic acid (C(26:0)), C(26:1), and C(30:0) to be downregulated in primary microglia at 1 and 24 hours A $\beta$  activation. Fatty acids of different acyl chain lengths and saturation status are known to have varying effects on immune cells[23]. For example, saturated long-chain (13-21 aliphatic tail carbons) and very-long-chain (22 or more carbons) fatty acids induce pro-inflammatory effects in macrophages via TNF- $\alpha$  and IL-6 secretion[24], [25] and in astrocytes[12]. More importantly, lipids play a massive role in regulating phagocytosis by modulating membrane fluidity. FFAs, glycerophospholipids, and sphingolipids make up the cell membrane architecture, and their acyl chain length and saturation/unsaturation states influence the phagocytic capacity of the cells. Given the impaired phagocytic function of

microglia in AD, it is imperative to probe further the effects and role of lipids on microglial phagocytosis of A $\beta$  in a disease context.

Since small molecules also regulate signaling cascades to control protein function and cell behavior, it is essential to understand how the entire cellular lipidome or metabolome network changes with external cues and signals (like in A $\beta$ ) in addition to probing just one or two specific molecules. Aspartate is of crucial significance in neuroinflammation since microglia releases aspartate during injury and regulates N-methyl-D-aspartate receptors on neurons. Further, arginine is involved in immune suppression via the inducible nitric oxide synthase pathways in microglia[26], [27].

#### **7.4.4 Lipidomics and metabolomics of 5xFAD and WT microglia**

In this study, we identified lipid-rich microglia that were higher in 5xFAD mice compared to age-matched WT mice. Lipid droplet (LD)-accumulating microglia have been shown to have phagocytic dysfunction in aged WT mice and are also seen primarily in inflammation[1], [28]. Furthermore, previous studies have characterized the lipids within the LDs in microglia to consist of neutral lipids including tri- and diacylglycerols (TAGs and DAGs) and cholesteryl esters (CEs). Our experiments indicate TAGs to be upregulated in primary microglia upon A $\beta$  treatment. We further confirmed the presence of LDs in microglia from 5xFAD mice. We showed that microglia exhibit sex-specificity in their LD accumulation, specifically, female microglia from 5xFAD brains uniformly or homogeneously produced LDs whereas only a sub-population of male microglia from 5xFAD mice showed an abundance of LDs. Investigating the sex-specificity of LDs as well as the lipidomic profiles of female and male microglia warrants further research. This may explain some of the underlying mechanisms involved in a higher rate of AD occurrence in females compared to males. Perhaps microglia hold the key to unlocking this mystery in AD. Other lines of investigation in the future should involve the roles played by other proteins in lipid and LD metabolism in microglia. TREM2 and APOE are two proteins that have been already identified to be critical in this process[29]. Several other proteins may be involved in this mechanism [30]and may provide clues to understanding the state of microglia over the course of AD and other disorders. The experiments outlined in this chapter has provided, for the first time, a window into how microglial lipidome changes in microglia due to A $\beta$  and also how microglia alter their LD

formation and metabolism in 5xFAD versus WT brains in a sex-dependent manner. We also identify an LD-associated protein—DGAT2 to be highly expressed in 5xFAD microglia. Further studies should delineate the specific roles of DGAT2 as well as other proteins involved in modulating LDs in microglia.

#### 7.4.5 Concluding thoughts

Immunometabolism of macrophage and microglia is a rapidly growing research area, and studies have shown how specific metabolites like succinate and itaconate regulate macrophage polarization and inflammatory function[31], [32]. Lipids and metabolites are essential biomolecules that regulate all aspects of cell function, however they are still understudied in glial cells like microglia and astrocytes. Specifically, the global changes (i.e., changes appearing in all the different lipid classes and lipid species in a cells) in microglia in response to A $\beta$  exposure *ex vivo* in culture or *in vivo* in a disease environment have not been investigated.

Lipid deposits were first observed in AD brains by Alois Alzheimer in 1907[33] and are ever since considered to play a critical role in AD pathology. One of the primary disease-risk genes in AD and its corresponding protein, Apolipoprotein E (APOE), mediates fat metabolism in the body and is the principal cholesterol carrier in the brain[34]. Lipids directly affect microglial function by modulating membrane proteins on the cell surface. In addition to changes in the cellular lipid and metabolites, microglia can also reprogram their environment and influence the function of surrounding neuron and glial cells by secreting various soluble factors like cytokines, chemokines, and other molecules encompassing the microglial lipid-secretome. We, therefore, asked how the acute treatment of A $\beta$  affected the secretory lipids and metabolites produced by microglia in culture? We performed MRM-profiling of lipids and metabolites isolated from the microglial conditioned media after A $\beta$  treatment at the different time points. We thus demonstrated that MRM-profiling can be used for the exploratory analysis of cellular and secretory lipids and metabolites.

This study forms a basis for understanding the direct effects of A $\beta$  on microglial cellular metabolism. MS technologies are rapidly evolving for evaluating markers in small-size samples and complex systems[35]–[37]. Developing new and novel ways to modulate such changes in the

cell pathways will be crucial for targeting neuroinflammation in AD and other neurological diseases. Further work is required to confirm the molecular structure of the lipids and metabolites detected in this study and understand how they affect microglial response to A $\beta$  in healthy and AD brains *in vivo*. The upstream and downstream signaling pathways influenced by these lipids and metabolites may reveal novel mechanisms of microglial cell function and AD initiation and progression.

## 7.5 References

- [1] J. Marschallinger *et al.*, “Lipid-droplet-accumulating microglia represent a dysfunctional and proinflammatory state in the aging brain,” *Nat. Neurosci.*, vol. 23, no. 2, pp. 194–208, Feb. 2020.
- [2] L. L. Listenberger *et al.*, “Triglyceride accumulation protects against fatty acid-induced lipotoxicity,” *Proc. Natl. Acad. Sci. U. S. A.*, vol. 100, no. 6, pp. 3077–3082, 2003.
- [3] R. De Simone, M. A. Ajmone-Cat, and L. Minghetti, “Atypical antiinflammatory activation of microglia induced by apoptotic neurons: Possible role of phosphatidylserine-phosphatidylserine receptor interaction,” *Mol. Neurobiol.*, vol. 29, no. 2, pp. 197–212, 2004.
- [4] R. De Simone, M. A. Ajmone-Cat, A. Nicolini, and L. Minghetti, “Expression of phosphatidylserine receptor and down-regulation of pro-inflammatory molecule production by its natural ligand in rat microglial cultures,” *J. Neuropathol. Exp. Neurol.*, vol. 61, no. 3, pp. 237–244, Mar. 2002.
- [5] O. Butovsky *et al.*, “Identification of a unique TGF- $\beta$ -dependent molecular and functional signature in microglia,” *Nat. Neurosci.*, vol. 17, no. 1, pp. 131–143, Jan. 2014.
- [6] C. J. Bohlen, F. C. Bennett, A. F. Tucker, H. Y. Collins, S. B. Mulinyawe, and B. A. Barres, “Diverse Requirements for Microglial Survival, Specification, and Function Revealed by Defined-Medium Cultures,” *Neuron*, vol. 94, no. 4, pp. 759–773.e8, May 2017.
- [7] H. Nilsson, M. Brown, E. Inwards, A. Stoeckman, and L. Listenberger, “Exploring Cellular Pathways of Saturated Fatty Acid Toxicity,” *FASEB J.*, vol. 33, no. S1, pp. 796.12–796.12, Apr. 2019.
- [8] G. B. Gordon, “Saturated free fatty acid toxicity. II. Lipid accumulation, ultrastructural alterations, and toxicity in mammalian cells in culture,” *Exp. Mol. Pathol.*, vol. 27, no. 2, pp. 262–276, Oct. 1977.
- [9] A. K. Azevedo-Martins, A. P. Monteiro, C. L. Lima, S. Lenzen, and R. Curi, “Fatty acid-induced toxicity and neutral lipid accumulation in insulin-producing RINm5F cells,” *Toxicol. Vitro.*, vol. 20, no. 7, pp. 1106–1113, Oct. 2006.

- [10] H. Wang, M. V. Airola, and K. Reue, "How lipid droplets 'TAG' along: Glycerolipid synthetic enzymes and lipid storage," *Biochimica et Biophysica Acta - Molecular and Cell Biology of Lipids*, vol. 1862, no. 10. Elsevier B.V., pp. 1131–1145, 01-Oct-2017.
- [11] L. L. Listenberger, D. S. Ory, and J. E. Schaffer, "Palmitate-induced Apoptosis Can Occur through a Ceramide-independent Pathway," *J. Biol. Chem.*, vol. 276, no. 18, pp. 14890–14895, 2001.
- [12] S. Gupta, A. G. Knight, S. Gupta, J. N. Keller, and A. J. Bruce-Keller, "Saturated long-chain fatty acids activate inflammatory signaling in astrocytes," *J. Neurochem.*, vol. 120, no. 6, pp. 1060–1071, Feb. 2012.
- [13] J. E. De Vries *et al.*, "Saturated but not mono-unsaturated fatty acids induce apoptotic cell death in neonatal rat ventricular myocytes," *J. Lipid Res.*, vol. 38, no. 7, pp. 1384–1394, 1997.
- [14] K. A. Guttenplan *et al.*, "Knockout of reactive astrocyte activating factors slows disease progression in an ALS mouse model," *Nat. Commun.*, vol. 11, no. 1, p. 3753, Dec. 2020.
- [15] S. Jawhar, A. Trawicka, C. Jenneckens, T. A. Bayer, and O. Wirths, "Motor deficits, neuron loss, and reduced anxiety coinciding with axonal degeneration and intraneuronal A $\beta$  aggregation in the 5XFAD mouse model of Alzheimer's disease," *Neurobiol. Aging*, vol. 33, no. 1, pp. 196.e29-196.e40, 2012.
- [16] B. C. Richard, A. Kurdakova, S. Baches, T. A. Bayer, S. Weggen, and O. Wirths, "Gene dosage dependent aggravation of the neurological phenotype in the 5XFAD mouse model of Alzheimer's disease," *J. Alzheimer's Dis.*, vol. 45, no. 4, pp. 1223–1236, 2015.
- [17] I. Diaz-Aparicio *et al.*, "Microglia actively remodel adult hippocampal neurogenesis through the phagocytosis secretome," *J. Neurosci.*, vol. 40, no. 7, pp. 1453–1482, Feb. 2020.
- [18] S. H. Baik *et al.*, "A Breakdown in Metabolic Reprogramming Causes Microglia Dysfunction in Alzheimer's Disease," *Cell Metab.*, vol. 30, no. 3, pp. 493-507.e6, 2019.
- [19] F. B. Cordeiro *et al.*, "Multiple reaction monitoring (MRM)-profiling for biomarker discovery applied to human polycystic ovarian syndrome," *Rapid Commun. Mass Spectrom.*, vol. 31, no. 17, pp. 1462–1470, Sep. 2017.
- [20] K. E. Yannell, C. R. Ferreira, S. E. Tichy, and R. G. Cooks, "Multiple reaction monitoring (MRM)-profiling with biomarker identification by LC-QTOF to characterize coronary artery disease," *Analyst*, vol. 143, no. 20, pp. 5014–5022, 2018.
- [21] Z. Xie *et al.*, "Multiple Reaction Monitoring Profiling (MRM-Profilng) of Lipids to Distinguish Strain-Level Differences in Microbial Resistance in Escherichia coli," *Anal. Chem.*, vol. 91, no. 17, pp. 11349–11354, Sep. 2019.

- [22] S. S. Dipali, C. R. Ferreira, L. T. Zhou, M. T. Pritchard, and F. E. Duncan, “Histologic analysis and lipid profiling reveal reproductive age-associated changes in peri-ovarian adipose tissue,” *Reprod. Biol. Endocrinol.*, vol. 17, no. 1, p. 46, Dec. 2019.
- [23] K. Huynh, G. Pernes, N. A. Mellett, P. J. Meikle, A. J. Murphy, and G. I. Lancaster, “Lipidomic profiling of murine macrophages treated with fatty acids of varying chain length and saturation status,” *Metabolites*, vol. 8, no. 2, p. 29, Apr. 2018.
- [24] T. Martins De Lima-Salgado, S. Coccuzzo Sampaio, M. Fernanda Cury-Boaventura, and R. Curi, “Modulatory effect of fatty acids on fungicidal activity, respiratory burst and TNF- $\alpha$  and IL-6 production in J774 murine macrophages,” *Br. J. Nutr.*, vol. 105, no. 8, pp. 1173–1179, Apr. 2011.
- [25] L. Håversen, K. N. Danielsson, L. Fogelstrand, and O. Wiklund, “Induction of proinflammatory cytokines by long-chain saturated fatty acids in human macrophages,” *Atherosclerosis*, vol. 202, no. 2, pp. 382–393, Feb. 2009.
- [26] M. J. Kan *et al.*, “Arginine deprivation and immune suppression in a mouse model of Alzheimer’s disease,” *J. Neurosci.*, vol. 35, no. 15, pp. 5969–5982, Apr. 2015.
- [27] J. Jung, H. Zeng, and T. Horng, “Metabolism as a guiding force for immunity,” *Nat. Cell Biol.*, vol. 21, no. 1, pp. 85–93, Jan. 2019.
- [28] B. C. Farmer, A. E. Walsh, J. C. Kluemper, and L. A. Johnson, “Lipid Droplets in Neurodegenerative Disorders,” *Frontiers in Neuroscience*, vol. 14, Frontiers Media S.A., p. 742, 29-Jul-2020.
- [29] B. A. Loving and K. D. Bruce, “Lipid and Lipoprotein Metabolism in Microglia,” *Frontiers in Physiology*, vol. 11, Frontiers Media S.A., p. 393, 28-Apr-2020.
- [30] K. D. Bruce *et al.*, “Lipoprotein lipase is a feature of alternatively-activated microglia and may facilitate lipid uptake in the CNS during demyelination,” *Front. Mol. Neurosci.*, vol. 11, Mar. 2018.
- [31] V. Lampropoulou *et al.*, “Itaconate Links Inhibition of Succinate Dehydrogenase with Macrophage Metabolic Remodeling and Regulation of Inflammation,” *Cell Metab.*, vol. 24, no. 1, pp. 158–166, 2016.
- [32] E. L. Mills *et al.*, “Succinate Dehydrogenase Supports Metabolic Repurposing of Mitochondria to Drive Inflammatory Macrophages,” *Cell*, vol. 167, no. 2, pp. 457–470.e13, Oct. 2016.
- [33] R. A. Stelzmann, H. Norman Schnitzlein, and F. Reed Murtagh, “An english translation of alzheimer’s 1907 paper, ‘über eine eigenartige erkankung der hirnrinde,’” *Clin. Anat.*, vol. 8, no. 6, pp. 429–431, 1995.

- [34] L. Puglielli, R. E. Tanzi, and D. M. Kovacs, “Alzheimer’s disease: The cholesterol connection,” *Nat. Neurosci.*, vol. 6, no. 4, pp. 345–351, Apr. 2003.
- [35] X. Gong *et al.*, “Single cell analysis with probe ESI-mass spectrometry: Detection of metabolites at cellular and subcellular levels,” *Anal. Chem.*, vol. 86, no. 8, pp. 3809–3816, 2014.
- [36] D. Petras, A. K. Jarmusch, and P. C. Dorrestein, “From single cells to our planet—recent advances in using mass spectrometry for spatially resolved metabolomics,” *Current Opinion in Chemical Biology*, vol. 36, pp. 24–31, 2017.
- [37] B. Ajami *et al.*, “Single-cell mass cytometry reveals distinct populations of brain myeloid cells in mouse neuroinflammation and neurodegeneration models,” *Nat. Neurosci.*, vol. 21, no. 4, pp. 541–551, Apr. 2018.



## CHAPTER 8.     PROTEOMIC, LIPIDOMIC, AND METABOLOMIC CHARACTERIZATION OF REACTIVE ASTROCYTES

Portions of this chapter will appear in a manuscript currently under minor revision.

Guttenplan K, Weigel M\*, Prakash P\*, Wijewardhane PR, Fine J, Neal M, Bruce KD, Chopra G, Gitler AD, Liddelow SA, Barres BA. Neurotoxic reactive astrocytes induce cell death via saturated lipids. *Nature*.

### 8.1   Introduction

Astrocytes in a healthy CNS play essential roles in every aspect of neurodevelopment and function. For example, they (i) promote neuronal development, (ii) secrete neurotransmitters and neurotrophic factors that regulate the states and functions of other CNS cells, (iii) support the blood brain barrier (BBB) and its function, (iv) modulate the extracellular ion concentrations, and (v) phagocytose neuronal synapses to maintain and promote neuroplasticity(1–3). In disease or injury, astrocytes undergo dramatic cellular changes and become ‘reactive’ to either promote recovery or exacerbate inflammation and toxicity. Thus, the functional states of reactive astrocytes were largely disputed for several years. Genomic analysis of reactive astrogliosis revealed that the cell state was dependent mainly on the type of inducing injury(4). For example, reactive astrocytes were identified to be beneficial/protective upon ischemic injury whereas they were toxic/detrimental when induced by lipopolysaccharide (LPS), a bacterial cell wall endotoxin(4). These were later termed as A1 (neurotoxic) and A2 (neurotrophic) astrocytes(5). Further, it was established that the A1 astrocytes are induced by classically activated microglia via the secretion of three main factors mainly, TNF- $\alpha$ , IL-1 $\alpha$ , and C1q *in vitro* and *in vivo*. These A1 astrocytes lose most normal supportive astrocytic functions such as the promotion of neuronal survival and outgrowth, promotion of synapse formation and function, and the phagocytosis of synapses and myelin debris. Instead, they become toxic and rapidly kill neurons as well as mature, differentiated oligodendrocytes via the secretion of a toxic factor. A1 astrocytes are present in acute injury and in several neurodegenerative diseases including AD where they may contribute to disease progression and are identified/marked via the intense expression of the complement 3 (C3) protein. The astrocyte-secreted toxic factor was also shown to be specifically toxic to the subtype of motor neurons most vulnerable in amyotrophic lateral sclerosis (ALS), similar to findings that cultured

astrocytes from mouse models of ALS are toxic to motor neurons(6, 7). In vivo, the inhibition of reactive astrocytes in a mouse with global knock out of IL-1 $\alpha$ , TNF $\alpha$ , and C1q prevented the death of retinal ganglion cells normally seen after optic nerve crushes or in the bead occlusion model of glaucoma(8) as well as extended the lifespan of Sod1<sup>G93A</sup> ALS model mice(9). How A1 astrocytes cause cytotoxicity i.e. what neurotoxic factor(s) are released by A1 astrocytes has not been known until now. Chemical compounds or biological molecules that inhibit A1 astrocyte formation or block the action of the neurotoxic factor may help save the neurons and oligodendrocytes in inflammatory conditions during injury and disease.

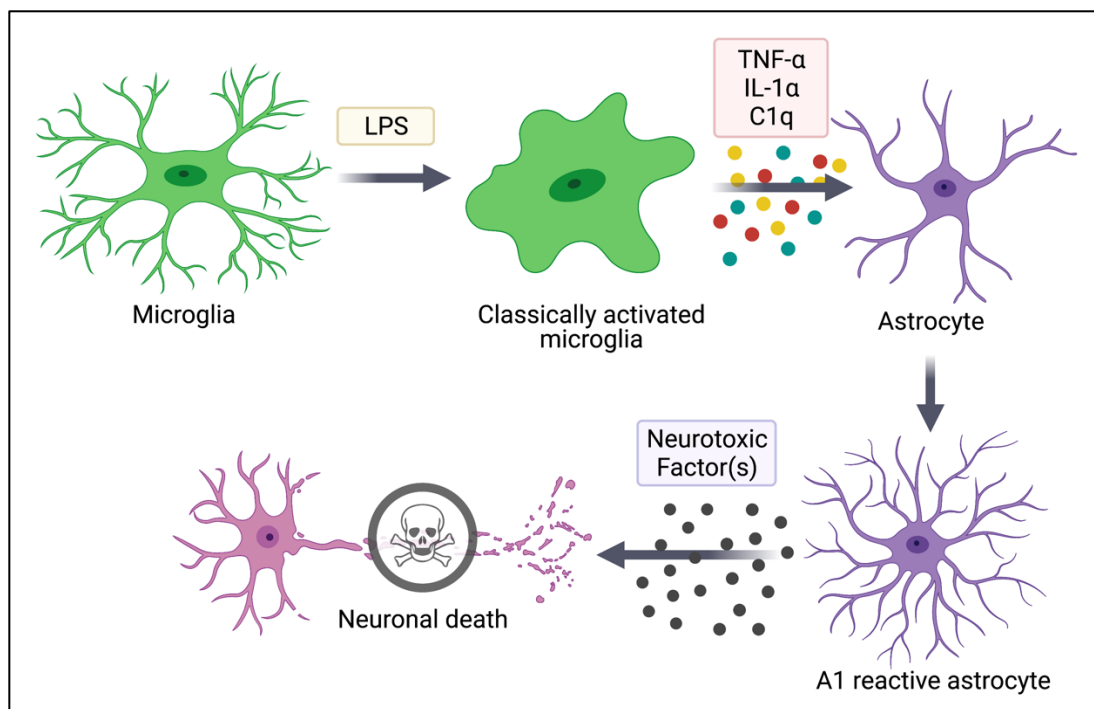


**Figure 8.1** Activated microglia induce neurotoxic reactive astrocytes. Microglia become classically activated with several factors such as the bacterial endotoxin (LPS) and even signals arising from damaged neurons. These activated microglia release astrocyte-activating signals (TNF- $\alpha$ , IL-1 $\alpha$ , and C1q) that induce astrocytes to become reactive. These A1 or neuroinflammatory reactive astrocytes directly cause neuronal death via the secretion of an unknown neurotoxic factor. Only previously damaged neurons are susceptible to the reactive-astrocyte-induced death, however, the mechanism is still unknown. The identity of this astrocytic toxic factor was a mystery to date.

## **8.2 Profiling of reactive astrocytes and their conditioned medium**

Besides C3, what protein markers identify A1 astrocytes in culture and in tissue? Further, what proteomic changes are induced in A1 astrocytes and their secretory milieu when they are activated by microglia? Could the neurotoxic factor that causes neuron and oligodendrocyte cell death be a protein molecule? To answer these questions, proteomic profiling of A1 astrocytes as well as the astrocyte conditioned media (ACM) was performed. Neurotoxic reactive astrocytes can be generated in culture by treating them with recombinant TNF- $\alpha$ , IL-1 $\alpha$ , and C1q (i.e. the activated microglia-derived factors). These cells secrete the neurotoxic factor into their conditioned media that directly kills neurons and mature oligodendrocytes but not other cells when applied onto them. Thus, the changes in the proteome, lipidome, and metabolome in the astrocytes (cells) as well as the ACM are characterized to identify the changes occurring due to their induction. The cells and ACM with the vehicle (PBS) treatment only are taken as controls. The reactive astrocytes and ACM samples used in this study were prepared and provided by Dr. Kevin Gattenplan. The frozen cell pellets and the ACM were used as the starting material for protein, lipid, or metabolite extraction and downstream proteomic and lipidomic characterization.

### **8.2.1 Sample preparation for the proteomic analysis of reactive astrocytes**

The cell lysates were thawed at room temperature and homogenized using the Precellys lysing kits (Bertin Instruments). The bicinchoninic acid assay (BCA) was performed to determine the total protein in each sample, and 20  $\mu$ g of protein (volume equivalent) from each sample was precipitated overnight at -20 °C with 4x volume of ice-cold acetone. The precipitates were pelleted at 13.5k RPM for 10 mins at 4°C, the supernatant discarded, and pellets dried in a vacuum centrifuge for 15 mins. The dried pellets were then resuspended in a mixture of 15  $\mu$ L water with 5  $\mu$ L of 4x Laemmli buffer and subjected to heating at 70°C for 10 mins. The samples were separated in the 1D gel at 200 V for 20 mins, and the bands on the gel were stained with the Coomassie blue solution for 1 hour. The gels were then rinsed several times with water, and each lane was excised into 6 gel slices for in-gel digestion per the previously described protocol (11). The sliced gel samples were washed 3x times with 25 mM ammonium bicarbonate (ABC) and 50% acetonitrile (ACN), and 1x times with 100% ACN to completely de-stain the gels and dried in a vacuum centrifuge for 15 mins. Reduction and alkylation of cysteines were carried out using 10

mM dithiothreitol (DTT) in 25 mM ABC at 55°C for 1 hour and 55 mM iodoacetamide (IAA) in 25 mM ABC at room temperature in the dark for 45 min respectively. Dried gel pieces were transferred to Barocycler tubes and digested for 2 hours in a Barocycler at 50°C and 20,000 psi (50 seconds at 20,000 psi, 10 seconds at atmospheric pressure for a total of 120 cycles or 2 hours) using trypsin/Lys-C mix (Promega #V5071) at an enzyme-to-substrate ratio of 1:25. After digestion, supernatants containing the peptides were removed, and the peptides were extracted using 60% ACN/5% trifluoroacetic acid (TFA). The peptide samples were vacuum dried and re-suspended in 15 uL of sample loading buffer (0.1% (v/v) formic acid in 3% ACN), and 5 uL was used for LC-MS/MS analysis.

### **8.2.2 Sample preparation for the proteomic analysis of reactive astrocyte conditioned medium**

The frozen ACM samples were thawed at room temperature, and the BCA was performed to determine the total protein in each sample. 50 ug of protein (equivalent volume) from each ACM sample was precipitated overnight at -20 °C with 4x volume of ice-cold acetone. The next day, the precipitated samples were pelleted at 13.5 k RPM at 4 °C for 10 minutes. The supernatants were discarded, and the precipitated pellets were dissolved in 10 uL of 8M urea containing 10 mM DTT and incubated at 37 °C for 1 hour for reduction. Next, alkylation was performed using 10 uL alkylating reagent (195 uL ACN+1 uL triethylphosphine+4 uL of IAA) by incubating the samples for 1 hour at 37 °C. The reduced and alkylated samples were then dried in a vacuum centrifuge. For in-solution digestion<sup>1</sup>, trypsin/Lys-C mix (Promega) was prepared by dissolving the stock reagent in 400 uL of 25 mM ABC. 80 uL of the trypsin/Lys-C mix was added to each sample for digestion in a Barocycler (50 °C; 60 cycles: 50 seconds at 20 kPSI and 10 seconds at 1 ATM). Finally, the peptides were desalted using MicroSpin columns (C18 silica; The Nest Group). The dried, purified peptides were re-suspended in 3% ACN in 0.1% formic acid to a final concentration of 1 ug/uL, and 1 uL (1 ug) was loaded to the HPLC system.

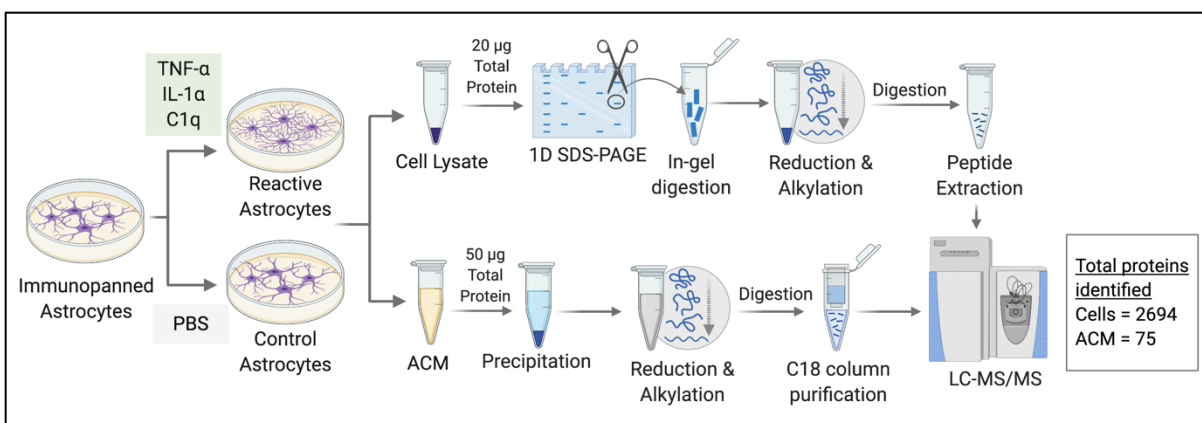


**Figure 8.2** Sample preparation for proteomics of A1 reactive astrocytes and ACM. A total of 2694 and 75 proteins were identified in cells and ACM respectively.

### 8.2.3 Liquid Chromatography-Mass Spectrometry/Mass Spectrometry

The peptides were analyzed in a Dionex UltiMate 3000 RSLC nano System (Thermo Fisher Scientific, Odense, Denmark) coupled on-line to Orbitrap Fusion Lumos Mass Spectrometer (Thermo Fisher Scientific, Waltham, MA, USA) as described previously(12). Briefly, reverse-phase peptide separation was accomplished using a trap column (300 µm ID×5 mm) packed with 5 µm 100 Å PepMap C18 medium coupled to a 50-cm long×75 µm inner diameter analytical column packed with 2 µm 100 Å PepMap C18 silica (Thermo Fisher Scientific). The column temperature was maintained at 50°C. The samples were loaded to the trap column in a loading buffer (3% acetonitrile in 0.1% FA) at a flow rate of 5 µL/min for 5 mins, and eluted from the analytical column at a flow rate of 200 nL/min using a 160-min LC gradient. The column was washed and equilibrated with three 30-min LC gradients before injecting the next sample. All data were acquired in the Orbitrap mass analyzer, and the data were collected using an HCD fragmentation scheme. For MS scans, the scan range was from 350 to 1600 m/z at a resolution of 120,000, the automatic gain control (AGC) target was set at  $4 \times 10^5$ , maximum injection time was 50 ms, dynamic exclusion was 30 secs, and intensity threshold was  $5.0 \times 10^4$ . MS data were acquired in the Data Dependent mode with a cycle time of 5s/scan. The MS/MS data were collected at a resolution of 15,000.

#### 8.2.4 Data analysis

LC-MS/MS data were analyzed using MaxQuant software(13) (version 1.6.3.3) by searching the *Rattus norvegicus* protein sequence database downloaded from the UniProt (www.uniprot.org) in March 2020. The following parameters were edited during search: precursor mass tolerance of 10 ppm; enzyme specificity of trypsin/Lys-C enzyme allowing up to 2 missed cleavages; oxidation of methionine (M) as a variable modification and iodoethanol (C) as a fixed modification. False discovery rate (FDR) of peptide spectral match (PSM) and protein identification was set to 0.01. Proteins with LFQ # 0 and MS/MS (spectral counts)  $\geq 2$  were only considered as true identification and used for statistical analysis in the Perseus software platform. The edgeR package(14, 15) in R was used to analyze the data obtained from MaxQuant. Briefly, the label-free quantitation (LFQ) intensity values of the five reactive astrocytes versus the five control astrocytes were used to calculate the log fold change ( $\log_2FC$ ), p-value, and the Benjamini-Hochberg (BH) method to obtain FDR values(16). for each identified protein. We analyzed the data such that each protein had at least 1 non-zero LFQ value, 2 non-zero LFQ values, 4 non-zero LFQ values, 6 non-zero LFQ values, 8 non-zero LFQ values, and 10 non-zero values (*termed 1x, 2x, 4x, 6x, 8x, and 10x respectively*) between the reactive and control groups (Figure 8.2). However, we selected 4x data analysis for results and figures based on the total contribution of principal components showcasing greater than 90% variation in reactive and control astrocytes datasets for both cells and ACM. The significant proteins were selected based on  $FDR < 0.1$ . There is no difference in  $\log_2FC$ , p-value, FDR between different datasets for the same protein. The 1x data shows the largest number of differentially expressed proteins that is also accessible at <http://astrocyte-omics.appspot.com>.

	ASTROCYTES		ACM	
	Number of significant proteins	Variation in data shown by PCA plots	Number of significant proteins	Variation in data shown by PCA plots
1x	1010	41.8%	112	Plot not generated
2x	409	67.2%	51	82.5%
4x	176	90.1%	17	94.5%
6x	6	99.4%	1	Plot not generated
8x	7	97.5%	0	Plot not generated
10x	707	76%	12	89.1%

**Figure 8.3** Number of significant proteins and PCA variation based on number of replicates of protein mass spectrometry that were required to have a non-zero spectral count to be considered for analysis. 4 of 10 (4x) was chosen for final analysis.

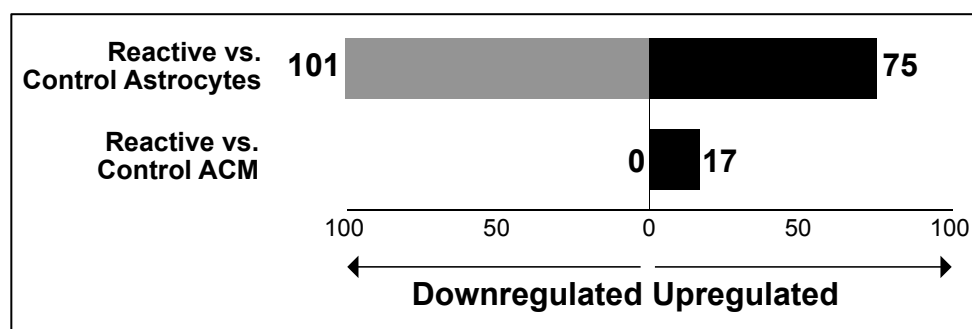


**Figure 8.4** Number of differentially regulated proteins in reactive astrocytes and ACM. The cells had 75 upregulated and 101 downregulated proteins. The ACM had 17 upregulated and 0 downregulated proteins. Data based on the 4x analysis described above.

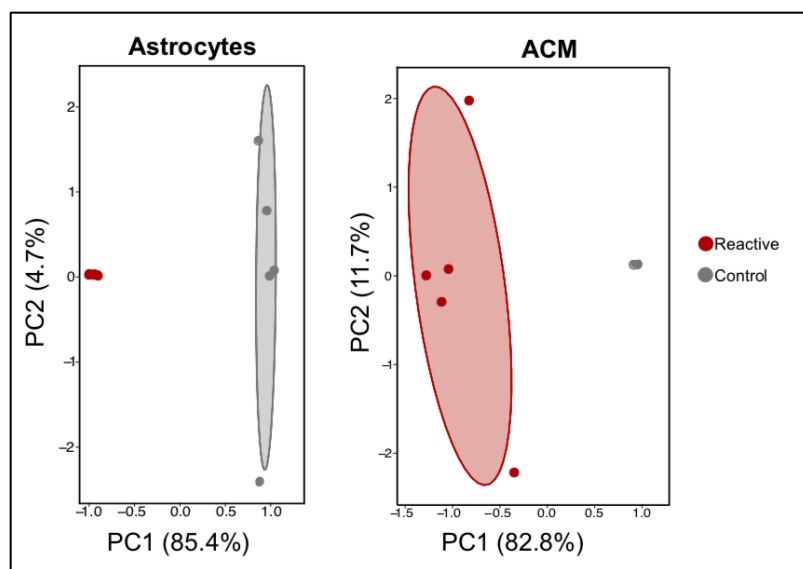


**Figure 8.5** Principal component analysis (PCA) plots shows separation in the proteomes of reactive and control astrocytes. Variation in more than 90% of the sample and control data is seen in each category showcasing the separation of the reactive and control astrocytes and ACM proteome.

### 8.2.5 Reactive astrocytes and ACM upregulate several previously known as well as unknown unique proteins

Interestingly, while 176 of 2694 detected proteins changed in abundance within reactive astrocytes (based on PCA contribution), most of these changes correspond to known reactivity signature genes, with the inflammatory astrocyte protein complement component C3 showing the largest increase (FDR  $2.12\text{E-}27$  and  $\text{Log}_2\text{FC}$  33.26). Additionally, proteins like SERPING1, LCN2, CLU (APOJ), SOD2, etc. were also increased in reactive astrocytes. Interestingly, *Serping1* and *Lcn2* were previously identified via genomic analysis to be markers of reactive astrocytes(4). Next, in the astrocyte secreted proteins (ACM), there was an expected increase in the abundance of astrocyte reactivity proteins such as C3, LCN2, and others in addition to classical astrocyte secreted factors such as SPARC10. Cp (Ceruloplasmin) was the most abundant protein in the reactive ACM (FDR  $2\text{E-}20$  and  $\text{Log}_2\text{FC}$  32.05). Many complement proteins as well as chemokines were highly upregulated in the reactive ACM including C1qb, C1s, C1r, Ccl2, and Ccl7 indicating an intense immune response corresponding to the cellular state and reactivity. The top 20 upregulated and downregulated proteins in both the cells and the ACM (upregulated only) are listed in the tables below. The complete datasets comprising all the identified proteins along with their fold change and significance is provided in the <http://astrocyte-omics.appspot.com> website.



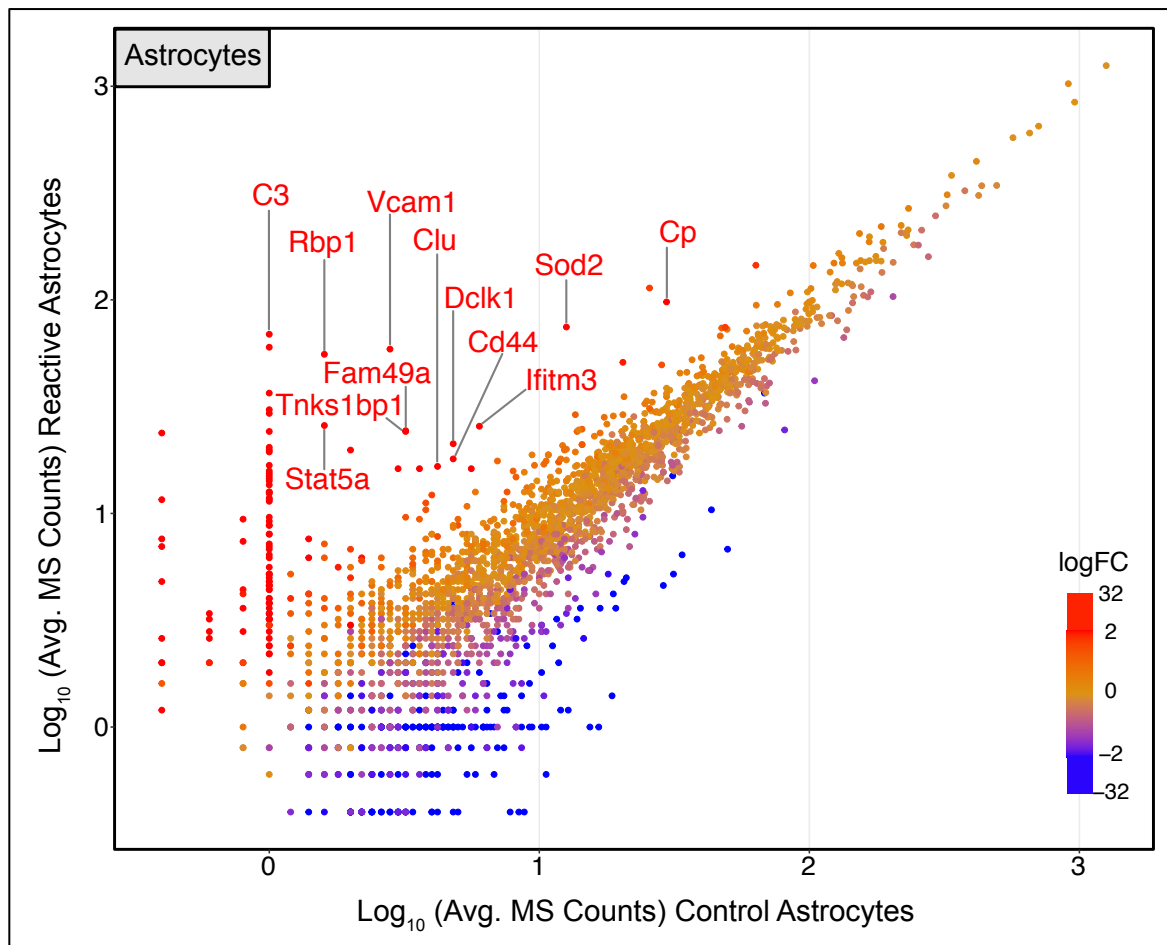


**Figure 8.6** Scatter plot shows the significant proteins in astrocytes due to their reactivity. Red and blue points indicate the proteins in highest and lowest abundance based on the Log<sub>2</sub>FC values respectively. Select relevant upregulated proteins like C3, CLU, SOD2, etc. are labeled.

**Table 8-1** Top 20 upregulated proteins in astrocytes.

<b>Protein ID</b>	<b>Gene names</b>	<b>Log<sub>2</sub>FC</b>	<b>FDR</b>
M0RBJ7	C3	33.2617396	2.12E-27
P09034	Ass1	32.3184515	3.19E-27
Q5U2Z4	Nfkb2	32.0294308	3.19E-27
Q9JKB7	Gda	31.587464	3.75E-27
F1LW83	Mpa2l	31.4802754	3.75E-27
D3ZYQ3	Tnfaip2	31.2734255	3.79E-27
Q4V8K1	Steap4	31.1983556	3.79E-27
Q00238	Icam1	30.4298686	7.14E-27
Q6P734	Serping1	30.3534644	7.14E-27
Q9WTV1	Chi3l1	30.2250176	7.14E-27
Q8R427	Abcb1b	30.2056668	7.14E-27
D3ZV82	LOC685067	30.166563	7.14E-27
M0R3N4	Vat1l	30.0950229	7.14E-27
E9PT22	Inf2	30.0738352	7.14E-27
M0RC17	Chl1	30.0022573	7.14E-27
F1M9F6	Gbp5	29.9553623	7.14E-27
F1LQH2	Nfkb1	29.8389829	7.37E-27
G3V6L4	Kif5c	29.693184	7.93E-27
P30152	Lcn2	29.6021665	8.14E-27
D3ZA22	Trim47	29.5555776	8.26E-27

**Table 8-2** Top 20 downregulated proteins in astrocytes.

Protein ID	Gene names	Log <sub>2</sub> FC	FDR
Q68FU7	Coq6	-29.970565	7.14E-27
G3V8G4	Bcan	-29.845883	7.37E-27
A0A0G2K327	Osbp11a	-29.787615	7.49E-27
P84039	Enpp5	-29.662662	7.93E-27
P02793	Ftl1	-29.018658	1.32E-26
A0A0G2K872	Cadm3	-28.976881	1.33E-26
Q6P762	Man2b1	-28.861268	1.33E-26
P23978	Slc6a1	-28.807476	1.33E-26
Q9JHZ9	Slc38a3	-28.798088	1.33E-26
D3ZVG3	Nup11	-28.764791	1.34E-26
A0A0G2K4X5	Zhx3	-28.736723	1.36E-26
A0A0G2JZ69	Sptan1	-28.619009	1.49E-26
B1WBY5	Dnajc11	-28.523749	1.55E-26
F2Z3T7	Isoc1	-28.516671	1.55E-26
B4F773	Ttyh1	-28.496712	1.55E-26
D3ZUM2	Sarm1	-28.46833	1.55E-26
P48303	S1pr1	-28.334299	1.72E-26
P07171	Calb1	-28.171863	1.85E-26
D3ZII1	Rftn2	-28.143412	1.85E-26
P22791	Hmgcs2	-28.123663	1.85E-26

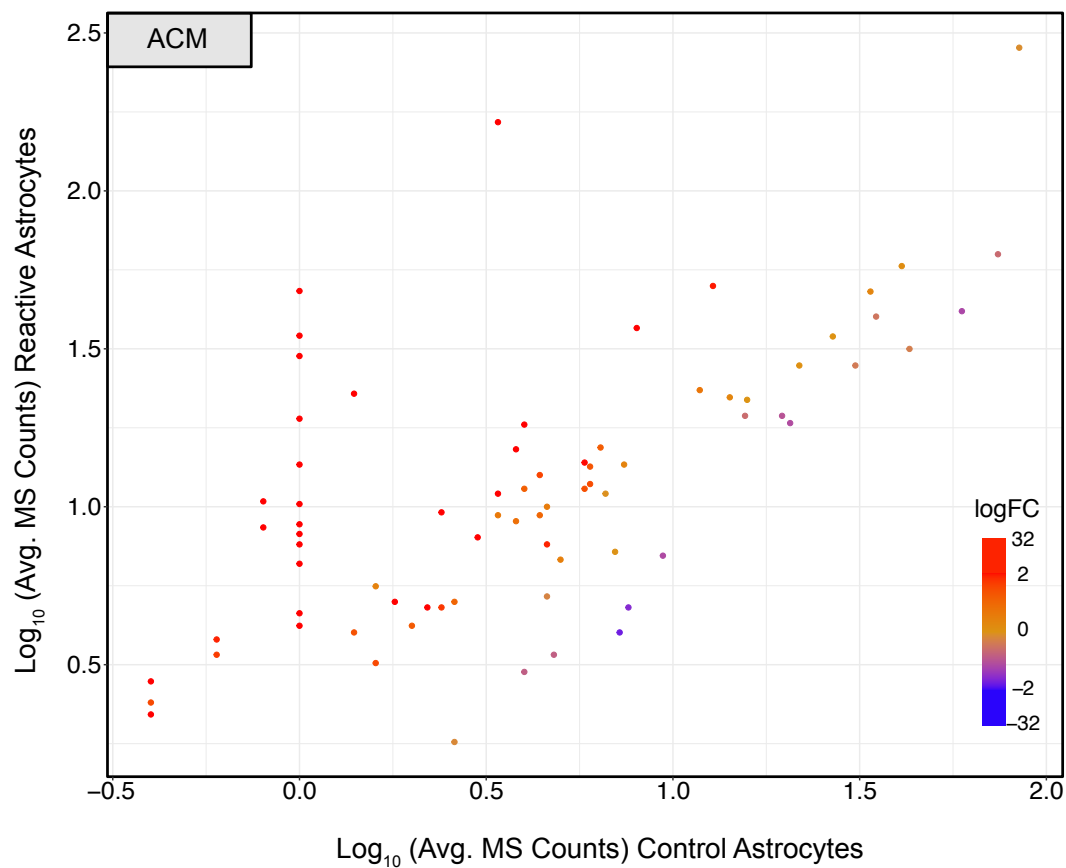


**Figure 8.7** Scatter plot shows the significant proteins in ACM due to the reactivity of the astrocytes. Red and blue points indicate the proteins in highest and lowest abundance based on the logFC values respectively.

**Table 8-3** Top 17 upregulated proteins in ACM.

<b>Protein IDs</b>	<b>Gene names</b>	<b>Log<sub>2</sub>FC</b>	<b>FDR</b>
G3V7K3	Cp	32.0541441	2.00E-20
Q9WTV1	Chi3l1	31.79356268	2.00E-20
P30152	Lcn2	31.74187379	2.00E-20
Q6P734	Serping1	31.40810148	2.01E-20
G3V7N9	C1qb	30.181602	4.71E-20
G3V7L3	C1s	29.65959113	5.80E-20
P14844	Ccl2	29.56044697	5.80E-20
B5DEH7	C1r	29.15260139	7.26E-20
P15473	Igfbp3	28.81786643	8.65E-20
Q6P6Q5	App	28.62017577	9.26E-20
Q6GMN4	Csf1	28.12422999	1.25E-19
Q63083	Nucb1	28.064853	1.25E-19
F1LM16	Serpine1	27.90164919	1.25E-19
P11762	Lgals1	27.8919931	1.25E-19
Q9QXY8	Ccl7	27.53495669	1.60E-19
P04797	Gapdh	26.72763152	3.04E-19
M0RBF1	C3	8.127599072	0.004892255

### **8.3 Lipid and metabolite profiling of reactive astrocytes and their conditioned media**

#### **8.3.1 Sample preparation for lipidomics**

Lipid and metabolite extracts from astrocytes and ACM were prepared using a slightly modified Bligh & Dyer extraction procedure(17). Briefly, the frozen cell pellets were thawed for 10 mins at room temperature, and 200 uL ultrapure water was added to promote cell lysis, followed by 450 uL methanol and 250 uL HPLC-grade chloroform. The samples were vortexed for 10 seconds, resulting in a one-phase solution, and incubated at 4 °C for 15 mins. Next, 250 uL ultrapure water and 250 uL chloroform were added, creating a biphasic solution. The samples were centrifuged at 16,000 x g for 10 mins resulting in three phases in the tubes. The bottom organic phase containing the lipids was transferred to new tubes. The middle phase consisting of proteins was discarded, and the upper polar phase containing the metabolites was transferred to separate tubes. The organic and polar phase solvents were evaporated in a vacuum concentrator leaving behind the dried lipid and metabolite extracts. The same protocol was used to extract the lipids and metabolites from the ACM samples. The volumes of the solvents were scaled to 2.5 times per 500 uL of the sample volume.

#### **8.3.2 MRM-profiling for lipids and metabolites**

Multiple Reaction Monitoring (MRM)-profiling of the extracted lipids and metabolites was performed as described previously(18–21). The dried lipid extracts were dissolved in 200 uL methanol:chloroform (3:1 v/v) to make lipid stock solutions and transferred to glass LC vials. The lipids were further diluted 200 times (cells) and 100 times (media) in injection solvent (acetonitrile:methanol:ammonium acetate 300 mM 3:6.65:0.35 (v/v)). The dried metabolites were resuspended in 200 uL (cells) and 1000 uL (media) of MeOH:ACN (1:1 v/v) to make stock solutions. The metabolite stock solutions were diluted 5 times (cells) and 250 times (media) in the injection solvent. The injection solvent alone without any lipids or metabolites was used as the “blank” sample. The injection solvent containing the quantitative mass spectrometry internal standard consisting of a mixture of 13 deuterated lipid internal standards at a concentration of 100 µg/mL each (Avanti Polar Lipids, #330731) was used as the “quality control” sample to monitor their peaks over time to confirm the proper working of the instrument. MS data was acquired by flow-injection (no chromatographic separation) from 8 µL of diluted lipid extract stock solution

delivered (per sample per method) using a micro-autosampler (G1377A) to the ESI source of an Agilent 6410 triple quadrupole MS. This method enabled the interrogation of the relative amounts of numerous lipid species within ten major lipid classes based on the LipidMaps database. Triacylglycerides (TAGs) were divided into 2 separate methods (TAG1 and TAG2) based on the fatty acid residues' neutral losses as the product ions. Specifically, TAG1 method screened for 16:0, 16:1, 18:0 and 18:1 fatty acids and TAG2 method screened for 18:2, 20:0, and 20:4 fatty acids. The raw MS data obtained for lipids and metabolites were analyzed using an in-house script. The lists containing MRM transitions and the respective ion intensity values were exported for statistical analysis.

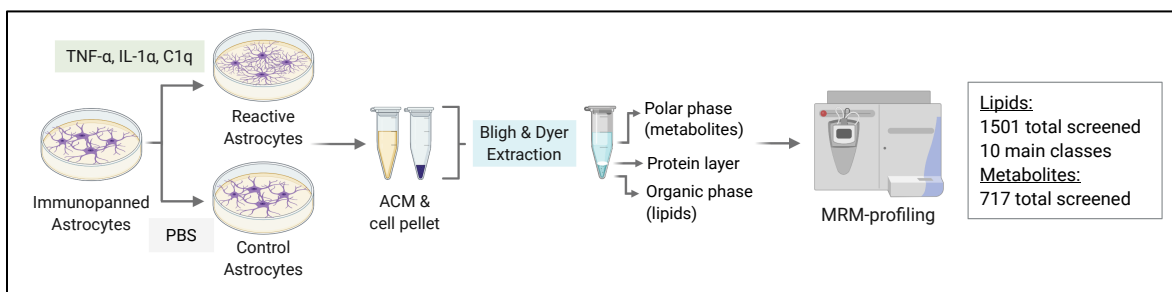


**Figure 8.8** Lipidomics pipeline for A1 astrocytes and ACM.

### 8.3.3 Data analysis

All statistics for the comparisons of MRM transitions of the lipids and metabolites between reactive astrocytes compared to control astrocytes were calculated using the edgeR package(14). Here, the ion count for a given molecule (lipid or metabolite) was referred to using the subscript  $s$  for the sample (cell replicate for a class of analyte) and  $b$  for the specific molecule (lipid or metabolite). An additional ‘intercept’ sample was added to model the experimental blank performed using just the injection media to ensure that all comparisons are significant with respect to this blank control. The edgeR package fits a generalized linear model to the following log-linear relationship for the mean-variance:  $\log \mu_{bs} = X_b^T \beta_g + \log N_s$ , for each molecule  $b$  in sample  $s$  where the sum of all ion intensity for sample  $s$  sums to  $N_s$ . This allowed for the calculation of the coefficient of variation (CV) for the ion count for a molecule in a sample ( $y_{bs}$ ) using the following relationship  $CV^2(y_{bs}) = 1/\mu_{bs} + \Phi_b$ , where  $\Phi_b$  is the dispersion of the molecule. This dispersion term was estimated using the common dispersion method(15). These values were used to calculate

the associated  $\log_2FC$  between the reactive and control astrocytes and the p-values were obtained using the likelihood ratio test. These p-values were then adjusted for multiple testing using the BH method to  $FDR(16)$ . The lipid or metabolite was considered significant when  $FDR < 0.1$ .

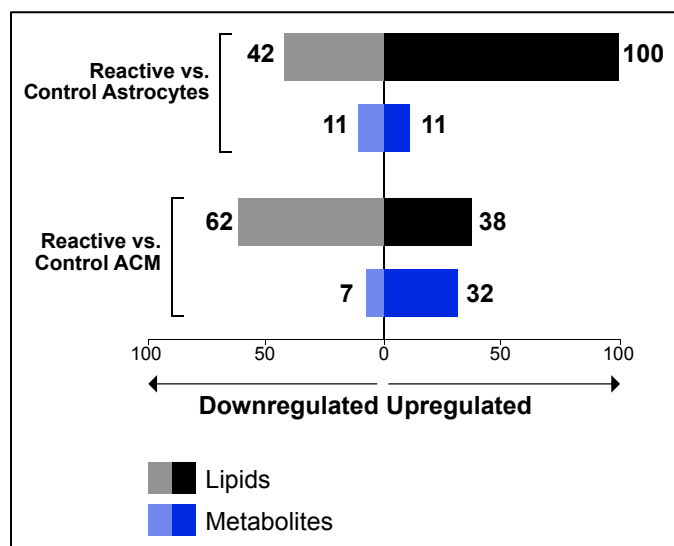


**Figure 8.9** Number of differentially regulated lipids and metabolites in reactive astrocytes and ACM. Lipids are shown in black/grey and metabolites are shown in blue (dark/pale).

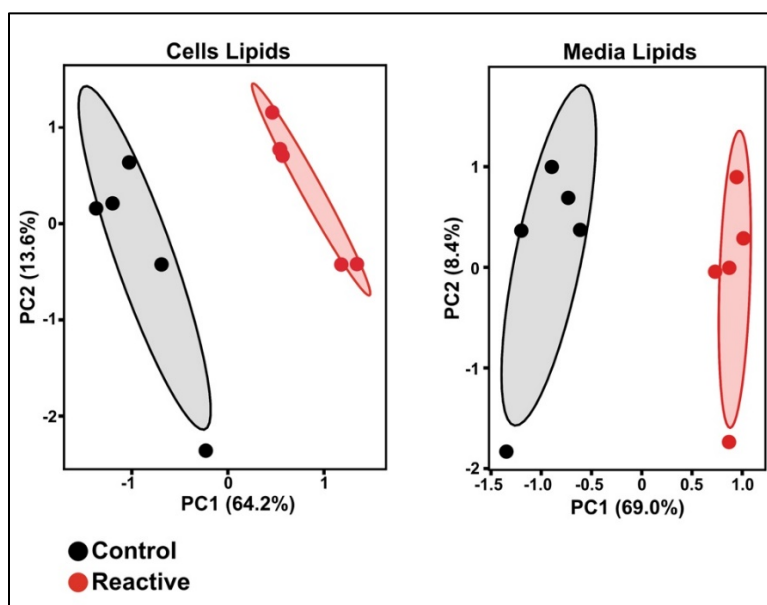


**Figure 8.10** Principal component analysis (PCA) plots shows separation in the lipidome of reactive and control astrocytes. Variation in more than 70% of the sample and control data is seen in each category showcasing the separation of the reactive and control astrocytes and ACM lipidome.



### 8.3.4 Saturated phosphatidylcholines are upregulated in reactive astrocytes

Astrocytes showed dramatic changes to their lipidome due to reactivity induced by activated microglial factors. The unbiased lipidomics (1501 lipids from 10 classes) performed on the cell extracts from quiescent and reactive astrocytes to determine if there was a shift in the cellular lipidome identified phosphatidylcholines (PCs) to be upregulated in reactive astrocytes. Prominently, the cells exhibited an upregulation of PCs with very-long chain fatty acid acyl chains (30-40 carbon atoms). Interestingly, triacylglycerols were largely downregulated in these reactive astrocytes.

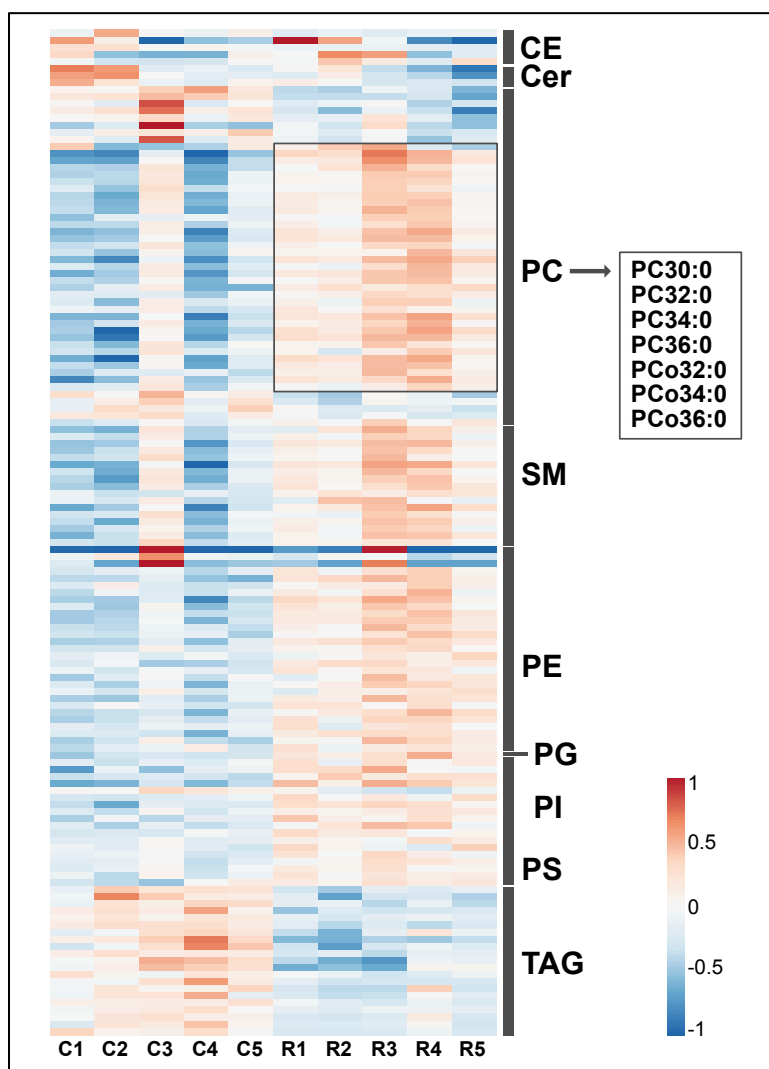


**Figure 8.11** Heatmap of cell lipids demonstrating the lipid class-specific changes in control (C) and reactive (R) astrocytes. The clear transition from blue (downregulated) to red (upregulated) shows the changes in cellular states via lipid-mediated mechanisms.

**Table 8-4** Top 20 upregulated lipids in A1 reactive astrocytes.

Lipid	Log <sub>2</sub> FC	FDR
PC (30:0)	1.04648533	9.92E-29
PC (36:8)	0.84286341	2.37E-18
SM (d18:0/16:0)	0.82367632	6.31E-18
PI (36:2)	0.82184952	1.04E-17
PC (30:1)	0.81901744	7.82E-18
PCo(34:0)	0.80697386	2.84E-17
PCo(32:0)	0.7824955	2.07E-16
PE (34:1)	0.78144499	2.10E-16
PCo(36:1)	0.78083488	2.53E-16
PCo(34:1)	0.77688997	2.53E-16
SM (d18:1/16:0)	0.74871137	3.52E-15
PE (32:1)	0.69892307	5.26E-13
PC (36:1)	0.67600936	2.10E-12
PCo(38:2)	0.64594058	4.19E-11
SM (d16:1/24:0)	0.64558435	2.38E-11
PC (36:2)	0.64537487	2.38E-11
PC (38:2)	0.64206551	3.43E-11
PEo (36:1)	0.61160868	6.37E-10
PE (38:2)	0.60175192	7.20E-10
PE (36:2)	0.59964553	6.94E-10

**Table 8-5** Top 20 downregulated lipids in A1 reactive astrocytes.

<b>Lipid</b>	<b>Log<sub>2</sub>FC</b>	<b>FDR</b>
TAG(50:4)_FA 16:1	-0.852679	3.10E-18
Lyso_PC(18:1)	-0.7243119	5.04E-14
Lyso_PC(16:1)	-0.7165528	1.07E-13
TAG(52:3)_FA 16:1	-0.6533062	4.06E-11
TAG(48:2)_FA 16:1	-0.6458235	7.49E-11
Lyso_PC(16:0)	-0.6074569	5.16E-10
PE (20:1)	-0.5843464	3.35E-09
TAG(48:3)_FA 16:1	-0.5792601	1.14E-08
TAG(50:4)_FA 18:1	-0.5611166	2.41E-08
TAG(52:3)_FA 18:1	-0.5511802	3.08E-08
Cer(d18:1/18:1(9Z))	-0.5192937	1.87E-07
TAG(50:3)_FA 16:0	-0.5128251	4.16E-07
Cer(d18:1/18:0)	-0.481071	1.41E-06
TAG(52:4)_FA 18:1	-0.4745916	4.45E-06
PCo(38:5)	-0.4682077	3.59E-06
TAG(48:2)_FA 16:0	-0.4672459	6.63E-06
PE (22:4)	-0.4485133	1.53E-05
TAG(48:2)_FA 18:1	-0.4166882	9.46E-05
TAG(54:6)_FA 20:4	-0.4109757	1.62E-04
TAG(52:3)_FA 16:0	-0.3916732	3.22E-04

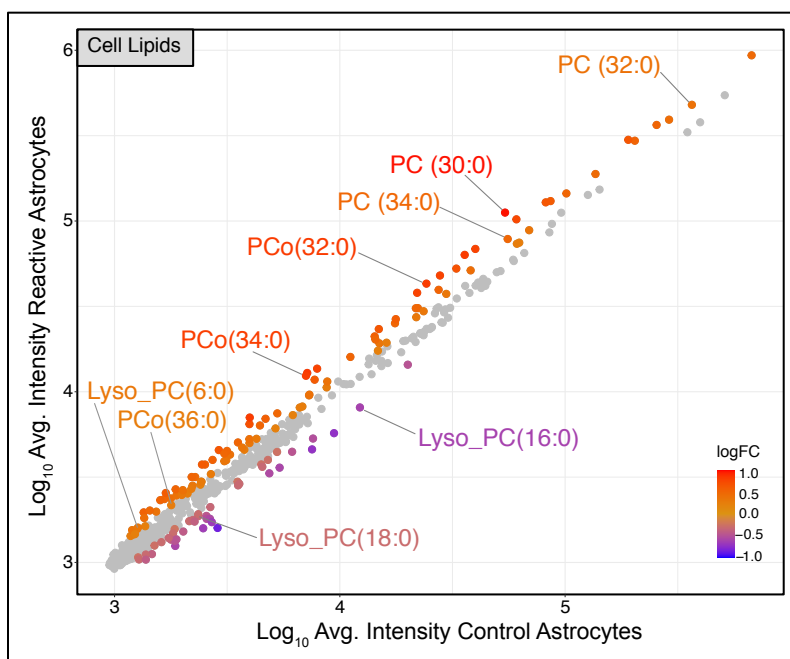


**Figure 8.12** Scatter plot of cell lipids shows the variation of the significant lipids from the unchanged lipids shown as grey points. Lipids in orange/red are upregulated and lipids in blue/purple are downregulated.

### 8.3.5 Long-chain saturated free fatty acids are upregulated in reactive ACM

The toxic factor that causes neurotoxicity must be present in the ACM of reactive astrocytes. The ACM of reactive astrocytes largely upregulated long-chain free fatty acids (FFAs) compared to the ACM of control astrocytes. FFAs have been previously studied to cause cellular toxicity in various in vitro cell models as well as in animal models. Thus, FFAs from the reactive astrocyte ACM were tested as possible candidates for the neurotoxin.

Interestingly, while PCs were upregulated in the reactive cells, they were not up in the ACM. Given that PCs are downregulated in the ACM suggests that apart from PCs being made in cells and localized to the cell membranes, they may also be taken up by reactive astrocytes via phagocytic mechanisms. Furthermore, it is not well known if reactive astrocytes are “suicidal” or apoptotic or even ready to be engulfed by microglia and macrophages via PC-mediated mechanisms. The changes in PCs in media is unlike changes in FFAs which are clearly produced in reactive astrocytes and are then released from the cells into the conditioned media. Additionally, a few triacylglycerols (TAGs) are also upregulated in the ACM of reactive astrocytes. The slight upregulation of TAGs in reactive ACM but their downregulation in reactive cells is also worth

noting and could explain some of the underlying changes to astrocytic metabolism due to their reactivity.

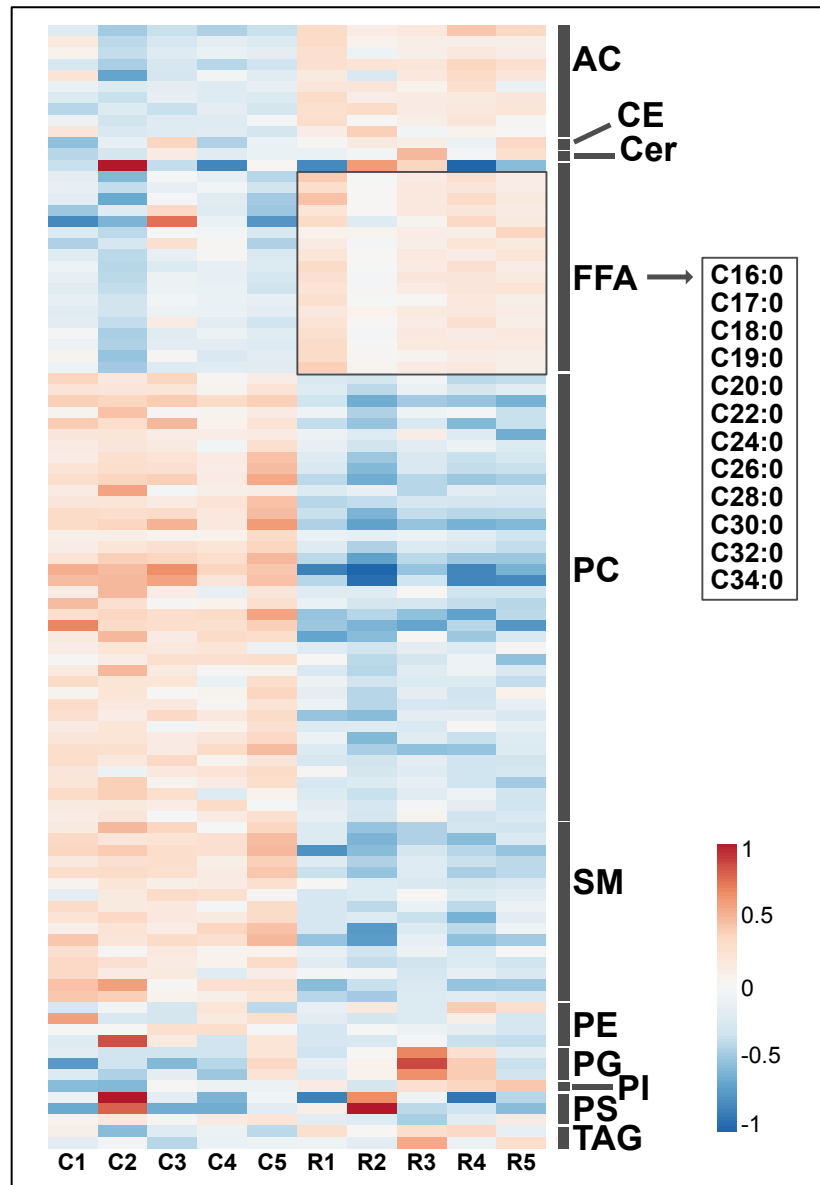


**Figure 8.13** Heatmap of media lipids demonstrating the lipid class-specific changes in control (C) and reactive (R) astrocytes. The clear transition from blue (downregulated) to red (upregulated) shows the changes in cellular states via lipid-mediated mechanisms.

**Table 8-6** Top 25 upregulated lipids in ACM.

<b>Lipid</b>	<b>Log<sub>2</sub>FC</b>	<b>FDR</b>
(5Z,8Z)-3-hydroxytetradecadienoylcarnitine	0.63612985	3.96E-10
(9Z,12Z)-3-hydroxyhexadecadienoylcarnitine	0.61183183	1.99E-09
PG (24:0)	0.52191518	1.06E-06
C18:0	0.51885585	6.93E-07
Hexacosanoyl carnitine	0.50755528	1.55E-06
PI (22:1)	0.43391365	1.15E-04
C16:0	0.43165515	8.41E-05
cis-5-Tetradecenoylcarnitine	0.40938238	2.66E-04
C34:0	0.39250291	5.37E-04
TAG(48:0)_FA 16:0	0.38845622	9.51E-04
C24:5	0.37696806	0.0010519
C24:0	0.37572473	0.00109041
C30:0	0.37360696	0.00120436
C17:0	0.35792068	0.00235367
C24:1	0.35702963	0.00242519
PG (26:0)	0.35558356	0.00353044
C28:0	0.33803343	0.00517633
C19:0	0.33108191	0.00675516
C22:1	0.33014949	0.00702716
C20:1	0.32235662	0.00932669
C20:0	0.32187949	0.00932669
C26:0	0.31583177	0.0114129
C26:1	0.31511251	0.01160081
3-hydroxypalmitoleoylcarnitine, Heptadecanoyl carnitine	0.30779834	0.01575244
(7Z,10Z)-hexadecadienoylcarnitine	0.30311785	0.01842848

**Table 8-7** Top 25 downregulated lipids in ACM.

<b>Lipid</b>	<b>Log<sub>2</sub>FC</b>	<b>FDR</b>
PC (36:3)	-1.2370878	5.86E-37
PC (36:4)	-1.0811477	7.00E-28
PC (38:4)	-0.9706337	1.29E-22
PC (34:2)	-0.9563433	1.29E-22
Lyso_PC(16:1)	-0.8731724	7.97E-19
PC (38:3)	-0.867268	2.49E-18
SM (d16:1/24:1)	-0.8566176	5.67E-18
PC (36:2)	-0.8354067	2.11E-17
PC (32:2)	-0.8140561	2.09E-16
SM (d18:1/20:0)	-0.7944475	9.80E-16
SM (d18:2/22:1)	-0.7491798	1.78E-13
PC (34:1)	-0.7332569	1.75E-13
Lyso_PC(18:1)	-0.7090613	1.50E-12
SM (d16:1/24:0)	-0.7036546	2.33E-12
PCo(36:3)	-0.675519	4.95E-11
SM (d18:0/20:0)	-0.6680054	3.19E-11
PC (38:5)	-0.6494334	4.06E-10
SM (d16:1/22:1)	-0.6273938	1.10E-09
PC (32:1)	-0.6237352	7.83E-10
SM (d18:1/18:1)9Z))	-0.5686099	5.56E-08
PC (34:0)	-0.5619356	6.31E-08
SM (d18:1/18:0)	-0.5565666	8.70E-08
SM (d18:0/18:0)	-0.5555712	8.51E-08
PCo(34:2)	-0.5528723	1.57E-07
PC (32:0)	-0.5525186	9.34E-08

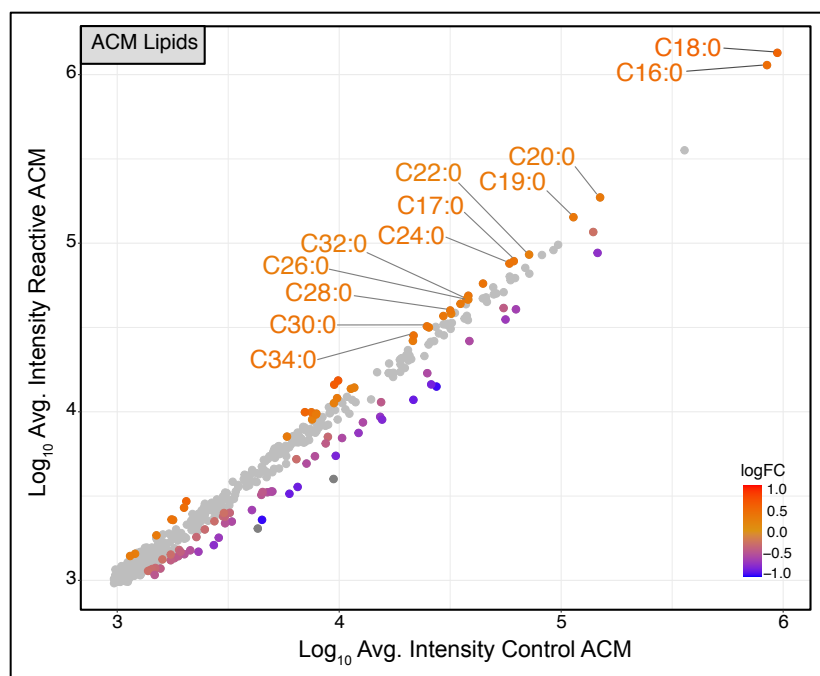


**Figure 8.14** Scatter plot of media lipids shows the variation of the significant lipids from the unchanged lipids shown as grey points. Lipids in orange/red are upregulated and lipids in blue/purple are downregulated. C18:0, C16:0, C20:0, C19:0 are the highly upregulated lipids in the reactive ACM.

### 8.3.6 Metabolome characterization of reactive astrocytes and their conditioned medium

In addition to lipids, the changes in cellular and media metabolites was also evaluated using MRM-profiling. The reactive ACM contained more differentially regulated metabolites and more upregulated metabolites compared to the cells. L-Glutamate was found to be upregulated in both reactive astrocytes (FDR  $6.95 \times 10^{-13}$ ,  $\text{Log}_2\text{FC}$  0.94) and their conditioned media (FDR 0.0065,  $\text{Log}_2\text{FC}$  0.421).



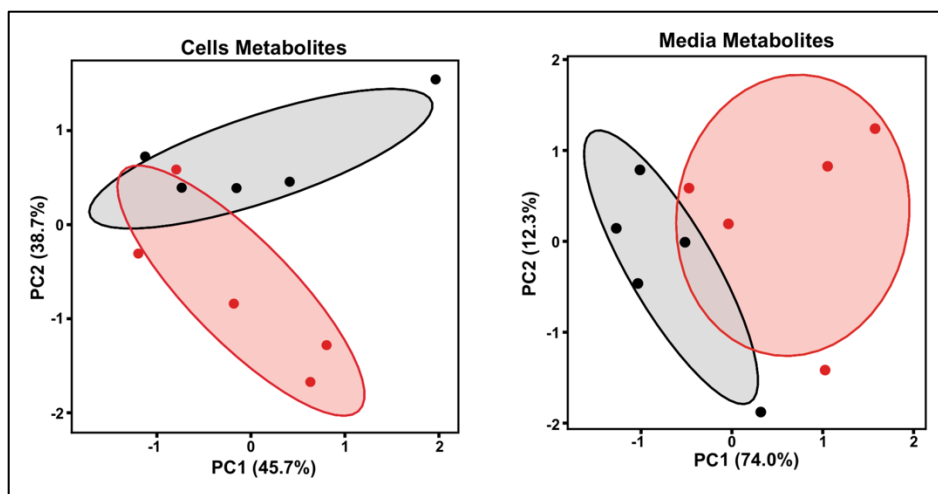


**Figure 8.15** Principal component analysis (PCA) plots do not show slight but not complete separation in the metabolome of reactive and control astrocytes.

**Table 8-8** Upregulated metabolites in reactive astrocytes.

Metabolite	Log <sub>2</sub> FC	FDR
Creatine	1.00287422	1.58E-14
Glutamic acid; L-Glutamate	0.93500221	6.95E-13
Hypotaurine	0.68519846	1.65E-06
DL-Homoserine; L-Threonine	0.61022672	3.63E-05
Hypoxanthine	0.36956263	0.06060315

**Table 8-9** Downregulated metabolites in reactive astrocytes.

Metabolite	Log <sub>2</sub> FC	FDR
Glutamine	-0.5728887	1.65E-04
Progesterone	-0.521588	9.44E-04
DL-3,4-Dihydroxymandelic acid	-0.4986236	0.00221337
L-Isoleucine; L-Leucine	-0.4686074	0.00476935
Bilirubin	-0.4460899	0.00978438
4-Hydroxy-L-proline	-0.4096564	0.02297377
Valine	-0.4071264	0.02323833
Asparagine	-0.3969348	0.02929837
L-Phenylalanine	-0.3439278	0.09971966

**Table 8-10** Upregulated metabolites in reactive ACM.

Metabolite	Log <sub>2</sub> FC	FDR
L-2-Aminobutyric acid	0.69427001	8.58E-07
Valine	0.65192878	3.94E-06
4-Hydroxy-L-proline	0.6323613	7.06E-06
L-Isoleucine	0.60960043	1.41E-05
D(-)-hydroxy butyric acid	0.60640509	1.41E-05
L-Leucine	0.5984328	1.58E-05
Histidine	0.5856986	2.45E-05
Trazodone	0.57521784	3.27E-05
Asparagine	0.54671031	8.62E-05
L-Proline	0.54181104	9.66E-05
L-Phenylalanine	0.51357249	2.75E-04
Methionine	0.48214758	8.86E-04
D-Glucose	0.47832045	0.00104529
D-Fructose 6-phosphate	0.44823014	0.00280356
UDP	0.44527015	0.00313062
DL-Homoserine	0.43108819	0.00460911
Glutamine	0.4211057	0.00657365
L-Phenylalanine	0.41856011	0.00658365
Hypoxanthine	0.39957587	0.01337282
Pantothenic acid	0.36923832	0.03001779
D-Ribulose 5-phosphate	0.36121745	0.03265702
4-Hydroxy-L-proline	0.3563933	0.03735371
L-Serine	0.35601888	0.03735371
Arginine	0.35166995	0.03844652
Succinic acid	0.34825891	0.04210226
L-Lysine	0.33922641	0.05178197
Lactic acid	0.33802022	0.05468144

**Table 8-11** Downregulated metabolites in reactive ACM.

Metabolite	Log <sub>2</sub> FC	FDR
Alanine	-0.5741813	3.27E-05
L-Threonine	-0.3787722	0.02507007
5'-CMP	-0.3681325	0.03001779
Anthranilic acid	-0.3538115	0.03844652
Cytidine	-0.3317984	0.06359155

#### 8.4 Knocking out the *Elov11* gene in reactive astrocytes changes their lipid profiles

Because shorter length and unsaturated phosphatidylcholines and free fatty acids are essential for the structure of the cell, the metabolic enzyme ELOVL1 was targeted for deletion. ELOVL1 is the enzyme specifically responsible for the synthesis of the longer chain, fully-saturated lipids(22) that was upregulated in the lipid mass spectrometry experiment. An *Elov11*<sup>flox/flox</sup> line was crossed with a Gfap-Cre line to generate an astrocyte-specific *Elov11* conditional knockout mouse (cKO). Unlike the global knockout of *Elov11*, which is embryonically lethal, mice with an astrocyte-specific cKO of *Elov11* are viable and fertile with no obvious behavioral or survival phenotypes.

The experiments corresponding to the generation of the mouse line, preparation of the cell and ACM samples were conducted by Dr. Kevin Guttenplan. The frozen cell pellets and ACM from the *Elov11*-cKO and WT mice were used as the starting material in this experiment to perform the characterization of the PC and FFA profiles of reactive astrocytes.

Astrocytes from WT and *Elov11* cKO mice were purified and the lipidome of reactive WT vs reactive *Elov11* cKO mice was compared. The lipidome of the *Elov11*-cKO and WT astrocytes separated in the PCA plots validating the changes to the lipid profiles due to *Elov11* deletion.

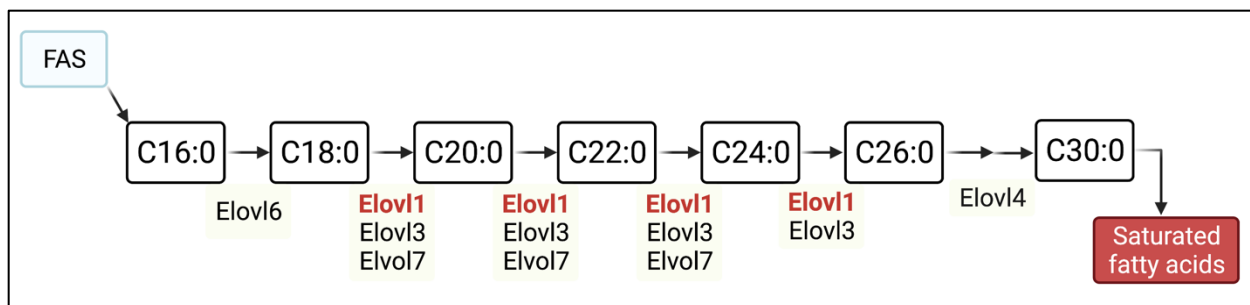


**Figure 8.16** Long chain and very long-chain fatty acid biosynthesis. Elovl1 (red) is key in several steps of the synthesis to make saturated fatty acids. FAS is fatty acid synthase.

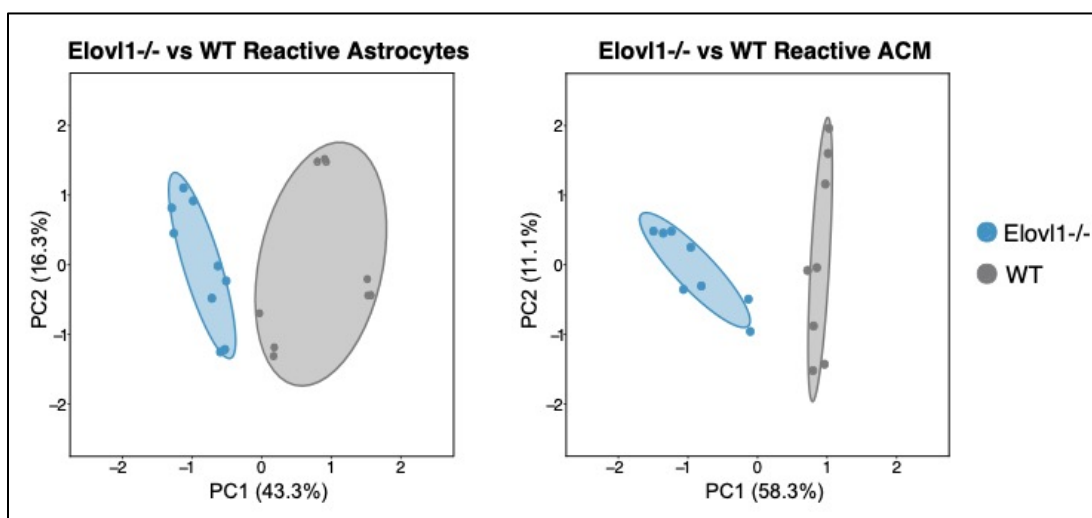


**Figure 8.17** Principal component analysis (PCA) plots shows separation in the lipidome of reactive and control astrocytes. Variation in more than 60% of the sample and control data is seen in each category showcasing the separation of the *Elovl1*-cKO reactive and control astrocytes and ACM lipidome.

As expected, the *Elovl1*-cKO reactive astrocytes showed a decrease in long-chain saturated FFAs compared to the WT reactive astrocytes. For example, C20:0, C22:0, C19:0, C24:0, C16:0, C17:0, etc. were downregulated in reactive astrocytes with *Elovl1* deletion. This validated that targeting of *Elovl1* reduced saturated lipids in astrocytes.

**Table 8-12** Top 20 downregulated lipids in *Elovl1*-cKO reactive astrocytes compared to WT reactive astrocytes.

Lipid	Log <sub>2</sub> FC	FDR
C20:0	-2.1337222	3.57E-116
C22:0	-1.0614026	1.85E-30
C22:6	-0.9788238	4.29E-26
C19:0	-0.9434302	2.11E-24
Lyso_PC(20:3)	-0.8604094	3.18E-20
PCo(32:3)	-0.6338684	3.92E-11
C20:1	-0.6084669	1.75E-10
Lyso_PC(19:3)	-0.573501	4.59E-09
C24:5	-0.5039944	2.38E-07
C16:1	-0.4875828	6.39E-07
C18:2	-0.4722271	1.36E-06
C22:1	-0.4334341	1.14E-05
C17:1	-0.4304586	1.31E-05
C24:0	-0.4278276	1.41E-05
C24:1	-0.4096295	3.39E-05
Lyso_PC(20:2)	-0.3706563	2.28E-04
C24:6	-0.3697049	1.96E-04
C18:1	-0.3203105	0.00148149
C18:0	-0.3130576	0.0019727
C17:0	-0.3018277	0.00304401

**Table 8-13** Top 20 upregulated lipids in *Elovl1*-cKO reactive astrocytes compared to WT reactive astrocytes.

Lipid	Log <sub>2</sub> FC	FDR
PC (32:3)	0.709534	5.67E-14
C15:1	0.63257617	3.25E-11
SM (d18:1/18:1)9Z))	0.5524984	9.99E-09
SM (d18:1/18:0)	0.48165826	8.01E-07
PC (32:2)	0.48148501	8.01E-07
PCo(38:4)	0.45416212	4.14E-06
C20:3	0.45023123	4.50E-06
PC (30:2)	0.41971007	2.19E-05
PCo(34:1)	0.41514455	2.62E-05
PCo(38:3)	0.39924737	6.15E-05
SM (d18:1/16:0)	0.39452647	6.97E-05
PCo(32:2)	0.39300024	7.87E-05
SM (d16:1/22:1)	0.39076749	8.03E-05
SM (d16:1/18:1)	0.38936552	8.85E-05
C14:1	0.38725678	8.85E-05
PC (38:3)	0.38414331	1.01E-04
PC (40:4)	0.38117007	1.19E-04
PCo(34:2)	0.35989115	3.03E-04
PC (34:3)	0.35159154	4.30E-04
PC (32:0)	0.34801528	4.91E-04

**Table 8-14** Top 19 downregulated lipids in *Elovl1*-cKO reactive ACM compared to WT ACM.

<b>Lipid</b>	<b>Log<sub>2</sub>FC</b>	<b>FDR</b>
C24:6	-0.6757876	2.16E-23
C20:3	-0.6592589	2.02E-22
C16:1	-0.4413498	3.89E-10
C15:1	-0.4327595	7.84E-10
Lyso_PC(20:3)	-0.3836129	8.28E-08
Lyso_PC(12:0)	-0.3697682	4.68E-07
C12:0	-0.2932304	6.18E-05
C32:0	-0.2895406	7.72E-05
C12:1	-0.2859954	9.30E-05
C24:5	-0.2857569	9.30E-05
C17:1	-0.2751099	1.80E-04
C15:0	-0.2679019	2.66E-04
Lyso_PC(10:0)	-0.2408067	0.00232475
Lyso_PC(20:2)	-0.2297349	0.00353771
C19:0	-0.1841237	0.021125
C20:1	-0.1540922	0.06903866
Lyso_PC(20:5)	-0.1508414	0.09606421
C24:0	-0.1473253	0.08444761
C14:1	-0.1424976	0.09922171



**Table 8-15** Top 19 upregulated lipids in *Elov11*-cKO reactive ACM compared to WT ACM.

Lipid	Log <sub>2</sub> FC	FDR
PC (40:0)	0.81735712	1.16E-32
SM (d18:2/24:1)	0.47290793	4.17E-11
SM (d18:0/22:0)	0.43384928	1.53E-09
SM (d18:1/16:0)	0.41620915	4.23E-09
SM (d18:1/24:1)15Z))	0.38913408	6.40E-08
PC (38:3)	0.37816888	1.83E-07
SM (d18:1/18:0)	0.36430845	4.31E-07
PC (38:7)	0.33605687	3.96E-06
PC (36:1)	0.32692208	7.98E-06
PC (32:2)	0.32605719	8.02E-06
PC (38:1)	0.31595081	2.57E-05
PC (34:0)	0.3107131	2.57E-05
SM (d18:1/18:1)9Z))	0.30149977	6.18E-05
SM (d18:1/24:0)	0.28201815	1.76E-04
PC (34:1)	0.27233279	2.12E-04
PCo(34:1)	0.26956586	2.86E-04
SM (d18:0/20:0)	0.26834333	2.74E-04
PC (32:1)	0.25947623	4.40E-04
Lyso_PC(16:0)	0.25740499	5.03E-04

The reactive ACM from *Elov11* cKO mice was significantly less toxic to oligodendrocytes *in vitro* as well as towards retinal ganglion cells following axon crush *in vivo* than the reactive ACM from WT mice thereby confirming that this lipid class mediated neurotoxicity (data available in the Nature paper; currently under minor revision). Upon concentrating the conditioned media 10-fold, there was a slight toxicity of *Elov11* cKO ACM to oligodendrocytes, however, the identically concentrated WT ACM was much more toxic to the cells, consistent with the decrease but not complete elimination of these toxic lipids in *Elov11* cKO ACM.

## 8.5 Concluding thoughts

These experiments provide the most comprehensive characterization of the proteome, lipidome, and metabolome of reactive astrocytes to date. The proteomic profiling identified several previously known as well as unknown proteins to be upregulated in reactive astrocytes and their conditioned media. Specifically, we saw the complement protein 3 (C3) to be upregulated in the cells as well as the ACM. This protein (and not the canonical GFAP) was previously used as a marker to label reactive astrocytes in cells and in pathological tissue. Identifying this protein in both our cells and ACM further validated the robustness of our datasets. Furthermore, we identified proteins such as LCN2 (Lipocalin 2) and SERPING1, whose corresponding genes were previously identified as strong markers of reactive astrocytes via genomic analysis. Interestingly, we also identified several other complement proteins in the reactive ACM like C1QB, C1R, C1S, etc. indicating a strong immune response and further studies to delineate the underlying mechanisms will be critical to understand other functional roles of reactive astrocytes.

Our lipidomics characterization showed that the lipidome of astrocytes changes dramatically with reactivity. We identified an upregulation of several PCs comprising of long and saturated acyl chains in the reactive astrocytes compared to WT astrocytes. Specifically, we identified PC(30:0), PC(32:0), PC(34:0), PC(36:0), etc. along with a few PEs with unsaturated acyl chains to be upregulated in reactive astrocytes. In the reactive ACM, we saw a striking upregulation of saturated long-chain FFAs to be upregulated, including, C18:0, C16:0, C34:0, C24:0, C30:0, C17:0, etc. These datasets demonstrate the dramatic changes occurring in the lipid profiles of reactive astrocytes. Furthermore, these characterizations were instrumental in the identification of the neurotoxic factor(s) released by reactive astrocytes (into their ACM) that were responsible for the

killing of damaged neurons *in vitro* and *in vivo*. Dr. Kevin Guttenplan used these datasets to identify and validate that saturated lipids released by reactive astrocytes (specifically, saturated PCs upregulated in the cells and saturated FFAs upregulated in the ACM) caused the death of neurons and mature oligodendrocytes *in vitro* and *in vivo* (i.e. reactive astrocytes induce neuronal death via saturated lipids; data not shown). These findings highlight both the important role of the astrocyte reactivity response in CNS injury and neurodegeneration and the relatively unexplored role of lipids in CNS signaling. These experiments demonstrate that astrocytes are prodigious secreters of lipids and more detailed study of their lipid-mediated functions will likely lead to fruitful discoveries.

Much of the scientific focus on astrocytes has been on their secreted proteins, likely in part due to the technical barriers to studying molecular classes such as lipids. Techniques like MRM-profiling and other sensitive/robust mass spectrometry methods are therefore essential to elucidate the identity and structures of lipid and metabolite molecules that are implicated in astrocyte signaling in health and disease or injury. There is also growing literature surrounding the formation of lipid droplets in glia in health and disease(23), which further demonstrates the potential impact of lipid metabolism on CNS physiology. Any potential connections between the changes in lipid secretion studied here and the formation or function of lipid droplets should be untangled in future work. For example, Chapter 7 has detailed the ability of microglia to form lipid droplets with A $\beta$  exposure *in vitro* and *in vivo* in the 5xFAD mice. I showed that microglia upregulate FFAs that may be cytotoxic with initial exposure and treatment with A $\beta$ . It was hypothesized that microglia overcome the FFA-induced cytotoxicity by upregulating TAGs in their lipid droplets. Thus, several outstanding questions remain such as, Do microglia develop a similar phenotype upon an exposure to reactive astrocyte-induced FFA secretion? Do reactive astrocytes themselves make lipid droplets to circumvent FFA-induced cytotoxicity via a positive feedback loop? Unlike neurons and mature oligodendrocytes that are susceptible to the saturated lipids secreted by reactive astrocytes, microglia may be able to overcome the FFA-induced toxicity via lipid droplet formation (Chapter 7). Further experiments in these directions will reveal novel cellular mechanisms involved in overcoming lipid-mediated cytotoxicity by microglia and astrocytes in injury and neurodegeneration.

## 8.6 References

- [1] B. A. Barres, What is a glial cell? *Glia*. 43, 4–5 (2003).
- [2] N. J. Allen, B. A. Barres, Neuroscience: Glia - more than just brain glue. *Nature*. 457 (2009), pp. 675–677.
- [3] J. B. Zuchero, B. A. Barres, Glia in mammalian development and disease. *Dev.* 142, 3805–3809 (2015).
- [4] J. L. Zamanian, L. Xu, L. C. Foo, N. Nouri, L. Zhou, R. G. Giffard, B. A. Barres, Genomic analysis of reactive astrogliosis. *J. Neurosci.* (2012), doi:10.1523/JNEUROSCI.6221-11.2012.
- [5] S. A. Liddelow, K. A. Guttenplan, L. E. Clarke, F. C. Bennett, C. J. Bohlen, L. Schirmer, M. L. Bennett, A. E. Münch, W. S. Chung, T. C. Peterson, D. K. Wilton, A. Frouin, B. A. Napier, N. Panicker, M. Kumar, M. S. Buckwalter, D. H. Rowitch, V. L. Dawson, T. M. Dawson, B. Stevens, B. A. Barres, Neurotoxic reactive astrocytes are induced by activated microglia. *Nature*. 541, 481–487 (2017).
- [6] M. Nagai, D. B. Re, T. Nagata, A. Chalazonitis, T. M. Jessell, H. Wichterle, S. Przedborski, Astrocytes expressing ALS-linked mutated SOD1 release factors selectively toxic to motor neurons. *Nat. Neurosci.* 10, 615–622 (2007).
- [7] F. P. Di Giorgio, M. A. Carrasco, M. C. Siao, T. Maniatis, K. Eggan, Non-cell autonomous effect of glia on motor neurons in an embryonic stem cell-based ALS model. *Nat. Neurosci.* (2007), doi:10.1038/nn1885.
- [8] K. A. Guttenplan, B. K. Stafford, R. N. El-Danaf, D. I. Adler, A. E. Münch, M. K. Weigel, A. D. Huberman, S. A. Liddelow, Neurotoxic Reactive Astrocytes Drive Neuronal Death after Retinal Injury. *Cell Rep.* 31 (2020), doi:10.1016/j.celrep.2020.107776.
- [9] K. A. Guttenplan, M. K. Weigel, D. I. Adler, J. Couthouis, S. A. Liddelow, A. D. Gitler, B. A. Barres, Knockout of reactive astrocyte activating factors slows disease progression in an ALS mouse model. *Nat. Commun.* 11 (2020), doi:10.1038/s41467-020-17514-9.
- [10] S. A. Liddelow, B. A. Barres, Reactive Astrocytes: Production, Function, and Therapeutic Potential. *Immunity* (2017), , doi:10.1016/j.immuni.2017.06.006.
- [11] V. E. Hedrick, M. N. LaLand, E. S. Nakayasu, L. N. Paul, Digestion, Purification, and Enrichment of Protein Samples for Mass Spectrometry. *Curr. Protoc. Chem. Biol.* 7, 201–222 (2015).
- [12] A. J. Barabas, U. K. Aryal, B. N. Gaskill, Proteome characterization of used nesting material and potential protein sources from group housed male mice, *Mus musculus*. *Sci. Rep.* 9 (2019), doi:10.1038/s41598-019-53903-x.

- [13] S. Tyanova, T. Temu, P. Sinitcyn, A. Carlson, M. Y. Hein, T. Geiger, M. Mann, J. Cox, The Perseus computational platform for comprehensive analysis of (prote)omics data. *Nat. Methods*. 13 (2016), pp. 731–740.
- [14] M. D. Robinson, D. J. McCarthy, G. K. Smyth, edgeR: A Bioconductor package for differential expression analysis of digital gene expression data. *Bioinformatics*. 26, 139–140 (2009).
- [15] D. J. McCarthy, Y. Chen, G. K. Smyth, Differential expression analysis of multifactor RNA-Seq experiments with respect to biological variation. *Nucleic Acids Res.* 40, 4288–4297 (2012).
- [16] Y. Benjamini, Y. Hochberg, Controlling the False Discovery Rate: A Practical and Powerful Approach to Multiple Testing. *J. R. Stat. Soc. Ser. B.* 57, 289–300 (1995).
- [17] E. G. Bligh, W. J. Dyer, A RAPID METHOD OF TOTAL LIPID EXTRACTION AND PURIFICATION. *Can. J. Biochem. Physiol.* 37, 911–917 (1959).
- [18] C. R. Ferreira, K. E. Yannell, B. Mollenhauer, R. D. Espy, F. B. Cordeiro, Z. Ouyang, R. G. Cooks, Chemical profiling of cerebrospinal fluid by multiple reaction monitoring mass spectrometry. *Analyst*. 141, 5252–5255 (2016).
- [19] C. B. de Lima, C. R. Ferreira, M. P. Milazzotto, T. J. P. Sobreira, A. A. Vireque, R. G. Cooks, Comprehensive lipid profiling of early stage oocytes and embryos by MRM profiling. *J. Mass Spectrom.* 53, 1247–1252 (2018).
- [20] Z. Xie, L. E. Gonzalez, C. R. Ferreira, A. Vorsilak, D. Frabutt, T. J. P. Sobreira, M. Pugia, R. G. Cooks, Multiple Reaction Monitoring Profiling (MRM-Profilng) of Lipids to Distinguish Strain-Level Differences in Microbial Resistance in Escherichia coli. *Anal. Chem.* 91, 11349–11354 (2019).
- [21] K. E. Yannell, C. R. Ferreira, S. E. Tichy, R. G. Cooks, Multiple reaction monitoring (MRM)-profiling with biomarker identification by LC-QTOF to characterize coronary artery disease. *Analyst*. 143, 5014–5022 (2018).
- [22] H. Guillou, D. Zadavec, P. G. P. Martin, A. Jacobsson, The key roles of elongases and desaturases in mammalian fatty acid metabolism: Insights from transgenic mice. *Prog. Lipid Res.* (2010), , doi:10.1016/j.plipres.2009.12.002.
- [23] J. Marschallinger, T. Iram, M. Zardeneta, S. E. Lee, B. Lehallier, M. S. Haney, J. V. Pluvinage, V. Mathur, O. Hahn, D. W. Morgens, J. Kim, J. Tevini, T. K. Felder, H. Wolinski, C. R. Bertozzi, M. C. Bassik, L. Aigner, T. Wyss-Coray, Lipid-droplet-accumulating microglia represent a dysfunctional and proinflammatory state in the aging brain. *Nat. Neurosci.* 23, 194–208 (2020).

## CHAPTER 9. MODULATING MICROGLIAL FUNCTION WITH STEROID COMPOUNDS

Portions of this chapter are available as an undergraduate thesis.

“Small Molecules Modulating Microglial Inflammatory Response *In Vitro*” by Gabrielle C. Williams, Department of Biochemistry, College of Agriculture, Purdue University, West Lafayette, IN 47906

### 9.1 Abstract

Microglia are the brain’s resident immune cells that are critical for maintaining tissue homeostasis in health and disease conditions. During injury or insult, the resting microglia undergo dramatic cellular changes and produce TNF- $\alpha$ , IL-1 $\alpha$ , nitric oxide (NO), etc. to mediate neuroinflammation. The cytokines released by activated microglia can influence the state and function of the neighboring cells in the environment such as astrocytes and neurons thereby leading to a cascade of downstream cellular events. Modulating some of these functional changes in microglia by using small chemical or biological molecules may be useful in alleviating neuroinflammation itself. In this study, we evaluated the effect of several FDA-approved steroidal compounds on the inflammatory response of BV-2 as well as primary mouse microglial cells. Specifically, the effect of the compounds on the secretion of NO, IL-1 $\alpha$ , and TNF- $\alpha$  by microglia that were activated with a classical inflammatory trigger lipopolysaccharide were determined. We show that out of the seven compounds tested, dexamethasone—a potent anti-inflammatory compound and an immunosuppressant, can modulate inflammatory function at nanomolar level concentrations in both BV2 as well as primary mouse microglia. Furthermore, we performed exploratory lipidomics on dexamethasone-treated activated microglial cells to investigate the lipidomic changes occurring in the drug-treated cells in culture. We found that dexamethasone upregulated several phosphatidylcholines and sphingomyelins and downregulated select phosphatidylserines—signaling lipids that are predominantly found on the plasma membrane. The underlying cellular and molecular mechanisms of these lipidomic changes in these cells are yet to be delineated. We conclude that dexamethasone is a potent immunomodulator of microglial function.

## 9.2 Introduction

Microglia are the brain's resident macrophages that remove the Alzheimer's disease (AD)-associated toxic amyloid beta ( $A\beta$ ) plaques by the process of phagocytosis and play a vital role in regulating neuroinflammation through various signaling pathways[1], [2]. As  $A\beta$  accumulates in the brain, microglia become "activated" and adopt a pro-inflammatory phenotype. Neuroinflammation is a characteristic feature of AD and also other neurodegenerative disorders that are mostly characterized by the progressive loss of neurons[3]–[5]. Currently, there are only a handful drugs approved by the Food and Drug Administration (FDA) for human use to moderate AD symptoms and there are no treatments that directly target the disease[6], [7]. The presence of  $A\beta$  plaques, dying neurons, and other cells in addition to the release of inflammatory molecules drive neuroinflammation in AD brains.

In addition to microglia, astrocytes are also affected by (and contribute to) neuroinflammation and have shown to contribute to the clearance of dying neurons in a mouse model of AD[8]. Astrocytes are star-shaped glial cells that are essential for neuronal support and survival. Activated microglia release inflammatory mediators which contribute to astrocyte activation resulting in reactive astrocytes formation. Specifically, interleukin 1 alpha ( $IL-1\alpha$ ), tumor necrosis factor alpha ( $TNF-\alpha$ ), and complement component 1q ( $C1q$ ) are inflammatory proteins released by microglia which are known to directly induce reactive astrocytes (or A1 astrocytes) to become toxic to neurons both *in vitro* and *in vivo*[9]–[11]. Thus, inhibiting or suppressing the release of these factors or their action may be an alternate way to prevent direct astrocyte-induced neurotoxicity *in vitro* and *in vivo*.

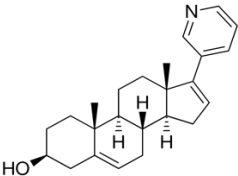
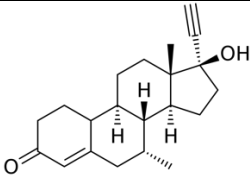
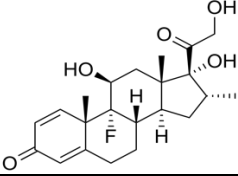
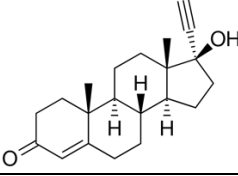
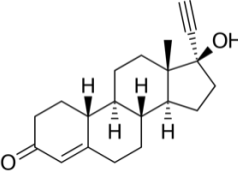
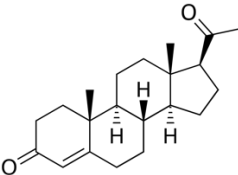
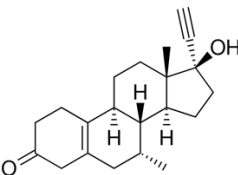
In this study, we utilized *in vitro* models of microglia comprising of a BV2 rodent cell line and primary mouse microglial cells to evaluate the effect of steroidal compounds on microglial function. Steroids are a class of organic compounds that contain a characteristic configuration of four cycloalkane rings fused together. Steroids play important roles in the regulation of several cellular functions; they regulate a wide range of metabolic, immune, and reproductive functions. The steroidal scaffold is present in many FDA-approved drugs. In this study, we evaluate the effects of seven FDA-approved steroid compounds on the inflammatory function of microglia. The cells were treated with lipopolysaccharide (LPS), a bacterial endotoxin that leads to a non-

specific activation of microglia that has been well characterized *in vitro* and *in vivo*[12]–[14]. For example, previous studies have demonstrated that LPS treatment of BV2 microglia results in secretion of interleukin 1 beta (IL-1 $\beta$ ), IL-6, etc[15]. However, the molecules that reduce the microglial secretion of both IL-1 $\alpha$  and TNF- $\alpha$ , which may in turn reduce reactive astrocyte induction may thus be used to promote the survival of neurons. Another characteristic of inflammation and AD is increased oxidative stress and increased reactive nitrogen species such as nitric oxide (NO)[16]. Therefore, we also hypothesized that decreasing the production of NO from microglial cells would further decrease the stress in the culture microenvironment, which may be beneficial in alleviating neuroinflammation.

Due to the vital role of microglia in mediating the secretion of inflammatory molecules, targeting these cells therapeutically may be a promising approach to modulate neuroinflammation. However, the development of a new drug has proven to take a significant amount of time, money, and resources. A simple solution to this problem is to repurpose existing drugs[17]. Since a single compound targets multiple protein in a human proteome[17], [18], using existing approved drugs can be used to identify and target the protein pathways that are implicated in neuroinflammation. Targeting microglial function via the release of inflammatory mediators like IL-1 $\alpha$  or TNF- $\alpha$  using small molecules is a promising approach, beginning with developing *in vitro* microglial models for inflammation that will be useful to investigate microglial function in AD. Here, we used several anti-inflammatory/steroidal compounds approved for various disease conditions to evaluate their effect on microglial function. Specifically, we evaluated microglial NO production and IL-1 $\alpha$  and TNF- $\alpha$  secretion by LPS-activated microglia with drug treatment. A detailed sandwich Enzyme Linked Immunosorbent Assay (ELISA) was developed independently to determine cytokine secretion the BV2 and primary microglia conditioned medium. We found that dexamethasone, a corticosteroid, reduces microglial secretion of IL-1 $\alpha$ , TNF- $\alpha$ , and NO under LPS inflammation in culture. Further, dexamethasone treatment caused an increase in phosphatidylcholine and a decrease in select phosphatidylserine in microglial cells suggesting changes in the cellular signaling events at the treatment conditions. Thus, we demonstrate that the pro-inflammatory response of microglia can be modulated with steroidal small molecules for better understanding microglial inflammatory responses.



**Table 9-1** List of the compound, abbreviation used, class of compound, and indication that the compound has been approved for in the United States. N/A indicates not approved or discontinued.

Drug name (ABBREVIATION)	Chemical Structure	Drug Class	Approved for
Abiraterone (ABI)		Progesterone derivative	Prostate cancer
Delta-4-Tibolone (D4T)		Synthetic androgen; active metabolite of tibolone	N/A
Dexamethasone (DEX)		Glucocorticoid	Inflammation
Ethisterone (ETH)		Progesterone receptor agonist; testosterone derivative	N/A
Norethisterone (NOR)		Progesterone receptor agonist; Ethisterone derivative	Hormonal contraception, Gynecological disorders
Progesterone (PRO)		Progesterone receptor agonist	Contraception, Menopausal hormone therapy
Tibolone (TIB)		Estrogen receptor agonist	Postmenopausal osteoporosis and menopausal symptoms

### **9.3 Materials and methods**

#### **9.3.1 Materials**

BV2 mouse microglial cells were provided by Dr. Linda J. Van Eldik (University of Kentucky, USA). The following were purchased from Corning: DMEM (Dulbecco's Modified Eagle's medium)/Hams F-12 50/50 Mix (#10-090-CV), L-Glutamine (#25-005-CI), Primaria anion/cation coated 24-well plate (#353847). The following were purchased from BioLegend: Purified anti-mouse TNF- $\alpha$  antibody (#510802), biotin anti-mouse TNF- $\alpha$  antibody (#506312), purified anti-mouse IL-1 $\alpha$  antibody (#512402), biotin anti-mouse IL-1 $\alpha$  antibody (#512504), and Av-HRP (#405103). Pierce 1-Step Turbo TMB-ELISA substrate (#PI34022) and recombinant TNF- $\alpha$  and IL-1 $\alpha$  were purchased from Fisher Scientific. Fetal bovine serum (FBS) was purchased from Atlanta Biologics. Penicillin/Streptomycin was purchased from Invitrogen. Cell Titer Blue dye was purchased from Promega. Griess assay reagents were prepared in the laboratory as per Promega instructions (#G2930). Cytation5 was the instrument used to read plates and was purchased from BioTek.

#### **9.3.2 BV2 microglial culture**

BV2 mouse microglial cells maintained at 37 °C and 5% CO<sub>2</sub> in DMEM/Hams F-12 50/50 Mix containing 10% FBS, 1% L-Glutamine, and 1% Penicillin/Streptomycin.

#### **9.3.3 Primary mouse microglia isolation and culture**

Previously described protocol was followed. CD11b<sup>+</sup> primary microglia were isolated from mice aged around 3 months of age. C57BL6 mice were euthanized with CO<sub>2</sub> following the Purdue University Animal Care and Use Committee guidelines, perfused brains were removed and cut into small pieces before homogenizing them in DPBS++ with 0.4% DNaseI on the tissue dissociator at 37 °C. After filtering the cells through a 70  $\mu$ m filter, myelin was removed two times, first using gradient centrifugation with Percoll PLUS reagent followed by myelin removal beads on the magnetic column separators. After myelin removal, CD11b<sup>+</sup> cells were selected from the single cell suspension using the CD11b beads as per the manufacturer's instructions. The CD11b<sup>+</sup> cells were finally resuspended in microglia growth media, further diluted in TIC (TGF- $\beta$ , IL-34, and cholesterol containing) media containing 2% FBS before seeding 0.1x10<sup>6</sup> cells/500  $\mu$ L/well

of a 24-well Primaria plate coated with 1 µg/mL mouse collagen. Primary mouse microglial cells were maintained at 37 °C and 10% CO<sub>2</sub> in TIC (TGF-β, IL-34, and cholesterol containing) microglial growth media containing 2% FBS with half-media change every other day until the day of Aβ treatment (12-14 days).

#### **9.3.4 Activation of BV2 microglia with LPS and drug treatment**

BV2 cells were seeded at a density of 3x10<sup>4</sup> cells per well in a 96-well flat bottom plate for 24 hours. The adherent cells were first activated with 100 µL 100 ng/mL LPS and subsequently treated with 100 µL drug. Drug dilutions were prepared at 2 µM and 200 nM in conditioned media. Once LPS and drug were added to the wells, the respective final concentrations for the cells become 50 ng/mL LPS and 1 µM and 100 nM drug. After 24 hours, supernatant was removed for Griess assay and ELISA, CTB assay was used to determine cell viability.

#### **9.3.5 Activation of primary mouse microglia with lipopolysaccharide and drug treatment**

Four of the steroid compounds which were tested on BV2 cells; Abiraterone, delta-4-Tibolone, Dexamethasone, and Ethisterone, were selected for further experimentation of primary cells based on their activity in BV2 cells. Primary microglial cells were isolated and seeded as previously described and cultured until visibly differentiated and confluent (12-14 days). On the day of treatment, adherent cells were first activated with 100 µL of 100 ng/mL LPS and subsequently treated with 100 µL of the drug. Drug dilutions were prepared at 2 µM in conditioned media. Once LPS and drug were added to the wells, the respective final concentrations for the cells become 50 ng/mL LPS and 1 µM drug. After 24 hours, supernatant was removed for Griess assay and ELISA, CTB assay was used to determine cell viability.

#### **9.3.6 Enzyme Linked Immunosorbent Assay for TNF-α and IL-1α production**

To determine whether drug treatment successfully decreased pro-inflammatory cytokines, TNF-α and IL-1α, the levels were quantified using Enzyme Linked Immunosorbent Assay (ELISA). 50 µL purified anti-mouse TNF-α (4 µg/mL) or IL-1α (1.5 µg/mL) antibody was diluted in coating buffer (0.15% anhydrous Na<sub>2</sub>CO<sub>3</sub> and 0.293% anhydrous NaHCO<sub>2</sub> in PBS) and added to the wells. The plate was sealed and incubated overnight at 4 °C. Coating buffer with purified antibody was

discarded and the plate was washed 3 times with wash buffer (0.05% Tween20 in PBS). 200  $\mu$ L blocking buffer (0.05% Tween20 and 1% BSA in PBS) was added to each well. The plate was sealed and incubated at room temperature for 2 hours. Blocking buffer was discarded and the plate was washed 3 times with wash buffer. 50  $\mu$ L cell supernatant was added to each well in triplicate along with standard dilutions for TNF- $\alpha$  (0-1000 pg/mL) and IL-1 $\alpha$  (0-500 pg/mL) diluted in conditioned media added in duplicate. The plate was sealed and incubated at room temperature for 2 hours. The supernatant and standards were discarded, and the plate was washed 3 times with wash buffer. 50  $\mu$ L biotin anti-mouse TNF- $\alpha$  (1  $\mu$ g/mL) or IL-1 $\alpha$  (0.2  $\mu$ g/mL) antibody diluted in blocking buffer was added to each well. The plate was sealed and incubated at room temperature for 1 hour. Biotin antibody was discarded, and the plate was washed 3 times with wash buffer. Av-HRP was diluted 1:1000 in blocking buffer and 50  $\mu$ L was added to each well. The plate was sealed and incubated at room temperature for 30 minutes. Av-HRP was discarded from the wells and the plate was washed 5 times with wash buffer. 50  $\mu$ L TMB substrate was added to each well. The plate was sealed and incubated at room temperature for 30 minutes at which point formation of a blue color was observed. 50  $\mu$ L stop solution (1M H<sub>2</sub>SO<sub>4</sub>) was added to each well resulting in a yellow colored solution. The absorbance at 450 nm was taken using Cytation5 instrument and Gen5 software.

### **9.3.7 Griess assay to evaluate Nitric Oxide production**

To determine whether drug treatment successfully decreases Nitric Oxide (NO), the levels were quantified using Griess assay. 50  $\mu$ L of cell supernatant was transferred from original treated plate containing BV2 cells to a new 96-well flat bottom plate and kept on ice. In the dark, 25  $\mu$ L 1% sulfanilamide in 5% H<sub>3</sub>PO<sub>4</sub> was added to each well, the plate was covered in foil and kept on ice for 5 minutes. 25  $\mu$ L 0.1% N-(1-Naphthyl)-ethylenediamine dihydrochloride (NED) in H<sub>2</sub>O was added to each well, the plate was covered in foil and kept on ice for 10 minutes. Absorbance at 540 nm was read using Cytation5 instrument and Gen5 software.

### **9.3.8 Cell Titer Blue assay**

The purpose of the Cell Titer Blue (CTB) assay is two-fold: to determine whether the drugs affect the viability of the cells and to normalize cytokine and NO production to the number of viable

cells per well. CTB dye was diluted at a 5:100 ratio of dye to conditioned media and kept in the dark. All media was aspirated from the treated wells that contain BV2 cells. 200  $\mu$ L diluted CTB dye was added to each well, covered in foil, and incubated at 37 °C for 3 hours. After incubation, the fluorescence of the plate was taken as outlined in “data analysis”. Viable cell values were calculated as a percent of the no LPS control.

### **9.3.9 Exploratory lipidomics**

Primary mouse microglia were cultured in TIC media with 2% serum for 10-14 days as described above. The cells were then activated with 100  $\mu$ L of 100 ng/mL LPS and immediately subsequently treated with 100  $\mu$ L of 1  $\mu$ M dexamethasone for 24 hours. After 24 hours, the cell media was aspirated and the cells were gently detached from the wells, pelleted at 500 x g for 5 mins and stored at -80 °C for lipid extraction. The lipids were extracted using the Bligh & Dyer protocol[19] and subjected to Multiple Reaction Monitoring (MRM)-profiling[20] for exploratory lipidomic analysis (Appendix B). The differentially regulated lipids between dexamethasone treated microglia vs. vehicle-treated control microglia were evaluation as described (Appendix B).

### **9.3.10 Data analysis**

CTB data was gathered by taking the fluorescence of the plate with excitation at 560 nm and emission at 590 nm using Cytation5 instrument with Gen5 software. Data was analyzed using the no LPS wells as the control, assuming 100% viability, all other values provided from treated wells were normalized to the control wells to provide a percent viability.

Griess data was gathered by taking the absorbance of the plate at 540 nm using a Cytation5 instrument with Gen5 software. The standard curve was fit with a linear equation, forced through the origin. Media was used as a blank and this value was subtracted from the raw data provided for each treatment. The equation for the standard curve was used to interpret NO concentration in each well. These values were normalized to the percent viability.

ELISA data was gathered by taking the absorbance of the plate at 450 nm using a Cytation5 instrument with Gen5 software. GraphPad Prism was used to analyze standard curves, interpolate

raw values, and create plots. TNF- $\alpha$  standard was fit to a second order polynomial equation. IL-1 $\alpha$  standard was fit to a hyperbolic equation. The standard curve for the TNF- $\alpha$  and IL-1 $\alpha$  was used to interpolate the raw values for the respective cytokine to provide the concentration of TNF- $\alpha$  or IL-1 $\alpha$  produced from each treatment. These concentrations were normalized to the percent viability of the respective treatment.

Statistical analysis was performed using GraphPad Prism and data were presented as mean  $\pm$  SD. Three independent experiments were analyzed using one-way ANOVA. To classify and indicate significant values, the following *p*-values were used; \**p* < 0.05; \*\**p* < 0.005; \*\*\**p* < 0.001.

## **9.4 Results**

### **9.4.1 BV2 microglial cells secrete TNF- $\alpha$ and IL-1 $\alpha$ with LPS activation**

To determine the levels of TNF- $\alpha$  and IL-1 $\alpha$  secretion by BV2 with LPS activation, cytokine levels were evaluated using ELISA. Cells treated with LPS only were used as a control for baseline secretion levels of TNF- $\alpha$  and IL-1 $\alpha$ . It has been previously demonstrated that activated BV2 murine microglial cell line produces IL-1 $\beta$ , IL-6, etc.; however, IL-1 $\alpha$  secretion with LPS activation has not been studied in these cells. Control BV2 cells without any activation produced 4 pg/mL TNF- $\alpha$  compared to the LPS-treated cells which produced 166 pg/mL TNF- $\alpha$  (a 4,150% increase). Control cells produced 0.25 pg/mL IL-1 $\alpha$  whereas LPS treated cells produced 29 pg/mL IL-1 $\alpha$  (a 11,600% increase) indicating a robust cytokine response with activation. These results confirm that the BV2 cells are a good model to study microglial secretion of TNF- $\alpha$  and IL-1 $\alpha$  under therapeutic influence in culture. Activation of BV2 cells in this study was performed for 24 hours, which can be considered to be indicative of acute inflammation. We propose further studies to evaluate IL-1 $\alpha$  and TNF- $\alpha$  production by activated cells for several days or a week to evaluate microglial inflammatory response with chronic activation in culture.

### **9.4.2 BV2 microglial cells secrete NO with LPS activation**

To determine the level of NO secreted by BV2 under LPS activation, NO production was quantified using Griess assay. BV2 microglia produced a robust NO response under LPS activation, indicating 8,874% more NO than the control cells without LPS activation. This trend of LPS

inducing NO secretion by activated microglial cells has been demonstrated often in literature when evaluating drug influence on inflammation. Given the simultaneous increase of IL-1 $\alpha$ , TNF- $\alpha$ , and NO under LPS-induced acute inflammation in culture, it is evident that multiple pathways are being modulated in the cells and thus it would be beneficial to consider a multi-pathway targeted approach when formulating pre-clinical drug discovery experiments. LPS inflammation induces the production of several inflammatory factors by microglia and thus a single factor cannot be considered as an in vitro model of acute or chronic inflammation.

#### **9.4.3 Primary mouse microglial cells secrete TNF- $\alpha$ and IL-1 $\alpha$ but do not secrete NO with LPS activation at the tested concentrations**

To determine the levels of TNF- $\alpha$  and IL-1 $\alpha$  secreted by LPS-activated CD11b<sup>+</sup> primary microglial cells, cytokine and NO levels were evaluated using ELISA and Griess assay, respectively. Similar to BV2 microglia, LPS treatment had no distinguishable effect on the viability of the CD11b<sup>+</sup> cells indicating no toxicity with treatment. The cells showed a slight increase in IL-1 $\alpha$  secretion when activated with LPS compared to the no-LPS treated controls. Similarly, TNF- $\alpha$  was also slightly increased in the presence of LPS compared to the control cells. Interestingly, we did not observe an increase in NO secretion when the cells were activated with LPS. No distinguishable levels of NO were present in these cells per the Griess assay. This could be due to many things such as low sensitivity of equipment, old reagents, or simply biology i.e. the concentration of the LPS used to detect NO from these cells may be low or perhaps another activating factor (for example, IFN- $\gamma$ ) may be required to induce NO secretion from these cells.

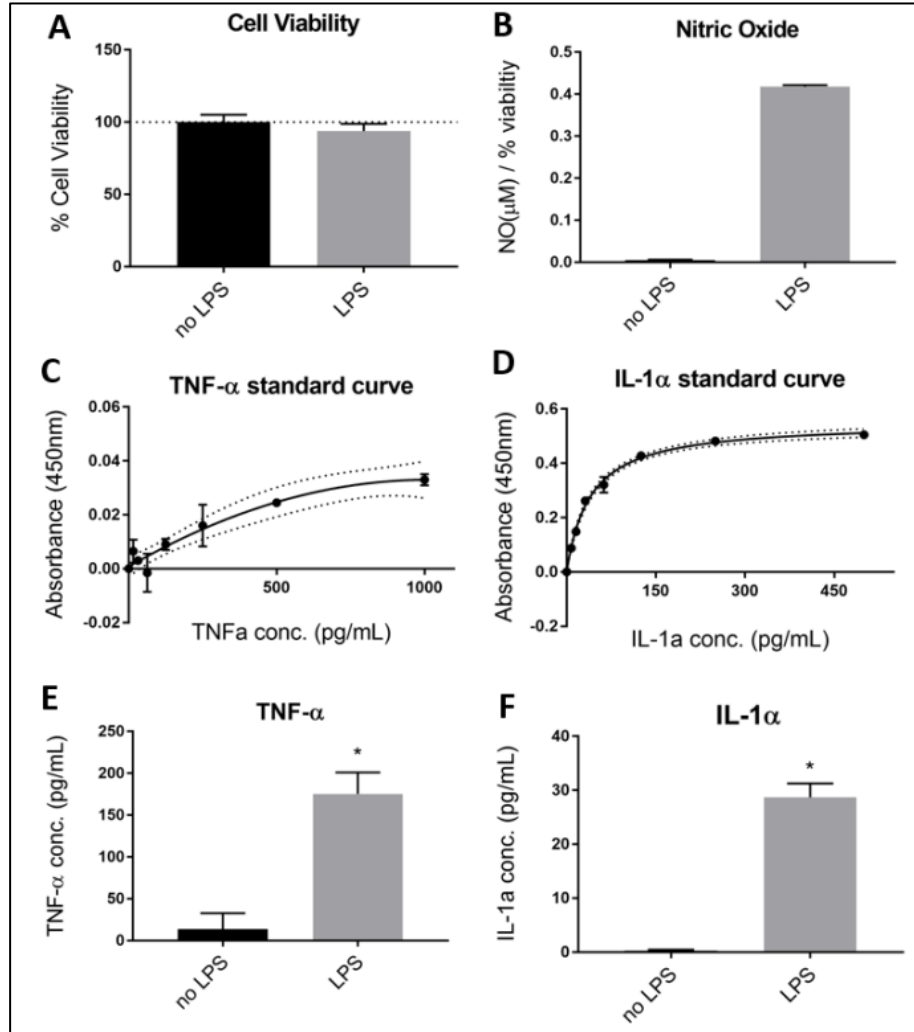


**Figure 9.1** BV2 microglia produce TNF- $\alpha$ , IL-1 $\alpha$ , and NO with LPS activation. (A) Cell viability with LPS treatment is calculated by considering vehicle-treated cells as 100% viable. (B) NO production from BV2 cells is significantly increased with LPS. (C) Standard curve of TNF- $\alpha$  and (D) IL-1 $\alpha$  for ELISA using recombinant proteins. (E) BV2 secretion of TNF- $\alpha$  and (F) IL-1 $\alpha$  is significantly increased in the presence of LPS.



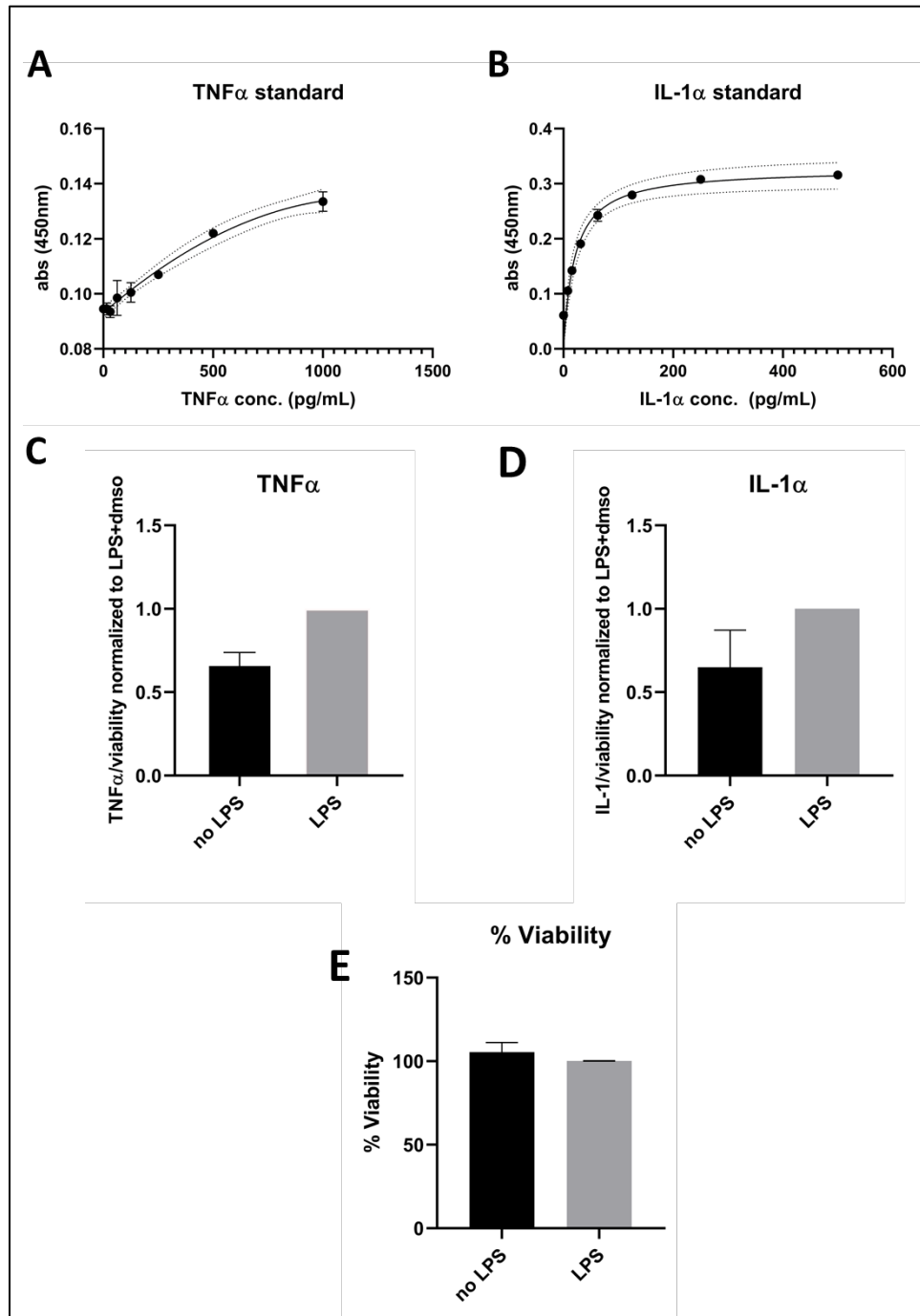


**Figure 9.2** CD11b<sup>+</sup> cells produce TNF- $\alpha$  and IL-1 $\alpha$  under the influence of LPS (50 ng/mL) activation. (A) Standard curve of TNF- $\alpha$  and (B) IL-1 $\alpha$  for ELISA using recombinant proteins. CD11b<sup>+</sup> cells secretion of (C) TNF- $\alpha$  (D) and IL-1 $\alpha$  is significantly increased in the presence of LPS. (E) Cell viability is normalized to control well which is considered 100% viable. LPS treatment does not alter the viability of CD11b<sup>+</sup> cells at the tested conditions.

#### **9.4.4 Dexamethasone reduced NO, TNF- $\alpha$ , and IL-1 $\alpha$ secretion from LPS-activated BV2 microglia**

To evaluate whether the steroid drugs could suppress the release of inflammatory mediators from activated BV2 microglial cells, LPS was introduced to the cells immediately before the respective drug was added. Cells that were not treated with LPS were used as a control for the baseline release of these cytokines. Cells treated with only LPS were used as a positive control to evaluate the influence of the drug on cytokine release. Treatment of the steroids showed no decreased cell viability and around 100% viability was maintained indicating no toxicity of the drugs at the applied concentrations. Abiraterone showed a significant decrease of IL-1 $\alpha$  secretion at 1  $\mu$ M concentration while all other drugs did not contribute to increased secretion at both concentrations of 1  $\mu$ M and 100 nM. All but Ethisterone showed a slight decrease of TNF- $\alpha$  secretion at both concentrations. All compounds resulted in no significant distinguishable change in NO at both concentrations. Abiraterone, delta-4-Tibolone, Dexamethasone, and Ethisterone showed consistent activity at decreasing cytokine release from BV2 cells and were chosen for further studies in CD11b<sup>+</sup> primary cells.

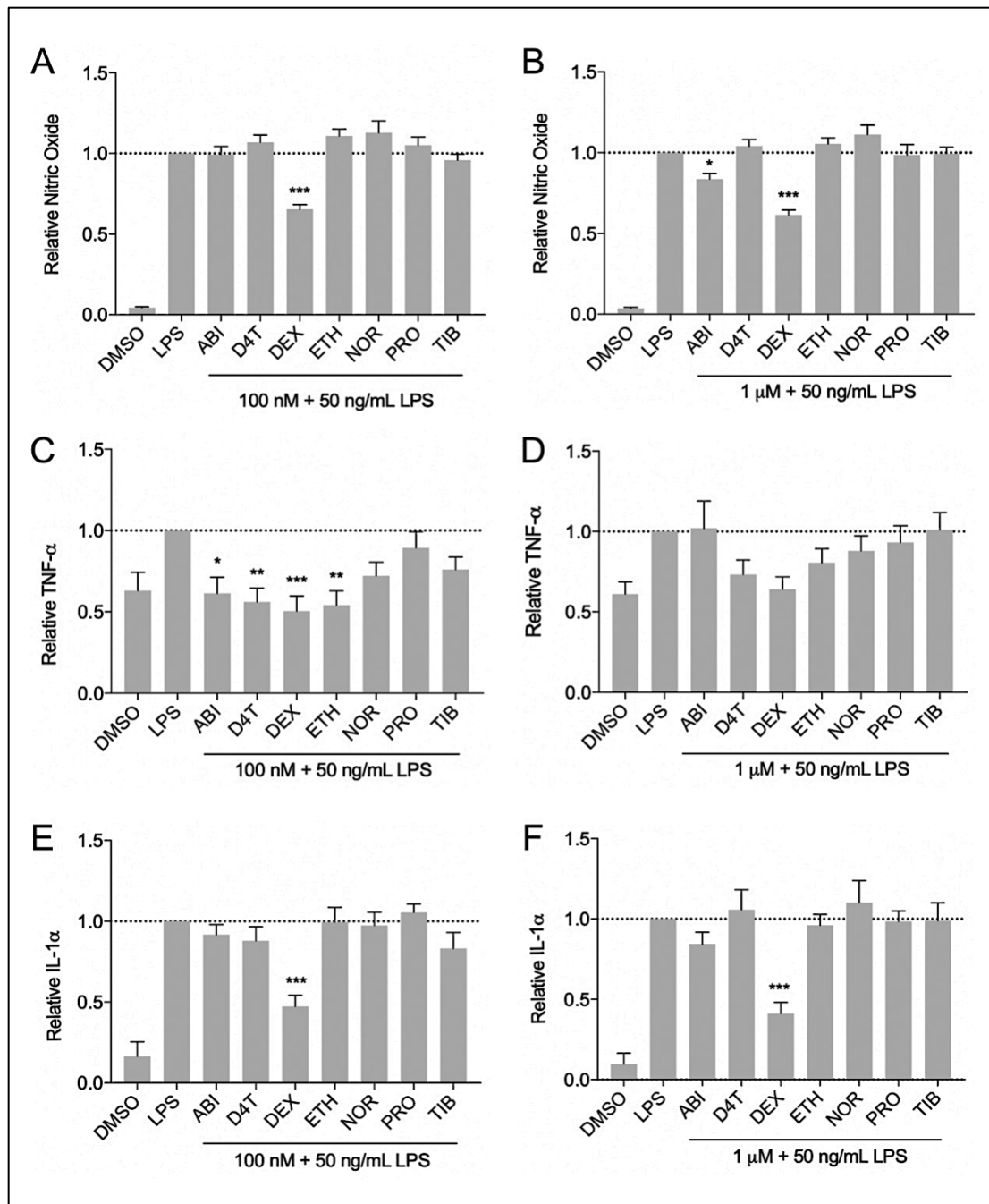


**Figure 9.3** Select steroidal drugs reduce the secretion of NO, TNF- $\alpha$ , and IL-1 $\alpha$  by LPS-activated microglia. (A) DEX suppresses NO secretion by LPS-activated BV2 microglia at both 100 nM and (B) 1  $\mu$ M. (C) DEX significantly suppresses TNF- $\alpha$  secretion at 100 nM along with D4T, ETH, and ABI. (D) None of the drugs significantly reduce TNF- $\alpha$  at 1  $\mu$ M, however, DEX treatment has the most observable cytokine reduction at this dose. (E) DEX significantly suppresses IL-1 $\alpha$  secretion at both 100 nM and (F) 1  $\mu$ M. The secretion of NO, TNF- $\alpha$ , and IL-1 $\alpha$  with LPS treatment alone was selected as a control and set to 1.0.

#### 9.4.5 Steroid Treatment on CD11b<sup>+</sup> Cells

The four selected steroids selected from BV2 steroid treatments were used with LPS activated primary cells which were subsequently evaluated for the same cytokines, NO, and for viability as primary cells serve as a more accurate model for evaluating specific responses such as inflammation. Combined data for LPS activated CD11b<sup>+</sup> cells demonstrate a slight decrease in TNF- $\alpha$  secretion and a significant decrease in IL-1 $\alpha$  secretion with delta-4-Tibolone treatment. Individual data for TNF- $\alpha$  suggests potential activity of Dexamethasone to decrease cytokine secretion, though combined data suggests an indistinguishable change. TNF- $\alpha$  and IL-1 $\alpha$  data is a combination of two biological replicates with each consisting of 3 technical replicates. As the technical replicate error bars are consistently low, the large biological replicate error could be due to varying biology of the mice used. Further experiments are proposed to help determine the cause and to generate more precise data.

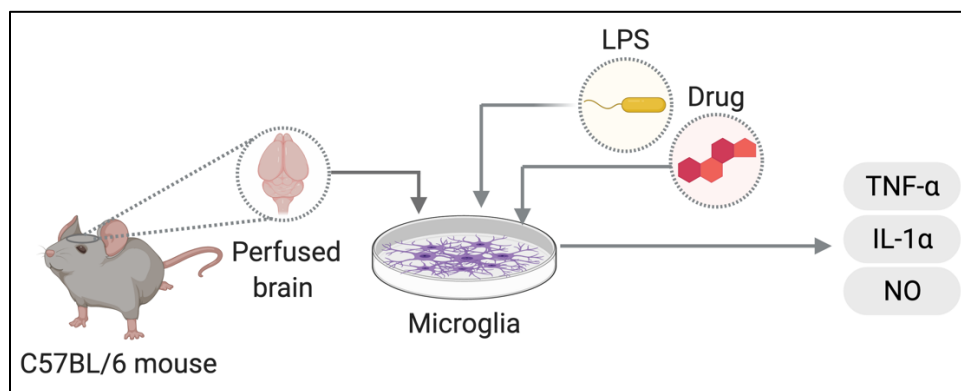


**Figure 9.4** Schematic for evaluating NO, TNF- $\alpha$ , and IL-1 $\alpha$  in LPS-activated microglia upon drug treatment.

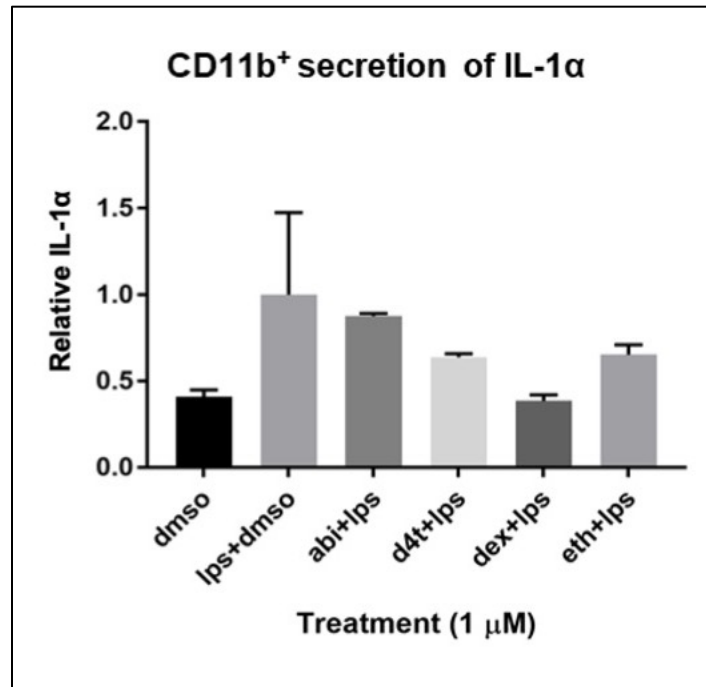


**Figure 9.5** CD11b<sup>+</sup> microglial secretion of IL-1α with LPS activation and under the treatment of various steroid compounds, abi, d4t, dex, and eth.

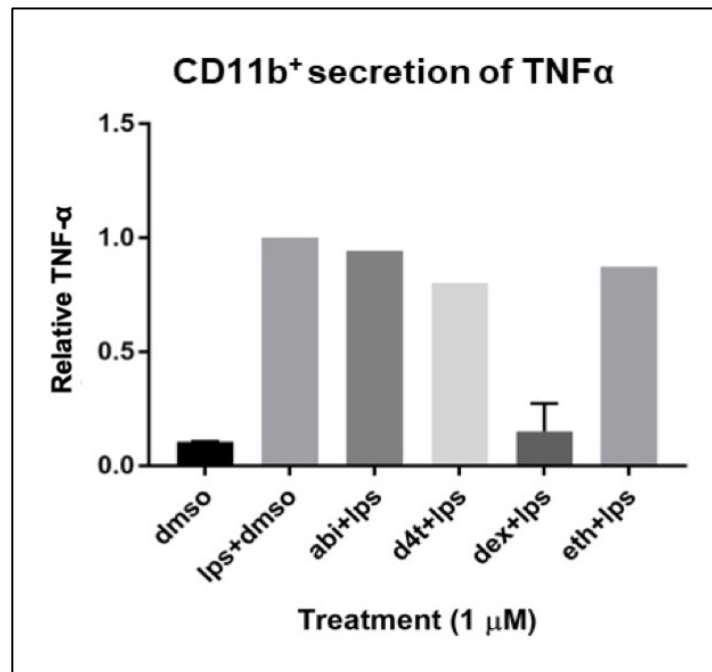


**Figure 9.6** CD11b<sup>+</sup> microglial secretion of TN-α with LPS activation and under the treatment of various steroid compounds, abi, d4t, dex, and eth.

#### 9.4.6 A few phosphatidylcholines are upregulated in LPS activated CD11b<sup>+</sup> cells with dexamethasone treatment

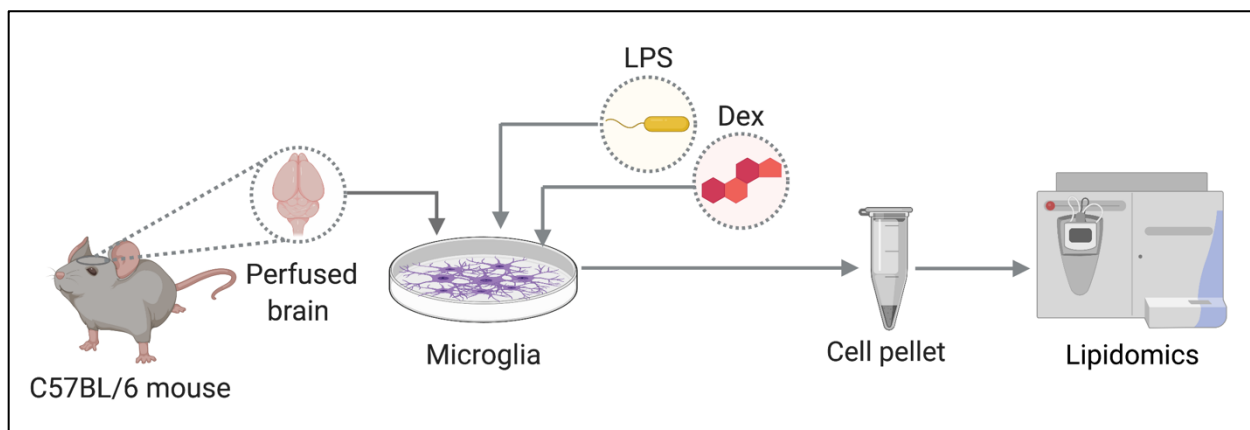


**Figure 9.7** Schematic for shotgun exploratory lipidomics performed on dexamethasone-treated activated microglial cells.

Dexamethasone is a corticosteroid that modulates the activity of glucocorticoid receptor (GR) on the cellular plasma membrane[21], [22]. We asked what lipids are affected in microglia with dexamethasone treatment? It has been shown that glucocorticoids in the periphery can either increase or decrease lipid storage in adipose tissues[23]. Given that lipid-rich microglia present a state of cellular dysfunction[24], it is important to ask if how the “suppressed” immune response in dexamethasone-treated microglia influences the cellular lipid changes. By performing shotgun exploratory lipidomics on primary microglia, we found that dexamethasone overwhelmingly upregulated phosphatidylcholine and sphingomyelin (PC-SM) that are predominantly present on the microglial cell membranes and involved in signaling events. Specifically, we found eleven PC-SMs that were abundant in microglia and most of the lipids contained fatty acid chains with one or more C=C bonds (i.e. unsaturated acyl chains). The top-most upregulated lipid was a long-chain saturated PC (PC(30:0)). The anti-inflammatory effects of PCs has been relatively well-documented in peripheral macrophages [25], [26]and warrants further studies in microglia.

**Table 9-2** Upregulated lipids in LPS activated CD11b<sup>+</sup> microglia due to dexamethasone treatment (FDR<0.1)

Lipid	Log <sub>2</sub> FC	FDR
PC(30:0)	0.83500374	0.00859162
PC(32:1)	0.7576662	0.02667424
PC(32:0), PCp(32:4)	0.74584955	0.02667424
PC(36:4)	0.74460968	0.02667424
SM(d18:0/18:0)	0.71210164	0.04506314
SM(d18:0/16:0)	0.67733482	0.07252048
PE(38:4)	0.67651736	0.07252048
PC(36:3)	0.66940565	0.0754214
PC(38:4)	0.65222848	0.0956145
SM(d18:2/24:1)	0.64560095	0.0975554
PC(32:2)	0.64274788	0.0975554

#### 9.4.7 A few phosphatidylserines are downregulated in LPS activated CD11b<sup>+</sup> cells with dexamethasone treatment

We found three phosphatidylserines (PS) to be depleted or downregulated in LPS-activated primary microglia with dexamethasone treatment. Given that PS lipids are upregulated in apoptotic cells in toxic environments, we may speculate that dexamethasone treatment, at the tested concentrations, suppresses toxicity and apoptosis and favors the proliferative capacity of microglia. Further studies should further evaluate how the changes to microglial lipidome with dexamethasone influences cellular behavior and function.

**Table 9-3** Downregulated lipids in LPS activated CD11b<sup>+</sup> microglia due to dexamethasone treatment (FDR<0.1)

Lipid	Log <sub>2</sub> FC	FDR
PSo(18:0)	-1.1221927	1.37E-05
PS(14:1)	-0.9619304	0.0005851
PS(32:2)	-0.8198402	0.00924964

## 9.5 Discussion

In this study, BV2 murine microglial cells and CD11b<sup>+</sup> primary mouse cells were used to evaluate TNF- $\alpha$ , IL-1 $\alpha$ , and NO production with respect to cell viability under LPS induced activation. Compounds approved for treatment of diabetes, inflammation, pain, opioid overdose, as well as various steroids were tested for the potential therapeutic influence on LPS-activated or “inflamed” microglia in culture. The influence of some of these compounds on neurons and microglia in an inflammatory environment has been previously evaluated. The anti-inflammatory effect of steroidal compounds on microglia have been demonstrated before; however, the effect of these drugs on IL-1 $\alpha$  has not been previously studied. Due to the immediate relation of this cytokine to astrocyte activation, a drug that is able to significantly decrease IL-1 $\alpha$  may be an ideal candidate for suppressing the microglial activation of astrocytes that results in neuronal death.

We also demonstrate that Abiraterone, Delta-4-Tibolone, Dexamethasone, and Ethisterone are able to decrease TNF- $\alpha$  cytokine release from LPS activated BV2 microglial cells while maintaining 100% viability. Delta-4-Tibolone and Dexamethasone data suggests that these drugs are sufficient to decrease cytokine activity in primary CD11b<sup>+</sup> cells, yet further studies are needed to ensure this activity in primary cells. Steroid compounds have been implicated to have anti-inflammatory effects through their interaction with hormone receptors. Dexamethasone has been studied in many ways in treatment to microglia and has indeed shown decreased pro-inflammatory cytokines[27], [28]. Dexamethasone consistently reduced the secretion of NO, TNF- $\alpha$ , and IL-1 $\alpha$  in microglia suggesting potent anti-inflammatory or immune-suppressive activity. Studying microglial inflammatory response to hormonal receptor modulators has merit since hormones have been shown to regulate microglial function in various disease conditions. Demonstrating the activity of other steroids which have not yet been studied with microglia implicate new hormone receptors in inflammation and provide new targets for research and therapy.

Although it has been shown that the specific factors such as IL-1 $\alpha$ , TNF- $\alpha$ , and C1q released from microglia are responsible for inducing reactive astrocytes, and that these reactive astrocytes lead to neuronal death[29], the mechanism for which astrocytes lead to the death of neurons has just been discovered (unpublished; Chapter 8). Since identity of the reactive astrocyte toxic factor was unknown for a long time, inhibiting the action of microglial factors (TNF- $\alpha$ , IL-1 $\alpha$ , and C1q) was



one way to prevent reactive astrocytes to be induced and thus prevent neurotoxicity. We now have evidence of the exact identity of some of these astrocyte-derived toxic molecules, a combination of released long-chain saturated free fatty acids (FFA) and phosphatidylcholines (PC) (Chapter 8). Thus, inhibiting or suppressing the release of these factors or their action may be an alternate way to prevent direct astrocyte-induced neurotoxicity *in vitro* and *in vivo*.

It has been recently proposed that there are more than two subpopulations of microglia (i.e. M1 and M2 microglia)[30], [31]. The concept of multiple microglial states, i.e., microglia do not have just one activated state, rather they are a heterogeneous population of cell with diverse activation states is dependent on the environmental cues. These concepts highlight critical details to consider while delineating microglial cell biology and immune response in health and diseases. Given the heterogeneity of these cells, we should probe microglial inflammatory response in a target specific manner that is relevant to the specific disease condition. Even though LPS has been shown to effectively activate microglial cells in culture (and *in vivo*), microglia may show different activity or activation states based on the disease condition and state of severity, sex and age of the animal, etc. Since LPS is a non-specific activator of microglia, the effect of specific disease-relevant activators such as A $\beta$ ,  $\alpha$ -synuclein, prion proteins, etc. on microglia should be further evaluated.

Demonstrating activity of approved compounds not only provides possibilities for quick and cost-effective new therapies for inflammatory autoimmune diseases like Alzheimer's disease, it most importantly provides a basis for exploring new targets of research. Utilizing the known interactions of all the FDA approved compounds evaluated in this research allows us to select the proteins and receptors that correspond to the active drugs as the basis of studies that can help provide insight to the mechanisms of dysfunctional microglia and inflammation as a whole. If the active drug shows a decrease in an inflammatory response, this likely implicates the protein or receptor in the inflammatory response pathway. Developing new and novel ways to modulate microglial immune response will be crucial for targeting neuroinflammation in AD and other neurological diseases.

## 9.6 References

- [1] V. H. Perry, J. A. R. Nicoll, and C. Holmes, “Microglia in neurodegenerative disease,” *Nat. Rev. Neurol.*, vol. 6, no. 4, pp. 193–201, Apr. 2010.
- [2] H. Sarlus and M. T. Heneka, “Microglia in Alzheimer’s disease,” *J. Clin. Invest.*, vol. 127, no. 9, pp. 3240–3249, Sep. 2017.
- [3] M. T. Heneka *et al.*, “Neuroinflammation in Alzheimer’s disease,” *Lancet Neurol.*, vol. 14, no. 4, pp. 388–405, Apr. 2015.
- [4] M. S. Ho, “Microglia in parkinson’s disease,” in *Advances in Experimental Medicine and Biology*, vol. 1175, Springer New York LLC, 2019, pp. 335–353.
- [5] D. J. Loane and A. Kumar, “Microglia in the TBI brain: The good, the bad, and the dysregulated,” *Experimental Neurology*, vol. 275, pp. 316–327, 2016.
- [6] J. Cummings, G. Lee, A. Ritter, and K. Zhong, “Alzheimer’s disease drug development pipeline: 2018,” *Alzheimer’s Dement. Transl. Res. Clin. Interv.*, vol. 4, no. 1, pp. 195–214, Jan. 2018.
- [7] R. Anand, K. D. Gill, and A. A. Mahdi, “Therapeutics of Alzheimer’s disease: Past, present and future,” *Neuropharmacology*, vol. 76, no. PART A, pp. 27–50, Jan. 2014.
- [8] W.-T. Chen *et al.*, “Spatial Transcriptomics and In Situ Sequencing to Study Alzheimer’s Disease,” *Cell*, vol. 182, no. 4, pp. 976–991.e19, Aug. 2020.
- [9] S. A. Liddelow *et al.*, “Neurotoxic reactive astrocytes are induced by activated microglia,” *Nature*, vol. 541, no. 7638, pp. 481–487, Jan. 2017.
- [10] K. A. Guttenplan *et al.*, “Neurotoxic Reactive Astrocytes Drive Neuronal Death after Retinal Injury,” *Cell Rep.*, vol. 31, no. 12, 2020.
- [11] K. A. Guttenplan *et al.*, “Knockout of reactive astrocyte activating factors slows disease progression in an ALS mouse model,” *Nat. Commun.*, vol. 11, no. 1, p. 3753, Dec. 2020.
- [12] S. Lund *et al.*, “The dynamics of the LPS triggered inflammatory response of murine microglia under different culture and in vivo conditions,” *J. Neuroimmunol.*, vol. 180, no. 1–2, pp. 71–87, Nov. 2006.
- [13] S. Lively and L. C. Schlichter, “Microglia responses to pro-inflammatory stimuli (LPS, IFN $\gamma$ +TNF $\alpha$ ) and reprogramming by resolving cytokines (IL-4, IL-10),” *Front. Cell. Neurosci.*, vol. 12, Jul. 2018.

- [14] X. jing Dai *et al.*, “Activation of BV2 microglia by lipopolysaccharide triggers an inflammatory reaction in PC12 cell apoptosis through a toll-like receptor 4-dependent pathway,” *Cell Stress Chaperones*, vol. 20, no. 2, pp. 321–331, Feb. 2015.
- [15] A. Nagai *et al.*, “Generation and characterization of immortalized human microglial cell lines: Expression of cytokines and chemokines,” *Neurobiol. Dis.*, vol. 8, no. 6, pp. 1057–1068, 2001.
- [16] A. Contestabile, B. Monti, and E. Polazzi, “Neuronal-glia Interactions Define the Role of Nitric Oxide in Neural Functional Processes,” *Curr. Neuropharmacol.*, vol. 10, no. 4, pp. 303–310, Dec. 2012.
- [17] G. Chopra and R. Samudrala, “Exploring Polypharmacology in Drug Discovery and Repurposing Using the CANDO Platform,” *Curr. Pharm. Des.*, vol. 22, no. 21, pp. 3109–3123, 2016.
- [18] G. Chopra, S. Kaushik, P. L. Elkin, and R. Samudrala, “Combating Ebola with repurposed therapeutics using the CANDO platform,” *Molecules*, vol. 21, no. 12, 2016.
- [19] E. G. Bligh and W. J. Dyer, “A RAPID METHOD OF TOTAL LIPID EXTRACTION AND PURIFICATION,” *Can. J. Biochem. Physiol.*, vol. 37, no. 1, pp. 911–917, Jan. 1959.
- [20] Z. Xie, C. R. Ferreira, A. A. Virequ, and R. G. Cooks, “Multiple reaction monitoring profiling (MRM profiling): Small molecule exploratory analysis guided by chemical functionality,” *Chem. Phys. Lipids*, vol. 235, Mar. 2021.
- [21] R. Dey and B. Bishayi, “Dexamethasone exhibits its anti-inflammatory effects in *S. aureus* induced microglial inflammation via modulating TLR-2 and glucocorticoid receptor expression,” *Int. Immunopharmacol.*, vol. 75, p. 105806, Oct. 2019.
- [22] X. Feng *et al.*, “Glucocorticoid-Driven NLRP3 Inflammasome Activation in Hippocampal Microglia Mediates Chronic Stress-Induced Depressive-Like Behaviors,” *Front. Mol. Neurosci.*, vol. 12, 2019.
- [23] R. A. Lee, C. A. Harris, and J.-C. Wang, “Glucocorticoid Receptor and Adipocyte Biology,” *Nucl. Recept. Res.*, vol. 5, 2018.
- [24] J. Marschallinger *et al.*, “Lipid-droplet-accumulating microglia represent a dysfunctional and proinflammatory state in the aging brain,” *Nat. Neurosci.*, vol. 23, no. 2, pp. 194–208, Feb. 2020.
- [25] I. Treede *et al.*, “Anti-inflammatory effects of phosphatidylcholine,” *J. Biol. Chem.*, vol. 282, no. 37, pp. 27155–27164, Sep. 2007.

- [26] M. Chen *et al.*, “Phosphatidylcholine regulates NF- $\kappa$ B activation in attenuation of LPS-induced inflammation: evidence from in vitro study,” *Animal Cells Syst. (Seoul)*., vol. 22, no. 1, pp. 7–14, Jan. 2018.
- [27] M. J. Park, H. S. Park, M. J. You, J. Yoo, S. H. Kim, and M. S. Kwon, “Dexamethasone Induces a Specific Form of Ramified Dysfunctional Microglia,” *Mol. Neurobiol.*, vol. 56, no. 2, pp. 1421–1436, Feb. 2019.
- [28] D. Hinkerohe *et al.*, “Dexamethasone prevents LPS-induced microglial activation and astroglial impairment in an experimental bacterial meningitis co-culture model,” *Brain Res.*, vol. 1329, pp. 45–54, May 2010.
- [29] S. A. Liddelow *et al.*, “Neurotoxic reactive astrocytes are induced by activated microglia,” *Nature*, vol. 541, no. 7638, pp. 481–487, Jan. 2017.
- [30] V. Stratoulis, J. L. Venero, M. Tremblay, and B. Joseph, “Microglial subtypes: diversity within the microglial community,” *EMBO J.*, vol. 38, no. 17, Sep. 2019.
- [31] T. Masuda, R. Sankowski, O. Staszewski, and M. Prinz, “Microglia Heterogeneity in the Single-Cell Era,” *Cell Rep.*, vol. 30, no. 5, pp. 1271–1281, Feb. 2020.

## CHAPTER 10. CHEMICAL NEUROIMMUNOLOGY—CURRENT AND FUTURE PERSPECTIVE

### 10.1 Preface

Neuroimmunology—the intersection of neuroscience and immunology is a relatively new field of neuroscience that has garnered a lot of interest over the last few years. My thesis has introduced another dimension to this field by introducing chemistry and chemical biology to tackle new challenges and ideas to better understand glial cell states and function. Chemical neuroimmunology utilizes novel chemical tools such as pH-responsive probes and newly developed mass spectrometry techniques such as multiple reaction monitoring-profiling to characterize glial biology's underlying cellular and molecular mechanisms. These toolsets provide insights into new and previously unknown *functional* biomolecules (proteins, lipids, metabolites) uniquely involved in glial cellular processes such as phagocytosis, lipid metabolism, and lipid droplet accumulation, cytokine secretion, cell-cell communication like microglia-astrocyte cross-talk, etc. There is a need to introduce bold ideas to this field that will accelerate research and translate the findings from the bench to the bedside to better human health. I believe that chemical neuroimmunology has the opportunity to harness the robust and sensitive nature of analytical chemistry methodologies to probe glial cells using *in vitro* to *in vivo* models. Furthermore, methods to modulate glial cell function using creative chemistries may help develop targeted immunotherapies to change the course of a disease.

### 10.2 Beyond genes and proteins—Lipids and metabolites

No doubt, single-cell RNA sequencing (scRNA-seq) technologies have revolutionized the field of microglia and astrocyte biology in the recent past[1]–[4]. These techniques introduced us to the concept of diverse glial cell states and heterogeneous glial cell populations existing in different environments. For example, microglia were once thought to exhibit two “activated” states, namely, M1 (classically activated; pro-inflammatory) and M2 (alternate activated; anti-inflammatory). Today, we are able to characterize microglia into multiple different states based on their location within the CNS, sex, and age of the animal, course of the disease, etc. Microglia may exhibit multiple cellular phenotypes even within a healthy brain. Similarly, reactive astrocytes are

currently considered to exhibit two activated phenotypes, namely, A1 (neurotoxic) and A2 (neurotrophic)[5], [6]. However, the idea of multiple reactive astrocyte cell subsets is now broadly accepted in the scientific community, and select studies indicate the dynamic nature of astrocytic response towards an inflammatory trigger. Thus, microglia and astrocytes are a population of highly heterogeneous cells exhibiting diverse phenotypes, and their cell states constantly change based on their environment.

Even though scRNA-seq studies have broadened our definitions of glial cell heterogeneity over the years, we are yet to define glial cell states with respect to their lipid and metabolite profiles. Glial cell states and subsets in terms of their global lipid and metabolite profiles do not exist to date. No doubt, the genomic profiles of glia provide us detailed transcriptomic state of the cells. However, gene expression may not always correspond to protein expression. Furthermore, proteins, lipids, and metabolites are functional molecules that regulate the signaling events within the cells and even in the extracellular space. Identifying these molecules in the serum or cerebrospinal fluid (CSF) in different conditions may provide a window into the cell states. For example, I have described how the reactive astrocytic lipidome changes dramatically upon reactivity compared to its metabolome. We observe an abundance of saturated lipids produced by these cells that are toxic to neurons and oligodendrocytes. Thus, we may speculate on the progression of a neurodegenerative disease based on the identification and quantification of the saturated lipids in a relevant biological sample such as the serum or CSF. However, this is not possible with genes. Therefore, it is time to incorporate these functional biomolecules into our broader definition and study of glial function. As highlighted through the course of this thesis, one may now appreciate the critical roles played by lipids in regulating glial function in response to inflammatory triggers such as LPS and more specific target substrates like A $\beta$ , myelin, etc.

### **10.3 Redefining glial cell states**

In the periphery, we identify T cells by the proteins they express on their plasma membranes and their intracellular transcription factor profiles. The subsets of T cells have broadened over the years from CD8 and CD4 T cells into multiple subpopulations of T cells such as Th1, Th2, Th17, Th22, regulatory T cells (Tregs), etc.—each with defined functions. Similar function-dependent subsets of glial cells in terms of lipids and metabolites may pave the way to understand the fundamental

nature of cellular responses and provide insights into changes occurring throughout a disease. For example, lipids may be utilized as functional biomarkers of impaired microglia to diagnose early-onset AD. The proposition for defining lipid-specific glial cell subsets is not related to generating new nomenclatures (especially in a field already crowded by a myriad of jargons) but it is related to better characterizing the states of cells in a specific pathological environment. Thus, defining functional subsets of glia will become paramount to our understanding of disease mechanism in itself.

Furthermore, we have to redefine our view of what encompasses a ‘cell state.’ A state of a cell is a function of its internal omics profiles and its ever-changing environment. Hence, a cell state is never static but will change over time in a given condition. Being able to predict such cellular changes using functional biomarkers will become important in the future. This endeavor may bridge multiple fields of science such as chemistry, biology, and computer science to make intelligent predictions about the nature of a cell in a given specific (or a dynamic) environment to diagnose the cell state and its response to its environment.

#### **10.4 New chemical tools to modulate glial function**

In chapters 3-5, I have introduced three new tools to understand the glial response to A $\beta$ . The recombinant A $\beta$  peptide may be substituted for the synthetic A $\beta$  peptide that is commercially available at a higher cost and is more challenging to produce. In contrast, producing recombinant A $\beta$  using bacteria in the lab solves some of these issues and provides a continuous supply of the peptide for a higher number of experiments. We have shown that the recombinant A $\beta$  behaves similarly to the synthetic A $\beta$  in its aggregation characteristics. This peptide, now produced in more significant amounts (around 15-20 mg per 1 L of bacterial culture), may also be used to perform new chemistries such as conjugation with pH-dependent fluorophores to track the intracellular localization of A $\beta$  within glial cells.

A pH-dependent A $\beta$  fluorescent probe (A $\beta^{\text{pH}}$ ) was introduced in the next chapter that brought this idea to fruition. Here, we showed that by conjugating a pH-sensitive fluorescent dye to A $\beta$ , we can visualize and track its uptake by glial cells in various modalities, including in vitro cultures of glia, in the brain tissue slices, and in vivo in the retina, hippocampus, and cortex. We showed that the

fluorescence occurring from the internalized A $\beta$ <sup>pH</sup> could also be visualized in fixed cells and be used to sort the cells via flow cytometry. Furthermore, we were able to show, for the first time, the internalization of A $\beta$  in live animals in real-time. We observed that microglia take up A $\beta$  much more than astrocytes in all these different conditions. Interestingly, these preliminary proof-of-concept experiments generated many new questions about glial biology that can be followed in future experiments. For example, in the retina, we saw that astrocytes do not take up A $\beta$  even at the 1 hour treatment time tested in the experiment. Furthermore, all the experiments were performed in healthy (wild-type) brain environments and healthy cell cultures. It will be interesting to see how the phagocytic functions of microglia and astrocytes get affected in diseased or inflammatory environments and the extent of the changes that occur in these conditions. Previous studies have demonstrated that microglia become functionally impaired and lose their phagocytic capacity in later stages of AD. Others have also reported that when microglia are phagocytically suppressed, astrocytes take over this function in a more pronounced manner[7] and that microglia and astrocytes both play orchestrated roles in the removal of dying neurons in different regions of the brain[8]. How these phagocytic roles are employed by glial cells in AD and other neurological disorders will be exciting lines of research worth exploring in future studies.

Other neuronal and non-neuronal CNS substrates can also be conjugated with similar pH-dependent fluorescent probes to study their internalization mechanism and clearance from the pathological tissue environment (Figure 10.1). For example, misfolded hyperphosphorylated tau proteins form neurofibrillary tangles within the neurons and can get discharged into the extracellular space when the neurons start to disintegrate. These extracellular tau deposits induce microglial activation and their phagocytic uptake. Similarly, disintegrating myelin from the axonal sheaths is observed in Multiple Sclerosis and other neurological disorders. Microglia in these conditions also act as robust first responders during the initial stages of the disease but exhibit altered phenotypes as the disease progresses. The underlying glial phagocytic mechanisms involved in this process have not yet been well defined to date. Conjugating substrates like tau and myelin (and several other molecules shown below) with pH-sensitive fluorophores will allow us to track the cellular mechanisms occurring within the cells under pathological conditions using live-cell imaging and even two-photon imaging for *in vivo* visualization. These cells with unique phenotypes and properties can then be separated via fluorescent-activated cell sorting (FACS). The



downstream molecules defining these cell states can be identified using omics technologies or other immunological and biochemical assays. The overarching question in all such experimental and disease paradigms pertains to the role of glial cell dysfunction in chronic inflammation and disease. How do glia become dysfunctional? What are the cellular processes that define glial states in such environments? What molecules are involved? These are some of the questions that will drive the development of new chemical tools in neuroimmunology.

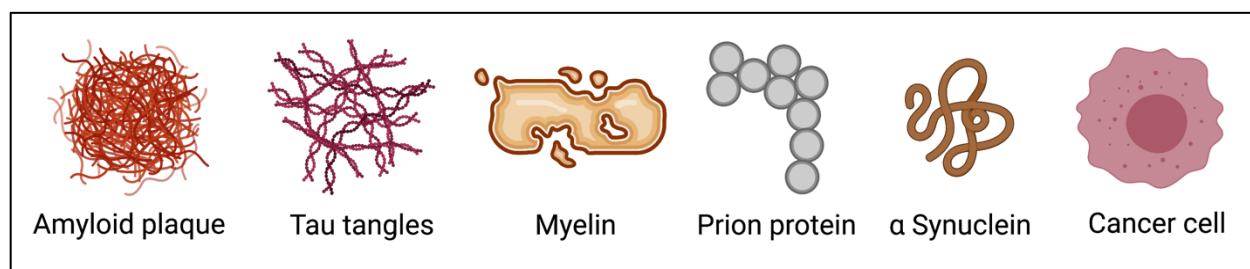


**Figure 10.1** Various neuronal and non-neuronal substrates that are implicated in neurodegenerative and neurological disorders. Microglia and astrocytes phagocytose these substrates in normal conditions but exhibit altered phagocytic capacities in diseased conditions. Conjugating these substrates with different types of fluorophores and probes will allow us to track their internalization by glial cells and separate these cells via FACS for their molecular characterization.

Near infra-red (NIR) fluorescent probes are widely used in biomedical imaging. These chemical probes can penetrate deep into the tissue[9] and exhibit low cytotoxicity, and are used for *in vivo* imaging[10]. While several NIR probes exist to date, pH-sensitive NIR probes have not yet been developed to the best of my knowledge. Similar to the  $A\beta^{pH}$  probe generated in our lab, NIR-based pH-sensitive  $A\beta$  probes will exhibit fluorescence in the far-red range uniquely in the acidic environments within the cells. These probes will have additional advantages over the  $A\beta^{pH}$  probe due to the following reasons: (1) they can be used in parallel with other probes that emit green fluorescence within the cells (like the BODIPY 443/505 probe used to image lipid droplets), (2) they can be used to image phagocytic cells in animals, (3) since they exhibit far red fluorescence in acidic environments, they can be used in GFP-reporter mice such as the *Cx3cr1*-GFP reporter mice wherein all the macrophages/microglia expressing CX3CR1 will exhibit green fluorescence, and they can be directly imaged without the need for an antibody. Therefore, developing such a probe will be a game-changer for the field to visualize cell states and phagocytic activity in animals.

## 10.5 New chemical techniques to characterize glial cell states

I have introduced MRM-profiling for the characterization of lipid and metabolite profiles in microglia and astrocytes. This is a relatively new and simplified exploratory lipidomics method developed here at Purdue and focuses on identifying molecules based on their functional groups. This method allows us to increase the amount of chemical information acquired and enables faster analysis in a short time. Furthermore, only a small amount of the sample is required (around 10,000 cells per sample may be used; about 100,000 cells per sample is preferred for microglia). Even though MRM-profiling is a valuable technique for lipidomics and metabolomics profiling of glial cell states, it does have certain shortcomings. For example, this technique does not perform structure characterization of the lipid molecules. The lipids of interest identified in this technique have to be validated further using chromatography techniques to confirm their identity and structure. New analytical chemistry techniques are being developed to identify lipid structures in microglia and astrocytes. Elucidating structures will allow us to chemically modify the molecules in order to change cell function or induce a specific cell state.

Using this technique, I was able to define microglial cell states with A $\beta$  exposure and treatment. With initial A $\beta$  exposure in culture (1 hour), I saw that the microglia produced an abundance of free fatty acids (FFA). Thus, FFA-rich microglia corresponds to a cell state in response to an acute inflammatory trigger like A $\beta$ . Furthermore, with prolonged A $\beta$  treatment, I showed that microglia produce an abundance of Triacylglycerides (TAGs) which are neutral lipids that are predominantly present in the cellular lipid droplets (LDs) in aged brains and also in cells under inflammatory conditions. We also show an upregulation of LDs in microglia from 5xFAD brains (5-7 months of age). These brains exhibit increased A $\beta$  pathogenesis, microgliosis, and inflammation. Thus, a TAG/LD-rich microglial cell state points to the progression of inflammation in the environment. TAGs/LDs are energy storage entities within a cell. I hypothesize that microglia accumulate TAGs/LDs in inflammation in order to protect themselves from external toxicity. That is, microglia may go into a state of “hibernation” by accumulating energy storage molecules in adverse conditions. These findings raise important questions about other cells in similar environments. These questions warrant further investigation.

1. What is unique to microglia that allows them to circumvent A $\beta$ -induced cytotoxicity by transforming themselves into this lipid-rich hibernation state?
2. What changes occur in astrocytes and other cells in the same environment? The TAG/LD accumulation state in microglia may not necessarily be disease-specific, i.e., it could be a response to inflammation in general and similar microglial cell states may be observed in TBI, MS, etc.
3. Do reactive astrocytes and the saturated lipids produced by reactive astrocytes induce similar cell states in microglia (Figure 10.2)? While reactive astrocytes kill neurons and mature oligodendrocytes via saturated lipids (saturated FFAs and PCs), microglia are not subjected to similar lipid-induced cytotoxicity. Does the ability of microglia to make TAGs/LDs to overcome FFA abundance along with the underlying mechanism involved (i.e., TAG formation with the help of DGAT2 and other proteins) prevent them from dying? Do neurons and oligodendrocytes lack these protective cellular mechanisms that render them susceptible to lipid (or FFA in particular)-induced cytotoxicity?

It would also be interesting to approach these questions from an evolution standpoint, i.e., Evolution has designed cells and higher-order organisms to protect themselves in the face of adversity. This response and the underlying mechanisms may be heightened in immune cells that are constantly exposed to pathogens and toxic entities.

## **10.6 Departing thoughts**

There are several genetic tools and techniques already present to study glial biology[11]. There is a limitation of chemical tools that can be used to externally modulate cells and their environment to change their cellular state and function. I hope that my thesis work has convinced the readers about how we can harness chemical science to study the biology of glial cells. I have mainly focused on glial cell phagocytosis, cytokine secretion, glial lipid/metabolite identification, and profile characterization. While the advent of new chemistries and technologies will significantly benefit the field of neuroimmunology, such advances must be based on fundamental biological questions.

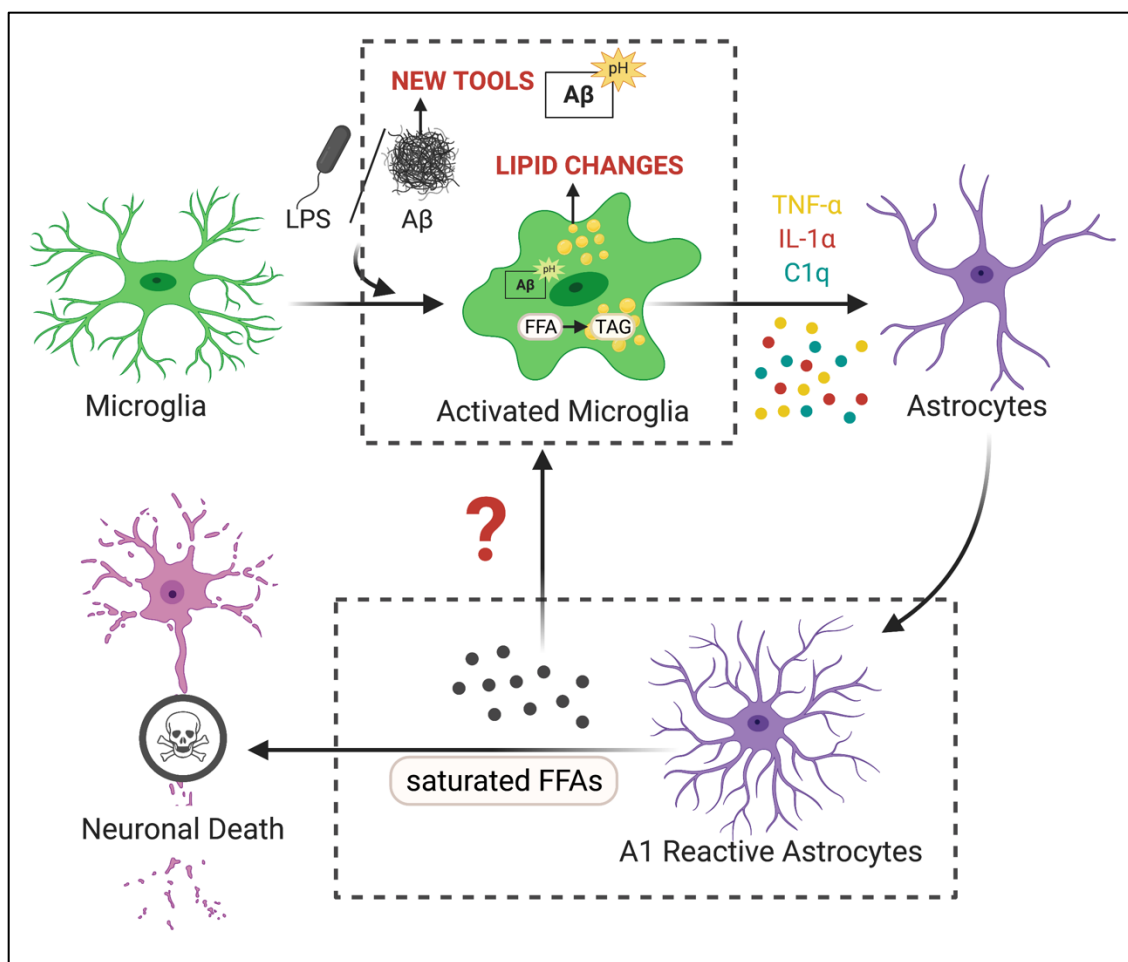


**Figure 10.2** Overview of my thesis. New Tools: Development of recombinant A $\beta$ , A $\beta^{\text{pH}}$ , and other pH-sensitive fluorophores to study A $\beta$ -specific phagocytosis and response in microglia (and astrocytes); Lipid Changes: Changes in microglial lipidome and metabolome landscape due to A $\beta$ , underlying mechanisms of lipid-induced cytotoxic and protective mechanisms; Reactive astrocytes: Characterizing reactive astrocytic proteome, lipidome, and metabolome. Lipidomics identified upregulation of saturated PCs and FFAs in reactive astrocytes and ACM, respectively.

How these molecules influence microglial cell state and whether microglia develop a lipid droplet-rich phenotype in this environment warrants further investigation.

## 10.7 References

- [1] H. Keren-Shaul *et al.*, “A Unique Microglia Type Associated with Restricting Development of Alzheimer’s Disease,” *Cell*, vol. 169, no. 7, pp. 1276–1290.e17, Jun. 2017.
- [2] T. Masuda, R. Sankowski, O. Staszewski, and M. Prinz, “Microglia Heterogeneity in the Single-Cell Era,” *Cell Rep.*, vol. 30, no. 5, pp. 1271–1281, Feb. 2020.
- [3] V. Stratoulis, J. L. Venero, M. Tremblay, and B. Joseph, “Microglial subtypes: diversity within the microglial community,” *EMBO J.*, vol. 38, no. 17, Sep. 2019.

- [4] Q. Li *et al.*, “Developmental Heterogeneity of Microglia and Brain Myeloid Cells Revealed by Deep Single-Cell RNA Sequencing,” *Neuron*, vol. 101, no. 2, pp. 207–223.e10, Jan. 2019.
- [5] S. A. Liddelow and B. A. Barres, “Reactive Astrocytes: Production, Function, and Therapeutic Potential,” *Immunity*. 2017.
- [6] S. A. Liddelow *et al.*, “Neurotoxic reactive astrocytes are induced by activated microglia,” *Nature*, vol. 541, no. 7638, pp. 481–487, Jan. 2017.
- [7] H. Konishi *et al.*, “Astrocytic phagocytosis is a compensatory mechanism for microglial dysfunction,” *EMBO J.*, vol. 39, no. 22, p. e104464, Nov. 2020.
- [8] E. C. Damisah *et al.*, “Astrocytes and microglia play orchestrated roles and respect phagocytic territories during neuronal corpse removal in vivo,” *Sci. Adv.*, vol. 6, no. 26, 2020.
- [9] Z. Guo, S. Park, J. Yoon, and I. Shin, “Recent progress in the development of near-infrared fluorescent probes for bioimaging applications,” *Chemical Society Reviews*, vol. 43, no. 1. Royal Society of Chemistry, pp. 16–29, 07-Jan-2014.
- [10] M. Staderini, M. A. Martín, M. L. Bolognesi, and J. C. Menéndez, “Imaging of  $\beta$ -amyloid plaques by near infrared fluorescent tracers: A new frontier for chemical neuroscience,” *Chemical Society Reviews*, vol. 44, no. 7. Royal Society of Chemistry, pp. 1807–1819, 07-Apr-2015.
- [11] M. L. Bennett *et al.*, “New tools for studying microglia in the mouse and human CNS,” *Proc. Natl. Acad. Sci. U. S. A.*, vol. 113, no. 12, pp. E1738–E1746, Mar. 2016.

## **APPENDIX A. ISOLATION AND CULTURE OF MICROGLIA FROM ADULT MOUSE BRAINS**

### **A.1 Background**

Isolation and culture of microglia from adult mice presents several hurdles due to the following reasons: (i) microglia are embedded within the brain parenchyma thereby requiring extensive tissue dissociation during their isolation; (ii) the adult rodent brain contains large quantities of myelin – a lipid-rich structure that hinders the isolation of cells; (iii) only about 5-10% of the cells in the brain are microglia, thus the number of microglia obtained per brain is far less compared to other glial cells[1]. The following protocol addresses some of these challenges by optimizing every step of the isolation process including the reagents used. Microglia are isolated from perfused brains upon tissue dissociation and two rounds of myelin removal. CD11b magnetic beads are used to pull down microglia from a suspension of all brain cells using magnetic columns. Although CD11b is not a microglia-specific marker i.e. it is also expressed on peripheral macrophages, we are able to obtain relatively pure microglia due to perfusion of the brain at the beginning of the protocol. The isolated cells are cultured in highly defined media containing TGF- $\beta$ , IL-34, and cholesterol (the main astrocytic-derived factors required for microglial survival and growth) [2] along with 2.0-2.5% serum. The cells develop processes around day 7-10 and respond to stimuli such as the A $\beta$  challenge in culture. Thus, this protocol is efficient for culturing microglia ex vivo for the use of various immunological and biochemical assays.

### **A.2 Reagents, buffers, and media preparation**

The following stock reagents are made and stored as described previously[2], [3]. The following tables contain the protocol for using these stock solutions to make microglia growth media (MGM) and TIC media for the culture of mouse microglial cells. Both the media are stored at 4 °C.

**Table A.1.** Microglia Growth Media (MGM). The base media for MGM is DMEM-F12 without phenol red. To make 100 mL of MGM, replace 4.104 mL from 100 mL of DMEM-F12 media with the following reagents.

Serial No.	Reagent	Stock Conc.	Vol. of Stock to add	Final Conc. in MGM
1.	Insulin	0.5 mg/mL	1 mL	5 µg/mL
2.	Apo-transferrin	10 mg/mL	1 mL	100 µg/mL
3.	L-Glutamine	200 mM	1 mL	2 mM
4.	Pen-Strep	10k units/mL-10k µg/mL	1 mL	100 units/mL-100 µg/mL
5.	N-Acetyl Cysteine	5 mg/mL	100 µL	5 µg/mL
6.	Sodium selenite	2.5 mg/mL	4 µL	100 ng/mL

**Table A.2.** TIC Media (MGM containing TGF- $\beta$ , IL-34, and cholesterol). Replace 1.083 mL from 50 mL of MGM with the following reagents to make 50 mL TIC media. Add cholesterol to warm media (pre-warmed at 37 °C) to facilitate dissolution. Don't add more than 1.5 µg/mL cholesterol or it will precipitate out. Do not filter the cholesterol-containing media. Equilibrate TIC media at 37 °C for 30 mins to 1 hour before adding to cells to insure optimal pH.

Serial No.	Reagent	Stock Conc.	Vol. of Stock to add	Final Conc. in TIC media
1.	Heparan sulfate	1 mg/mL	500 µL	10 µg/mL
2.	IL-34	10 µg/mL	500 µL	100 ng/mL
3.	TGF- $\beta$ 2	4 µg/mL	25 µL	2 ng/mL
4.	Cholesterol	1.5 mg/mL	50 µL	1.5 µg/mL
5.	Oleic acid	0.67 mg/mL	7.5 µL	0.1 µg/mL
6.	Gondoic acid	0.1 mg/mL	0.5 µL	0.001 µg/mL

### ***Dounce buffer***

15 mM HEPES + 0.5% Glucose in HBSS. On the day of the experiment, add 20  $\mu$ L of 0.4% DNase-I to 5 mL Dounce buffer in a C-tube for each brain.

### ***MACS buffer***

0.5% BSA and 25 mM EDTA in PBS i.e., 0.5 g BSA + 58.45 mg EDTA in 100 mL 1x PBS.

## **A.3 Tissue dissociation and collection**

1. Euthanize mouse by CO<sub>2</sub> asphyxiation (3 minutes at level 3).
2. Transcardially perfuse with 10-30 mL ice cold PBS.

*Optional:* 50  $\mu$ g/mL heparin can be added to the PBS to facilitate thinning of blood.

3. Dissect whole brain and transfer to a 3 cm dish on ice with cold Dounce buffer.
4. Chop the brain into 1 mm<sup>3</sup> chunks with a cold scalpel blade and transfer to the ice-cold C-tube with 5 mL Dounce buffer containing 0.4% DNase-I.

*Note:* 100  $\mu$ L 0.4% DNase-I in 25 mL HBSS (or 20  $\mu$ L 0.4% DNase-I in 5 mL HBSS).

5. Collect each individual brain as per above into one C-tube and dissociate the tissue on the Octo Heat Dissociator with the correct program (37C\_ABKD).

## **A.4 Myelin removal**

Note: The volumes mentioned below are for one brain, scale volume for more brains.

1. Prepare myelin separation buffer (MSB): 9 mL Percoll Plus + 1 mL DPBS<sup>++</sup> with Ca<sup>2+</sup> and Mg<sup>2+</sup> ions.
2. Bring the C-tubes to the hood and place on ice. Further dissociate the tissue chunks with a 5 mL pipet and transfer to a 50 mL falcon tube with a 70  $\mu$ m filter placed on ice.
3. Bring the volume of the suspension to 33.5 mL with the Dounce buffer and add 10 mL MSB per tube to bring the volume to 43.5 mL. This results in 23% final MSB in 43.5 mL final volume.
4. Mix well by inverting up and down many times. Centrifuge at 500 x g for 15 mins at 4C on slow break (9 acceleration, 3 deceleration).



5. Aspirate the myelin and the supernatant and resuspend the pellet in 1800  $\mu$ L MACS buffer. Pass the cell suspension through a 70  $\mu$ m filter to remove any cell clumps.
6. Add 200  $\mu$ L myelin removal beads (Miltenyi). Mix well, do not vortex.
7. Incubate at 4 °C fridge for 15 mins in dark.
8. During incubation, prepare LS columns (one LS column per brain) by washing 3x times with 3 mL MACS buffer. Discard the wash buffer collected in the tubes.
9. After step #12, wash the suspension with 10x the labeling volume i.e. add 18 mL MACS buffer (since labeling volume was 1800  $\mu$ L). Mix well.
10. Centrifuge at 300 x g for 10 mins at 4 °C on slow break.
11. Aspirate supernatant completely and resuspend pellet with 1000  $\mu$ L MACS buffer. Filter through a 70  $\mu$ m filter and make sure the cell suspension is homogeneous.
12. Apply the 1000  $\mu$ L filtered cell suspension to an LS column (myelin remains in the column and unlabeled cells pass through).
13. Wash the column with 1 mL MACS buffer 2x times. Collect the single cell suspension that passed through the tubes (*these are unlabeled cells with myelin removed*).
14. Determine cell number with a hemocytometer (9  $\mu$ L cell suspension + 1  $\mu$ L trypan blue).

#### **A.5 CD11b<sup>+</sup> cell selection**

1. Centrifuge the unlabeled cell suspension at 300 x g for 10 mins at 4 °C on slow break.
2. Aspirate supernatant completely and resuspend in 90  $\mu$ L MACS Buffer per 10<sup>7</sup> total cells.
3. Add 10  $\mu$ L CD11b microbeads (Miltenyi) per 10<sup>7</sup> total cells.
4. Gently mix well and incubate at 4 °C fridge for 15 mins.
5. During the incubation time, wash the LS column with 3 mL MACS Buffer 3x times.
6. After step #24, wash the cell suspension by adding 1-2 mL buffer per 10<sup>7</sup> cells.
7. Centrifuge at 300 x g for 10 mins at 4 °C on slow break.
8. Keep the TIC medium and MGM in 37 °C incubator with 10% CO<sub>2</sub> for equilibration for 30 mins.
9. Coat the wells with collagen IV and place in 37 °C incubator. Stock collagen IV = 200  $\mu$ g/mL. Dilute 1:100 to final conc. of 2  $\mu$ g/mL in MGM. Coat for 15-60 mins.
10. Pipet off supernatant completely and resuspend up to 108 cells in 500  $\mu$ L buffer.

11. Apply cell suspension to the LS column. Collect unlabeled cells that pass through and wash column with 3 mL MACS Buffer 2x to 3x times.
12. Remove column from the stand and place on a 15 mL falcon tube on ice. Add 5 mL MACS buffer into the column and flush the CD11b<sup>+</sup> cells using a plunger.
13. Determine CD11b<sup>+</sup> cell count using a hemocytometer (9  $\mu$ L cell suspension + 1  $\mu$ L trypan blue).

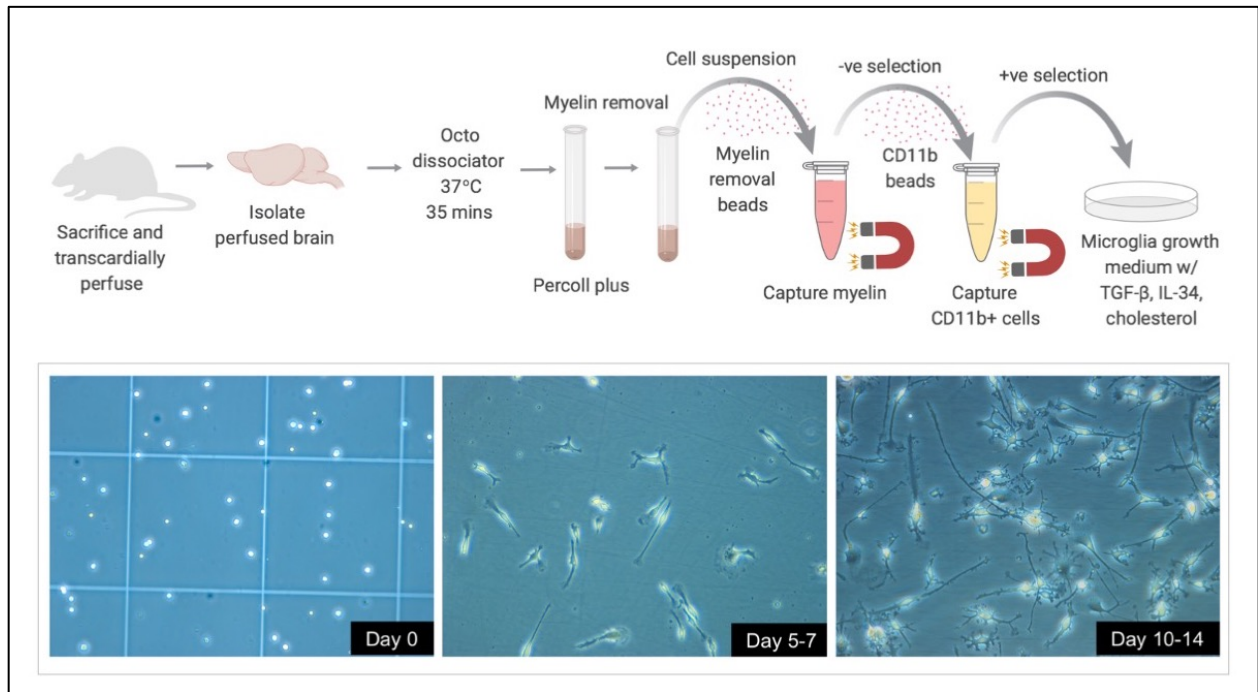


**Figure A.1** (Top) Illustration depicting the optimized protocol for isolation of primary mouse microglia and culture in reduced serum media. (Bottom) Growth and differentiation of seeded cells in a dish over time.

#### A.6 Seeding CD11b<sup>+</sup> cells

1. Centrifuge cell suspension at 300 x g for 10 mins at 4 °C on slow break.
2. Aspirate the buffer completely and resuspended the cells in MGM.
3. Count the cells with a hemocytometer (9  $\mu$ L cell suspension + 1  $\mu$ L trypan blue).
4. Dilute the cell suspension to the required concentration in TIC medium. ( $0.1 \times 10^6$  cells/well in a 24-well plate. Seed 100  $\mu$ L per well).
5. Incubate at 37 °C for 5-10 mins to allow the cells to adhere. Top up volume by adding pre-warmed TIC medium to the wells.

## A.7 References

- [1] C. J. Bohlen, F. C. Bennett, and M. L. Bennett, "Isolation and Culture of Microglia," *Curr. Protoc. Immunol.*, vol. 125, no. 1, p. e70, Jun. 2019.
- [2] C. J. Bohlen, F. C. Bennett, A. F. Tucker, H. Y. Collins, S. B. Mulinyawe, and B. A. Barres, "Diverse Requirements for Microglial Survival, Specification, and Function Revealed by Defined-Medium Cultures," *Neuron*, vol. 94, no. 4, pp. 759-773.e8, May 2017.
- [3] H. Y. Collins and C. J. Bohlen, "Isolation and culture of rodent microglia to promote a dynamic ramified morphology in serum-free medium," *J. Vis. Exp.*, 2018.

## **APPENDIX B. EXPLORATORY LIPIDOME AND METABOLOME ANALYSIS BY MULTIPLE REACTION MONITORING (MRM)-PROFILING**

### **B.1 Background**

MRM-profiling is a fast and highly sensitive analytical strategy used in exploratory lipidomics and metabolomics[1]. It was developed in the laboratory of Prof. Graham Cooks at Purdue University.

Most traditional MS exploratory approaches for small molecule profiling are based on LC separation and full mass scans followed by product ion scans. On the other hand, MRM-profiling relies on direct sample injection, and the functional groups are monitored using neutral loss and precursor MS/MS scans. Rather than detecting signals associated with individual molecules (as in conventional product ion MS/MS), MRM focuses on the functional groups. The most discriminant precursor/product transitions observed from screens of representative pooled samples are used to analyze individual samples in minimum times using very small amounts of sample.

The main challenge related to MRM-profiling is the difficulty in identifying the molecular structure of small molecules. Since the technique does not use LC separation, etc., the select lipids of interest have to be further validated using the other analytical techniques for structure elucidation. The main advantages of MRM-profiling are the sensitivity and speed the method. The merit of the technique has been recently demonstrated by its application on biomarker discovery for the following disease conditions: human polycystic ovarian syndrome[2], diet compliance[3], coronary artery disease[4], and for better understanding of the lipid metabolism in bovine preimplantation embryos[5], aging mice[6], to detect bacterial resistance[7] and colostrum impact on the reproductive system of newborn piglets[8].

### **B.2 Methods**

#### **B.2.1 Bligh & Dyer protocol for lipid and metabolite extraction**

The Bligh & Dyer protocol is used for sample extraction[9]. The frozen cell pellets and the conditioned medium are brought to room temperature and the following steps are carried out.

1. Add 200  $\mu\text{L}$  of ultrapure water, 450  $\mu\text{L}$  methanol and 250  $\mu\text{L}$  chloroform (HPLC grade). Mix, vortex 10 sec. This should become a 1-phase solution. If after letting the microtube sitting for few seconds two layers are observed, add 100  $\mu\text{L}$  methanol.
2. Allow the solution to sit at 4  $^{\circ}\text{C}$  for 15min.
3. Add 250  $\mu\text{L}$  ultrapure water and 250  $\mu\text{L}$  chloroform. It will be possible to notice that the solution becomes biphasic.
4. Centrifuge for 10 min at 16,000 x g. The upper phase of the solution is the polar phase, and bottom phase is the organic phase where the lipids are. There will probably be a middle whitish 'ring' corresponding to proteins.
5. Carefully transfer the bottom phase (that's where the lipids are) to a clean microtube. The lipid phase solution can be split into 4 microtubes (to provide more aliquots for analysis).
6. Evaporate the solvent in the microtubes using nitrogen stream on in a speed-vac.
7. Store the dried lipid extracts in -80  $^{\circ}\text{C}$  freezer until mass spectrometry.

### B.2.2 Multiple Reaction Monitoring (MRM)-profiling

MRM-profiling is a two-step strategy (discovery step/screening step) for small molecule biomarker identification, first reported in 2016 (2). For this study, MRM-profiling is performed using the screening methods described by de Lima *et al.*, 2018 (6) and Dipali *et al.*, 2019.

Briefly, the first step of the MRM-profiling approach consists of using lists of MRMs based on the Lipid Maps database for 15 different lipid classes (Lyso PC, PC, SM, Lyso PE, PE, Lyso PI, PI, Lyso PG, PG, Lyso PS, PS, TAGs, cholesteryl esters, acyl-carnitines, and FFA). Each MRM consists of a molecular ion of mass-to-charge ratio ( $m/z$ ) and the expected diagnostic product ion for each lipid class or fatty acyl residue. Triacylglycerols (TAGs) are monitored by the parent ion of their ammonium adducts and the product ion corresponding to the neutral loss of specific fatty acyl residues [palmitic (C16:0), palmitoleic (C16:1), stearic (C18:0), oleic (C18:1), linoleic (C18:2), arachidic (C20:0) and arachidonic (C20:4)]. Free fatty acids are monitored at the negative ion mode only by the parent ion. The final list of MRMs contains around 1,586 entries corresponding to 14,184 Lipid Maps entries (the constitutional isomers were combined into a single entry). The screening step of MRM-profiling is performed in representative pools from each

study group. Only MRMs presenting ion intensity at least 30% than a blank sample for at least one of the experimental pools will be used for interrogating individual samples in the screening phase.

In the second step, MRM profiling of individual samples is performed for the entire sample set by interrogating the samples only for the MRMs detected as higher than in a blank extraction sample during the discovery step.

For both steps, dry lipid extracts (from Bligh & Dyer extraction) are re-suspended in ACN+MeOH+300mM NH<sub>4</sub>Ac 3:6.65:0.35 (v/v). A micro-autosampler (G1377A) is used to deliver 8 µL per sample by flow injection for the screening of each lipid class to the ionization source of an Agilent 6410 QQQ mass spectrometer (Agilent Technologies, Santa Clara, CA, USA). The autosampler's capillary pump is operated with a pressure of 150 bar and a ten µL/min flow. The capillary voltage will be 3.5-5 kV, and the gas flow was 5.1 L/min at 300 °C.

### B.3 Data analysis

All statistics determined for the comparisons between experimental cells versus control cells are calculated using the edgeR package[10]. Here, the ion count for a given biomarker (i.e., lipid or metabolite) is referred to using the subscript  $s$  for the sample (cell replicate for a class of analyte) and  $b$  for the specific biomarker (i.e., a single lipid). An additional 'intercept' sample is added to model the experimental blank performed using just the injection media to ensure that all comparisons are significant with respect to this control. The edgeR package fits a generalized linear model to the following log-linear relationship for the mean-variance:  $\log \mu_{bs} = X_b^T \beta_g + \log N_s$  for each biomarker  $b$  in sample  $s$  where the sum of all ion intensity for sample  $s$  sums to  $N_s$ . This allows for the calculation of the coefficient of variation (CV) for the ion count for a biomarker in a sample ( $y_{bs}$ ) using the following relationship  $CV^2(y_{bs}) = 1/\mu_{bs} + \Phi_b$  Where  $\Phi_b$  is the dispersion of the biomarker, this dispersion term is estimated using the common dispersion method[11]. These values are used to calculate the associated log-fold change between reactive and control cells and the p-values obtained using the likelihood ratio test. These p-values are then adjusted for multiple testing using the BH method to get false discovery rates[12].

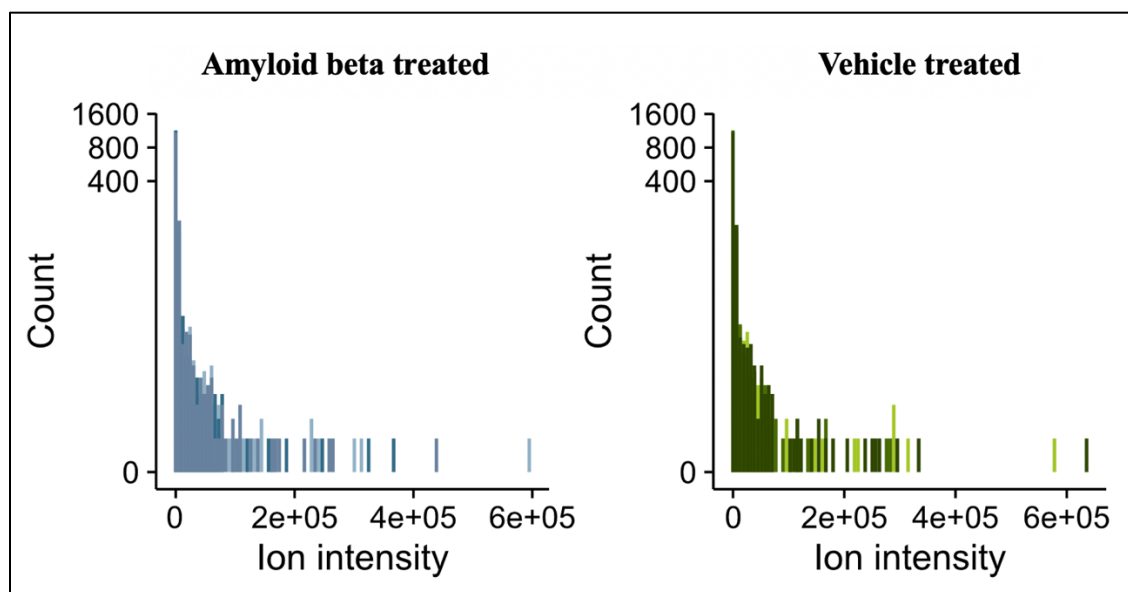


**Figure B.1** Sample Ion Intensity distributions for BV2 cells. These plots have hallmark characteristics of a negative binomial distribution. These features include the fact that the majority of the ion counts are near 0 and that the distributions have a long right-hand tail.

#### B.4 References

- [1] Z. Xie, C. R. Ferreira, A. A. Virequ, and R. G. Cooks, "Multiple reaction monitoring profiling (MRM profiling): Small molecule exploratory analysis guided by chemical functionality," *Chem. Phys. Lipids*, vol. 235, Mar. 2021.
- [2] F. B. Cordeiro *et al.*, "Multiple reaction monitoring (MRM)-profiling for biomarker discovery applied to human polycystic ovarian syndrome," *Rapid Commun. Mass Spectrom.*, vol. 31, no. 17, pp. 1462–1470, Sep. 2017.
- [3] J. Dhillon, C. R. Ferreira, T. J. P. Sobreira, and R. D. Mattes, "Multiple reaction monitoring profiling to assess compliance with an almond consumption intervention," *Curr. Dev. Nutr.*, vol. 1, no. 9, 2017.
- [4] K. E. Yannell, C. R. Ferreira, S. E. Tichy, and R. G. Cooks, "Multiple reaction monitoring (MRM)-profiling with biomarker identification by LC-QTOF to characterize coronary artery disease," *Analyst*, vol. 143, no. 20, pp. 5014–5022, 2018.
- [5] C. B. de Lima, C. R. Ferreira, M. P. Milazzotto, T. J. P. Sobreira, A. A. Vireque, and R. G. Cooks, "Comprehensive lipid profiling of early stage oocytes and embryos by MRM profiling," *J. Mass Spectrom.*, vol. 53, no. 12, pp. 1247–1252, Dec. 2018.
- [6] S. S. Dipali, C. R. Ferreira, L. T. Zhou, M. T. Pritchard, and F. E. Duncan, "Histologic analysis and lipid profiling reveal reproductive age-associated changes in peri-ovarian adipose tissue," *Reprod. Biol. Endocrinol.*, vol. 17, no. 1, p. 46, Dec. 2019.

- [7] Z. Xie *et al.*, “Multiple Reaction Monitoring Profiling (MRM-Profilng) of Lipids to Distinguish Strain-Level Differences in Microbial Resistance in *Escherichia coli*,” *Anal. Chem.*, vol. 91, no. 17, pp. 11349–11354, Sep. 2019.
- [8] T. Casey, K. L. Harlow, C. R. Ferreira, T. J. P. Sobreira, A. Schinckel, and K. Stewart, “The potential of identifying replacement gilts by screening for lipid biomarkers in reproductive tract swabs taken at weaning,” *J. Appl. Anim. Res.*, vol. 46, no. 1, pp. 667–676, 2018.
- [9] E. G. Bligh and W. J. Dyer, “A RAPID METHOD OF TOTAL LIPID EXTRACTION AND PURIFICATION,” *Can. J. Biochem. Physiol.*, vol. 37, no. 1, pp. 911–917, Jan. 1959.
- [10] M. D. Robinson, D. J. McCarthy, and G. K. Smyth, “edgeR: A Bioconductor package for differential expression analysis of digital gene expression data,” *Bioinformatics*, vol. 26, no. 1, pp. 139–140, Jan. 2009.
- [11] D. J. McCarthy, Y. Chen, and G. K. Smyth, “Differential expression analysis of multifactor RNA-Seq experiments with respect to biological variation,” *Nucleic Acids Res.*, vol. 40, no. 10, pp. 4288–4297, May 2012.
- [12] Y. Benjamini and Y. Hochberg, “Controlling the False Discovery Rate: A Practical and Powerful Approach to Multiple Testing,” *J. R. Stat. Soc. Ser. B*, vol. 57, no. 1, pp. 289–300, Jan. 1995.



## APPENDIX C.    PROTEOMIC ANALYSIS OF BV2 MICROGLIA WITH AMYLOID

### C.1    Introduction

In this study, I evaluated the changes in the global proteome of BV2 microglia that were acutely exposed to A $\beta$  in culture. Although BV2 cells do not accurately mirror the characteristics of microglia *in vivo*[1], they may share similar phagocytic machinery as primary microglia[2]. First, using live cell imaging and flow cytometry, I showed that BV2 microglia treated with 500 nM aggregated A $\beta^{\text{pH}}$  (Chapter 4) readily phagocytose the aggregates within 1 hour of exposure. The pH-sensitive human A $\beta$ 1-42 peptide conjugate (A $\beta^{\text{pH}}$ ) is non-fluorescent outside the cells and exhibits green fluorescence at pH  $\sim$ 4.5 upon internalization into the intracellular acidic phagosomal compartments of the cells. This experiment showed the dramatic changes occurring in BV2 microglia within 1 hour of A $\beta$  treatment. Next, I asked, what downstream proteomic changes occur in these cells that may be involved in the almost-immediate change in cell state and phagocytic function due to A $\beta$ ? I performed label-free quantitative proteomics to identify all the cellular proteins in A $\beta$ -treated as well as vehicle-treated control BV2 microglia and then evaluated the proteins that were differentially regulated in the cells due to A $\beta$ . A total of 3743 proteins/protein families were identified in the A $\beta$ -treated BV2 microglia and 3745 proteins/protein families were identified in the vehicle-treated control microglia and 3250 proteins (84.5%) were common to both. Over a hundred proteins were uniquely identified in microglia acutely treated with A $\beta$  compared to the vehicle-treated control microglia. Additionally, 46 proteins were differentially regulated (FDR<0.1) in these cells due to A $\beta$ , out of which 19 and 27 proteins were up and downregulated, respectively. This dataset provides a comprehensive view of the dynamic changes in BV2 microglia's proteome with acute exposure to A $\beta$  in culture.

### C.2    Methods

#### C.2.1    BV2 microglia cell culture

BV2 microglial cells were kindly provided by Dr. Linda J. Van Eldik (University of Kentucky, USA). DMEM (Dulbecco's Modified Eagle's medium)/Hams F-12 50/50 Mix (#10-090-CV) and L-Glutamine (#25-005-CI) were purchased from Corning. Fetal bovine serum (FBS) was from

Atlanta Biologics, Penicillin/Streptomycin was from Invitrogen. BV2 microglial cells were maintained at 37 °C and 5% CO<sub>2</sub> in DMEM/Hams F-12 50/50 Mix containing 10% FBS, 1% L-Glutamine, and 1% Penicillin/Streptomycin.

### **C.2.2 A $\beta$ 42 preparation and treatment**

Human amyloid beta 1-42 peptide was purchased from AnaSpec (#20276). The A $\beta$ 42 peptide was first dissolved in 2 mM NaOH at a concentration of 1 mg/mL and incubated at 37 °C for 24 hrs to initiate aggregation. The aggregated peptide was stored at -80 °C and diluted to 500 nM in the cell culture media for the subsequent proteomic experiments.

For the proteomics experiment, the cells were seeded at a concentration of 0.16 million cells/mL in a 6-well plate for 24 hours and treated with 500 nM A $\beta$ 42 for 1 hour to facilitate their phagocytosis by the BV2 cells. After 1 hour, the cells were washed with 10 mM cold phosphate buffered saline (PBS) 3 times and manually detached from the wells. The cells were then centrifuged at 500 x g for 6 min at 4 °C, supernatant removed, and the cell pellets stored at -20 °C for protein extraction. Four independent experiments were performed (biological replicates).

### **C.2.3 BV2 microglial phagocytosis of A $\beta$ 42**

For live-cell imaging on IncuCyte, the cells were seeded in a 96-well plate at the concentration of 5000 cells/200  $\mu$ L/well for around 16-18 hours overnight. The next day, the cells were treated with 500 nM A $\beta^{\text{pH}}$  and immediately transferred to the IncuCyte for imaging. The cells were imaged for 1 hour to evaluate the phagocytosis of A $\beta^{\text{pH}}$  over this time. For flow cytometry experiments, the cells were seeded at the concentration of 0.16 million cells/mL in a 6-well plate for around 16-18 hours overnight. The next day, the cells were treated with 500 nM A $\beta^{\text{pH}}$  for 1 hour to facilitate their phagocytosis (during this time the plate was kept at 37 °C). After 1 hour, the plate was brought to the hood and placed on ice. The media containing A $\beta^{\text{pH}}$  was removed and the cells were washed with cold 1x PBS 2-3 times and manually detached from the wells. The cells were pelleted at 500 x g for 5 mins and resuspended in around 500  $\mu$ L 1x PBS. The cells were then stained with the live/dead Zombie Violet dye (BioLegend #423113) per the manufacturer's protocol. After staining, the were once again pelleted as above to remove the dye-containing PBS and resuspended in fresh

1x PBS. The cells were then taken for flow cytometry analysis to evaluate the green fluorescence within the cells indicating the phagocytic uptake of A $\beta$ <sup>pH</sup>.

#### **C.2.4 Protein extraction and digestion (Sample preparation for LC-MS/MS)**

The protocol previously detailed for cellular proteins was followed (Basic protocol 1)[3]. Briefly, BV2 microglia treated with 500 nM A $\beta$ 42 for 1 hour were pelleted by washing with cold 10 mM PBS and centrifugation at 500 x g for 6 mins at 4 °C. The pelleted cells were lysed by homogenization in 8M urea in a bath sonicator for 15 mins. The homogenized cells were centrifuged at 14,000 rpm for 15 mins at 4 °C and the proteins were precipitated with 5 equivalents (v/v) of ice-cold acetone overnight at -20 °C. The proteins were centrifuged at 14,000 rpm for 15 mins at 4 °C and dissolved in 8M urea. Protein concentration was determined with BCA assay using BSA as a standard. Based on the protein concentration in each sample, 50 ug of total protein reduced with 10 mM dithiothreitol (DTT) at 55 °C for 45 min and cysteine alkylation performed with 20 mM iodoacetamide at room temperature under dark for 45 min. The proteins were then digested using trypsin and Lys-C mix at a 1:25 (w/w) enzyme-to-protein ratio at 37 °C overnight. The digested peptides were cleaned using C18 micro spin columns using the manufacturer's protocol. The peptides were then eluted with 0.1% formic acid (FA) in 80% acetonitrile (ACN). The eluted peptides were vacuum dried and re-suspended in 0.1% FA in 3% ACN. Peptide concentration was determined with the BCA assay as above and adjusted to 1  $\mu$ g/ $\mu$ L for LC-MS/MS. The LC-MS/MS data was acquired as previously described (Chapter 8; Section 8.2.3).

#### **C.2.5 Data analysis**

The proteomic data generated from this experiment was analyzed as described in Appendix B (B.3 Data analysis).

### **C.3 Results**

#### **C.3.1 BV2 microglia phagocytose A $\beta$ within 1 hour of treatment**

Phagocytosis is a well-orchestrated mechanism wherein the target prey particles are recognized by the phagocytes and engulfed into their intracellular organelle called phagosomes[4]. Enzymatic digestion of the internalized particles is initiated in the phagolysosomes which is formed by the

fusion of the phagosomes with the lysosomes[4]. BV2 microglia were treated with 500 nM A $\beta$ 42 for 1 hour which is sufficient to cause its phagocytic uptake by majority of the cells and the control cells were treated with corresponding amount of 2 mM NaOH diluted in media. We observed that cells treated with 500 nM A $\beta^{\text{pH}}$  readily phagocytosed the peptides within 1 hour as shown by flow cytometry and live cell imaging. The A $\beta^{\text{pH}}$ —pH-sensitive Protonex green labeled A $\beta$ 42 (Chapter 4) is non-fluorescent outside the cells and exhibits green fluorescence at ~pH 4.0 upon internalization into the intracellular acidic compartments of the cells. Thus, majority of the microglia in culture were phagocytic towards the A $\beta$ 42 at the given time point and concentration.

### **C.3.2 Global proteomic changes in BV2 microglia with 1 hour A $\beta$ treatment**

A total of 4990 proteins were identified in the study (out of 54478 peptide sequences screened). The data was analyzed such that each protein had at least 1 non-zero label free quantitation (LFQ) value, 2 non-zero LFQ values, 4 non-zero LFQ values, and 8 non-zero LFQ values (called 1x, 2x, 4x, and 8x respectively) between the A $\beta$  and vehicle groups. However, we selected 2x data analysis for results and figures based on the total contribution of principal components showcasing greater than 70% variation in A $\beta$  and vehicle-treated microglia dataset. There is no difference in log2FC, p-value, and FDR values between different datasets for the same protein. The 1x data shows the largest number of differentially expressed proteins (i.e. 468 proteins; FDR<0.1), however the PCA plots do not separate the proteomes of A $\beta$  and vehicle groups and therefore, 2x dataset was chosen.

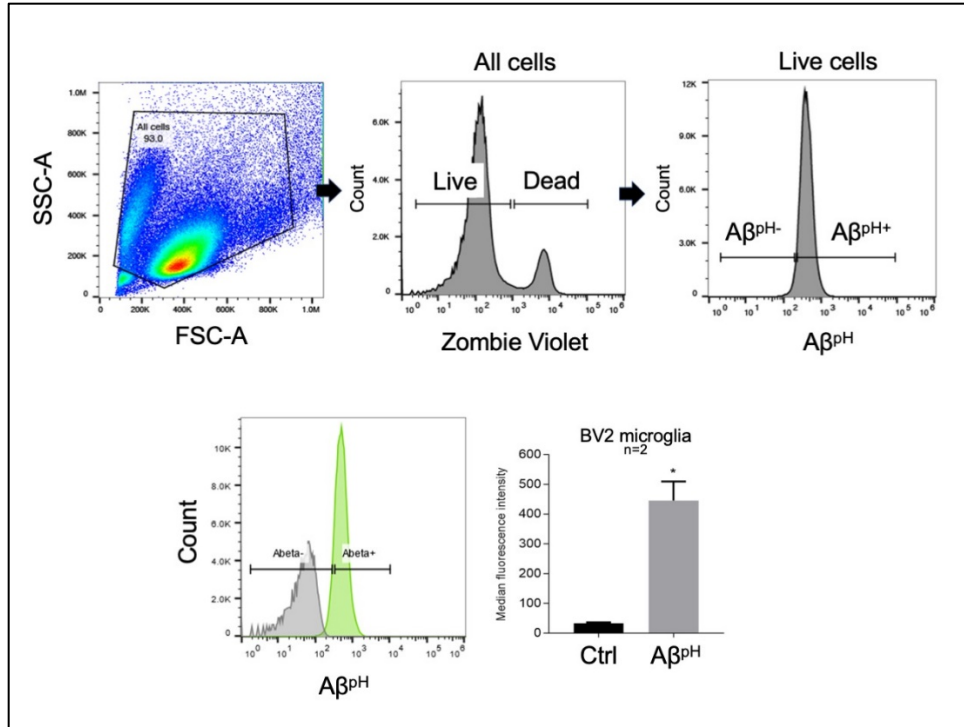


**Figure C.1** (Top) Gating strategy for evaluating the phagocytosis of A $\beta^{pH}$  by BV2 microglia. BV2 microglia phagocytose 500 nM A $\beta^{pH}$  within 1 hour of treatment in culture.

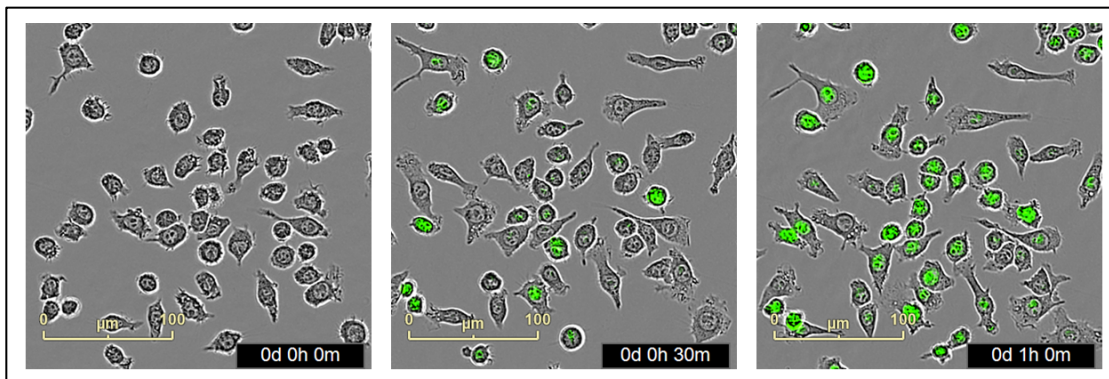


**Figure C.2** Live cell imaging of A $\beta^{pH}$  phagocytosis by BV2 microglia.

**Table C-1** Principal components analysis of protein mass spectrometry data. Number of significant proteins and PCA variation based on number of replicates of protein mass spectrometry that were required to have a non-zero spectral count to be considered for analysis. 2 of 8 (2x) was chosen for final analysis.

Dataset	Number of significant proteins (FDR<0.1)	Number of upregulated proteins	Number of downregulated proteins	Variation in data shown by the PCA plots
1x	468	112	356	59.0
2x	46	19	27	59.3
3x	15	6	9	78.9
4x	15	7	8	98.9
8x	5	3	2	77.1

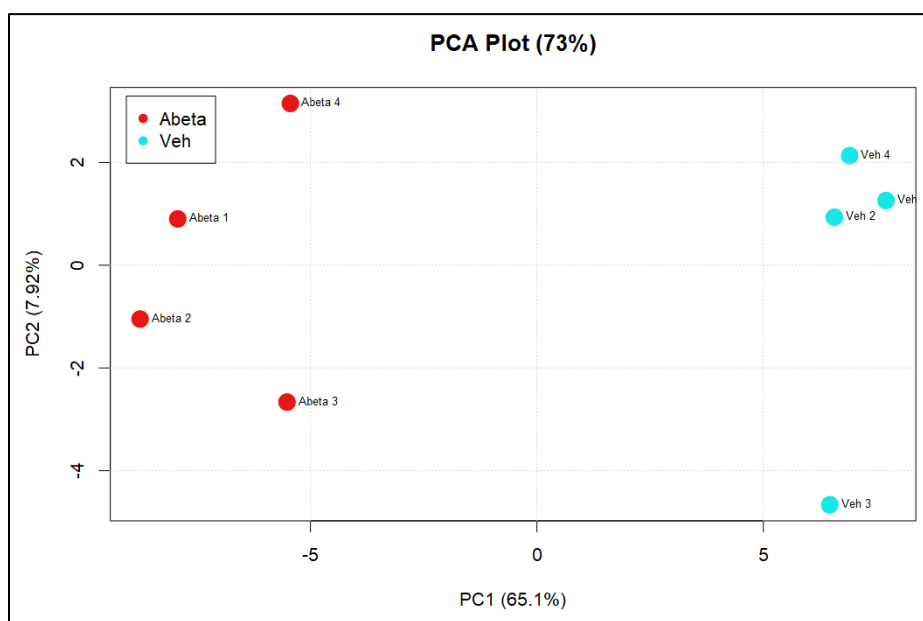


**Figure C.3** Principal Component Analysis (PCA) plot showing separation of BV2 microglial proteomes with A $\beta$  (red) and vehicle (blue) treatment. PC1 and PC2 correspond to 65.1% and 7.92% respectively indicating the data representing 73%.

### **C.3.3 Upregulated proteins in BV2 microglia with 1 hour A $\beta$ treatment**

Out of the several upregulated proteins (fold change >1.5) identified in the A $\beta$  treated microglia, there were transmembrane proteins (App, Pkp4, Mfsd5), cytoplasm and cytosolic proteins (Bphl, Wdr37, Prkra, etc.), nuclear proteins (Tfdp1, Mtf2, Pimreg, Pus7l, Vrk3, Atad5), and proteins associated with mitochondrion (Fmc1) and Golgi apparatus (Cog6, Atp2c1). The highest upregulated protein in A $\beta$  treated microglia was the amyloid beta (A4) protein (Gene: App). The top 3 most upregulated proteins are associated with the plasma membrane and cytoskeleton which are involved in the cellular process of migration and endocytosis, thereby suggesting a dynamic state of the cells with initial A $\beta$  exposure. The phagocytic and endocytic pathways are closely associated molecular pathways within the cells. The specific roles of several proteins identified in this datasets has still not been characterized in microglia.

### **C.3.4 Downregulated proteins in BV2 microglia with 1 hour A $\beta$ treatment**

Out of the downregulated proteins (fold change <1.5) identified in the A $\beta$  treated microglia, the nuclear and cytoplasm and cytosolic proteins were the most abundant. A few proteins were localized in the cytoskeleton (Chd3, Trip10), mitochondrion (Coa6, mt-Cytb), Golgi apparatus (Trip10), and Peroxisome (Serhl). Interestingly, the TRIP10 protein (thyroid hormone receptor interactor 10; also known as CIP4) localizes to several subcellular regions within the cell including the plasma membrane, cytoskeleton, Golgi apparatus, and lysosome. This protein is required for translocation of GLUT4 to the plasma membrane and is also heavily involved in phagocytosis[5]. Specifically, TRIP10 is required for the reorganization of the actin cytoskeleton during endocytosis[6]. This protein also binds to lipids such as phosphatidylinositol 4,5-bisphosphate and phosphatidylserine. Thus, TRIP10 warrants further research in the context of microglial response to A $\beta$ . Calcium-regulated heat-stable protein 1 (Carhsp1) is another interesting protein in this dataset. This protein is an important mediator of inflammation and is critical for TNF- $\alpha$  production by both resting and lipopolysaccharide (LPS)-stimulated macrophages[7]. Finally, while the literature on the role of CD300a protein is limited[8], [9], its function in the context of microglial phagocytosis must be further evaluated. This membrane protein is expressed on myeloid lineages and specific subsets of CD4<sup>+</sup> T cells. CD300a has a cytoplasmic tail containing an immunoreceptor tyrosine-based inhibitory motif—an inhibitory receptor found on immune cells[10], [11].

**Table C-2** Upregulated proteins in A $\beta$ -treated BV2 microglia

Protein ID	Protein name	Gene	Log <sub>2</sub> FC	FDR
Q6GR78	Amyloid-beta A4 protein	App	33.876	1.03E-33
Q3UV17	Keratin, type II cytoskeletal 2 oral	Krt76	30.809	4.84E-32
A2AS45	Plakophilin-4	Pkp4	28.943	3.84E-31
Q6RUT7	Protein CCSMST1	Ccsmst1	27.668	1.49E-30
A0A068E	NA	NA	27.348	1.49E-30
Q9CR13	Protein FMC1 homolog	Fmc1	27.344	1.49E-30
Q8C7Y2	Conserved oligomeric Golgi complex subunit 6	Cog6	27.259	1.55E-30
Q9D297	Transcription factor Dp-1	Tfdp1	26.706	2.54E-30
E9QAD3	Metal-response element- binding transcription factor 2	Mtf2	26.498	2.87E-30
Q8R164	Valacyclovir hydrolase	Bphl	26.274	3.34E-30
Q5RIU2	Protein PIMREG	Pimreg	26.039	3.78E-30
A0A0U1RP6	NA	NA	25.902	4.13E-30
H3BK66	WD repeat-containing protein 37	Wdr37	25.894	4.13E-30
Q8CE46	Pseudouridylate synthase 7 homolog-like protein	Pus71	25.826	4.32E-30
Q9WTX2	Interferon-inducible double- stranded RNA-dependent protein kinase activator A	Prkra	25.792	4.42E-30
E9PW85	Inactive serine/threonine- protein kinase VRK3	Vrk3	25.739	4.66E-30
Q8BMS7	Calcium-transporting ATPase	Atp2c1	25.435	7.13E-30
B2RUJ4	ATPase family AAA domain- containing protein 5	Atad5	25.363	7.54E-30
Q921Y4	Molybdate-anion transporter	Mfsd5	25.065	1.05E-29



**Table C-3** Downregulated proteins in A $\beta$ -treated BV2 microglia

<b>Protein</b>	<b>Protein name</b>	<b>Gene</b>	<b>Log<sub>2</sub>FC</b>	<b>FDR</b>
F7C528	DNA helicase	Chd3	-29.650	1.79E-31
Q5M9P7	Calcium regulated heat stable protein 1	Carhsp1	-27.961	1.31E-30
Q8BGD8	Cytochrome c oxidase assembly factor 6 homolog	Coa6	-27.511	1.49E-30
Q8R2R3	Alpha- and gamma-adaptin-binding protein p34	Aagab	-27.467	1.49E-30
F8WIA3	Predicted gene 20604	Gm20604	-27.433	1.49E-30
Q9CQ86	Migration and invasion enhancer 1	Mien1	-26.832	2.54E-30
Q8VC65	Nurim	Nrm	-26.819	2.54E-30
F6TCF9	BAG family molecular chaperone regulator 1	Bag1	-26.696	2.54E-30
Q8VC93	Eri3 protein	Eri3	-26.664	2.54E-30
Q3V2F9	Cytochrome b	mt-Cytb	-26.647	2.54E-30
Q7TQE1	Mediator of RNA polymerase II transcription subunit 15	Med15	-26.579	2.67E-30
Q6SJQ0	CMRF35-like molecule 8	Cd300a	-26.375	3.12E-30
Q7M752	Pantothenate kinase 3	Pank3	-26.374	3.12E-30
A0A140LJ	NA	NA	-26.308	3.29E-30
Q8CJ53	Cdc42-interacting protein 4	Trip10	-26.200	3.44E-30
Q80XK9	Serine hydrolase-like	Serhl	-26.195	3.44E-30
Q3TL71	Heterogeneous nuclear ribonucleoprotein K	Hnrnpk	-26.154	3.52E-30
B9EHE8	R3hdm1 protein	R3hdm1	-26.058	3.78E-30
Q91YX0	Protein THEMIS2	Themis2	-26.041	3.78E-30
Q6DIC0	Probable global transcription activator SNF2L2	Smarca2	-25.923	4.13E-30
A6H6S8	BCL2-associated athanogene 4	Bag4	-25.919	4.13E-30
Q3UV38	Uncharacterized protein	Tpcn1	-25.872	4.13E-30
A0A087WP6	NA	NA	-25.367	7.54E-30
A0A1L1SQZ	NA	NA	-25.287	8.19E-30
Q3TDA1	Oxysterol-binding protein	Osbpl2	-25.261	8.32E-30
Q8C142	Low density lipoprotein receptor adapter protein 1	Ldlrap1	-25.194	8.97E-30
Q8K368	Fanconi anemia group I protein homolog	Fanci	-25.178	8.98E-30

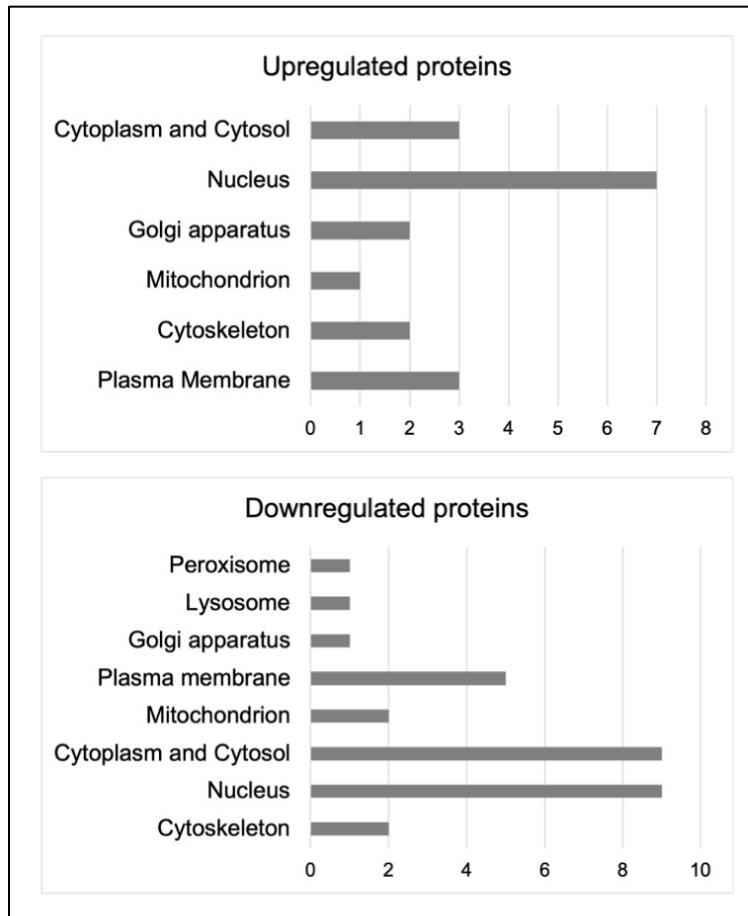


**Figure C.4** Subcellular localization of differentially regulated proteins identified in A $\beta$ -treated BV2 microglia.

#### C.4 Concluding thoughts

This study provides a window into the initial changes occurring in microglia upon A $\beta$  exposure in culture. We observe uptake of A $\beta^{\text{pH}}$  within this short amount of time indicating changes in cellular reorganization and function in response to A $\beta$ . We provide the datasets containing the upregulated and downregulated proteins in microglia with A $\beta$  and highlight a few interesting proteins worthy of investigation in future experiments. We also identify several new and previously unknown proteins related to microglial function. The proteins associated with the plasma membrane and cellular cytoskeleton may be directly involved in phagocytosis of A $\beta$ . The initial identification and screening of phagocytic targets in BV2 microglia may be functionally validated in *ex vivo* cultures of primary microglia as well as in microglia *in vivo*.

## C.5 References

- [1] O. Butovsky *et al.*, “Identification of a unique TGF- $\beta$ -dependent molecular and functional signature in microglia,” *Nat. Neurosci.*, vol. 17, no. 1, pp. 131–143, Jan. 2014.
- [2] J. V. Pluvinaud *et al.*, “CD22 blockade restores homeostatic microglial phagocytosis in ageing brains,” *Nature*, vol. 568, no. 7751, pp. 187–192, 2019.
- [3] V. E. Hedrick, M. N. LaLand, E. S. Nakayasu, and L. N. Paul, “Digestion, Purification, and Enrichment of Protein Samples for Mass Spectrometry,” *Curr. Protoc. Chem. Biol.*, vol. 7, no. 3, pp. 201–222, Nov. 2015.
- [4] S. Gordon, “Phagocytosis: An Immunobiologic Process,” *Immunity*, vol. 44, no. 3, pp. 463–475, 2016.
- [5] S. Linder, K. Hufner, U. Wintergerst, and M. Aepfelbacher, “Microtubule-dependent formation of podosomal adhesion structures in primary human macrophages,” *J. Cell Sci.*, vol. 113, pp. 4165–4176, 2000.
- [6] C. C. Hsu *et al.*, “Functional characterization of Trip10 in cancer cell growth and survival,” *J. Biomed. Sci.*, vol. 18, no. 1, p. 12, Feb. 2011.
- [7] J. R. Pfeiffer, B. L. McAvoy, R. E. Fecteau, K. M. Deleault, and S. A. Brooks, “CARHSP1 Is Required for Effective Tumor Necrosis Factor Alpha mRNA Stabilization and Localizes to Processing Bodies and Exosomes,” *Mol. Cell. Biol.*, vol. 31, no. 2, pp. 277–286, Jan. 2011.
- [8] F. Borrego, “The CD300 molecules: An emerging family of regulators of the immune system,” *Blood*, vol. 121, no. 11, pp. 1951–1960, 2013.
- [9] X. Carnec *et al.*, “The Phosphatidylserine and Phosphatidylethanolamine Receptor CD300a Binds Dengue Virus and Enhances Infection,” *J. Virol.*, vol. 90, no. 1, pp. 92–102, 2016.
- [10] V. R. Simhadri, J. F. Andersen, E. Calvo, S. C. Choi, J. E. Coligan, and F. Borrego, “Human CD300a binds to phosphatidylethanolamine and phosphatidylserine, and modulates the phagocytosis of dead cells,” *Blood*, vol. 119, no. 12, pp. 2799–2809, 2012.
- [11] Y. Cao, T. Ao, X. Wang, W. Wei, J. Fan, and X. Tian, “CD300a and CD300f molecules regulate the function of leukocytes,” *International Immunopharmacology*, vol. 93. Elsevier B.V., 01-Apr-2021.

## **APPENDIX D.    PROTEOMIC ANALYSIS OF MYELOID-DERIVED SUPPRESSOR CELLS**

Portions of this section are from a manuscript in preparation.

Kischuk EM\*, Fine JA\*, Wijewardhane PR, Prakash P, Lantz TC, Majumder J, Ratliff TL, Chopra G. Small-molecule immunomodulators targeting myeloid derived suppressor cells function in solid tumor microenvironments. (In preparation)

### **D.1    Background**

Myeloid-derived suppressor cells (MDSCs) are a heterogeneous population of immature myeloid cells that expand from precursors in the bone marrow under pathological inflammatory conditions such as cancer. MDSCs are functionally defined by the ability to suppress the proliferation and effector functions of T cells. Thus, inhibiting the activity of MDSCs may pave way for the T cells to respond to and kill cancer cells. Higher levels of MDSCs correlate with immunotherapy failure. Thus, the problematic role of MDSCs in cancer therapy has driven efforts to better characterize the underlying biology of these cells and identify molecules that suppress the function of MDSCs.

A novel machine learning method was developed by the Chopra lab that uses a profile of upregulated genes in suppressive MDSCs to predict molecules that interact with the putative protein targets. Active molecules were defined as those that reduced nitric oxide (NO) production, a key mechanism of MDSC-mediated T cell suppression. One lead molecule was identified in this study, which was called JM81, that showed significant activity on MDSCs i.e. JM81 reduced NO secretion by MDSCs and also reduced MDSCs suppression of T cell under pathological conditions.

The question then was, what proteins are affected in MDSCs upon JM81 treatment? The class of proteins or proteins that are affected in this paradigm may explain the mechanism of NO reduction. These proteins may also indicate towards other immunological mechanisms that underlie this cellular response. I performed the proteomics experiments to evaluate the changes to the MDSCs proteome upon JM81 treatment. The MDSCs samples were prepared by Dr. Erin Kischuk, the JM81 compound was computationally predicted by Dr. Jonathan Fine, and the compound was synthesized by Prageeth R. Wijewardhane.

## D.2 Method

MDSCs (Ly6C<sup>+</sup>Ly6G<sup>neg</sup> cells) isolated from tumor-bearing mice after four days of *in vivo* treatment with JM81 or vehicle were frozen at -80 °C. The frozen cells were resuspended in 100 mM ammonium bicarbonate buffer and sonicated in an ice-cold bath-sonicator for 15 minutes to break down the cell pellets. The cells were then completely lysed in a barocycler and the homogenized cells were transferred to Eppendorf tubes and centrifuged at 14,000 rpm for 15 minutes at 4 °C. The supernatant were transferred to new tubes and 4 volume (v/v) of pre-chilled (-20 °C) acetone was added and incubated overnight at -20 °C to precipitate the proteins. The next morning, the acetone-fractions left in -20 °C containing the precipitated proteins were centrifuged at 14,000 rpm for 15 minutes at 4 °C to pellet the proteins. The protein pellets were dissolved in 8 M urea for 1 hour at room temperature (RT) and the protein concentration was quantified using bicinchoninic acid (BCA) assay using bovine serum albumin as a standard. About 50 µg protein from each sample was taken and incubated with 10 mM dithiothreitol at 37 °C for 45 minutes for reduction of disulfide bonds. Next, the samples were brought to RT and incubated with 20 mM 2-iodoacetamide for 45 minutes in the dark at RT for cysteine alkylation. The proteins were digested by adding trypsin/lys-c in 1:25 ratio (2 ug trypsin per sample) and the samples were treated with 35,000 psi in a barocycler for 1 hour. The digested peptides were cleaned in C18 columns per manufacturer's protocol and purified peptides were finally eluted in 80% acetonitrile (ACN) and 0.1% formic acid (FA). The samples were vacuum dried and re-suspended in 0.1% FA in 3% ACN. The peptide concentration was determined with BCA assay as before and adjusted to 1 µg/µL and 5 uL for LC-MS/MS analysis.

The data on LC-MS/MS was acquired as detailed in Chapter 8 (section 8.3.2) and the resulting bioinformatic data was analyzed as detailed in Appendix B (section B.2).

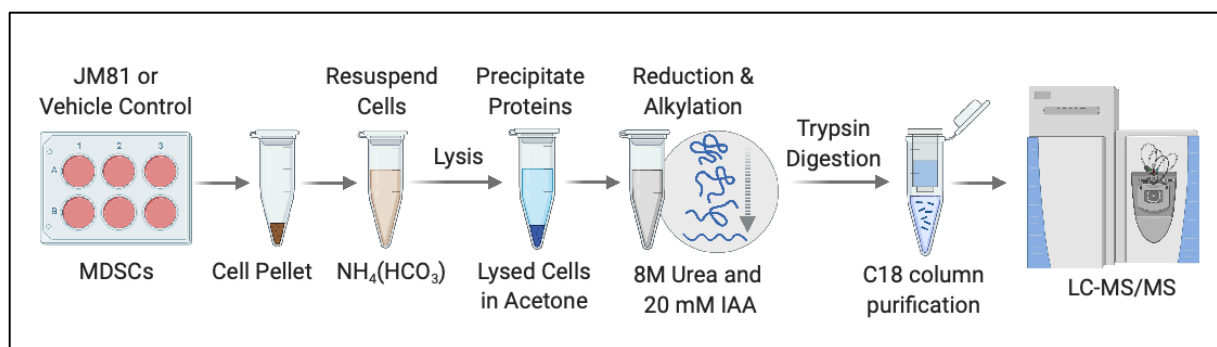


**Figure D.1** Schematic diagram of sample preparation of JM81/Vehicle-treated MDSCs for proteomics analysis. There were 3 biological replicates of JM81 and Vehicle-treated samples.

### D.3 Results

A total of 3988 proteins were identified in this study. Out of all the proteins identified, 64 proteins were found to be significant ( $\text{FDR} < 0.1$ ) and differentially regulated between the JM81-treated and vehicle treated (control) MDSCs. Thirty five proteins were upregulated and twenty nine proteins were downregulated in JM81-treated MDSCs compared to the control cells.

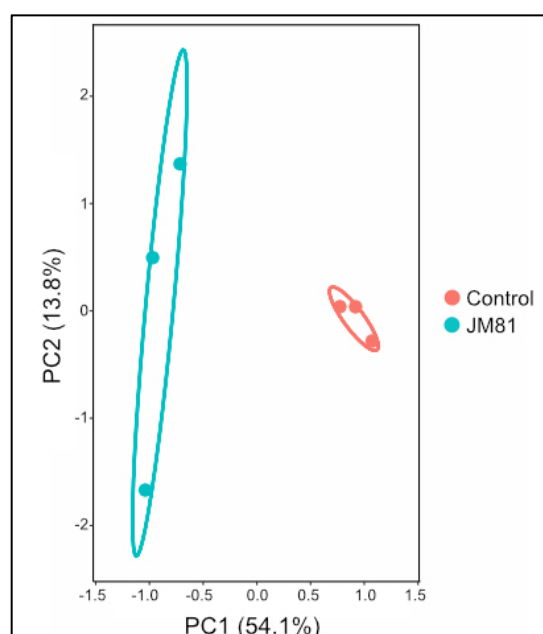


**Figure D.2** Principal component analysis (PCA) plots shows separation in the proteomes of JM81-treated versus control MDSCs. Variation in more than 67% of the sample and control data is seen showcasing the separation of the proteomes of both groups.

**Table D-1** Top 20 upregulated proteins in JM81-treated MDSCs compared to the control cells

Protein ID	Protein names	Gene names	FDR	Log <sub>2</sub> FC
P0CW03	Lymphocyte antigen 6C2	Ly6c2	4.77E-17	30.327
P63213	Guanine nucleotide-binding protein G(I)/G(S)/G(O) subunit gamma-2	Gng2	4.85E-17	29.604
Q3TEN9	Glycerol kinase	Gyk;Gk	5.50E-17	28.426
Q8C297	Transmembrane protein 14C	Tmem14c	5.50E-17	28.246
Q4FJR7	Eukaryotic translation initiation factor 1A, X-chromosomal;Eukaryotic translation initiation factor 1A	Eif1a;Eif1ax;Gm5662	5.50E-17	28.042
Q99KD5	Protein unc-45 homolog A	Unc45a	5.50E-17	28.033
A2A4J8	Vacuolar protein-sorting-associated protein 25	Vps25	5.50E-17	27.952
Q3U7A7	Proteasome subunit beta type;Proteasome subunit beta type-9	Psmb9	5.50E-17	27.838
Q6PFQ7	Ras GTPase-activating protein 4	Rasa4	5.50E-17	27.618
B7ZMR0	Protein FAM63A	Fam63a	5.50E-17	27.353
W0TGY1	NADH-ubiquinone oxidoreductase chain 4	ND4;mt-Nd4;Mtnd4	5.50E-17	27.230
Q05CR0	NA	LOC72520	5.50E-17	27.194
A9UGK3	Ran-binding protein 10	Ranbp10	5.50E-17	27.179
A0A338P6W1	E3 ubiquitin-protein ligase RBBP6	Rbbp6	5.50E-17	27.161
E9Q1V3	Dihydroorotate dehydrogenase (quinone), mitochondrial	Dhodh	5.50E-17	27.121
Q3TAJ6	Gamma-tubulin complex component 3	Tubgcp3	5.50E-17	27.053
Q9JM13	Rab5 GDP/GTP exchange factor	Rabgef1	5.50E-17	27.053
Q7TQ39	NA	gag	5.50E-17	26.992
Q99LG2	Transportin-2	Tnpo2	5.50E-17	26.876
Q3TPG4	Nucleolar protein 10	Nol10	5.50E-17	26.745

**Table D-2** Top 20 downregulated proteins in JM81-treated MDSCs compared to the control cells

Protein ID	Protein names	Gene names	FDR	Log <sub>2</sub> FC
Q8BFZ3	Beta-actin-like protein 2	Actbl2	1.49E-18	-35.469
E9Q4K7	Kinesin-like protein	Kif13b	4.77E-17	-29.956
Q99MR8	Methylcrotonoyl-CoA carboxylase subunit alpha, mitochondrial	Mccc1	5.50E-17	-29.123
Q9JM79	Napsin-A	Napsa	5.50E-17	-28.355
Q3UZQ3	Elongation factor 1-alpha	Eef1a1	5.50E-17	-27.965
O55239	Nicotinamide N-methyltransferase	Nnmt	5.50E-17	-27.710
A0A286Y DP0	Centrin-3	Cetn3	5.50E-17	-27.582
Q3TKB7	28S ribosomal protein S18b, mitochondrial	Mrps18b	5.50E-17	-27.536
E9Q265	Sulfatase-modifying factor 1	Sumf1	5.50E-17	-27.321
Q3TMB5	Thyroid receptor-interacting protein 6	Trip6	5.50E-17	-27.226
Q7TMR0	Lysosomal Pro-X carboxypeptidase	Prcp	5.50E-17	-26.899
Q9CSN5	Peptidyl-prolyl cis-trans isomerase-like 4	Ppil4	5.50E-17	-26.863
B2CC69	Interferon regulatory factor 5	Irf5	5.50E-17	-26.829
Q8VE10	N-alpha-acetyltransferase 40	Naa40	5.50E-17	-26.798
E9PXM6	Equilibrative nucleoside transporter 1	Slc29a1	5.50E-17	-26.769
P97287	Induced myeloid leukemia cell differentiation protein Mcl-1 homolog	Mcl1	5.50E-17	-26.631
Q9CSZ5	Transforming growth factor beta regulator 1	Tbreg1;mFLJ00213	5.50E-17	-26.508
A0A0G2JF 16	Coiled-coil domain-containing protein 12	Ccdc12	5.50E-17	-26.461
Q52KC5	Coiled-coil-helix-coiled-coil-helix domain-containing protein 5	Chchd5	5.50E-17	-26.446
Q8C0L8	Conserved oligomeric Golgi complex subunit 5	Cog5	5.50E-17	-26.398



## APPENDIX E. ONLINE RESOURCE FOR GLIAL OMICS DATASETS

The lipidomics and metabolomics experiments conducted in this thesis generated large datasets with hundreds of lipid and metabolite molecules. In addition to identifying the molecules, we also determined the changes occurring to these molecules with changes in their environment. For example, we evaluated how the lipids and metabolites changes in microglia with A $\beta$  treatment, astrocytes with microglial TNF- $\alpha$ , IL-1 $\alpha$ , and C1q treatment (reactive astrocytes), microglia with dexamethasone treatment, etc. Visualizing these changes in an interactive setting is a powerful way to understand the data and also refer to molecules of interest in the future.

We have developed an online resource in order to access these datasets and also visualize the changes in their abundance with a change in their environment. This resource can be accessed on the following websites. (Please note: any updates or changes to the web addresses in the future will be updated on the Chopra lab website at chopralab.org and on the lab twitter at @chopralab).

- <http://lipidomics.appspot.com> for microglial lipidomics data
- <http://gliametabolites.appspot.com> for microglial metabolomics data
- <http://astrocyte-omics.appspot.com> for astrocyte proteomics, lipidomics, and metabolomics data

Some of the main features of the websites are follows:

- Navigate between different datasets on the same page. The current available datasets on the website are: primary mouse microglial lipids (cellular and microglial conditioned medium), BV2 microglial lipids, mouse microglial metabolites (cellular and microglial conditioned medium)
- User may view changes to microglial lipids over time on the same plot i.e. changes to lipid abundance with A $\beta$  treatment at 1, 12, and 24 hour time point
- Reactive astrocyte resource includes cellular data as well as reactive astrocyte conditioned medium data
- User may view changes to astrocytic lipids in cells versus conditioned media on the same plot, i.e. view if a lipid becomes depleted in the cells and shows abundance in the conditioned media

- Also includes data from reactive and control astrocytes from the *Elovl1*<sup>-/-</sup> mice for the two main lipid classes, namely, phosphatidylcholine and sphingomyelin and free fatty acids
- Information section containing the names of all the main lipid classes included in the datasets for easy reference for the user
- Information section also includes links to the wiki page for each lipid class for further learning of lipid literature including structure and nomenclature of lipids
- Download section will include the link to download the main raw datasets used in the manuscripts and also used to build the resource
- Easy access to contact information in case of further questions

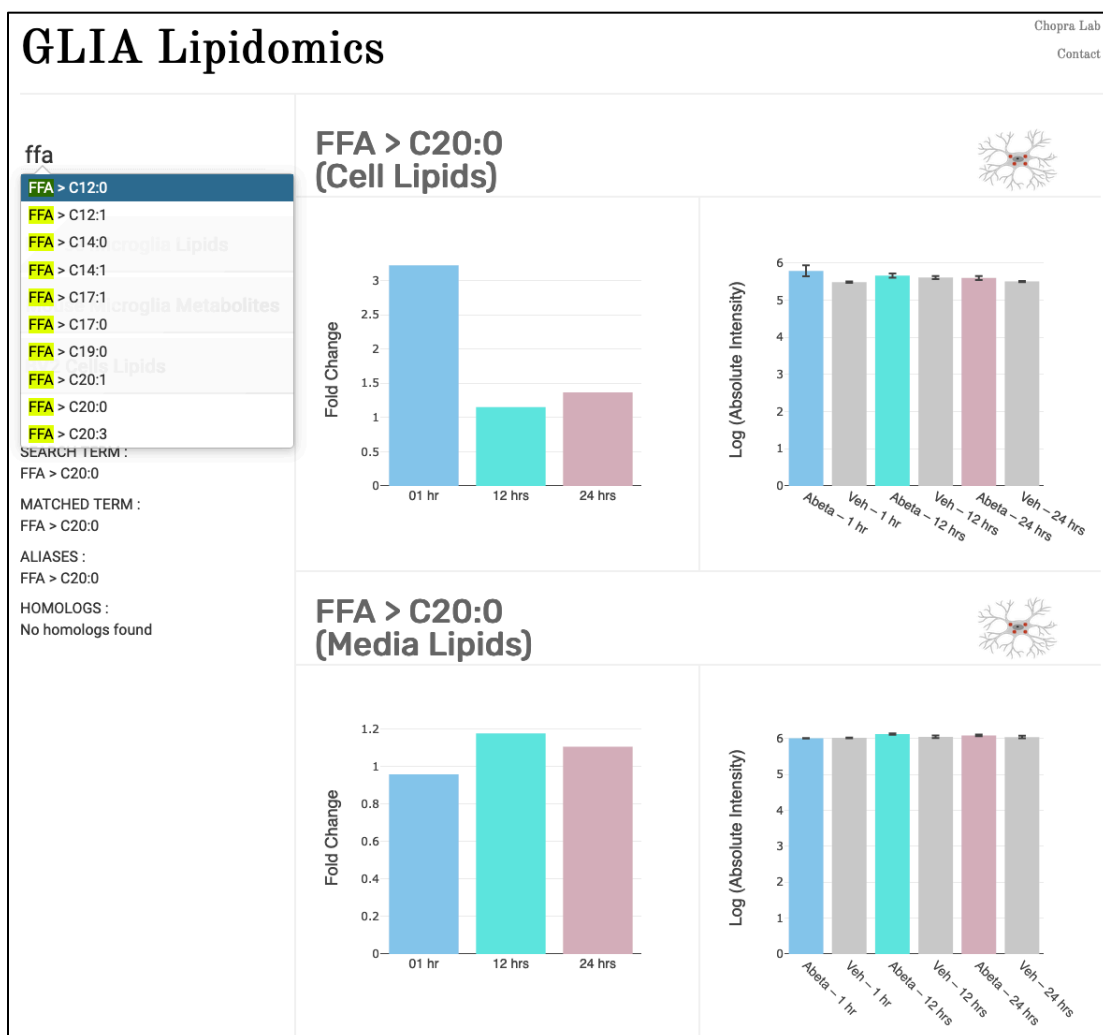


**Figure E.1** View of the microglia lipidomics website. An example of free fatty acid (FFA) is shown. The user starts by typing “FFA” into the search bar in order to view the list of lipids species included in the main lipid class. The result for C20:0 is shown here wherein the lipid in the cells is abundant at 1 hour of A $\beta$  treatment but depletes over time at 12 and 24 hours. The absolute intensity values are also shown on the right.

[INFO](#)
[DOWNLOAD](#)
[CITATION](#)

---

**LIPID CLASSES AND INFORMATION (LIPID MAPS CLASSIFICATION)**

1. Acyl Carnities (AC)  
Fatty Acyls (Wiki) > Fatty esters > Fatty acyl carnities
2. Cholesteryl Esters (CE)  
Sterol Lipids (Wiki) > Sterols > Sterol esters
3. Ceramides (Cer)  
Sphingolipids (Wiki) > Ceramides
4. Free Fatty Acids (FFA)  
Fatty Acyls (Wiki) > Fatty Acids and Conjugates
5. Phosphatidylcholine and sphingomyelin (PC and SM)  
Glycerophospholipids (Wiki) > Glycerophosphocholines
6. Phosphatidylethanolamine (PE)  
Glycerophospholipids (Wiki) > Glycerophosphoethanolamines
7. Phosphatidylglycerol (PG)  
Glycerophospholipids (Wiki) > Glycerophosphoglycerols
8. Phosphatidylinositol (PI)  
Glycerophospholipids (Wiki) > Glycerophosphoinositols
9. Phosphatidylserine (PS)  
Glycerophospholipids (Wiki) > Glycerophosphoserines
10. Triacylglycerols (TAG)  
Glycerolipids (Wiki) > Triacylglycerols > Triacylglycerols

**MICE** C57BL/6J male and female, P150-P215 adult mice

**CELL PURIFICATION AND CULTURE** Microglia were isolated and cultured as follows. Briefly, brains were harvested from adult mice following transcardial perfused with 1x PBS. The brain tissue were cut into 1 mm<sup>3</sup> pieces and dissociated in dounce buffer containing DNase-I at 37 °C on GentleMACS Octo Dissociator (Miltenyi). To obtain a single cell suspension, the dissociated tissue was passed through a 70 µm filter. Next, two rounds of myelin removal was performed. First, myelin was removed via gradient centrifugation using Percoll Plus reagent (GE Healthcare). Second, myelin removal beads (Miltenyi) was used to remove the remaining myelin to obtain a myelin-free cell mixture. Lastly, microglia cells were selected from the single cell mixture using CD11b<sup>+</sup> beads on LS columns (Miltenyi). The total cell number was counted on a hemocytometer and 0.1 million cells/0.5 mL/well were seeded on a 24-well Primaria plate (Corning). Cells were cultured for 10-14 div in low serum (2%)-containing TIC media (Bohlen et al., 2017).

**TREATMENT** Microglia were treated with 500 nM aggregated human amyloid beta 1-42 (AnaSpec) for 1, 12, or 24 hours. After the time period, the cells were collected with ice-cold PBS, pelleted at 500 x g, and flash frozen until lipidomic analysis.

**LIPIDOMICS** Total cellular and media lipids and metabolites were extracted using Bligh and Dyer method. Multiple-Reaction Monitoring (MRM) Profiling was perform via direct injection on the Agilent 6410 triple quadruple mass spectrometer. n = 5 biological replicates per group (amyloid beta-treated and vehicle-treated).

**Figure E.2** The bottom half of the webpage is shown here. This space mainly contains the information corresponding to the main lipid classes along with useful links. This space also contains the section for downloading the raw dataset (excel file) and the citation to be used.

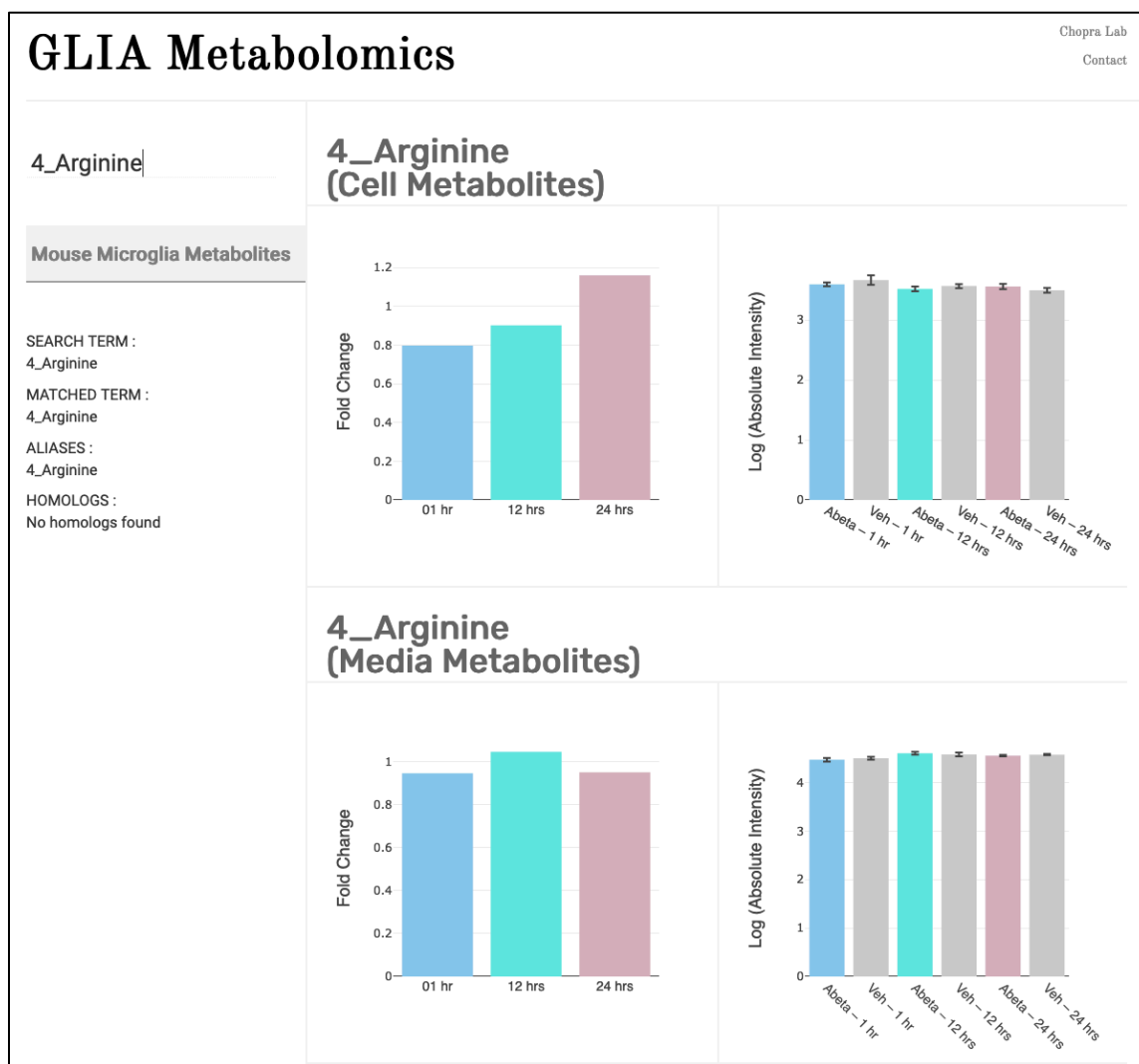


**Figure E.3** The webpage for microglial metabolites is shown here. As an example, the changes in microglial arginine with A $\beta$  treatment over time is displayed (fold change). Arginine is abundant in the cells with 24 hours of A $\beta$  treatment. The absolute intensity plots are also shown on the right.

# Astrocyte Omics

Chopra Lab

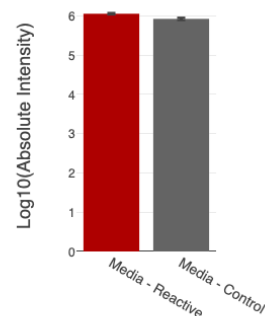
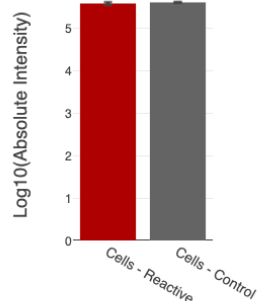
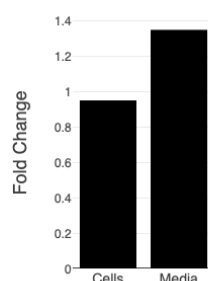
FFA > C16:0

Lipids

Proteins

Metabolites

FFA > C16:0  
(Reactive Vs Control)



FFA > C16:0  
(EKO Reactive Vs WT Reactive)

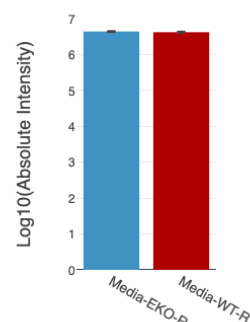
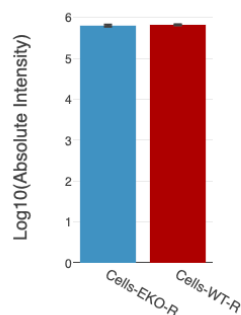
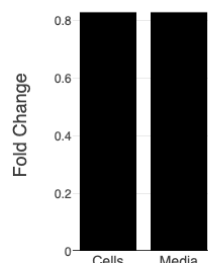


**Figure E.4** The webpage for astrocyte lipids is shown here. As an example, the changes in the saturated free fatty acid C16:0 is displayed in the plots. The lipid C16:0 is abundant in the astrocyte conditioned media (labeled as media) compared to the cells. The bottom plots correspond to the data obtained from the *Elovl1*<sup>-/-</sup> astrocyte data.

## VITA

### EDUCATION

- 2015-2021     **Doctor of Philosophy, Chemistry**  
Purdue University Interdisciplinary Life Sciences (PULSe) program  
Department of Chemistry  
Purdue University, West Lafayette, IN, USA
- 2013-2015     **Master of Science, Biological Sciences**  
Purdue University Northwest (Calumet campus), Hammond, IN, USA
- 2009-2013     **Bachelor of Engineering, Biotechnology**  
PES Institute of Technology (now PES University), Bangalore, India

### RESEARCH EXPERIENCE

- 2016-2021     **Graduate Research Assistant**  
Advisor: Dr. Gaurav Chopra, Chemistry Department  
Thesis Characterizing microglial response to amyloid: From new tools to new molecules
- 2015-2016     **Graduate Research Assistant**  
Laboratory rotations in the labs of Drs. Kavita Shah (Chemistry), Richard van Rijn (Medicinal Chemistry & Molecular Pharmacology), Jenna Rickus (Bioengineering), and Gaurav Chopra (Chemistry)
- 2013-2015     **Graduate Student Researcher**  
Advisor: Dr. Radmila Sarac Stanic, Biology Department  
Project: Understanding the role of GIRK ion channel hydrophobic pocket

## **FUNDING & FELLOWSHIPS**

- 2020-2021     Eli Lilly-Stark Neurosciences Predoctoral Research Fellowship in  
Neurodegeneration by the Indiana Clinical and Translational Sciences Institute  
(Role: PI)
- 2018-2019     Graduate Research Assistantship by Purdue Research Foundation
- 2014-2015     Graduate Research Grant by the Graduate Office, Purdue University Northwest  
(Role: PI)

## **AWARDS & HONORS**

- 2021            PULSe Outstanding Graduate Student in Research Award, Purdue University  
Interdisciplinary Life Sciences program
- 2021            Guy Mellon Award in Analytical Chemistry, Department of Chemistry, Purdue  
University
- 2019            Outstanding Graduate Student Mentor Award, Summer Undergraduate Research  
Fellowship (SURF) program, Purdue University
- 2018            Young Investigator Scholarship, Alzheimer's Drug Discovery Foundation
- 2018            Travel Grant Award, Graduate Woman in Science Program, Purdue University
- 2018            Travel Grant Award, Purdue Graduate Student Government
- 2017            Travel Grant Award, Purdue Institute of Inflammation, Immunology, and  
Infectious Disease
- 2015            First Place in Graduate Student Oral Presentation, Student Research Day, Purdue  
University Northwest
- 2013            First Class with Distinction Award, PES University



## PUBLICATIONS

<sup>†</sup> Indicates equal contribution <sup>#</sup> Indicates undergraduate trainee mentored by PP

1. **Prakash P<sup>†</sup>**, Lantz TC<sup>†#</sup>, Jethava KP, Chopra G. Rapid, refined, & robust method for expression, purification, & characterization of recombinant human amyloid beta 1-42. *Methods Protoc.* 2019, 2, 48.
2. **Prakash P<sup>†</sup>**, Jethava KP<sup>†</sup>, Korte N<sup>†</sup>, Izquierdo P<sup>†</sup>, Favuzzi E, Rose I, Guttenplan K, Dutta S, Rochet JC, Fishell G, Liddelow SA, Attwell D, Chopra G. Monitoring phagocytic uptake of amyloid  $\beta$  into glial cell lysosomes in real-time. (In revision at *Chemical Science*) Preprint available on bioRxiv: <https://doi.org/10.1101/2020.03.29.002857>
3. Guttenplan K, Weigel M<sup>†</sup>, **Prakash P<sup>†</sup>**, Wijewardhane PR, Fine J, Neal M, Bruce K, Chopra G, Gitler A, Liddelow SA, Barres BA. Neurotoxic reactive astrocytes induce cell death via saturated lipids. (In minor revision at *Nature*)
4. Jethava KP<sup>†</sup>, **Prakash P<sup>†</sup>**, Manchanda P, Arora H, Chopra G. One Scaffold—Different Organelles Sensors: pH-Activable Fluorescent Probes for Targeting Live Primary Microglial Cell Organelles. (In review)
5. **Prakash P<sup>†</sup>**, Wijewardhane PR<sup>†</sup>, Manchanda P, Randolph C, Thayer EA<sup>#</sup>, Fine JA, Chopra, G. Characterizing microglial lipidome and metabolome with amyloid  $\beta$ . (In preparation)
6. Kischuk EM, Fine JA, Wijewardhane PR, **Prakash P**, Lantz TC, Majumder J, Ratliff TL, Chopra G. Small-molecule immunomodulators targeting myeloid derived suppressor cells function in solid tumor micro-environments. (In preparation)
7. Fine JA, Majumder J, Adulnirath A, Wijewardhane PR, Lantz TC, **Prakash P**, Chopra G. Protein network targeting to combat prostate cancer. (In preparation)

## PUBLISHED ABSTRACTS AND ORAL/POSTER PRESENTATIONS

First author was the primary presenter. # Indicates undergraduate trainee mentored by PP

1. **Prakash P**, Wijewardhane PK, Chopra G. Microglial Lipidome and Metabolome with Amyloid  $\beta$  Exposure and Phagocytosis. SfN Global Connectome. January 11th-13th, 2021.
2. **Prakash P**, Fine JA, Thayer EA<sup>#</sup>, Ferreira CR, Chopra G. What do microglia make when they eat A $\beta$ ? Glia in Health & Disease-Cold Spring Harbor Laboratory, July 16<sup>th</sup>-19<sup>th</sup>, 2020.  
*\*Selected for oral talk.*
3. Adulnirath A, **Prakash P**, Chopra G. Do primary mouse microglia live a good life in culture? Glia in Health & Disease-Cold Spring Harbor Laboratory. July 16<sup>th</sup>-19<sup>th</sup>, 2020.
4. **Prakash P**, Fine JA, Thayer EA<sup>#</sup>, Ferreira CR, Chopra G. Multiple-Reaction Monitoring (MRM)-Profiling Reveals Distinct Lipid & Metabolite Profiles in Microglia with Amyloid Beta Exposure. 68th ASMS Conference on Mass Spectrometry & Allied Topics, May 31<sup>st</sup>-June 4<sup>th</sup>, 2020.
5. **Prakash P**, Jethava KP, Thayer EA<sup>#</sup>, Williams GC<sup>#</sup>, Izquierdo P, Nils K, Favuzzi E, Fishell G, Attwell D, Chopra G. Identifying molecular modulators of amyloid beta phagocytosis. 2019 Indiana CTSI Annual Meeting, September 13<sup>th</sup>, 2019; Indiana University–Purdue University Indianapolis, Indiana.
6. Thayer EA<sup>#</sup>, **Prakash P**, Chopra G. Amyloid beta-mediated inflammatory response in microglia. The SURF Symposium. August 2019; Purdue University.  
*\*EAT selected for oral talk*

7. **Prakash P**, Jethava KP, Chopra G. Characterizing microglial phagocytosis with novel pH-dependent fluorescent amyloid- $\beta$  and  $\alpha$ -synuclein sensors. 2019 Annual Meeting of the Greater Indiana Society for Neuroscience, March 22<sup>nd</sup>, 2019; Indianapolis, Indiana.
8. **Prakash P**, Jethava KP, Chopra G. A pH-Dependent Fluorogenic Amyloid-Beta Reporter for the Characterization of Phagocytosis in Live Microglial Cells: Implications for Alzheimer's Disease Research. 19<sup>th</sup> International Conference on Alzheimer's Drug Discovery, September 17<sup>th</sup>-18<sup>th</sup>, 2018; Jersey City, New Jersey.  
*\*Invited for postercast talk.*
8. Thayer EA<sup>#</sup>, **Prakash P**, Chopra G. Role of cyclic GMP-AMP Synthase in Microglial Immune Response. 3rd Annual ECI Undergraduate Research Conference, November 17<sup>th</sup>, 2018; University of Illinois Urbana Champaign, Champaign, Illinois.  
*\*EAT won outstanding poster award from UIUC women chemists committee*
9. **Prakash P**, Jethava KP, Chopra G. Do activated microglia get “exhausted” resulting in loss of function? Development of pH-dependent fluorescent amyloid- $\beta$  and  $\alpha$ -synuclein sensors to study microglial phagocytosis. Glia in Health & Disease-Cold Spring Harbor Laboratory, July 19<sup>th</sup>-23<sup>rd</sup>, 2018; Cold Spring Harbor, New York.
10. Williams GC<sup>#</sup>, **Prakash P**, Chopra G. Targeting Pro-Inflammatory Function of Microglia Using Small Molecules to Combat Neurodegeneration. The SURF Symposium. Paper 100. August 2, 2018; Purdue University.  
*\*GCW selected for oral talk*
11. **Prakash P**, Williams GC<sup>#</sup>, Thayer EA<sup>#</sup>, Fine JA, Chopra G. Combination drug repurposing for synergistic effect of enhancing phagocytosis and reduce neurotoxicity during neurodegeneration based on disease-disease relationships. Keystone Symposia—Neuroinflammation: Concepts, Characteristics, Consequences (E5), June 19<sup>th</sup>-23<sup>rd</sup>, 2017; Keystone, Colorado.

## TEACHING EXPERIENCE

2018	Teaching Assistant, Principles of Biochemistry, Purdue University
2016-2017	Teaching Assistant & Lab Instructor: General Chemistry, Purdue University
2015-2015	Biology & Chemistry Tutor, Academic Center for Excellence, Purdue University Northwest
2013-2015	TA & Lab Instructor: General Chemistry, Purdue University Northwest

## RESEARCH MENTORING

2019-2021	Palak Manchanda, Graduate Student-Chemistry
2016-2020	Gabrielle C. Williams, Undergrad-Biochemistry (Honors) <i>*2018 SURF program mentor</i>
2018-2020	Elizabeth A. Thayer, Undergrad-ACS Biochemistry (Honors) <i>*2019 SURF program mentor</i>
2018-2019	Travis C. Lantz, Undergrad-ACS Chemistry (Honors)
2017-2018	Dawn N. Tilley, Undergrad-Chemistry & Biology

## OUTREACH, SERVICE, & ENGAGEMENT

### Invited Talks

04/2021	Keynote Presentation at the PULSe Spring Reception
03/2021	Lilly-Stark Neurodegeneration Retreat
10/2020	Glia Journal Club, New York University Langone Health
01/2018	The Purdue Lecture Hall Series
03/2018	Invited Lecture: Principles of Biochemistry, Purdue University

### Organizational Boards

2017-19	Graduate Ambassador, Purdue Institute of Inflammation, Immunology, and Infectious Disease
2016-17	Vice President, PULSe Graduate Student Organization

**Volunteering**

2017,18        Science Fair Judge, Annual Lafayette Regional Science and Engineering Fair  
2016,17,19    Spring Fest: “Exploring the brain” station, West Lafayette, IN  
2016,17        Science in Schools at Wea Ridge Elementary School, West Lafayette, IN

**PROFESSIONAL MEMBERSHIPS**

American Association for the Advancement of Science  
Society for Neuroscience